65. Paik, C. Y. and Hochreiter, L. E., 1986, "Analysis of FLECHT SEASET 163-Rod Blocked Bundle Data Using COBRA-TF," NUREG/CR-4166.

66. Paleev, I. I. and Filippovich, B. S., 1966, "Phenomena of Liquid Transfer in Two-Phase Dispersed Annular Flow," *International Journal Heat Mass Transfer*, Vol. 9, pp. 1089-1093.

67. Ransom, V. H. and Trapp, J. A., 1980, "The RELAP5 Choked Flow Model and Application to a Large Scale Flow Test," *ANS/ASME/NRC International Topical Meeting on Nuclear Reactor Thermal-Hydraulics*, Saratoga Springs, New York, pp. 799-819.

68. Shiller, L. and Nauman, A. Z., 1933, Ver. Deut. Ing., 77, pp. 318-320.

69. Smoglie, C., 1984, "Two Phase Flow Through Small Break Branches in a Horizontal Pipe with Stratified Flow," Kernforschungszentrum Karlsruhe Report KfK 3861.

70. Smoglie, C. and Reimann, J., 1986, "Two-Phase Flow Through Small Branches in a Horizontal Pipe with Stratified Flow," *Int J Multiphase Flow*, Vol. 12, No. 4, pp. 609-625.

71. Taitel, Y. and Dukler, A. E., 1976, "A Model for Predicting Flow Regime Transitions in Horizontal and Near Horizontal Gas-Liquid Flow," *AIChE Journal*, Vol. 22, No. 1, pp. 47-55.

72. Takeuchi, K., et al., 1982, "Experimental Studies on the Behavior of a Small Droplet Impinging Upon a Hot Surface," *Proceedings of the Second International Conference on Liquid Atomization and Spray Systems*, pp. 397-404.

73. Tatterson, D. F., et al., 1977, "Drop Sizes in Annular Gas-Liquid Flows," *AIChE Journal*, Vol. 23, No. 1, pp. 68-76.

74. Thurgood, M. J., et al., 1983, "COBRA/TRAC – A Thermal-Hydraulics Code for Transient Analysis of Nuclear Reactor Vessels and Primary Coolant Systems," Vol. 1, PNL-4385, NUREG/CR-3046.

75. Vennard, J. K., 1961, Elementary Fluid Mechanics, Fourth Edition, John Wiley Sons' Publishers.

76. Wachters, L. H. J. and Westerling, N. A. J., 1966, "The Heat Transfer From a Hot Wall to Impinging Water Drops in a Spheroidal State," *Chem. Eng. Sci.*, Vol. 21, pp. 1047-1056.

77. Wallis, G. B., 1969, One-Dimensional Two-Phase Flow, McGraw-Hill.

78. Wallis, G. and Dobson, J., 1973, "The Onset of Slugging in Horizontal Stratified Air-Water Flow," *Int. J. Multiphase Flow*, Vol. 1, pp. 173-193.

79. Whalley, P. B., et al., 1973, "Experimental Wave and Entrainment Measurements in Vertical Annular Two-Phase Flow," AERE-R7521, Atomic Energy Research Establishment, Harwell, England.

80. Whalley, P. B., 1981, "Two-Phase Pressure Drop Design Report Part 5: The Calculation of Frictional Pressure Gradients in Two-Phase Flow," Atomic Energy Research Establishment report AERE-R9793, HTFS DR28, Rev.

81. White, F. M., 1979, Fluid Mechanics, McGraw-Hill Book Co., New York.

82. Wurtz, J., 1978, "An Experimental and Theoretical Investigation of Annular Steam-Water Flow in Tubes and Annuli at 30 to 90 Bar," Report No. 372, RISO National Laboratory, Denmark.

83. Yao, S. C., Hochreiter, L. E., and Cai, K. Y., 1988, "Dynamics of Droplets Impacting on Thin Heated Strips," *Transactions of the ASME, Journal of Heat Transfer*, Vol. 110, pg. 214.

84. Young, M. Y., et al., 1984, "BART-A1: A Computer Code for the Best Estimate Analysis of Reflood Transients," WCAP-9561-P-A.

Table 5-1 Comparisons of Pressure Loss at Sudden Contraction (Vessel Component)

a,c

Table 5-2 Comparisons of Pressure Loss at Sudden Expansion (Vessel Component)

a,c

Table 5-3 Comparisons of Pressure Loss at Combination of Sudden Contraction and Expansion (Vessel Component)

a,c

Table 5-4 Wall Shear Dependence Upon Pipe Diameter

Facility	Cold-leg D (m)	Wall shear Pressure Gradient ($Pa.m^{-1}$)
Full-Size Plant	0.698	446.0
LOFT	0.284	1353.0
Semiscale	0.067	7635.0

Table 5-5a Irreversible Pressure Loss Coefficient

Abrupt Contraction Standard Loss-Coefficient Data

A_{j+1}/A_j	0.0	0.04	0.16	0.36	0.64	1.0
K	0.5	0.45	0.38	0.28	0.14	0.0

Table 5-5b [ ]^{a,c} a,c

Table 5-6 Comparisons of Pressure Loss at Sudden Contraction (1D Loop Component)

a,c

Table 5-7 Comparisons of Pressure Loss at Sudden Expansion (1D Loop Component)

a,c

Table 5-8 Comparisons of Pressure Loss at Combination of Sudden Contraction and Expansion (1D Loop Component)

a,c

Table 5-9 Critical Height Correlation Constant

a,c

Table 5-10 Donor Modification for Liquid Drain Logic

Momentum Cell or Cell Face	V_v: Vapor Velocity	Donor α_v	V_l: Liquid Velocity	Donor α_l
j (Top of Node-J)	>0	$\alpha_{v,J+1}$	>0	$\alpha_{l,J+1}$
	<0	Normal Donor	<0	Normal Donor
j-1 (Bottom of Node-J)	>0	Normal Donor	>0	Normal Donor
	<0	$\alpha_{v,J-1}$	<0	$\alpha_{l,J-1}$

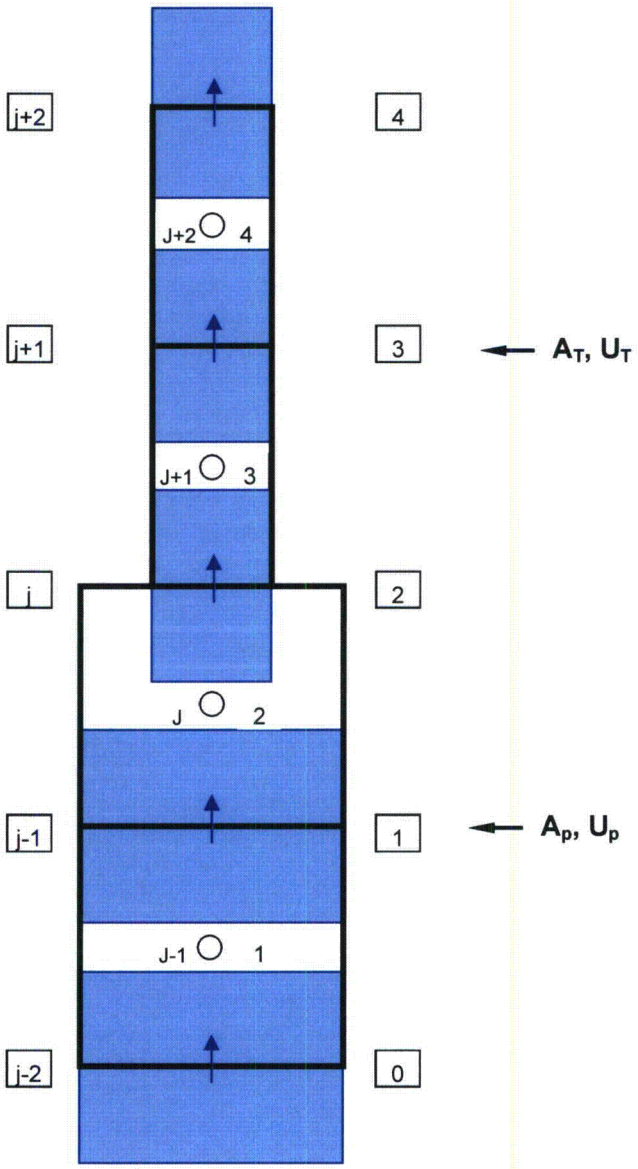

Figure 5-1 One-Dimensional Vessel Channel with Area Change

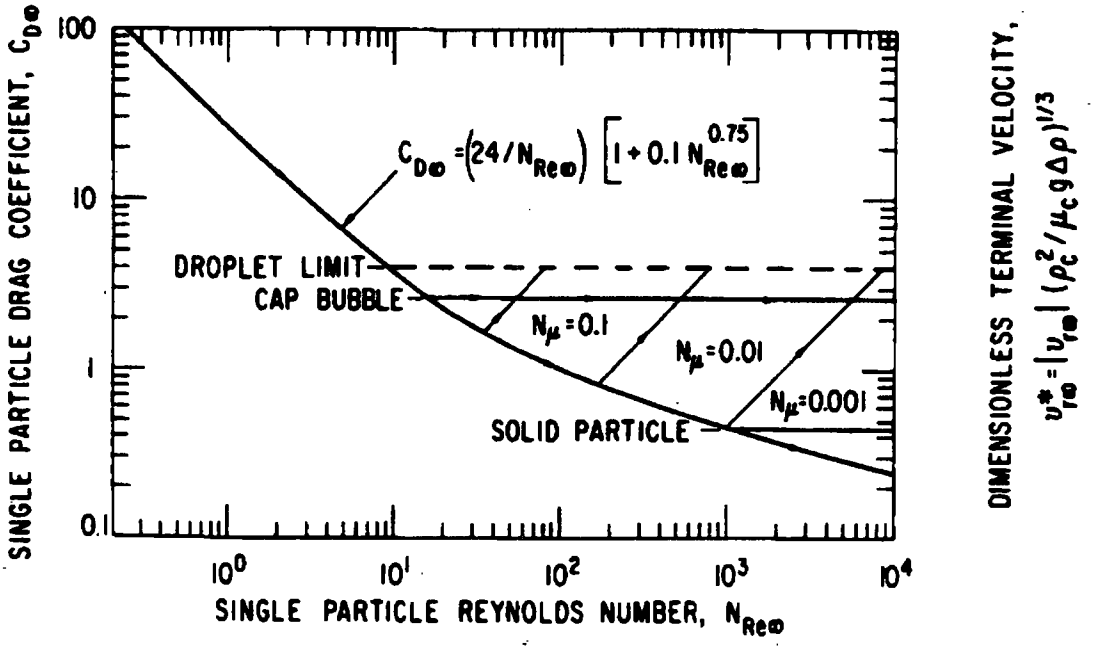

Figure 5-2 Bubble Drag Coefficients (Ishii and Chawla, 1979)

[a,c

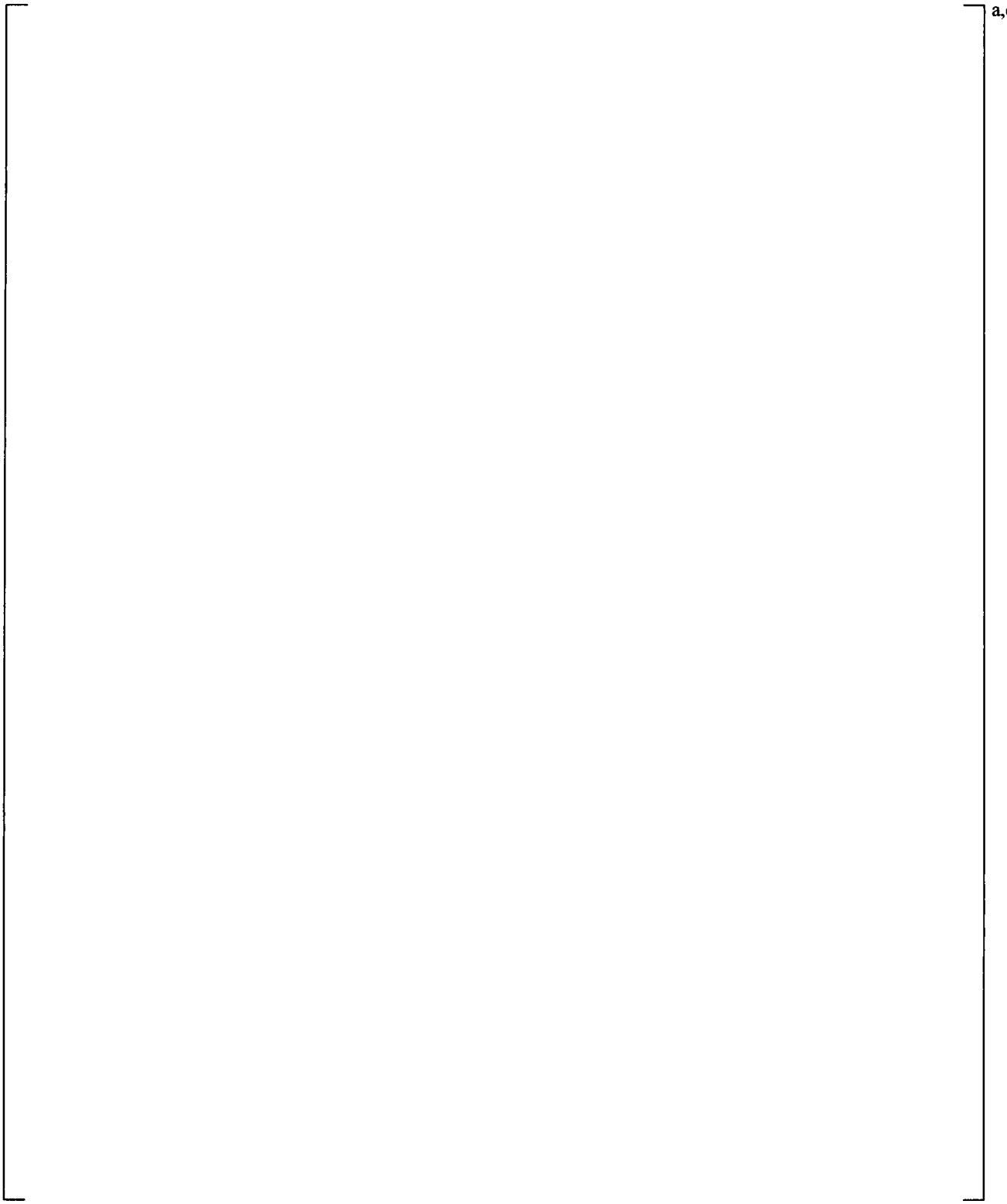

]

Figure 5-3 Effect of Ramps on Interfacial Friction Factor. (a) Small Bubble Regime, (b) Large Bubble Regime

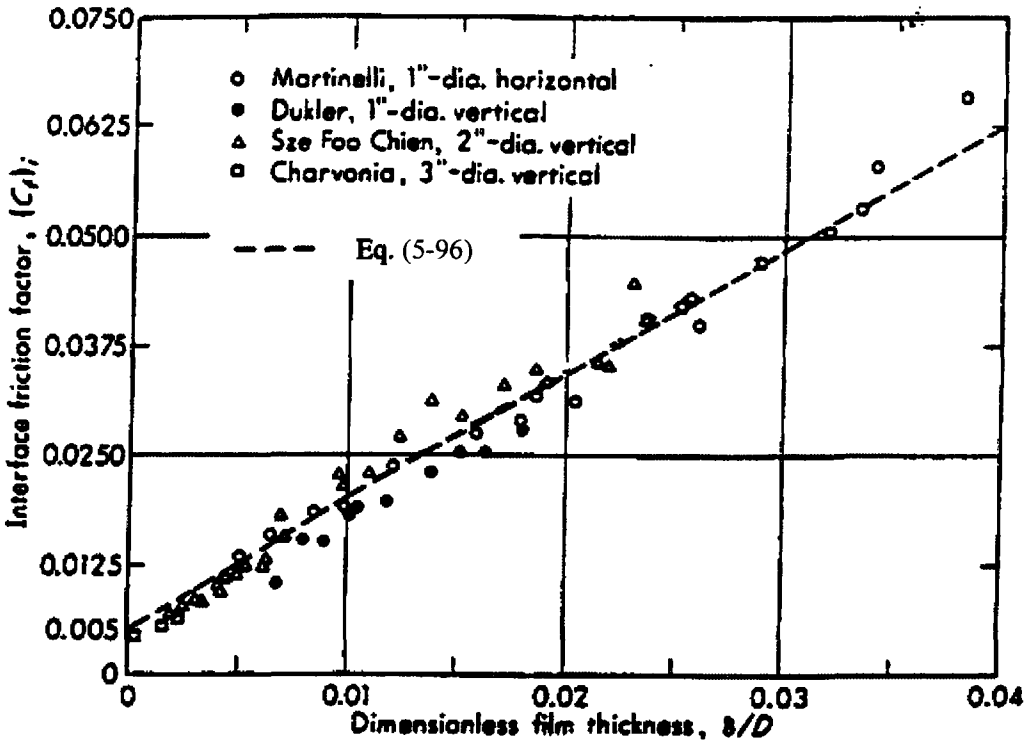

Figure 5-4 Interfacial Friction Factor for Smooth Films (Wallis, 1969)

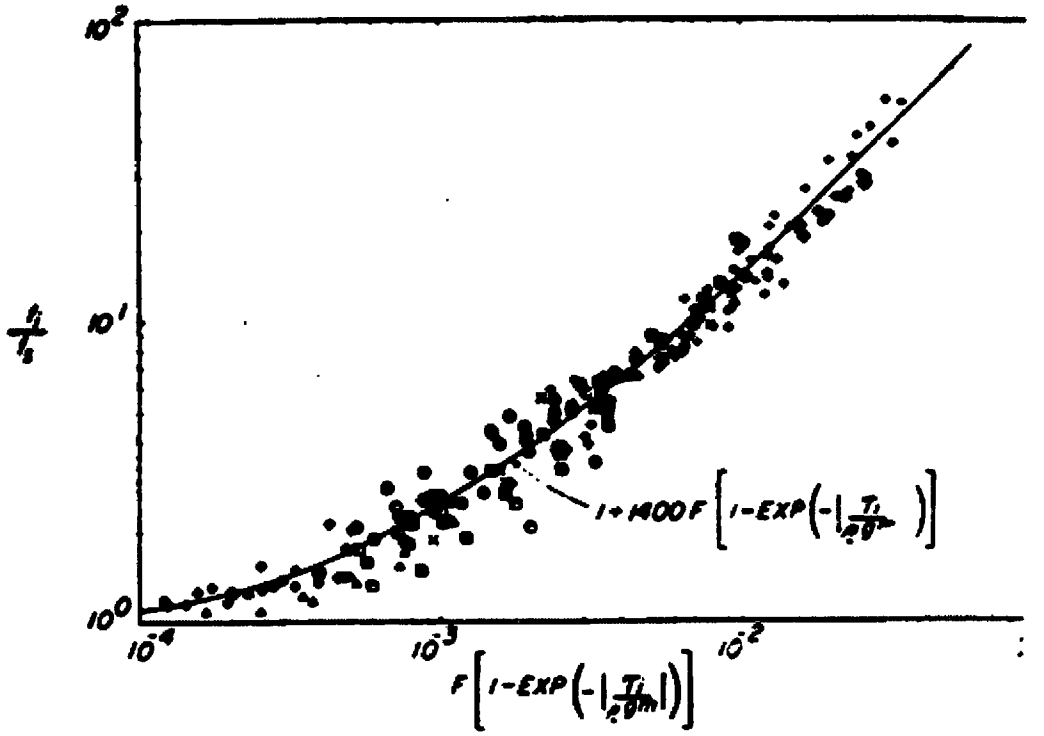

Final form of friction factor correlation, vertical flow

Figure 5-5 Hanstock and Hanratty (1976) Film Flow Interfacial Shear

[a,c

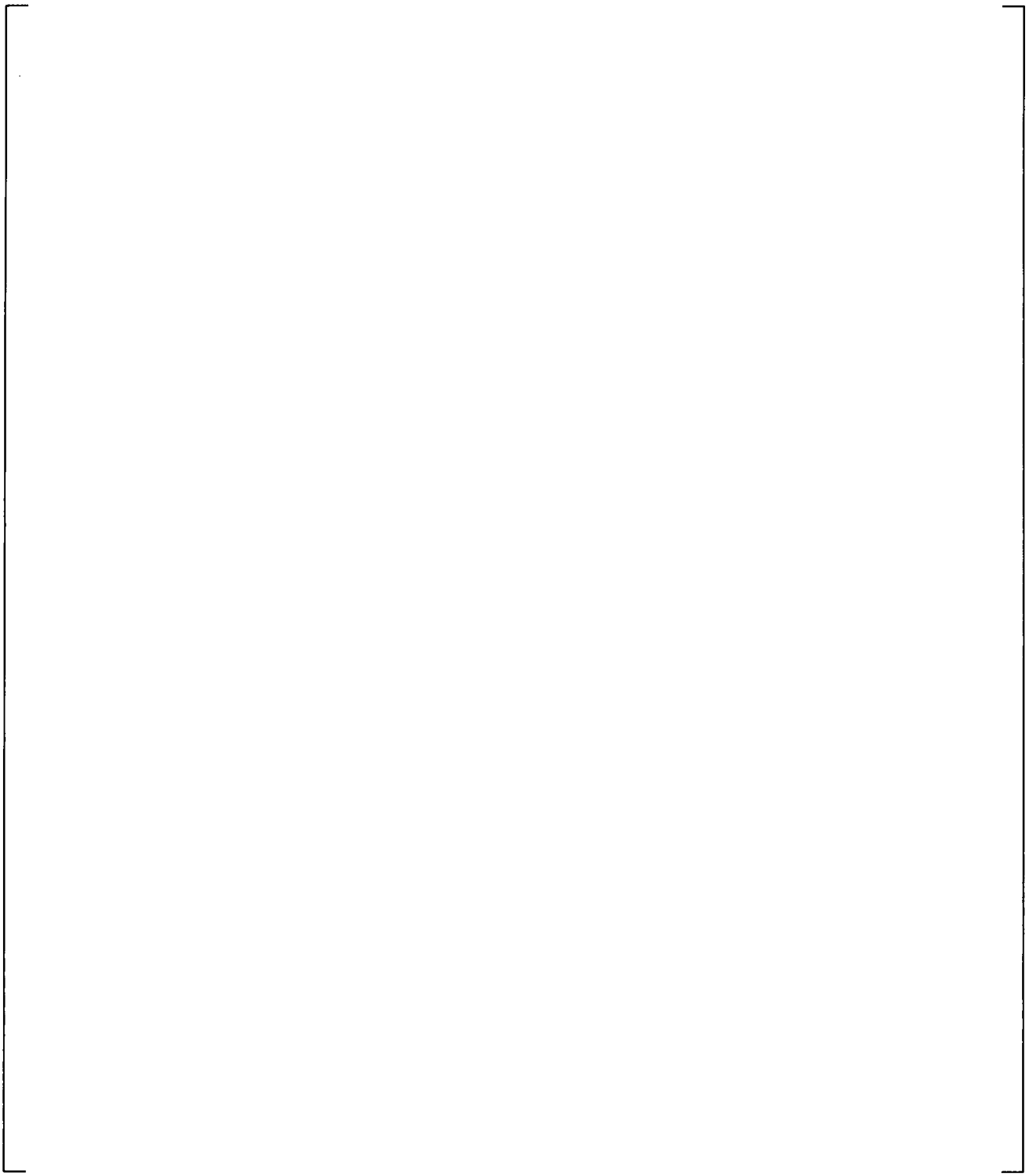

]

Figure 5-6a Comparison of Droplet Data Range and Droplet Size Limits in WCOBRA/TRAC-TF2 at 40 psia

[a,c

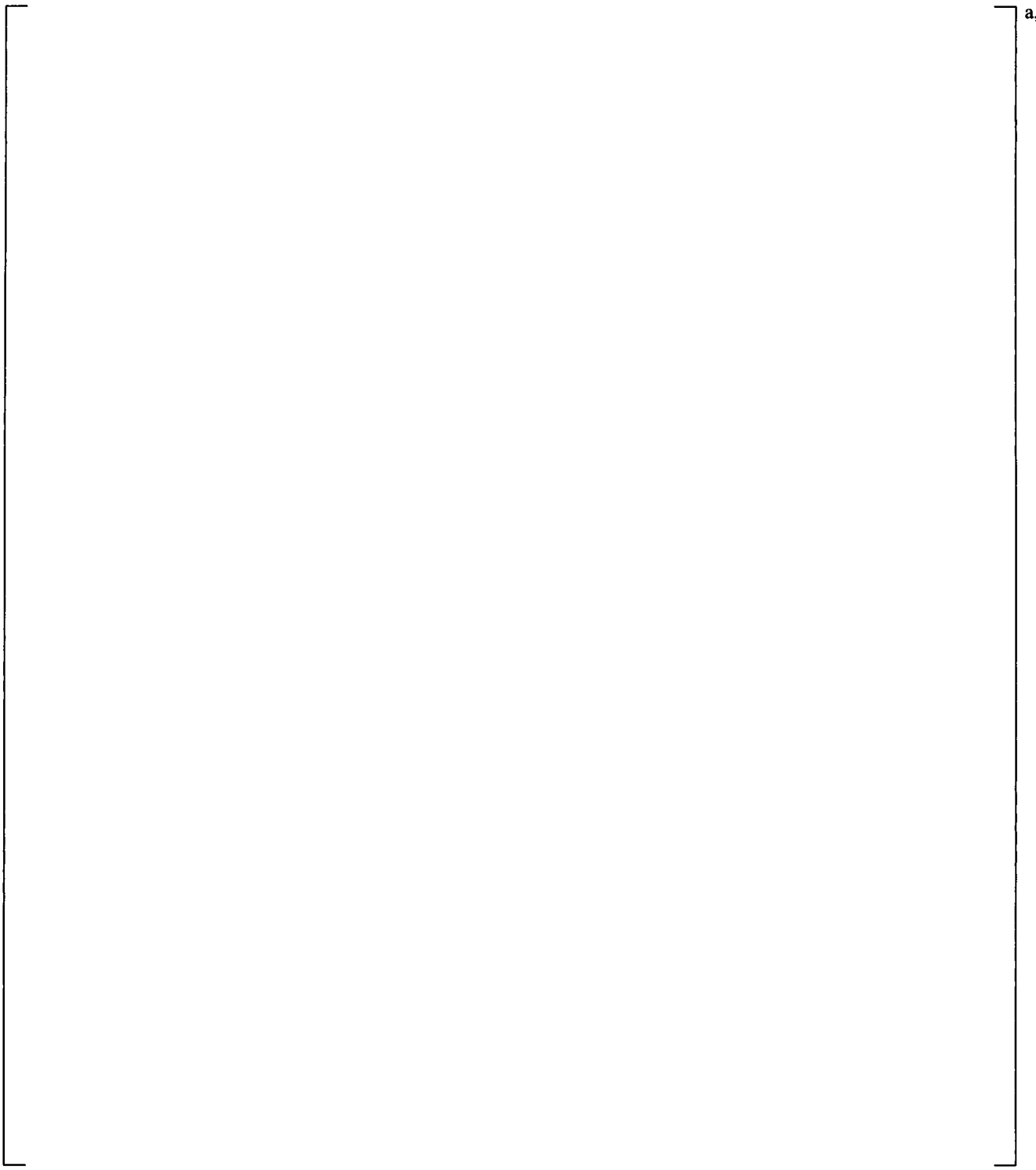

]

Figure 5-6b Comparison of Droplet Data Range and Droplet Size Limits in WCOBRA/TRAC-TF2 at 20 psia

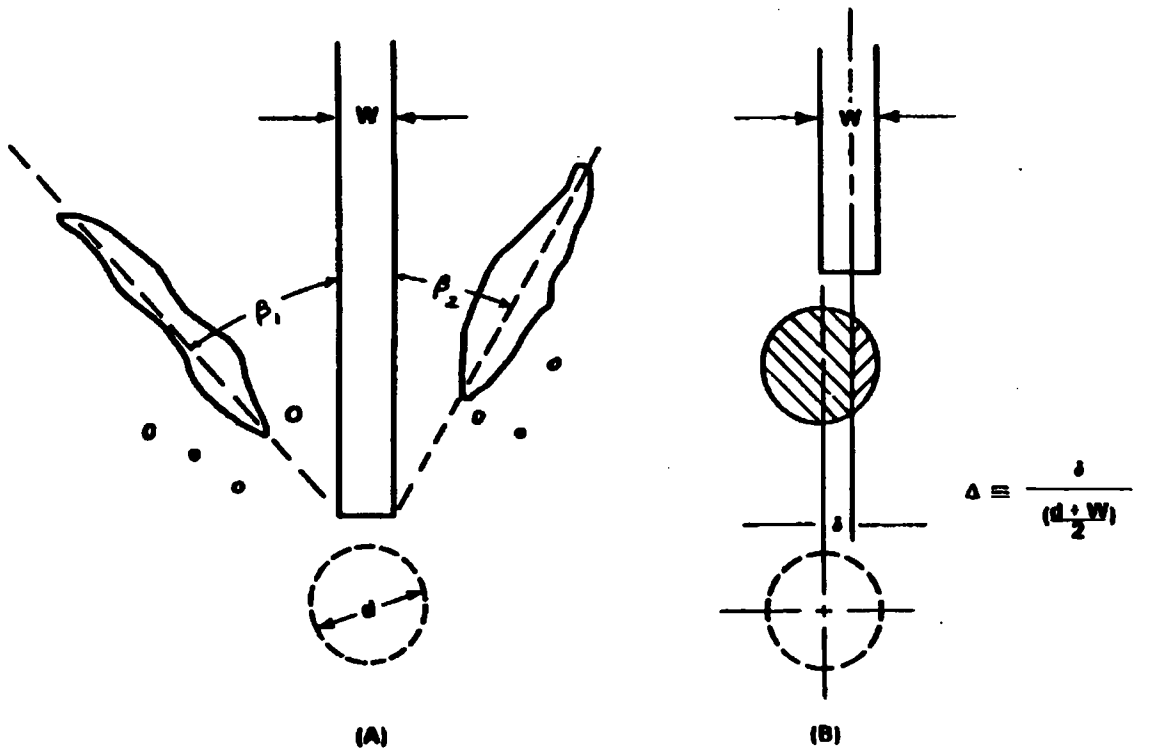

Figure 5-7 Impingement of a Droplet on a Grid Spacer
(a) Shattering Process
(b) Definition of Droplet Offset Parameter

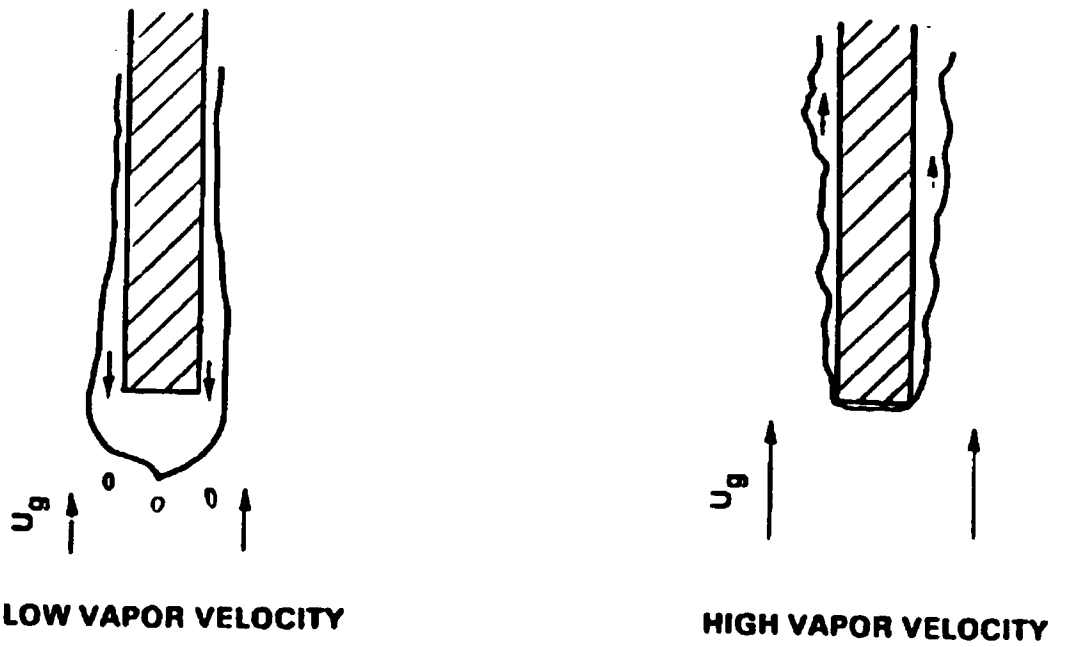

Figure 5-7c Leading Edge of a Wetted Grid; Effect of Vapor Velocity

[a,c

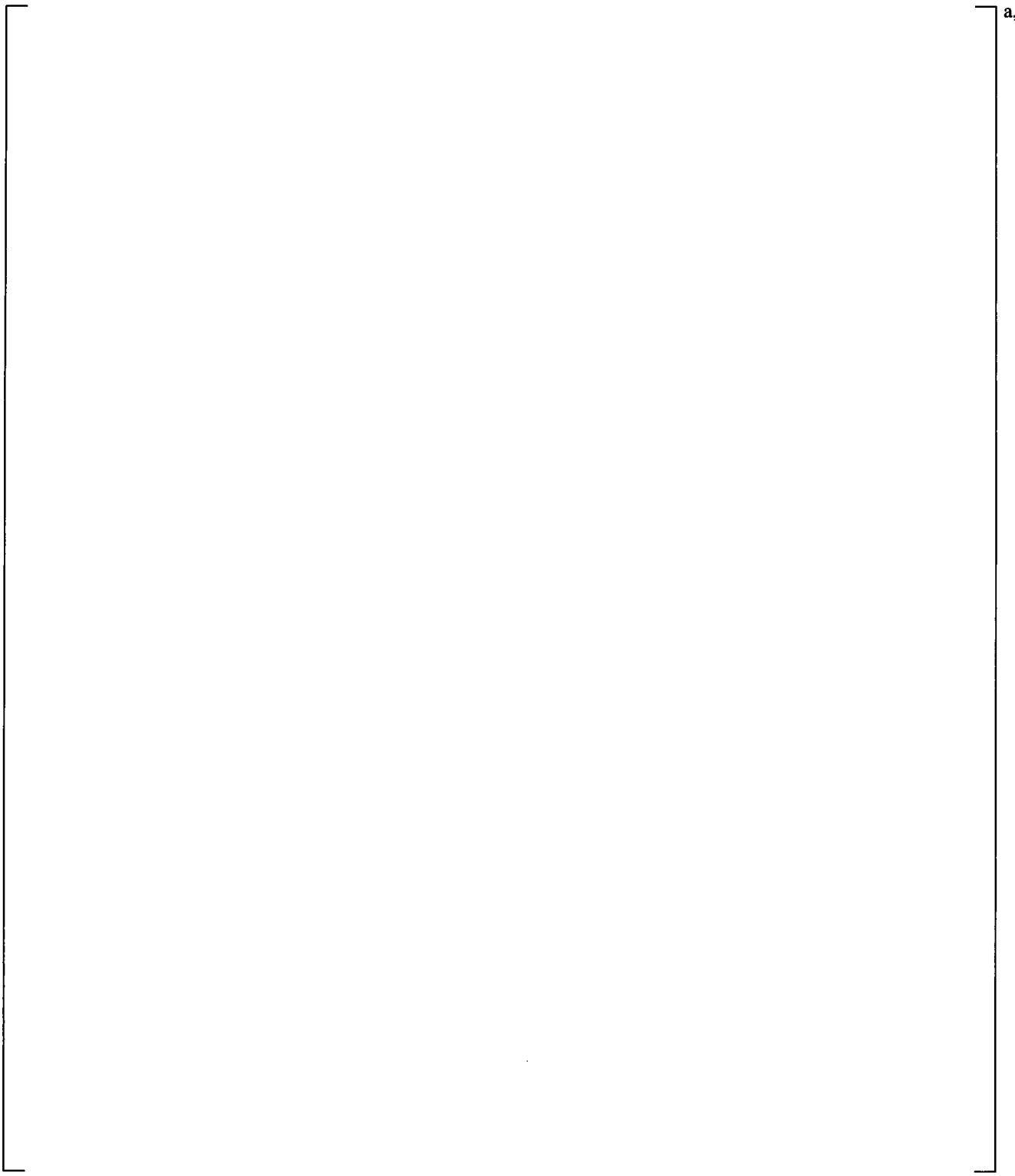

]

Figure 5-8 The Relationship of Droplet Diameter Ratio versus Droplet Weber Number

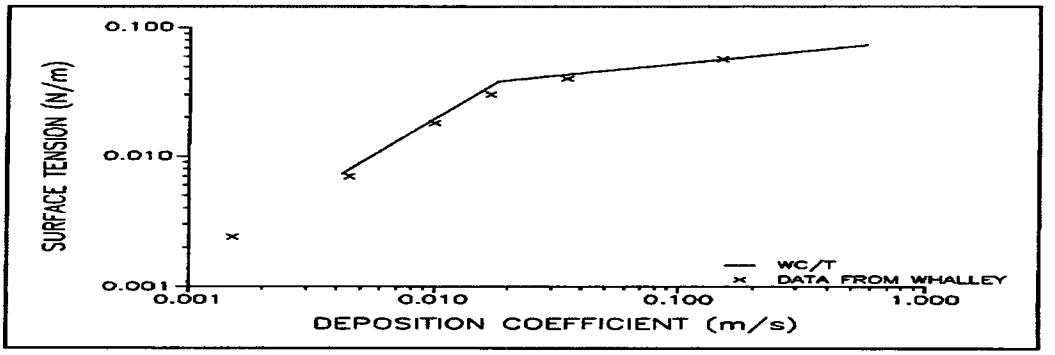

Figure 5-9 Comparison of Equation 5-189 with Data from Whalley (1973)

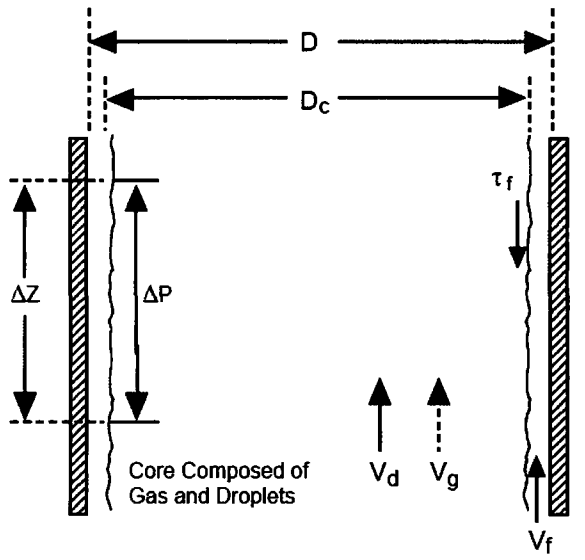

Figure 5-10 Core to Film Momentum Balance in Annular Film Flow

a,c

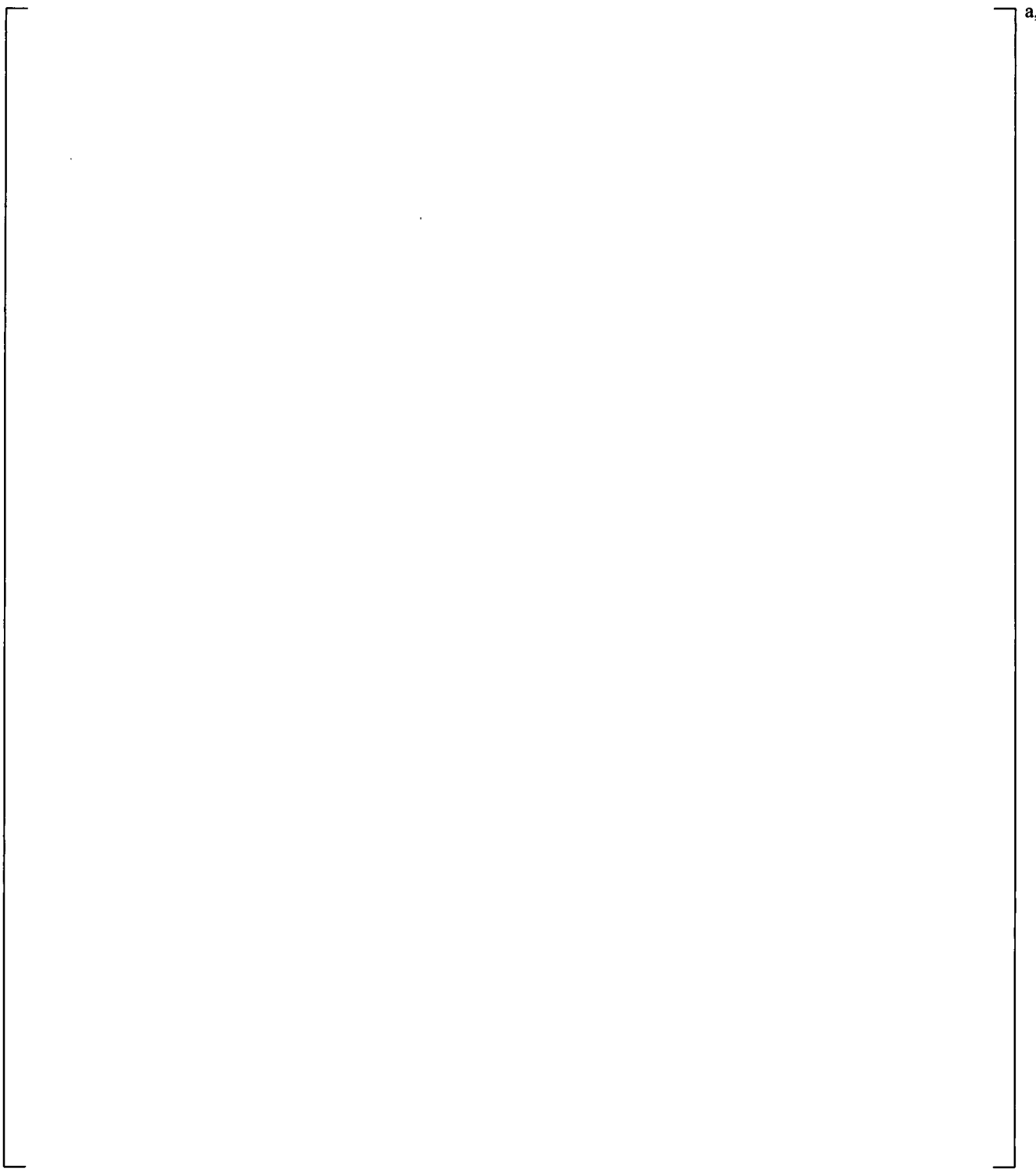

Figure 5-11 Comparison of the Wall Friction Factors from the Churchill Model and the Blasius Model (Wall Roughness 5.0E-5 m, Pipe Diameter 0.7 m)

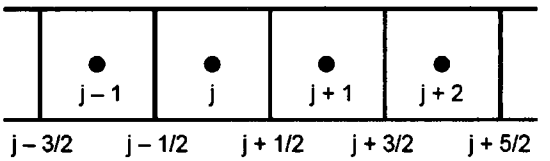

Figure 5-12 WCOBRA/TRAC-TF2 1D Noding

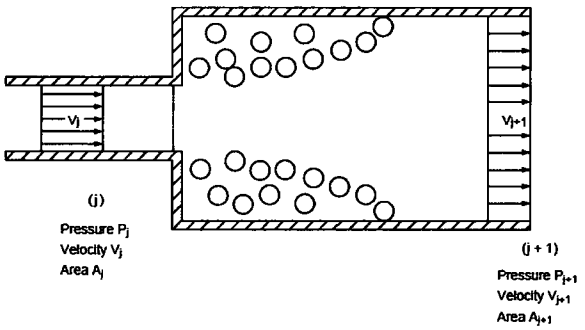

Figure 5-13 Abrupt Expansion in 1D Component

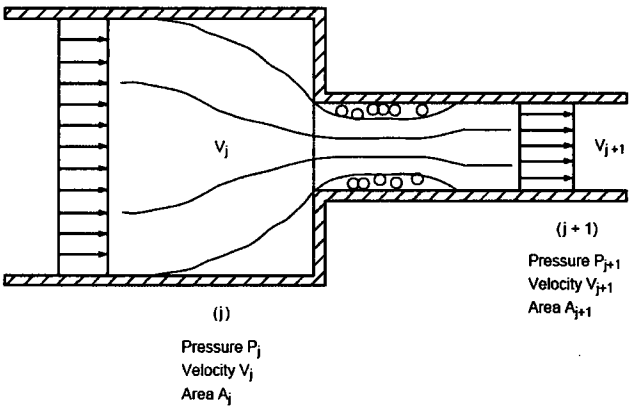

Figure 5-14 Abrupt Contraction in 1D Component

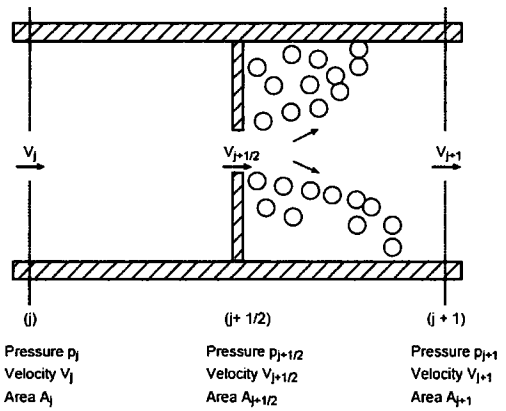

Figure 5-15 Sharp-Edged Thin-Plate Orifice

a,c

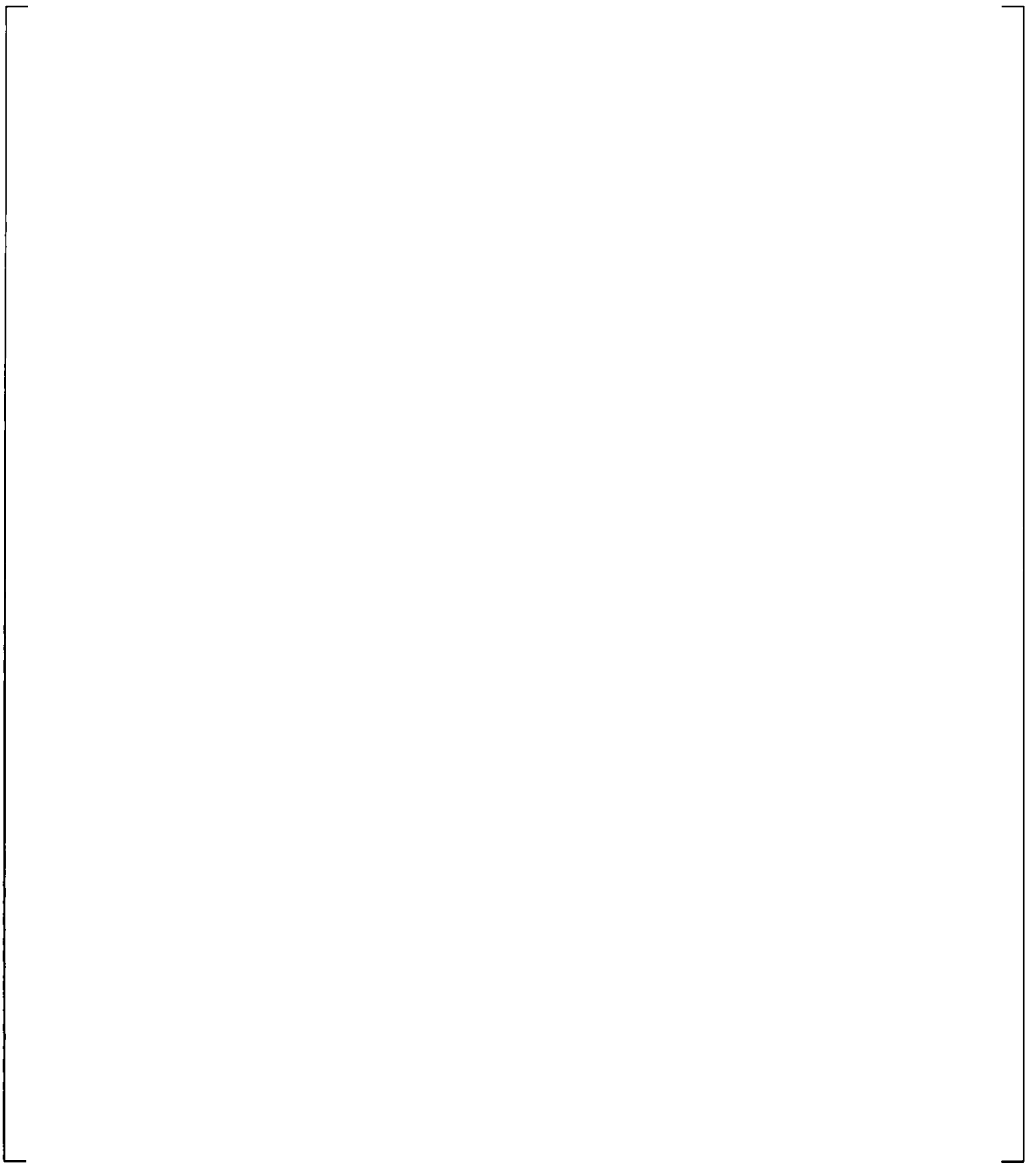

Figure 5-16 Horizontal 1D Component Connected to a PWR Downcomer Channel

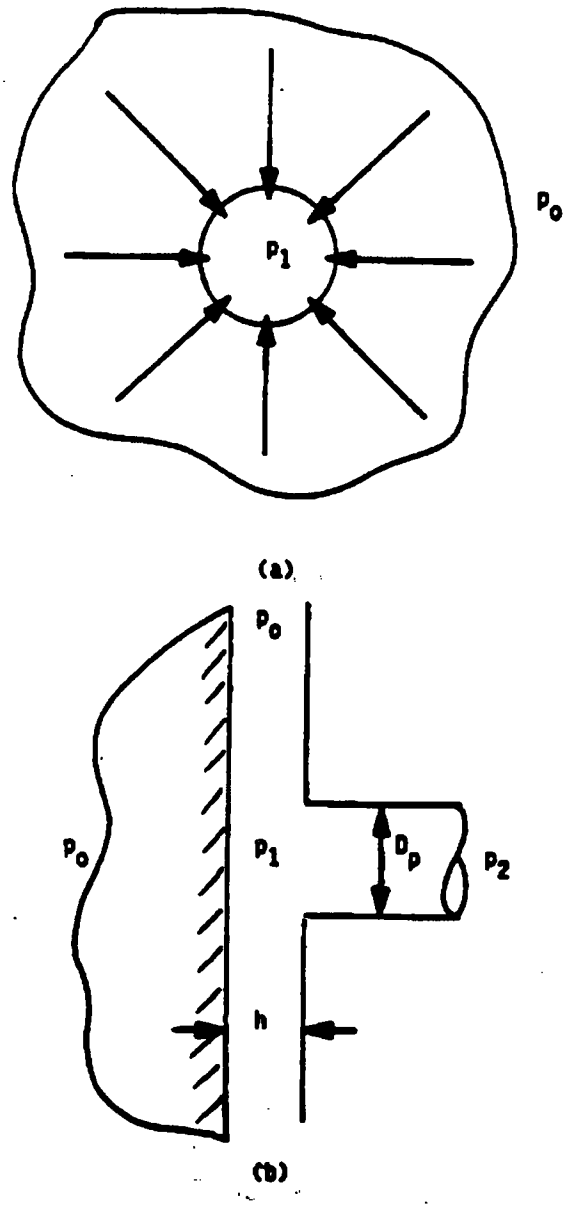

Figure 5-17 Broken Cold Leg Nozzle Junction to Vessel

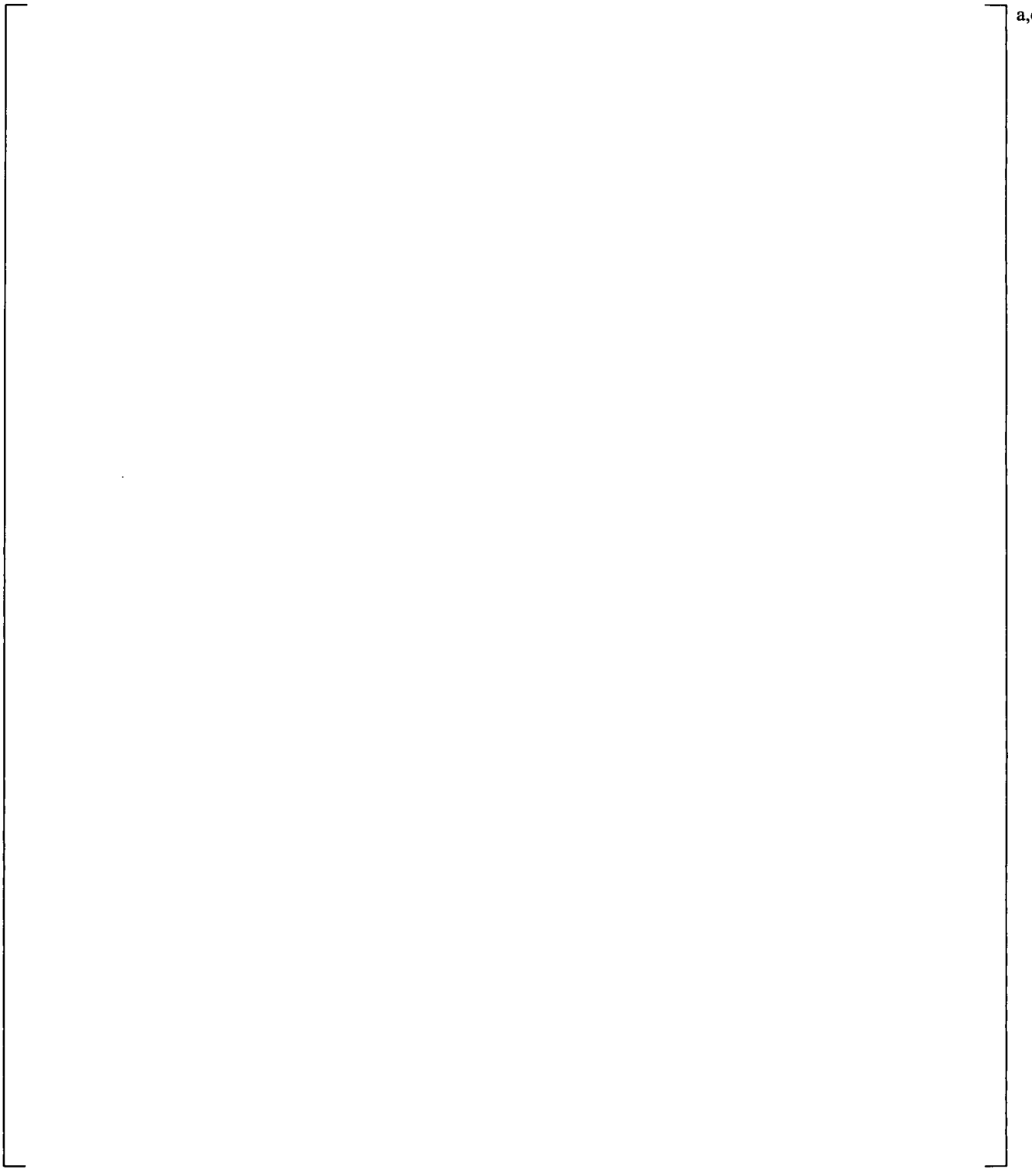

a,c

Figure 5-18 Horizontal 1D Component Connected to a PWR Upper Plenum Hot Leg Nozzle

[a,c

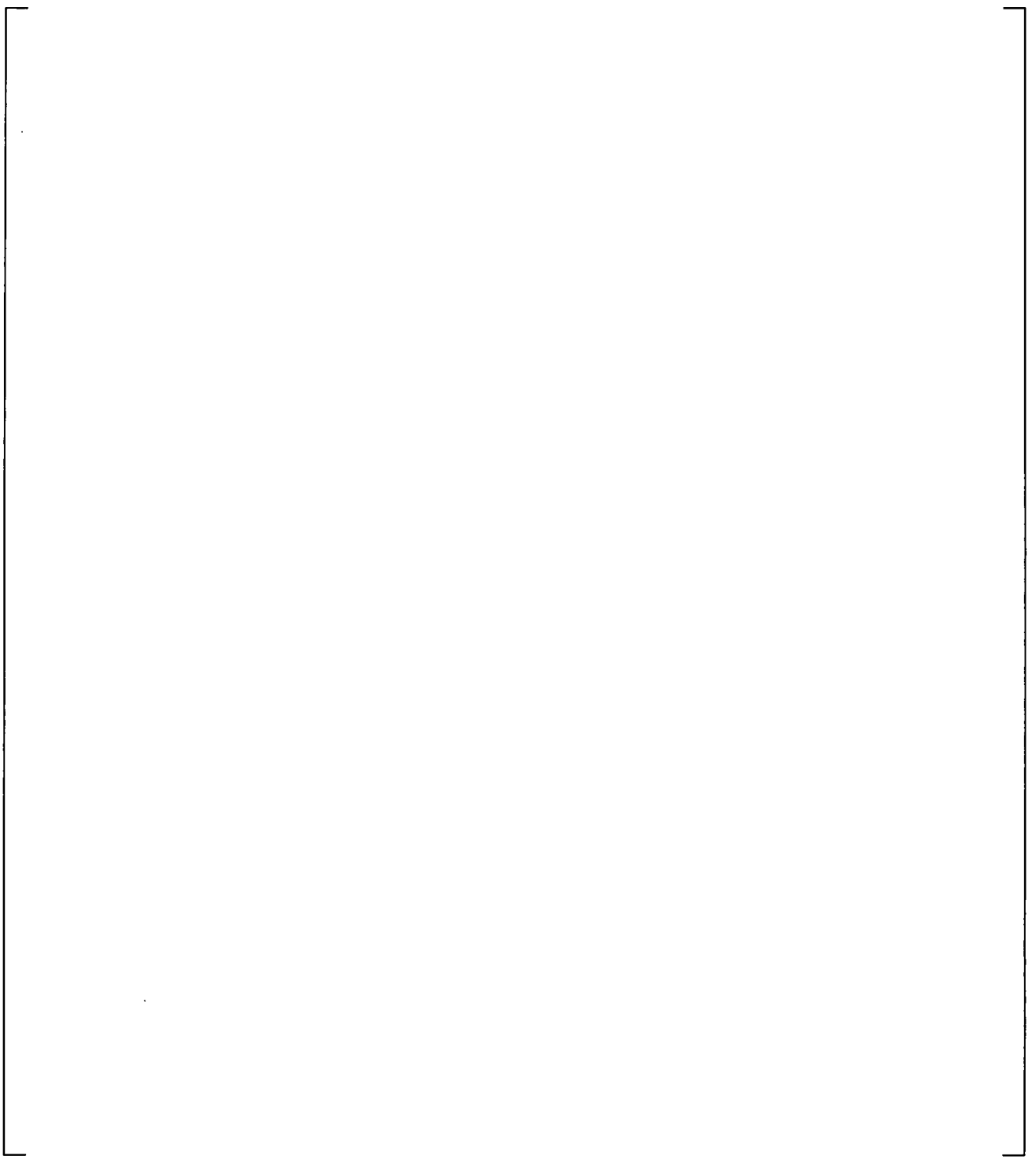

]

Figure 5-19 TRAC-P [ ]^{a,c} Sub-models of the Choked Flow Models

$$\underline{\underline{A}} = \begin{bmatrix} \alpha\left[\left(\frac{\partial \rho_a}{\partial T}\right)_{Pa}\frac{d_T}{d_{Pv}} + \rho_v^*\right] + (1-\alpha)\rho_\ell^* & \rho_g - \rho_\ell & 0 & 0 & \alpha\left(\frac{\partial \rho_a}{\partial P}\right)_T + (1-\alpha)\left(\frac{\partial \rho_\ell}{\partial P}\right)_T \\ 0 & 0 & \alpha\rho_g + Ca(1-\alpha)\rho_m & -Ca(1-\alpha)\rho_m & 0 \\ 0 & 0 & -Ca(1-\alpha)\rho_m & (1-\alpha)\rho_\ell + Ca(1-\alpha)\rho_m & 0 \\ \alpha\left[-\rho_v^* s_v^* + s_v \rho_v^* + \frac{d_T}{d_{Pv}}\left(\rho_a\left(\frac{\partial s_a}{\partial T}\right)_{Pa} + s_a\left(\frac{\rho_a}{\partial T}\right)_{Pa}\right)\right] + (1-\alpha)\left[\rho_\ell s_\ell + \rho_\ell s_\ell^*\right] & (\rho_g s_g - \rho_\ell s_\ell) & 0 & 0 & \alpha\left[\rho_a\left(\frac{\partial s_a}{\partial P}\right)_T + s_a\left(\frac{\partial \rho_a}{\partial P}\right)_T\right] + (1-\alpha)\left[\rho_\ell\left(\frac{\partial s_\ell}{\partial P}\right)_T + s_\ell\left(\frac{\partial \rho_\ell}{\partial P_{1\ell}}\right)_T\right] \\ \alpha\left(\frac{\partial \rho_a}{\partial T}\right)_{Pa}\frac{d_T}{d_{Pv}} & \rho_a & 0 & 0 & \alpha\left(\frac{\partial \rho_a}{\partial P}\right)_T \end{bmatrix} \begin{bmatrix} \frac{\partial P_v}{\partial t} \\ \frac{\partial \alpha}{\partial t} \\ \frac{\partial V_g}{\partial t} \\ \frac{\partial V_\ell}{\partial t} \\ \frac{\partial P_a}{\partial t} \end{bmatrix}$$

Figure 5-20 WCOBRA/TRAC-TF2 Two-phase Choked Flow Model Matrix A

$$\underline{B} = \begin{bmatrix} V_g \alpha \left[\left(\frac{\partial \rho_a}{\partial T} \right)_{Pa} \frac{d_T}{d_{Pv}} + \rho_v^* \right] + V_\ell (1-\alpha) \rho_\ell^* & \rho_g V_g - \rho_\ell V_\ell & \partial \rho_g & (1-\alpha)\rho_\ell & V_g \alpha \left(\frac{\partial \rho_a}{\partial P\delta} \right)_T + V_\ell (1-\alpha) \left(\frac{\partial \rho_\ell}{\partial P} \right)_T \\ \alpha & 0 & V_g \alpha \rho_g + V_\ell C a (1-\alpha) \rho_m & -V_g C a (1-\alpha) \rho_m & \alpha \\ (1-\alpha) & 0 & -V_\ell C a (1-\alpha) \rho_m & V_g C a (1-\alpha) \rho_m + V_\ell (1-\alpha) \rho_\ell & (1-\alpha) \\ V_g \alpha \left[\begin{array}{l} -\rho_v^* s_v^* + s_v \rho_v^* + \frac{d_T}{d_{Pv}} \\ \left(\rho_a \left(\frac{\partial s_a}{\partial T} \right)_{Pa} + s_a \left(\frac{\partial \rho_a}{\partial T} \right)_{Pa} \right) \end{array} \right] + V_\ell (1-\alpha) \left[\rho_\ell s_\ell^* + s_\ell \rho_\ell^* \right] & (V_g \rho_g s_g - V_\ell \rho_\ell s_\ell) & \alpha \rho_g s_g & (1-\alpha) \rho_\ell s_\ell & V_g \alpha \left[\rho_a \left(\frac{\partial s_a}{\partial P_a} \right)_T + s_a \left(\frac{\partial \rho_a}{\partial P_a} \right)_T \right] + V_\ell (1-\alpha) \left[\rho_\ell \left(\frac{\partial s_\ell}{\partial P} \right)_T + s_\ell \left(\frac{\partial \rho_\ell}{\partial P} \right)_T \right] \\ V_g \alpha \left(\frac{\partial \rho_a}{\partial T} \right)_{Pa} \frac{d_T}{d_{Pv}} & \rho_a & \alpha \rho_a & 0 & V_g \alpha \left(\frac{\partial \rho_a}{\partial P_a} \right)_T \end{bmatrix} \begin{bmatrix} \frac{\partial P_v}{\partial x} \\ \frac{\partial \alpha}{\partial x} \\ \frac{\partial V_g}{\partial x} \\ \frac{\partial V_\ell}{\partial x} \\ \frac{\partial P_a}{\partial x} \end{bmatrix}$$

Figure 5-21 WCOBRA/TRAC-TF2 Two-phase Choked Flow Model Matrix B

a,c

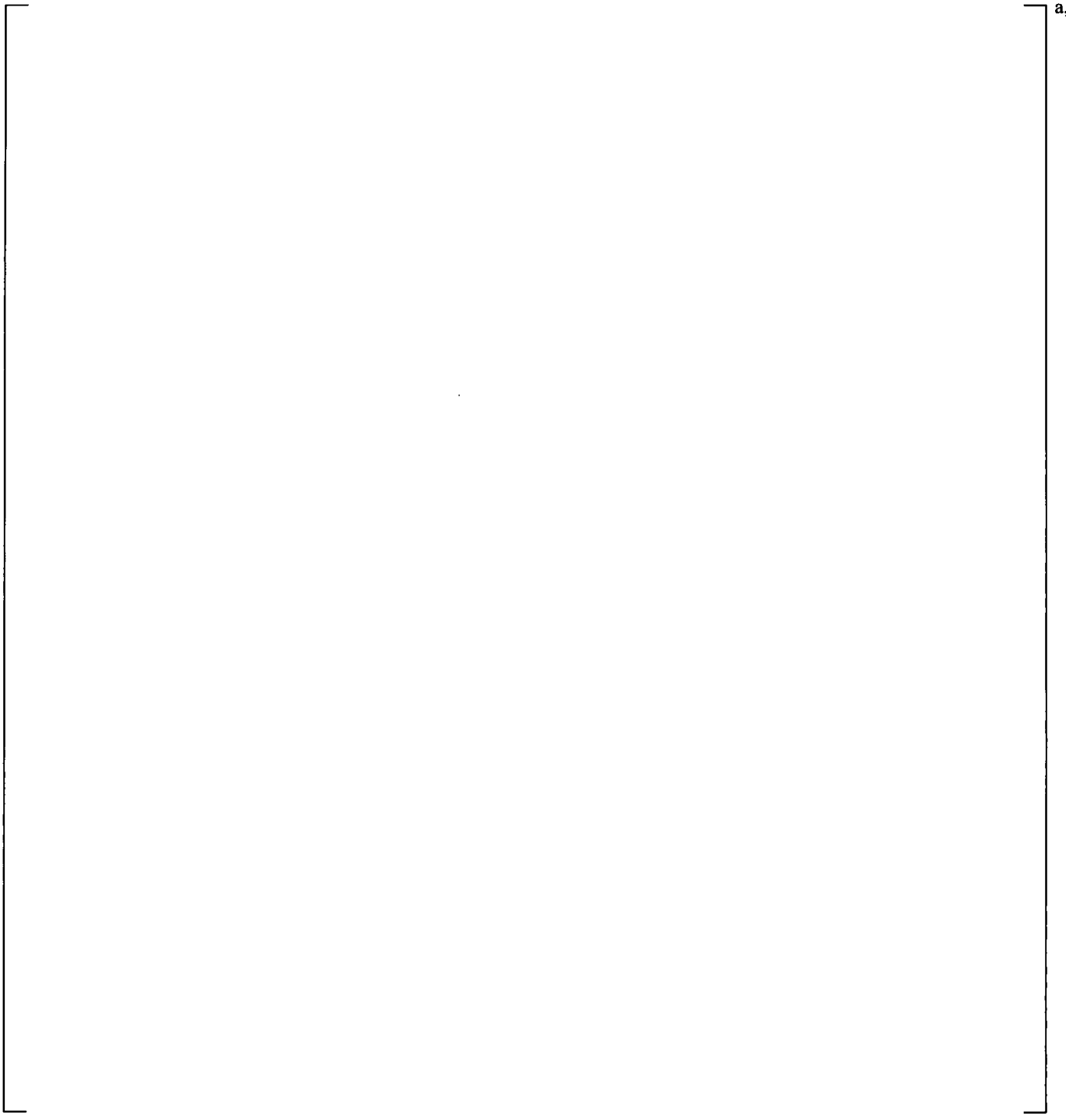

Figure 5-22 WCOBRA/TRAC-TF2 Sub-models with Homogeneous Non-equilibrium Relaxation Model Option

a,c

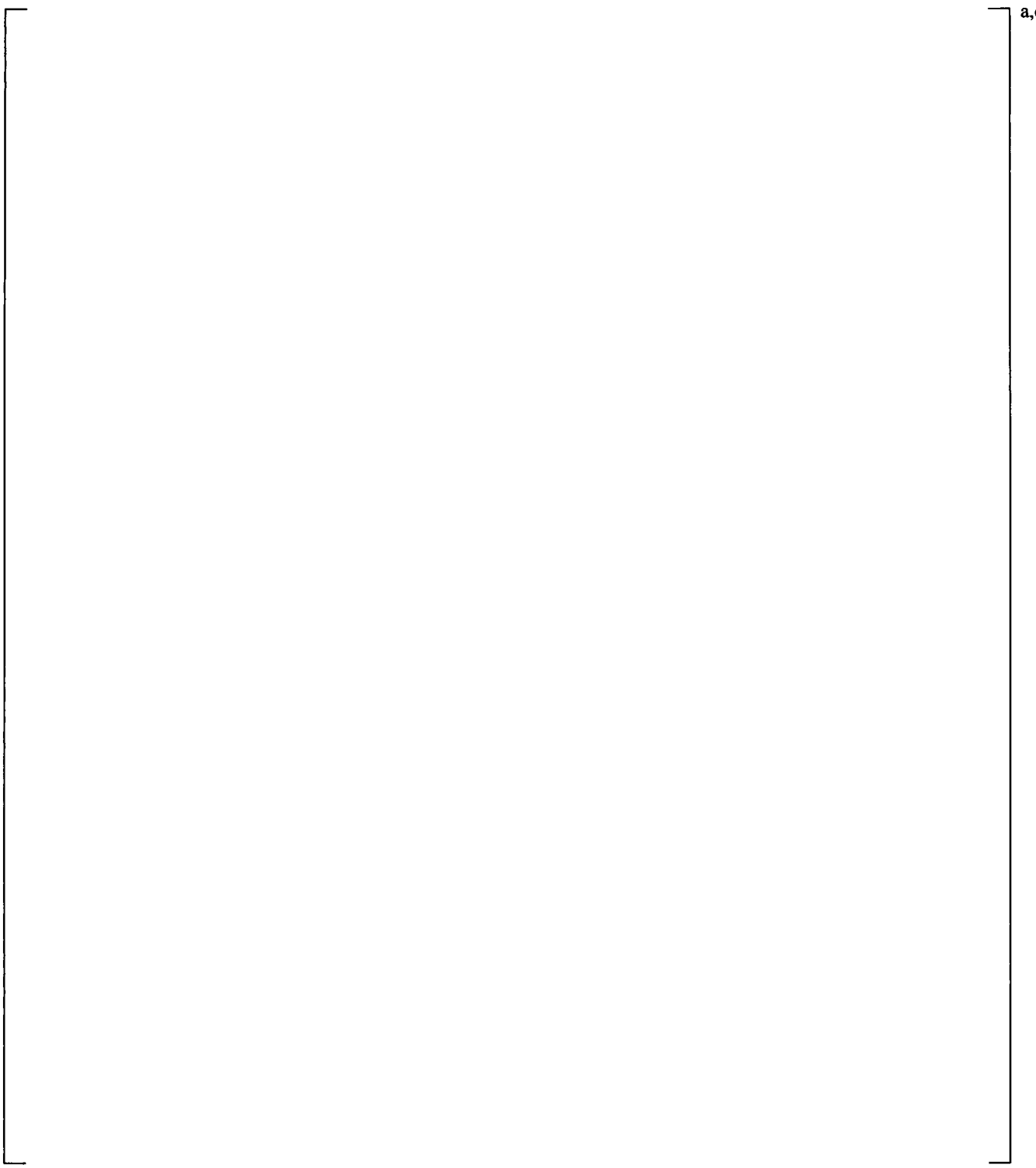

Figure 5-23 Area Ratio in Homogeneous Non-equilibrium Relaxation Model

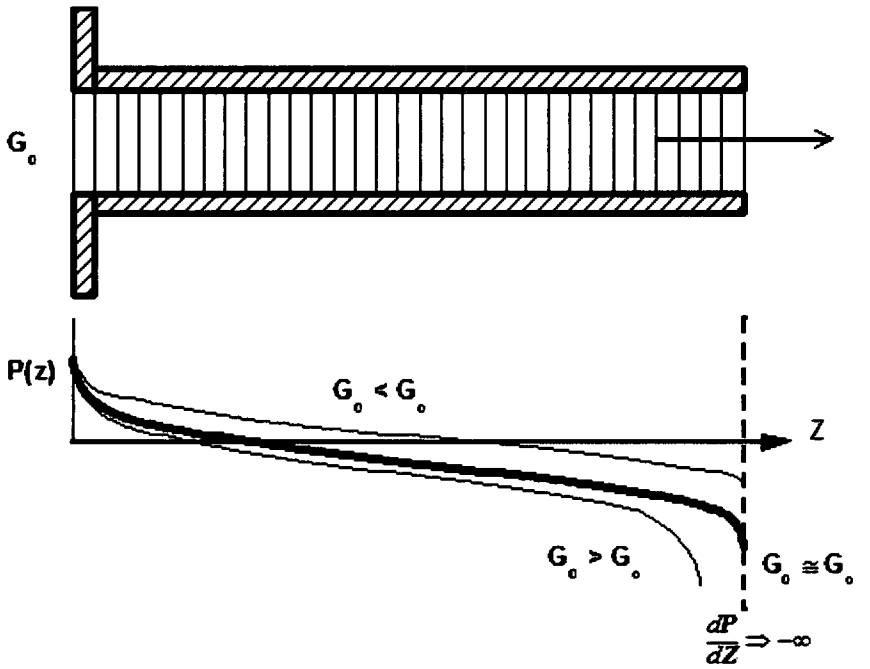

Figure 5-24 WCOBRA/TRAC-TF2 Choked Critical Flow Model

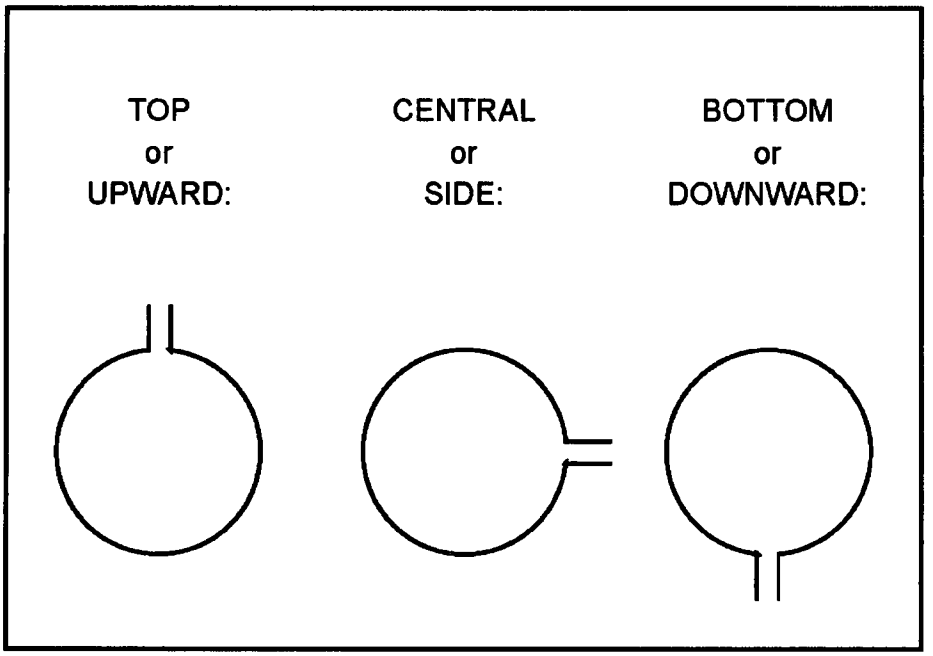

Figure 5-25 Possible Offtake Geometries

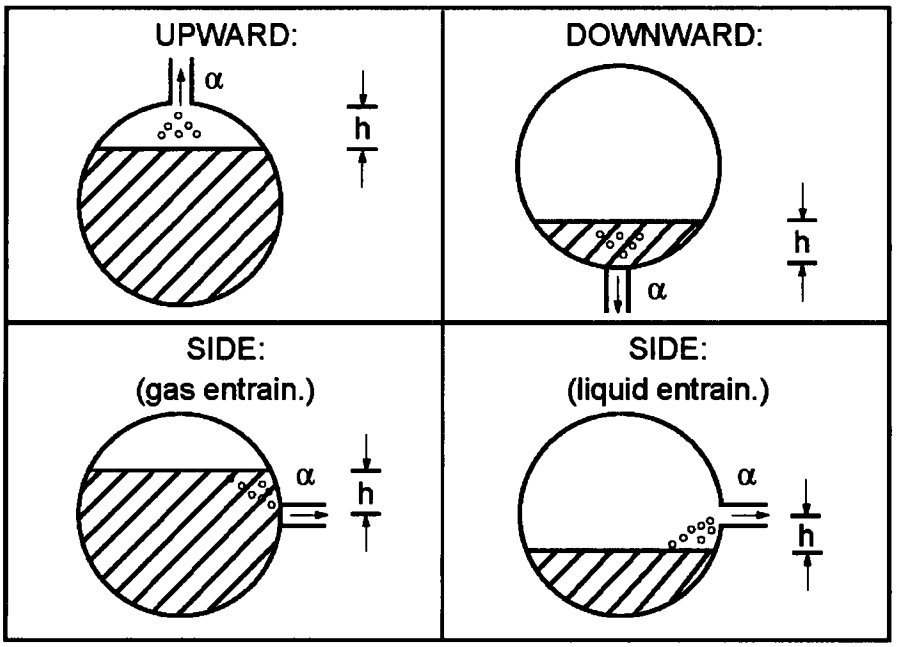

Figure 5-26 Determination of Actual Characteristic Height, h

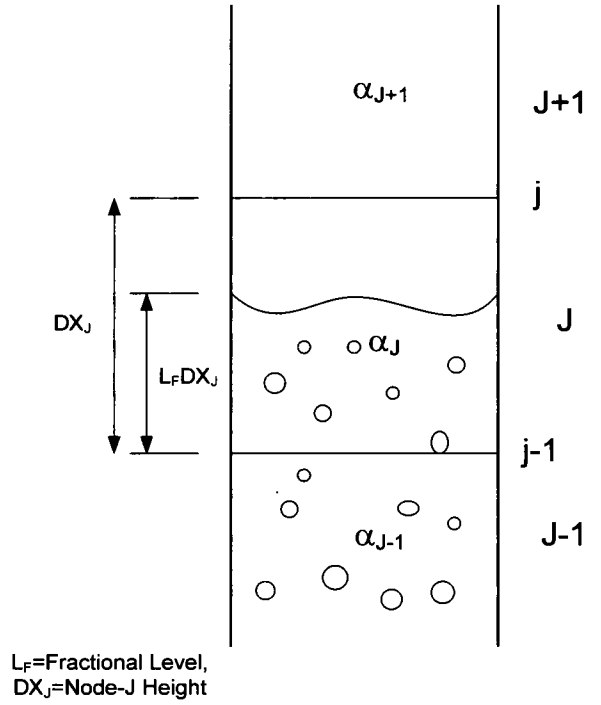

Figure 5-27 Mixture Level in Node J in a Channel

6 WCOBRA/TRAC-TF2 INTERFACIAL HEAT AND MASS TRANSFER MODELS

6.1 INTRODUCTION

The heat and mass transfer between the liquid and vapor phases depends on the interfacial heat transfer coefficient h_i and the interfacial area A_i. WCOBRA/TRAC-TF2 combines these quantities into interfacial heat transfer factors ($h_i A_i$) for the vessel component and into liquid side and vapor side interfacial heat transfer factors in the one-dimensional components. Section 4 discussed calculation of the interfacial area. This section describes the models, correlations, and assumptions used in the WCOBRA/TRAC-TF2 vessel and one-dimensional components to determine the interfacial heat transfer coefficients and the interfacial heat transfer factors. The interfacial heat transfer coefficients depend on the flow regime and on whether the fluid is subcooled or superheated.

In a postulated Loss-of-Coolant Accident (LOCA), and in the integral effects tests (IETs) and separate effects tests (SETs) that approximate parts of a LOCA, not all of the interfacial heat transfer terms are of equal importance. In the vessel, evaporation of saturated liquid droplets and films into superheated vapor is clearly the most dominant interfacial heat transfer process. Condensation to subcooled liquid also occurs as emergency core cooling (ECC) liquid enters the vessel or the loops. Superheated liquid and subcooled vapor are inherently unstable and are rarely encountered. Thus, the interfacial heat transfer coefficients from the interface to superheated vapor and from the interface to subcooled liquid are the most important terms to consider.

The following sections describe, by flow regime, the correlations used for the calculations of the interfacial heat transfer coefficients and interfacial heat transfer factors in the WCOBRA/TRAC-TF2 vessel component and one-dimensional components.

6.2 VESSEL COMPONENT INTERFACIAL HEAT AND MASS TRANSFER MODELS

6.2.1 Small Bubble Regime

Model Basis

In the small bubble flow regime, the vapor side heat transfer coefficient for superheated vapor is assumed to be a constant:

$$h_{i,SHV} = 2.78 \frac{Btu}{ft^2 - s - °F} \tag{6-1}$$

For subcooled vapor, a large constant value is assumed for the interfacial heat transfer coefficient:

$$h_{i,SCV} = 2780.0 \frac{Btu}{ft^2 - s - °F} \tag{6-2}$$

The interfacial area for subcooled vapor is:

[ ]a,c (6-3)

where $A_X \Delta X$ is the cell volume.

The expression given by Equation 6-3 is essentially a [

]a,c The constant coefficient was originally arrived at by making assumptions on bubble or drop size, although it should be taken mainly as an empirical constant.

In the small bubble regime, the liquid side interfacial heat transfer coefficient to subcooled liquid is calculated using a correlation by [ ]a,c:

[ ]a,c (6-4)

where:

$$Re_b = \frac{\rho_\ell U_{br} D_b}{\mu_\ell} \quad (6\text{-}5)$$

and Pr_ℓ is the liquid Prandtl number.

Use of this equation in the small bubble regime assumes [

]a,c.

For superheated liquid, a large value is assumed in order to drive the liquid towards saturation:

$$h_{i,SHL} = 278.0 \frac{Btu}{ft^2 - s - °F} \quad (6\text{-}6)$$

Model As Coded

Calculations of the interfacial heat transfer coefficients and the quantities ($h_i A_i$) for each regime are performed in subroutine INTFR. Only the ($h_i A_i$) terms are returned for use by the rest of the code, so their calculations will be described in this section.

For evaporation to superheated vapor in the small bubble regime, ($h_i A_i$) is coded as:

$$(h_i A_i)_{SB,SHV} = h_{i,SHV} A_{i,SB} \quad (6\text{-}7)$$

where $h_{i,SHV}$ is given by Equation 6-1 and the interfacial area is given by Equation 4-22.

For superheated liquid evaporation ($h_i A_i$) is:

$$(h_i A_i)_{SB,SHL} = 278.0\, A_{i,SB} \tag{6-8}$$

The condensation terms in the small bubble regime are calculated as discussed in the following paragraphs.

For subcooled vapor,

$$(h_i A_i)_{SB,SCV} = h_{i,SCV}\, A_{i,SCV} \tag{6-9}$$

For subcooled liquid, the interfacial area is subjected to an additional ramp if there is a large void fraction gradient. If the difference in void fraction between two adjacent hydraulic cells is greater than [ ]^{a,c}, indicating that a transition to large bubble or churn-turbulent flow occurs nearby, the interfacial area is modified in the following manner:

$$A_{i,SCL} = F_{\Delta\alpha} A_X + (1 - F_{\Delta\alpha})\, A_{i,SB} \tag{6-10}$$

where A_X is the cell axial flow area and $A_{i,SB}$ is the small bubble interfacial area from Equation 4-22.

[

]^{a,c}

The interfacial heat transfer coefficient to subcooled liquid is calculated using Equation 6-4 and [

]^{a,c}

$$\left[\qquad\qquad\right]^{a,c} \tag{6-11}$$

where,[

]^{a,c}

[

]^{a,c}

[ ]^{a,c}

it follows that:

[ ]^{a,c} (6-12)

The interfacial heat transfer factor for subcooled liquid in the small bubble regime is then calculated as:

[ ]^{a,c} (6-13)

where the interfacial area $A_{i,SCL}$ is given by Equation 6-10.

Scaling Considerations and Conclusions

The formulation used in the small bubble regime is scale independent, since it is based on an individual bubble in the flow stream. The key process for the small bubble regime is the flow of saturated steam bubbles in subcooled water and for this combination the interfacial heat transfer is modeled with an appropriate expression. Metastable states are prevented from establishing by setting interfacial heat transfer coefficients to large values. The droplet size and interfacial area is calculated as discussed in Section 4. For subcooled liquid, the interfacial area is subjected to an additional ramp (Equation 6-10) if there is a large void fraction gradient to reflect a condition where a transition to large bubble or churn-turbulent flow occurs nearby.

The models and correlations for the ($h_i A_i$) terms for the small bubble regime are fully exercised as part of the WCOBRA/TRAC-TF2 verification and validation (V&V) presented in Volume 2. Noding consistency between the modeling of the SETs and IETs further ensures that any bias and scaling effect is properly accounted for in the overall code bias and uncertainty.

6.2.2 Small to Large Bubble Regime

Model Basis

In the small to large bubble regime, large vapor bubbles (slugs) are gradually calculated to form above a void fraction of [ ]^{a,c}, while a dispersion of small bubbles is assumed to exist in the continuous liquid phase. The interfacial area for large bubbles was described in Section 4.2.3.

The interfacial heat transfer coefficient to large bubbles for superheated vapor uses the correlation suggested by Lee and Ryley (1968):

$$h_{i,LR} = \frac{k_v}{D_h}(2.0 + 0.74\, Re_b^{1/2}\, Pr_v^{1/3}) \tag{6-14}$$

The Lee-Ryley correlation was originally developed for the evaporation of droplets in superheated steam.

The value of $h_{i,LR}$ given by Equation 6-14 assumes all of the vapor is in the form of large bubbles in calculating the bubble Reynolds number Re_b and that the bubbles nearly fill the hydraulic cell, making $D_b \approx D_h$. Pr_v is the vapor Prandtl number. The use of this correlation in this regime is an extrapolation. However, bubbles of superheated steam are unlikely to occur extensively in a LOCA transient, since the large interfacial area will quickly drive the steam to saturation.

For superheated liquid, a constant value is assumed,

$$h_{i,SHL} = 278.0 \frac{Btu}{ft^2 - s - °F} \tag{6-15}$$

[

]^{a,c}

For subcooled vapor, a constant value is assumed for the interfacial heat transfer coefficient:

$$h_{i,SCV} = 2780.0 \frac{Btu}{ft^2 - s - °F} \tag{6-16}$$

Model as Coded

The calculations of the interfacial heat transfer coefficients and the quantity ($h_i A_i$) are performed in subroutine INTFR. In the small to large bubble regime, values of ($h_i A_i$) for large bubbles are ramped with ($h_i A_i$) for small bubbles to obtain a ($h_i A_i$) for the small to large bubble regime. The small bubble values were discussed in Section 6.2.1.

The quantities ($h_i A_i$) for large bubbles are calculated as follows.

For superheated vapor,

$$(h_i A_i)_{LB,SHV} = h_{i,LR}\, A_{i,SLB} \tag{6-17}$$

where $A_{i,SLB}$ is given by Equation 4-36, and $h_{i,LR}$ is from Equation 6-14.

For superheated liquid,

$$(h_i A_i)_{LB,SHL} = h_{i,SHL} A_{i,SLB} \quad (6\text{-}18)$$

For subcooled liquid, the interfacial area is modified if there is a large void fraction gradient ($\Delta\alpha >$ [ ]^{a,c}) between two adjacent hydraulic cells, indicating a more separated flow regime. When the void gradient is large, the interfacial area for subcooled liquid is calculated as:

[ ]^{a,c} (6-19)

[

]^{a,c}

The subcooled liquid term ($h_i A_i$) is then calculated as:

[ ]^{a,c} (6-20)

where [ ]^{a,c}.

After these calculations are performed for large bubbles, the final values of ($h_i A_i$) for the small to large bubble regime are obtained. The ramp between the small bubble and large bubble values is the same as that described in Section 4.2.3, so only the final expressions are listed here. These are:

For superheated vapor,

[ ]^{a,c} (6-21)

For superheated liquid,

[ ]^{a,c} (6-22)

For subcooled liquid,

[ ]^{a,c} (6-23)

and for subcooled vapor,

[ ]^{a,c} (6-24)

Scaling Considerations and Conclusions

As with the small bubble regime, the key process is the flow of saturated vapor bubbles in subcooled water and an appropriate expression is used for this process. Similar scaling considerations and conclusions discussed for the small bubble regime apply here. These models and correlations are fully exercised as part of the WCOBRA/TRAC-TF2 V&V presented in Volume 2. Noding consistency between the modeling of the SETs and IETs further ensures that any bias and scaling effect is properly accounted for in the overall code bias and uncertainty.

6.2.3 Churn-Turbulent Regime

Model Basis

In the churn-turbulent flow regime, flow is transitioned from large bubble at α_{LB} = [ ]^{a,c} to film at $\alpha = \alpha_{crit}$ as described in Section 4. Droplets can appear in the flow from entrainment and from adjoining channels.

For superheated vapor, the interfacial heat transfer coefficient from the liquid film is based on:

$$h_{i,v\ell} = \frac{f_{i,\ell}\,\rho_v\,C_{pv}\left|\underline{U}_{v\ell}\right|}{2\,Pr_v^{2/3}} \tag{6-25}$$

For superheated vapor from droplets, the interfacial heat transfer coefficient is given by the Lee-Ryley (1968) correlation:

$$h_{i,LR} = \frac{k_v}{D_d}[2.0 + 0.74\,Re_d^{1/2}\,Pr_v^{1/3}] \tag{6-26}$$

For superheated liquid films, there are three possible expressions for the interfacial heat transfer coefficient. The first of these expressions is derived from the Colburn analogy (Colburn, 1933) using friction factors by Hughmark (1973):

[ ]^{a,c} (6-27)

where:

[ ]^{a,c} (6-28)

The second expression is from conduction through a liquid film:

$$h_i^* = \frac{2k_\ell}{\delta_\ell} \tag{6-29}$$

where δ_ℓ is the liquid film thickness.The third expression assumes the constant value:

$$h_i^{**} = 278.0 \tag{6-30}$$

The interfacial heat transfer coefficient from the interface to the liquid for liquid drops is from Andersen (1973):

$$h_{i,drop} = C\frac{\pi^2}{3}\frac{k_\ell}{r_d} \tag{6-31}$$

where the value of C is taken as [ ]^{a,c}

The interfacial heat transfer coefficient from the interface to subcooled liquid films is also based on the Hughmark (1973) expression:

$$h_{i,SCL,v\ell} = h_{i,HM} \tag{6-32}$$

where $h_{i,HM}$ is given by Equation 6-27. This value is limited by the upper limit heat transfer coefficient $h_{i\ell,max}$ described in Section 6.2.1.

For subcooled liquid drops, the expression from Andersen (1973) is again applied:

$$h_{i,SCL,ve} = h_{i,drop} \tag{6-33}$$

where $h_{i,drop}$ is from Equation 6-31.

The interfacial heat transfer coefficient from the interface to subcooled vapor is assumed to be a large constant for both liquid films and droplets to drive the vapor toward saturation. The value given by Equation 6-16 is again applied.

Model as Coded

Calculations of the interfacial heat transfer coefficients for the churn-turbulent regime are performed in subroutine INTFR. The evaporation and condensation ($h_i A_i$) terms are calculated for large bubbles, as described in Section 6.2.2, and for annular films and drops as described below. The interfacial heat transfer coefficient is then calculated for the churn-turbulent regime using a linear interpolation of the large bubble values at α_{LB}=[ ]^{a,c} and the film/drop values at α_{crit}, where α_{crit} is calculated using Equation 4-42.

The term ($h_i A_i$) from the interface to vapor for liquid films and drops in superheated vapor is calculated as:

[ ]^{a,c} (6-34)

where [

]^{a,c}.

For superheated liquid, ($h_i A_i$) is calculated as:

[ ]^{a,c} (6-35)

where [

]^{a,c}.

The interfacial area used with the Hughmark (1973) correlation, $A^*_{i,film}$, is a modification of the film interfacial area to take into account a large void fraction gradient, and is calculated as:

[ ]^{a,c} (6-36)

where [ ]^{a,c}.

For subcooled liquid, the interfacial heat transfer coefficient from the interface to the liquid is calculated as:

[ ]^{a,c} (6-37)

subject to the upper limit on the liquid side interfacial heat transfer coefficient described in Section 6.2.1.
[ ]^{a,c}

The interfacial areas $A^*_{i,film}$ and $A_{i,drop}$ are calculated with Equations 6-36 and 4-45.

The quantity ($h_i A_i$) for subcooled vapor is calculated as:

$$(h_i A_i)_{FD,SCV} = h_{i,SCV}\ A_{i,SCV} \quad (6\text{-}38)$$

where $h_{i,SCV}$ is an assumed large constant value given by Equation 6-16 and $A_{i,SCV}$ is given by Equation 6-3.

[

]^{a,c}

[ ]a,c (6-39)

where [

]a,c

The ($h_i A_i$) terms for interfacial heat transfer in the churn-turbulent regime are then calculated as:

$$(h_i A_i)_{CT,SHV} = F_{CT}(h_i A_i)_{FD,SHV} + (1 - F_{CT})(h_i A_i)_{LB,SHV} \quad (6\text{-}40)$$

$$(h_i A_i)_{CT,SHL} = F_{CT}(h_i A_i)_{FD,SHL} + (1 - F_{CT})(h_i A_i)_{LB,SHL} \quad (6\text{-}41)$$

$$(h_i A_i)_{CT,SCL} = F_{CT}(h_i A_i)_{FD,SCL} + (1 - F_{CT})(h_i A_i)_{LB,SCL} \quad (6\text{-}42)$$

$$(h_i A_i)_{CT,SCV} = 2780.0\ A_{i,SCV} \quad (6\text{-}43)$$

Scaling Considerations and Conclusions

The interfacial heat transfer factors in the churn-turbulent regime are obtained as an interpolation between the large bubble values at α_{LB}=[ ]a,c and the film/drop values at α_{crit}, where α_{crit} is calculated using Equation 4-42. These models and correlations are fully exercised as part of the WCOBRA/TRAC-TF2 V&V presented in Volume 2. Noding consistency between the modeling of the SETs and IETs further ensures that any bias and scaling effect is properly accounted for in the overall code bias and uncertainty.

6.2.4 Film/Drop Regime

Model Basis

The film/drop regime is assumed to exist when the vapor fraction is greater than the critical vapor fraction for transition to annular flow (α_{crit}). The value of α_{crit} was described in Section 4.2.4, and is given by Equation 4-42.

The correlations for the interfacial heat transfer coefficient in the film/drop flow regime are the same as those in the churn-turbulent regime. The difference between the film/drop regime ($h_i A_i$) and the churn-turbulent regime ($h_i A_i$) enters through the interfacial areas A_i of the two regimes. In the churn-turbulent regime, the interfacial area is dominated by the large bubble area. In the film/drop regime, the entrainment rate is high, and the ($h_i A_i$) term due to droplets thus has greater importance.

Model as Coded

For superheated vapor, the interfacial heat transfer factor is calculated as:

[ ]a,c (6-44)

[

]a,c

For superheated liquid, ($h_i A_i$) is calculated as:

[ ]a,c (6-45)

[

]a,c

The interfacial area used with the Hughmark (1973) correlation $A^*_{i,film}$ is a modification of the film interfacial area and is calculated as:

[ ]a,c (6-46)

[

]a,c

For subcooled liquid, the interfacial heat transfer coefficient from the interface to the liquid is calculated as:

[ ]a,c (6-47)

The quantity ($h_i A_i$) for subcooled vapor is calculated as:

$$(h_i A_i)_{FD,SCV} = h_{i,SCV} A_{i,SCV} \quad (6\text{-}48)$$

where $h_{i,SCV}$ is an assumed large constant value given by Equation 6-16 and $A_{i,SCV}$ is given by Equation 6-3.

Scaling Considerations and Conclusions

The interfacial heat transfer correlations for the film/drop regime were originally validated for a limited range of conditions. These models and correlations are fully exercised as part of the WCOBRA/TRAC-TF2 V&V presented in Volume 2. Noding consistency between the modeling of the SETs and IETs further ensures that any bias and scaling effect is properly accounted for in the overall code bias and uncertainty. This regime was also considered by Chow et al. (1989), and no bias relative to scale was found.

6.2.5 Inverted Annular Regime

Model Basis

The inverted annular flow regime is selected when the liquid is subcooled, and the cell contains a heated structure with a surface temperature exceeding T_{sat} + [ ]^{a,c}. The continuous liquid in this regime is assumed to be in an annular column separated from the wall by a thin film of vapor.

The interfacial heat transfer coefficient from both continuous liquid and droplets to superheated vapor is based on a correlation by Forslund and Rohsenow (1968). This expression is:

$$Nu_d = 2 + 0.55 Re_d^{1/2} Pr_v^{1/3} \tag{6-49}$$

where the Prandtl number is evaluated at the vapor film temperature.

The Forslund-Rohsenow correlation is modified as suggested by Yuen and Chen (1978) to account for the reduction in the drop heat transfer due to evaporation. Yuen and Chen recommend the following expression for interfacial heat transfer from drops:

$$Nu_d (1 + B) = 2 + 0.6\, Re_d^{1/2} Pr_v^{1/3} \tag{6-50}$$

where the mass transfer number B is defined as:

$$B = \frac{H_v - H_g}{H_{fg}} \tag{6-51}$$

Where: H_v is the vapor phase enthalpy at bulk vapor temperature;

H_g is the vapor phase enthalpy at saturation temperature;

H_{fg} is the latent heat.

For the subcooled continuous liquid and droplets, the interfacial heat transfer coefficient is assumed to be given by:

$$h^*_{i,ve} = C \frac{\pi^2}{3} \frac{k_\ell}{R_d} \tag{6-52}$$

for droplets, and for continuous liquid by:

$$\left[\qquad \right]^{a,c} \tag{6-53}$$

with C, assumed to be C = [ ]^{a,c}.

For subcooled vapor, a large interfacial heat transfer coefficient is assumed:

$$h_{i,SCV} = 2780 \frac{Btu}{ft^2 - s - °F} \tag{6-54}$$

Model as Coded

Interfacial areas for the inverted annular column and for droplets that may appear were described in Section 4.3.2. Values of ($h_i A_i$) are calculated in subroutine INTFR and returned to subroutine XSCHEM for use in the solution of the conservation equations.

The ($h_i A_i$) for superheated vapor is calculated as:

$$(h_i A_i)_{IVA,SHV} = h_{i,FR,v\ell} A_{i,film} + h_{i,FR,ve} A_{i,drop} \tag{6-55}$$

where $h_{i,FR,v\ell}$ and $h_{i,FR,ve}$ are modified versions of the Forslund Rohsenow (1968) correlation, coded in subroutine INTFR as:

[ ]^{a,c} (6-56)

and

[ ]^{a,c} (6-57)

[

]^{a,c}

The interfacial areas $A_{i,film}$ and $A_{i,drop}$ are given by Equations 4-54 and 4-55, respectively.

For subcooled liquid, the ($h_i A_i$) term is calculated by:

[ ]^{a,c} (6-58)

where $h^*_{i,v\ell}$ is determined from Equation 6-53, $h^*_{i,ve}$ from Equation 6-52, and $h_{i\ell,max}$ from Equation 6-12.

The $(h_i A_i)$ term for subcooled vapor is calculated as:

$$(h_i A_i)_{IVA,SCV} = h_{i,SCV} A_{i,SCV} \tag{6-59}$$

where $h_{i,SCV}$ and $A_{i,SCV}$ are calculated by Equations 6-54 and 6-3, respectively.

Although not used in the inverted annular regime, a value of $(h_i A_i)$ for superheated liquid is also calculated. This term is calculated as:

$$(h_i A_i)_{IVA,SHL} = 278.0\, A_{i,film} + 27.8\, A_{i,drop} \tag{6-60}$$

Scaling Considerations and Conclusions

The key process in the inverted annular regime is condensation to the subcooled liquid $(h_i A_i)_{IVA,SCL}$. Appropriate correlations were selected to represent these terms. The inverted annular flow regime is applicable to conditions expected in a PWR during a LOCA event and no scaling limitation in its formulation was identified. The models and correlations for this regime are applied in a large number of separate and integral effects tests as discussed in Volume 2.

6.2.6 Inverted Liquid Slug Regime

Model Basis

The inverted liquid slug regime is selected when the liquid is saturated or superheated and the cell contains a heated structure with a surface temperature exceeding T_{sat} + 75°F. The continuous liquid in this regime is assumed to be in the form of large liquid slugs. Droplets occur through entrainment.

The interfacial heat transfer coefficient from the liquid and droplets interface to superheated vapor in this regime is also estimated using the modified Forslund-Rohsenow (1968) correlation. This correlation was originally developed to determine the interfacial heat transfer coefficient from droplets to superheated vapor and is described in Section 6.2.5.

For superheated liquid, the heat transfer coefficient from the interface to the liquid is assumed to be a constant value of:

$$h_{i,v\ell} = 278.0 \frac{Btu}{ft^2 - s - °F} \tag{6-61}$$

for continuous liquid and:

$$h_{i,ve} = 27.8 \frac{Btu}{ft^2 - s - °F} \tag{6-62}$$

for drops.

For subcooled vapor, a large interfacial heat transfer coefficient is assumed,

$$h_{i,SCV} = 2780 \frac{Btu}{ft^2 - s - °F} \tag{6-63}$$

Model as Coded

Interfacial areas for the inverted liquid slugs and for droplets were described in Section 4.3.3. Values of $(h_i A_i)$ are calculated in subroutine INTFR and returned to subroutine XSCHEM for use in solution of the conservation equations.

The $(h_i A_i)$ for superheated vapor is calculated as:

$$(h_i A_i)_{IVS,SHV} = h_{i,FR,v\ell}\, A_{i,film} + h_{i,FR,ve}\, A_{i,drop} \tag{6-64}$$

where $h_{i,FR,v\ell}$ and $h_{i,FR,ve}$ are modified versions of the Forslund-Rohsenow (1968) correlation, coded in INTFR as:

[ ]a,c (6-65)

and

[ ]a,c (6-66)

where B is given by Equation 6-51.

The interfacial areas $A_{i,film}$ and $A_{i,drop}$ are given by Equations 4-60 and 4-61, respectively.

For the superheated liquid, the value of $(h_i A_i)$ is calculated from:

$$(h_i A_i)_{IVS,SHL} = h_{i,v\ell}\, A_{i,film} + h_{i,ve}\, A_{i,drop} \tag{6-67}$$

where $h_{i,v\ell}$ and $h_{i,ve}$ are the constant values given by Equations 6-61 and 6-62.

The $(h_i A_i)$ term for subcooled vapor is calculated as:

$$(h_i A_i)_{IVS,SCV} = h_{i,SCV} A_{i,SCV} \tag{6-68}$$

where $h_{i,SCV}$ and $A_{i,SCV}$ are calculated by Equations 6-63 and 6-3, respectively.

Although not used explicitly in the inverted liquid slug regime, a value of $(h_i A_i)$ for subcooled liquid is also calculated. This term is calculated as:

[ ]a,c (6-69)

[ ]a,c

Scaling Considerations and Conclusions

The key process in the inverted liquid slug flow regime is evaporation to superheated vapor $(h_i A_i)_{IVS,SHV}$. An appropriate correlation is used to represent this term. The inverted liquid slug flow regime is applicable to conditions expected in a PWR during a LOCA event and no scaling limitation in its formulation was identified. The models and correlations for this regime are assessed in a large number of separate and integral effects tests as discussed in Volume 2.

6.2.7 Dispersed Droplet Flow Regime

Model Basis

The dispersed droplet flow regime occurs when the continuous liquid field becomes completely entrained. Interfacial heat transfer is then due to droplets only.

The interfacial heat transfer coefficient to superheated vapor is given by the [ ]a,c:

[ ]a,c (6-70)

[ ]a,c

[ ]a,c (6-71)

For the interfacial heat transfer coefficient to superheated liquid, a constant value is assumed:

$$h_{i,ve} = 27.8 \frac{Btu}{ft^2 - s - °F} \quad (6\text{-}72)$$

The interfacial heat transfer coefficient to subcooled liquid droplets is calculated using the equation by Andersen (1973):

$$h^{*}_{i,ve} = C\frac{\pi^2}{3}\frac{k_f}{R_d} \tag{6-73}$$

with C = [ ]^{a,c}.

For subcooled vapor a large interfacial heat transfer coefficient is assumed:

$$h_{i,SCV} = 2780\frac{Btu}{ft^2 - s - °F} \tag{6-74}$$

Model as Coded

The quantity (h_i A_i) for the dispersed droplet regime is calculated as follows.

For superheated vapor,

$$(h_i A_i)_{DD,SHV} = h_{i,FR,ve}\, A_{i,drop} \tag{6-75}$$

For superheated liquid,

$$(h_i A_i)_{DD,SHL} = h_{i,ve}\, A_{i,drop} \tag{6-76}$$

For subcooled liquid,

[ ]^{a,c} (6-77)

and for subcooled vapor,

$$(h_i A_i)_{DD,SCV} = h_{i,SCV}\, A_{i,SCV} \tag{6-78}$$

where $A_{i,drop}$ is given by Equation 4-78 and $A_{i,SCV}$ by Equation 6-3.

Scaling Considerations and Conclusions

The key processes in the dispersed droplet flow regime are condensation to the subcooled drops (h_i A_i)$_{DD,SCL}$ and evaporation to superheated vapor (h_i A_i)$_{DD,SHV}$. The inverted liquid slug flow regime is applicable to conditions expected in a PWR during a LOCA event and no scaling limitation in its formulation was identified. Models and correlations for this regime are assessed in a number of separate and integral effects tests as discussed in Volume 2.

6.2.8 Falling Film Regime

Model Basis

The falling film regime is selected in a cell when the [

]^{a,c}. Both continuous liquid films and droplets occur.

The correlations used for the interfacial heat transfer coefficients in the falling regime have all been described in previous sections. The modified Forslund-Rohsenow correlation is used for superheated vapor, the Andersen correlation is used for subcooled liquid, and constant values are used for h_i for subcooled vapor and superheated liquid.

Model as Coded

In the falling film regime, the $(h_i A_i)$ terms are calculated as follows.

For superheated vapor,

$$(h_i A_i)_{FF,SHV} = h_{i,FR,v\ell}\, A_{i,film} + h_{i,FR,ve}\, A_{i,drop} \tag{6-79}$$

For subcooled liquid,

[ ]^{a,c} (6-80)

For superheated liquid,

$$(h_i A_i)_{FF,SHL} = h_{i,v\ell}\, A_{i,film} + h_{i,ve}\, A_{i,drop} \tag{6-81}$$

and for subcooled vapor,

$$(h_i A_i)_{FF,SCV} = h_{i,SCV}\, A_{i,SCV} \tag{6-82}$$

where:

$h_{i,FR,v\ell}$ is given by Equation 6-56,

$h_{i,FR,ve}$ is given by Equation 6-57,

[

]^{a,c}

$h_{i,v\ell}$ is given by Equation 6-61,

$h_{i,ve}$ is given by Equation 6-62,

$h_{i,SCV}$ is given by Equation 6-63,

[ ]^{a,c}

$A_{i,film}$ is given by Equation 4-64,

$A_{i,drop}$ is given by Equation 4-65,

$A_{i,SCV}$ is given by Equation 6-3.

Scaling Considerations and Conclusions

The key processes in the falling film regime are condensation to the subcooled liquid $(h_i A_i)_{FF,SCL}$ and evaporation to superheated vapor $(h_i A_i)_{FF,SHV}$. Appropriate correlations were selected to represent these terms and no major scaling issue was identified in the model. Models and correlations for this regime are assessed in a number of separate and integral effects tests as discussed in Volume 2.

6.2.9 Top Deluge Flow Regime

Model Basis

The top deluge regime is selected in a cell when the [ ]^{a,c}. Both continuous liquid and droplets can occur; however, since entrainment is low, most of the liquid remains in the continuous liquid field. Thus, for interfacial heat transfer, the $(h_i A_i)$ for continuous liquid is of greater importance.

The models and correlations for the top deluge regime are the same as those described in previous subsections.

Model as Coded

The interfacial heat transfer terms for the top deluge flow regime are coded identically to those for the falling film regime. Thus, for superheated vapor,

$$(h_i A_i)_{TD,SHV} = h^*_{i,FR,v\ell}\, A_{i,film} + h^*_{i,FR,ve} A_{i,drop} \tag{6-83}$$

For subcooled liquid,

[ ]^{a,c} (6-84)

For superheated liquid,

$$(h_i A_i)_{TD,SHL} = h_{i,v\ell}\, A_{i,film} + h_{i,ve} A_{i,drop} \tag{6-85}$$

and for subcooled vapor,

$$(h_i A_i)_{TD,SCV} = h_{i,SCV}\ A_{i,SCV} \tag{6-86}$$

where:

$h^*_{i,FR,v\ell}$ is given by Equation 6-56,

$h^*_{,FR,ve}$ is given by Equation 6-57,

[ ]^{a,c}

$h_{i,v\ell}$ is given by Equation 6-61,

$h_{i,ve}$ is given by Equation 6-62,

$h_{i,SCV}$ is given by Equation 6-63,

[ ]^{a,c}

$A_{i,film}$ is given by Equation 4-66,

$A_{i,drop}$ is given by Equation 4-67,

$A_{i,SCV}$ is given by Equation 6-3.

Scaling Considerations and Conclusions

The key processes in the falling film regime are condensation to the subcooled liquid $(h_i A_i)_{FF,SCL}$ and evaporation to superheated vapor $(h_i A_i)_{FF,SHV}$. Appropriate correlations were selected to represent these terms and no major scaling issue was identified in the model. Models and correlations for this regime are assessed in a number of separate and integral effects tests as discussed in Volume 2.

6.2.10 Effect of Grid Spacers on Interfacial Heat Transfer

Model Basis

Spacer grids have an important effect on interfacial heat transfer. Since the grids are unpowered and have a large surface area to volume ratio, they can quench before the fuel rods. If the grid quenches, a liquid film can cover the grid, which creates an additional liquid surface area. This thin liquid film readily evaporates and acts to desuperheat the vapor in a non-equilibrium two-phase droplet flow. Because the grid blocks a portion of the fuel assembly flow area, the velocity of the vapor passing through the grid is higher than velocities nearby in the fuel bundle. As a result the vapor-film relative velocity at the grid is larger, so that a wetted grid has a higher interfacial heat transfer coefficient compared to nearby droplets.

The additional interfacial heat transfer due to a wetted grid is accounted for in WCOBRA/TRAC-TF2 by an additional $(h_i A_i)$ term which augments the $(h_i A_i)$ term calculated for the droplet flow. Since the grid height is small compared to the height of the momentum cell in which it is placed and the fuel rods are not yet quenched, a continuous liquid film is not formed in the momentum cell by de-entrainment from the droplet field. Thus, mass conservation calculations are unaffected by the assumption that a thin film is assumed to form on the grid. Rather, mass that would form the liquid film is left in the droplet field and

the evaporation of this mass is taken into account through an ($h_i A_i$) term calculated for the wetted grid, $(h_i A_i)_{grid}$. A simple radiation heat transfer model is used to determine if the grid can be wetted. This grid rewet model is described in Section 7.2.9.

[

]^{a,c}

[ ]^{a,c} (6-87)

[

]^{a,c}

[ ]^{a,c} (6-88)

[ ]^{a,c}

[ ]^{a,c} (6-89)

In Equation 6-89, the exponent on the [

]^{a,c}.

The liquid film interfacial area $A_{i,grid}$ is assumed to be equal to the grid metal surface area.

Model as Coded

For a grid to rewet, its temperature must be below the rewet temperature, and there must be sufficient liquid in the flow to form a film. Calculations are first performed in subroutine HEAT to determine the grid temperature T_{grid}. A flag to indicate if the grid can rewet, I_{wet}, is passed from HEAT to subroutine INTFR, where the interfacial heat transfer calculations are performed. The value of I_{wet} is:

[ ]^{a,c} (6-90)

[

]^{a,c}

The value of ($h_i A_i$) is then calculated as:

[ ]^{a,c} (6-91)

[
]a,c

[a,c

(6-92)

[

]a,c

Finally, the interfacial heat transfer factor for superheated vapor is augmented by $(h_i A_i)_{grid}$.

$$(h_i A_i)_{fr,SHV} = (h_i A_i)^*_{fr,SHV} + (h_i A_i)_{grid} \quad (6\text{-}93)$$

where the flow regime "fr" in this case may be any of the hot wall flow regimes where the void fraction can be greater than [ ]a,c. The term $(h_i A_i)^*_{fr,SHV}$ is the interfacial heat transfer factor calculated for each regime as described in previous sections.

Scaling Considerations and Conclusions

The grid model, including the grid interfacial heat transfer augmentation, is used in WCOBRA/TRAC-TF2 simulations of Full Length Emergency Cooling Heat Transfer (FLECHT)-Separate Effects and System Effects Test (SEASET), FLECHT Low Flooding Rate, FLECHT Top-Skewed Power, Flooding Experiment with Blocked Arrays (FEBA), and Cylindrical Core Test Facility (CCTF) reflood tests, as well as the Oak Ridge National Lab (ORNL) Thermal-Hydraulic Test Facility (THTF) and G-1 loop blowdown tests. The test bundles in these experiments were full scale in height and used prototypic PWR spacer grids, including both mixing vane and non-mixing vane grid types. The grid models were developed based on data for full scale grids.

6.2.11 Effect of Non-Condensables

Model Basis

The rate of steam condensation is suppressed in the presence of a non-condensable gas such as nitrogen, hydrogen, and inert gases. Non-condensable gases can arise in a PWR from several sources during a loss-of-coolant accident. As the RCS de-pressurizes, dissolved gas will come out of solution throughout the primary side. During accumulator injection, some of the nitrogen cover gas can be swept into the cold legs and additional nitrogen can flow into the system after most of the accumulator water inventory has been depleted. Air from the containment can be ingested into the RCS at the break during the refill phase

of a LOCA. Hydrogen, resulting from cladding oxidation, can also be present in the RCS. If fuel rod burst occurs, the gas mixture inside the fuel rod is released to the RCS. The FULL SPECTRUM LOCA (FSLOCA) methodology only models the nitrogen in the RCS resulting from accumulator injection and the air ingested from containment is calculated approximately using nitrogen. The amount of other non-condensable gases in the RCS is insignificant, so they are neglected.

There are two major effects from non-condensables. First, the non-condensables affect the interfacial heat and mass transfer rate by reducing the steam partial pressure (Dalton's law) in the bulk mixture and thus, the saturation temperature of the steam. The interfacial heat transfer factor for the steam is reduced by being multiplied by the steam partial pressure. The interfacial heat transfer rate on the liquid side is reduced during condensation, because the saturation temperature reduces with a lower steam partial pressure. The impact of the steam partial pressure in the bulk gas mixture on interfacial heat and mass transfer is further discussed in Section 6.2.13.

Second, during a condensation process, as the vapor-gas mixture flows to the liquid-vapor interface, the vapor phase is condensed to the liquid phase. Thus, the non-condensable gases accumulate at the interface and create an additional resistance to the flow of vapor toward the liquid-vapor interface. This gas concentration near the interface reduces the condensation rate further. This effect is more significant when the gas partial pressure in the bulk mixture is relatively small and the condensation rate is high. Thus, condensation suppression models are necessary to account for the further reduction of the condensation rate.

Numerous experimental studies have demonstrated this effect, including those by Dehbi, Golay, and Kazimi (1991), Slegers and Seban (1970), Sklover and Rodivilin (1976), and Young and Bajorek (1997). The Young and Bajorek model was selected for the FSLOCA methodology.

Young and Bajorek analyzed the non-condensable concentration near a liquid-gas interface during the condensation process. They argued that, under stagnant flow conditions, the condensation process is limited by the ability of the vapor to diffuse through the gas collecting near the surface. They developed a condensation suppression model (Young and Bajorek, 1997) from first principles using surface renew theory and gas diffusion theory. The model is used to develop a condensation suppression factor that is applied to the liquid side interfacial heat transfer factor ($h_i A_i$) for subcooled liquid.

[

]^{a,c}

$$\left[\qquad\qquad \right]^{a,c} \qquad (6\text{-}95)^{1}$$

where:

---

[1] Equation 6-94 intentionally omitted.

[ ]a,c (6-96)

[

]a,c

[ ]a,c (6-97)

[

]a,c

Model as Coded

[

]a,c The coded condensation suppression model is shown in the following equation,

[ ]a,c (6-98)

In the code, the condensation suppression factor is limited to the range:

[ ]a,c (6-99)

Scaling Considerations and Conclusions

The condensation suppression model is used to simulate the effect of non-condensable gases in IETs/SETs/PWR analysis. Discussion of the effect of non-condensable gases on the ACHILLES, Loss-of-Fluid Test (LOFT), and PWR transient is presented in Section 20.1.4. Additional assessment of the effect of non-condensables is provided via numerical "thought problems" in Section 23.2.7. The simulation results indicate that the model provides an adequate approximation of the condensation suppression process.

6.2.12 Condensation Ramp Model at Low Pressure

WCOBRA/TRAC-TF2 provides a condensation ramp to reduce the condensation rate at low pressure.
[

]a,c

Model as Coded

The condensation ramp function F_{CONT} is calculated as:

[ ]a,c (6-100)

[

]^{a,c}

Scaling Considerations and Conclusions

The condensation ramp is applied at very low pressure [ ]^{a,c} to compensate for numerical instabilities when extreme low pressures are induced by condensation. It is not expected to impact the results of any simulation. The possible bias or scaling of the model is of no concern. Although the model is simple, simulation results indicate that it provides adequate protection from code failure.

6.2.13 Vessel Component Interfacial Mass Transfer

Model Basis

The vessel component model for interfacial mass transfer is obtained from the energy jump condition by neglecting the mechanical terms and averaging. Wheeler et al. (1986), showed that this yields:

$$\Gamma''' = \frac{-q'''_{i\ell} - q'''_{iv}}{\Delta H_{\ell v}} \tag{6-101}$$

where:

$$\Delta H_{\ell v} = H_g - H_\ell \text{ for vaporization} \tag{6-102}$$

$$\Delta H_{\ell v} = H_v - H_f \text{ for condensation} \tag{6-103}$$

The interfacial heat transfer for phase k, q'''_{ik} is given by:

$$q'''_{ik} = (h_i A'''_i)(T_{sat} - T_k) \tag{6-104}$$

where h_i is the interfacial heat transfer coefficient and A'''_i is the average interfacial area per unit volume.

In the vessel component, the vapor generation rate is divided into five interfacial components: evaporation due to superheated vapor (SHV), the condensation due to subcooled vapor (SCV), the evaporation due to superheated liquid (SEL), the condensation due to subcooled liquid (SCL), the liquid flashing (SHL), and one component for boiling at the wall. The total vapor generation rate is given by the combination of these five interfacial components and the boiling at the wall. Table 6-1 shows the phase change phenomena and how these components are related to saturation, $T_{sat}(P)$, and dew-point

temperatures, $T_{dp} = T_{sat}(P_v)$. The symbols P and P_v refer to the pressure of the gas mixture and the steam partial pressure (Dalton's law), respectively.

The interfacial transfer terms associated with each phase when the phases are in non-equilibrium were described in the previous subsections. One way for non-equilibrium conditions to be created is for the liquid or vapor phase to receive heating or cooling from an external surface. The models used to calculate the heat transfer between the external surface ("wall") and the phases are described in Section 7. In nearly all situations, some portion of the total wall heat flux is considered to flow from the wall directly to the phase. Subsequent heating or cooling of that phase then results from interfacial heat and mass transfer as described in this section.

For most heat transfer regimes, some portion of the total heat flux from the wall is allocated to a term Q_b, or h_{wb} $(T_w - T_{sat})$, called the "boiling heat flux." This term then appears as an additive term in the net evaporation rate. The reason for doing this is to more accurately model situations such as subcooled nucleate boiling. In this heat transfer regime, the bulk fluid is still subcooled, but the liquid layer near the wall has reached saturation. Additional heating of this liquid layer creates bubbles, which then enter the bulk liquid and condense. Use of the boiling term allows vapor to be created via the net evaporation term, even though the liquid is subcooled. Because WCOBRA/TRAC-TF2 uses only one liquid energy equation, if the wall heat flux were to be allocated only to the liquid, vapor generation would not occur until the bulk fluid became saturated and slightly superheated.

A similar situation exists for film boiling situations in which the bulk liquid is subcooled. The vapor generation occurs at the interface between the liquid and the thin vapor film surrounding the wall as heat is conducted across the vapor film. Although the vapor film is superheated, most of the heat passes directly to the liquid layer. As more vapors are created, the film thickens and the hot wall begins to superheat the vapor, which then loses its superheat by interfacial heat transfer.

Transition boiling is a situation in which part of the wall is transferring directly to the vapor, and part of the wall is transferring directly to the liquid, usually at a high heat flux rate. Under these conditions, it is more numerically stable to pass the wall heat directly to the boiling term, rather than allow the liquid to superheat and then evaporate.

The way in which the total heat flux from the heat transfer models is split up among Q_{wf}, Q_{wv}, and Q_b is described for each heat transfer regime in Section 7.

The net vapor generation rate is given as the sum of five interfacial components, given below, and the boiling term. The interfacial mass transfer terms for Superheated Vapor (SHV), Subcooled Vapor (SCV), evaporation (SEL), Subcooled Liquid (SCL) and Superheated Liquid (SHL) are defined as follows:

Superheated Vapor (SHV),

$$\begin{cases} \Gamma''' _{SHV} = \dfrac{\left(h_i A_i'''\right)_{fr,SHV} \cdot \left(H_v - H_{g,dp}\right)}{C_{Pv,dp} \cdot \left(H_{g,dp} - H_\ell\right)} & \text{if } H_v \geq H_{g,dp} \\ \Gamma''' _{SHV} = 0 & \text{if } H_v < H_{g,dp} \end{cases} \quad (6\text{-}105)$$

Subcooled Vapor (SCV),

$$\begin{cases} -\Gamma''' _{SCV} = 0 & \text{if } H_v \geq H_{g,dp} \\ -\Gamma''' _{SCV} = \dfrac{P_v}{P} \dfrac{\left(h_i A_i'''\right)_{fr,SCV} \cdot \left(H_v - H_{g,dp}\right)}{C_{Pv,dp} \cdot \left(H_v - H_{f,dp}\right)} & \text{if } H_v < H_{g,dp} \end{cases} \quad (6\text{-}106)$$

Evaporation (SEL),

$$\begin{cases} \Gamma''' _{SEL} = \dfrac{\left(h_i A_i'''\right)_{fr,SEL} \cdot \left(H_\ell - H_{f,dp}\right)}{C_{P\ell,dp} \cdot \left(H_{g,dp} - H_\ell\right)} & \text{if } H_\ell \geq H_{f,dp} \\ \Gamma''' _{SEL} = 0 & \text{if } H_\ell < H_{f,dp} \end{cases} \quad (6\text{-}107)$$

Subcooled Liquid (SCL),

$$\begin{cases} -\Gamma''' _{SCL} = 0 & \text{if } H_\ell \geq H_{f,dp} \\ -\Gamma''' _{SCL} = \dfrac{\left(h_i A_i'''\right)_{fr,SCL} \cdot \left(H_\ell - H_{f,dp}\right)}{C_{P\ell,dp} \cdot \left(H_v - H_{f,dp}\right)} & \text{if } H_\ell < H_{f,dp} \end{cases} \quad (6\text{-}108)$$

Superheated Liquid (SHL),

$$\begin{cases} \Gamma''' _{SHL} = \dfrac{\left(h_i A_i'''\right)_{fr,SHL} \cdot \left(H_\ell - H_f\right)}{C_{P\ell} \cdot \left(H_g - H_\ell\right)} & \text{if } H_\ell \geq H_f \\ \Gamma''' _{SHL} = 0 & \text{if } H_\ell < H_f \end{cases} \quad (6\text{-}109)$$

where "fr" denotes the flow regime dependence.

The total vapor generation rate is given by:

$$\Gamma''' = \Gamma'''_{SHV} - \Gamma'''_{SCV} + \Gamma'''_{SEL} - \Gamma'''_{SCL} + \Gamma'''_{SHL} + Q'''_b / (H_g - H_\ell) \tag{6-110}$$

which is seen to be the sum of the evaporative, condensive, and flashing contributions, plus the boiling term.

The fraction η of the total vapor generation coming from the entrained liquid is given by:

[ ] a,c (6-111)

for evaporation, and for condensation by:

[ ] a,c (6-112)

Model as Coded

Calculations are first performed as described in Sections 6.2.1 through 6.2.9 to determine (h_i A_i) for each flow regime and fluid condition (SHV, SEL, SCV, SCL, SHL). If there is a grid, the (h_i A_i) value for superheated vapor is augmented by $(h_i A_i)_{grid}$ as described in Section 6.2.10. The calculation of the interfacial mass transfer is performed next in subroutine XSCHEM.

It is convenient to discuss the interfacial heat transfer factors (h_i A_i) for this calculation in terms of the array variable representing (h_i A_i) at mesh cell (I, J).

Thus, for any flow regime "fr" let:

$$HASHV(I,J) = (h_i A_i)_{fr,SHV} \tag{6-113}$$

$$HASCV(I,J) = (h_i A_i)_{fr,SCV} \tag{6-114}$$

$$HASCL(I,J) = (h_i A_i)_{fr,SCL} \tag{6-115}$$

$$HASHL(I,J) = (h_i A_i)_{fr,SHL} \tag{6-116}$$

For the evaporation due to the superheated liquid (SEL), the interfacial heat transfer factors ($h_i A_i$) is given by Equation 6-117 regardless the flow regime (fr).

[ ]a,c (6-117)

A sensible heat transfer term to the non-condensable gas is also defined:

$$HASNC(I,J) = (h_i A_i)_{non-condensable} \quad (6\text{-}118)$$

[

]a,c This model is judged reasonable for the calculation of interfacial mass transfer.

A temporary interfacial area is defined as:

[ ]a,c (6-119)

where [ ]a,c.

Finally, the interfacial heat transfer factors for the cell (I, J) are calculated as:

[ ]a,c (6-120)

(6-121)

(6-122)

(6-123)

(6-124)

The individual components of the interfacial mass transfer are calculated as:

[ ]a,c (6-125)

[a,c

(6-126)

(6-127)

(6-128)

(6-129)

]

[

]a,c

[a,c

(6-130)

(6-131)

(6-132)

]

[
]a,c

[a,c]

(6-133)

(6-134)

(6-135)

Finally, the interfacial mass transfer is calculated as the sum of the evaporative, condensive, flashing, and boiling terms. Q_b is defined by Equation 7-189.

$$\Gamma''' = \Gamma'''_{SHV} - \Gamma'''_{SCV} + \Gamma'''_{SEL} - \Gamma'''_{SCL} + \Gamma'''_{SHL} + Q'''_b / (H_g - H_\ell) \tag{6-136}$$

Scaling Considerations and Conclusions

The model for interfacial mass transfer is based on conservation principles. Nearly all of the simulations reported in Volume 2 include two-phase flow and some degree of thermal non-equilibrium. As such, the interfacial mass transfer model in WCOBRA/TRAC-TF2 has been validated against experimental data. The vessel model for interfacial mass transfer is not dependent on scale.

6.3 ONE-DIMENSIONAL COMPONENT INTERFACIAL HEAT AND MASS TRANSFER MODELS

WCOBRA/TRAC-TF2 solves non-equilibrium, two-phase-flow equations where the liquid and the gas phases are not in thermodynamic equilibrium. As a result, the different phasic temperatures lead to a heat and mass exchange between the phases through the interface. The interfacial transport is calculated in subroutine TF1DS for the 1D components.

The gas phase is assumed to be a homogeneous mixture of vapor and non-condensable gas in thermodynamic equilibrium. Further, the mixture obeys Dalton's law. The rate of change of the gas-phase sensible energy is given by:

$$q_g = \underbrace{\frac{P_s}{P} H_{CHTI} (T_g - T_{sv})}_{\text{gas to interface}} + \underbrace{\frac{P_a}{P} H_{CHTA} (T_g - T_\ell)}_{\text{gas to liquid}} \tag{6-137}$$

where H is the heat transfer factor, defined as the product of the convective heat transfer coefficient and the interfacial area. The first term in Equation 6-137 corresponds to heat transfer to or from the interface (q_{ig}) and is converted to or released as latent heat through phase change. The second term is the direct sensible heat exchange between the liquid and the gas.

Similarly, the rate of change of the liquid-phase sensible energy is given by:

$$q_\ell = \underbrace{\left\{H_{ALVE}(T_\ell - T_{sv}) + H_{ALV}\langle T_\ell - T_{sat}\rangle'\right\}}_{\text{liquid to interface}} + \underbrace{\frac{P_a}{P} H_{CHTA}(T_\ell - T_g)}_{\text{liquid to gas}} \quad (6\text{-}138)$$

Likewise, the first term ($q_{i\ell}$) accounts for the sensible heat transferred to or from the interface where it is converted to or released as latent heat, and the second term is the direct sensible heat exchange between the liquid and the gas. In WCOBRA/TRAC-TF2, evaporation and flashing are accounted for separately. Consequently, there are two liquid-side interfacial heat transfer factors, H_{ALV} and H_{ALVE}. For condensation and evaporation, H_{ALVE} is used. As shown in Figure 6-4, evaporation occurs if $T_{sv} < T_\ell < T_{sat}$ and flashing occurs if $T_\ell > T_{sat}$.

H_{ALV} is used during flashing. Note that the flashing term is incorporated into Equation 6-138 through a piecewise function, which is defined as follows:

$$\langle T_\ell - T_{sat}\rangle' = \begin{cases} 0 & \text{if } T_\ell \le T_{sat} \\ T_\ell - T_{sat} & \text{if } T_\ell > T_{sat} \end{cases} \quad (6\text{-}139)$$

When Equations 6-137 and 6-138 are added, the direct sensible heat transfer terms cancel out, and the mass transfer rate per unit volume as a result of interfacial heat transfer between the phases is calculated as:

$$\Gamma_i = \frac{q_{ig} + q_{i\ell}}{B_{cell}(h_v^* - h_\ell^*)} \quad (6\text{-}140)$$

where:

$$q_{i\ell} = \underbrace{H_{ALVE}(T_\ell - T_{sv})}_{\text{evaporation or condensation}} + \underbrace{H_{ALV}\langle T_\ell - T_{sat}\rangle'}_{\text{flashing}} \quad (6\text{-}141)$$

and

$$q_{ig} = \frac{P_s}{P} H_{CHTI}(T_g - T_{sv}) \quad (6\text{-}142)$$

A positive Γ_i indicates vapor generation and a negative Γ_i indicates liquid generation. Notice that while q_{ig} is negative, $q_{i\ell}$ may be positive, and vice versa. The net vapor or liquid generation is determined by the relative magnitude of these quantities and is illustrated in Figure 6-5. The total rate of phase change also includes the effect of subcooled boiling and is given by:

$$\Gamma = \Gamma_i + \Gamma_{sub} \quad (6\text{-}143)$$

where Γ_{sub} is determined through wall heat transfer and is given in Section 6.3.8.

To calculate q_g, q_ℓ, and Γ_i, closure relationships for the interfacial area and liquid- and vapor-side heat transfer coefficients, which provide H_{ALVE}, H_{ALV}, H_{CHTI}, and H_{CHTA}, are needed. In general, the interfacial area and convective heat transfer coefficients depend on the flow pattern and are calculated in conjunction with a flow regime map. The flow regime map of WCOBRA/TRAC-TF2 is discussed in Section 4 and the details are not repeated here. For the sake of completeness, the basic flow regime map is redrawn in Figure 6-6.

6.3.1 Bubbly Slug Flow Regime

In this section, the interfacial heat transfer coefficient of the three regions in Figure 6-6 labeled "bubbly flow," "bubbly slug transition," and "bubbly slug," here referred to as bubbly slug flow, is discussed. The logic used in determining pure bubbly and transition flows is explained in Section 4 and is repeated below.

For void fractions less than 30%, slugs do not form, irrespective of the mass flux. For void fractions between 30% and 50%, slugs and bubbles coexist for $G < 2000$ kg/m^2-s and slug formation is prohibited for $G > 2700$ kg/m^2-s. The intermediate mass-flux range is treated as a transition region.

The convective-heat transfer coefficients during condensation and flashing are described below. The direct sensible heat transfer between gas and liquid also is possible only in the presence of non-condensables. However, these models are flow regime dependent and very similar to vapor-to-interface heat transfer models. Consequently, the calculation of H_{CHTA} is included in this section, even though it is meaningless unless non-condensables are present.

Model Basis

If the liquid temperature is smaller than the saturation temperature, the liquid side is in condensation mode. To calculate the heat transfer coefficient during condensation, the correlation developed by Chen and Mayinger (1992) is used. The correlation is given by:

$$Nu = 0.185\, Re^{0.7} \sqrt{Pr_\ell} \tag{6-144}$$

where:

$$Nu = \frac{h_{i\ell} D_b}{k_\ell} \tag{6-144a}$$

and

$$Re = \frac{\rho_\ell D_b (V_g - V_\ell)}{\mu_\ell} \tag{6-144b}$$

In their experiments, bubbles were produced by blowing saturated vapor into subcooled liquid slowly moving downward. Heat transfer data are obtained at the interface of condensing bubbles using

holographic interferometry and high-speed photography. Ethanol, propanol, refrigerant-113, and water were used as working fluids. These fluids provided Prandtl numbers ranging from 1.96 to 14.4. The experimental Reynolds number ranged from ~350 to ~7000. However, the Reynolds number for only water data had a shorter range from ~4000 to ~7000. In deriving the correlation given by Equation 6-144, Chen and Mayinger used the experimentally observed bubble detachment diameter in defining Re and Nu. In the code, the Sauter mean diameter is given by:

$$D_b = 2\,L_o \tag{6-145}$$

where L_o is the Laplace coefficient defined as:

$$L_o = \sqrt{\frac{\sigma}{g\,(\rho_\ell - \rho_g)}} \tag{6-146}$$

Chen and Mayinger recommend the use of their correlation for $Re < 10^4$ and $Ja < 80$. The Jakob number, Ja, is the ratio of liquid sensible heat to latent heat and is defined as:

$$Ja = \frac{\rho_\ell c_{p,\ell} \Delta T_{sub}}{\rho_g h_{fg}} \tag{6-147}$$

For $Ja < 80$, the condensation is controlled by heat transfer at the phase interface. If $Ja > 100$, the collapse of the vapor bubble is controlled by the inertia of the liquid mass when entering into the space set free by the condensing bubble. The Chen and Mayinger correlation is valid for heat transfer-controlled condensation. However, in the code, it is also used in the inertia-controlled regime, independently of the Jakob number.

At high Reynolds numbers, it is assumed that the Nusselt number is independent of the Reynolds number. This upper limit is calculated through the Chen and Mayinger correlation by setting $Re = 10^4$, which yields:

$$Nu_{max} = 116.7\,\sqrt{Pr_\ell} \tag{6-148}$$

For water, $Re = 10^4$ corresponds to 0.5–0.6 m/s bubble-relative velocities, which are higher than observed terminal bubble-rise velocities. Thus, for quasi-steady conditions, the Reynolds numbers are usually smaller than 10^4. At low Reynolds numbers, the Chen and Mayinger correlation yields Nusselt numbers smaller than solid-sphere correlations, which is not realistic. Thus, the solid-sphere heat transfer correlation of Whitaker (Whitaker, 1972) is used as the lower limit of the Nusselt number. The original correlation is given by:

$$Nu = 2 + (0.4\,\sqrt{Re} + 0.06\,Re^{2/3})\,Pr_\ell^{0.4} \left(\frac{\mu_w}{\mu_\infty}\right) \tag{6-149}$$

where the Reynolds and Nusselt numbers are defined based upon the sphere diameter, and μ_w and μ_∞ are the fluid viscosities at the sphere wall and far field, respectively. In the code, the viscosity correction is neglected and the bubble diameter is used for Reynolds number. The following equation is obtained:

$$Nu = 2 + (0.4\sqrt{Re} + 0.06\,Re^{2/3})\,Pr_\ell^{0.4} \tag{6-150}$$

Figure 6-7 shows the code-calculated Nu as a function of Re for two values of Pr that are representative of high and low limits for water. Once the liquid-side heat transfer coefficient is obtained, the heat transfer factor for condensation is calculated as:

$$H_{ALVE,bubbly\ slug} = h_{i\ell} A_{i,bubbly\ slug} \tag{6-151}$$

where $A_{i,bubbly\ slug}$ is the total interfacial area given in Section 4.4.2.

During flashing, where $T_\ell > T_{sat}$, the liquid-side heat transfer factor is calculated using the following approximate model:

$$\left[\qquad\qquad\right]^{a,c} \tag{6-152}$$

The basis for this model is its high magnitude, which quickly decreases the liquid temperature to saturation temperature. The flashing heat transfer coefficients are heuristic and are developed specifically for implementation into WCOBRA/TRAC-TF2. This model is flow regime independent and is used for all flow patterns. It will be used in the other flow regimes as well.

For both condensation and flashing, the vapor-to-interface and gas-to-liquid heat transfer coefficients are given by:

$$h_{g\ell} = h_{ig} = 1000\ W/m^2K \tag{6-153}$$

Thus,

$$H_{CHTA,bubbly\ slug} = H_{CHTI,bubbly\ slug} = 1000\ A_{i,bubbly\ slug} \tag{6-154}$$

This is also an engineering approximation. This model is motivated by the fact that during quasi-steady conditions, the vapor-side heat transfer coefficient is commonly about an order of magnitude smaller than the liquid-side heat transfer coefficients.

In subcooled boiling, vapor is generated near the heater wall even though the bulk liquid is subcooled. However, part of this vapor condenses when in contact with the subcooled bulk liquid. Thus, during subcooled boiling, a mechanistic model is required to account for this interfacial condensation. The model suggested by Lahey and Moody (Lahey and Moody, 1977) is used:

$$q_{cond} = H_o \frac{D_h}{4} h_{fg} \frac{\rho_\ell \rho_g}{\rho_\ell - \rho_g} \alpha (T_{sv} - T_\ell) \quad (6\text{-}155)$$

where H_o is an empirical constant and q_{cond} is the interfacial condensation heat flux. Setting:

$$\pi D_h q_{cond} \Delta x = H_{ALVE,sub} (T_{sv} - T_\ell) \quad (6\text{-}156)$$

then:

$$H_{ALVE,sub} = H_o B_{cell} h_{fg} \frac{\rho_\ell \rho_g}{\rho_\ell - \rho_g} \alpha \quad (6\text{-}157)$$

The code uses $H_o = 0.075$ (s-K)$^{-1}$ as suggested by Lahey and Moody.

Model as Coded

Calculations of the interfacial heat transfer coefficients and the interfacial areas are performed in subroutine HTIF for 1D components. The liquid side heat transfer factors $ALVE_{bubblyslug}$ and $ALV_{bubblyslug}$, and the vapor side heat transfer factors $CHTI_{bubblyslug}$ and $CHTA_{bubblyslug}$, are calculated as follows:

In the case of liquid subcooling ($T_\ell < T_{sv}$), the liquid side heat transfer coefficient is calculated as:

$$h_{i\ell} = \begin{cases} \text{maximum} \begin{cases} \frac{k_\ell}{D_b} \cdot \left(0.185\, Re^{0.7} \sqrt{Pr_\ell}\right) \\ \frac{k_\ell}{D_b} \cdot \left[2 + \left(0.4 \sqrt{Re} + 0.06\, Re^{2/3}\right) Pr_\ell^{0.4}\right] \end{cases} & Re \le 10^4 \\ \frac{k_\ell}{D_b} \cdot \left(116.7 \sqrt{Pr_\ell}\right) & Re > 10^4 \end{cases} \quad (6\text{-}158)$$

and the liquid side heat transfer factor is then determined as:

$$H_{ALVE,bubbly\ slug} = h_{i\ell} A_{i,bubbly\ slug} \quad (6\text{-}159)$$

where $A_{i,bubblyslug}$ is the interfacial area defined in Section 4.4.2.

During flashing, where $T_\ell > T_{sat}$, the liquid side heat transfer factor is calculated using following equation:

[ ] a,c (6-160)

For both condensation and flashing, the vapor-to-interface and gas-to-liquid heat transfer coefficients are given by Equations 6-153 and 6-154.

To account for the effect of subcooled boiling (assumed to occur only in bubbly flow), the subcooled boiling heat transfer factor is superimposed on the bubbly flow liquid side heat transfer factor through a weighting factor as:

$$H_{ALVE,bubbly,sub} = W_{sub} H_{ALVE,sub} + (1 - W_{sub})\ H_{ALVE,bubbly} \tag{6-161}$$

where the weighting factor is given by:

$$0 \le W_{sub} = 10\,(0.2 - \alpha) \le 1 \tag{6-162}$$

and the $H_{ALVE,sub}$ is defined in Equation 6-157.

As shown by Equation 6-162, if the void fraction is greater than 0.2, the weighting factor becomes zero. Thus, for the subcooled-boiling effect to be present in the interfacial heat transfer, the following conditions must be satisfied:

1. The liquid temperature must be less than saturation temperature.
2. Subcooled boiling must be occurring ($h_\Gamma > 0$).
3. The void fraction must be less than 20%.

Scaling Considerations and Conclusions

An assessment of the interfacial heat transfer model of Chen and Mayinger (1992) regarding the experimental bubble condensation data over a range of pressure from 1.0 to 6.2 MPa, subcooling from 15 to 100 K, and a Reynolds number up to 5000, was provided in Section F1.1.4 of LA-UR-00-910 (Spore, et al., 2000). As discussed therein, the models for the interfacial heat transfer for the bubbly flow regime are rather simplistic but are judged to be adequate for the purpose of simulating LOCA events in a PWR. The interfacial heat transfer in bubbly flow is relatively large and both phases are near saturation. Therefore, inaccuracies in the model have a small or negligible effect on the results.

6.3.2 Churn Flow Regime

Model Basis

The churn flow regime is assumed when $0.5 < \alpha < 0.75$. This regime is modeled as a simple transition between the bubbly or slug and annular-mist flow regimes. Interfacial areas and heat transfer coefficients are calculated for the slug and annular-mist flow regimes, and then values for the churn flow regime are calculated using the weighting factor W_t, given by Equation 4-88 described in Section 4.4.3.

Model as Coded

The closure parameters are obtained from the following relationship:

$$X_{transition} = (1 - W_t)X_{bubbly\ slug_{(\alpha = 0.5)}} + W_t X_{annular\ mist_{(\alpha = 0.75)}} \quad (6\text{-}163)$$

where X corresponds to either A_i, H_{ALVE}, H_{ALV}, H_{CHTI}, or H_{CHTA}. The linear weighting factor, W_t, is defined based upon the void fraction as follows:

$$0 \le W_t = \frac{(\alpha - 0.5)}{(0.75 - 0.5)} \le 1 \quad (6\text{-}164)$$

Note that for flashing, the calculated value of H_{ALV} is compared with Equation 6-152 and the maximum is chosen.

Scaling Considerations and Conclusions

The churn flow regime is designed to be a simple transition between bubbly slug and annular-mist flows. Therefore, the same considerations to the regimes of bubbly slug flow and annular-mist flow apply.

6.3.3 Annular-Mist Flow Regime

Model Basis

The annular-mist flow regime is assumed when $\alpha \ge 0.75$, independent of mass flux. A schematic of the flow pattern in annular-mist flow is shown in Figure 6-8. As shown, the liquid flows as droplets in the gas core and also forms a liquid film on a solid wall. Therefore, a more rigorous treatment requires at least two fields for the liquid phase. In the 1D components of WCOBRA/TRAC-TF2, the liquid phase is represented as a single field. Thus, the characteristics of liquid droplets and film must be properly accounted for by a single field. The following generic equation shows the way the various closure parameters are calculated in annular-mist flow:

$$X = (1 - W_f)(X_{drop} + X_{film}) + W_f X_{drop,max} \quad (6\text{-}165)$$

where X represents either H_{ALVE}, H_{ALV}, H_{CHTI} or H_{CHTA}. The weighting factor, W_f, given in Equation 6-166, is introduced to account for the fact that beyond a certain limit in phasic velocities, all the liquid will be entrained in the form of droplets, thus no liquid film will exist. The phasic velocities are compared to a critical velocity defined based upon the Helmholtz instability and given by Equation 6-167.

$$W_f = \begin{cases} 0 & \text{if } \max(V_\ell, V_g) < 10\ V_c \\ 0.5\dfrac{\max(V_\ell, V_g)}{V_c} - 5 & \text{if } 10\ V_c \le \max(V_\ell, V_g) \le 12\ V_c \\ 1 & \text{if } \max(V_\ell, V_g) > 12\ V_c \end{cases} \quad (6\text{-}166)$$

$$V_c = \left[\frac{g\sigma(\rho_\ell - \rho_g)}{\rho_g^2}\right]^{1/4} \quad (6\text{-}167)$$

Figure 6-9 illustrates the transition from annular-mist to mist flow as a function of pressure for saturated water. As shown in the figure, the critical velocity is a strong function of pressure and decreases rapidly with increasing pressure.

During condensation and flashing, the heat transfer factors are calculated as:

$$H_{ALVE} = (1 - W_f)(H_{ALVE,drop} + H_{ALVE,film}) + W_f H_{ALVE,drop,max} \quad (6\text{-}168)$$

$$H_{ALV} = (1 - W_f)(H_{ALV,drop} + H_{ALV,film}) + W_f H_{ALV,drop,max} \quad (6\text{-}169)$$

$$H_{CHTI} = (1 - W_f)(H_{CHTI,drop} + H_{CHTI,film}) + W_f H_{CHTI,drop,max} \quad (6\text{-}170)$$

and

$$H_{CHTA} = (1 - W_f)(H_{CHTA,drop} + H_{CHTA,film}) + W_f H_{CHTA,drop,max} \quad (6\text{-}171)$$

During flashing, the maximum H_{ALV} predicted by either Equation 6-169 or Equation 6-152 is used. Liquid- and vapor-side heat transfer coefficients for the droplets and liquid film are described in the following subsections.

Mist Flow Heat Transfer Coefficients

The liquid-side interfacial heat transfer coefficient, $h_{i\ell}$, is calculated using the transient conduction solution in liquid droplets. The conduction solution is calculated using the equation by Andersen (1973):

$$Nu = \frac{2\pi^2}{3} C_c \quad (6\text{-}172)$$

where:

$$Nu = \frac{h_{i\ell} D_d}{k_\ell} \quad (6\text{-}173)$$

and

$$\left[\quad\right]^{a,c} \quad (6\text{-}174)$$

where D_d is defined in Equation 4-95. Knowing the liquid-side heat transfer coefficient, the heat transfer factors become:

$$H_{ALVE,drop} = h_{i\ell} A_{i,drop} \quad (6\text{-}175)$$

$$H_{ALVE,drop,max} = h_{i\ell} A_{i,drop,max} \quad (6\text{-}176)$$

during condensation, and:

$$H_{ALV,drop} = h_{i\ell} A_{i,drop} \tag{6-177}$$

$$H_{ALV,drop,max} = h_{i\ell} A_{i,drop,max} \tag{6-178}$$

during flashing.

The above interfacial area terms are calculated as described in Section 4.4.4.

During both condensation and evaporation, the vapor-side heat transfer coefficient is calculated using the correlation developed by Ryskin (1987), given by:

$$Nu = 2 + 0.92\sqrt{V^*_{max}\, Pe} \tag{6-179}$$

In Equation 6-179, the Nusselt and Peclet numbers are defined as:

$$Nu = \frac{h_{ig} D_d}{k_g} \tag{6-180}$$

and

$$Pe = Re_g\, Pr_g = \frac{\rho_g c_{p,g} D_d V_r}{k_g} \tag{6-181}$$

respectively, where V_r is obtained from a force balance between gravity and drag using an interfacial-drag coefficient of 0.44, which yields (Ishii, 1977),

$$V_r = 2.462 \sqrt{g \frac{\rho_\ell - \rho_g}{\rho_g} \frac{D_d}{2}} \tag{6-182}$$

The maximum dimensionless circulation velocity at the surface of the drop is defined as:

$$V^*_{max} = \frac{1.5}{1 + \frac{2.8\,(1+2\lambda)\,(2+3\kappa)}{(2+3\lambda)\sqrt{Re_g}}} \tag{6-183}$$

where:

$$Re_g = \frac{\rho_g D_d V_r}{\mu_g} \tag{6-184}$$

$$\lambda = \sqrt{\frac{\rho_\ell \mu_\ell}{\rho_g \mu_g}} \tag{6-185}$$

and

$$\kappa = \frac{\mu_\ell}{\mu_g} \tag{6-186}$$

Thus, the vapor-side heat transfer factors can be calculated as:

$$H_{CHTI,drop} = h_{ig,drop} A_{i,drop} \tag{6-187}$$

and

$$H_{CHTI,drop,max} = h_{ig,drop} A_{i,drop,max} \tag{6-188}$$

The same model given by Equation 6-179 is used to calculate the direct sensible heat transfer factor, H_{CHTA}, between the gas and liquid phases. In order to calculate H_{CHTA}, the mixture properties are replaced by non-condensable gas properties in the model, i.e.:

$$Nu = \frac{h_{g\ell} D_d}{k_a} \tag{6-189}$$

and

$$Pe = Re_g \, Pr_a = \frac{\mu_a \rho_g c_{p,a} D_d V_r}{\mu_g k_a} \tag{6-190}$$

and the circulation velocity is similarly expressed by:

$$V^*_{max} = \frac{1.5}{1 + \frac{2.8(1+2\lambda)(2+3\kappa)}{(2+3\lambda)\sqrt{Re_g}}} \tag{6-191}$$

$$\lambda = \sqrt{\frac{\rho_\ell \mu_\ell}{\rho_a \mu_a}} \tag{6-192}$$

and

$$\kappa = \frac{\mu_\ell}{\mu_a} \tag{6-193}$$

And the appropriate heat transfer factors are defined such that:

$$H_{CHTA,drop} = h_{g\ell,drop} A_{i,drop} \tag{6-194}$$

and

$$H_{CHTI,drop,max} = h_{g\ell,drop} A_{i,drop,max} \tag{6-195}$$

Annular-mist Flow Heat Transfer Coefficients

For the liquid film, both the liquid- and vapor-side heat transfer coefficients are calculated using a Stanton number correlation given by:

[ ]^{a,c} (6-196)

This correlation was originally developed by Bankoff (Bankoff, 1980) for the liquid-side heat transfer coefficient during stratified co-current steam-water flow. For saturated water, the effect of slip ratio and pressure on the calculated Stanton number is illustrated in Figure 6-10. For the original correlation, the Stanton number is defined based upon the liquid properties and liquid velocity. In the code, the Stanton number is defined as:

$$St \equiv \frac{h_{i\ell}}{\rho_\ell c_{p,\ell} V_\ell} \tag{6-197}$$

$$St \equiv \frac{h_{ig}}{\rho_g c_{p,g} \left| V_g - V_\ell \right|} \tag{6-198}$$

or

$$St \equiv \frac{h_{g\ell}}{\rho_a c_{p,a} \left| V_g - V_\ell \right|} \tag{6-199}$$

to calculate the liquid-side, the vapor-to-interface, or the gas-to-liquid heat transfer coefficient.

Thus, the heat transfer factors can be obtained as:

$$H_{ALVE,film} = h_{i\ell} A_{i,film} \tag{6-200}$$

$$H_{ALV,film} = h_{i\ell} A_{i,film} \tag{6-201}$$

$$H_{CHTI,film} = h_{i\ell} A_{i,film} \tag{6-202}$$

and

$$H_{CHTA,film} = h_{g\ell} A_{i,film} \tag{6-203}$$

Model as Coded

For the annular-mist flow regime, H_{ALVE}, H_{ALV}, H_{CHTI} or H_{CHTA} for the mist and annular-mist flows are calculated as described in the 'Model Basis' section above.

Scaling Considerations and Conclusions

Developmental assessment for the annular-mist flow regime interfacial heat transfer can be found in Section F1.2.3 of the TRAC-M Theory Manual, LA-UR-00-910 (Spore, et al., 2000). While the models are physically based, data assessment is limited and model deficiencies are identified in that report. However, for the purpose of modeling LOCA transients, the importance of the annular-mist interfacial heat transfer is limited to condensation in the cold leg as cold safety injection (SI) water is injected in the pipe. As discussed in Section 6.3.6, a special cold leg condensation model was developed to simulate the SI water direct condensation. The cold leg condensation model is also applied to the annular-mist flow regime in the cold leg node connected to the SI line. Detailed assessment of the model is provided in Section 17 over a wide range of conditions and scales. Therefore the uncertainty in the condensation models is accounted for in the overall WCOBRA/TRAC-TF2 code bias and uncertainty.

6.3.4 Horizontal Stratified Flow Regime

Model Basis

The criteria for the selection of the horizontal stratified flow regime were discussed in Section 4.4.5. The closure of the mass, momentum, and energy equations requires the interfacial heat transfer coefficients $h_{i\ell}$, h_{ig}, and $h_{g\ell}$. These coefficients are needed to define the heat transfer rates per unit volume for the interface-to-liquid heat transfer, the interface-to-gas heat transfer, and the liquid-to-gas sensible heat transfer, respectively. This section will elaborate on the individual models for horizontal stratified flow as coded within WCOBRA/TRAC-TF2.

Model as Coded

By definition, the heat transfer factor for a given flow regime is expressed as the product of the interfacial heat transfer coefficient and the interfacial area corresponding to that flow regime. The following sections will focus on four specific heat transfer factors:

$$H_{ALV} = \left(h_{i\ell}\right)_{flashing} \cdot A_i \tag{6-204}$$

$$H_{ALVE} = \left(h_{i\ell}\right)_{evap/cond} \cdot A_i \tag{6-205}$$

$$H_{CHTI} = h_{ig} \cdot A_i \tag{6-206}$$

$$H_{CHTA} = h_{g\ell} \cdot A_i \tag{6-207}$$

The heat transfer factors H_{ALV} and H_{ALVE} correspond to interface-to-liquid heat transfer via flashing for $T_\ell \geq T_{sat}$ and via evaporation or condensation for $T_\ell < T_{sv}$. Similarly, the heat transfer factors H_{CHTI} and H_{CHTA} correspond to interface-to-gas heat transfer and liquid-to-gas sensible heat transfer, respectively.

Under fully stratified flow conditions, the liquid-side heat transfer coefficient is evaluated using the constant Stanton number criterion suggested by Linehan et al. (1972), where:

$$St = \frac{h_{i\ell,st}}{\rho_\ell c_{p,\ell} V_\ell} = 0.0073 \tag{6-208}$$

The liquid-side heat transfer factors thus are defined by:

$$H_{ALVE,strat} = h_{i\ell,st} \cdot A_{i,st} \tag{6-209}$$

for evaporation/condensation, where the stratified flow interfacial area is calculated as discussed in Section 4. For flashing,

$$H_{ALV,st} = H_{ALV,map,st} \tag{6-210}$$

When the flow is not fully stratified (interpolation region), the code interpolates between the heat transfer factors for stratified flow, as calculated above, and the values otherwise determined with respect to the basic flow regime map. In general form, this can be expressed as:

$$X_{map,st} = (1 - W_{st}) \cdot X_{map} + W_{st} \cdot X_{st} \tag{6-211}$$

where X represents the heat transfer factors H_{ALVE} and H_{ALV} and where $0 \leq W_{st} \leq 1$. The weighting factor W_{st} is calculated using Equation 4-117 in Section 4.

[

$$\left[\right]^{a,c}_{a,c} \tag{6-212}$$

where:

$$\left[\right]_{a,c} \tag{6-213}$$

The basis for this model is its high magnitude, which quickly decreases the liquid temperature to saturation temperature. This model is flow regime independent and is used for all flow patterns.

Finally, no modifications are made to the vapor-side and sensible heat transfer factors for stratified flow. Thus,

$$H_{CHTI,map,st} = H_{CHTI,map} \tag{6-214}$$

and

$$H_{CHTA,map,st} = H_{CHTA,map} \tag{6-215}$$

It is noted, if the cold leg condensation model is turned on, the liquid side heat transfer factor and vapor side heat transfer factor are subject to the cold leg condensation model which is discussed in Section 6.3.6.

Scaling Considerations and Conclusions

As discussed for annular-mist flow, the Bankoff correlation (1980), which is used to estimate the heat transfer coefficient in liquid films, was originally developed for stratified condensing co-current flow. Spore et al. (2000) compared the constant Stanton number criterion proposed by Linehan et al. (1972) with the Bankoff correlation. The comparison shows that if the slip ratio is on the order of unity, the two correlations are in order of magnitude agreement. Increasing the pressure increases the Stanton number predicted by the Bankoff correlation. However, even with pressure variation, it is still considered that the Bankoff and the Linehan et al. correlations are accurate within ±100%, which is considered to be satisfactory. Furthermore, Spore et al. (2000) compared the Kim (1985) model, which is an empirical model developed from the condensation rates in countercurrent stratified flow with a wide Re range, with the Linehan model. The constant Stanton number correlation (Linehan et al., 1972) is the same order of magnitude as the majority of Kim's data.

Given the nature of PWR LOCA transients (both large and small breaks), the accuracy of the interfacial heat transfer model for horizontal stratified flow is only a lower order factor compared with the transition between stratified flow to bubbly flow, which dictates an enormous difference in interfacial heat transfer, and the special cold leg condensation model in Section 6.3.6. Thus, the Linehan (1972) model is an acceptable solution for the prediction of interfacial heat transfer for horizontal stratified flow in WCOBRA/TRAC-TF2. Moreover, as indicated in Section 6.3.6, the cold leg condensation model is applied to the horizontal stratified flow regime in the cold leg node connected to the SI line. Detailed assessment of the model is provided in Section 17 over a wide range of conditions and scales. Therefore, the uncertainty of the condensation models is accounted for in the overall WCOBRA/TRAC-TF2 code bias and uncertainty.

6.3.5 Wavy Dispersed Flow Regime

Model Basis

[

]^{a,c}

Model as Coded

The liquid field and the droplet field parameters are combined as follows:

$$\left[\qquad\qquad\right]^{a,c} \tag{6-216}$$

[

]^{a,c}

After solving for the liquid side heat transfer coefficient, the relevant condensation heat transfer factors can be defined such that:

$$H_{ALVE,drop} = h_{i\ell,drop} \cdot A_{i,drop} \tag{6-217}$$

The above interfacial area terms likewise are calculated as specified in Section 4.4.6.

[

]^{a,c}

$$H_{CHTI,drop} = h_{ig,drop} \cdot A_{i,drop} \quad (6\text{-}218)$$

[

]^{a,c}

$$H_{CHTA,drop} = h_{g\ell,drop} \cdot A_{i,drop} \quad (6\text{-}219)$$

As with the liquid-side and vapor-side models, the above interfacial heat transfer terms and the droplet diameter D_d are calculated as described in Section 4.4.6.

Alternatively, for the bulk liquid layer, all three heat transfer coefficients ($h_{i\ell}$, h_{ig}, and $h_{g\ell}$) are defined as a function of the Stanton number such that:

[ ]^{a,c} (6-220)

[

]^{a,c}

The bulk liquid layer field heat transfer factors in turn are defined by:

$$H_{ALVE,layer} = h_{i\ell,layer} \cdot A_{i,layer} \quad (6\text{-}221)$$

$$H_{CHTI,layer} = h_{ig,layer} \cdot A_{i,layer} \quad (6\text{-}222)$$

$$H_{CHTA,layer} = h_{g\ell,layer} \cdot A_{i,layer} \quad (6\text{-}223)$$

where the bulk liquid layer interfacial area defined in Section 4.4.6.

Scaling Considerations and Conclusions

[

]^{a,c} Therefore, the uncertainty in the condensation models is accounted for in the overall WCOBRA/TRAC-TF2 code bias and uncertainty.

6.3.6 Special Model: Cold Leg Condensation Model

Model Basis

Following a postulated Small Break LOCA (SBLOCA) in a PWR, steam is generated in the reactor core by decay heat. To help core recovery, cold water from the emergency core cooling system (ECCS) is injected into the cold leg. As the SI comes into contact with the steam in the cold leg, direct contact condensation occurs. The direct contact condensation in the cold leg due to safety injection is usually called SI condensation in literatures. In this report, the name of cold leg condensation is used to include both SBLOCA and Large Break LOCA (LBLOCA). The cold leg condensation is expected to have a rather important effect on the thermal hydraulic behavior of the system.

In particular, the large amount of condensation results in steam volume reduction in the RCS and RCS pressure is reduced. The lower RCS pressure leads to an increase in the SI flow rate and a decrease in break flow. The increase in the SI flow rate helps maintain the RCS mass inventory and core water level, and also accelerates the RCS depressurization process. Once the RCS pressure reduces to the accumulator check valve setpoint pressure, injection of accumulator water leads to core recovery. In general, the cold leg condensation impacts the RCS pressure transient, the SI flow rate, the break flow which then determines the system inventory, the core water level, the steam generation rate which in turn affects condensation, and the accumulator injection. As a result, a mis-prediction of the direct condensation could lead to compensating errors and mis-prediction of the transient. [

]^{a,c}

The pressure range when this type of condensation is expected to occur is from loop seal clearance [ ]^{a,c} to the accumulator setpoint pressure [ ]^{a,c} (Figure 6-11), but the lower bound could be extended to lower pressure if the condensation by accumulator (ACC) water is considered.

One of the main features of cold leg condensation is that the flow in the cold leg is expected to be in the horizontal stratified flow regime. Compared with bubbly flow, stratified flow is characterized by low liquid-gas interface area and low interfacial heat transfer coefficients. However, as SI water is injected into the cold leg, this leads to turbulence and mixing in the region, which enhance the cold leg condensation rate.

For LBLOCA, condensation is of the highest relative importance during the refill period. The condensation process in the cold leg helps to reduce ECC bypass flow at the top of the downcomer, promoting ECC penetration. The condensation effects are reduced during the reflood period as the accumulators end their injection and the lower flow pumped injection continues, but condensation still influences the break flow rate, the downcomer and core water inventory, and the water subcooling in the downcomer. [ ]^{a,c} Different from stratified flow during the cold leg condensation in SBLOCA, the flow regime in the cold leg during a large break LOCA is rather complicated.

To correctly predict this condensation contribution, a specific cold leg condensation model is developed. [ ]^{a,c}

[ ]^{a,c} The condensation correlation is developed using Westinghouse Condensation on Safety Injection (COSI) experimental data (Gros d'Aillon, 1987) and was then implemented in WCOBRA/TRAC-TF2.

During a SBLOCA, when cold SI water is injected into the cold leg with stratified flow, condensation exists in the SI jet surface and the stratified flow interface. The interaction between the SI jet and the water layer in the cold leg leads to a more complicated steam-water interface. To simplify the construction of the empirical condensation model, [

]^{a,c}. In reality the flow regime in the region near the jet will be very complicated, but this is a level of detail that is beyond the coarseness of the model considered for the purpose of LOCA simulation.

In the vicinity of the SI injection, the turbulence brought in by the SI jet as it impinges on the stratified liquid layer in the cold leg agitates the bulk liquid. This region is usually called the mixing zone (Figure 6-12), because the SI jet impinges into the stratified cold leg water and causes rapid mixing there.

The COSI experiment results showed that a large fraction of total condensation occurs in this mixing zone. The temperature profile from thermocouple rakes showed the similarity between the profile near the SI jet and the profile further downstream (Gros d'Aillon, 1987). Furthermore, Shimeck (1988) indicated that the Framatome COSI test facility considered a much shorter cold leg length than the Westinghouse test facility, but comparison between the Framatome test data and the Westinghouse test data showed that a much shorter cold leg only led to a very moderate decrease in the condensation heat transfer rate. Thus, the cold leg condensation model assumes that the majority of condensation occurs in a small region near the SI injection port and the condensation outside the mixing zone is negligible. This assumption is also adopted by several existing cold leg condensation models (Shimeck 1988; Janicot and Bestion 1993).

The cold leg condensation model [

]^{a,c} will be validated against LBLOCA cold leg condensation experiments in Sections 17 and 19.

Model as Coded

When the flow in the cold leg is stratified without SI injection, the vapor and liquid phases are co-current flow and separated by the horizontal interface. There is condensation in the stratified flow due to the subcooled liquid layer. However, the condensation rate is extremely low because a saturated layer of liquid will develop near the interface which will insulate the bulk of the cold liquid from the vapor. Due to the low turbulence, the layer of saturated liquid developing in the proximity of the interface essentially limits the condensation rate to the rate of conduction heat transfer within the liquid layer.

[

]^{a,c}

[

]^{a,c}

The condensation heat transfer rate at the vapor-liquid interface near the mixing zone is expressed as a function of heat transfer area, heat transfer coefficient and temperature difference.

$$Q_{cond} = A_i h_i (T_{sat}(P) - T_{SI}) \tag{6-224}$$

where h_i is the interfacial heat transfer coefficient, A_i is the interfacial area and the temperature gradient is the temperature difference between the saturated steam and the SI water. The interfacial heat transfer area A_i is a complicated value to determine. The area of the mixing zone is used as the heat transfer area A_i, and can be affected by several factors.

[

]^{a,c}

$$\left[\quad\right]^{a,c} \tag{6-225}$$

[ ]^{a,c} The condensation heat transfer coefficient is represented by the following dimensionless Nusselt number:

$$Nu = \frac{hL_c}{k_\ell} \tag{6-226}$$

where k_ℓ is the thermal conductivity of the SI water and L_c is the characteristic length determined by the cold leg diameter and liquid volume fraction. [

]^{a,c} Combining Equations 6-224, 6-225, and 6-226 leads to:

$$Nu = \frac{hL_c}{k_\ell} = \frac{Q_{cond}}{A\Delta T}\frac{L_c}{k_\ell} = \frac{Q_{cond}}{d_{SI}k_\ell \Delta T} \tag{6-227}$$

[

]^{a,c}

Since the turbulence in the bulk liquid of the cold leg is brought in by the SI jet, the turbulence intensity will be related to the SI jet Reynolds number, which is defined using the SI water velocity, density, viscosity, and SI pipe diameter as follows:

[ ]^a,c (6-228)

where [ ]^a,c.

In a heat transfer problem, the Prandtl number usually indicates the relative magnitude between the momentum boundary layer and the thermal boundary layer, while the Reynolds number only reflects the momentum boundary layer. The Prandtl number is defined as follows:

$$Pr_\ell = \frac{c_{p,\ell}\mu_\ell}{k_\ell} \tag{6-229}$$

where $c_{p,\ell}$ is the liquid specific heat. The Prandtl number is a function of system pressure and temperature.

Next, a correlation between the Nusselt number and Reynolds number is established in a form similar to the traditional forced convection heat transfer correlation:

$$Nu = CRe_\ell^m Pr_\ell^n \tag{6-230}$$

where the coefficients C, m, and n are to be determined using [ ]^a,c.

During the cold leg condensation process, the SI water is heated up from the SI temperature in the SI pipe to the saturation temperature at the vapor-liquid interface. The fluid properties depend on a reference fluid temperature, [ ]^a,c.

The reference fluid temperature during the cold leg condensation process could be determined by the temperature profile inside the liquid. [

]^a,c

[ ]^a,c (6-231)

$$\rho_\ell = \rho(T_{\ell,ref}) \tag{6-232}$$

$$\mu_\ell = \mu(T_{\ell,ref}) \quad (6\text{-}233)$$

$$k_\ell = k(T_{\ell,ref}) \quad (6\text{-}234)$$

$$c_{p,\ell} = c_p(T_{\ell,ref}) \quad (6\text{-}235)$$

[

]^{a,c} were selected to determine the fitting coefficients. A different set of data was then utilized to validate the model. The Westinghouse horizontal injection COSI dataset, Framatome COSI (Gros d'Aillon, 1987) dataset and Rig-of-Safety Assessment (ROSA) cold leg condensation (Kawaji et al., 1986) dataset were used to independently perform the validation and verification of the model, discussed in Section 17.

The coefficients C, m, and n were determined to be [ ]^{a,c}. Therefore, the correlation for cold leg condensation is given by:

[ ]^{a,c} (6-236)

The comparison between the calculated Nusselt number and the measured Nusselt number for the fitted data points is shown in Figure 6-15.

The cold leg condensation heat transfer rate is calculated using the Nusselt number, [ ]^{a,c}

[ ]^{a,c} (6-236a)

[

]^{a,c}

[ ]^{a,c} (6-236b)

[

]^{a,c}

Scaling and Applicability Considerations

The cold leg condensation correlation was obtained using data from the Westinghouse vertical COSI test facility, which geometrically is a 1:100 scale of a PWR cold leg. The SI line configuration in the Westinghouse vertical COSI facility is a [ ]^{a,c}. The steam temperature and SI temperature ranges are other scaling issues that need to be addressed.

Important scaling parameters associated with the cold leg condensation are shown for IETs, SETs, and PWRs in Table 6-2. The Westinghouse horizontal injection COSI tests, Framatome COSI tests, ROSA SB-CL-05 COSI tests, Upper Plenum Test Facility (UPTF) test 8A and UPTF test 25A are part of the verification and validation. Beaver Valley Unit 1 and V. C. Summer Unit 1 are the pilot plants for the FSLOCA methodology.

The pressure range of the Westinghouse COSI test is [ ]^{a,c}, which is a good representation of the pressure range for cold leg condensation during a postulated PWR SBLOCA. The Framatome COSI test has a pressure as low as [ ]^{a,c}, which extends the applicability of the cold leg condensation model for small break LOCA analysis. The pressure of UPTF 8A and 25A reaches 0.26 MPa, which covers the pressure range of a large break LOCA.

The SI temperature range of the Westinghouse COSI tests is only [ ]^{a,c}. However, the upper limit of the SI temperature in the Framatome COSI tests is [ ]^{a,c}. The range of [ ]^{a,c} is representative of typical plant SI temperature.

The Westinghouse COSI facility has orientations of [ ]^{a,c}. The orientation of SI line in the Framatome COSI facility is [ ]^{a,c}. The orientation of the SI line in the UPTF test facility is 0°-60°. A sensitivity study of the SI injection angle is provided in Section 17.3.4.

The cold leg diameter is not included in the cold leg condensation correlation. Thus, it is not a scaling factor. The influence of the SI pipe diameter is combined into the Reynolds number. The range of Reynolds numbers in the Westinghouse vertical injection COSI tests is [ ]^{a,c}, which is lower than the range in the pilot plants [ ]^{a,c}. However, UPTF is a full scale facility, which covers full scale large break LOCA. The Reynolds number range of UPTF 8A and UPTF 25A is 2.61×10^{5} to 1.05×10^{7}, which covers conditions expected in a small or large break LOCA.

The Prandtl number range of the Westinghouse COSI test is consistent with the range for the pilot plants.

Cold Leg Water Level Effect

[

]^{a,c}

SI Jet Break-up

[

]^{a,c}

Steam Superheating During Cold Leg Condensation

[

]^{a,c}

[

]a,c

SI Line Running Partial Full

[

]a,c

[a,c] (6-237)

[ ]a,c [a,c] (6-238)

[

]a,c

[

]^{a,c}

[

]^{a,c}

Conclusions

A cold leg condensation model is developed for evaluating the condensation heat transfer rate due to SI injection in a SBLOCA. [

]^{a,c} The Nusselt number of the condensation is correlated to the liquid Reynolds number and the Prandtl number using [ ]^{a,c}. Scaling and applicability issues with respect to the cold leg geometry, the system pressure, the SI temperature, cold leg water level, SI line running partially full, SI jet break-up, and the steam superheating are addressed.

6.3.7 Effect of Non-Condensables

The treatment of the effect of non-condensable gas on the condensation is the same for 1D and Vessel components in WCOBRA/TRAC-TF2. Section 6.2.11 already provide the complete description of the condensation suppression model handling the effect of the non-condensable gas in the 1D component which results in the calculation of the suppression factor x_{cond} applied to Eq. 6-257.

The effect of non-condensables on the evaporation in 1D components is discussed next.

In the presence of non-condensables, WCOBRA/TRAC-TF2 modifies the liquid-side heat transfer factor H_{ALVE} during evaporation using the model from Skelland (1985). Under evaporation conditions ($T_{sv} < T_\ell < T_{SAT}$), H_{ALVE} is calculated by a diffusion model in which:

$$H_{ALVE,nc} = h_M h_{fg} (\rho_s - \rho_g + \rho_a) A_i \frac{1}{(T_\ell - T_{sv})} \tag{6-239}$$

Where h_M is the mass transfer coefficient (m/s), h_{fg} is the latent heat (J/kg), ρ_s is the density of steam at interface (kg/m^3), ρ_g is the density of gas mixture (kg/m^3), ρ_a is the non-condensable density in the gas mixture (kg/m^3), A_i is the interfacial area (m^2), T_ℓ is the liquid temperature (K), and T_{SV} is the saturation temperature at the steam partial pressure (K).

The steam density ρ_s at the interface is estimated using the ideal gas approximation.

$$\rho_s = \frac{(P_{sat})_{T_{sat}=T_\ell}}{R_s T_\ell} \tag{6-240}$$

where R_s is the ideal gas constant for steam and is set equal to 462 J/kg-K. The mass transfer coefficient h_M is determined, independent of flow regime, as a function of the Sherwood number.

$$Sh = \frac{h_M D_h}{D_o} \tag{6-241}$$

where:

$$Sh = \begin{cases} 3.656 & Re \le 2300 \\ 0.023\, Re^{0.8}\, Sc^{1/3} & Re > 2300 \end{cases} \tag{6-242}$$

for the Schmidt number:

$$Sc = \frac{\mu_g}{\rho_g D_o} \tag{6-243}$$

and the Reynolds number:

$$Re = \frac{G_g D_h}{\mu_g} \tag{6-244}$$

The diffusion coefficient D_o (m^2/s) is evaluated from:

$$D_o = \frac{10^{-3}}{P}\left(-699.2438 + 4.9249\, T_g + 0.0171\, T_g^2\right) \tag{6-245}$$

where P is the gas mixture pressure (Pa) and T_g is the gas mixture temperature (K). The diffusion coefficient is a curve fit to the theoretical equation for diffusion of steam in air for T_g between 273 K and 600 K.

The mass transfer modeling for evaporation is based on the heat and mass transfer analogy. The analogy has been shown to be correct for the conditions for which the heat transfer coefficient correlation is correct.

Model As Coded

[ ]^{a,c}

[ ]a,c (6-246)

[

[ ]a,c
]a,c (6-247)

Scaling Considerations and Conclusions

Section 6.2.11 already provides the complete description of the non-condensable condensation suppression factor x_{cond} for the VESSEL (3D) component. The same model is used for the 1D components. The formulation for the 1D component also accounts of the effect of non-condensables on the evaporation. The possible bias or scaling of the model is of no concern.

6.3.8 One-Dimensional Component Interfacial Mass Transfer

Model Basis

The total mass transfer rate is actually the sum of two components: mass transfer caused by interfacial heat transfer Γ_i and mass transfer caused by subcooled boiling at a heated wall Γ_{sub}:

$$\Gamma = \Gamma_i + \Gamma_{sub} \tag{6-248}$$

As previously noted, the interfacial mass transfer caused by interfacial heat transfer is defined by the jump relation:

$$\Gamma_i = \frac{q_{i\ell} + q_{ig}}{(h_g - h_\ell)} \tag{6-249}$$

The individual terms for interfacial heat transfer rate to the gas and to the liquid were defined in Section 4. To solve for the heat transfer rate, the flow regime dependent interfacial area and interfacial heat transfer coefficients must be determined, which are presented in Sections 4.4 and 6.3, respectively. A positive value for Γ_i indicates vapor generation at the interface. Conversely, a negative value indicates liquid generation.

The interfacial mass transfer caused by subcooled boiling likewise is defined by the equation:

$$\Gamma_{sub} = \frac{h_\Gamma A_w (T_w - T_\ell)}{B_{cell} (h_g - h_\ell)} \tag{6-250}$$

The subcooled-boiling term is important for hydraulic cells coupled to a heated wall. Specifically, the term is included to improve the prediction of void fraction near the saturation point. For subcooled boiling

to take place, the cell-averaged liquid temperature must be below the saturation temperature; at the same time, the wall temperature must be above T_{sat}.

When the above conditions are satisfied, the actual mass transfer rate is in turn dependent on the subcooled-boiling liquid heat transfer coefficient h_Γ, as defined by:

$$h_\Gamma = W_{sb} h_{w\ell} F_e \tag{6-251}$$

where $h_{w\ell}$ is the wall-to-liquid heat transfer coefficient as presented in Section 7. The subcooled-boiling weighting factor, W_{sb}, is empirically based and is calculated such that:

$$0 \le W_{sb} = 5\left(0.7 - \alpha\right) \le 1 \tag{6-252}$$

W_{sb} equals 1.0 for void fractions ranging from 0.0 to 0.5. Above a void fraction of 0.5, the weighting factor ramps linearly to zero. Finally, F_e is the evaporation fraction based on Lahey's mechanistic model (Lahey, 1978), where:

$$0 \le F_e = \frac{T_\ell - T_{\ell d}}{\max\left(1, \left(T_{sv} - T_{\ell d}\right)\right)} \le 1 \tag{6-253}$$

The liquid temperature at bubble detachment $T_{\ell d}$ provides the criterion by which bubbles reside solely on the wall or bubbles may detach and move into the bulk fluid without collapsing. As demonstrated by the above equation, when $T_{\ell d}$ exceeds the bulk liquid temperature, the evaporation fraction, and thus the mass transfer rate, becomes zero. In this way, the code does not calculate any void generation associated with bubbles residing solely on the wall. However, once the bulk fluid temperature exceeds $T_{\ell d}$, the bubbles may detach and the calculated mass transfer rate then becomes nonzero.

The value of the liquid temperature at bubble detachment is determined via the modified Saha-Zuber correlation for the point of net vapor generation. Saha and Zuber (Saha and Zuber, 1974) correlated the point of net vapor generation as a function of Nusselt, Stanton, and Peclet numbers, where:

$$\mathrm{Nu} = 455 \qquad \text{if } \mathrm{Pe} \le 70{,}000 \tag{6-254}$$

and

$$\mathrm{St} = 0.0065 \qquad \text{if } \mathrm{Pe} > 70{,}000 \tag{6-255}$$

Therefore, the liquid temperature at bubble departure, $T_{\ell d}$, is computed by:

$$T_{\ell d} = \begin{cases} T_{sv} - \dfrac{\mathrm{Nu}^*}{0.0065 \times 70000}, & \text{if } \mathrm{Pe} \le 70000 \\ T_{sv} - \dfrac{\mathrm{Nu}^*}{0.0065 \times \mathrm{Pe}}, & \text{if } \mathrm{Pe} > 70000 \end{cases} \tag{6-256}$$

where Nu* is a modified Nusselt number.

$$Nu^* = \frac{q_{w\ell} D_h}{k_\ell} \tag{6-256a}$$

For HTSTR components in WCOBRA/TRAC-TF2, the subcooled-boiling heat transfer is calculated in subroutine HTCOR.

Model As Coded

The interfacial heat transfer is calculated as (in the coding, the sign convention is reversed):

$$q_{i\ell} = x_{cond} F_{CONT} F_{r1} H_{ALVE} (T_\ell - T_{sat}) \tag{6-257}$$

$$q_{ig} = F_{r2} H_{CHTI} (T_g - T_{sat}) \tag{6-258}$$

and finally,

$$\Gamma_i = \frac{q_{i\ell} + q_{ig}}{(h_g - h_\ell)} \tag{6-259}$$

The condensation suppression factor x_{cond} and the condensation ramps F_{CONT} are calculated as described in Section 6.2.11 and Section 6.2.12, respectively. The terms F_{r1} and F_{r2} are defined as:

[ ]^{a,c} (6-260)

and

[ ]^{a,c} (6-261)

to provide implicit ramping as the fluid approaches single-phase conditions.

Scaling Considerations and Conclusions

The model for interfacial mass transfer in WCOBRA/TRAC-TF2 one-dimensional components is scale independent. In the original Saha-Zuber correlation (1974), the subcooled boiling heat transfer coefficient covered a wide range of channel sizes and geometries, including 7 mm inner diameter and 13 mm outer diameter annular geometries through 63 mm channels. The correlation is expected to be independent of scale.

6.3.9 Additional Remarks on Interfacial Heat Transfer Models as Coded

Flashing Heat Transfer

The flashing heat transfer model is applied to the liquid side heat transfer regardless of the flow regime. The formula is given by Equation 6-152. The basis for this model is its high magnitude, which quickly decreases the liquid temperature to saturation temperature. This model is flow regime independent and is used for all flow patterns.

Condensation Ramp Model at Low Pressure

The condensation ramp model at low pressure is the same for 1D and Vessel components in WCOBRA/TRAC-TF2. See Section 6.2.12 for the complete description of the condensation ramp model.

Limits for Subcooled Vapor

If the vapor temperature is less than the saturation temperature, the vapor-side heat transfer factor is limited by:

$$H_{CHTI,map/stratified/NC} \leq 10^6 \times B_{cell} \tag{6-262}$$

Then, the final value of H_{CHTI} is further modified based upon the degree of subcooling as follows:

$$H_{CHTI,map/stratified/NC} = H_{CHTI,map/stratified/NC} \times \exp(T_{sv} - T_g) \tag{6-263}$$

where:

$$0 \leq T_{sv} - T_g \leq 7$$

If the gas temperature is less than the liquid temperature, the magnitude of H_{CHTA} is similarly modified as:

$$H_{CHTA,map/stratified/NC} \leq 10^6 \times B_{cell} \tag{6-264}$$

Then, the final value of H_{CHTA} is further modified based upon the temperature difference as follows:

$$H_{CHTA,map/stratified/NC} = H_{CHTA,map/stratified/NC} \times \exp(T_\ell - T_g) \tag{6-265}$$

where:

$$0 \leq T_\ell - T_g \leq 7$$

Kinetic Theory Limits on Liquid-Side Heat Transfer

In WCOBRA/TRAC-TF2, the liquid-side heat transfer coefficient is limited according to kinetic theory. It is assumed that the condensation or evaporation rate cannot exceed the molecular flux towards the interface. Using the linearized approximation of kinetic theory, the maximum limit of $h_{i\ell}$ is coded as:

$$h_{i\ell,max} = \sqrt{\frac{M_s}{2\pi R_s}} \times \frac{\rho_g h_{fg}^2}{T_g^{1.5}} \quad \text{if } T_\ell < T_{sv} \tag{6-266}$$

where M_s is the molecular weight of water. The liquid-side heat transfer factor during condensation or evaporation is limited as:

$$0.1\, B_{cell} \le H_{ALVE,map/stratified/nc} \le A_i h_{i\ell,max} \tag{6-267}$$

Time Smoothing (Old-Time/New-Time Averaging)

No old-time/new-time averaging is applied if the phasic temperature crosses the saturation line, the cell was single phase at the previous time step, or the magnitudes of H_{ALV}, H_{ALVE}, H_{CHTI}, and H_{CHTA} were less than 10^{-10} at the previous time step. Otherwise time smoothing techniques are applied. The time smoothing techniques are addressed in Section 3.

6.4 REFERENCES

1. Andersen, J. G. M., 1973, "REMI/HEAT COOL, A Model for Evaluation of Core Heat-Up and Emergency Core Spray Cooling System Performance for Light-Water-Cooled Nuclear Power Reactors," Report No. 296, RISO National Lab Denmark.

2. Bankoff, S. G., 1980, "Some Condensation Studies Pertinent to LWR Safety," *Int. J. Multiphase Flow*, Vol. 6, pp. 51-67.

3. Bin, A. K., 1993, "Gas Entrainment by Plunging Liquid Jets," *Chemical Engineering Science*, Vol. 48, No. 21, pp. 3585-3630.

4. Chen, Y. M. and Mayinger, F., 1992, "Measurement of Heat Transfer at the Phase Interface of Condensing Bubbles," *Int. J. Multiphase Flow*, Vol. 18, No. 6, pp. 877-890.

5. Chow, S. K., et al., 1989, "Assessment of Scaling Uncertainties for PWR Plant Large-Break LOCA Analysis," EPRI NP-6602.

6. Colburn, A. P., 1933, "A Method of Correlating Forced Convection Heat-Transfer Data and a Comparison with Fluid Friction," *Trans Am Inst Chem Eng*, Vol. 29, pp. 174-210.

7. Dehbi, A. A., Golay, M. W. and Kazimi, M. S., 1991, "The Effects of Noncondensable Gases on Steam Condensation Under Turbulent Natural Convection Conditions," Rpt. No. MIT-ANP-TR-004, Dept. of Nucl. Engr., MIT.

8. Dittus, F. W. and Boelter, L. M. K., 1930, "Heat Transfer in Automobile Radiators of the Tubular Type," University of California Engineering Publications.

9. Forslund, R. P. and Rohsenow, W. M., 1968, "Dispersed Flow Film Boiling," *J. Heat Transfer*, Vol. 87, pp. 399-407.

10. Gros d'Aillon, M., 1987, "Essais De Condensation En Regime Permanent," (COSI Report), SETh/LETC/87-45.

11. Hughmark, G. A., 1973, "Film Thickness Entrainment and Pressure Drop in Upward Annular and Dispersed Flow," *AICHE J.*, Vol. 19, pp. 1062-1065.

12. Ishii, M., 1977, "One Dimensional Drift-Flux Model and Constitutive Equations for Relative Motion Between Phases in Various Two-Phase Flow Regimes," ANL-77-47.

13. Kawaji M., et al., 1986, "ROSA-IV/LSTF 5% Cold Leg Break LOCA Experiment Data Report: Run SB-CL-05," JAERI-memo 61-056.

14. Janicot, A. and Bestion, D., 1993, "Condensation Modelling for ECC injection," *Nuclear Engineering and Design*, Vol. 145, pp. 37-45.

15. Kim, H. J., 1985, "Local Properties of Countercurrent Stratified Steam-Water Flow," US Nuclear Regulatory Commission, NUREG/CR-4417.

16. Lahey, R. T. Jr. and Moody, F. J., 1977, "The Thermal-Hydraulics of a Boiling Water Nuclear Reactor," ANS monograph.

17. Lahey, R. T., 1978, "A Mechanistic Subcooled Boiling Model," *Proc. 6th Int. Heat Transfer Conf.*, Toronto, Canada, Vol. 1, pp. 293–297.

18. Lee, K. and Ryley, D. J., 1968, "The Evaporation of Water Droplets in Superheated Steam," *Trans A.S.M.E. J Heat Transfer*, Vol. 90, pp. 445-451.

19. Linehan, J. H., Petrick, M. and El Wakil, M. M., 1972, "The condensation of saturated vapor on a subcooled film during stratified flow," *Chem. Eng. Symp. Series*, Vol. 66, No.102, pp. 11–20.

20. Rowe, P. N., Claxton, K. T. and Lewis, J. B., 1965, "Heat and Mass Transfer from a Single Sphere in an Extensive Flowing Fluid," *Trans. Instn. Chem. Engrs.*, 43, T14-T31.

21. Ryskin, G., 1987, "Heat or Mass Transfer from a Moving Drop – Some Approximate Relations for the Nusselt Number," *Int. Comm. Heat Mass Transfer*, Vol. 14, pp. 741-749.

22. Saha, P. and Zuber, N., 1974 "Point of Net Vapor Generation and Vapor Void Fraction in Subcooled Boiling," *Proc. 5th Int. Heat Transfer Conf.*, Tokyo, Japan, Paper B4.7.

23. Shimeck, D.J., 1988, "COSI SI/Steam Condensation Experiment Analysis," WCAP-11767.

24. Skelland, A. H. P., 1985, Diffusional Mass Transfer, Robert E. Kreiger Publishing Co., Malabar, Florida.

25. Sklover, G. G. and Rodivilin, M. D., 1976, "Condensation on Water Jets with a Cross Flow of Steam," Teploenergetika 23, 48 51.

26. Slegers, L. and Seban, R. A., 1970, "Laminar Film Condensation of Steam Containing Small Concentrations of Air," *Int. J. Heat Mass Trans.*, Vol. 13, pp. 1941-1947.

27. Spore, J.W., et al., 2000, "TRAC-M/FORTRAN 90 (Version 3.0) Theory Manual," LA-UR-00-910.

28. Wallis, G. B., 1968, "Use of the Reynolds Flux Concept for Analyzing One-Dimensional Two-phase Flow, Part I, Derivation and Verification of Basic Analytical Techniques," *Int. J. Heat Mass Transfer*, Vol. II, pp 445-458.

29. Wallis, G. B., Crowley, C. J. and Hagi, Y., 1977, "Conditions for a Pipe to Run Full When Discharging Liquid Into a Space Filled With Gas," *Journal of Fluids Engineering*, pp. 405-413.

30. Wheeler, C. L., et al., 1986, "COBRA-NC: A Thermal-Hydraulic Code for Transient Analysis of Nuclear Reactor Components," Vol. 1, NUREG/CR-3262, PNL-4710.

31. Whitaker, S., 1972, "Forced Convection Heat Transfer Correlations for Flow in Pipes, Past Flat Plates, Single Cylinders, Single Spheres, and for Flow in Packed Beds and Tube Bundles," *AIChE Journal*, Vol. 18 (2), pp. 361-371.

32. Yao, S. C., Hochreiter, L. E. and Leech, J. J., 1982, "Heat Transfer Augmentation in Rod Bundles Near Grid Spacers," *J. Heat Transfer*, Vol. 104, pp. 76-81.

33. Young, M. Y., et al., 1984, "BART-A1: A Computer Code for Best Estimate Analysis of Reflood Transients," WCAP-9561-P-A and WCAP-9695-A (Non-Proprietary).

34. Young, M.Y. and Bajorek, S.M., 1997, "The Effect of Noncondensables on Condensation in Reactor LOCA Transients," *AICHE SYMPOSIUM SERIES*, Vol. 314, pp 6-13.

35. Yuen, M. C. and Chen, L. W., 1978, "Heat transfer Measurements of Evaporating Liquid Droplets," *Int J Heat and Mass Transfer*, Vol. 21, pp. 537-542.

Table 6-1 The Selection Logic for Condensation, Evaporation, and Flashing for 3D Vessel			
Vapor	SCV $T_v (=T_{gas}) < T_{dp}$	SHV $T_v (=T_{gas}) > T_{dp}$	
Liquid	SCL $T_l < T_{dp} (<=T_{sat})$	SEL $T_{dp} < T_l <= T_{sat}$	SHL $T_l > T_{sat}$
The subscript dp refers to dew point, i.e., $T_{dp} = T_{sat}(P_v)$, where P_v is the steam partial pressure.			

Table 6-2 [ ]a,c

a,c

a,c

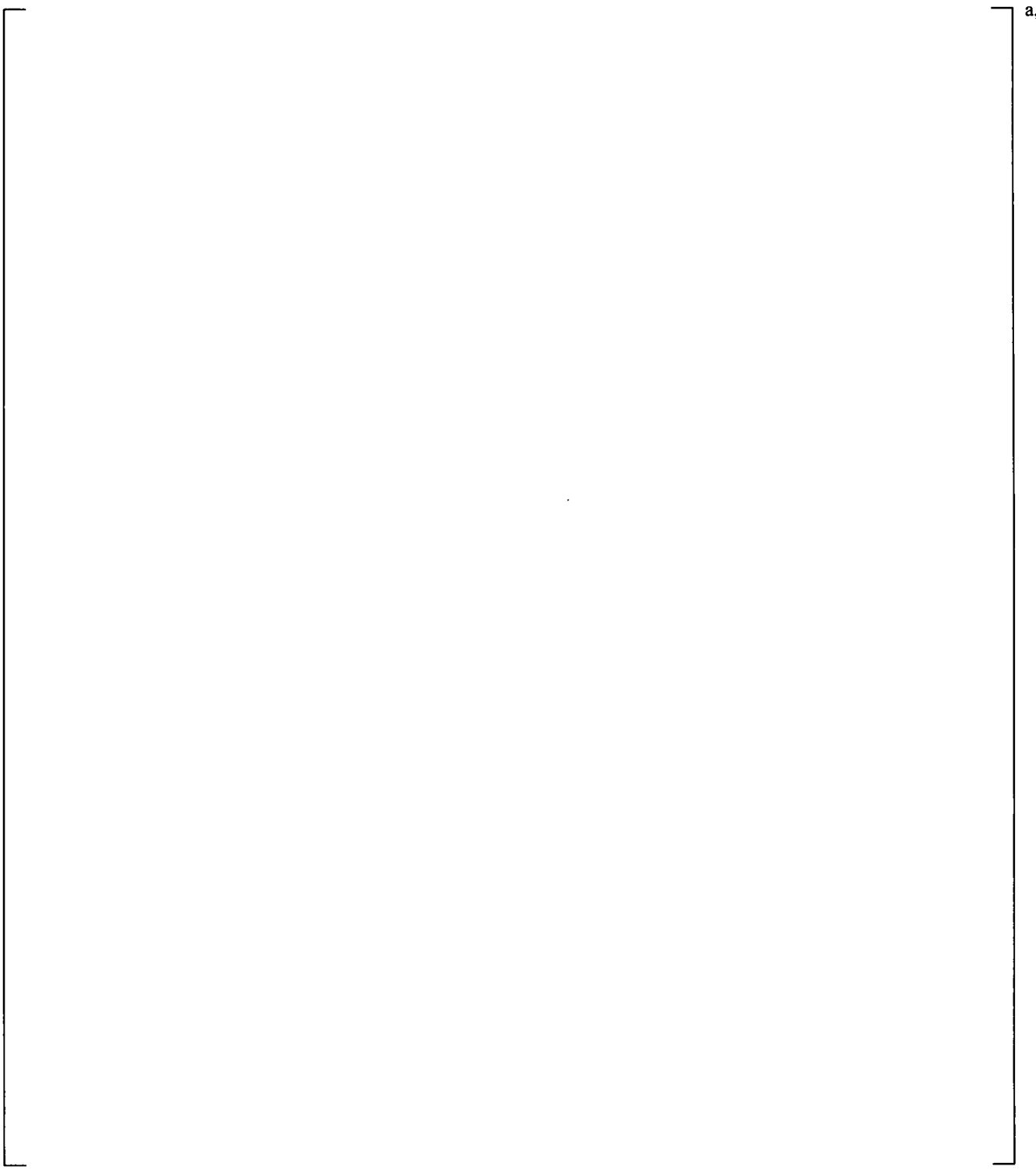

Figure 6-1 Large Void Fraction Gradient Ramp for Subcooled Liquid Interfacial Area

a,c

Figure 6-2 Suppression Factor at Various Liquid Side Heat Transfer Coefficients at 0.1 MPa and 1.0 MPa using the Revised Young-Bajorek Model

[a,c

]

Figure 6-3 Illustration of Condensation Ramp Model, Variable PCONT1 Represents ΔP_{cont}

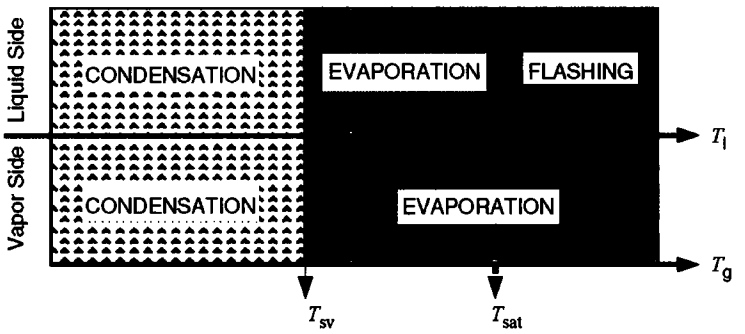

Figure 6-4 Illustration of the Selection Logic for Condensation, Evaporation, and Flashing for 1D Components

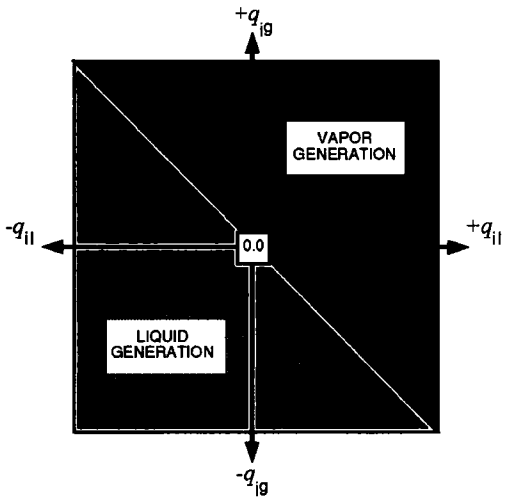

Figure 6-5 Interfacial Mass Transfer Map for 1D Components

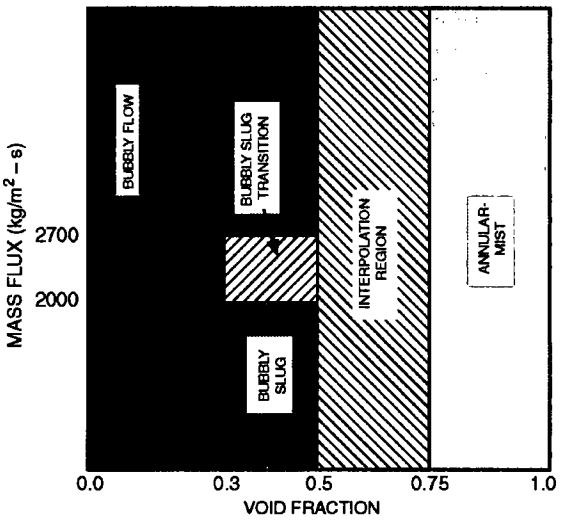

Figure 6-6 WCOBRA/TRAC-TF2 Basic Flow Regime Map for 1D Components

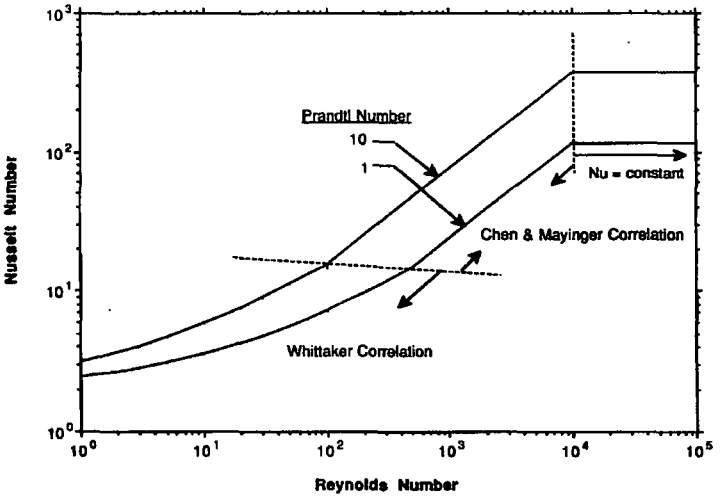

Figure 6-7 Liquid Side Heat Transfer Coefficient Model During Condensation in Bubbly Slug Flow for 1D Components

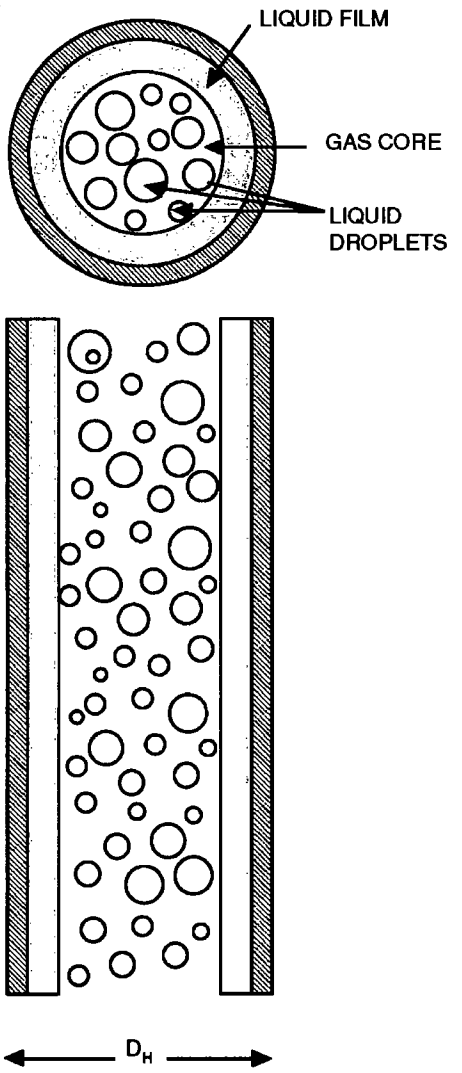

Figure 6-8 Schematic of Flow Pattern in Annular-Mist Flow

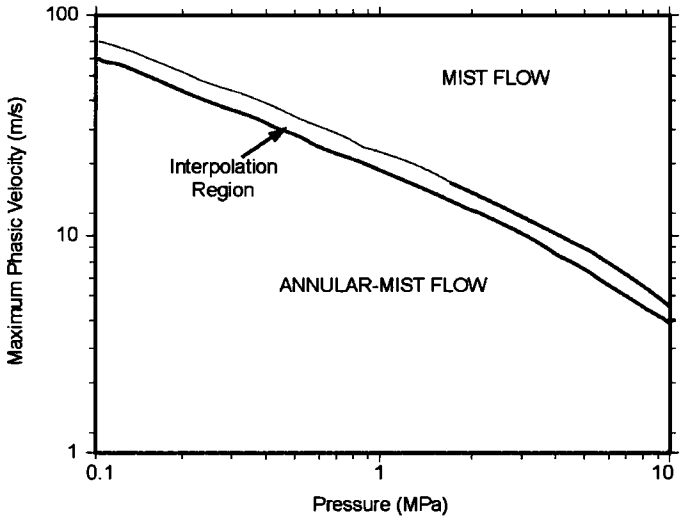

Figure 6-9 Transition from Annular-Mist to Mist Flow as a Function of Pressure for Saturated Water

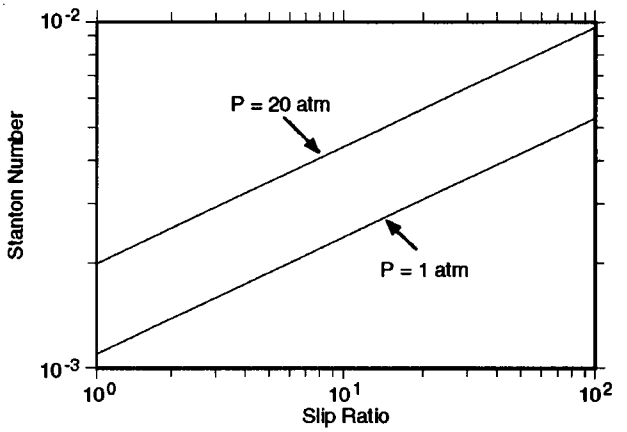

Figure 6-10 Calculated Stanton Numbers for Liquid-Film Flow using Saturated Water Properties

[a,c

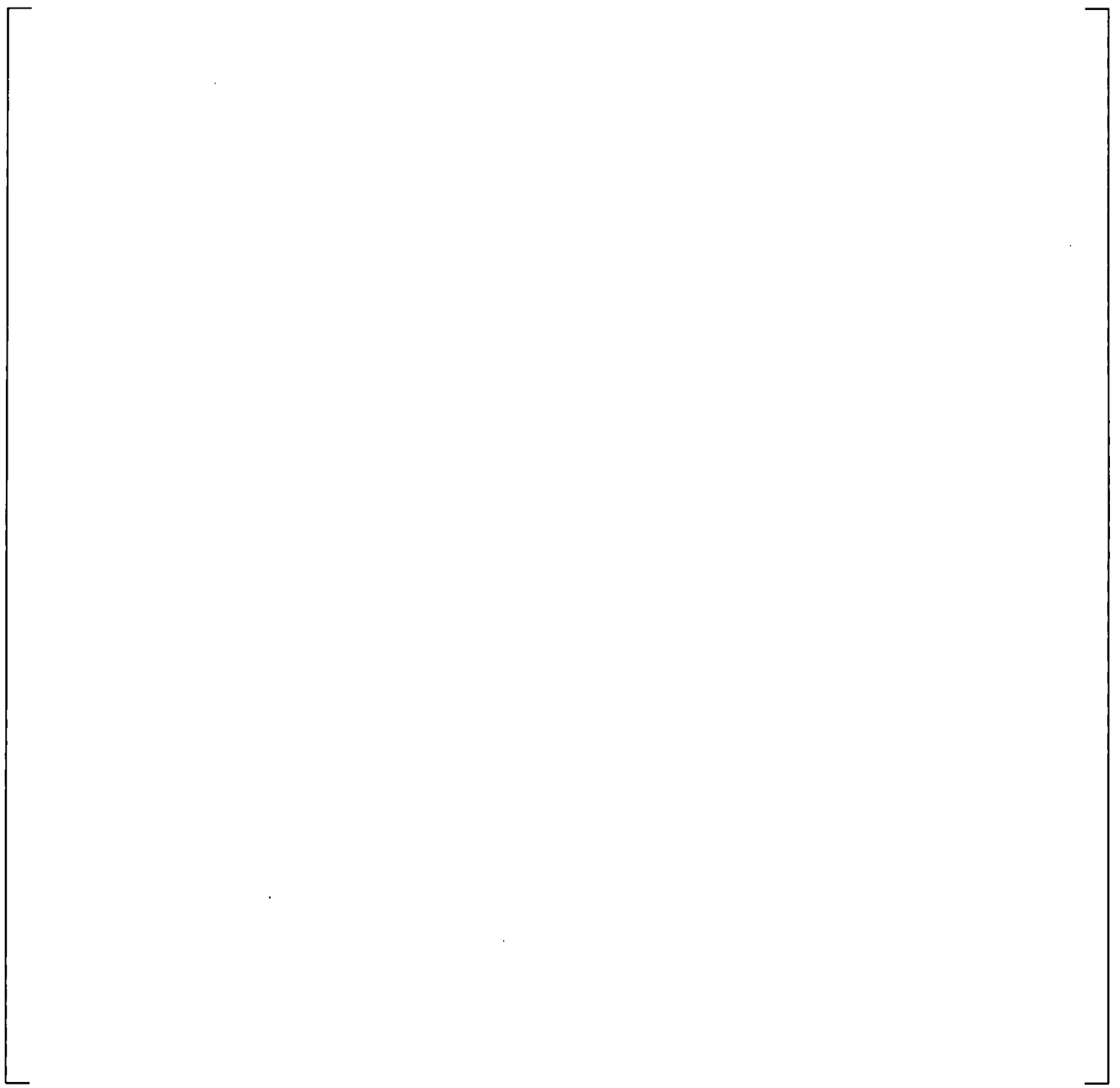

]

Figure 6-11 Small Break LOCA Pressure Response (DLW SBLOCA Reference Transient)

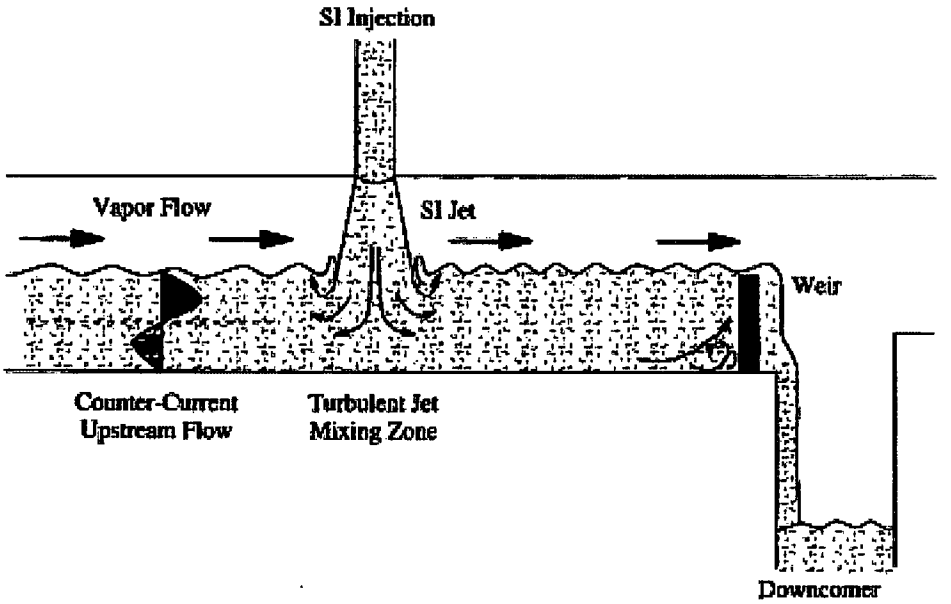

Figure 6-12 Schematic of Flow Regime and Condensation in COSI Experiments

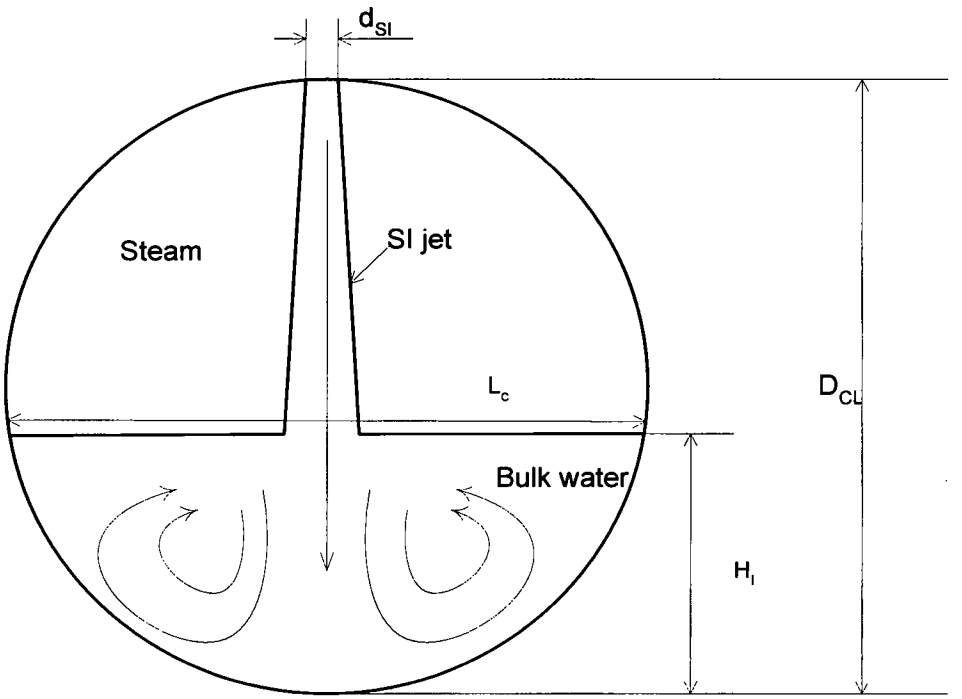

Figure 6-13 Cross Section of Cold Leg Near the Safety Injection

a,c

Figure 6-14 Temperature Profile of the Bulk Water in the Cold Leg Measured in Westinghouse COSI Test (Test No. 010, Point 5)

[a,c

]

Figure 6-15 Comparison Between the Measured Nusselt Number and Calculated Nusselt Number from the Cold Leg Condensation Correlation

[ ] a,c

Figure 6-16 Comparison of Measured Condensation Heat Transfer Rates Under Different Cold Leg Water Level Cases

7 WCOBRA/TRAC-TF2 WALL HEAT TRANSFER MODELS

7.1 INTRODUCTION

This section describes the wall to fluid heat transfer models in WCOBRA/TRAC-TF2. These models and correlations determine the temperature response of the fuel, cladding, and structural components of a pressurized water reactor (PWR) during normal operations and transients. Separate heat transfer packages are used for the vessel (COBRA/TF) and one-dimensional (TRAC-P [ ]^{a,c}) components. In general, the two packages are similar for pre-Critical Heat Flux (CHF) heat transfer. For post-CHF heat transfer, the vessel component contains models that are more refined. This is due to the intended application of each package. The vessel component heat transfer package is used in the core and reactor vessel, where post-CHF heat transfer, dispersed droplet film boiling and single phase vapor, in particular, are expected to be important. Other RCS structures such as the loop piping, pumps, and steam generators utilize the one-dimensional component heat transfer package. Post-CHF heat transfer is much less common in these components and does not require the same amount of detail as the vessel.

For both the vessel and one-dimensional components, the heat transfer calculations are performed at the beginning of each time step before the hydrodynamic solution. The heat transfer coefficients based on the previous time step fluid conditions are used to advance the conduction solution in the affected material structures. Heat release rates are explicitly coupled to the hydrodynamic solution as source terms in the fluid energy equation. The coupling of the heat transfer rate to the fluid energy equation is described in Section 7.2.10 for the vessel component and in Section 7.3.11 for one-dimensional components.

7.2 VESSEL COMPONENT WALL HEAT TRANSFER MODELS

The vessel heat transfer package consists of a library of heat transfer correlations and the selection logic to determine which correlation is appropriate for a given set of hydrodynamic conditions. The heat transfer correlations and selection logic produce a continuous boiling curve, as shown in Figure 7.2-1. The heat transfer regime selection logic is shown in Figure 7.2-2. The following list gives the heat transfer regimes used in the WCOBRA/TRAC-TF2 vessel component heat transfer package.

Mode 1 Single-phase liquid convection (SPL)
Mode 2 Subcooled nucleate boiling (SUBC)
Mode 3 Saturated nucleate boiling (NUCB)
Mode 4 Transition boiling (TRAN)
Mode 5 Inverted annular film boiling (IAFB)
Mode 6 Inverted annular dispersed flow (IADF)
Mode 7 Dispersed droplet film boiling (DFFB)
Mode 8 Single-phase vapor (SPV)

Figure 7.2-3 shows a heat transfer regime map, indicating where each of the modes apply.

For each regime, three heat transfer coefficients are determined. These are: h_{wv}, the heat transfer coefficient from the wall to vapor, $h_{w\ell}$ the heat transfer coefficient from the wall to liquid for sensible heat, and h_{wb} the heat transfer coefficient from the wall to liquid for latent heat. The use of $h_{w\ell}$ and h_{wb} to partition the heat transfer to the liquid phases is discussed in Section 7.2.11. The following sections

describe, by heat transfer regime, the correlations used by the vessel component to determine h_{wv}, $h_{w\ell}$, and h_{wb}.

7.2.1 Convection to Single-Phase Liquid

Model Basis

The WCOBRA/TRAC-TF2 vessel heat transfer routines employ two correlations to calculate the heat transfer coefficients to single-phase liquid. For laminar flow, the heat transfer coefficient is limited to the value recommended by (Kim, 1979):

$$h_{w\ell,lam} = 7.86\left(\frac{k_\ell}{D_h}\right) \tag{7-1}$$

where k_ℓ is the liquid thermal conductivity.

For turbulent flow, the (Dittus and Boelter, 1930) correlation is used to calculate the single-phase heat transfer coefficient to liquid:

$$h_{w\ell,DB} = 0.023\left(\frac{k_\ell}{D_h}\right)\left(\frac{G_\ell D_h}{\mu_\ell}\right)^{0.8}(Pr_\ell)^n \tag{7-2}$$

where n = 0.4 for heating and n = 0.3 for cooling. All liquid properties are evaluated at the bulk liquid pressure and enthalpy.

Model as Coded

The Dittus-Boelter correlation is coded as listed with [ ]^{a,c} for all usage. Heat transfer coefficients are calculated using the Dittus-Boelter correlation and the expression for laminar external tube flow, and the maximum value is selected as the heat transfer coefficient for forced convection to single-phase liquid. Natural convection and radiation heat transfer are not considered. The correlation is also applied in the transition region between laminar and fully turbulent flow.

The wall to liquid single-phase heat transfer coefficient is calculated as:

$$h_{w\ell,SPL} = F_{SPL} \times \max\begin{Bmatrix} h_{w\ell,lam} \\ h_{w\ell,DB} \end{Bmatrix} \tag{7-3}$$

where, F_{SPL} is a ramp applied to account for liquid deficient heat transfer and is defined as:

$$\left[\quad\right]^{a,c} \tag{7-4}$$

Since T_f is less than T_{sat} for the single-phase liquid regime, boiling does not occur and:

$$h_{wb,SPL} = 0 \tag{7-5}$$

A heat transfer coefficient to vapor for the single-phase liquid regime is also calculated, with a ramp applied to account for liquid deficient heat transfer, as:

$$h_{wv,SPL} = (1.0 - F_{vap})\, h_{wv,FC} \tag{7-6}$$

[ ] a,c

(7-7)

$h_{wv,FC}$ is calculated from Equation 7-160. The effect of $(1.0 - F_{vap})$ is to set the vapor phase heat transfer coefficient to 0.0, except at relatively high void fraction.

Scaling Considerations and Conclusions

In the two correlations for heat transfer to single-phase liquid, scaling is accounted for by selection of an appropriate hydraulic diameter. In Equation 7-2, the heat transfer coefficient is seen to be a weak function of D_h, and thus is not a strong function of scale. These models are assessed by simulating a large number of prototypical rod bundles experiments with WCOBRA/TRAC-TF2. The assessment is presented in Volume 2 of this report.

7.2.2 Saturated and Subcooled Nucleate Boiling

Model Basis

When the wall temperature is greater than saturation but less than the temperature at the critical heat flux and liquid is present, the (Chen, 1963) correlation is used. This correlation assumes that both nucleation and convective mechanisms occur and that the contributions made by the two mechanisms are additive. The Chen correlation automatically makes the transition to single-phase forced convection at low wall superheat, and to pool boiling at low flow rate. The convective component is represented by a Dittus-Boelter type of expression where the thermal conductivity, Reynolds number, and the Prandtl number are replaced by effective values associated with the two-phase flow. To account for increased convection caused by the formation of vapor bubbles, a multiplier is applied to the convective part of the correlation.

A (Forster and Zuber, 1955) type of pool boiling equation is used for the nucleate boiling component of the correlation. The pool boiling expression relates a bubble Nusselt number to a bubble Reynolds number and a liquid Prandtl number. It can be shown that the product of growth rate and bubble radius is

constant for a given superheat. In pool boiling and convective boiling, the superheat is not constant across the boundary layer. This effect can be neglected in pool boiling since the boundary layer is generally large in comparison to the vapor bubble. In convective boiling, however, the boundary layer is thinner and the temperature gradients steeper. The difference between the wall superheat and the mean superheat to which the bubble is exposed must be considered. A suppression factor, S_{CHEN}, is used to modify the nucleate boiling part of the correlation and account for this effect.

The equations for the Chen correlation are as follows:

$$h_{CHEN} = h_{FC} + h_{NB} \tag{7-8}$$

$$h_{FC} = 0.023 F_{CHEN} \left(\frac{k_\ell}{D_h} \right) Re_\ell^{0.8} Pr_\ell^{0.4} \tag{7-9}$$

$$Re_\ell = \frac{G_\ell D_h}{\mu_\ell} \tag{7-10}$$

$$h_{NB} = 0.00122 S_{CHEN} \left(\frac{k_\ell^{0.79} C_{p_\ell}^{0.45} \rho_\ell^{0.49} g_c^{0.25}}{\sigma^{0.5} \mu_\ell^{0.29} H_{fg}^{0.24} \rho_v^{0.24}} \right) \left(T_w - T_\ell \right)^{0.24} \left(P_w - P \right)^{0.75} \tag{7-11}$$

where F_{CHEN} is the Reynolds number factor shown in Figure 7.2-4 as a function of the inverse Martinelli factor, χ_{TT}^{-1}. The boiling suppression factor, S_{CHEN}, is shown in Figure 7.2-5, and P_w is the saturation pressure corresponding to T_w. Additionally, see the nomenclature following equation 7-90 for common variable definitions, where the ℓ and v subscripts denote liquid and vapor, respectively.

The inverse Martinelli factor is given by:

$$\chi_{TT}^{-1} = \left(\frac{x}{1-x} \right)^{0.9} \left(\frac{\rho_f}{\rho_g} \right)^{0.5} \left(\frac{\mu_g}{\mu_f} \right)^{0.1} \tag{7-12}$$

and the Reynolds number factor is determined as:

$$F_{CHEN} = MAX \begin{Bmatrix} 1.0 \\ 2.34 \left(X_{TT}^{-1} + 0.213 \right)^{0.736} \end{Bmatrix} \tag{7-13}$$

The boundary for the maximum function for F_{CHEN} exists at $\chi^{-1}{}_{TT} \approx 0.1$. The boiling suppression factor recommended by (Thurgood et al., 1983) is given by:

$$S_{CHEN} = \begin{cases} \left(1 + 0.12\ Re_{2\phi}^{1.14}\right)^{-1} & Re_{2\phi} \le 32.5 \\ MAX\left\{ \begin{matrix} \left(1 + 0.42\ Re_{2\phi}^{0.78}\right)^{-1} \\ 0.1 \end{matrix} \right. & Re_{2\phi} > 32.5 \end{cases} \quad (7\text{-}14)$$

$$Re_{2\phi} = \left(10^{-4}\right) Re_{\ell}\ F_{CHEN}^{1.25} \quad (7\text{-}15)$$

Note that the limit in Equation 7-14 has been modified to limit S_{CHEN} to 0.1 (Thurgood et al., 1983) to make the transition more continuous.

Subcooled Nucleate Boiling

The Chen correlation, though developed for saturated boiling, may be extended into the subcooled region. As discussed above, the Chen correlation superimposes a forced convective and nucleate boiling component. For subcooled boiling:

$$q''_{SUBC} = q''_{FC} + q''_{NB} \quad (7\text{-}16)$$

The nucleate boiling heat flux is evaluated as:

$$q''_{NB} = h_{NB}\left(T_w - T_{sat}\right) \quad (7\text{-}17)$$

where h_{NB} is defined by Equation 7-11, and the suppression factor, S_{CHEN}, is calculated from Equation 7-14. The forced convection heat flux is computed from Equation 7-9 using subcooled liquid properties and setting the flow factor, F_{CHEN}, to unity so that:

$$q''_{FC} = 0.023\left(\frac{k_{\ell}}{D_h}\right) Re_{\ell}^{0.8}\ Pr_{\ell}^{0.4}\left(T_w - T_{\ell}\right) \quad (7\text{-}18)$$

where T_{ℓ} is the local bulk fluid temperature and Re_{ℓ} is calculated using Equation 7-10.

(Moles and Shaw, 1972) compared the Chen correlation to boiling data for several fluids and reported satisfactory agreement for low to moderate subcoolings.

During subcooled boiling, vapor generation occurs and a significant void fraction ($\alpha_v \sim 0.6$) may exist despite the presence of subcooled liquid. In this regime, four processes are of interest:

1. forced convection to liquid;
2. vapor generation at the wall;
3. condensation near the wall; and
4. bulk condensation (subcooled liquid core).

Condensation occurring because of the presence of vapor in the subcooled liquid core is calculated implicitly during the solution of the energy equations and does not affect the determination of phasic heat

inputs. Forced convection to liquid is treated using Equation 7-18 for the heat input to the liquid energy equation. The nucleate boiling component of the Chen correlation, Equation 7-11, defines the amount of heat available to cause vapor generation at the wall.

The near-wall condensation is estimated using the (Hancox and Nicoll, 1971) correlation for heat flux at the point where all the bubbles generated collapse in the near-wall region:

$$q''_{HN} = 0.4\left(\frac{C_{\rho_f}\mu_f}{D_h}\right)\left(\frac{G_\ell D_h}{\mu_f}\right)^{0.662}(T_{sat} - T_\ell) \tag{7-19}$$

where T_{sat} is the local saturation temperature.

The heat flux dissipated in near-wall condensation for a flowing system is calculated as:

$$q''_{cond} = q''_{HN} - q''_{SPL} \tag{7-20}$$

Subtracting the near wall condensation from the amount of energy available for vapor generation yields:

$$q_\Gamma = \left(q''_{NB} - q''_{cond}\right)A_w \tag{7-21}$$

where A_w is the wall surface area.

However, a fraction of q_Γ is expended to heat up the subcooled liquid "pumped" into the saturated thermal boundary layer. This fraction is given by the following expression derived from the (Rouhani and Axelsson, 1970) model for the core geometry as:

$$\varepsilon_\rho = \frac{(\rho_f/\rho_g)(H_f - H_\ell)}{H_{fg} + (\rho_f/\rho_g)(H_f - H_\ell)} \tag{7-22}$$

$$\varepsilon_\Gamma = (1 - \varepsilon_p)\frac{H_{fg}}{H_{fg} + (\rho_f/\rho_g)(H_f - H_\ell)} \tag{7-23}$$

where:

ε_p = fraction of heat from the near-wall boiling component that contributes to sensible heating of the bulk fluid

ε_Γ = fraction of total wall heat flux that generates vapor at the wall

Finally, the amount of energy available for vapor generation is:

$$q_\Gamma = \left(q''_{NB} - q''_{cond}\right)\varepsilon_\Gamma A_w \tag{7-24}$$

and, adding all the heat inputs to the liquid:

$$q_\ell = \left[q''_{SPL} + (1-\varepsilon_\Gamma)q''_{NB} + \varepsilon_\Gamma q''_{cond}\right]A_w \tag{7-25}$$

ε_Γ is implemented as the subcooled boiling modifier, F^*_{SCB} which will be discussed in the Model as Coded section.

The heat source term for vapor generation, q_Γ, enters the liquid energy equation as an explicit vapor generation rate and will partially condense because of the implicit bulk condensation.

Model as Coded

Nucleate boiling heat transfer coefficients are calculated when the wall temperature is $T_{sat} \leq T_{wall} < T_{CHF}$.

Calculations are first performed in subroutine BOILING to determine χ_{TT}^{-1}, $Re_{2\phi}$, F_{CHEN} and S_{CHEN}. To obtain χ_{TT}^{-1}, the quality is calculated as:

[ ] a,c (7-26)

The inverse Martinelli factor is then calculated as:

[ ] a,c (7-27)

For saturated liquid ($T_\ell \geq T_{sat}$), the convective enhancement factor F_{CHEN} is calculated:

[ ] a,c (7-28)

and the value of $Re_{2\phi}$ is:

$$Re_{2\phi} = \left(10^{-4}\right)F_{CHEN}^{1.25}\,Re_\ell \tag{7-29}$$

For subcooled liquid, χ_{TT}^{-1} is not calculated and $Re_{2\phi}$ is calculated as:

$$Re_{2\phi} = \left(10^{-4}\right)Re_\ell \tag{7-30}$$

which is equivalent to assuming $F_{CHEN} = 1.0$ in Equation 7-29.

The boiling suppression factor is then calculated for both saturated and subcooled liquid as:

[ ] a,c (7-31)

The $(P_w - P)$ term in the Chen correlation is approximated using the Clausius-Clapeyron equation as:

[ ] a,c (7-32)

(7-33)

(7-34)

For saturated nucleate boiling, the heat transfer coefficient to liquid for sensible heat is calculated as:

$$h_{w\ell,NUCB} = F_{CHEN}\, h_{w\ell,SPL} + h_{NB} \tag{7-35}$$

$$h_{NB} = 0.00122\, S_{CHEN}\left[\frac{k_f^{0.79}\, C_{pf}^{0.45}\, \rho_f^{0.49}\, g_c^{0.25}}{\sigma^{0.5}\, \mu_f^{0.29}\left(H_{fg}\rho_g\right)^{0.24}}\right]\left(T_w - T_f\right)^{0.24}\left(P_w - P\right)^{0.75} F_B \tag{7-36}$$

and $h_{w\ell,SPL}$ is given by Equation 7-3. This allows transition to laminar convection when Re_ℓ decreases, The function F_B insures a smooth decrease in the boiling term as dryout occurs:

[ ] a,c (7-37)

The derivative of the Chen boiling heat transfer coefficient is used to calculate the wall to fluid heat transfer for nodes in the nucleate boiling regime as described in Section 7.2.10. This derivative is calculated as:

[ ]a,c (7-38)

Since the liquid must be saturated to be in this regime and the interfacial heat transfer rates are high, all of the heat transfer results in evaporation. The heat transfer coefficient for latent heat is set to 0.0 to avoid double accounting.

$$h_{wb,NUCB} = 0.0 \tag{7-39}$$

The heat transfer coefficient to vapor is calculated using Equation 7-6, as it was for the single-phase liquid regime. That is:

$$h_{wv,NUCB} = h_{wv,SPL} = (1 - F_{vap})\, h_{wv,FC} \tag{7-40}$$

For subcooled nucleate boiling, a ramp is imposed on the correlation to avoid sharp discontinuities in the vapor generation rate at small liquid subcoolings. A subcooled boiling modifier is defined as:

[ ]a,c (7-41)

This multiplier is used to determine the split etween latent and sensible heating for subcooled liquid. A numerical ramp is applied between [ ]a,c subcooling to gradually decrease F^*_{SCB}.

This subcooled boiling modifier is defined as:

[ ]a,c (7-42)

(7-43)

for [ ]^{a,c}. For liquid subcoolings less than [ ]^{a,c}, $F_{SCB} = 1.0$.

Subcooled nucleate boiling heat transfer coefficients are then estimated after calculating:

[ ]^{a,c} (7-44)

where the Hancox-Nicoll correlation is used to obtain q''_{HN}, calculated by Equation 7-19 without modification.

The fraction of heat in subcooled boiling that goes into vapor generation, F_{GAM}, is then calculated as:

[ ]^{a,c} (7-45)

Finally, the subcooled nucleate boiling heat transfer coefficients are calculated as:

[ ]^{a,c} (7-46)

[

]^{a,c}

[ ]^{a,c} (7-47)

The heat transfer coefficient to vapor is calculated using Equation 7-6 as it was for the single-phase liquid regime. That is,

$$h_{wv,SUBC} = h_{wv,SPL} = (1 - F_{vap})\, h_{wv,FC} \tag{7-48}$$

Scaling Considerations and Conclusions

In the correlations used for subcooled and saturated nucleate boiling, the forced convection component scales with characteristic length, which is the flow channel hydraulic diameter. These models are assessed by simulating a large number of prototypical rod bundles experiments with WCOBRA/TRAC-TF2. The assessment is presented in Volume 2 of this report.

7.2.3 Critical Heat Flux and Wall Temperature at CHF

Model Basis

The intersection of the nucleate boiling and transition boiling heat transfer regimes occurs at the CHF. To provide for an upper limit to the nucleate boiling regime and a continuous transition to other regimes, the CHF point $\left(q''_{CHF}, T_{CHF}\right)$ must be specified.

Three CHF regimes are considered: modified pool boiling for use during flow reversal, forced convective departure from nucleate boiling (DNB), and annular film dryout.

Pool Boiling DNB

Pool boiling DNB is selected when:[

]^{a,c}

The pool boiling critical heat flux is given by modification of the (Zuber et al., 1961) equation, as recommended by (Bjornard and Griffith, 1977):

$$q''_{CHF} = 0.9\left(1.0 - \alpha_v\right)\frac{\pi}{24} H_{fg}\, \rho_g^{0.5} \left[g_c\, g\sigma\left(\rho_f - \rho_g\right)\right]^{0.25} \tag{7-49}$$

Forced-Convection DNB

Forced-convection DNB is considered when:[

]^{a,c}

The critical heat flux is determined by the CHF look-up table from (Groeneveld, 2007), which is based on quality, mass flux and pressure.

Annular Film Dryout

If annular flow exists, the departure from nucleate boiling is caused by film dryout. In this regime, the heat flux is not limited by a correlation, but rather forced convection vaporization exists until the film dries out. Film dryout is a complex function of the film flow rate, the applied heat flux, and the entrainment/de-entrainment rate, and is determined by the solution of the hydrodynamic equations. This approach was pioneered by (Whalley, Hutchinson, and Hewitt, 1973) and (Whalley, 1976) and has been applied successfully to the analysis of the single tube tests conducted by (Bennett et al., 1967).

To be consistent with the remainder of the heat transfer package, the critical heat flux point for annular film dryout must be defined. A value of [ ]^{a,c} wall superheat has been selected, and the critical heat flux is set to that given by the modified Griffith-Zuber equation (Equation 7-49). The onset of film boiling is not affected by this definition since film boiling is controlled by film dryout. The critical heat flux is ramped between the annular film dryout regime and the pool boiling and forced-convection DNB regimes.

Critical Heat Flux Temperature

To define the boiling curve, it is necessary to know the surface temperature at which CHF occurs. An iterative procedure is used to find the wall temperature at which the heat flux from the (Chen, 1963) nucleate boiling correlation is equal to the critical heat flux. Thus,

$$q''_{CHEN}(T_{CHF}) = q''_{CHF} \tag{7-50}$$

Model as Coded

Calculations to estimate the critical heat flux for vessel component structures are performed in subroutine BOILING. The search is currently limited to:

[ ]^{a,c} (7-51)

The quality and mass flux is calculated and then used with the pressure to determine the critical heat flux from the Groeneveld look-up table is first, and then the Griffith-Zuber critical heat flux is calculated as:

[ ]^{a,c} (7-52)

[

]^{a,c}

The CHF based on flow is calculated as:

$$q''^{*}_{CHF} = \begin{cases} q''_{CHF,Groeneveld} & |G| \geq 30 \frac{g}{cm^2 \cdot s} \\ F_{flow} \times \max\begin{cases} q''_{CHF,Groeneveld} \\ q''_{CHF,Zuber} \end{cases} + (1.0 - F_{flow}) q''_{CHF,Groeneveld} & |G| < 30 \frac{g}{cm^2 \cdot s} \end{cases} \tag{7-53}$$

[ ]a,c (7-54)

where G is the total mass flux in g/cm^2·s.

Next, the CHF based on [ ]^{a,c} is calculated as:

[ ]a,c (7-55)

(7-56)

If the flow is approaching annular dryout, q''_{CHF} is [ ]^{a,c}, and:

$$q''_{CHF} = F_{ad}\, q''_{CHF} \quad (7\text{-}57)$$

[ ]a,c (7-58)

The critical heat flux at the wall surface is then modified to account for the transition to SPV:

[ ]a,c (7-59)

(7-60)

(7-61)

The term in Equation 7-59 representing the heat flux to vapor assumes that $\Delta T_{CHF} =$ [ ]^{a,c}.

Numerical damping is finally applied to avoid rapid changes with time. The critical heat flux then is:

$$\left[\quad\right]^{a,c} \tag{7-62}$$

where $\tilde{q}''_{CHF}$ is calculated by Equation 7-59 and q''^{n}_{CHF} is the critical heat flux calculated for the previous time step.

Scaling Considerations and Conclusions

The correlations used for critical heat flux scale with hydraulic diameter. These models are assessed by simulating a large number of prototypical rod bundles experiments with WCOBRA/TRAC-TF2. The assessment is presented in Volume 2 of this report.

7.2.4 Transition Boiling

Model Basis

The transition boiling heat transfer regime exists between the critical heat flux (q''_{CHF}, T_{CHF}) and the minimum film boiling point (q''_{MIN}, T_{MIN}). In this regime, liquid makes only intermittent contact with the wall. The vessel component in WCOBRA/TRAC-TF2 uses three separate models to estimate the transition boiling heat transfer coefficient. These values are compared, and the maximum is used to calculate the transition boiling heat flux.

Model 1

The first model used to estimate transition boiling heat transfer coefficients is based on a mechanistic approach to the heat transfer. This model is similar to those suggested by (Iloeje et al., 1974) and (Ganic and Rohsenow, 1977). Transition boiling heat transfer is assumed to be composed of both wet wall and dry wall heat transfer components. In this model, the transition boiling heat flux is expressed as:

$$q''_{TBI} = q''_{cwv} + q''_{rwv} + q''_{rw\ell} + q''_{dcht} \tag{7-63}$$

where:

q''_{cwv} = heat transfer by convection from wall to vapor
q''_{rwv} = radiation heat transfer from wall to vapor
$q''_{rw\ell}$ = radiation heat transfer from wall to liquid
q''_{dcht} = direct contact heat transfer from wall to liquid

The heat transfer by convection from wall to vapor, q''_{cwv}, is determined by:

$$q''_{cwv} = h_{wv,FC}\left(T_w - T_v\right) \tag{7-64}$$

and the heat transfer by radiation from wall to vapor, q''_{rwv}, is determined by:

$$q''_{rwv} = h_{wv,RAD}\left(T_w - T_v\right) \tag{7-65}$$

where the expressions for $h_{wv,FC}$ and $h_{wv,RAD}$ are described in Section 7.2.8.

The heat transfer by radiation from wall to entrained liquid droplets, $q''_{rw\ell}$, is based on void fraction, and equal to that from the film boiling models as discussed in Sections 7.2.6 and 7.2.7:

[ ]^{a,c} (7-66)

The direct contact heat transfer term, q''_{dcht}, is composed of terms representing direct contact heat transfer to the continuous and entrained liquid fields as:

$$q''_{dcht} = q''_{dcht,\ell} + q''_{dcht,e} \tag{7-67}$$

The direct contact heat transfer to the entrained field is calculated using a model developed by (Forslund and Rohsenow, 1968):

[ ]^{a,c} (7-68)

[

]^{a,c}

[ ]^{a,c} (7-69)

The direct contact heat transfer to the continuous liquid field is modeled by assuming the liquid maintains wall contact only intermittently with an effectiveness, ε_{wet}. The continuous liquid direct contact heat transfer is given by:

$$q''_{dcht,\ell} = h_{w\ell,SPL}\,\varepsilon_{wet}\left(T_w - T_\ell\right) \tag{7-70}$$

The contact effectiveness is defined similar to (Ganic and Rohsenow, 1977) as:

[ ] a,c (7-71)

In their original work, Ganic and Rohsenow assumed m = 2. However, this assumption gives unrealistic values at high pressure. In (Bajorek et al., 1998), the coefficient m was redefined to be:

[ ] a,c (7-72)

This is carried forward into WCOBRA/TRAC-TF2. Figure 7.2-6 shows the effectiveness function compared to values obtained for droplets by (Wachters and Westerling, 1966), (Corman, 1966), (Gaugler, 1966), and (Pedersen, 1967) at atmospheric pressure. Figure 7.2-7 shows the variation of ε_{wet} as coded at higher pressure.

Model 2

The second model for transition boiling also expresses the heat flux as the sum of wet wall and dry wall contributions. The wet wall contribution to the heat flux is assumed to be a function of the critical heat fluxes:

$$q''_{TB2} = q''_{cwv} + q''_{rwv} + q''_{rw\ell} + q''_{wet} \tag{7-73}$$

where:

q''_{cwv} = heat transfer by convection from wall to vapor; Equation 7-64
q''_{rwv} = radiation heat transfer from wall to vapor; Equation 7-65
$q''_{rw\ell}$ = radiation heat transfer from wall to liquid; Equation 7-66
q''_{wet} = heat transfer from wall to liquid for the "wetted" portion, as:

$$q''_{wet} = F_{film}\, F_{wet}\, q''_{CHF} \tag{7-74}$$

q''_{CHF} is the critical heat flux calculated from Equation 7-62. (Bjornard and Griffith, 1977) reported that the fraction of wetted wall, F_{wet}, as:

$$F_{wet} = \left(\frac{T_W - T_{MIN}}{T_{CHF} - T_{MIN}} \right)^2 \tag{7-75}$$

provides good agreement with data as described by (Groeneveld and Fung, 1976) and with (McCreery et al., 1977). F_{film} is used to account for the disappearance of the liquid, and is calculated as:

[ ]a,c (7-76)

The ramp, F_{film}, is shown in Figure 7.2-8.

Model 3

A third transition boiling model is applied in the region near a top-down quench front. For a top-down quench, the void fraction can be very high (0.95-0.99) and yet still produce a significant quench rate. The transition boiling heat flux for this model is based on Zuber's estimate of the critical heat flux as:

$$q''_{TB3} = q''_{cwv} + q''_{rwv} + q''_{rw\ell} + q''_{TQ} \quad (7\text{-}77)$$

where:

q''_{cwv} = heat transfer by convection from wall to vapor; Equation 7-64
q''_{rwv} = radiation heat transfer from wall to vapor; Equation 7-65
$q''_{rw\ell}$ = radiation heat transfer from wall to liquid; Equation 7-66
q''_{TQ} = heat transfer from wall to liquid for top-down quench, as:

[ ]a,c (7-78a)

where L_{QF} is the distance in feet from the top quench front; F_{wet} is given by Equation 7-75; and, the Zuber critical heat flux is given by:

[ ]a,c (7-78b)

Model as Coded

The transition boiling heat transfer coefficients are calculated in subroutine HCOOL when the wall temperature is between T_{CHF} and T_{MIN}. These coefficients are calculated as follows.

The model for q''_{TB1} uses a liquid contact effectiveness ε_{wet} that was defined by Equations 7-71 and 7-72. Limits are placed on the calculated value of ε_{wet} to insure that only reasonable values are employed in subsequent calculations. The maximum value allowed for ε_{wet} is [ ]^{a,c}. A value less than [ ]^{a,c} is used based on the assumption that during stable nucleate boiling some fraction of the wall at any given moment is effectively covered by vapor. A minimum value of [ ]^{a,c} is used as a lower limit for ε_{wet}. So, the liquid contact effectiveness is calculated as:

[ ]a,c (7-79)

where the exponent m is given by Equation 7-72 and T_w and T_{sat} are in °F.

The wet wall components of heat transfer for Model 1 and Model 2 are then calculated, and the maximum is selected:

$$q''^{*}_{wet} = \max\begin{Bmatrix} q''_{dcht,\ell} + q''_{dcht,e} \\ F_{film}\, F_{wet}\, q''_{CHF} \end{Bmatrix} \quad (7\text{-}80)$$

where $q''_{dcht,\ell}$ is calculated by Equation 7-70; $q''_{dcht,e}$ by Equation 7-68 except [ ]^{a,c}; F_{wet} by Equation 7-75; F_{film} by Equation 7-76; and q''_{CHF} by Equation 7-62 without modification.

Model 3 is considered only if the wall location is within [ ]^{a,c} feet of a top quench front. If L_{QF} is < [ ]^{a,c} feet, the wetted wall transition boiling heat flux is selected as:

[ ]a,c (7-81)

where $q''^{*}_{TB,wet}$ is given by Equation 7-80; F_{film} is given by Equation 7-76; q''_{Zuber} is given by Equation 7-78b; and F^{*}_{wet} is given by:

[ ]a,c (7-82)

(7-83)

The transition boiling regime heat transfer coefficients are then calculated as:

[a,c] (7-84)

[a,c] (7-85)

$$h_{wv,TB} = h_{wv,FC} + h_{wv,RAD} \quad (7\text{-}86)$$

The first term in Equation 7-84 represents radiation from the wall to the liquid phase and is calculated with Equation 7-66, and $q''_{CHF,Zuber}$ is calculated with Equation 7-52. In these expressions, $h_{wv,FC}$ by Equation 7-160; $h_{wv,rad}$ by Equation 7-161; and the term F_{SCB} is intended to direct more heat to sensible heating as the liquid subcooling increases (Section 7.2.2) and is calculated by Equation 7-43.

Scaling Considerations and Conclusions

The set of correlations used for transition boiling heat transfer scale with hydraulic diameter. These models are assessed by simulating a large number of prototypical rod bundles experiments with WCOBRA/TRAC-TF2. The assessment is presented in Volume 2 of this report.

7.2.5 Minimum Film Boiling Wall Temperature

Model Basis

The transition boiling regime is bounded by the CHF point and the minimum stable film boiling point. It is assumed that the minimum film boiling temperature is the wall temperature that results in an instantaneous contact temperature equal to the homogeneous nucleation temperature, T_{hn}. Using a contact temperature correction to include the effects of surface thermal properties, the minimum film boiling temperature is:

$$T_{MIN,hn} = T_{hn} + (T_{hn} - T_\ell)\left[\frac{(k\rho C_p)_\ell}{(k\rho C_p)_w}\right]^{0.5} \quad (7\text{-}87)$$

where the homogeneous nucleation temperature (T_{hn}) is given as a function of pressure by a simple curve fit:

$$T_{hn} = 705.44 - (4.722\times10^{-2})\Delta P_{crit} + (2.3907\times10^{-5})\Delta P_{crit}^2 - (5.8193\times10^{-9})\Delta P_{crit}^3 \quad (7\text{-}88)$$

where $\Delta P_{crit} = 3203.6 - P$ psi and T_{hn} in °F.

The minimum film boiling temperature is specified as the larger of either Equation 7-87 or that given by Henry's modification (Henry, 1974) of the Berenson correlation:

$$T_{MIN,Henry} = T_B + 0.42(T_B - T_\ell)\left\{\left[\frac{(k\rho C_p)_\ell}{(k\rho C_p)_w}\right]^{0.5}\left[\frac{H_{fg}}{C_{p_w}(T_B - T_{sat})}\right]\right\}^{0.6} \quad (7\text{-}89)$$

$$T_B = T_{sat} + 0.127\frac{\rho_v H_{fg}}{k_v}\left[\frac{g(\rho_\ell - \rho_v)}{(\rho_\ell + \rho_v)}\right]^{\frac{2}{3}}\left[\frac{g_c \sigma}{g(\rho_\ell - \rho_v)}\right]^{\frac{1}{2}}\left[\frac{\mu_v}{g(\rho_\ell - \rho_v)}\right]^{\frac{1}{3}} \quad (7\text{-}90)$$

where:

C_{P_ℓ} = liquid specific heat (BTU/lbm-°F)
C_{Pw} = wall specific heat (BTU/lbm-°F)
g = gravitational constant (ft/hr^2)
g_c = conversion factor (equal to g but in ft-lbm/lbf-hr^2)
H_{fg} = heat of formation (BTU/lbm)
k_ℓ = liquid thermal conductivity (BTU/hr-ft-°F)
k_v = vapor thermal conductivity (BTU/hr-ft-°F)
k_w = wall thermal conductivity (BTU/hr-ft-°F)
ρ_ℓ = liquid density (lbm/ft^3)
ρ_v = vapor density (lbm/ft^3)
ρ_w = wall density (lbm/ft^3)
σ = surface tension (lbf/ft)
T_ℓ = liquid temperature (°F)
T_{sat} = saturation temperature (°F)
μ_v = vapor viscosity (lbm/ft-hr)

Model as Coded

The minimum film boiling temperature for all unheated structures (except for spacer grids; see Equation 7-175) is assumed to be T_{MIN} = [ ]^{a,c}. For heated structures, T_{MIN} is calculated as:

[ ]^{a,c} (7-91)

where the [ ]^{a,c} properties in Equations 7-87, 7-88 and 7-89 are taken to be at [ ]^{a,c}, and the [ ]^{a,c} properties are taken to be at the [ ]^{a,c}. The [ ]^{a,c}

[

]^{a,c}

Scaling Considerations and Conclusions

The minimum film boiling temperature has been found to occur over a range of values that depends on the fluid conditions and the surface properties. This is calculated in WCOBRA/TRAC-TF2 by appropriate correlations, and the value of T_{MIN} is limited to a range of values observed in experiments. The correlations depend on the thermal properties of the wall and of the coolant and do not depend on the system geometry, and are therefore scale independent. Since Equation 7-89 can give unreasonable values at high pressures, limits are placed on T_{MIN} to keep the calculated values in a reasonable range. The correlations for T_{MIN} and the limitations on permissible values have been assessed by their use in simulations of prototypical rod bundle test facilities reported in Volume 2 of this report.

7.2.6 Inverted Annular Film Boiling

Model Basis

The WCOBRA/TRAC-TF2 vessel heat transfer package assumes that the flow has an inverted annular pattern if the wall temperature is greater than the minimum stable film boiling temperature, $T_w > T_{MIN}$, and the void fraction is less than [ ]^{a,c}. Below a void fraction of [ ]^{a,c}, the inverted annular film boiling heat transfer coefficient uses a modified form of the (Bromley, 1950) correlation. The revised form of the Bromley correlation used in WCOBRA/TRAC-TF2 is documented in (Pomerantz, 1964). For void fractions in the range [ ]^{a,c}, the heat transfer coefficients are interpolated between those of this version of the Bromley equation and heat transfer coefficients for dispersed droplet flow. The modified version of the Bromley equation, given by (Pomerantz, 1964) is:

$$h_{Bromley} = 0.62\left(\frac{D_h}{\lambda}\right)^{0.172}\left[\frac{k_v^3 \rho_v (\rho_\ell - \rho_v) H_{fg} g}{D_h \mu_v (T_w - T_{sat})}\right]^{\frac{1}{4}} \tag{7-92}$$

where, the critical wavelength (λ) is:

$$\lambda = 2\pi\left[\frac{g_c \sigma}{g(\rho_\ell - \rho_v)}\right]^{\frac{1}{2}} \tag{7-93}$$

Radiation heat transfer from the wall to liquid in an inverted annular column is based on radiation between two concentric cylinders. The radiative heat flux from the wall to the liquid can be expressed as:

$$q''_{rw\ell} = \frac{\sigma_{SB}\left(T_w^4 - T_{sat}^4\right)}{\frac{A_w}{A_\ell}\left(\frac{1.0}{\varepsilon_\ell}\right) + \left(\frac{1.0}{\varepsilon_w} - 1.0\right)} \tag{7-94}$$

where:

A_w = wall surface area
A_ℓ = inverted annular column surface area
σ_{SB} = Stefan-Boltzmann constant
ε_w = wall emissivity
ε_ℓ = liquid emissivity

For α_v [ ]^{a,c}, the heat flux in inverted annular flow is:

$$q''_{IAFB} = q''_{Bromley} + q''_{rw\ell} \tag{7-95}$$

If [ ]^{a,c}, the inverted annular heat flux is linearly interpolated between q''_{IAFB} and the heat flux in dispersed flow film boiling, q''_{DFFB}, which is described in Section 7.2.7.

Model as Coded

Calculation of the inverted annular regime heat transfer coefficients are performed in subroutine HCOOL. Heat transfer coefficients are defined for the vapor phase and for sensible and latent heating of the liquid.

To estimate these heat transfer coefficients, the Bromley film boiling heat flux is estimated as:

$$q''_{Bromley} = h_{Bromley}(T_w - T_{sat}) \tag{7-96}$$

Equation 7-92 is used to calculate $h_{Bromley}$, with the exception that [ ]^{a,c}. The value of $q''_{Bromley}$ from Equation 7-96 is compared to the dispersed flow heat flux (described in the next section). If the dispersed flow heat flux is [

]^{a,c}

[ ] a,c (7-97)

where [ ]^{a,c}.

Vapor superheat and void fraction are taken into account by defining:

[ ] a,c (7-98)

The liquid and additional vapor phase contributions from the Bromley correlation are then calculated as:

$$q''_{w\ell,Bromley} = (1.0 - F_{IAFB}) q''^{*}_{Bromley} \tag{7-99}$$

$$q''_{wv,Bromley} = F_{IAFB}\, q''^{*}_{Bromley} \tag{7-100}$$

The radiation heat transfer from the wall to an inverted annular column is calculated using Equation 7-94 with the assumptions that ε_w = [ ]^{a,c} and ε_ℓ = [ ]^{a,c}. [

]^{a,c}

[ ] a,c (7-101)

An additional assumption is made that [

]^{a,c} so that Equation 7-94 is reduced to:

$$q''_{rw\ell} = F'_{w\ell}\left(T_w^4 - T_{sat}^4\right) \tag{7-102}$$

[ ] a,c (7-103)

The radiation heat transfer coefficients are then calculated as:

$$h_{rw\ell} = F'_{w\ell}\frac{T_w^4 - T_{sat}^4}{T_w - T_\ell} \tag{7-104}$$

For Equation 7-104, it is assumed that the surface temperature of the liquid drops and liquid column is [ ]^{a,c}.

For α_v [ ]^{a,c}, the regime is denoted as the inverted annular film boiling regime and the heat transfer given by:

$$h_{wv,IAFB} = h_{wv,FC} + h_{wv,RAD} + \frac{q''_{wv,Bromley}}{T_w - T_v} \tag{7-105}$$

$$h_{w\ell,IAFB} = h_{rw\ell} \tag{7-106}$$

$$h_{wb,IAFB} = \frac{q''_{w\ell,Bromley}}{T_w - T_{sat}} \tag{7-107}$$

where:

$h_{wv,FC}$ is given by Equation 7-160;

$h_{wv,RAD}$ is given by Equation 7-161;

$q''_{wv,Bromley}$ is given by Equation 7-100;

$h_{rw\ell}$ is given by Equation 7-104; and

$q''_{w\ell,Bromley}$ is given by Equation 7-99.

If [ ]^{a,c}, the heat transfer coefficients are calculated using a linear void fraction ramp between the Bromley heat flux and the dispersed droplet regime heat flux. In this void fraction range, the heat transfer regime is designated the inverted annular dispersed flow regime.

The ramp is defined as:

$$\left[\qquad\qquad\right]^{a,c} \tag{7-108}$$

and the heat transfer coefficients for the inverted annular dispersed flow regime are calculated as:

$$h_{wv,IADF} = F_{IADF}\, h_{wv,IAFB} + (1.0 - F_{IADF}) h_{wv,DFFB} \tag{7-109}$$

$$h_{w\ell,IADF} = F_{IADF}\, h_{w\ell,IAFB} + (1.0 - F_{IADF}) h_{w\ell,DFFB} \tag{7-110}$$

$$h_{wb,IADF} = F_{IADF}\, h_{wb,IAFB} + (1.0 - F_{IADF}) h_{wb,DFFB} \tag{7-111}$$

where:

F_{IADF} is given by Equation 7-108;

$h_{wv,IAFB}$ is given by Equation 7-105;

$h_{wv,DFFB}$ is given by Equation 7-142;

$h_{w\ell,IAFB}$ is given by Equation 7-106;

$h_{w\ell,DFFB}$ is given by Equation 7-143;

$h_{wb,IAFB}$ is given by Equation 7-107; and,

$h_{wb,DFFB}$ is given by Equation 7-144.

Figure 7.2-9 illustrates the effect of the various ramps in the film boiling regimes. As the wall temperature increases, a higher proportion of the overall heat transfer goes to the vapor phase while direct contact heat transfer and radiation to the liquid phases diminishes. As void fraction increases the heat transfer to the liquid phases decreases to zero.

Scaling Considerations and Conclusions

The inverted annular heat transfer regime is characterized by the separation of the liquid field from the heated surface by a thin layer of vapor. Only a very limited amount of liquid-wall contact is assumed to be possible. The main components of the heat transfer are convection to vapor and thermal radiation to the inverted liquid annular column. As the inverted annular column breaks up, there is a transition to dispersed droplet film boiling. These processes are represented in WCOBRA/TRAC-TF2 by appropriate correlations. Each of the main mechanisms of heat transfer is modeled. A smooth transition to dispersed droplet film boiling is provided.

The modified Bromley correlation (Equation 7-92) uses the hydraulic diameter (D_h) as the length scale. (Bjornard and Griffith, 1977) note that while there is some disagreement in the literature as to whether the hydraulic diameter, the rod diameter, or the critical wavelength should be used, all three yield virtually the same results. Thus, the Bromley correlation is seen to be relatively scale independent.

The models and correlations for the inverted annular heat transfer regime have been assessed through their use in reflood separate effects tests (Volume 2 of this report) and in the Cylindrical Core Test Facility (CCTF) and Loss-of-Fluid Test (LOFT) integral tests. In particular, inverted annular heat transfer is important in reflood separate effects tests with high reflood rates.

7.2.7 Dispersed Flow Film Boiling

Model Basis

Dispersed flow film boiling is assumed when the void fraction is greater than [ ]^{a,c} and the wall temperature is greater than T_{MIN}. It is calculated as a "two-step" method where the dominant heat transfer mode is forced convection to superheated steam. The steam superheat is then determined by the interfacial heat transfer rate to the entrained droplets as part of the hydrodynamic solution. The dispersed flow film boiling heat flux is composed of four components. The total heat flux is given by:

$$q''_{DFFB} = q''_{cwv} + q''_{rwv} + q''_{rwe} + q''_{dcht,e} \tag{7-112}$$

where:

q''_{cwv} = convective heat flux to vapor
q''_{rwv} = radiative heat flux to vapor
q''_{rwe} = radiative heat flux to droplets
$q''_{dcht,e}$ = drop-wall direct contact heat transfer

A discussion of each of these components of the dispersed flow heat flux follows.

Forced Convection to Vapor

The convective heat flux to vapor flowing through a rod bundle in a dispersed droplet flow is increased by the interfacial shear with the droplets and by an increase in the turbulence due to the support grids. In WCOBRA/TRAC-TF2, the convective heat flux to vapor in dispersed flow film boiling is expressed as:

$$q''_{cwv} = F_{grid}\, F_{2\phi}\, h_{wv,FC} \left(T_w - T_v\right) \tag{7-113}$$

where:

$h_{wv,FC}$ = heat transfer coefficient to single phase vapor;
F_{grid} = grid heat transfer enhancement factor;
$F_{2\phi}$ = two-phase enhancement factor.

The heat transfer coefficient to single-phase vapor $\left(h_{wv,FC}\right)$ is determined from Equation 7-160. A description of the grid heat transfer enhancement factor $\left(F_{grid}\right)$, radiation heat flux, droplet impingement heat flux and two-phase enhancement factor $\left(F_{2\phi}\right)$ follow.

Grid Heat Transfer Enhancement Factor

Spacer grids are structural members in the reactor core which support the fuel rods at a prescribed rod-to-rod pitch. Since the grid reduces the fuel assembly flow area, the flow contracts and then expands downstream of each grid. As the flow is accelerated within the grid and then expands downstream, it disrupts and reestablishes the fluid and thermal boundary layers on the fuel rod, increasing local heat transfer within and downstream of the grid. Several single-phase experiments clearly showed that the continuous phase heat transfer downstream of a spacer grid can be modeled as an entrance effect phenomenon in which the abrupt contraction and expansion result in the establishment of a new boundary layer downstream of the grid.

This entrance effect heat transfer decays exponentially downstream of the grid, as shown in Figure 7.2-10. (Chiou, Hochreiter, and Young, 1986) summarized the single-phase and two-phase experiments that demonstrated the grid convective enhancement effect, and provided a complete description of the effect of grids on the flow.

The flow acceleration and consequent deceleration as the coolant flows past grid spacer cause a local increase in heat transfer rates downstream because of the creation of free turbulence and the separation and reestablishment of the boundary layer.

The correlation for single-phase enhancement downstream of a spacer grid used in WCOBRA/TRAC-TF2 was developed by [ ]^{a,c}:

$$\left[\right]^{a,c} \tag{7-114}$$

[

]^{a,c}

[

]^{a,c}

Radiation Heat Transfer in Dispersed Flow

The (Sun, Gonzalez, and Tien, 1976) model is used to account for radiation heat transfer to vapor and droplets in the dispersed flow film boiling regime. They showed that for a dispersed droplet flow, the wall, vapor, and droplets can be treated as single nodes in a radiation network analysis if the flow is assumed to be optically thin. The gray body factors are:

$$F_{we} = \frac{1.0}{R_2\left(1.0 + \frac{R_3}{R_1} + \frac{R_3}{R_2}\right)} \tag{7-115}$$

$$F_{wv} = \frac{1.0}{R_1\left(1.0 + \frac{R_3}{R_1} + \frac{R_3}{R_2}\right)} \tag{7-116}$$

where:

$$R_1 = \frac{1.0 - \varepsilon_v}{\varepsilon_v\left(1.0 - \varepsilon_v \varepsilon_\ell\right)} \tag{7-117}$$

$$R_2 = \frac{1.0 - \varepsilon_\ell}{\varepsilon_\ell\left(1.0 - \varepsilon_v \varepsilon_\ell\right)} \tag{7-118}$$

$$R_3 = \frac{1.0}{1.0 - \varepsilon_v \varepsilon_\ell} + \frac{1.0 - \varepsilon_w}{\varepsilon_w} \tag{7-119}$$

$$\varepsilon_v = 1.0 - \exp\left(-a_v L_b\right) \tag{7-120}$$

$$\varepsilon_\ell = 1.0 - \exp\left(-a_\ell L_b\right) \tag{7-121}$$

The parameter L_b is the mean beam length and is assumed to be equal to [ ]^{a,c}. The terms a_v and a_ℓ are the vapor and liquid absorption coefficients and ε_v, ε_ℓ, and ε_w are the vapor, liquid, and wall emissivities, respectively.

The liquid absorption coefficient is defined as:

$$a_\ell = \psi_a \frac{\pi D_d^2 N_d}{4} \tag{7-122}$$

where D_d is a droplet diameter and N_d is a droplet number density. The parameter ψ_a is the absorption efficiency and has a value of [ ]^{a,c} for drops in the range [ ]^{a,c}.

The droplet number density can be expressed as:

$$N_d = \frac{6.0(1.0-\alpha_v)}{\pi D_d^3} \tag{7-123}$$

such that Equation 7-122 becomes:

$$a_\ell = 1.11 \frac{1.0-\alpha_v}{D_d} \ (ft^{-1}) \tag{7-124}$$

The vapor absorption coefficient is given by:

$$a_v = \left(\frac{P}{14.7}\right)\left[5.6\left(\frac{1000.0}{T_v+460.0}\right)^3 - 0.3\left(\frac{1000.0}{T_v+460.0}\right)^4\right](ft^{-1}) \tag{7-125}$$

which is from (Abu-Romia and Tien, 1967).

The fluid emissivities are then given by:

$$\varepsilon_v = 1.0 - \exp(-0.85 a_v L_b) \tag{7-126}$$

$$\varepsilon_\ell = 1.0 - \exp(-0.85 a_\ell L_b) \tag{7-127}$$

where the beam length (L_b) is assumed to be equal to [ ]^{a,c}. Additional information on Equations 7-126 to 7-127 can be found in (Yao, Hochreiter and Dodge, 1979).

Finally, the radiative heat transfer coefficients from wall-to-vapor and wall-to-droplet can be calculated as:

$$h_{rwv} = F_{wv} \frac{T_w^4 - T_v^4}{T_w - T_v} \tag{7-128}$$

$$h_{rwe} = F_{we}\frac{T_w^4 - T_{sat}^4}{T_w - T_{sat}} \quad (7\text{-}129)$$

Droplet Impingement Heat Flux

Forslund and Rohsenow developed a model for calculating the direct contact heat transfer for the dispersed droplet field (Forslund and Rohsenow, 1968):

[ ]^{a,c} (7-130)

[ ]^{a,c}

[ ]^{a,c} (7-131)

[

]^{a,c}

[ ]^{a,c} (7-132)

(7-133)

[

]^{a,c}

[ ]^{a,c} (7-134)

[

]^{a,c}

[

]^{a,c}

Two-Phase Enhancement

Some dispersed flow experiments, such as those described by (Spencer and Young, 1980), (Lee et al., 1981) and (Drucker and Dhir, 1984), have shown that interfacial shear between dispersed particles and a continuous phase increases the turbulence level and enhances the convective heat transfer. The two-phase enhancement factor for dispersed flow, $F_{2\phi}$, is approximated by an extension of the analogy between wall shear stress and heat transfer, described by (Kays, 1966).

The wall shear stress can be written as:

$$\tau_w = \frac{1}{2}\rho_v f_w \frac{U_v^2}{D_h} \tag{7-135}$$

and the interfacial shear stress due to the droplets by:

$$\tau_d = \frac{3}{4}\alpha_e \rho_v C_{D_d} \frac{(U_v - U_d)^2}{D_d} \tag{7-136}$$

and the total shear stress level for the two-phase dispersed flow field as:

$$\tau_{2\phi} = \tau_w + \tau_d \tag{7-137}$$

where:

f_w = wall friction factor [ ]^{a,c}

C_{D_d} = droplet drag coefficient

D_d = drop diameter

α_e = volume fraction of entrained drops

From the momentum – heat transfer analogy, the turbulent convective heat transfer coefficient is proportional to the square root of the shear stress, given by (Kays, 1966) as:

$$h_{wv,SPV} \propto \sqrt{\tau_w} \tag{7-138}$$

The two-phase enhancement factor can be defined as the ratio of convective heat transfer in a two-phase dispersed droplet field to that for single phase vapor as:

$$F_{2\phi} = \frac{h_{cwv,2\phi}}{h_{cvw,SPV}} = \sqrt{\frac{\tau_{2\phi}}{\tau_w}} \tag{7-139}$$

or, using Equation 7-137:

$$F_{2\phi} = \sqrt{1.0 + \frac{\tau_d}{\tau_w}} \tag{7-140}$$

Using Equations 7-135 and 7-136, the shear stress ratio is calculated as:

$$\frac{\tau_d}{\tau_w} = 1.5\alpha_e \left(\frac{D_h}{D_d}\right)\left(\frac{C_{D_d}}{f_w}\right)\left(1.0 - \frac{U_d}{U_v}\right)^2 \tag{7-141}$$

Instantaneous local values of the variables α_e, D_d, C_{Dd}, f_w, U_v and U_d are used to evaluate Equation 7-141. A comparison of the two-phase enhancement inferred from FLECHT reflood tests is shown in Figure 7.2-11. The figure also shows a correlation for turbulence enhancement developed from separate air/water tests and from rod bundle tests at UCLA for EPRI by (Drucker and Dhir, 1984).

Model as Coded

The heat transfer coefficients for the dispersed flow film boiling regime are calculated in subroutine HCOOL. The heat transfer coefficients are calculated as follows:

$$h_{wv,DFFB} = F_{grid}\, F_{2\phi}\, h_{wv,FC} + h_{rwv} \tag{7-142}$$

$$h_{w\ell,DFFB} = h_{rwe} \tag{7-143}$$

$$h_{wb,DFFB} = 0 \tag{7-144}[1]$$

where:

$h_{wv,FC}$ = forced convection heat transfer wall to vapor, Equation 7-160;

h_{rwv} = radiation heat transfer wall to vapor, Equation 7-152;

h_{rwe} = radiation heat transfer wall to droplets, Equation 7-153;

[1] Equation 7-145 intentionally omitted.

F_{grid} = grid enhancement multiplier, Equation 7-114;

$F_{2\phi}$ = two-phase enhancement multiplier, Equations 7-140 and 7-141 and limited to [ ]^{a,c}.

The liquid absorption coefficient is calculated as:

[ ]^{a,c} (7-146)

[ ]^{a,c}.

The liquid emissivity is calculated as:

[ ]^{a,c} (7-147)

where the mean beam length is assumed to be the [ ]^{a,c}.

The vapor absorption coefficient is calculated as:

$$a_v = \left(\frac{P}{14.7}\right)\left[5.6\left(\frac{1000}{T_v}\right)^2 - 0.3\left(\frac{1000}{T_v}\right)^4\right] ft^{-1} \quad (7\text{-}148)$$

where P is the pressure in psia and T_v is the vapor temperature in Rankine.

The vapor emissivity by:

[ ]^{a,c} (7-149)

The gray body factors are then calculated:

$$F'_{wv} = \frac{\sigma_{SB}}{R_1\left(1 + \frac{R_3}{R_1} + \frac{R_3}{R_2}\right)} \quad (7\text{-}150)$$

[ ]^{a,c} (7-151)

where R_1, R_2, and R_3 are calculated by Equations 7-117 to 7-119, and the Stefan-Boltzmann constant is $\sigma_{SB} = 1.713 \times 10^{-9} \frac{Btu}{hr \cdot ft^2 \cdot {}^\circ R^4}$.

The radiation heat transfer coefficients are then calculated as:

$$h_{rwv} = F'_{wv} \frac{(T_w^4 - T_v^4)}{(T_w - T_v)} \quad (7\text{-}152)$$

$$h_{rwe} = F'_{we} \frac{(T_w^4 - T_{sat}^4)}{(T_w - T_\ell)} \quad (7\text{-}153)$$

Scaling Considerations and Conclusions

Though the predictive performance of the model depends on the interfacial heat transfer between the vapor and droplets, the key process in dispersed flow film boiling is convective heat transfer to vapor. In the WCOBRA/TRAC-TF2 model, this process is represented by appropriate convective heat transfer correlations and modified by factors to account for the effect of droplets and grids.

The convective heat transfer correlations used in the dispersed flow film boiling regime scale with hydraulic diameter. The radiation heat transfer coefficients assume that the mean beam length is equal to the [ ]^{a,c}, so that h_{rwv} and h_{rwe} also scale with the [ ]^{a,c}. The direct contact heat transfer also scales with the [ ]^{a,c}.

The model for dispersed flow film boiling heat transfer was assessed by simulations of reflood, blowdown and refill separate effects tests (Volume 2 of this report). These tests utilized full-scale fuel assemblies and therefore validate the use of this model for analysis of PWR fuel bundles.

7.2.8 Single-Phase Vapor

Model Basis

Heat transfer to single-phase vapor (SPV) is assumed when $\alpha_v >$ [ ]^{a,c}. The WCOBRA/TRAC-TF2 vessel component uses four correlations to determine the heat transfer coefficients for convection to single-phase vapor which is added to a heat transfer coefficient for radiation to vapor. The maximum value of these convection correlations is chosen, along with the radiation component, as the heat transfer coefficient to be used to calculate the heat flux to provide a continuous and smooth transition between

heat transfer regimes. These convective correlations are the (McAdams, 1954) correlation for turbulent natural convection, a constant Nusselt number value for laminar forced convection, the (Dittus and Boelter, 1930) equation and an expression proposed by (Wong and Hochreiter, 1981) for turbulent forced convection. This section presents each correlation and describes its basis.

The McAdams correlation for turbulent free convection over vertical plates and cylinders is given by:

$$h_{wv,nc} = 0.13\left(\frac{k_v}{L}\right)(Gr_v\, Pr_v)^{0.333} \tag{7-154}$$

where the Grashof number (Gr_v) is defined by:

$$Gr_v = \frac{g\beta|T_w - T_v|L^3 \rho_v^2}{\mu_v^2} \tag{7-155}$$

where:

β = thermal expansion coefficient
L = characteristic length, and is taken to be the hydraulic diameter

and Prandtl number (Pr_v) defined by:

$$Pr_v = \frac{\mu_v C_{p_v}}{k_v} \tag{7-156}$$

The form of the McAdams correlation results from the analysis of the boundary layer on a vertical surface, at uniform temperature and in an infinite fluid at rest. It is assumed that the flow in the boundary layer is buoyancy induced, and is primarily parallel to the surface. Although the coefficients for this correlation were originally developed by fitting the equation to data from vertical flat plates in air, the McAdams correlation has also been found to provide good estimates of the heat transfer coefficients for vertical planes and short horizontal surfaces in water, oils, alcohols, and air. This correlation is valid in the range $10^9 < GrPr < 10^{13}$.

For laminar flow, the heat transfer coefficient to vapor is determined from Lee et al., 1981, to be a constant Nusselt number of 10. Thus, for laminar vapor flow the heat transfer coefficient is given by:

$$h_{wv,lam} = 10.0\left(\frac{k_v}{D_h}\right) \tag{7-157}$$

where k_v is the film thermal conductivity for vapor.

This expression for the laminar flow heat transfer coefficient is in the same form as that for fully developed laminar flow in a circular pipe with a constant wall heat flux. The Nusselt number for internal tube flow with constant wall heat flux is 4.364. For laminar external flows, it has been shown that the

calculated Nusselt number is higher. (Kim, 1979) showed that the Nusselt number for an infinite rod bundle with a square rod to pitch ratio of 1.33 is 7.86.

For forced turbulent flow, convective vapor heat transfer coefficients are determined by the Dittus-Boelter equation and a correlation proposed by (Wong and Hochreiter, 1981) that is based on experimental rod bundle data. The Dittus-Boelter equation was originally developed for turbulent flow within smooth tubes in automobile radiators. It has since proven acceptable for many other applications involving turbulent flows. It is given by:

$$h_{wv,DB} = 0.023\left(\frac{k_v}{D_h}\right)\left(\frac{G_v D_h}{\mu_v}\right)^{0.8}(Pr_v)^n \tag{7-158}$$

where n = 0.4 for heating and n = 0.3 for cooling. All vapor properties are evaluated at the mean film temperature.

The expression proposed by (Wong and Hochreiter, 1981) is:

$$h_{wv,WH} = 0.0797\left(\frac{k_v}{D_h}\right)\left(\frac{G_v D_h}{\mu_v}\right)^{0.6774}(Pr_v)^{0.3333} \tag{7-159}$$

This correlation is a linear regression fit to experimental data obtained from steam cooling heat transfer tests run in a 17x17 rod bundle at [ ]^{a,c}. This correlation predicts heat transfer coefficients that are larger than those predicted by the Dittus-Boelter equation for Reynolds numbers less than 25,000.

The radiation to vapor heat transfer coefficient is the same as that developed for dispersed flow film boiling as given by Equation 7-128 in Section 7.2.7.

Model as Coded

The set of four correlations are coded as presented above, with all fluid properties evaluated at the mean film temperature. These correlations are applied to both vertical and horizontal surfaces in the vessel and use the hydraulic diameter of the flow channel, D_h, as the characteristic length.

For heated structures, the heat transfer coefficient to single-phase vapor is calculated as:

$$h_{wv,FC} = \begin{cases} \max \begin{cases} h_{wv,DB} \\ h_{wv,lam} \\ h_{wv,nc} \quad \text{if } Re_{film} <[\quad\quad]^{a,c} \end{cases} & \text{if } [\quad\quad]^{a,c} \\ \max \begin{cases} h_{wv,DB} \\ h_{wv,WH} \\ h_{wv,lam} \\ h_{wv,nc} \quad \text{if } Re_{film} <[\quad\quad]^{a,c} \end{cases} & \text{if } [\quad\quad]^{a,c} \end{cases} \tag{7-160}$$

When the [ ]^{a,c} is less than [ ]^{a,c}, the correlation proposed by (Wong and Hochreiter, 1981) is included in the determination of the forced convection heat transfer, and when the vapor film Reynolds number is less than [ ]^{a,c}, the McAdams correlation for turbulent natural convection is also considered.

Continuity between free and forced convection and between laminar and turbulent flow is assured by selecting the maximum value of the heat transfer coefficients. The Dittus-Boelter equation is coded with the [

]^{a,c}

The radiation heat transfer coefficient is calculated in a similar manner as that for dispersed flow film boiling as:

$$h_{wv,RAD} = F'_{wv} \frac{(T_w^4 - T_v^4)}{(T_w - T_v)} \tag{7-161}$$

with F'_{wv} calculated from Equation 7-150.

If grids are present in the flow, the convective heat transfer to single-phase vapor is enhanced. This is accounted for by multiplying the convective heat transfer coefficient by a factor F_{grid} that models the grid effect. The total heat transfer to vapor is calculated as:

$$h_{wv,SPV} = F_{grid} h_{wv,FC} + h_{wv,RAD} \tag{7-162}$$

The effect of the grid on convective heat transfer and calculation of F_{grid} is described in Section 7.2.7.

For unheated structures, $F_{grid} = 1.0$ and $h_{wv,FC}$ is selected as:

$$h_{wv,FC} = \max \begin{cases} h_{wv,DB} \\ h_{wv,lam} \\ h_{wv,nc} \quad \text{if } Re_{film} <[\quad\quad]^{a,c} \end{cases} \tag{7-163}$$

$$h_{wv,lam} = 7.86\left(\frac{k_v}{D_h}\right) \quad (7\text{-}164)$$

The single-phase vapor regime is assumed when $\alpha_v >$ [ ]^{a,c}. Only heat transfer to vapor is calculated for this regime, and:

$$h_{w\ell,SPV} = 0 \quad (7\text{-}165)$$

$$h_{wb,SPV} = 0 \quad (7\text{-}166)$$

Scaling Considerations and Conclusions

The four correlations used to calculate the single-phase heat transfer coefficient to vapor scale by using an appropriate characteristic length. In WCOBRA/TRAC-TF2, the channel hydraulic diameter is used for the characteristic length. The McAdams correlation is not affected by choice of the characteristic length since that term cancels out of the expression for the heat transfer coefficient. The hydraulic diameter affects the calculation of the natural convection heat transfer coefficient only through its use in the Reynolds number in the selection logic to determine the appropriate heat transfer mode. Therefore the scale dependence of the McAdams correlation is not large.

The Wong and Hochreiter correlation was developed directly from experimental data from a full scale rod bundle at [ ]^{a,c}. Therefore, the only scale dependent concerns are over the application of this correlation to rod bundle arrays different from the 17x17 rod bundle and [ ]^{a,c} used to generate the experimental data on which the correlation is based. To preclude the Wong and Hochreiter correlation from being applied outside [ ]^{a,c} in which it was developed, a [ ]^{a,c} is used to consider this correlation in the heat transfer to vapor calculation. Therefore, the set of equations used by WCOBRA/TRAC-TF2 to calculate single phase vapor heat transfer coefficients is not strongly dependent on scale.

The expressions used to determine the wall to vapor heat transfer coefficient for single-phase vapor are well known. The set of correlations used for this heat transfer coefficient has been assessed in the separate and integral effects tests simulated by WCOBRA/TRAC-TF2. Most of the experiments were conducted in prototypical rod bundles test facilities. The assessment is presented in Volume 2 of this report.

7.2.9 Grid Rewet Model

Model Basis

Spacer grids have important effects on heat transfer in a rod bundle. Since the grids are unpowered, they can quench before the fuel rods. When the grids quench, they create additional liquid surface area which de-superheats vapor in a non-equilibrium, two-phase, dispersed droplet flow. The film on a wetted grid also has a higher interfacial heat transfer coefficient as compared to the droplets, since the relative velocity at the grid is higher. Rewetting of the grids is important and must be accounted for in a best-estimate analysis.

[

]^{a,c}

$$[\quad]^{a,c} \tag{7-167}$$

The grid temperature from Equation 7-167 is:

$$[\quad]^{a,c} \tag{7-168}$$

where [

]^{a,c}.

The radiation heat transfer from the rods to the grid is given by:

$$[\quad]^{a,c} \tag{7-169}$$

where [ ]^{a,c}.

The grid is permitted to rewet if sufficient liquid is available, and if T_{grid} drops below the minimum film boiling temperature T_{MIN}.

Model as Coded

The emissivities of the rod and the grid are assumed to be $\varepsilon_w = \varepsilon_{grid}$ = [ ]^{a,c}, and the value of D_{grid} is taken to be:

$$[\quad]^{a,c} \tag{7-170}$$

where P_{rod} is the fuel rod pitch.

The radiative heat flux to the grid is then calculated explicitly using the grid temperature from the previous time step T^n_{grid} as:

$$[\quad]^{a,c} \tag{7-171}$$

and the new time grid temperature is calculated as:

[ ]a,c (7-172)

(7-173)

In Equation 7-173, [
]a,c.

The grid temperature is then numerically damped to prevent rapid changes as:

[ ]a,c (7-174)

The minimum film boiling temperature for the grid is estimated as:

[ ]a,c (7-175)

where T_{MIN} is calculated by Equation 7-91. In effect, Equation 7-175 insures that the [
]a,c.

A flag to indicate possible grid rewet is then set:

$$I_{wet} = \begin{cases} 1 & \text{if } T_{grid} < T_{MIN,g} \\ 0 & \text{if } T_{grid} \geq T_{MIN,g} \end{cases} \quad (7\text{-}176)$$

This flag is then used as described in Section 6.2.10 in the calculation of interfacial heat transfer due to evaporation of the liquid film on the grid.

Scaling Considerations and Conclusions

The primary processes in the initial quenching of a grid are convection to steam and radiation from the rods. Because the grid strap mass is small, it is assumed to quickly rewet once a quench front is established. The simple WCOBRA/TRAC-TF2 grid rewet model accounts for the convection and radiation processes by using appropriate expressions. The grid rewet model is independent of scale, and depends on the structural design of the spacer grids and rod bundle arrays.

The model has been assessed by its use in simulations of reflood separate and integral effects tests (Volume 2 of this report), and in blowdown test simulations (grid rewet not important for level swell or small break integral tests). Full size prototype PWR grids, as well as supplier grids, were modeled in these tests.

7.2.10 Wall to Fluid Heat Transfer

Model Basis

The heat transfer coefficients h_{wv}, $h_{w\ell}$ and h_{wb} are used to determine the heat transfer to the vapor field, the combined liquid fields (continuous liquid and entrained liquid), and the fraction of the heat transfer from subcooled boiling that results in vapor generation. Sections 7.2.1 through 7.2.8 described the models and correlations used to determine the heat transfer coefficients for the vessel component. This section discusses the use of these coefficients in the determination of the wall to fluid heat transfer.

The heat transfer rates, used as boundary conditions in the fluid energy equations at each heat transfer node location, are given by:

$$Q_{wv} = h_{vap} A_w (T_w - T_v) \tag{7-177}$$

$$Q_{w\ell} = h_{liq} A_w (T_w - T_\ell) \tag{7-178}$$

where A_w represents the heat transfer node surface area. The calculation of h_{vap} and h_{liq} from the values of h_{wv}, $h_{w\ell}$ and h_{wb} follow.

Model as Coded

Calculations to determine h_{wv}, $h_{w\ell}$ and h_{wb} are performed in subroutine HCOOL for the appropriate heat transfer regime. These coefficients are returned to subroutine HEAT, where h_{vap} and h_{liq} are calculated and used to determine Q_{wv} and $Q_{w\ell}$.

First, two ramps are defined which smooth changes in the heat transfer coefficients as either the liquid or vapor phase is depleted.

These are:

[ ] a,c (7-179)

(7-180)

The wall to vapor heat transfer coefficient is calculated using numerical damping with the new and old time step values as:

[ ]a,c (7-181)

and similarly, a wall to liquid heat transfer coefficient by:

[ ]a,c (7-182)

where, C_l = [ ]^{a,c} for non-heated structures and C_l = [ ]^{a,c} for heated structures, m = [ ]^{a,c} for non-heated structures and m = [ ]^{a,c} for heat structures, and the superscript n denotes the old time step value. The ratio of heat transfer for latent heat to the overall heat transfer to liquid is calculated as:

[ ]a,c (7-183)

For solution of the conduction equation, described in Section 8, the derivative of the wall to liquid heat transfer coefficient with respect to temperature is needed for heat transfer nodes in the nucleate boiling regime. This is calculated as:

[ ]a,c (7-184)

where $\frac{dh_{Chen}}{dT_w}$ is given by Equation 7-38 for the nucleate boiling regime, and is 0.0 for all other heat transfer regimes.

The wall to liquid heat transfer coefficient is then calculated as:

[ ]a,c (7-185)

where T_w^n is the wall temperature for the heat transfer node from the previous timestep. From the definition and use of $\frac{dh_{Chen}}{dT_w}$ in Equation 7-184, $h_{liq} = h_{liq}^*$ from Equation 7-182 except for nucleate boiling.

The phasic heat transfer rates are then calculated as:

[ ]a,c (7-186)

(7-187)

The rate of heat transfer that causes subcooled boiling vapor generation, Q_b, is calculated as:

[ ]a,c (7-188)

(7-189)

where [ ]a,c.

Scaling Considerations and Conclusions

The calculation of the phasic heat transfer rates uses the conventional definition of heat flux. Ramps are imposed to insure smooth behavior as a phase is depleted, and numerical damping is used to prevent numerical oscillations that could result from the explicit/implicit coupling of the fluid and structures. The coupling of the thermal-hydraulic calculation to the fuel rod and structural calculations is general and scaling concerns are not applicable.

7.2.11 Heat Flux Splitting in WCOBRA/TRAC-TF2

In the preceding sections, three types of heat transfer coefficient were described: heat transfer to vapor (h_{wv}) (for example, Equation 7-48), heat transfer to liquid ($h_{w\ell}$ (for example, Equation 7-46), and heat transfer due to boiling, (h_{wb}) (for example, Equation 7-47). This section further describes how these components are derived from the overall heat transfer correlations.

WCOBRA/TRAC-TF2 is similar to other two fluid models in that it requires the splitting of the heat flux from a heated surface to each phase being considered. In the calculation of a Loss-of-Coolant Accident (LOCA) transient, the transition must be made from heat transfer entirely to the liquid (normal steady state conditions), to heat transfer partially to the liquid and partially to the vapor (transition boiling), to heat transfer entirely to the vapor (steam cooling), and back again (quenching and long term cooling). The problem encountered when doing this is also similar to other two fluid models; how to take heat flux correlations and models which describe the total heat flux from the wall to the fluid, and apportion this total heat flux properly among the phases being modeled in the code.

In WCOBRA/TRAC-TF2, the total heat flow rate is divided among three paths: the wall to liquid path ($Q_{w\ell}$) the wall to interface path (Q_{wi}), and the wall to vapor path (Q_{wv}) (note that Q_{wi} and h_{wi} are equivalent to Q_{wb} and h_{wb} in previous sections; the interface path description is felt to more accurately describe the process).

The heat flow to the bulk liquid ($Q_{w\ell}$) represents heat flow mechanisms in which energy is deposited, or mixed, into the bulk liquid phase, and where the driving force for such heat transfer is best described by the temperature difference between the wall and the bulk liquid. This energy transfer heats the liquid, raising its temperature. Examples of such mechanisms are:

- Energy transferred by conduction or by turbulent eddies from the region near the wall surface.
- Energy transferred by conduction or by turbulent eddies from the region near the vapor-liquid interface.
- Energy deposited by radiation from the wall to the liquid.

The heat flow to the liquid interface (Q_{wi}) represents heat flow mechanisms in which energy is deposited locally in the liquid phase, near the interface between the liquid and either the wall or the vapor. Since the liquid near the interface is saturated when next to the vapor, and may also be saturated near the wall, the energy deposited will cause the liquid to evaporate or boil. The energy is therefore dissipated by local vapor generation before there is time to transfer the energy to the bulk fluid. The energy may ultimately be deposited into the bulk fluid as the generated vapor enters the main stream and condenses. Mechanisms in which energy is deposited this way are:

- Energy transferred by nucleate boiling, where bubbles are created at the wall surface. These bubbles then detach and mix with the bulk liquid which may be subcooled.
- Energy transferred by conduction across a thin vapor layer adjacent to the wall, to the vapor liquid interface, as in pool film boiling.

The wall to vapor heat flow (Q_{wv}) represents heat flow mechanisms in which energy is deposited in the bulk vapor phase. Examples of such mechanisms are:

- Energy transferred by conduction or by turbulent eddies from the near-wall region.
- Energy deposited by radiation from the wall to the vapor.

The wall to interface heat transfer is sometimes referred to as the "latent" heat transfer, while the other heat transfers are sometimes referred to as the "sensible" heat transfer.

The total heat flow from the wall is described by the following equation:

$$Q_w = Q_{w\ell} + Q_{wi} + Q_{wv} \tag{7-190}$$

$$Q_w = h_{w\ell} A_{w\ell}(T_w - T_\ell) + h_{wi} A_{wi}(T_w - T_i) + h_{wv} A_{wv}(T_w - T_v) \quad (7\text{-}191)$$

where $h_{w\ell}$, h_{wi}, and h_{wv} are the local heat transfer coefficients from the wall to the bulk liquid phase, the wall to the vapor liquid interface, and the wall to the bulk vapor phase. These will be described in more detail later. $A_{w\ell}$, A_{wi}, A_{wv} are the areas over which each process is assumed to take place. Described in terms of heat flux q" (heat flow divided by total surface area), Equation 7-190 becomes:

$$q''_w = q''_{w\ell}\,\varepsilon_{w\ell} + q''_{wi}\,\varepsilon_{wi} + q''_{wv}\,\varepsilon_{wv} \quad (7\text{-}192)$$

$$q''_w = h_{w\ell}\varepsilon_{w\ell}(T_w - T_\ell) + h_{wi}\varepsilon_{wi}(T_w - T_i) + h_{wv}\varepsilon_{wv}(T_w - T_v) \quad (7\text{-}193)$$

where the epsilons are the fractional areas for each path. The ε's are somewhat analogous to the vapor fraction α, and the q"s are somewhat analogous to, for example, vapor volumetric flux j_v (total vapor flow divided by total flow area). Unlike the fluid phase situation, the heat transfer area fractions do not have to add up to 1.0. This is because different heat transfer mechanisms can easily be visualized as acting over the same surface area. Radiation to vapor, for example, acts over the entire surface area simultaneously with forced convection to vapor. However, in order to properly apply the model, the h's and ε's need to be defined consistent with the heat flux equation outlined above, and also consistent with a physical picture about the heat transfer mechanisms involved. How this is done for each heat transfer regime in WCOBRA/TRAC-TF2 is described in the following section.

7.2.11.1 Single-Phase Liquid

In this regime, heat is transferred to the bulk liquid or vapor by conduction or by turbulent eddies. The Dittus-Boelter equation (Equation 7-2) is used for turbulent forced convection conditions, for example. The fractional areas along the various paths are:

[ ] a,c (7-194)

(7-195)

(7-196)

The overall heat flux is:

[ ] a,c (7-197)

(7-198)

(7-199)

[ ]a,c (7-200)

7.2.11.2 Saturated Nucleate Boiling

In this regime, the total heat flux is calculated using a model which accounts for nucleate boiling under forced convection conditions. The Chen correlation (Section 7.2.2) is an example of this type of model. This model assumes the heat transfer is made up of a forced convection component (q''_{fc}), transferring sensible heat, and a nucleate boiling component (q''_{nb}), transferring latent heat, as shown at the top of Figure 7.2-12. However, the code is set up such that all of the heat from the wall is used for liquid sensible heating, and the interfacial heat transfer models handle the actual boiling due to code calculated super-heated liquid; that is:

[ ]a,c (7-201)

(7-202)

(7-203)

Equation 7-192 becomes:

[ ]a,c (7-204)

(7-205)

(7-206)

(7-207)

7.2.11.3 Subcooled Nucleate Boiling

In this regime, the total heat flux is calculated using Chen, but it is assumed that at high liquid subcoolings [

]a,c

[ ]a,c (7-208)

(7-209)

(7-210)

[ ]a,c (7-211)

7.2.11.4 Transition Boiling

In this regime the surface is assumed to be dry and heat transfer to the vapor occurs by forced convection (q''_{wv}), but the surface is contacted intermittently by liquid as illustrated in Figure 7.2-13. Since the wall temperature is relatively high, radiation to cooler vapor (q''_{rv}) and liquid ($q''_{r\ell}$) is assumed to take place. In this and in other models described below, radiation is always superimposed (i.e., acts over the entire surface). [

]^{a,c} The resulting heat flux equation is:

[ ]a,c (7-212)

(7-213)

(7-214)

(7-215)

(7-216)

(7-217)

7.2.11.5 Inverted Annular Film Boiling

In inverted annular film boiling, the wall is assumed to be dry and covered by a vapor film surrounded by a more or less continuous liquid field (which may contain vapor), as shown at the bottom of Figure 7.2-14. [

]^{a,c}

$$[\qquad\qquad]^{a,c} \tag{7-218}$$

[

]^{a,c} The resulting heat flux equation is:

$$[\qquad\qquad]^{a,c} \tag{7-219}$$

(7-220)

(7-221)

(7-222)

(7-223)

(7-224)

7.2.11.6 Inverted Annular Dispersed Flow Film Boiling and Dispersed Droplet Film Boiling

The Inverted Annular Dispersed Flow (IADF) regime is visualized as a dry wall surface surrounded by a discontinuous liquid field consisting of large drops whose surfaces approach the wall, and a population of small drops in the vapor field (top of Figure 7.2-14). [

]^{a,c}

[

]^{a,c} The heat flux equation is:

[ ]^{a,c} (7-225)

[ ]^{a,c} (7-226)

(7-227)

(7-228)

(7-229)

(7-230)

In the instances where superposition is used, one of the heat flux components is assumed to dominate while the others represent perturbations, so the assumption introduces small errors. The potential also exists for compensating error if the functional dependence of a heat transfer component with flow rate or vapor fraction is incorrect, or if the phasic temperature, particularly of vapor, is not correctly calculated. The assessments in Volume 2 of this report are designed to find such compensating errors if they exist.

Note: In presentations of heat transfer coefficients calculated by WCOBRA/TRAC-TF2, the terms "HTCV" and "HTCL" are sometimes used. These are defined as follows:

$$HTCV = \frac{q''_{wv}}{T_w - T_v} \quad (7\text{-}231)$$

$$HTCL = \frac{q''_{wi} + q''_{w\ell}}{T_w - T_\ell} \quad (7\text{-}232)$$

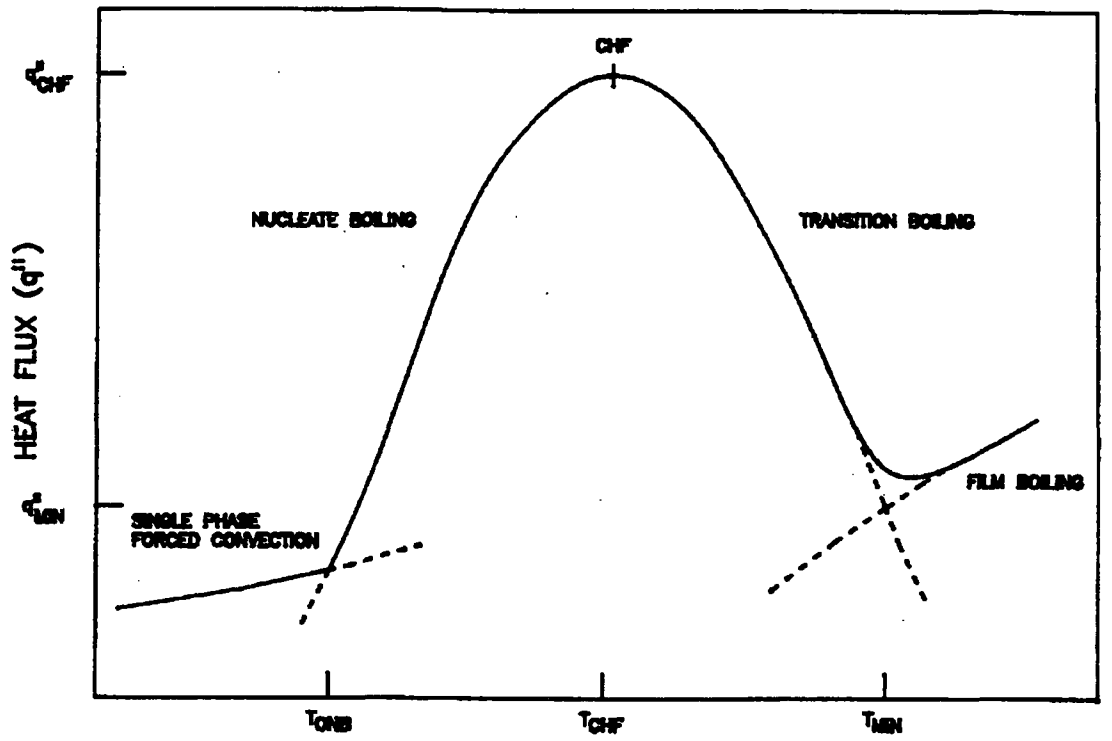

Figure 7.2-1 Boiling Curve

[a,c

]

Figure 7.2-2 Heat Transfer Regime Selection Logic for Vessel Component

a,c

Figure 7.2-3 Heat Transfer Regime Map for Vessel Component

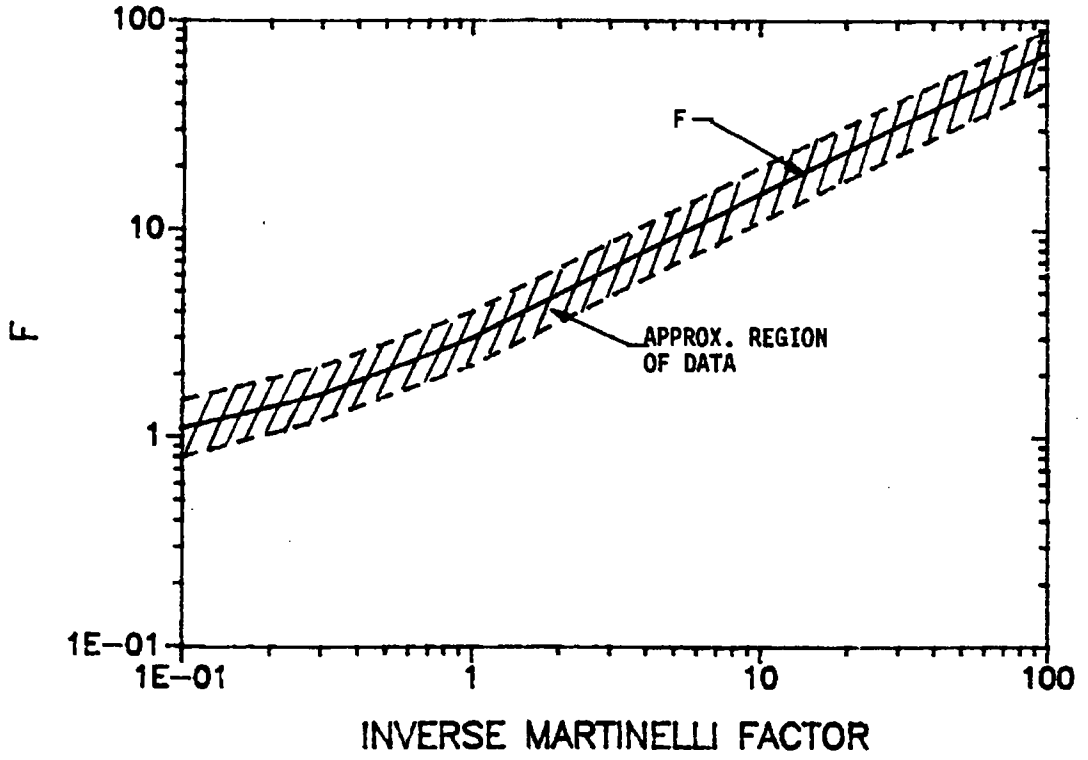

Figure 7.2-4 Chen Correlation Convective Multiplier F_{CHEN}

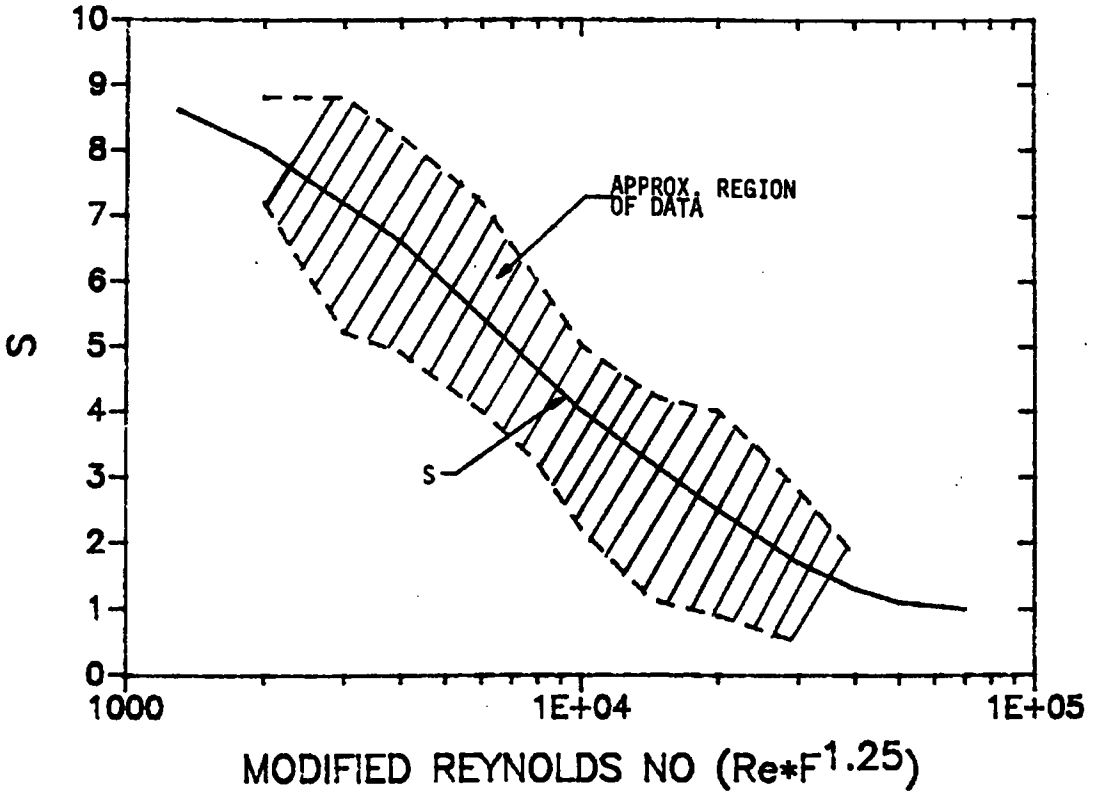

Figure 7.2-5 Chen Boiling Suppression Factor S_{CHEN}

[a,c]

Figure 7.2-6 Droplet Contact Effectiveness (as coded) at Atmospheric Pressure

[a,c

]

Figure 7.2-7 Droplet Contact Effectiveness (as coded) at High Pressure

a,c

Figure 7.2-8 Transition Boiling (Model 2) Ramp F_{FILM}

a,c

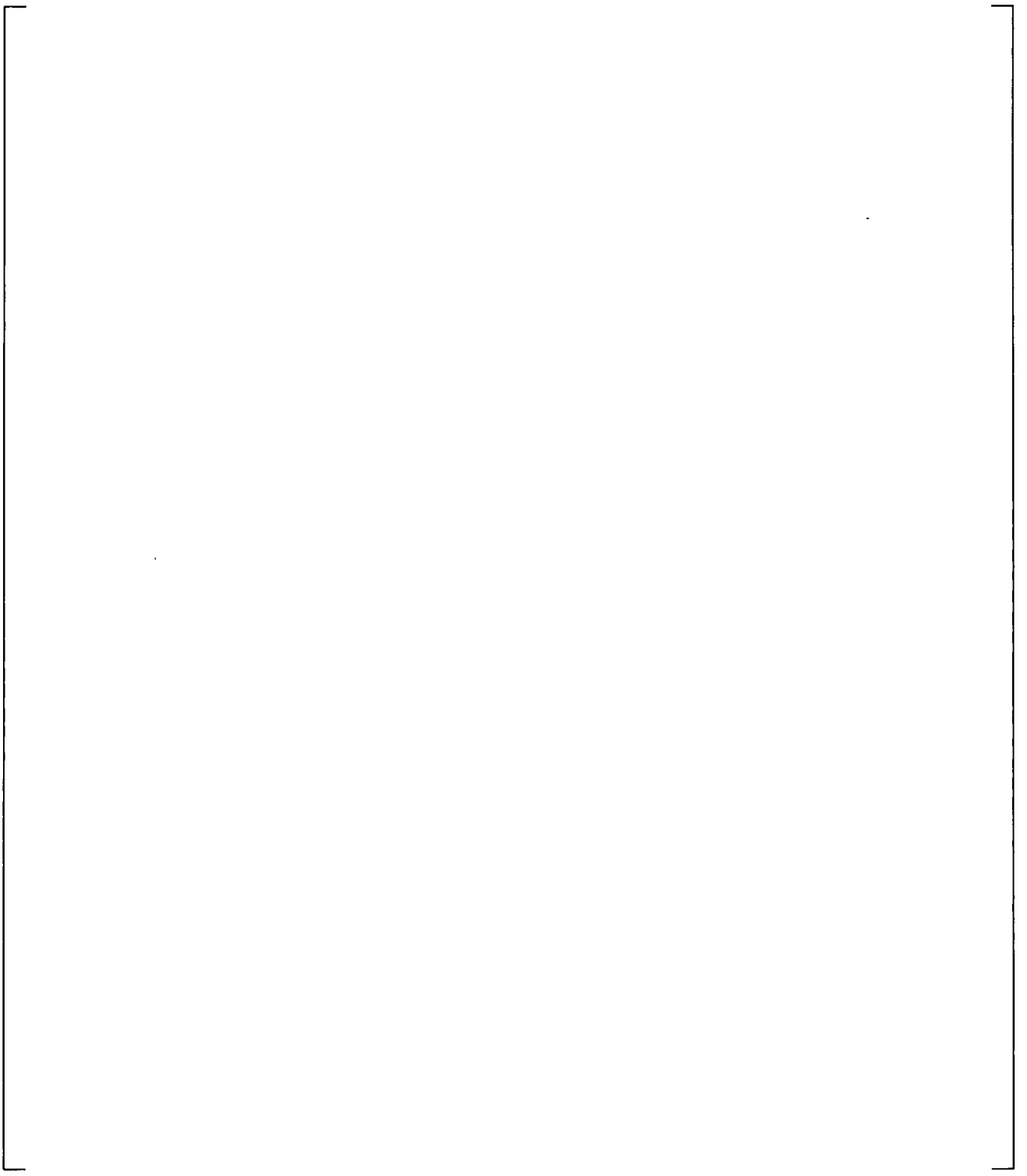

Figure 7.2-9 Film Boiling Model Components

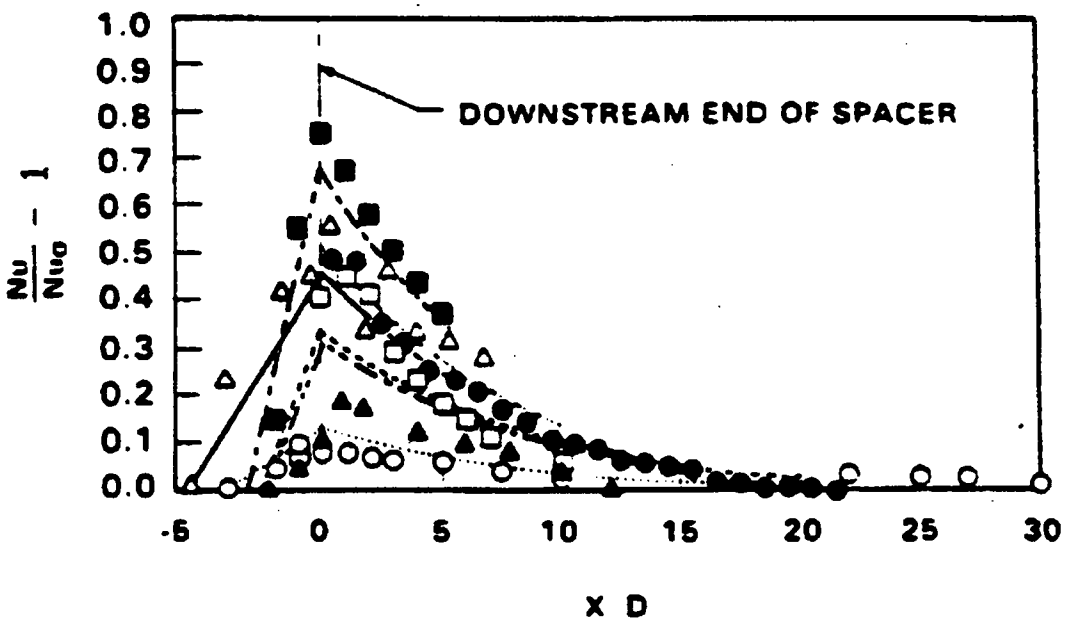

Symbol	Author	Type of grid reported in reference	$Re \times 10^{-4}$	ϵ	Calculated $\frac{Nu}{Nu_0} - 1 = 5.55\,\epsilon^2$
■	Rehme	B.3	12.7	0.348	0.672
Δ	Velcek	6 cm	15.5	0.289	0.463
●	Kidd	4.3	5	0.245	0.333
□	Krett	C	9.5	0.303	0.509
▲	Velcek	5 mm	12.5	0.237	0.311
○	Hudina	lb. smooth	1.5 ~ 5	0.156	0.135

Figure 7.2-10 Effect of Spacer Grids on Convective Heat Transfer (from Chiou, et al., 1986)

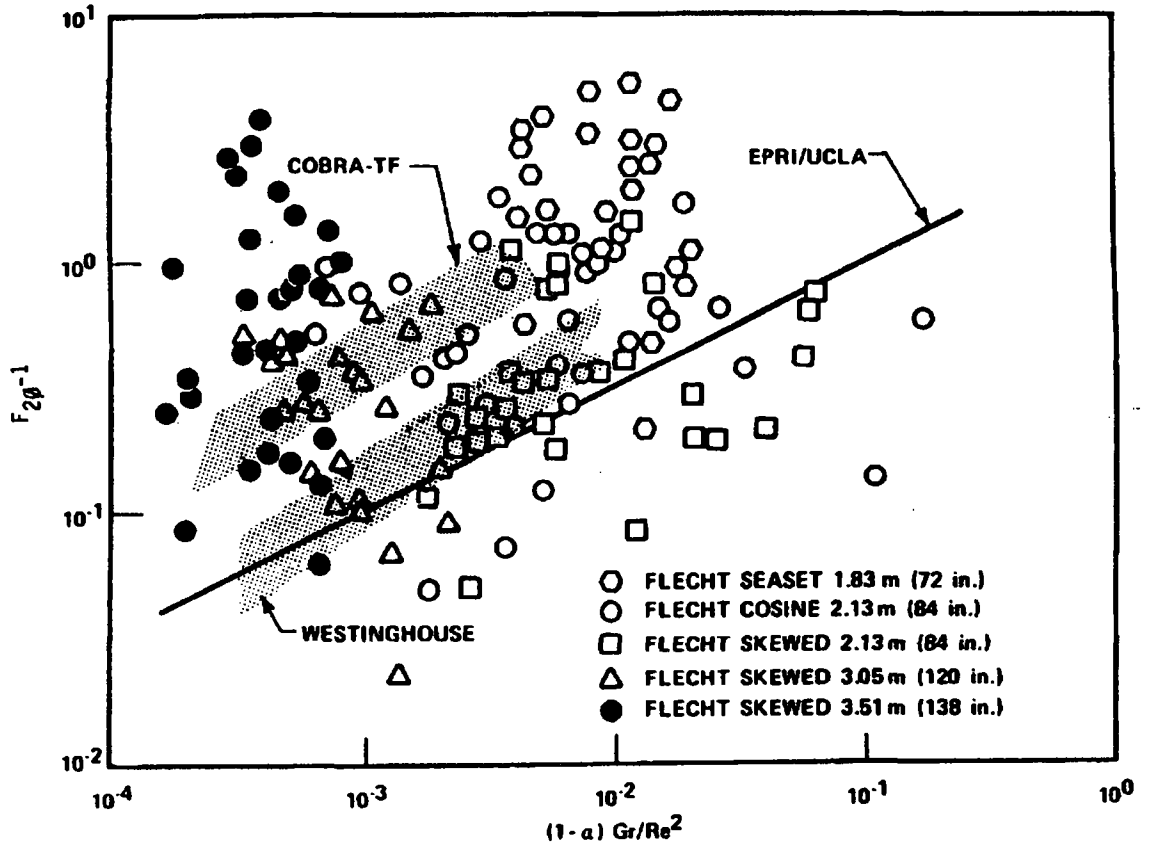

Figure 7.2-11 Enhancement of Convective Heat Transfer Due to Droplets

a,c

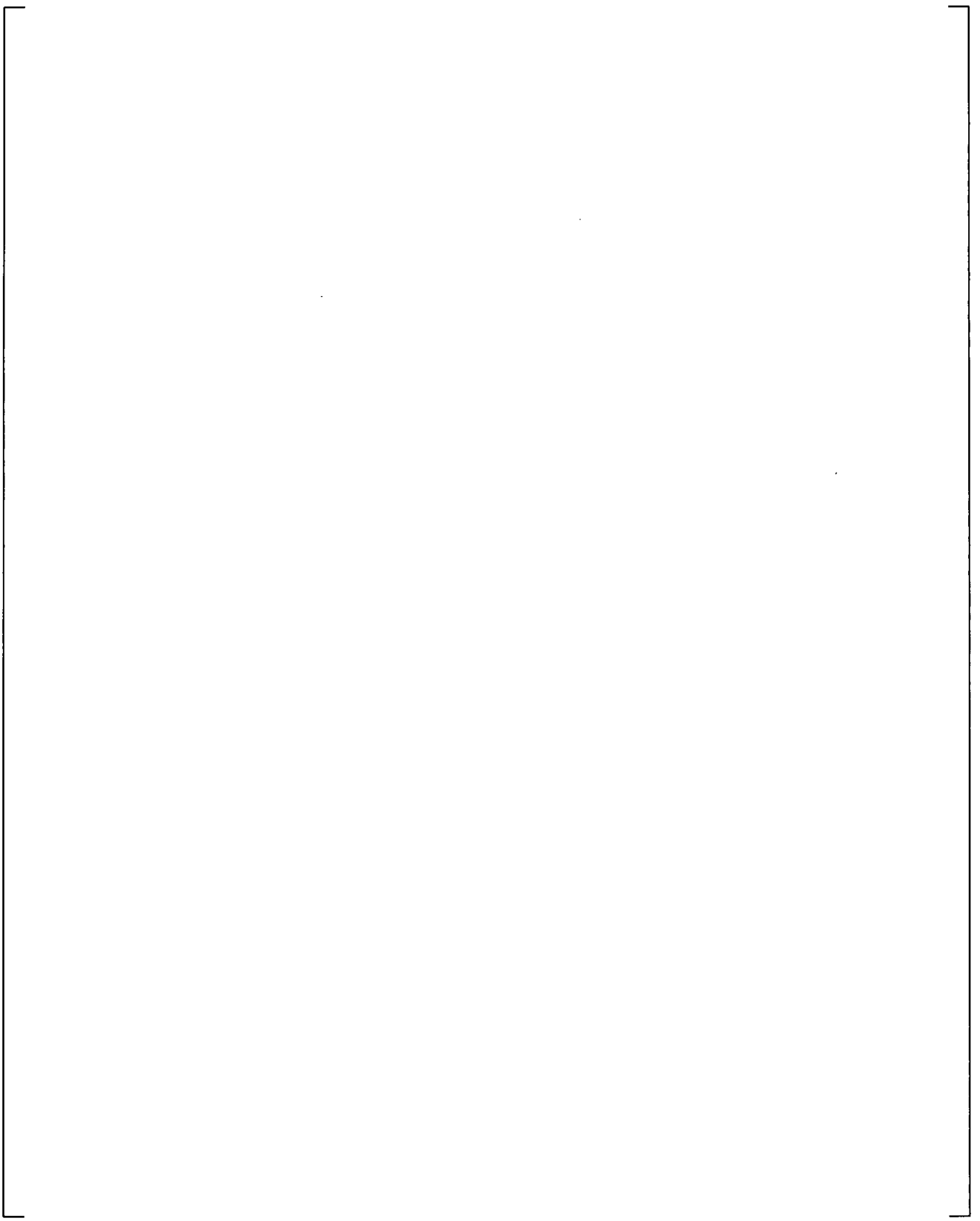

Figure 7.2-12 Heat Flux Paths for Nucleate Boiling

a,c

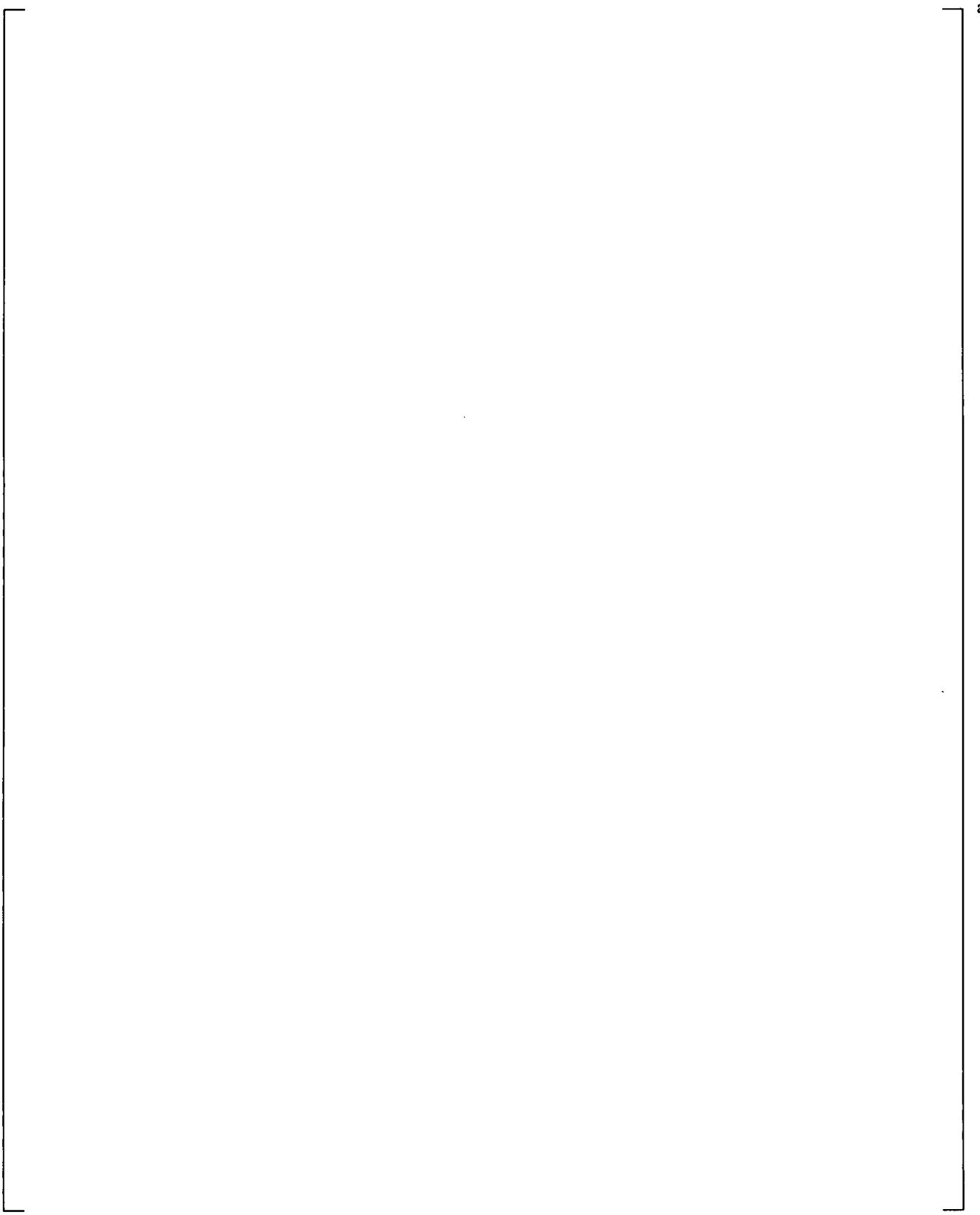

Figure 7.2-13 Heat Flux Paths for Transition Boiling and Dispersed Flow Film Boiling

a,c

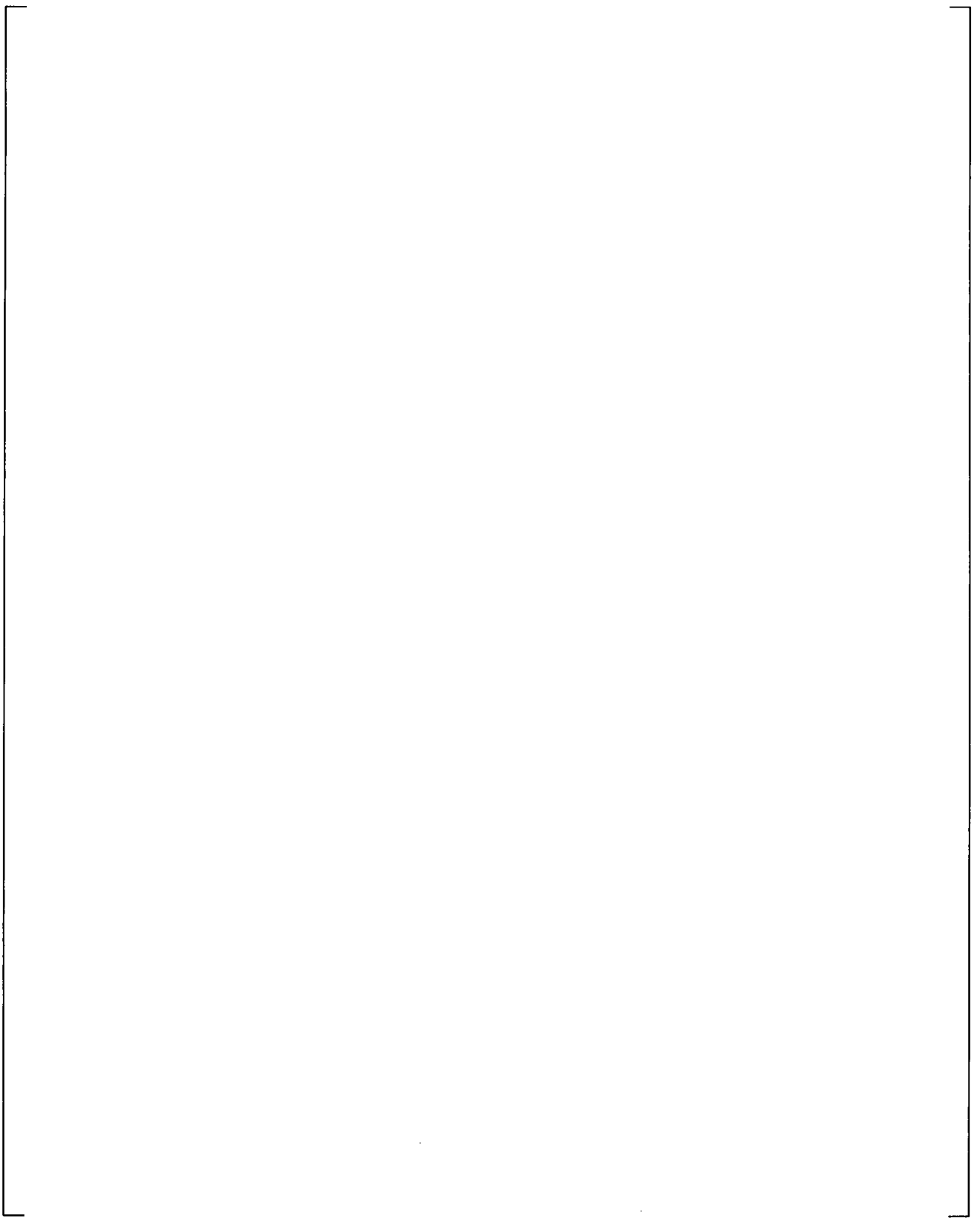

Figure 7.2-14 Heat Flux Paths for Film Boiling

7.3 ONE-DIMENSIONAL COMPONENT WALL HEAT TRANSFER

This section describes the models and correlations used in WCOBRA/TRAC-TF2 to determine the heat transfer coefficients in the one-dimensional components. The heat transfer coding logic in WCOBRA/TRAC-TF2 for the one-dimensional components is taken from TRAC-P [ ]^{a,c}. The expressions and coding for this package are in the metric system of units. While the heat transfer logic in TRAC-P [ ]^{a,c} can generate a full boiling curve with all the heat transfer regimes being modeled, the loops quickly void during most transients and are then filled with vapor; so heat transfer rates are low, and single phase vapor convection is dominant. The exception is during the natural circulation of a small break LOCA and in the steam generator during blowdown. The steam generator is initially a heat sink during the early portion of blowdown and natural circulation, and then it becomes a heat source. As such, during blowdown, the dispersed flow film boiling model is important, and during natural circulation, both the single-phase liquid and two-phase models are important. After loop seal clearing, the steam generator may become a heat sink, as it condenses the steam entering from core boiloff. For this situation, the condensation model is important.

The selection and calculation of heat transfer coefficients is controlled by subroutine HTCOR, which defines eight different heat transfer regimes. These regimes and the code assigned identification number (IDREG) for each region are shown in Table 7.3-1.

The following sections discuss the correlations used in the regimes denoted in Table 7.3-1, in addition to calculations performed for the critical heat flux and the minimum stable film boiling temperature. Figure 7.3-1 presents the coding logic that determines the heat transfer regime for WCOBRA/TRAC-TF2 one-dimensional components.

7.3.1 Single-Phase Liquid Natural Convection

Model Basis

Conventional heat transfer correlations are used for single-phase flow situations. The code has logic to determine natural convection, forced laminar convection or turbulent flow forced convection. Natural convection heat transfer is assumed when the quantity (Gr_ℓ / Re_ℓ^2) is greater than [ ]^{a,c} or if Re_ℓ = 0.0,

where:

$$Re_\ell = \frac{\rho_\ell U_\ell D_h}{\mu_\ell} \tag{7-233}$$

$$Gr_\ell = \frac{g_c \beta | T_w - T_\ell | \rho_\ell^2 D_h^3}{\mu_\ell^2} \tag{7-234}$$

β is the thermal expansion coefficient and D_h is the hydraulic diameter.

Heat transfer coefficients for laminar natural convection are calculated by the (McAdams, 1954) correlation:

$$h_{w\ell,lnc} = 0.59\left(Gr_\ell Pr_\ell\right)^{1/4}\frac{k_\ell}{D_h}, \qquad \left(Gr_\ell Pr_\ell\right) \le 10^9 \tag{7-235}$$

For turbulent flow, the heat transfer coefficients are calculated as suggested by (Holman, 1976) as:

$$h_{w\ell,tnc} = 0.10\left(Gr_\ell Pr_\ell\right)^{1/3}\frac{k_\ell}{D_h}, \qquad 10^9 < \left(Gr_\ell Pr_\ell\right) \le 10^{13} \tag{7-236}$$

Model as Coded

The natural convection heat transfer coefficients $h_{w\ell,lnc}$ and $h_{w\ell,tnc}$ are calculated in subroutine HTCOR. The heat transfer coefficient to vapor $h_{wv,nc}$ is set to zero. All thermal properties except ρ_ℓ and β are evaluated at the liquid temperature. The properties ρ_ℓ and β are approximated as:

[ ] a,c (7-237)

(7-238)

where T_{film} is the average of the wall and fluid temperatures.

The heat transfer coefficient selected by subroutine HTCOR for this regime is the maximum value predicted by Equations 7-235 and 7-236. That is:

$$h_{w\ell,nc} = \text{maximum}\begin{Bmatrix} h_{w\ell,lnc} \\ h_{w\ell,tnc} \end{Bmatrix} \tag{7-239}$$

By using the maximum, the laminar correlation is actually applied up to a value of $Gr_\ell Pr_\ell = 1.794 \times 10^9$.

Scaling Considerations and Conclusions

The natural convection heat transfer correlations used by the one-dimensional component heat transfer package are generally accepted correlations from open literature. The correlations use the hydraulic diameter as the characteristic length, rather than a vertical height which would be more appropriate. However, in turbulent natural convection, the heat transfer coefficient is not dependent on a characteristic dimension, and in laminar natural convection, the heat transfer coefficient is only weakly dependent on the characteristic length.

The most important region where natural convection heat transfer may occur during a LOCA transient is the steam generator secondary side. The heat transfer in this situation is from the secondary side fluid to the primary side dispersed flow two-phase mixture. Once the transient begins, the reactor power quickly drops to less than 5 percent of full power, and the secondary side heat transfer area is considerably over-sized relative to the transient core power. The small uncertainty in the secondary side heat transfer coefficient will have almost no effect on the heat transfer to the primary fluid.

The WCOBRA/TRAC-TF2 code is compared in Section 19 to the CCTF experiments which have an unpressurized secondary side steam generator. The calculations indicate super-heating of the incoming primary two-phase mixture, which is consistent with the experimental data, as well as stratification of the secondary side through heat released by natural convection. Since the CCTF steam generators are full height and have similar tube diameter and pitch to a PWR steam generator, there should be no scale effects of the natural convection models. In addition, the WCOBRA/TRAC-TF2 code is compared in Section 21 to the Rig-of-Safety Assessment (ROSA) experiments which are full height and have similar tube diameter and pitch to a PWR steam generator. Since these tests are full length and use prototypical PWR dimensions, the scaling issue is properly assessed.

7.3.2 Single-Phase Liquid Forced Convection

Model Basis

Heat transfer coefficients for both laminar and turbulent flows are calculated. For laminar flow, a theoretical analysis (Rohsenow and Choi, 1961) is used:

$$h_{w\ell,lfc} = 4.0 \frac{k_\ell}{D_h} \tag{7-240}$$

This equation represents a compromise between the analytically developed equations for uniform wall heat flux and uniform wall temperature for fully developed laminar flow in round tubes assuming a parabolic velocity profile. For the fully developed turbulent-flow regime, the (Dittus and Boelter, 1930) equation is used and is given by:

$$h_{w\ell,tfc} = 0.023 \frac{k_\ell}{D_h} Re_\ell^{0.8} Pr_\ell^{0.4} \tag{7-241}$$

The liquid Reynolds number is:

$$Re_\ell = \frac{\rho_\ell |U_\ell| (1-\alpha) D_h}{\mu_\ell} \tag{7-242}$$

The liquid Prandtl number is:

$$Pr_\ell = \left(\frac{\mu c_p}{k} \right)_\ell \tag{7-243}$$

Model as Coded

Both correlations given by Equations 7-240 and 7-241 are evaluated in subroutine CHEN and the maximum is selected as the single-phase liquid forced heat transfer coefficient.

The fluid properties in both correlations are evaluated at the liquid temperature and pressure. The velocity used to calculate the Reynolds number is the absolute value of the liquid velocity.

Scaling Considerations and Conclusions

The one-dimensional components use forced convection heat transfer coefficients that are accepted correlations from open literature. The laminar and turbulent flow correlations represent the geometry of the systems through the use of the hydraulic diameter, which is scale independent. These correlations have been applied to experiments with different scales to model the heat transfer in the one-dimensional components, such as CCTF, ROSA and the LOFT loops (Volume 2 of this report). The most important loop component, from a heat transfer perspective, is the steam generator, since it can be a heat source or sink during the transient. The CCTF generator used full height steam generator tubes with diameters which are typical of PWR steam generators. Since these correlations have been assessed on large- and full-scale components, any scaling issue is properly assessed.

7.3.3 Nucleate Boiling

Model Basis

The (Chen, 1963) correlation is used in the nucleate boiling heat transfer regime. The correlation assumes that both boiling and forced convective mechanisms occur and that the contributions made by the two mechanisms are additive. The convective component is assumed to be represented by a modified Dittus-Boelter equation where the thermal conductivity, Reynolds number, and Prandtl number are effective values associated with the two-phase flow. The liquid properties are used for the Reynolds number since a liquid film is assumed to exist on the wall. The values of the Prandtl number for liquid and vapor are normally of the same order of magnitude and it is reasonable to expect the two-phase Prandtl number to have a similar value. A parameter, $F_{CHEN} \geq 1.0$, which is a function of the Martinelli parameter (χ), is used to modify the convective part of the correlation, h_{forc} (called the macroterm), to account for increased agitation caused by the formation of vapor bubbles. The factor F_{CHEN} is the ratio of an effective two-phase Reynolds number to the single-phase liquid Reynolds number.

The basis for the nucleate boiling component of the correlation is the analysis of (Forster and Zuber. 1955) for pool boiling. Their analysis relates a bubble Nusselt number to a bubble Reynolds number and a liquid Prandtl number. It can be shown that the product of growth rate and bubble radius is constant for a given degree of superheat. In pool boiling and convective boiling, the superheat is not constant across the boundary layer. In pool boiling, this effect can be neglected. In forced convective boiling, the boundary layer is thinner and temperature gradients are steeper. The difference between the wall superheat and the mean superheat to which the bubble is exposed must be considered. A suppression factor, S_{CHEN}, modifies the nucleate boiling part of the correlation, h_{nucb} (called the microterm), to account for this effect, and is a function of the two-phase Reynolds number.

The Chen model provides the transition from a liquid forced convection flow into fully developed nucleate boiling. As the quality in the flow increases, the two-phase convection increases and merges with the nucleate boiling portion of the correlation.

The equations for the Chen correlation are as follows:

$$q_{total} = h_{forc}(T_w - T_\ell) + h_{nucb}(T_w - T_{sat}) \tag{7-244}$$

where:

$$h_{forc} = 0.023 \frac{k_\ell}{D_h} \left(\frac{|U_\ell| \rho_\ell (1-\alpha) D_h}{\mu_\ell} \right)^{0.8} \left(\frac{\mu C_p}{k} \right)_\ell^{0.4} F_{CHEN} \tag{7-245}$$

$$h_{nucb} = 0.00122 \frac{k_\ell^{0.79} C_{p\ell}^{0.45} \rho_\ell^{0.49}}{\sigma^{0.5} \mu_\ell^{0.29} H_{fg}^{0.24} \rho_v^{0.24}} (T_w - T_{sat})^{0.24} (P_w - P)^{0.75} S_{CHEN} \tag{7-246}$$

F_{CHEN} is defined as:

$$F_{CHEN} = \begin{cases} 1.0 & \text{for } \chi_{TT}^{-1} \le 0.10 \\ 2.35 \left(\chi_{TT}^{-1} + 0.213 \right)^{0.736} & \text{for } \chi_{TT}^{-1} > 0.10 \end{cases} \tag{7-247}$$

where:

$$\chi_{TT}^{-1} = (\text{Martinelli factor})^{-1} = \left(\frac{x}{1-x} \right)^{0.9} \left(\frac{\rho_f}{\rho_g} \right)^{0.5} \left(\frac{\mu_g}{\mu_f} \right)^{0.1} \tag{7-248}$$

The suppression factor (S_{CHEN}) is defined as:

$$S_{CHEN} = \begin{cases} \left(1 + 0.12\, Re_{TP}^{1.14} \right)^{-1} & Re_{TP} < 32.5 \\ \left(1 + 0.42\, Re_{TP}^{0.78} \right)^{-1} & 32.5 \le Re_{TP} \le 70.0 \end{cases} \tag{7-249}$$

The two-phase Reynolds number is defined as:

$$Re_{TP} = 10^{-4} \frac{|U_\ell| \rho_\ell (1-\alpha) D_h}{\mu_\ell} F_{CHEN}^{1.25} \tag{7-250}$$

The Chen correlation provides the transition from forced convection liquid flow to nucleate boiling by enhancing the convective heat transfer with a two-phase Reynolds number and suppressing the boiling heat transfer as the convective portion of the heat transfer increases. As the void fraction or flow quality increases, the nucleation in the wall film becomes suppressed and the boiling contribution is decreased.

(Lahey and Moody, 1977) have shown how the Chen correlation merges with the fully developed nucleate boiling correlation by (Jens and Lottes, 1951) and the high void fraction dryout correlation by (Dengler and Addoms, 1956). As Lahey and Moody indicate, the Chen correlation merges with the nucleate boiling correlation at low quality where the two-phase Reynolds number is low and also merges with the high quality dryout correlation as the quality increases and the convection is enhanced at the expense of the nucleate boiling term in the correlation.

Model as Coded

The quantities h_{forc} and h_{nucb} are calculated in subroutine CHEN and the vapor heat transfer coefficient is calculated in subroutine HVNB.

The vapor heat transfer coefficient is defined using the natural-convection and forced-convection correlations given by:

$$h_{NC} = 0.13 k_g \left[\frac{\rho_g^2 g |T_w - T_g|}{\mu_g^2 T_g} \right]^{0.333} \cdot Pr_g^{0.333} \tag{7-251}$$

$$h_{dr} = 0.023 \, Re_{TP}^{0.8} \, Pr_g^{0.4} \left(\frac{k_g}{D_h} \right) \tag{7-252}$$

where:

$$Re_{TP} = \frac{\left(|U_g| \alpha + |U_\ell| (1-\alpha) \right)}{\mu_g} \cdot (\rho_g D_h) \tag{7-253}$$

and:

$$Pr_g = \left(\frac{c_p \mu}{k} \right)_g \tag{7-254}$$

Equation 7-251 is a correlation for natural convection for vertical planes and cylinders in the turbulent-flow regime where [ ]^{a,c}. It should be noted that in Equation 7-251, the characteristic length has dropped out and β has been approximated by [ ]^{a,c}. Equation 7-252 is the (Dougall and Rohsenow, 1963) correlation. In subroutine HVNB, if the void fraction is [ ]^{a,c}, the vapor heat transfer coefficient, h_{wg}, is set to 0.0. If the void fraction is [ ]^{a,c}, h_{wg} is the maximum of the values given by Equations 7-251 and 7-252. Linear interpolation is done between 0.0 and max(h_{NC}, h_{dr}) for void fractions between [ ]^{a,c}.

Because the Chen correlation was developed to represent the total heat flux and a vapor heat transfer coefficient is used for the phasic heat transfer, the liquid heat transfer coefficient is given by:

$$h_{w\ell} = \left[h_{forc}\left(T_w - T_\ell\right) + h_{nucb}\left(T_w - T_{sat}\right) - h_{wg}\left(T_w - T_g\right)\right] / \left(T_w - T_\ell\right) \quad (7\text{-}255)$$

The maximum value of the Martinelli parameter χ_{TT}^{-1} is limited to [ ]^{a,c}, and the maximum value of the two-phase Reynolds number, as defined in Equation 7-250, is limited to [ ]^{a,c}.

As the quality and void fraction approach unity, Re_{TP} and χ_{TT}^{-1} approach zero, resulting in F_{CHEN} = [ ]^{a,c}. The suppression factor, S_{CHEN}, should approach zero as $\alpha \rightarrow 1.0$. From the definition of S_{CHEN} in Equations 7-186 and 7-187, it is clear that [

]^{a,c} That is:

[ ]^{a,c} (7-256)

At high void fractions ($\alpha > \alpha_c = 0.98$), the heat transfer coefficients are revised by [ ]^{a,c} between the current values of $h_{w\ell}$ and h_{wg} and those for single-phase vapor ($h_{w\ell} = 0.0$ and $h_{wg} = h_{wg,spv}$) so that:

[ ]^{a,c} (7-257)

(7-258)

(7-259)

At high void fractions:

[ ]^{a,c} (7-260)

(7-261)

Scaling Considerations and Conclusions

The Chen correlation was originally used in TRAC-P [ ]^{a,c} for boiling in rod bundle arrays. The Chen correlation described here is used for loop components where the structure wall temperature exceeds T_{sat} and an evaporating liquid film exists on the walls. The components are mostly larger pipes whose geometry can be characterized by the hydraulic diameter. The void fraction in these structures is usually very high for most of the transient so that only a portion of the Chen correlation is used for the total heat transfer, while the forced convection to vapor is the primary mode of heat transfer. Another location where the Chen correlation may be applied is in the steam generator tubes as the reactor system depressurizes. This occurs very early in blowdown. Since the steam generators are vertical tubes, there should not be any scaling effects.

Most of the data from which the correlations were developed were for boiling inside vertical tubes. The Chen correlation, although semi-empirical, does have a physical basis. It works well for a variety of fluids (including water), covers both the low- and high-quality regions, and transforms into the Forster-Zuber correlation for pool boiling at low flows.

The WCOBRA/TRAC-TF2 one-dimensional structure heat transfer models are validated as part of different scaled tests such as LOFT, ROSA and CCTF in Volume 2 of this report, in which the walls are super-heated relative to the fluid for a period of the transient. Since these correlations have been assessed on large- and full-scale components, any scaling issue is properly assessed.

7.3.4 Critical Heat Flux

Model Basis

The critical heat flux is predicted by WCOBRA/TRAC-TF2 for one-dimensional components using the (Biasi, 1967) correlation with modifications at low mass velocities and high void fractions.

The Biasi correlation consists of the following two equations, and the maximum CHF value calculated by these equations is used:

$$q''_{CHF} = \frac{1883}{D_h^m G^{1/6}}\left[\frac{F(P)}{G^{1/6}} - x\right] \tag{7-262}$$

$$q''_{CHF} = \frac{3780}{D_h^m G^{0.6}} H(P)(1-x) \tag{7-263}$$

where:

q''_{CHF} = critical heat flux, (W/cm^2)
m = 0.4 for $D_h \geq 1$ cm, 0.6 for $D_h < 1$ cm
$F(P) = 0.7249 + 0.099P \exp(-0.032P)$
$H(P) = -1.159 + \frac{8.99P}{10 + P^2} + 0.149P \exp(-0.019P)$

D_h = diameter (cm)
G = mass flux ($g \cdot cm^{-2} \cdot s^{-1}$)
P = pressure (bar)
x = equilibrium quality

Typically Equation 7-162 is for low quality and Equation 7-163 is for high quality. For a given mass flux and tube diameter, the switch-over quality between the two equations is shown as a function of pressure in Figure 7.3-2 taken from (Liles et al., 1988). As seen in this figure, the switch-over quality is not constant and varies between 0.3 and 0.68 within the pressure range of the Biasi correlation. It exhibits a peak between 2 and 3 MPa.

The Biasi correlation was originally correlated over a data base containing 4551 CHF data points. The ranges of the CHF parameters within this data base are as follows:

$$0.3\,cm < D_h < 3.75\,cm$$

$$20\,cm < L < 600\,cm$$

$$0.27\,MPa < P < 14.0\,MPa$$

$$10\,g \cdot cm^{-2} \cdot s^{-1} < G < 600\,g \cdot cm^{-2} \cdot s^{-1}$$

$$x_{inlet} < 0$$

$$\frac{1}{1+\rho_\ell/\rho_v} < x < 1$$

Model as Coded

The Biasi correlation is written in cgs units. Thus, Equations 7-162 and 7-163 yield the CHF in W/cm^2. To obtain the CHF directly in W/m^2, Equations 7-162 and 7-163 are multiplied by 10^4 in the code. All the other constants remain unchanged.

In WCOBRA/TRAC-TF2, the critical heat flux calculations for one-dimensional components are done in subroutines CHF and CHF1, and are used in HTCOR. The critical heat flux temperature is needed in HTCOR to differentiate between the nucleate boiling and transition boiling regimes. The critical heat flux temperature is also needed for computing the heat transfer coefficient in the transition boiling regime.

In the subroutine CHF, the value of the critical heat flux calculated in subroutine CHF1 is used with the Chen nucleate boiling heat transfer correlation to obtain the corresponding critical heat flux temperature. This requires an iterative solution which is done by the Newton-Raphson procedures. The iteration is started by using [ ]^{a,c} as the initial guess. The latest calculated value of T_{CHF} is used in subsequent iterations. The magnitude of the critical heat flux temperature is bound at the lower and upper ends as follows:

[ ]a,c (7-264)

Scaling Considerations and Conclusions

The Biasi correlation has been developed based on CHF test data for tubes from 0.12 inches in diameter to 1.47 inches in diameter and tube lengths up to 20 feet, which cover prototypical steam generator tube diameters.

The range of fluid conditions for which this correlation was developed covers expected PWR steam generator conditions during reflood. The correlation is used in a geometry of the same configuration as it was originally developed. Therefore, no scaling issues are expected when applying this correlation for the steam generator component. The correlation has been tested in the WCOBRA/TRAC-TF2 analysis of the LOFT, ROSA and CCTF experiments (Volume 2 of this report), all of which have heated steam generators.

The application of the Biasi correlation to the WCOBRA/TRAC-TF2 one-dimensional components and the steam generator is within the range of conditions for which the correlation was developed.

7.3.5 Transition Boiling

Model Basis

The transition boiling regime spans the boiling curve between the critical heat flux and the minimum film boiling point. It is assumed that transition boiling heat transfer is composed of both nucleate boiling (wet wall) and film boiling (dry wall) heat transfer components. Each component is weighted by a factor F_{wet}, the fraction of wall area that is wet. The equations used in the transition boiling regime are from (Bjornard and Griffith, 1977):

$$q''_{tb} = F_{wet} q''_{CHF} + (1 - F_{wet}) q''_{MIN} \tag{7-265}$$

$$F_{wet} = \left(\frac{T_w - T_{MIN}}{T_{CHF} - T_{MIN}} \right)^2 \tag{7-266}$$

In Equations 7-265 and 7-266, T_{MIN} is the wall temperature of the minimum stable film boiling point, while q''_{MIN} is the heat flux at that wall temperature. The transition boiling heat flux is simply a ramp between the critical heat flux (q''_{CHF}) at T_{CHF} to the film boiling heat flux, q''_{MIN} at T_{MIN}. The methods and correlations used to calculate q''_{MIN} at T_{MIN} will be discussed in following sections on film boiling. The critical heat flux q''_{CHF} is calculated as presented in Section 7.3.4. The heat flux q''_{MIN} at the minimum stable film boiling temperature T_{MIN} is given as:

$$q''_{MIN} = h_{w\ell,min}(T_{MIN} - T_\ell) + h_{wv,min}(T_{MIN} - T_v) + h_{dffb}(T_{MIN} - T_{sat}) \tag{7-267}$$

For this expression, the heat transfer coefficient $h_{wv,min}$ is evaluated as the maximum of the natural convection or the (Dougall and Rohsenow, 1963) correlations, or:

$$h_{wv,min} = \max\left(h_{NC}, h_{dr}\right) \tag{7-268}$$

Both the natural-convection and the Dougall-Rohsenow correlations were presented in Section 7.3.3. For purposes of computing $h_{wv,min}$, however, the appropriate properties in either correlation are evaluated at the minimum stable film-boiling temperature T_{MIN}. Similarly, the liquid heat transfer coefficient $h_{w\ell,min}$ is calculated by:

$$h_{w\ell,min} = h_{rw\ell,fb}\left(\frac{T_{MIN} - T_{sat}}{T_{MIN} - T_{\ell}}\right) \tag{7-269}$$

Where $h_{rw\ell,fb}$ is calculated using Equation 7-285 with T_w set to T_{MIN}. The heat transfer coefficient h_{dffb} is calculated using Equation 7-289 with T_w set to T_{MIN}.

Based on the value of $h_{wv,min}$ and the above calculation of the total heat flux for transition boiling, the wall-to-liquid phasic heat transfer coefficient can be determined from:

$$h_{w\ell} = \frac{q''_{tb} - h_{wv}\left(T_w - T_v\right)}{\left(T_w - T_{\ell}\right)} \tag{7-270}$$

In those situations where the cell void fraction is [ ]^{a,c}, a final interpolation is performed on the total heat flux q''_{tb} to provide a smooth transition between heat transfer regimes.

Model as Coded

Calculations for the transition boiling regime are performed primarily in subroutine HTCOR. Subroutines CHEN, CHF, CHF1, DFHT, TMSFB, HLFILM and HVFILM are called by HTCOR to perform various calculations such as the critical heat flux and minimum stable film boiling temperature. The transition boiling regime is assumed if,

$$T_w \leq T_{MIN}$$

$$T_w > T_{CHF}$$

$$x_{eq} < 1.0$$

where x_{eq} is the equilibrium quality defined as:

$$x_{eq} = \frac{(H_{mix} - H_f)}{H_{fg}} \tag{7-271}$$

where H is an enthalpy.

A "total" transition boiling heat transfer coefficient is calculated as:

[ ]a,c (7-272)

F_{wet} is calculated using Equation 7-266.

The vapor phase heat transfer coefficient assumes film boiling and is calculated in subroutine HVFILM as:

[ ]a,c (7-273a)

The calculation of $h_{wv,nc}$ and $h_{wv,dr}$ is discussed in Section 7.3.7.

The liquid phase heat transfer coefficient is then calculated as:

[ ]a,c (7-273b)

If the void fraction is less than or equal to [ ]^{a,c}, the values of $\overline{h_{wv,tb}}$ and $\overline{h_{w\ell,tb}}$ from Equations 7-273a and 7-273b become the final values and are used in subsequent calculations. That is:

$$h_{wv,tb} = \overline{h_{wv,tb}} \quad (7\text{-}274a)$$

$$h_{w\ell,tb} = \overline{h_{w\ell,tb}} \quad (7\text{-}274b)$$

If the void fraction is greater than [ ]^{a,c}, a single-phase heat transfer coefficient for the vapor phase, $h_{wv,spv}$, is calculated as described in Section 7.3.8, and the heat transfer coefficients are linearly ramped as follows:

[ ]a,c (7-275a)

for the vapor phase heat transfer coefficient, and:

[ ]^{a,c} (7-275b)

where:

[ ]^{a,c} (7-275c)

for the liquid phase heat transfer coefficient. Equation 7-275a decreases the vapor phase coefficient to that of the single-phase vapor regime as the void fraction approaches [ ]^{a,c}, and Equations 7-275b and 7-275c linearly ramp the liquid phase coefficient to 0.0.

Scaling Considerations and Conclusions

A simple transition boiling model is used in the one-dimensional components to provide a smooth transition between the CHF point and the minimum film boiling point on the boiling curve. This model is most important in modeling the steam generator heat release during reflood and has been validated on prototypical steam generator data.

The expressions used to calculate the transition boiling heat flux are based mainly on data from tubes and annuli. In WCOBRA/TRAC-TF2 this transition boiling model is used primarily for steam generator tubes during reflood when a two-phase mixture enters the tubes. The steam generator tube wall temperature can be in the range where transition boiling is calculated to occur.

WCOBRA/TRAC-TF2 has been validated against experiments, such as CCTF and ROSA (Volume 2 of this report), which have prototypical, full height, steam generator tubes with a hot pressurized secondary fluid as the heat source. Since these correlations have been assessed on large- and full-scale components, any scaling issue is properly assessed.

7.3.6 Minimum Film Boiling Temperature

Model Basis

The minimum stable film boiling temperature T_{MIN} is the temperature at the intersection point between the transition boiling and the film boiling heat transfer regimes. It is also used in determining the transition boiling heat flux. In WCOBRA/TRAC-TF2 one-dimensional components, the minimum film boiling temperature is calculated to be the maximum of the homogeneous nucleation temperature and the correlation by (Iloeje et al., 1975). The homogeneous nucleation model for T_{MIN} is given as:

$$T_{MIN,hn} = T_{hn} + (T_{hn} - T_{\ell})R^{1/2} \quad (7\text{-}276)$$

where T_{hn} is the homogenous nucleation temperature and given by a third order polynomial taken from the COBRA-TF code as:

$$T_{hn} = 705.44 - \left(4.722 \times 10^{-2}\right)DP + \left(2.3907 \times 10^{-5}\right)DP^2 - \left(5.8193 \times 10^{-9}\right)DP^3 \quad (7\text{-}277)$$

where:

$$DP = 3203.6 - P \quad (7\text{-}278)$$

$$R = \frac{\left(k \rho c_p\right)_\ell}{\left(k \rho c_p\right)_w} \quad (7\text{-}279)$$

T_{hn} is in units of °F; P is in units of psia; DP is in units of psi; and R is the ratio of the fluid properties at the fluid temperature and wall temperature, where the subscript "ℓ" indicates liquid properties and the subscript "w" refers to wall properties.

T_{MIN} is also calculated using the (Iloeje et al., 1975) correlation developed for liquid nitrogen. The Iloeje correlation is empirical and depends on the mass flux and equilibrium quality as follows:

$$T_{MIN,I} = T_{sat} + 0.29\Delta T_B \left(1.0 - 0.295 \cdot x^{2.45}\right)\left[1.0 + \left(G \times 10^{-4}\right)^{0.49}\right] \quad (7\text{-}280)$$

where:

$$\Delta T_B = 0.127 \cdot \frac{\rho_v H_{fg}}{k_v}\left[\frac{g\left(\rho_\ell - \rho_v\right)}{\rho_\ell + \rho_v}\right]^{2/3}\left[\frac{g_c \sigma}{g\left(\rho_\ell - \rho_v\right)}\right]^{0.5}\left[\frac{\mu_\ell}{g\left(\rho_\ell - \rho_v\right)}\right]^{1/3} \quad (7\text{-}281)$$

and x is the equilibrium quality.

The liquid properties should be evaluated at the film temperature:

$$T_{film} = 0.5\left(T_w + T_{sat}\right) \quad (7\text{-}282)$$

where T_{sat} is the saturation temperature.

The one-dimensional component heat transfer package logic chooses the maximum of the saturation temperature, the homogeneous nucleation value, or the Iloeje value for T_{MIN}. That is:

$$T_{MIN} = \max\begin{cases} T_{MIN,hn} \\ T_{MIN,I} \\ T_{sat} + 0.0001\,K \end{cases} \quad (7\text{-}283)$$

There are limits placed on the (Iloeje et al., 1975) correlation to keep it within its database. [

]^{a,c} The liquid properties are calculated at the film temperature as defined in Equation 7-282, and the vapor properties are evaluated at T_{sat}.

Scaling Considerations and Conclusions

The component where WCOBRA/TRAC-TF2 is most likely to use the calculated value of T_{MIN} is in the steam generator during reflood. The homogeneous nucleation equation is a thermodynamic limit and as such does not have any scale dependency. The (Iloeje et al., 1975) correlation is an empirical fit to water data and requires validation. The one-dimensional component heat transfer package has been used in the analysis of the CCTF reflood test, which has full height steam generators. The tests use prototypical steam generator tube dimensions and lengths such that there should not be a scaling concern.

7.3.7 Film Boiling Heat Transfer

Model Basis

The film-boiling heat transfer regime incorporates several different correlations to describe fully-developed film boiling. The film boiling regime is assumed to occur when the wall temperature exceeds the minimum stable film boiling temperature ($T_w > T_{MIN}$). The wall-to-vapor and wall-to-liquid heat transfer are calculated separately. The wall-to-liquid heat transfer coefficient is assumed to be the sum of three components: radiation, film boiling and dispersed flow film boiling. The film boiling liquid heat transfer coefficient is given by:

[ ]^{a,c} (7-284)

where the radiative component is:

[ ]^{a,c} (7-285)

In the above correlation, σ_{SB} is the Stefan-Boltzmann constant and ε_w is the wall emissivity (assumed to be [ ]^{a,c}). The (Bromley, 1950) correlation is given as:

$$h_{Brom} = 0.62 \left\{ \frac{\rho_v k_v^3 (\rho_\ell - \rho_v) g h'_{fg}}{\mu_v (T_w - T_{sat}) \lambda} \right\}^{0.25} \quad (7\text{-}286)$$

where:

$$h'_{fg} = H_{fg} + 0.5 C_{pv} (T_v - T_{sat}) \quad (7\text{-}287)$$

The critical wavelength is:

$$\lambda = 2\pi\left[\frac{\sigma}{g(\rho_\ell - \rho_v)}\right]^{1/2} \tag{7-288}$$

The dispersed flow film boiling portion is given as the smaller of the modified (Forslund and Rohsenow, 1968) correlation and the modified Bromley correlation, where:

[ ]^{a,c} (7-289)

In the Forslund-Rohsenow correlation, [

]^{a,c}

[ ]^{a,c} (7-290)

D_d is the droplet diameter based upon a critical Weber number (We_d) of [ ]^{a,c}:

$$D_d = \frac{We_d\,\sigma}{\rho_v (U_v - U_d)^2} \tag{7-291}$$

The drop diameter in Equation 7-291 is restricted to the range [ ]^{a,c} meters. The temperature ratio in Equation 7-289 [

]^{a,c}.

The wall-to-vapor film boiling heat transfer coefficient calculated in this heat transfer regime is the greater of the (Dougall and Rohsenow, 1963) correlation ($h_{wv,DR}$) and the turbulent natural convection ($h_{wv,nc}$) correlation.

The Dougall-Rohsenow correlation is given as follows:

$$h_{wv,DR} = 0.023\frac{k_v}{D_h}\left[\rho_v\frac{\{\alpha_v U_v + (1-\alpha_v)U_\ell\}D_h}{\mu_v}\right]^{0.8}[Pr_v]^{0.4} \tag{7-292}$$

The natural convection correlation to vapor is given from (McAdams, 1954) as:

$$h_{wv,nc} = 0.13\,k_v\left[\frac{\rho_v^2 g_c (T_w - T_v)}{\mu_v^2 T_v}\right]^{1/3} Pr_v^{1/3} \tag{7-293}$$

Model as Coded

Separate liquid and vapor heat transfer components are calculated for the film boiling heat transfer. For the heat transfer to liquid, Equation 7-284 is used. For vapor void fractions [ ]^{a,c}, h_{dffb} is set to zero, and for vapor void fractions [ ]^{a,c}, h_{Brom} is set to zero. For vapor void fractions between [ ]^{a,c}, h_{Brom} and h_{dffb} are calculated as follows:

[ ]^{a,c} (7-294)

and:

[ ]^{a,c} (7-295)

where:

[ ]^{a,c} (7-296)

For the heat transfer to vapor in film boiling, the code chooses the largest of the h_{wv} correlations given in Equations 7-292 and 7-293.

That is:

$$h_{wv,fb} = \text{maximum}\begin{cases} h_{wv,nc} \\ h_{wv,DR} \end{cases} \quad (7\text{-}297)$$

For void fractions above [ ]^{a,c} is used to reach forced convection to vapor at [ ]^{a,c}.

Scaling Considerations and Conclusions

The film boiling models in WCOBRA/TRAC-TF2 one-dimensional components model calculate the energy split between the liquid phase and vapor phase.

The correlations used for film boiling have been primarily developed on tube flow geometries. The most significant location where these correlations are likely to be applied is the steam generator tubes during blowdown and reflood. The one-dimensional component film boiling model has been used to model the ROSA, LOFT and CCTF tests (Volume 2 of this report), which have steam generator components that have prototypical PWR dimensions. Since these correlations have been assessed on large- and full-scale components, any scaling issue is properly assessed.

7.3.8 Convection to Single-Phase Vapor

Model Basis

In this heat transfer regime the wall to vapor heat transfer coefficient is selected as the larger of the (McAdams, 1954) turbulent natural convection heat transfer coefficient $h_{wv,tnc}$ or the forced convection heat transfer coefficient using either (Sieder and Tate, 1936) equation or the (Dittus and Boelter, 1930) equation $h_{wv,tfc}$. The choice of equation is dependent on the [ ]^{a,c} where:

[ ]^{a,c} (7-298)

For turbulent natural convection, the McAdams correlation for turbulent natural convection from horizontal cylinders is used as:

$$h_{wv,tnc} = 0.13\left(Gr_v \cdot Pr_v\right)^{1/3}\left(\frac{k_v}{D_h}\right) \tag{7-299}$$

where:

$$Gr_v = \frac{g_c \beta \rho_v^2 |T_w - T_v| D_h^3}{\mu_v^2} \tag{7-300}$$

with β approximated as:

[ ]^{a,c} (7-301)

If [ ]^{a,c}, the code uses the Sieder-Tate equation, given by:

$$h_{wv,tfc} = 0.027\left(\frac{k_v}{D_h}\right) Re_v^{0.8}\, Pr_v^{0.3333}\left(\frac{\mu_v}{\mu_w}\right)^{0.14} \tag{7-302}$$

If [ ]^{a,c}, the code calculates $h_{wv,tfc}$ from the Dittus-Boelter relation such that:

$$h_{wv,tfc} = 0.023\left(\frac{k_v}{D_h}\right) Re_v^{0.8}\, Pr_v^{0.4} \tag{7-303}$$

where:

$$Re_v = \frac{\rho_v |U_v| D_h}{\mu_v} \tag{7-304}$$

Model as Coded

The heat transfer coefficients for single-phase vapor are evaluated in subroutine HTCOR. The Reynolds number is limited to a minimum value of [ ]^{a,c}. The vapor heat transfer coefficient is found as follows:

$$h_{wv,spv} = \text{maximum}\left(h_{wv,tnc}, h_{wv,tfc}\right) \tag{7-305}$$

All properties are evaluated at [ ]^{a,c} in Equations 7-299 and 7-304 and at [ ]^{a,c} in Equation 7-302, except μ_w, which is evaluated at the wall temperature, T_w. The velocity in the Reynolds number is the absolute value of the axial vapor velocity. The hydraulic diameter of the flow passage is used as the characteristic length. In order to avoid extra calls to the thermodynamics properties subroutine, THERMO, densities evaluated at either the [ ]^{a,c} temperatures are approximated by [ ]^{a,c} as follows:

[ ]^{a,c} (7-306)

and:

[ ]^{a,c} (7-307)

Under the conditions that the cell void fraction is between [ ]^{a,c}, WCOBRA/TRAC-TF2 interpolates between the single-phase heat transfer coefficients described in this section and the appropriate two-phase heat transfer coefficients.

A test is made on the void fraction. If [ ]^{a,c}, two-phase liquid and vapor heat transfer coefficients are calculated. For void fractions between [ ]^{a,c}, the vapor heat transfer coefficient is found by interpolating between the single-phase and two-phase results and the liquid heat transfer coefficient is found by interpolating between a value of zero and the two-phase results. The resulting coefficients are therefore:

[ ]^{a,c} (7-308)

(7-309)

where h_{wf} and h_{wg} are the liquid and vapor two-phase heat transfer coefficients and $h_{wv,spv}$ is the heat transfer coefficient for single-phase vapor. If [ ]^{a,c}, two passes are made, first with [ ]^{a,c}, and then with [ ]^{a,c}. Finally, linear interpolation is done for both h_{wf} and h_{wg} using their values computed at [ ]^{a,c}.

Scaling Considerations and Conclusions

Existing, well known correlations are used for the single-phase vapor heat transfer. The application of these correlations is most important in the steam generator tubes, whose geometry is similar to that used in the original formulation for the correlations.

The correlations used in heat transfer to single-phase vapor are well known and have been applied to a wide variety of fluids and geometries. A length scale does not appear in the expression for turbulent natural convection, and the Dittus-Boelter equation does not have significant scale dependence.

These correlations have been tested on a wide range of scaled and full-scale system components as part of the WCOBRA/TRAC-TF2 validation (Volume 2 of this report).

7.3.9 Heat Transfer to Two-Phase Mixtures

Model Basis

For one-dimensional components, WCOBRA/TRAC-TF2 includes a regime that is unique in that it is not part of the boiling curve discussed previously. The regime is used only when the input flag ICHF = 0 is specified, which instructs the component to ignore CHF calculations.

The liquid heat transfer coefficient uses the (Rohsenow and Choi, 1961) expression for laminar forced convection, $h_{w\ell,lfc}$, and the (Dittus and Boelter, 1930) correlation for turbulent forced convection, $h_{w\ell,tfc}$:

$$h_{w\ell,lfc} = \frac{4.0\, k_\ell}{D_h} \tag{7-310}$$

$$h_{w\ell,tfc} = 0.023 \frac{k_\ell}{D_h} Re_m^{0.8}\, Pr_m^{0.4} \tag{7-311}$$

where:

$$Pr_m = \frac{c_{p\ell}\, \mu_\ell}{k_\ell} \tag{7-312}$$

$$Re_m = \frac{G_m\, D_h}{\mu_m} \tag{7-313}$$

$$\mu_m = \frac{1}{\frac{x}{\mu_v} + \frac{1-x}{\mu_\ell}} \tag{7-314}$$

The term μ_m is the two-phase viscosity proposed by (McAdams, Woods, and Bryan, 1942), x is the flow quality, and G_m is the product of mixture velocity (U_m), and mixture density (ρ_m).

Alternatively, the wall-to-gas heat transfer coefficient is given by:

$$h_{wv} = \begin{cases} 0.0 \\ \max\left(h_{wv,tnc}, h_{wv,tfc}\right) \end{cases} \quad \left[\qquad \right]^{a,c} \tag{7-315}$$

where the coefficient $h_{wv,tnc}$ is evaluated from the turbulent natural-convection correlation. The Dittus-Boelter correlation is applied for turbulent forced convection to vapor, $h_{wv,tfc}$.

That is:

$$h_{wv,tnc} = 0.13\left(Gr_v \cdot Pr_v\right)^{1/3}\left(\frac{k_v}{D_h}\right) \tag{7-316}$$

$$h_{wv,tfc} = 0.023\left(\frac{k_v}{D_h}\right) Re_v^{0.8}\, Pr_v^{0.4} \tag{7-317}$$

where:

$$Re_v = \frac{\rho_v\, U_v\, D_h}{\mu_v} \tag{7-318}$$

$$Pr_v = \frac{c_{pv}\, \mu_v}{k_v} \tag{7-319}$$

Model as Coded

The heat transfer coefficients for heat transfer in this regime are evaluated in subroutine HTCOR.

Turbulent and laminar liquid phase heat transfer coefficients are calculated with Equations 7-310 and 7-311. In the region where [

]^{a,c}. The liquid phase heat transfer coefficient in this range is calculated by selecting the maximum convective heat transfer coefficient:

$$\tilde{h}_{w\ell,2\phi} = \text{maximum}\left(h_{w\ell,lfc}, h_{w\ell,tfc}\right) \tag{7-320a}$$

and then linearly interpolating as:

$$\left[\qquad \right]^{a,c} \tag{7-320b}$$

If [ ]^{a,c}, h_{wv}=0.0. Otherwise Equations 7-316 and 7-317 are used to evaluate h_{wv}. The value of h_{wv} is determined from the equation:

$$\tilde{h}_{wv,2\phi} = \text{maximum}\left(h_{wv,tnc}, h_{wv,tfc}\right) \quad (7\text{-}321a)$$

then a linear interpolation with void fraction is performed to determine the final value when the void fraction is greater than [ ]^{a,c}:

[ ]^{a,c} (7-321b)

where $h_{wv,spv}$ is calculated by Equation 7-305.

[

]^{a,c}

Figure 7.3-3 clarifies the selection process. In this figure, it is assumed that ICHF = 0, so that post-CHF regimes are not considered. For equilibrium quality greater than or equal to [ ]^{a,c}, the single-phase vapor regime is chosen and the vapor heat transfer coefficient is calculated using Equation 7-305. The liquid phase heat transfer coefficient is set to 0.0 in this regime. [

]^{a,c} The liquid phase heat transfer coefficient is calculated using Equation 7-320 and the vapor phase heat transfer coefficient is set to 0.0.

Scaling Considerations and Conclusions

The correlations used to determine the heat transfer coefficient in this regime scale weakly with hydraulic diameter. The WCOBRA/TRAC-TF2 one-dimensional component heat transfer package provides extra flexibility for specifying two-phase heat transfer coefficients. This portion of the package is used only in one-dimensional components where CHF is not a consideration. Use of this model is not considered a major contributor to the code bias and uncertainty.

7.3.10 Condensation Heat Transfer

Model Basis

WCOBRA/TRAC-TF2 includes a separate heat transfer regime to account for condensation heat transfer in one-dimensional components. The equilibrium quality x, is compared to the value defined as [ ]^{a,c} to determine which set of condensation correlations to use for the wall condensation regime (IDREG=11). The limiting value, [ ]^{a,c}, is based on the data used in development of the Chen correlation. This can be observed in Table 7.2 of (Collier and Thome, 1994), which summarizes the data used in the development of the Chen model.

The vapor heat transfer coefficient for condensation is determined from the maximum of the (McAdams, 1954) correlation:

$$h_{wv,tnc} = 0.13\left(Gr_v \cdot Pr_v\right)^{1/3}\left(\frac{k_v}{D_h}\right) \tag{7-322}$$

an approximation of the (Dittus and Boelter, 1930) equation as:

$$h_{wv,tfc} = 0.023\left(\frac{k_v}{D_h}\right)\cdot\left(\frac{\rho_v U_v D_h}{\mu_v}\right)^{0.8} Pr_v^{0.3} \tag{7-323}$$

a correlation based on Nusselt's theoretical analysis for the average heat transfer coefficient for a vapor condensing on a liquid film in laminar flow on a vertical wall:

$$h_{vcond,1} = 0.9428\left[\frac{\rho_\ell^2 g k_\ell^3 h_{fg}}{\mu_\ell L\left(T_{sv} - T_w\right)}\right]^{0.25} \tag{7-324}$$

and an empirical correlation used when the film Reynolds number is greater than [ ]^{a,c}:

$$h_{vcond,2} = 0.003\left[\frac{\rho_\ell^2 g k_\ell^3 L\left(T_{sv} - T_w\right)}{h_{fg}\mu_\ell^3}\right]^{0.5} \tag{7-325}$$

where L is the characteristic length.

For the liquid phase, the condensation heat transfer coefficients are determined from the maximum of the following correlations.

The (Rohsenow and Choi, 1961) equation for laminar forced convection flow in a pipe as:

$$h_{w\ell,lfc} = \frac{4.0\, k_\ell}{D_h} \tag{7-326}$$

and the (Chen, 1963) correlation with the suppression factor S_{CHEN} set to 0.0:

$$h_{w\ell,tfc} = 0.023\,\frac{k_\ell}{D_h}\left[\frac{\rho_\ell U_\ell\left(1.0-\alpha\right)D_h}{\mu_\ell}\right]^{0.8}\left(Pr_\ell\right)^{0.4} F_{CHEN} \tag{7-327}$$

where F_{CHEN} is defined in Equation 7-247. In evaluating F_{CHEN} for condensation, the minimum of [ ]^{a,c} is used for the quality.

Therefore:

$$h_{w\ell} = \text{maximum}\left(h_{w\ell,lfc}, h_{w\ell,tfc,}, h_{nc1}, h_{nc2}\right) \tag{7-328}$$

where:

$$h_{nc1} = 0.59\left(\frac{k_\ell}{D_h}\right) Gr_\ell^{0.25} Pr_\ell^{0.25} \tag{7-329}$$

$$h_{nc2} = 0.10\left(\frac{k_\ell}{D_h}\right) Gr_\ell^{0.3333} Pr_\ell^{0.3333} \tag{7-330}$$

Model as Coded

The condensation heat transfer regime (IDREG = 11) is assumed when the following conditions are each satisfied:[

]^{a,c}

where IQENCH is a flag indicating whether an interface exists (0 indicates no interface and 1 indicates an interface is present). When the conditions are satisfied, Equations 7-322 to 7-327 are evaluated in subroutine HTCOR to calculate a value for the vapor heat transfer coefficient, $h_{wv,cond}$. For long tubes, Equation 7-324 underestimates the heat transfer coefficient caused by ripples that develop on the liquid film. To account for this effect, a weighting factor WF ($0.0 \leq WF \leq 1.0$) based upon [ ]^{a,c} is calculated. This factor is used to combine the laminar and turbulent heat transfer coefficients $h_{vcond,1}$ and $h_{vcond,2}$ to determine a weighted average vapor heat transfer coefficient. For short lengths where [ ]^{a,c}, the laminar heat transfer coefficient $h_{vcond,1}$, is used; for large values [ ]^{a,c}, the larger of the turbulent and laminar heat transfer coefficients is used. The sink temperature for $h_{vcond,1}$ is then converted from [ ]^{a,c}. These equations are as follows:

[ ] a,c (7-331)

(7-332)

(7-333)

The vapor heat transfer coefficient for single-phase vapor (called h'_{wv} here to avoid confusion with the final result) and the heat transfer coefficient for a condensing vapor are then found as follows:

$$h'_{wv} = \max\left(h_{wv,tnc}, h_{wv,tfc}\right) \tag{7-334}$$

$$h_{wv,cond} = \max\left(h'_{wv}, \bar{h}_{vcond}\right) \tag{7-335}$$

For the liquid heat transfer coefficient, Equation 7-327 is evaluated in subroutine CHEN and the macroterm of the Chen correlation, h_{forc}, is returned to subroutine HTCOR (see Section 7.3.3). The microterm of the Chen correlation, h_{nucb}, is not evaluated in subroutine CHEN because in heat transfer regime 11, [ ]^{a,c}. An if-test in the subroutine will cause the calculation of hnucb to be bypassed when [ ]^{a,c}. The following equation, evaluated in subroutine CHEN, determines the macroterm, h_{forc}, which is returned to subroutine HTCOR:

$$\bar{h}_{forc} = \max\left(h_{w\ell,lfc}, h_{w\ell,tfc}\right) \tag{7-336}$$

Equations 7-329 and 7-330 are evaluated in subroutine HTCOR and the liquid heat transfer coefficient is determined as follows:

$$h_{w\ell,cond} = \max\left(h_{nc1}, h_{nc2}, \bar{h}_{forc}\right) \tag{7-337}$$

The final values for the liquid and vapor heat transfer coefficients are then determined by the following method:

If [ ]^{a,c}:

$$h_{w\ell} = 0.0 \tag{7-338}$$

$$h_{wv} = h_{wv,cond} \tag{7-339}$$

If [ ]^{a,c}:

[ ]^{a,c} (7-340)

(7-341)

If [ ]^{a,c}, the heat transfer coefficient for the liquid phase is calculated from the Chen correlation, with the suppression term $S_{CHEN} = 0.0$ and the heat transfer coefficient for the vapor phase set to 0.0. That is:

$$h_{w\ell} = \overline{h_{w\ell}} = \text{maximum}\left(h_{w\ell,lfc}, h_{w\ell,tfc}\right) \tag{7-342}$$

$$h_{wv} = 0.0 \tag{7-343}$$

Where $h_{w\ell,lfc}$ is again given by Equation 7-326, and $h_{w\ell,lfc}$ by Equation 7-327.

[

]^{a,c}

Scaling Considerations and Conclusions

These correlations model condensation as a forced or natural convection process assuming that all the resistance to the condensation is at the vapor-liquid interface. A detailed assessment of the condensation models against a number of separate and integral effect test facilities at various scales (including full scale UPTF data) is presented in Volume 2 of this report.

7.3.11 Wall to Fluid Heat Transfer

Model Basis

In the one-dimensional components, the total heat transfer from the wall is partitioned into the respective liquid and vapor phases. The total wall heat flux is given by:

$$q''_{total} = q''_{w\ell} + q''_{wv} \tag{7-344}$$

where:

$$q''_{w\ell} = h_{w\ell}\left(T_w - T_\ell\right) \tag{7-345}$$

$$q''_{wv} = h_{wv}\left(T_w - T_v\right) \tag{7-346}$$

The values of $h_{w\ell}$ and h_{wv} are regime dependent and are described in the previous subsections.

Model as Coded

The calculation of the wall heat flux for one-dimensional components is controlled by subroutine HTCOR. The details of the individual models are described in the previous subsections.

Scaling Conditions and Conclusions

Scaling considerations for each of the heat transfer correlations used for the wall-to-vapor and wall-to-liquid are discussed in their respective subsections. The WCOBRA/TRAC-TF2 one-dimensional heat transfer package uses correlations which have been tested by the simulation of different tests at different scales.

Table 7.3-1 One-Dimensional Component Heat Transfer Regimes	
IDREG	**Heat Transfer Regime**
1	Forced convection to single-phase liquid (fc)
2	Nucleate boiling (nb)
3	Transition boiling (tb)
4	Film boiling (fb)
6	Convection to single-phase vapor (spv)
7	Convection to two-phase mixtures (2ϕ)
11	Condensation (cond)
12	Natural convection to single-phase liquid (nc)

a,c

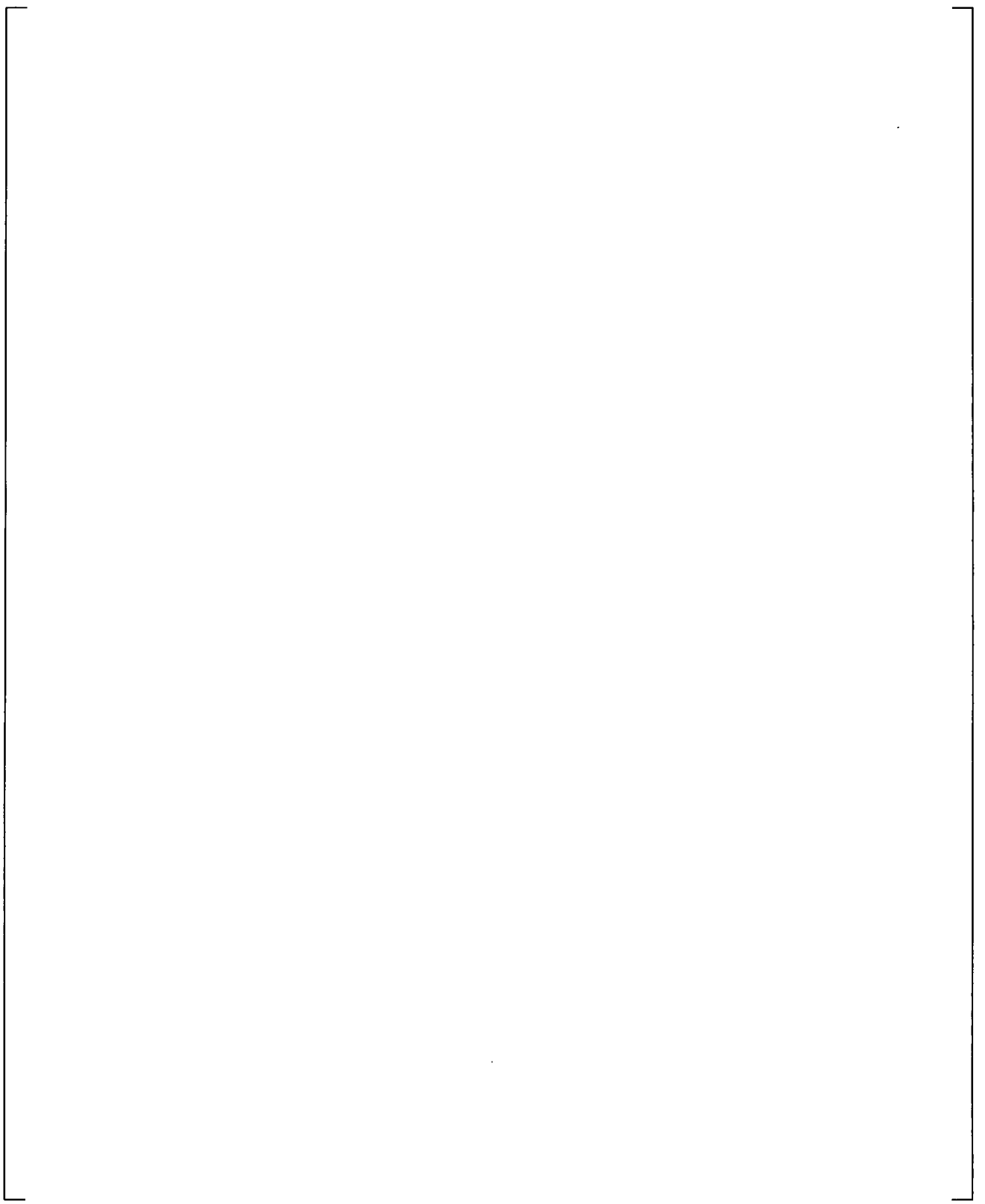

Figure 7.3-1 One-Dimensional Component Heat Transfer Regime Selection

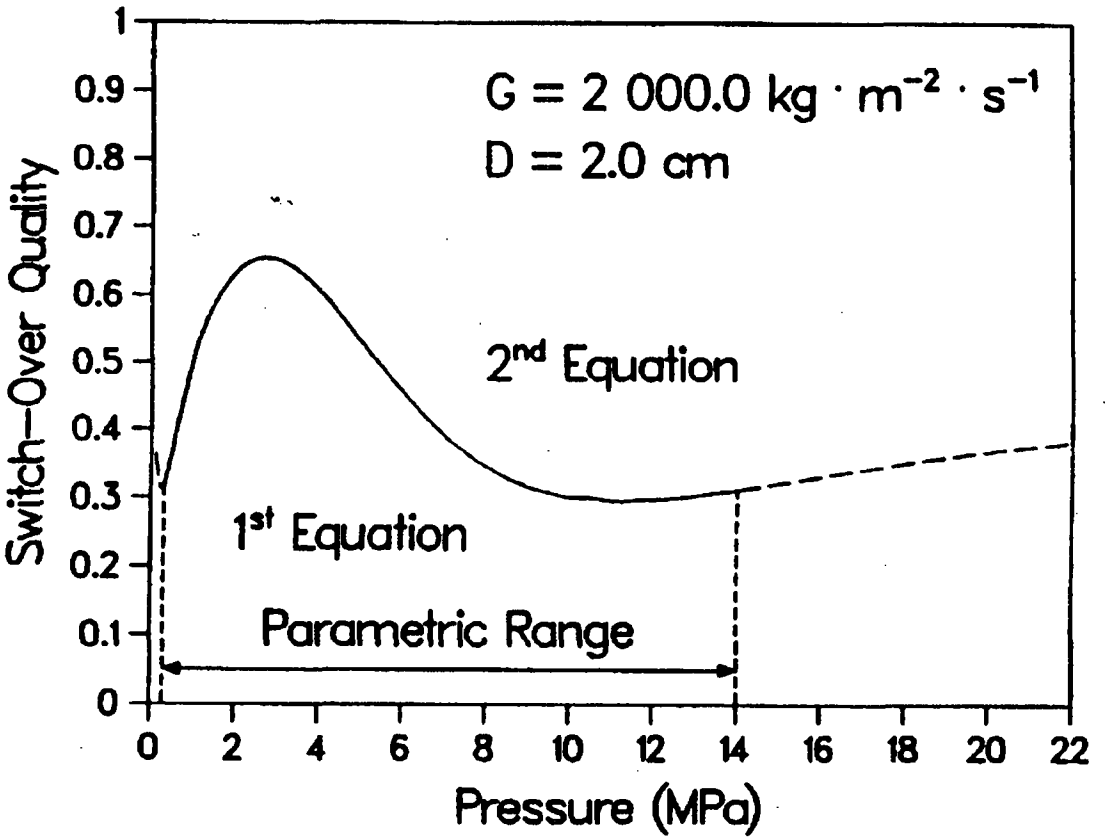

Figure 7.3-2 Biasi CHF Correlation Switch Over Quality (from Liles, D. R., et al., 1988)

a,c

Figure 7.3-3 One-Dimensional Component Heat Transfer Regime Selection Process at High Void and Quality

7.4 REFERENCES

1. Abu-Romia, M. M. and Tien, C. L., 1967, "Appropriate Mean Absorption Coefficients for Infrared Radiation of Gases," *J. Heat Transfer*, 89, pp. 321-327.

2. Bajorek, S. M., et al., 1998, "Code Qualification Document for Best Estimate LOCA Analysis," WCAP-12945-P-A, Volume 1, Revision 2, and Volumes 2 through 5, Revision 1, and WCAP-14747 (Non-Proprietary).

3. Bajorek, S. M., and Young, M. Y., 1998, "Assessment and Quantification of WCOBRA/TRAC-MOD7A Heat Transfer Coefficients for Blowdown Dispersed Flow Film Boiling," *ICONE*-6184, May 10-14.

4. Biasi, L., et al., 1967, "Studies on Burnout, Part 3," *Energia Nucleare*, Vol. 14, No. 9, pp. 530-536.

5. Bennett, A. W., et al., 1967, "Heat Transfer to Steam-Water Mixtures Flowing in Uniformly Heated Tubes in Which the Critical Heat Flux has been Exceeded," Report No. AERE-R5373, Atomic Energy Research Establishment, Harwell, England.

6. Bjornard, T. A. and Griffith, P., 1977, "PWR Blowdown Heat Transfer," *Thermal and Hydraulic Aspects of Nuclear Reactor Safety*, ASME, New York, Vol. 1, pp. 17-41.

7. Bromley, L. A., 1950, "Heat Transfer in Stable Film Boiling," *Chemical Engineering Progress*, Vol. 46, No. 5, pp. 221-226.

8. Chen, J. C., 1963, "A Correlation for Boiling Heat Transfer to Saturated Fluids in Convective Flow," ASME 63-HT-34.

9. Chiou, J. S., Hochreiter, L. E. and Young, M. Y., 1986, "Spacer Grid Heat Transfer Effects During Reflood," WCAP-10484.

10. Collier, J. G. and Thome, J. R., 1994, Convective Boiling and Condensation, 3rd Ed., Clarendon Press, Oxford.

11. Corman, J. C., 1966, "Water Cooling of a Thin, High Temperature Metal Strip," Ph.D. Thesis, Carnegie Institute of Technology.

12. Dengler, G. E. and Addoms, J. N., 1956, "Heat Transfer Mechanism for Vaporization of Water in Vertical Tube," *Chemical Engineering Progress Symposium*, Ser. 52, No. 18, pp. 95-103.

13. Dittus, F. W. and Boelter, L. M. K., 1930, "Heat Transfer in Automobile Radiators of the Tubular Type," *Publications in Engineering*, 2, Univ. of California, Berkeley, pp. 443-461.

14. Dougall, R. S. and Rohsenow, W. M., 1963, "Film Boiling on the Inside of Vertical Tubes with Upflow of the Fluid at Low Qualities," MIT Report 9079-26.

15. Drucker, M. and Dhir, V. K., 1984, "Studies of Single- and Two-Phase Heat Transfer in a Blocked Four-Rod Bundle," EPRI NP-3485.

16. Fineman, C. P., et al., May 1996, "Technical Evaluation Report, Westinghouse Code Qualification Document for Best Estimate Loss of Coolant Accident Analysis, WCAP-12945-P," INEL-95/0608.

17. Forslund, R. P. and Rohsenow, W. M., 1968, "Dispersed Flow Film Boiling," *J. Heat Trans.*, Vol. 90, No. 6, pp. 399-407.

18. Forster, H. K. and Zuber, N., 1955, "Dynamics of Vapor Bubbles and Boiling Heat Transfer," *AICHE J.*, Vol. 1 (4), pp. 531-535.

19. Gaugler, R. E. 1966, "An Experimental Study of Spray Cooling of High Temperature Surfaces," Ph.D. Thesis, Carnegie Institute of Technology.

20. Ganic, E. N. and Rohsenow, W. M., 1977, "Dispersed Flow Heat Transfer," *Int. J. Heat and Mass Transfer*, Vol. 20, pp. 855-866.

21. Gottula, R. C., et al., 1985, "Forced Convective, Nonequilibrium, Post-CHF Heat Transfer Experiment Data and Correlation Comparison Report," NUREG/CR-3193, Idaho National Engineering Laboratory.

22. Groeneveld, D. C. and Fung, K. K., 1976, "Forced Convective Transition Boiling – Review of Literature and Comparison of Predictive Methods," AECL-5543, Chalk River Nuclear Laboratories, Chalk River, Ontario.

23. Groeneveld, D. C., et al., 2007, "The 2006 CHF Look-up Table," *Nuclear Engineering and Design*, 237, pp. 1909-1922.

24. Hancox, W. T. and Nicoll, W. B., 1971, "A General Technique for the Prediction of Void Distributions in Nonsteady Two-Phase Forced Convection," *Int. J. Heat and Mass Transfer*, Vol. 14, pp. 1377-1394.

25. Henry, R. E., 1974, "A Correlation for the Minimum Film Boiling Temperature," *AICHE Symposium Series*, Vol. 138, pp. 81-90.

26. Holman, J. P., 1976, Heat Transfer, 4th Edition, McGrew-Hill Co., New York.

27. Iloeje, O. C., et al., 1974, "A Study of Wall Rewet and Heat Transfer in Disposed Vertical Flow," MIT Report 72718-92.

28. Iloeje, O. C., et al., 1975, "An Investigation of the Collapse and Surface Rewet in Film Boiling in Vertical Flow," *J. Heat Trans.*, Vol. 97, pp. 166-172.

29. Jens, W. H. and Lottes, P. A., 1951, "Analysis of Heat Transfer, Burnout, Pressure Drop and Density Data for High Pressure Water," USAEC Report ANL-4627.

30. Kays, W. M., 1966, Convective Heat and Mass Transfer, McGraw-Hill Book Company, New York.

31. Kim, J. H., 1979, "Heat Transfer in Longitudinal Laminar Flow Along Cylinders in a Square Array," Heat Transfer Over Rod or Tube Bundles, ASME, pp. 155-161.

32. Lahey, R. T. and Moody, F. J., 1977, The Thermal-Hydraulics of a Boiling Water Nuclear Reactor, American Nuclear Society.

33. Lee, N., et al., 1981, "PWR FLECHT SEASET Unblocked Bundle, Forced and Gravity Reflood Task Data Evaluation and Analysis Report," NUREG/CR-2256.

34. Lienhard, J. H. and Dhir, V. K., 1973, "Hydrodynamic Prediction of Peak Pool-Boiling Heat Fluxes from Finite Bodies," *J. Heat Transfer*, Vol. 95, No. 2, pp. 152-158.

35. Liles, D. R., et al., 1988, "TRAC-PF1/MOD1 Correlations and Models," NUREG-5069, LA-11208-MS.

36. McAdams, W. H., 1954, Heat Transmission, 3rd Edition, McGraw-Hill Co., New York.

37. McAdams, W. H., Woods, W. K. and Bryan, R. L., 1942, "Vaporization Inside Horizontal Tubes – II – Benzene-oil Mixtures," *Trans. ASME*, 64, 193.

38. McCreery, G. E., et al., 1977, "Thermal-Hydraulic Analysis of Semiscale MOD-1 Reflood Test Series (Gravity Feed Tests)," TREE-NUREG-1010.

39. Moles, F. D. and Shaw, J. F. G., 1972, "Boiling Heat Transfer to Subcooled Liquids Under Conditions of Forced Convection," *Trans. Inst. Chem. Eng.*, Vol. 50.

40. Pedersen, C. O., 1967, "The Dynamics and Heat Transfer Characteristics of Water Droplets Impinging on a Heated Surface," Ph. D. Thesis, Carnegie Institute of Technology.

41. Pomerantz, M. L., 1964, "Film Boiling on a Horizontal Tube in Increased Gravity Fields," *J. Heat Transfer*, 86 (2), pp. 213-219.

42. Rohsenow, W. M. and Choi, H., 1961, Heat, Mass and Momentum Transfer, Prentice-Hall, Inc., New York.

43. Rouhani, S. Z. and Axelsson, E., 1970, "Calculation of Void Volume Fraction in Subcooled and Quality Boiling Regions," *Int. J. Heat and Mass Transfer*, Vol. 13.

44. Sieder, E. N. and Tate, G. E., 1936, "Heat Transfer and Pressure Drop of Liquids in Tubes," *Industrial and Engineering Chemistry*, Vol. 28 (12), pp. 1429-1435.

45. Spencer, A. C. and Young, M. Y., 1980, "A Mechanistic Model for the Best-Estimate Analysis of Reflood Transients (the BART Code)," *19th National Heat Transfer Conference*, Orlando, FL, HTD, Vol. 7.

46. Sun, K. H., Gonzalez-Santalo, J. M. and Tien, C. L., 1976, "Calculations of Combined Radiation and Convection Heat Transfer in Rod Bundles Under Emergency Cooling Conditions," *Transactions of the ASME, Journal of Heat Transfer,* Vol. 98 (3), pp. 414 - 420.

47. Thurgood, M. J., et al., 1983, "COBRA/TRAC – A Thermal-Hydraulics Code for Transient Analysis of Nuclear Reactor Vessels and Primary Systems," Volume 1, NUREG/CR-3046.

48. Wachters, L. H. J. and Westerling, N. A. J., 1966, "The heat transfer from a hot wall to impinging water drops in the spheroidal state," *Chem. Eng. Sci.*, Vol. 21, pp. 1047-1056.

49. Whalley, P. B., 1976, "The Calculation of Dryout in a Rod Bundle," Report No. AERE-R8319, Atomic Energy Research Establishment, Harwell, England.

50. Whalley, P. B., Hutchinson, P. and Hewitt, G. F., 1973, "The Calculation of Critical Heat Flux in Forced Convection Boiling," Report No. AERE-R7520, Atomic Energy Research Establishment, Harwell, England.

51. Wong, S. and Hochreiter, L. E., January 1981, "Analysis of the FLECHT SEASET Unblocked Bundle Steam Cooling and Boiloff Tests," NUREG/CR-1533.

52. Yao, S. C., Hochreiter, L. E. and Dodge, C. E., 1979, "A Simple Method for Calculating Radiative Heat Transfer in Rod Bundles with Droplets and Vapor as Absorbing Media," *J. Heat Transfer*, 101, pp. 736-739.

53. Yao, S. C., Hochreiter, L. E. and Leech, J. J., 1982, "Heat Transfer Augmentation in Rod Bundles Near Grid Spacers," *J. Heat Trans.*, Vol. 104, pp. 76-81.

54. Yoder, et al., 1982, "Dispersed Flow Film Boiling in Rod Bundle Geometry-Steady State Heat Transfer Data and Correlation Comparisons," NUREG/CR-2435, ORNL-5822.

55. Zuber, N., et al., 1961, "The Hydrodynamic Crisis in Pool Boiling of Saturated and Subcooled Liquids," *International Developments in Heat Transfer*, Int. Heat Transfer Conf., Boulder, Colorado, Part II, No. 27, pp. 230-236.

8 WCOBRA/TRAC-TF2 MODELS FOR HEATED AND UNHEATED STRUCTURES

8.1 INTRODUCTION

The WCOBRA/TRAC-TF2 models for heated and unheated structures calculate the transient temperature response of the structures of interest, using the boundary conditions calculated by the heat transfer models and the fluid energy equations. This calculation consists of five major components:

- CONDUCTION MODEL — Specifies the conductor geometry and material properties, and solves the conduction equation.
- QUENCH FRONT MODEL — A "fine mesh-rezoning" method that calculates quench front propagation due to axial conduction and radial heat transfer.
- GAP CONDUCTANCE MODEL — A dynamic gap conductance model for a nuclear fuel rod.
- FUEL ROD DEFORMATION MODEL — Calculates the deformation of nuclear fuel rods, and the effects on core thermal-hydraulics.
- HEAT GENERATION MODEL — Determines the temporal and spatial variations in heat generation due to fission, gamma, and neutron energy deposition, fission product and actinide decay, and metal-water reaction in the cladding.

The conduction, quench front, gap conductance and fuel rod deformation models, and the metal-water reaction heat source are described in this section. The remaining heat sources are described in Section 9.

8.2 CONDUCTOR GEOMETRIES MODELED IN THE VESSEL

WCOBRA/TRAC-TF2 includes two general types of conductor models for the vessel component. The "rod" model is designed for heated structures such as nuclear fuel rods, heater rods, and tubes or walls which are expected to exceed the minimum film boiling temperature. This model allows the user to simulate most of the conductor geometries found in reactor vessels and heat transfer experiments. In addition, an "unheated conductor" model is provided for unpowered structures which are expected to remain below the minimum film boiling temperature.

Rods and unheated conductors are both used to model solid conducting structures in the vessel. There are two significant differences between them, however, one conceptual, the other numerical. Rods can model either active or passive elements, but unheated conductors are always passive. Unheated conductors cannot have internal heat sources. The quench front model with fine-mesh renoding can be applied to rods if needed, but unheated conductors are assumed never to require it.

A nuclear fuel rod model requiring minimal user input is built into the code as the "NUCL" rod option. Material properties can be specified by input or defaulted to uranium-dioxide and zircaloy. The default

properties are calculated using correlations from MATPRO-11 (Revision 1) (Hagrman, Reymann, and Manson, 1980). The standard conductor geometry for a nuclear fuel rod is illustrated in Figure 8-1. Only cylindrical fuel rods with fluid thermal connections on the rod exterior are considered with this modeling option.

A dynamic gap conductance model based on the GAPCON (Beyer et al., 1975 and Lanning et al., 1978) and FRAP (Dearian et al., 1977, Siefken et al., 1979, and Berna et al., 1978) computer codes is used for analyses of nuclear fuel rods. This model is discussed in Section 8.3.2. A fuel rod deformation model is also used for analyses of nuclear fuel rods. This model is discussed in Section 8.4.

Electric heater rods and other solid cylinders can be modeled with the "HROD" option. This option is available with the rod model and the unheated conductor model. These rods are modeled as concentric rings of different material regions, as shown in Figure 8-2. In each region the material type, number of radial nodes, width, and power factor are specified by input. Contact resistances are not calculated between material regions, but can be modeled by including a region one node wide with material properties that give it the appropriate thermal resistance.

Conductors, either tube or plate, with thermal connections to channels on either the inner or the outer surface are modeled with the "TUBE" and "WALL" options. The "WALL" option is available with the rod model and the unheated conductor model. The "TUBE" option is available with the unheated conductor model. The TUBE and WALL geometries, shown in Figure 8-3, are similar to the HROD geometry except for the interior coolant connections. Concentric and flat plate fuel elements, thermal walls and simple tubes can be modeled with these options.

Geometries simulated with the rod model may extend through any number of channel-splitting sections, but each heat transfer surface may only be connected to one channel in each section. Geometries simulated with the unheated conductor model may extend through one section only. Other limitations on the unheated conductor model are discussed in Section 8.7.

8.2.1 Conduction Equation

Model Basis

The modeling requirements of the vessel component include the ability to simulate generalized conductor geometries (fuel rods, electric heater rods, tubes, and walls) and temperature-dependent material properties. To accomplish this, a finite-difference form of the conduction equation has been employed.

The difference equations are formulated using the "heat balance" approach (Trent and Welty, 1974) which easily accommodates the following features:

- unequal mesh spacing
- temperature-dependent material properties
- space-dependent material properties
- internal resistances (such as those due to gaps)
- radial heat generation profiles

The finite-difference nodes of the conduction equation are modeled as control volumes connected by thermal resistances. They form a set of linearized equations solved by Gaussian elimination and back-substitution.

Model As Coded

The radial conduction equation for a control volume can be derived from a simple heat balance. For node i of Figure 8-4 this is:

$$(\rho C_p V)_i \frac{\partial T_i}{\partial t} = -Q_{i,i-1} - Q_{i,i+1} + Q_i''' V_i \tag{8-1}$$

where:

ρ	=	density (lbm/ft^3)
C_p	=	specific heat (Btu/lbm-°F)
V_i	=	node volume (ft^3)
T_i	=	node temperature (°F)
$Q_{i,i-1}$	=	radial heat flow from node (i) to (i-1) (Btu/sec)
$Q_{i,i+1}$	=	radial heat flow from node (i) to (i+1) (Btu/sec)
Q_i'''	=	volumetric heat generation rate (Btu/sec-ft^3)

The locations of radial conduction nodes are automatically calculated for a conductor geometry type. Each material region is divided into a specified number of subregions of equal radial thickness, and a conduction node is located at the center of mass of each subregion. This rule is followed for all nodes except the following:

- the node at the inside and outside surface of a "TUBE" or "WALL"
- outside surface of a heater rod
- fuel pellet exterior, cladding interior, and cladding exterior surface for a nuclear fuel rod

For these surfaces, a subregion half as wide as the other subregions is defined, and the node is located on the surface. The noding within a nuclear fuel rod is illustrated in Figure 8-5. (The fuel centerline temperature is calculated by Hermite interpolation.)

The radial positions of the conduction nodes are fixed; relocation due to thermal expansion is not calculated. To prevent an apparent loss of mass from the conductor because of density change with temperature, the term (ρV) is evaluated at the cold state density and dimensions, and defines the mass M_i associated with node i. So Equation 8-1 becomes:

$$(MC_p)_i \frac{\partial T_i}{\partial t} = -Q_{i,i-1} - Q_{i,i+1} + Q_i''' V_i \tag{8-2}$$

Heat transfer through a node is computed from the conductance (K) of the material and the temperature gradient across the node as:

$$Q_{i,j} = -K_{i,j}(T_j - T_i) \tag{8-3}$$

and

$$K_{i,j} = K_{j,i} \text{ for } j = \begin{cases} i-1 \\ i+1 \end{cases}$$

The conductance is defined as the inverse of the thermal resistance (R) between nodes and is computed as:

$$K_{i,i-1} = 1/(R_{i,i-1)} + R_{i-1,i}) \tag{8-4}$$

Thermal resistances are calculated for each node as a function of geometry and thermal conductivity. (See Section 8.2.2 for a complete explanation of this procedure.)

Substituting Equation 8-3 into 8-2 gives:

$$(MC_p)_i \frac{\partial T_i}{\partial t} = K_{i,i-1}(T_{i-1} - T_i) + K_{i,i+1}(T_{i+1} - T_i) + Q_i''' V_i \tag{8-5}$$

Forward differencing the temporal derivative in Equation 8-5 yields:

$$\frac{(MC_p)_i}{\Delta t}(T_i - T_i^n) = K_{i,i-1}(T_{i-1} - T_i) + K_{i,i+1}(T_{i+1} - T_i) + Q_i''' V_i \tag{8-6}$$

where:

Δt	=	time increment
n	=	old time level (all other temperatures are at the new time level)

To solve this equation, an implicit formulation is applied in the radial direction and the equation solved by Gaussian elimination for all nodes at that axial level. Axial conduction, if used, is treated as an explicit source term. The finite-difference equation for node (i) is then:

$$\frac{(MC_p)_i}{\Delta t}(T_i - T_i^n) = K_{i,i-1}(T_{i-1} - T_i) + K_{i,i+1}(T_{i+1} - T_i)$$

$$+ K_{i,j-1}(T_{j-1}^n - T_i^n) + K_{i,j+1}(T_{j+1}^n - T_i^n) + Q_i''' V_i \tag{8-7}$$

where the subscripts (j+1) and (j-1) represent the nodes at the same radial location and immediately above and below node i. If the stability criterion for the explicit axial conduction is exceeded, the timestep used

in the conduction equation is divided into two or more smaller timesteps and the conduction equation is solved for each of these.

Variations of Equation 8-7 are defined for the boundary nodes. The boundary condition applied to the conduction equation can be adiabatic or a surface heat transfer coefficient. Adiabatic boundary conditions are assigned to the center nodes of solid cylindrical rods (nuclear and heater rods) and at any surface node not connected to the fluid. Heat transfer coefficient boundary conditions are applied at surfaces connected to the fluid.

The heat transfer is coupled to the fluid channel through the heat transfer coefficient boundary condition. For each surface heat transfer node, both a heat transfer coefficient and a fluid sink temperature are specified for each phase of the fluid. Thus, the rod heat flux is given by:

$$q'' = h_{w\ell}(T_w - T_\ell^n) + h_{wv}(T_w - T_v^n) \tag{8-8}$$

where $h_{w\ell}$ and h_{wv} are the total heat transfer coefficients to the liquid and vapor fields, respectively (Section 7). The fraction of the rod surface area in contact with a given phase is accounted for in the heat transfer modeling (e.g., $h_{wv} = 0$ for annular flow).

The nucleate boiling heat flux depends very strongly on the wall surface temperature. Since the wall temperature is in turn affected strongly by the heat flux, the surface temperature solution may oscillate in nucleate boiling unless the heat transfer and wall temperature solution are coupled implicitly. This is done non-iteratively by including the "linearized" derivative of the heat transfer coefficient with respect to temperature in the surface boundary condition. Therefore, the heat flux from the surface to phase is given by:

$$q_\ell'' = h_{w\ell}^n(T_w - T_\ell^n) + \left(\frac{\partial h_{w\ell}^n}{\partial T_w}\right)(T_w - T_w^n)(T_w^n - T_\ell^n) \tag{8-9}$$

Rewriting Equation 8-7 for a surface node (w):

$$\frac{(MC_p)_w}{\Delta t}(T_w - T_w^n) = K_{w,w-1}(T_{w-1} - T_w) + K_{w,j-1}(T_{j-1}^n - T_w^n)$$

$$+ K_{w,j+1}(T_{j+1}^n - T_w^n)$$

$$- A_w\left[h_{w\ell}^n(T_w - T_\ell^n) + \left(\frac{\partial h_{w\ell}^n}{\partial T_w}\right)(T_w - T_w^n)(T_w^n - T_\ell^n)\right]$$

$$- A_w h_{wv}^n(T_w - T_v^n) + Q_w''' V_w \tag{8-10a}$$

where A_w is the heated surface area. Equation 8-10a is solved simultaneously with a set of equations for the interior nodes to determine the new time temperatures.

Finally, the liquid phase heat transfer coefficient and the nucleate boiling heat flux are updated by,

$$h_{w\ell} = h^n_{w\ell} + \left(\frac{\partial h_{w\ell}}{\partial T_w}\right)^n (T_w - T^n_w) \tag{8-10b}$$

and

$$q''_{w\ell} = h_{w\ell}(T_w - T^n_\ell) \tag{8-10c}$$

8.2.2 Calculation of Thermal Conductance

Model Basis

The internode conductance ($K_{i,i+1}$) between nodes i and i+1, as shown in Figure 8-6, is calculated from:

$$K_{i,i+1} = 1/(R_{i,i+1} + R_{i+1,i}) \tag{8-11}$$

The thermal resistance $R_{i,i+1}$ is the resistance to heat flow from node i to the boundary between nodes i and i+1. The thermal resistance $R_{i+1,i}$ is the resistance to heat flow from node i+1 to the boundary between i+1 and i. Formulas for these resistances for both plate and cylindrical geometries are given below.

Model As Coded

For a structure modeled as a flat plate, the steady, one-dimensional heat conduction equation with no internal generation is:

$$\frac{d^2T}{dx^2} = 0 \tag{8-12}$$

with the boundary conditions (Figure 8-7):

$$x = 0, T = T_1$$
$$x = L, T = T_2$$

Integrating Equation 8-12 and applying the boundary conditions gives the following formula for temperature distribution in the plate:

$$T = (T_2 - T_1)\left(\frac{x}{L}\right) + T_1 \tag{8-13}$$

where L = thickness of the plate.

The rate of heat transfer, from the Fourier equation, is:

$$q = -kA\frac{\partial T}{\partial x} = \frac{kA}{L}(T_1 - T_2) \tag{8-14}$$

where:

k	=	thermal conductivity of the plate
A	=	surface area perpendicular to the direction of heat flow

If the heat transfer is thought of as energy being pushed down a temperature gradient against some thermal resistance, q can be expressed as:

$$q = \frac{\Delta T}{R} \tag{8-15}$$

then:

$$R = \frac{L}{kA} \tag{8-16}$$

Therefore, the resistance from node i to the boundary between i and i+1 for a flat plate is:

$$R_{i,i+1} = \frac{\delta_{i,i+1}}{k_i A} \tag{8-17}$$

The total resistance from node i to node i+1 is ($R_{i,i+1} + R_{i+1,i}$). The conductance (K) between nodes i and i+1 is therefore:

$$K_{i,i+1} = K_{i+1,i} = \frac{k_i k_{i+1} A}{k_{i+1}\delta_{i,i+1} + k_i \delta_{i+1,i}} \tag{8-18}$$

where:

$\delta_{i,i+1}$	=	distance from node i to boundary between nodes i and i+1 (Figure 8-6)
A	=	surface area perpendicular to the direction of heat flow
k_i, k_{i+1}	=	thermal conductivity of the material in node i and i+1, respectively.

For steady radial flow of heat through the wall of a hollow cylinder (Figure 8-8) the conduction is:

$$\frac{1}{r}\frac{\partial}{\partial r}\left(r\frac{\partial T}{\partial r}\right) = 0 \tag{8-19}$$

with boundary conditions:

$$r = r_1, T = T_1$$

$$r = r_2, \ T = T_2$$

Integration of Equation 8-19 yields:

$$T = \frac{T_1 - T_2}{\ln\left(\frac{r_1}{r_2}\right)} \ln\left(\frac{r}{r_2}\right) + T_2 \tag{8-20}$$

The rate of heat flow is:

$$q = -k(2\pi r \Delta X)\frac{\partial T}{\partial r} \tag{8-21}$$

$$= \frac{2\pi k \Delta X}{\ln\left(\frac{r_2}{r_1}\right)}(T_1 - T_2)$$

and the resistance is:

$$R = \frac{\ln\left(\frac{r_2}{r_1}\right)}{2\pi k \Delta X} \tag{8-22}$$

where:

ΔX = node length in axial direction

Therefore, the resistance from node i to the boundary between i and i+1 for a cylinder is:

$$R_{i,i+1} = \frac{\ln\left[\frac{(r_i + \delta_{i,i+1})}{r_i}\right]}{2\pi k (\Delta X)} \tag{8-23}$$

where:

r_i = center of mass of node i
$\delta_{i,i+1}$ = radial distance from r_i to node boundary

The total resistance between nodes i and $i+1$ is $(R_{i,i+1} + R_{i+1,i})$, so the conductance is:

$$K_{i,i+1} = K_{i+1,i} = \frac{2\pi k_i k_{i+1} \Delta X}{k_{i+1} \ln (r_B / r_i) + k_i \ln (r_{i+1} / r_B)} \quad (8\text{-}24)$$

where $r_B = r_i + \delta_{i,i+1}$

The formulation for the hollow cylinder applies also to solid cylinders, simply by assuming an adiabatic condition on the inside boundary.

8.3 FUEL ROD MODELING

The fuel rod conductor has several special models to handle the unique situations that arise with heated conductors. These include a quench front renoding option and pellet-cladding gap conductance. These models are discussed in detail below.

8.3.1 Fuel Rod Quench Front Model

Model Basis

Coupled thermal-hydraulic numerical simulations of rewetting encounter difficulties with large axial computational mesh spacing which cannot adequately resolve the axial profile of temperature and surface heat flux across the quench front. During quenching, the entire boiling curve – from film boiling through transition boiling and critical heat flux to nucleate boiling – can be encompassed by one hydrodynamic mesh cell. Constraining the entire cell to be in one boiling regime is nonphysical and results in stepwise cell-by-cell quenching, producing flow oscillations that can obscure the correct hydrodynamic solution. Consequently, an integration of the boiling curve shape through the hydrodynamic computational cell must be performed to determine the fluid heat input.

User-specified fixed heat transfer nodes and a fine mesh-rezoning technique (Kelly, 1979) are employed in the vessel component of WCOBRA/TRAC-TF2 to surmount these difficulties. Fixed heat transfer nodes are used to model fuel rod conduction and cladding-fluid heat transfer with nodes that are smaller than the hydrodynamic cell size. These nodes are used throughout the transient. The fine mesh rezoning option allows the code to further resolve the quench front heat transfer. Fine mesh heat transfer cells with axial and radial conduction are superimposed upon the fixed heat transfer nodes, and a boiling heat transfer package is applied to each node.

By solving the two-dimensional conduction equation for a variable fine mesh at the quench front, propagation due either to quenching or dryout can be resolved and the surface heat flux integrated to provide the cell-averaged phasic heat inputs for the fluid energy equation. The resulting quench front velocity will be a function of:

- axial conduction
- boiling curve shape

- pre-quench heat transfer
- internal heat transfer within the rod

[

] [a,c]

Model as Coded

Resolution of axial temperature and surface heat flux excursions is achieved by rezoning the heat conductor mesh in their vicinity. Figure 8-9 illustrates a typical axial noding scheme. When axial temperature differences between adjacent heat transfer nodes within a continuity cell exceed splitting criteria, an additional node is inserted [ ]^{a,c} When the splitting criteria are exceeded at a continuity cell boundary, [ ]^{a,c} These scenarios are illustrated in Figure 8-10. The temperatures assigned to these nodes are computed so that energy is conserved. This splitting process continues (over a succession of timesteps) until the mesh is fine enough to resolve the surface temperature curve to the desired level of detail.

The correct temperature differences to be used as splitting criteria depend [ ]^{a,c}. They are further modified by functions of the wall temperature (when the wall temperature is [ ]^{a,c}) to ensure resolution of the surface heat flux profile in the vicinity of the quench front. The temperatures assigned to the inserted nodes are calculated from an energy balance:

$$\left[\qquad\qquad\right]^{a,c} \tag{8-25a}$$

where subscripts 1 and 2 represent the two original nodes, and subscript 3 represents the inserted node; subscripts O and N represent the old and new conduction node lengths, respectively.

Conversely, when a fine mesh has been established, but the disturbance has propagated downstream and the fine mesh is no longer necessary, adjacent nodes can be coalesced back down to one node. The decision to merge cells is based on [ ]^{a,c} between adjacent nodes. Eventually, all the fine mesh nodes in a region will coalesce, and only the original nodes will remain. The temperatures assigned to the adjacent nodes are calculated from an energy balance:

$$\left[\qquad\qquad\right]^{a,c} \tag{8-25b}$$

where subscript 3 represents the deleted node, and subscripts 1 and 2 represent the two remaining nodes; subscripts O and N represent the old and new nodes, respectively.

The fine mesh-rezoning model differs from other reflood models in that the fine mesh nodes are [ ]^{a,c}. The fine mesh nodes are split to create a graduated

mesh spacing that [ ]^{a,c}. This approach permits node sizes small enough to resolve axial conduction and the boiling curve shape at the quench front, and yet minimizes the number of nodes required. It ensures conservation of stored energy when cells are added, and simplifies coupling with the hydrodynamic solution. Figures 8-11 and 8-12 (taken from a simulation of a FLECHT low flooding rate test) illustrate the resolution of the cladding temperature profile and the surface heat flux in the vicinity of the quench front.

8.3.2 Pellet-Cladding Gap Conductance Model

Model Basis

The dynamic gap conductance model, originally developed for the VIPRE (Stewart et al., 1982) code, computes changes in the fuel rod structure and fill gas pressure that affect the gap conductance and fuel temperature during a transient. The method is based primarily on previous work on the GAPCON (Beyer et al., 1975, and Lanning et al., 1978) and FRAP (Dearien et al., 1977, Siefken et al., 1979, and Berna et al., 1978) series of fuel performance codes, but with the mechanics and fill gas pressure models greatly simplified. The material property correlations are taken exclusively from MATPRO-11 (Revision 1) (Hagrman, Reymann, and Manson, 1980); refer to Section 11.4.

Model As Coded

The pellet-cladding gap conductance has three components:

$$h_{gap} = h_{rad} + h_{gas} + h_{solid} \tag{8-26}$$

where:

h_{rad} = gap conductance due to thermal radiation

h_{gas} = gap conductance due to conduction in the fill gas

h_{solid} = gap conductance due to physical contact between the fuel pellet and the cladding

Each of these terms has associated with it certain models and assumptions. These are discussed in detail below. In all models, the gap is assumed axisymmetric.

Radiant Heat Transfer

The gap conductance due to radiant heat transfer is the ratio of the gap radiant heat flux, q_r'', to the temperature rise across the fuel/cladding gap:

$$h_{rad} = \frac{q_r''}{T_1 - T_2} \tag{8-27}$$

The radiant heat flux leaving the fuel surface, q_r'', is determined from the Stefan-Boltzmann equation using appropriate fuel cladding geometry factors, so that:

$$q_r'' = \sigma_{SB}\left[\frac{1}{\varepsilon_1} + \frac{A_1}{A_2}\left(\frac{1}{\varepsilon_2} - 1\right)\right]^{-1}\left[T_1^4 - T_2^4\right] \quad (8\text{-}28)$$

where:

A_1	=	fuel surface area (ft^2)
A_2	=	cladding surface area (ft^2)
ε_1	=	fuel surface emissivity
	=	min (0.8707, 1.311 - 2.447 x 10^{-4}T(°R))
ε_2	=	cladding surface emissivity
	=	0.75
T_1	=	fuel surface temperature (°R)
T_2	=	cladding surface temperature (°R)
σ_{SB}	=	Stefan-Boltzmann constant (1.714 x 10^{-9} Btu/hr-ft^2-°R^4)

The emissivity of the fuel is taken from function FEMISS of MATPRO-11 (Revision 0) (Hagrman and Reymann, 1979). The emissivity of the cladding inner surface is based on the data in subroutine ZOEMIS of MATPRO-11 (Revision 0).

Note that Revision 0 of function FEMISS has a lower bound of 0.4083, used for fuel temperatures in excess of 3230°F. Fuel surface temperatures never approach this value during any WCOBRA/TRAC-TF2 calculation which satisfies the peak cladding temperature (PCT) acceptance criterion, so the absence of this lower limit is inconsequential.

Conduction Heat Transfer in the Fill Gas

Heat conduction through the fill gas is calculated using the model developed for GAPCON-2 based on a linear regression analysis of Ross-Stoudt data by Lanning and Hann (1975). For a normal open gap the conductance is:

$$h_{gas} = \frac{k_{gas}}{\tau_g + 1.8(g_1 + g_2)} \quad (8\text{-}29)$$

where:

k_{gas}	=	fill gas mixture thermal conductivity (Btu/hr-ft-°F)
τ_g	=	gas gap width from deformation model (ft)
g_1	=	fuel pellet temperature jump distances (ft)
g_2	=	cladding temperature jump distances (ft)

The temperature jump distances compensate for the nonlinearity of the temperature gradient near the walls and the temperature discontinuities on the wall surface as illustrated in Figure 8-13. The nonlinear temperature gradient is due to the incomplete thermal mixing of the gas molecules near the surface. The surface temperature discontinuity results from the incomplete thermal accommodation of the gas molecules to the surface temperature.

The GAPCON-2 modification of the Lloyd model (Lloyd et al., 1973) is used to calculate the temperature jump distance. The Lloyd model compares well with available data and is used in both the FRAP and GAPCON-2 codes. The temperature jump distance term is evaluated with the relation.[1]

$$(g_1 + g_2) = 1.131(10^{-5}) \frac{k_{gas}(\overline{T}_g)^{1/2}}{P_{gas} \sum_{j=1}^{6} \frac{a_j x_j}{(M_j)^{1/2}}} \text{ (ft)} \tag{8-30}$$

where:

k_{gas}	=	fill gas mixture thermal conductivity (Btu/hr-ft-°F) (Section 11.4)
$\overline{T}_g$	=	gas gap average temperature (K)
x_j	=	mole fraction of jth gas
M_j	=	molecular weight of jth gas
a_j	=	accommodation coefficient of jth gas
P_{gas}	=	fill gas pressure (psia)

Measurements for helium and xenon on UO_2 by Ullman, Acharya, and Olander (1974) show that accommodation coefficients are temperature-dependent and vary for different gases. These dependencies are incorporated by using the GAPCON-2 curve fits to the Ullman data.

$$\alpha_{He} = 0.425 - 2.5(10^{-4})T$$

$$\alpha_{Xe} = 0.749 - 2.3(10^{-4})T \tag{8-31}$$

where T is in Kelvin (K).

The accommodation coefficients for other gases are approximated using a linear interpolation between those of helium and xenon based on molecular weight. This was found to correlate the data of Thomas (1967) with reasonable accuracy.

The gas mixture conductivity (k_{gas}) is determined from the conductivities of the constituent gases using a simplified version of the model in the MATPRO-11 subroutine GTHCON. Since the code uses the temperature jump model described above, the free molecular convection regime correction to the gas

1. Note that the equation as written in the GAPCON-2 manual is in error.

conductivity given in MATPRO is not required. The conductivities of helium, xenon, argon, krypton, hydrogen, and nitrogen gases are calculated using correlations from MATPRO-11 (Revision 1). The correlations compare favorably with the Chapman-Enskog theory used in GAPCON but are much easier to implement.

When fuel/cladding contact occurs, the heat conductance in the gas becomes:

$$h_{gas} = \frac{k_{gas}}{\left\{1.8\left[C(R_1 + R_2) + g_1 + g_2\right] - 4.2(10^{-7})\right\}} \quad (8\text{-}32)$$

where:

k_{gas} = fill gas mixture thermal conductivity (determined as for open gap)

g_1, g_2 = fuel pellet and cladding temperature jump distances (determined as for the open gap)

C = 1.98 exp [ ]^{a,c}, dimensionless constant where P_i is the contact pressure (in psi, determined by the fuel rod deformation model)

Fuel cladding contact is defined to occur when:

$$\tau_g \leq 3.6\ (R_1 + R_2) \quad (8\text{-}33)$$

where:

τ_g = gas gap width (from the fuel rod deformation model; discussed below)
R_1 = mean surface roughness of fuel pellet
R_2 = mean inside surface roughness

By this criterion, contact is assumed to occur because of waviness and mismatch of the fuel/cladding interface when the calculated gap width closes to within 3.6 times the combined surface roughnesses. This was determined by comparing measured gap widths with calculated gap widths from GAPCON (Hann, Beyer, and Parchen, 1973). A more complete discussion is available in the GAPCON-2 manual (Beyer et al., 1975).

Pellet-Cladding Contact Conductance

When the fuel and cladding are not in contact, h_{solid} must be zero. But when the deformation model determines that the gap between the fuel and cladding is small enough for contact to occur, the Mikic/Todreas model (Cooper, Mikic, and Yavonovich, 1969 and Todreas and Jacobs, 1973) is used to determine the contact conductance. Of the available models, it provides the best agreement with a wide range of contact conductance data (Lanning and Hahn, 1975 and Garnier and Begej, 1979).

In this model, h_{solid} is defined in terms of the physical properties of the materials and the geometry of the interface between them:

$$h_{solid} = \frac{5k_m}{(R_1^2 + R_2^2)^{1/2}} \left(\frac{P_{int}}{H_M}\right)^n \left(\frac{R_1}{\lambda_1}\right) \quad (8\text{-}34)$$

where:

k_m = $\frac{2k_1 k_2}{k_1 + k_2}$

k_1 = fuel thermal conductivity (Btu/hr-ft-°F)

k_2 = cladding thermal conductivity (Btu/hr-ft-°F)

R_1 = mean fuel surface roughness (ft)

R_2 = mean cladding surface roughness (ft)

$\frac{P_{int}}{H_M}$ = the dimensionless ratio of the interface pressure to the Meyer hardness

$\frac{R_1}{\lambda_1}$ = the dimensionless ratio of the mean fuel surface roughness and wave length distance between peaks)

The interfacial pressure (P_{int}) due to the differential fuel and cladding expansion, is calculated with the fuel rod deformation model and is non-dimensionalized using the Meyer hardness calculated from MATPRO-11 (Revision 1) subroutine CMHARD (Hagrman, Reymann, and Manson, 1980),

$$H_M = \exp\left(26.034 + T\left(-2.6394\times10^{-2} + T\left(4.3502\times10^{-5} - T\cdot 2.5621\times10^{-8}\right)\right)\right) \quad (8\text{-}34a)$$

Where H_M is the Meyer hardness (N/m^2), and T is the temperature (K). In the code, the Meyer hardness is limited to 0.001Psi (6.9Pa) to maintain computational stability. The exponent, n , on the ratio of interfacial pressure to Meyer hardness is defined (Thomas, 1967) as:

$$n = 1.0 \quad \text{if } (P_{int} / H_M) > 0.01$$

$$n = 0.5 \quad \text{if } (P_{int} / H_M) < 0.0001$$

For the intermediate range, the ratio is held constant:

$$\left(\frac{P_{int}}{H_M}\right)^n = 0.01 \quad \text{if } 0.0001 \le (P_{int}/H_M) \le 0.01$$

The ratio of fuel surface roughness to wave length is estimated as in GAPCON-2 by:

$$(\frac{R_1}{\lambda_1}) = \exp[0.5285 \ln (R_1) - 5.738] \quad (8\text{-}35)$$

where:

R_1 = mean fuel surface roughness (microinches)

Furthermore, the overall calculated conductance of the gap after pellet and cladding contact in GAPHTC is limited by the value of 3.0 E5 BTU/hr-ft^2-F. This value is selected to be outside the proper range used for calculation, but be able to improve robustness of fuel rod conductance calculation.

8.4 FUEL ROD DEFORMATION MODEL

Model Basis

Fuel pellet and cladding dimensional changes will occur during a loss-of-coolant accident as a result of the thermal and mechanical stresses present in a nuclear fuel rod. The fuel rod deformation model calculates these changes and their effects on the core transient thermal-hydraulics. WCOBRA/TRAC-TF2 calculates the effects of fuel rod deformation on the pellet-cladding gap conductance, the cladding dimensions used in the conduction equation and the calculation of cladding oxidation, the cladding surface heat transfer area, and the continuity and momentum areas of the fluid cells associated with the fuel rods. The modeling of each of these effects is discussed in this section.

Model as Coded

The fuel rod deformation mechanisms which are modeled in WCOBRA/TRAC-TF2 are described in Section 8.4.1. The effects of fuel rod deformation on the core transient thermal-hydraulics are discussed in Section 8.4.2.

8.4.1 Deformation Mechanisms

Fuel Pellet Thermal Expansion

The axial and diametral thermal expansion of the fuel is calculated using the MATPRO-11 (Revision 1) (Hagrman, Reymann, and Manson, 1980) FTHEXP subroutine correlation for thermally induced strain in UO_2. The correlation was simplified by omitting the corrections for molten fuel and mixed oxide (Pu). FTHEXP will return the same numerical value as the correlation in WCOBRA/TRAC-TF2, when FCOMP (weight percent PuO2) is equal to zero, and when T (fuel temperature) is less than FTMELT (fuel melting temperature). This is apparent by inspection of the subroutine listing in MATPRO.

In this model, the radial cracks in the fuel are assumed to relieve the hoop and radial stresses, allowing unrestrained radial movement of the fuel in each concentric radial node. The total radial movement at the fuel pellet surface is the sum of the expansion in all the fuel nodes.

$$(\Delta r_{th})_{fuel} = \sum_{i=1}^{NFUEL} \varepsilon_r(T_i)_j \Delta r_i \quad (8\text{-}36)$$

where:

$\varepsilon_r(T_i)_j$	=	thermal strain at axial node j and radial node i
	=	$1 \times 10^{-5} T_i + 0.04 \exp(-5000/T_i) - 0.003$
T_i	=	node temperature (K)
Δr_i	=	thickness of radial node i
NFUEL	=	number of radial nodes in the fuel

The stress-free axial thermal expansion of the fuel pellet stack is calculated in an analogous manner. The fuel pellet stack length change due to the thermal expansion is:

$$(\Delta \ell_{th})_{fuel} = \sum_{j=1}^{NDX} \varepsilon_z(\overline{T}_j) \Delta X_j \quad (8\text{-}37)$$

where:

$\varepsilon_z(\overline{T}_j)$	=	thermal strain at axial node j based on volume-averaged radial node temperatures
ΔX_j	=	height of axial node j
NDX	=	number of axial nodes

Cladding Thermal Expansion

The axial and radial thermal expansion of the cladding are calculated using the CTHEXP subroutine correlations from Hagrman, Reymann, and Manson (1980). The radial thermal expansion is calculated as:

$$(\Delta r_{th})_{clad} = \varepsilon_r(\overline{T}_j)\bar{r} \quad (8\text{-}38)$$

where:

$\varepsilon_r(\overline{T}_j)$	=	radial thermal strain at axial node j based on the average cladding temperature (Table 8-1)
$\bar{r}$	=	cladding mean radius (cold)

The axial thermal expansion of the cladding is:

$$(\Delta \ell_{th})_{clad} = \sum_{j=1}^{NDX} \varepsilon_Z (\overline{T}_j) \Delta X_j \quad (8\text{-}39)$$

where:

$\varepsilon_Z(\overline{T}_j)$ = axial thermal strain at axial node j based on average cladding temperature at node j (Table 8-1)

ΔX_j = height of axial node j

Cladding Elastic Deformation

When the pellet-cladding gap is open, elastic deformation of the cladding is driven by the difference between the fill gas and system pressures. If the gap closes, the cladding deformation is caused by the radial motion of the fuel. In both cases, the cladding is assumed sufficiently thin for the stress, strain, and temperature to be uniform throughout the cladding thickness.

In the open gap elastic deformation model, the cladding is considered as a thin cylindrical shell loaded by internal and external pressures. (Axisymmetric loading and deformation are assumed.) The radial and axial elastic deformation is the result of hoop stress and axial stress caused by pressure difference. These stresses are given by the following equations:

$$\sigma_\theta = \frac{r_i P_i - r_o P_o}{\tau_c} \quad (8\text{-}40)$$

$$\sigma_Z = \frac{\pi r_i^2 P_i - \pi r_o^2 P_o}{\pi (r_o^2 - r_i^2)} \quad (8\text{-}41)$$

where:

r_o = cladding outside radius

r_i = cladding inside radius

τ_c = cladding thickness

P_i = internal fill gas pressure (P_G if the gap is open, Equation 8-46; P_{int} if the gap is closed, Equation 8-49)

P_o = system pressure

The radial stress component is neglected, yielding the following relationships from Hook's Law:

$$\varepsilon_\theta = \frac{\Delta r}{\bar{r}} = \frac{1}{E}(\sigma_\theta - \nu\sigma_Z) \tag{8-42}$$

$$\varepsilon_Z = \frac{\Delta \ell}{\ell} = \frac{1}{E}(\sigma_Z - \nu\sigma_\theta) \tag{8-43}$$

where:

ε_θ	=	hoop strain
ε_Z	=	axial strain
E	=	modulus of elasticity (Young's modulus)
ν	=	Poisson ratio, $E/2G-1$ where G = shear modulus

The modulus of elasticity and the shear modulus are shown in Table 8-2.

The relations for the cladding radial and axial elastic deformations, then, are:

$$(\Delta r_{el})_{clad} = \varepsilon_\theta \bar{r} \tag{8-44}$$

$$(\Delta \ell_{el})_{clad} = \sum_{j=1}^{NDX} \varepsilon_Z \Delta X_j \tag{8-45}$$

where:

ε_θ	=	hoop strain at axial node j
$\bar{r}$	=	cladding mean radius
ε_Z	=	axial strain at axial node j
Δx_j	=	height of axial node j

The internal fill gas pressure used to determine the cladding elastic deformation when the gap is open is calculated from the relation:

$$P_G = \frac{M \cdot R}{\frac{V_P}{T_P} + \sum_{j=1}^{NDX} \pi \Delta X_j \frac{r_{ci}^2 - r_{fo}^2}{T_G} + \sum_{j=1}^{NDX} \pi \Delta X_j \frac{r_v^2}{T_V} + \sum_{j=1}^{NDX} \pi \Delta X_j \frac{r_{fvoid}^2}{T_F}} \tag{8-46}$$

where:

M	=	gram-moles of gas in fuel rod

V_p = gas plenum volume, including effects of fuel and cladding axial expansion (ft^3) (from Equations 8-37, 8-39, and 8-45)

T_p = gas plenum temperature (K) (defined as the temperature of the cladding at the top of the fuel rod + 10 K)

ΔX_j = computational cell length at axial level j (ft)

r_{ci} = cladding inside radius including thermal and elastic expansion, and creep deformation (ft) (from Equations 8-38, 8-44, and 8-59)

r_{fo} = fuel outside radius including thermal expansion (ft) (from Equation 8-36)

R = gas constant (6.1313 ft-lbf/g-mole-K)

r_v = radius of central void (ft) (from input data)

T_G = gas gap temperature (K)

T_v = central void temperature (K)

T_F = averaged fuel pellet temperature

r_{fvoid} = radius of additional fuel void in the fuel pellet

This is a static lumped pressure model, similar to those in FRAP or GAPCON. The pressure is assumed uniform throughout the fuel rod, with constant fission gas inventory.

In the closed gap deformation model, the cladding is considered as thin-wall tubing with a specified displacement at the inside and pressure loading at the outside surface. The radial fuel displacement at which contact occurs can be calculated as:

$$(\Delta r_{th})_{fuel} = (\Delta r_{th})_{clad} + (\Delta r_{cr})_{clad} + \tau_{g,cold} - \tau_g|_L \quad (8\text{-}47)$$

where:

$\tau_g|_L$ = fuel cladding gap width that defines the closed gap (i.e., 3.6 (R_1+R_2) as in Equation 8-33)

$\tau_{g,cold}$ = user-input cold fuel cladding gap width (including burnup-dependent effects)

$(\Delta r_{th})_{fuel}$ = fuel radial thermal expansion (Equation 8-36)

$(\Delta r_{th})_{clad}$ = cladding radial thermal expansion (Equation 8-38)

$(\Delta r_{cr})_{clad}$ = cladding creep deformation (Equation 8-59)

Fuel radial displacement due to contact is assumed negligible, so the radial elastic deformation of the cladding must be equal to the applied fuel displacement on the inside surface,

$$(\Delta r'_{th})_{fuel} = (\Delta r_{th})_{fuel} - (\Delta r_{th})_{clad} - (\Delta r_{cr})_{clad} + \tau_g|_L - \tau_{g,cold}$$

$$(\Delta r_{el})_{clad} = (\Delta r'_{th})_{fuel} \quad (8\text{-}48)$$

The pellet-cladding interfacial pressure generated by the applied displacement can be computed using the equilibrium stress (Equations 8-40 and 8-41), Hook's Law (Equations 8-42 and 8-43), and the applied displacement $(\Delta r'_{th})_{fuel}$. The interfacial pressure is:

$$P_{int} = \frac{(\Delta r'_{th})_{fuel} E\tau_c(r_o^2 - r_i^2)}{\bar{r}[r_i(r_o^2 - r_1^2) - r_1^2\tau_c\nu]} + P_o\frac{r_o(r_o^2 - r_1^2) - r_o^2\tau_c\nu}{r_i(r_o^2 - r_1^2) - r_1^2\tau_c\nu} \quad (8\text{-}49)$$

where:

$(\Delta r'_{th})_{fuel}$ = applied fuel displacement in cladding (from Equation 8-48)
E = modulus of elasticity
τ_c = cladding thickness
r_o = cladding outside radius
r_i = cladding inside radius
$\bar{r}$ = cladding mean radius
ν = Poisson's ratio for the cladding
P_o = system pressure (on the outside surface of the cladding)

The elastic deformation when the gap is closed is evaluated using the relation in Equation 8-44, but the internal pressure P_i is defined as the interfacial pressure P_{int} from Equation 8-49 instead of the fill gas pressure P_G from Equation 8-46.

Cladding Creep Deformation

The high-temperature creep model is based on tests performed at the Berkeley Nuclear Laboratories in the United Kingdom. Three cladding material options are available. The first is used for analyses of Westinghouse manufactured Zircaloy-4 cladding, and is based on the work of Donaldson, Healey, and Horwood (1985). The second is used for analyses of Westinghouse manufactured ZIRLO cladding, and is based on the work of Donaldson and Barnes (1989), and Donaldson, Barnes, and Hall (1989). An additional option is available for analyses of the Sandvik manufactured Zircaloy-4 cladding used in the National Research Universal (NRU) experiments, and is based on the work of Donaldson, Horwood, and Healey (1982).

The Berkeley test data indicate that high-temperature creep of the cladding materials of interest is well described by a power law stress dependence and an Arrhenius temperature dependence.

$$de/dt = A'\sigma^n \exp(-Q/RT) \quad (8\text{-}50)$$

where:

de/dt	=	creep rate (sec^{-1})
σ	=	hoop stress (MPa)
Q	=	activation energy, cal/gm-mole
R	=	gas constant, 1.987 cal/gm-mole/K
T	=	temperature (K)
t	=	time

and A', n are material-specific functions of T and σ. This relationship for creep is commonly referred to as the Norton creep equation.

The time-dependent hoop stress is given by:

$$\sigma(t) = (d(t)/2\tau(t))\, P(t) \quad (8\text{-}51)$$

where:

d(t)	=	mid-wall cladding diameter
	=	$d_o(1+\varepsilon(t))$, where d_o = initial mid-wall cladding diameter
$\tau(t)$	=	cladding thickness
	=	$\tau_o/(1+\varepsilon(t))$, where τ_o = initial cladding thickness
P(t)	=	cladding pressure differential
$\varepsilon(t)$	=	engineering strain

If the pressure is assumed to vary linearly over a small increment of time, such that,

$$P(t) = P_o + (dP/dt)\Delta t,$$

where:

P_o	=	cladding pressure differential at the beginning of the timestep

the time-dependent stress is given by:

$$\sigma(t) = \sigma_o(1+\varepsilon(t))^2 (1+((dP/dt)/P_o)\Delta t), \quad (8\text{-}52)$$

where:

σ_o = hoop stress at the beginning of the timestep

If the temperature is assumed to vary linearly over a small increment of time, such that:

$$T(t) = T_o + (dT/dt)\Delta t,$$

where:

T_o = temperature (K) at the beginning of the timestep

then:

$$\exp(-Q/RT(t)) = \exp(-Q/RT_o(1+((dT/dt)/T_o)\Delta t)) \quad (8\text{-}53)$$

A good approximation to this expression is:

$$\exp(-Q/RT(t)) = \exp(-Q/RT_o)(1+(dT/dt)(Q/RT_o^2)\Delta t \quad (8\text{-}54)$$

provided that $|(dT/dt)(Q/RT_o^2)|\Delta t \le 0.01$.

Substituting Equations 8-52 and 8-54 into 8-50 and allowing for the possibility of negative cladding pressure differentials yields:

$$de/dt = (|P_o|/P_o)A' \exp(-Q/RT_o)|\sigma_o|^n (1+\varepsilon)^{2n} \\ (1+((dP/dt)/P_o)\Delta t)^n (1+(dT/dt)(Q/RT_o^2)\Delta t) \quad (8\text{-}55)$$

The true strain is related to the engineering hoop strain by $e = \ln(1+\varepsilon)$. Therefore, $de = d\varepsilon/(1+\varepsilon)$. If we define:

$$C_1 = (|P_o|/P_o)A' \exp(-Q/RT_o)|\sigma_o|^n$$
$$C_2 = (dT/dt)(Q/RT_o^2)$$
$$C_3 = (dP/dt)/P_o$$

Equation 8-55 may be rewritten as:

$$d\varepsilon/(1+\varepsilon)^{2n+1} = C_1((1+C_2\Delta t)(1+C_3\Delta t)^n)dt$$

or

$$(1+\varepsilon)^{-(2n+1)}d\varepsilon = C_1(1+C_3\Delta t)^n dt + C_1C_2\Delta t(1+C_3\Delta t)^n dt \quad (8\text{-}56)$$

Integration may be performed using standard integral tables (for example, Beyer, 1978) which yields:

$$(-1/2n)((1+\varepsilon)^{-2n}-1)=C_1/C_3^2((C_3-C_2)((1+C_3\Delta t)^{n+1}-1)/(n+1) \quad (8\text{-}57)$$

$$+C_2((1+C_3\Delta t)^{n+2}-1)/(n+2))$$

The engineering hoop strain in the timestep Δt is therefore:

$$\varepsilon=[(1-2n(\text{Right Hand Side of Equation } 8-57)]^{-1/2n}-1 \quad (8\text{-}58)$$

The creep model used in WCOBRA/TRAC-TF2 calculates the incremental engineering hoop strain over a timestep Δt using Equation 8-58. The cladding creep deformation is then calculated as:

$$(\Delta r_{cr})_{clad}=\varepsilon(t)\bar{r} \quad (8\text{-}59)$$

where:

$\varepsilon(t)$	=	engineering hoop strain at end of timestep
$\bar{r}$	=	cladding mean radius

The maximum timestep for the integration of the Norton creep equation is limited so that $|C_2|\Delta t \le 0.01$ and the approximation to exp(-Q/RT(t)) remains valid. Details of the model application for the three available cladding options are summarized below.

[

]^{a,c}

Westinghouse Zircaloy-4 Cladding

Donaldson, Healey, and Horwood (1985) report Westinghouse manufactured Zircaloy-4 creep data obtained under constant pressure, constant temperature test conditions. Test specimens were heated to the specified temperature and the temperature was held constant for 10 minutes prior to pressurization. The creep test results indicate the existence of two types of creep behavior (Figure 8-14). Creep in the alpha and beta phases, and part of the mixed phase region, exhibits high stress sensitivity typical of a dislocation climb mechanism. In the low stress/low temperature portion of the mixed phase region the stress sensitivity is significantly reduced. In this region, the creep mechanism is superplastic creep.

Donaldson, Healey, and Horwood (1985) report additional creep test data for [

]^{a,c}

[

]^{a,c}

The creep rates shown in Figure 8-14 are programmed in WCOBRA/TRAC-TF2 in the form:

$$de/dt = A\sigma^n \tag{8-60}$$

where the coefficients A and n are functions of temperature and the creep mechanism (Table 8-3). To determine the coefficients A', Q and n for integration of Equation 8-50, the following procedure is used:

1. [ ]^{a,c}

$$\left[\quad\right]^{a,c} \tag{8-61}$$

where: [

]^{a,c}

2. [ ]^{a,c}

3. Calculate n from:

$$\left[\quad\right]^{a,c} \tag{8-62}$$

4. [ ]^{a,c}

5. Calculate Q from:

$$\left[\quad\right]^{a,c} \tag{8-63}$$

6. Calculate A from:

[ ]a,c (8-64)

Westinghouse ZIRLO® Cladding

Donaldson and Barnes (1989) and Donaldson, Barnes, and Hall (1989) report Westinghouse manufactured ZIRLO® cladding creep data obtained under similar test procedures as were used for the Zircaloy-4 tests, with the following notable exception. [

]a,c

The ZIRLO® cladding creep rates shown in Figure 8-15 are programmed in the form of Equation 8-60, with the coefficients **A** and **n** defined in Table 8-4. The procedure used to obtain the coefficients for the integration of the Norton creep equation is identical to that used for the Westinghouse Zircaloy-4 cladding option.

The ZIRLO® cladding creep model used in WCOBRA/TRAC-TF2 has previously been incorporated into the 1981 Evaluation Model with BASH and the NOTRUMP Evaluation Model (Davidson and Nuhfer, 1990). That reference describes a correction to the creep rate integration which is used in the alpha phase and the portion of the mixed phase region which exhibits dislocation creep, to more accurately predict the measured strain versus time. That correction is also used in WCOBRA/TRAC-TF2. Following integration of the Norton creep equation in the alpha phase and the mixed phase/dislocation creep regions, the strain accumulated during the timestep is reduced by an empirical expression which is a function of the strain accumulated in these regions, i.e.,

$$\varepsilon_e = \frac{\varepsilon}{(1+x)^m} \tag{8-65}$$

where:

ε_e	=	effective strain increment
ε	=	strain increment calculated by Equation 8-58
x	=	summation of ε_e in the strain hardening regimes
m	=	[ ]a,c for the alpha phase, [ ]a,c for the mixed phase/dislocation creep region

Sandvik (NRU) Zircaloy-4 Cladding

Donaldson, Horwood, and Healey (1982) report creep data for Sandvik Zircaloy-4 cladding specimens in the alpha phase. Testing was confined to the high alpha phase temperature range, based on the expected range of interest for the NRU Materials Test program.

The alpha phase Sandvik Zircaloy-4 cladding creep rates shown in Figure 8-16 are programmed in the form of Equation 8-60, with the coefficients A and n defined in Table 8-5. [

]^{a,c} The procedure used to obtain the coefficients for the integration of the Norton creep equation is identical to that used for the Westinghouse Zircaloy-4 cladding option.

Cladding Rupture

Loss of coolant accidents result in depressurization of the reactor coolant system and heatup of the nuclear fuel rods, due to insufficient cooling. The resulting stresses on the cladding may be sufficiently high to cause rupture of the cladding. Correlations which predict the occurrence of cladding rupture and the resulting cladding strains have been incorporated into WCOBRA/TRAC-TF2 for Zircaloy-4 cladding and for ZIRLO® cladding. These correlations are described below.

Zircaloy-4 Cladding

Powers and Meyer (1980) have reviewed zircaloy cladding rupture data from a wide range of experimental facilities and have recommended the cladding rupture correlation developed by Chapman (1979). The correlation is given by:

$$T_R = 3960 - \frac{20.4\sigma_E}{1+H} - \frac{8.51 \times 10^6 \sigma_E}{100(1+H)+2790\sigma_E} \qquad (8\text{-}66)$$

where:

T_R	=	rupture temperature (°C)
σ_E	=	engineering hoop stress (kpsi)
H	=	min (1.0, HUR/28°C/sec)
HUR	=	heatup rate

This correlation has been incorporated into WCOBRA/TRAC-TF2, and is used to predict the occurrence of cladding rupture for nuclear fuel rods clad with Zircaloy-4.

The cladding heatup rate in WCOBRA/TRAC-TF2 is treated in the same way as in the LOCTA-IV code (Bordelon et al., 1974). The approach can be explained by using Figure 8-17 which illustrates a number of potential scenarios. The instantaneous heatup rate is used until the cladding temperature is within [ ]^{a,c} of the cladding burst temperature. When this condition is reached (Point A) the cladding temperature and time are recorded to be used as a reference for the calculations. As long as the cladding temperature is [

]^{a,c}

[ ] a,c (8-67)

where: [

]^{a,c}

[

]^{a,c}

ZIRLO® Cladding

Westinghouse has conducted single rod burst tests of ZIRLO® cladding over a wide range of cladding pressure differentials (100 to 2000 psi), and heatup rates (5 to 50°F/sec) (Davidson and Nuhfer, 1990). The test results have been correlated in the form of rupture temperature as a function of engineering hoop stress, consistent with the Chapman approach. However, the ZIRLO® cladding rupture temperature correlation is not dependent on the heatup rate, as the data show no systematic heatup rate dependence.

The ZIRLO® cladding rupture correlation was defined using the mean of the 10°F/sec heatup rate data. Figure 8-19 shows a comparison of the measured burst temperatures and those predicted by the correlation. The correlation predicts the data well over the entire range of heatup rates included in the test matrix.

A correlation for the ZIRLO® cladding strain following rupture has been developed using the single rod burst test data reported in Davidson and Nuhfer (1990). The resulting correlation is shown with the

database in Figure 8-20. The WCOBRA/TRAC-TF2 correlation reflects the alpha phase and beta phase peaks, and [ ]^{a,c}

[

]^{a,c}

8.4.2 Effects of Fuel Rod Deformation on Core Thermal-Hydraulics

Transient Pellet-Cladding Gap

Before Cladding Rupture

Prior to cladding rupture the pellet-cladding gap width is calculated as:

$$\tau_g = \tau_{g,cold} - (\Delta r_{th})_{fuel} + (\Delta r_{th})_{clad} + (\Delta r_{el})_{clad} + (\Delta r_{cr})_{clad} \quad (8\text{-}68)$$

where:

$\tau_{g,cold}$	=	input value for pellet-cladding gap width
$(\Delta r_{th})_{fuel}$	=	pellet radial thermal expansion, from Equation 8-36
$(\Delta r_{th})_{clad}$	=	cladding radial thermal expansion, from Equation 8-38
$(\Delta r_{el})_{clad}$	=	cladding radial elastic deformation, from Equation 8-44
$(\Delta r_{cr})_{clad}$	=	cladding radial creep deformation, from Equation 8-59

This gap width is used in Equation 8-33 to determine if the gap is open or closed. If the gap is open, the gap conductance is calculated as described in Section 8.3.2 with h_{solid} set to zero. If the gap is closed, the gap conductance is calculated as described in Section 8.3.2, with the interfacial pressure from Equation 8-49 used to evaluate h_{solid}.

After Cladding Rupture

After cladding rupture occurs, the fuel rod deformation calculation is bypassed and the gap width at the time of rupture is used for the balance of the transient. [

]^{a,c}

[

]^{a,c}

The gap conductance for the heat transfer node containing the burst elevation is evaluated using the thermal conductivity of steam, after cladding rupture occurs.

[

]^{a,c}

Cladding Thermal Resistance

For analyses of nuclear fuel rods, the conduction model divides the fuel pellet into six radial nodes, and the cladding into two radial nodes. Node-to-node radial conduction is calculated using the conductance given by Equation 8-24. For undeformed cladding, the conductance is:

$$K = \frac{2\pi k_i k_o \Delta X}{k_o \ln\left(\frac{r_m}{r_i}\right) + k_i \ln\left(\frac{r_o}{r_m}\right)} \quad (8\text{-}70)^2$$

where:

K	=	conductance between inner and outer cladding nodes $\left(\frac{Btu}{hr\,°F}\right)$
k_i, k_o	=	thermal conductivity of inner and outer cladding nodes $\left(\frac{Btu}{hr\,°F}\right)$
ΔX	=	length of cladding (ft)
r_i	=	initial cladding inner radius (ft)
r_o	=	initial cladding outer radius (ft)
r_m	=	$0.5\ (r_i + r_o)$

The effects of cladding deformation on the cladding thermal resistance are accounted for by using the deformed dimensions r_i', r_o', and r_m' in Equation 8-70. Prior to burst, the deformed inner radius is approximated as:

$$r_i' = r_i + (\Delta r_{th})_{clad} + (\Delta r_{el})_{clad} + (\Delta r_{cr})_{clad} \quad (8\text{-}71)$$

where the Δr terms are given by Equations 8-38, 8-44, and 8-59. The deformed outer radius is calculated by conserving the cladding mass.

After burst occurs, the inner and outer radii of the heat transfer node containing the burst elevation are calculated as described above, for the transient pellet-cladding gap width.

Deformation of the fuel pellet due to thermal expansion has a negligible effect on the pellet node-to-node conduction. Therefore, the conductance between the pellet nodes is based on the undeformed pellet dimensions.

[

]^{a,c}

[2] Equation 8-69 intentionally omitted.

Heat Transfer From Cladding to Fluid

The heat transferred from the cladding of a nuclear fuel rod to the fluid is dependent on the cladding surface heat transfer area (Equation 8-10a). The cladding surface area of each heat transfer node is updated at each timestep, using the deformed cladding outer radius. The deformed cladding outer radius is calculated as described above.

[

]^{a,c}

Flow Blockage Due to Rod Deformation

Creep Deformation

The flow areas of the continuity cells in the core region are updated at each timestep to reflect the cladding creep deformation of the rods within each cell. The flow areas of the momentum cells in the core region are updated at each time step using the average outer rod diameter from the continuity cells above and below the center of the momentum cell.

Rupture Deformation

According to the experimental studies (Powers and Meyer, 1980; USNRC, 1988), the ballooning surface of cladding at the burst elevation of a fuel rod reduces flow area to the burst region, thus reduces the coolant flow area in the burst channel. In the Code Qualification Document (CQD) methodology, the flow area reduction factor is obtained following the recommend methodology in NUREG-0630 (Powers and Meyer, 1980). The flow area reduction factor accounts for a non-coplanar burst effect, hot assembly burst strain, and the presence of thimble tubes and instrumentation tubes. The flow area reduction factor is applied to both nominal flow area of continuity cell (ACONT) containing the hot assembly rod burst elevation, and two momentum cells (AMOM) at the top and bottom of continuity cell.

Since the total length of two momentum cells is much longer than the length of the ballooning area near burst elevation, this treatment will result in an excessive pressure loss in the fluid channel. Also, the code numerics will result in additional pressure losses (Section 5.3). Therefore, the coolant flow rate to the fluid channel containing burst rods is underestimated. The flow area predicted by the model in NUREG-0630 (Powers and Meyer, 1980) is a minimum flow area of the ballooning area. The fluid volume of the continuity node containing burst node is under-estimated. The underestimated coolant flow rate and the fluid volume leads to a reduced cooling effect for the rods in the channel.

[

]^{a,c}

[

]a,c

[ ]a,c

(8-72)

[

]a,c

[ ]a,c

(8-73)

[

]a,c

8.5 CLADDING REACTION MODEL

Model Basis

The zirconium base metal used in modern nuclear fuel rod cladding materials undergoes the following exothermic reaction with water or steam:

$$2H_2O + Zr \rightarrow 2H_2 + ZrO_2 + 140500 \text{ cal/mole Zr reacted} \quad (8\text{-}74)$$

This reaction may become significant under the high temperature conditions which may exist following a postulated LOCA.

At temperatures of about 1000K or greater, the zirconium-water reaction follows a parabolic rate law:

$$W \; dW/dt = A \exp(-B/RT)$$

where:

W	=	total oxygen consumed (gm/cm^2)
A	=	constant ($(gm/cm^2)^2/sec$)
B	=	activation energy (cal/gm mole)
R	=	gas constant (1.987 cal/gm mole/K)
T	=	temperature (K)

WCOBRA/TRAC-TF2 includes Cathcart and Pawel (1977) cladding reaction model which calculates the oxide buildup throughout the transient and the resulting heat generation in the cladding. The model is applied for Zircaloy-4 and ZIRLO® cladding materials, as described below.

Model as Coded

Cathcart and Pawel (1977) have examined the reaction of Zircaloy-4 in steam and have recommended a parabolic rate equation of:

$$W \; dW/dt = 0.1811 \exp(-39940/RT) \quad (8\text{-}75)$$

The uncertainty of the data fit [

]^{a,c}

[ ]^{a,c} (8-76)

where: [

]^{a,c}

The metal-water reaction calculation is performed in subroutine QOXIDE. The reaction rate of Equation 8-75 is converted to units of (ft Zr)^2/sec assuming a density of 409 lb/ft^3, resulting in:

$$\tau \; d\tau/dt = 3.69E - 5 \exp\left(-39940/RT\right) \tag{8-77}$$

where τ is the thickness of zirconium which has been reacted. Including the uncertainty on the reaction rate (only applied to [ ]^{a,c}), given by Equation 8-76, rearranging and integrating over a timestep Δt yields:

$$\int_{\tau_o}^{\tau} \tau \; d\tau = 3.69E-5 \int_0^{\Delta t} \exp\left(-39940/RT\right)\left(1+\delta_{Zr-4}/100\right)dt \tag{8-78}$$

Timesteps in WCOBRA/TRAC-TF2 are typically 0.01 seconds or less, due to hydraulic limitations. Therefore, the cladding temperature can be assumed constant over the timestep Δt, and Equation 8-78 may be integrated to yield:

$$\frac{\tau^2 - \tau_o^2}{2} = 3.69E-5 \exp\left(-39940/RT\right)\left(1+\delta_{Zr-4}/100\right)\Delta t \tag{8-79}$$

The thickness of cladding reacted at the end of the time step is then given by:

$$\tau = \left[\tau_o^2 + 7.38E-5 \exp\left(-39940/RT\right)\left(1+\delta_{Zr-4}/100\right)\Delta t\right]^{1/2} \tag{8-80}$$

The fuel rod deformation model described in Section 8.4 calculates changes in the cladding dimensions throughout a LOCA transient. The deformed cladding dimensions are used in the cladding reaction model calculation, as described below.

Before cladding burst is predicted to occur, the metal-water reaction occurs on the cladding outer surface only. The heat generation rate is given by:

$$q_o = Q_c \frac{\pi\left[\left(r'_{ox}\right)^2 - \left(r'_{ox} - \Delta r_{ox}\right)^2\right]\Delta X}{\Delta t} \tag{8-81}$$

where:

q_o = heat generated by outer surface reaction $\left(\frac{Btu}{sec}\right)$

Q_c = 1.123E6 $\left(\frac{Btu}{ft^3}\right)$

r'_{ox} = outer surface oxide radius prior to new oxidation (ft)

Δr_{ox} = cladding thickness oxidized over the timestep (ft)

ΔX = height of conduction node (ft)

Δt = timestep size (sec)

Prior to burst, the fuel rod deformation model updates the cladding outer radius at each timestep. [

]^{a,c}

[ ] a,c (8-82)

where: [

]^{a,c}

[ ] a,c (8-83)

[

]^{a,c}

Metal-water reaction on the cladding inner surface begins at the time the cladding bursts. Heat generation on the inner surface of the heat transfer node containing the hot rod burst elevation is calculated by:

[ ] a,c (8-84)

where:

[

]^{a,c}

[

]^{a,c}

[a,c] (8-85)

[ ]^{a,c}

The oxidation over the timestep is then calculated, and the heat generation is calculated using Equation 8-84.

8.6 [ ]^{a,c} MODEL

[

]^{a,c}

The FULL SPECTRUM LOCA (FSLOCA) methodology will model the hot assembly rods as [ ]^{a,c}

1. Hot Assembly (HA) Rod Component – A type of active nuclear fuel rod that describes all fuel rods in the hot assembly but the hot pin. [ ]^{a,c} A hot assembly rod is a fully functional fuel rod coupled with the thermal-hydraulic solution and core kinetics. The HA rod will consider all local uncertainty models at their nominal (as coded) value. The HA rod will deform consistently with the fuel rod deformation model discussed in Section 8.4, including creep deformation and rupture deformation. [

]^{a,c}

2. Hot Rod (HR) Component – A type of active nuclear fuel rod that describes the single fuel pin in the hot assembly, which represents a high power fuel pin. A hot rod is a partially functional fuel rod coupled with the thermal hydraulic solution and core kinetics. All the functions of the HA rod are applied to hot rod except the creep deformation and the rupture deformation are disabled for hot rod. The hot rod considers all applicable local uncertainty models at their nominal value.

3. [

]^{a,c}

[

]^{a,c}

A summary of functions of rods in the hot assembly is given in Table 8-6. The local uncertainties in Table 8-6 will be explained in Section 29.

The details of the [ ]^{a,c} model are listed below.

[

]^{a,c}

[

]^{a,c}

[

]^{a,c}

[

]^{a,c}

$$\left[\quad\right]^{a,c} \tag{8-86a}$$

[

]^{a,c}

[

]a,c

[ ]a,c

(8-86b)

[ ]a,c

[ ]a,c

(8-86c)

[

]a,c

[

]a,c

[

]^{a,c}

8.6.1 Fuel Relocation Following [ ]^{a,c} Burst

The phenomenon of fuel relocation following cladding burst was recognized in the early 1980s during various experimental studies, including those performed at the Power Burst Facility (PBF) in Idaho. A review and analysis of these tests was performed by Westinghouse and National Nuclear Corporation (NNC) during preparation of the safety case for Sizewell B in the United Kingdom; results of that analysis and application to the present situation are summarized below.

A number of short (approximately 3 feet) pre-irradiated and unirradiated test specimens were taken through depressurization and heatup transients at the PBF. Three tests were reported: LOC-3 and LOC-5 from Broughton (1981) and LOC-6 from Broughton (1983). The different tests were designed to cause rupture at different temperatures; LOC-3 in the alpha plus beta region (approximately 1680 F), LOC-5 in the beta region (approximately 2000 F), and LOC-6 in the alpha region (approximately 1470 F). The rods, which were highly enriched (12.5 percent), experienced variable ratings during pre-irradiation, on average about 12 kW/ft, with peak ratings as high as 18 kW/ft, which would be expected to promote more extensive fuel cracking than normal reactor conditions. Data about fuel relocation was available in the following forms from these tests:

1. Post-test neutron radiographs were available for most rods.

2. Niobium-95 gamma ray count rates were monitored after the tests to determine the axial location of the fuel.

3. Information from photo micrographs was presented in Broughton (1981) for tests LOC-3 and 5.

4. Photographs of the cross section of some of the rod specimens were available from the literature.

The relocation evidence from these tests was summarized by INEL in Broughton (1981) and as shown in Figure 8-29.

This figure shows the increase in fuel volume as a function of the increase in cladding volume after burst. A review of the data indicated some discrepancies with this figure, beyond the obvious one that the x and y axes show fraction, not percentage, change. [

]^{a,c} The data indicates that since the fuel volume increases

less than the cladding volume, the fuel does not completely fill the available cladding volume; there is a decrease in the fuel density along with an increase in the fuel volume. This change in fuel density can be described in terms of a [ ]^{a,c}

$$\left[\quad\right]^{a,c} \tag{8-87}$$

[

]^{a,c}

When the fuel relocates into the burst region, its mass increases. As a result, the heat generation rate within the burst zone is affected. The linear heat rate resulting from the fuel relocation is calculated in Equations 8-88 through 8-91.

The heat generation rate per unit mass of fuel (q_m) is related to the linear heat rate under normal conditions by:

$$q_m \frac{Btu}{s \cdot lb} = q' \frac{Btu}{s \cdot ft} \frac{1}{A_f} \frac{ft}{ft^3} \frac{1}{\rho_{uo2}} \frac{ft^3}{lb} \tag{8-88}$$

When burst occurs, the fuel mass in the burst region will [

]^{a,c}

$$\left[\quad\right]^{a,c} \tag{8-89}$$

[

]^{a,c}

$$\left[\quad\right]^{a,c} \tag{8-90}$$

[ ]^{a,c}

$$\left[\right]^{a,c} \quad (8\text{-}91)$$

[

]^{a,c}

8.6.2 Thermal Conductivity Model of Relocated Fuel

It was known that the fragments of fuel pellet relocate to the space created by the ballooning cladding after the rod burst. The relocated fuel is in the form of granular material, so that the fuel density after the relocation reduces. The relocation model predicts the change in fuel density with the variable packing fraction, which depends on factors, such as fuel type, fuel burnup, burst strain, etc. On the same token, the low fuel density after relocation affects the effective fuel conductivity after fuel relocation.

[

]^{a,c}

$$\left[\right]^{a,c} \quad (8\text{-}92)$$

[

]a,c

[a,c] (8-93)

[

]a,c

8.6.3 Burst Node Heat Transfer Enhancement Model

The study in NUREG-1230 (USNRC, 1988) suggests the flow blockage at the mid-plane was found to improve heat transfer both upstream and downstream of the blocked region. This was due to increased turbulence and atomization of entrained liquid droplets. The heat transfer was found to be enhanced near the region of blockage.

Paik and Hochreiter (1986) also suggested that the heat transfer may improve in fuel bundle with flow blockage rather than reduced. The heat transfer mechanism associated to the flow blockage is studied in NUREG-4166 (Paik and Hochreiter, 1986) and listed here:

- Single phase convective enhancement due to flow acceleration.
- Separation of boundary layer and reattachment of boundary layer.
- Droplets break-up in blocked region.
- Droplet impact heat transfer on the entrance region of the blockage.

The proper models for the mechanisms are also provided in NUREG-4166. None of the mechanisms are implemented in CQD methodology (Bajorek et al., 1998). Those models are suggested to be incorporated into FSLOCA methodology to realistically model heat transfer after rod burst. However, considering the complexity of the model and the far-reaching implications of a complete revision on the overall heat transfer and uncertainty methodology, only the model of [

]^{a,c}

[a,c] (8-94)

[

]^{a,c}

[ ]a,c (8-95)

[

]a,c

[ ]a,c (8-96)

[

|

|

]a,c

[ ]a,c (8-97)

[

]a,c

[ ]a,c (8-98)

[

]a,c

[ ]a,c (8-99)

[

]a,c

[ ]a,c (8-100)

[

]a,c

[ ]a,c (8-101)

[ ]a,c

[ ]a,c (8-102)

[

]a,c

8.7 UNHEATED CONDUCTOR MODEL IN THE VESSEL

Structural heat transfer surfaces in the vessel can be more efficiently modeled with the unheated conductor model. This option accesses the same conductor geometries (except for the nuclear fuel rod geometry) as the rod model, and uses the same heat transfer package. However, to economize computer time and storage, the unheated conductor model is limited in the following ways:

- No internal heat generation is included.

- Radial conduction only is used.
- No fine mesh-rezoning quench front model is included.
- Unheated conductors do not extend across section boundaries.
- The fluid solution cannot be forced into the "hot wall" flow regime.
- Vapor properties in the convective heat transfer correlations are evaluated at the bulk vapor temperature rather than the film temperature.
- The minimum film boiling temperature is set to a constant [ ]^{a,c}

These limitations only apply to the unheated conductor model and not to the rod model in general. Unheated conductors are used to model structural elements in the vessel for which expected peak temperatures are well below the minimum film boiling point.

8.8 CONDUCTOR MODELING IN ONE-DIMENSIONAL COMPONENTS

The thermal history of the solid material structure is obtained from a solution of the heat-conduction equation applied to different geometries. The HTSTR component in WCOBRA/TRAC-TF2 evaluates the dynamics of conduction and convection heat transfer in structure hardware elements in the reactor coolant systems. As a carryover from early versions of WCOBRA/TRAC, the PIPE, PUMP, TEE and VALVE hydraulic components also evaluate transient conduction and convection heat transfer across their cylindrical-geometry 1D flow channel wall. For user convenience, this heat transfer capability has remained a part of the modeling capability provided by these hydraulic components, even though it can be done with more modeling flexibility by an HTSTR component. However, whenever possible the user is encouraged to model heat transfer with HTSTR components coupled to hydraulic components because of the more flexible and extended features that an HTSTR component provides.

Model Basis

Because the heat flux in a solid material is a vector quantity, the following general equation describes the heat-conduction process in an arbitrary geometry:

$$\frac{\partial (\rho c_p T)}{\partial t} + \nabla \cdot \bar{q} = q''' \tag{8-103}$$

where ρ is the density, c_p is the specific heat, T is the temperature and q''' is the heat source/sink per unit volume.

In practice, the product ρc_p is assumed to be constant for purposes of calculating the time derivative.

The heat flux $\bar{q}$ can be expressed in terms of the temperature gradient by Fourier's law of conduction as follows:

$$\bar{q} = -k\nabla T \tag{8-104}$$

where k is the thermal conductivity. Therefore, Equation 8-103 becomes:

$$\rho c_\rho \frac{\partial T}{\partial t} = \nabla \cdot (k\nabla T) + q''' \tag{8-105}$$

Model as Coded

1D Component Cylindrical Wall Heat Conduction

The temperature distribution within the walls of the one-dimensional components is determined by subroutine CYLHT. A solution is obtained from a finite-difference approximation to the one-dimensional conduction equation in cylindrical coordinates,

$$\rho c_p \frac{\partial T}{\partial t} = \frac{1}{r}\left[\frac{\partial}{\partial r}\left(rk\frac{\partial T}{\partial r}\right)\right] + q''' \tag{8-106}$$

Alternatively, a lumped parameter solution is employed if the user specifies one conduction node.

The finite-difference equations are derived by applying an integral method (Roache, 1972) to the elemental volumes shown in Figure 8-34. The general form for the volume i $(1 < i < N)$ is:

$$\frac{r_{i-1/2}\,k_{i-1/2}}{\Delta r_{i-1}} T_{i-1}^{n+1} - \left\{\frac{r_{i-1/2}\,k_{i-1/2}}{\Delta r_{i-1}} + \frac{r_{i+1/2}\,k_{i+1/2}}{\Delta r_i}\right. \tag{8-107}$$

$$\left. + \frac{1}{2\Delta t}\left[\left(r_i\,\Delta r_{i-1} - \frac{\Delta r_{i-1}^2}{4}\right)(\rho c_p)_{i-1/2} + \left(r_i\,\Delta r_i + \frac{\Delta r_i^2}{4}\right)(\rho c_p)_{i+1/2}\right]\right\} T_i^{n+1}$$

$$+ \frac{r_{i+1/2}\,k_{i+1/2}}{\Delta r_i} T_{i+1}^{n+1} = -\frac{1}{2}\left\{\left(r_i \Delta r_{i-1} - \frac{\Delta r_{i-1}^2}{4}\right)\left[\frac{(\rho c_p)_{i-1/2}}{\Delta t} T_i^n + q'''\right]\right.$$

$$\left. + \left(r_i \Delta r_i + \frac{\Delta r_i^2}{4}\right)\left[\frac{(\rho c_p)_{i+1/2}}{\Delta t} T_i^n + q'''\right]\right\}$$

This formulation positions nodal points on material interfaces. Material properties are evaluated between nodes. The boundary conditions applied to the inner $(i = 1)$ and outer $(i = N)$ surfaces are:

$$-k\frac{\partial T}{\partial r}\Big|_{i=1,N} = \pm\left[h_{w\ell}(T_\ell - T_i) + h_{wv}(T_v - T_i)\right] \tag{8-108}$$

where T_ℓ and T_v are liquid and vapor temperatures, respectively; $h_{w\ell}$ and h_{wv} are the heat transfer coefficient for liquid and vapor phases, respectively.

Applying this boundary condition to the inner surface (i = 1), for example,

$$-\left\{\frac{r_{3/2}\,k_{3/2}}{\Delta r_1}+\frac{1}{2}\left[r_1\Delta r_1+\frac{\Delta r_1^2}{4}\right]\frac{(\rho c_p)_{3/2}}{\Delta t}+f_{ss}r_1\left(h_{wl}+h_{wv}\right)\right\}T_1^{n+1}+\frac{r_{3/2}\,k_{3/2}}{\Delta r_1}T_2^{n+1}$$

$$=-\frac{1}{2}\left(r_1\Delta r_1+\frac{\Delta r_1^2}{4}\right)\left[\frac{(\rho c_p)_{3/2}}{\Delta t}T_1^n+q'''\right]$$

$$+r_1\left[h_{w\ell}\left(f_t T_1^n-T_\ell^{n+1}\right)+h_{wv}\left(f_t T_1^n-T_v^{n+1}\right)\right] \qquad (8\text{-}109)$$

The parameters f_t and f_{ss} are 0 and 1, respectively, to provide maximum stability.

The resulting linear equations are solved in a sequential fashion for each of the cells in the component. For each cell a solution is achieved using Gaussian elimination.

If the user specifies one radial conduction node for the wall, the wall temperature is calculated using a lumped parameter solution:

$$T^{n+1}=\left\{\frac{1}{2}\left(2\Delta r+\frac{\Delta r^2}{r_i}\right)\left(\frac{\rho c_p}{\Delta t}T^n+q'''\right)+h_{w\ell_i}\left(T_{\ell_i}^{n+1}-f_t T^n\right)\right.$$

$$\left.+h_{wv_i}\left(T_{v_i}^{n+1}-f_t T^n\right)-\left(1+\frac{\Delta r}{r_i}\right)\left[h_{w\ell_o}\left(f_t T^n-T_{\ell_o}^{n+1}\right)+h_{wv_o}\left(f_t T^n-T_{v_o}^{n+1}\right)\right]\right\}$$

$$\cdot\left\{\frac{1}{2}\left(2\Delta r+\frac{\Delta r^2}{r_i}\right)\left(\frac{\rho c_p}{\Delta t}\right)+f_{ss}\left[h_{w\ell_i}+h_{wv_i}+\left(1+\frac{\Delta r}{r_i}\right)\left(h_{w\ell_o}+h_{wv_o}\right)\right]\right\}^{-1} \qquad (8\text{-}110)$$

The subscripts i and o refer to the inner and outer radii, respectively.

Slab and Rod Heat Conduction

The heat transfer modeling in an HTSTR-component is in either cylindrical or Cartesian 2D geometry. There are four numerical calculation options for computing temperature distribution in slabs and rods. For thin slabs or rods of small diameter where the radial temperature profile is flat and axial conduction is negligible, the user may choose the "lumped parameter" solution. This option gives the best calculational efficiency and should be used whenever it can be justified.

The second option is a 1D solution with implicit differencing in the radial direction and no conduction in the axial direction. This option is appropriate when steep axial temperature profiles do not exist.

The third option is a 2D solution with implicit differencing in the radial direction and explicit differencing in the axial direction. This allows the very small radial node spacing without severely limiting the time step. The explicit differencing in the axial direction does limit the maximum timestep size for axial spacing. In many cases, however, this maximum timestep size is much greater than that used for the fluid-dynamics calculation and is not restrictive. For those cases, the semi-implicit calculation gives good computational efficiency.

The fourth option is the fully implicit, 2D finite-difference calculation. This is the best choice for cases where the axial temperature gradient is very large. Then the very fine axial noding that is required would cause the time step to be severely limited if the semi-implicit calculation was used. These methods are discussed in the following sections.

Lumped Parameter Calculation

The lumped-parameter equation for cylindrical coordinates is Equation 8-110. If we choose $f_t = 0$ and $f_{ss} = 1$ for maximum stability, the equation reduces to:

$$T^{n+1} = \left\{\frac{1}{2}\left(2\Delta r + \frac{\Delta r^2}{r_i}\right)\left(\frac{\rho c_\rho}{\Delta t}T^n + q'''\right) + h_{w\ell_i}T_{\ell_i}^{n+1} + h_{wv_i}T_{v_i}^{n+1} + \left(1 + \frac{\Delta r}{r_i}\right)\left[h_{w\ell_o}T_{\ell_o}^{n+1} + h_{wv_o}T_{v_o}^{n+1}\right]\right\}$$

$$\left\{\frac{1}{2}\left(2\Delta r + \frac{\Delta r^2}{r_i}\right)\left(\frac{\rho c_\rho}{\Delta t}\right) + \left[h_{w\ell_i} + h_{wv_i} + \left(1 + \frac{\Delta r}{r_i}\right)\left(h_{w\ell_o} + h_{wv_o}\right)\right]\right\}^{-1} \quad (8\text{-}111)$$

For a solid rod, the axial temperatures are:

$$T^{n+1} = \left\{\frac{\Delta r}{2}\left[\frac{\rho c_\rho}{\Delta t}T^n + q'''\right] + h_{w\ell_o}T_{\ell_o}^{n+1} + h_{wv_o}T_{v_o}^{n+1}\right\}\left\{\frac{\Delta r \rho c_p}{2\Delta t} + h_{w\ell_o} + h_{wv_o}\right\}^{-1} \quad (8\text{-}112)$$

The lumped-parameter equation for the temperature of a slab is:

$$T^{n+1} = \left(\frac{\rho c_\rho \Delta x}{\Delta t}T^n + q'''\Delta x + h_{w\ell_o}T_{w\ell_o}^{n+1} + h_{wv_o}T_{v_o}^{n+1} + h_{w\ell_i}T_{\ell_i}^{n+1} + h_{wv_i}T_{v_i}^{n+1}\right)$$

$$\left(\frac{\rho c_p \Delta x}{\Delta t} + h_{w\ell_o} + h_{wv_o} + h_{w\ell_i} + h_{wv_i}\right)^{-1} \tag{8-113}$$

where Δx is the slab thickness.

Semi-implicit Calculation

Finite-difference equations are obtained by applying an integral method (Roache, 1972) to appropriate differential volumes. The noding within a structure (Figure 8-35) is staggered with respect to the nodes used in the fluid-dynamics calculations. The staggered mesh gives the advantage of providing axial numerical smoothing.

Consider a general differential volume shown in Figure 8-35. Using explicit differencing in the axial direction and implicit differencing in the radial direction, the finite-difference equation for this volume is:

$$\left\{(\rho c_p)_{ij}\frac{T_{ij}^{n+1} - T_{ij}^{n}}{\Delta t} - q_{ij}'''\right\}\frac{1}{2}\left[\left(r_i\Delta r_i + \frac{\Delta r_i^2}{4}\right) + \left(r_i\Delta r_{i-1} - \frac{\Delta r_{i-1}^2}{4}\right)\right]\left[\frac{\Delta z_j + \Delta z_{j-1}}{2}\right]$$

$$= \left\{r_{i+1/2}k_{i+1/2,j}\left(\frac{T_{i+1,j}^{n+1} - T_{ij}^{n+1}}{\Delta r_i}\right) + r_{i-1/2}k_{i-1/2,j}\left(\frac{T_{i-1,j}^{n+1} - T_{ij}^{n+1}}{\Delta r_{i-1}}\right)\right\}$$

$$\times\left[\frac{\Delta z_j + \Delta z_{j-1}}{2}\right] + \left\{k_{i,j+1/2}\left(\frac{T_{i,j+1}^{n} - T_{ij}^{n}}{\Delta z_j}\right) + k_{i,j-1/2}\left(\frac{T_{i,j-1}^{n} - T_{ij}^{n}}{\Delta z_{j-1}}\right)\right\}$$

$$\times\frac{1}{2}\left[\left(r_i\Delta r_i + \frac{\Delta r_i^2}{4}\right) + \left(r_i\Delta r_{i-1} - \frac{\Delta r_{i-1}^2}{4}\right)\right] \tag{8-114}$$

where $f_{ij}^{n} = f\left(t^{n}, r_i, z_j\right)$

The boundary conditions applied to the cylindrical structures are:

- The top ($z = z_u$) and bottom ($z = z_b$) of the rods are assumed to be insulated,

$$k\frac{\partial T}{\partial z}\bigg|_{z=z_b,z_u} = 0$$

- The outer/inner surface of the cylindrical structure are coupled to the fluid hydraulic conditions using Newton's law:

$$k\frac{\partial T}{\partial r}\bigg|_{r=r_0} = -h_{w\ell_o}\left(T_{w\ell_0} - T_{\ell_0}\right) - h_{wv_o}\left(T_{wv_0} - T_{v_0}\right)$$

$$k\frac{\partial T}{\partial r}\bigg|_{r=r_i} = -h_{w\ell_i}\left(T_{w\ell_i} - T_{\ell_i}\right) - h_{wv_i}\left(T_{wv_i} - T_{v_i}\right)$$

- If the structure is a solid rod, the rod centerline (r = 0) is a line of symmetry,

$$\frac{\partial T}{\partial r}\bigg|_{r=0} = 0$$

All properties (that is, ρ, c_p, and k) required by the difference equations are stored at the node locations. Linear interpolation is used to obtain properties between nodes (that is, at cell surfaces). A node located at the interface between two dissimilar materials requires two sets of properties. Consider the differential volume provided in Figure 8-36. Application of an integral technique to this volume results in the equation (after dividing through by the volume),

$$\overline{(\rho c_\rho)}_{ij}\left(\frac{T_{ij}^{n+1} - T_{ij}^{n}}{\Delta t}\right) - q_{ij}''' = \left\{r_{i+1/2}k_{i+1/2,j}\left(\frac{T_{i+1,j}^{n+1} - T_{ij}^{n+1}}{\Delta r_i}\right) + r_{i-1/2}k_{i-1/2,j}\right.$$

$$\left.\times\left(\frac{T_{i-1,j}^{n+1} - T_{ij}^{n+1}}{\Delta r_{i-1}}\right)\right\}\times\left[\frac{\left(r_i\Delta r_i + \frac{\Delta r_i^2}{4}\right) + \left(r_i\Delta r_{i-1} + \frac{\Delta r_{i-1}^2}{4}\right)}{2}\right]^{-1}$$

$$+\left\{\bar{k}_{i,j+1/2}\left(\frac{T_{i,j+1}^{n} - T_{ij}^{n}}{\Delta z_j}\right) + \bar{k}_{i,j-1/2}\left(\frac{T_{i,j+1}^{n} - T_{ij}^{n}}{\Delta z_{j-1}}\right)\right\}\left[\frac{\Delta z_j + \Delta z_{j-1}}{2}\right]^{-1} \qquad (8\text{-}115)$$

where:

$$\overline{(\rho c_\rho)}_{ij} \equiv \frac{\left[(\rho c_\rho)_{i^+,j}^{R^+}(\rho c_\rho)_{i^-,j}^{R^-}\right]}{R^+ + R^-}$$

and

$$\bar{k}_{i,j+1/2} = \frac{\left[k_{i^+,j+1/2}R^+ + k_{i^-,j+1/2}R^-\right]}{\left[R^+ + R^-\right]}$$

In the above equations,

$$R^{+} \equiv \left(r_i + \frac{\Delta r_i}{4} \right) \frac{\Delta r_i}{2} \tag{8-116}$$

and

$$R^{-} \equiv \left(r_i - \frac{\Delta r_{i-1}}{4} \right) \frac{\Delta r_{i-1}}{2} \tag{8-117}$$

The superscripts + and – refer to the material to the right and left of the interface.

The semi-implicit finite-difference formulation for the slab is identical to that of the rod except for the obvious geometric differences.

Fully Implicit Calculation

With the cell noding shown in Figure 8-35, the fully implicit finite-difference equation for 2D heat conduction is:

$$\begin{aligned}
&(\rho c_\rho)_{i,j} \left(\frac{T_{i,j}^{n+1} - T_{i,j}^{n}}{\Delta t} \right) V_{i,j} \\
&= q_{ij}''' V_{i,j} + k_{i+1/2,j} \left(\frac{T_{i+1,j}^{n+1} - T_{i,j}^{n+1}}{\Delta r_i} \right) A_{i+1/2} \\
&+ k_{i-1/2,j} \left(\frac{T_{i-1,j}^{n+1} - T_{i,j}^{n+1}}{\Delta r_{i-1}} \right) A_{i-1/2} \\
&+ k_{i,j+1/2} \left(\frac{T_{i,j+1}^{n+1} - T_{i,j}^{n+1}}{\Delta z_j} \right) A_i^{*} \\
&+ k_{i,j-1/2} \left(\frac{T_{i,j-1}^{n+1} - T_{i,j}^{n+1}}{\Delta z_{j-1}} \right) A_i^{*}
\end{aligned} \tag{8-118}$$

where V = cell volume, A = area in radial direction, A* = area in axial direction, and Δr = cell length in radial or x direction.

Note that this equation applies to both the slab and rod geometries, providing the areas and volumes of the cells are calculated correctly. Equation 8-118 can be written as:

$$a_{1,i,j} T_{i-1,j}^{n+1} + a_{2,i,j} T_{i,j}^{n+1} + a_{3,i,j} T_{i+1,j}^{n+1} + a_{4,i,j} T_{i,j-1}^{n+1} + a_{5,i,j} T_{i,j+1}^{n+1} = b_{i,j} \tag{8-119}$$

where:

$$a_{1,i,j} = -k_{i-1/2,j} A_{i-1/2} / \Delta r_{i-1}$$

$$\begin{aligned} a_{2,i,j} = (\rho c_\rho)_{i,j} V_{i,j} / \Delta t \\ + k_{i+1/2,j} A_{i+1/2} / \Delta r_i + k_{i-1/2,j} A_{i-1/2} / \Delta r_{i-1} \\ + k_{i,j+1/2,j} A_i^* / \Delta z_j + k_{i,j-1/2,j} A_i^* / \Delta z_{j-1} \end{aligned}$$

$$a_{3,i,j} = -k_{i+1/2,j} A_{i+1/2} / \Delta r_i$$

$$a_{4,i,j} = -k_{i,j-1/2} A_i^* / \Delta z_{j-i}$$

$$a_{5,i,j} = -k_{i,j+1/2} A_i^* / \Delta z_j$$

and

$$b_{i,j} = \left\{ q'''_{i,j} + (\rho c_\rho)_{i,j} T^n_{i,j} / \Delta t \right\} V_{i,j} \tag{8-120}$$

Equation 8-119 is rewritten in matrix notation as:

$$\underline{\underline{A}} \cdot \underline{T} = \underline{B} \tag{8-121}$$

or

$$\begin{pmatrix} \underline{\underline{D}}(1) & \underline{\underline{E}}(1) & & & & \\ \underline{\underline{C}}(2) & \underline{\underline{D}}(2) & \underline{\underline{E}}(2) & & & 0 \\ & \underline{\underline{C}}(3) & \underline{\underline{D}}(3) & \underline{\underline{E}}(3) & & \\ & 0 & & & & \\ 0 & & & & & \\ & & \underline{\underline{C}}(NZ-1) & \underline{\underline{D}}(NZ-1) & \underline{\underline{E}}(NZ-1) & \\ & & & \underline{\underline{C}}(NZ) & \underline{\underline{D}}(NZ) & \end{pmatrix} \begin{pmatrix} \underline{T}(1) \\ \underline{T}(2) \\ \underline{T}(3) \\ M \\ M \\ \underline{T}(NZ-1) \\ \underline{T}(NZ) \end{pmatrix} = \begin{pmatrix} \underline{B}(1) \\ \underline{B}(2) \\ \underline{B}(3) \\ M \\ M \\ \underline{B}(NZ-1) \\ \underline{B}(NZ) \end{pmatrix} \tag{8-122}$$

where:

$$\underline{T}^{(j)} = \begin{pmatrix} T_{1,j} \\ T_{2,j} \\ M \\ T_{NR,j} \end{pmatrix} (j = 1, NZ), \qquad \underline{B}^{(j)} = \begin{pmatrix} b_{1,j} \\ b_{2,j} \\ M \\ b_{NR,j} \end{pmatrix} (j = 1, NZ) \tag{8-123}$$

$$\underline{\underline{C}}^{(j)} = \begin{pmatrix} a_{4,1,j} & & & 0 \\ & a_{4,2,j} & & \\ & & 0 & \\ 0 & & & a_{4,NR,j} \end{pmatrix} (j = 2, NZ) \tag{8-124}$$

$$\underline{\underline{D}}^{(j)} = \begin{pmatrix} a_{2,1,j} & a_{3,1,j} & & \\ a_{1,2,j} & a_{2,2,j} & a_{3,2,j} & 0 \\ & a_{1,3,j} & a_{2,3,j} & a_{3,3,j} \\ & & 0 & \\ & 0 & & a_{1,NR,j} \quad a_{1,NR,j} \end{pmatrix} (j = 1, NZ) \tag{8-125}$$

and

$$\underline{\underline{E}}^{(j)} = \begin{pmatrix} a_{5,1,j} & & & 0 \\ & a_{5,2,j} & & \\ & & 0 & \\ 0 & & & a_{5,NR,j} \end{pmatrix} (j = 1, NZ-1) \tag{8-126}$$

Matrix $\underline{\underline{A}}$ is a symmetrical banded matrix. To solve for the temperatures, matrix $\underline{\underline{A}}$ is inverted by a modified Cholesky method. Then the temperatures are computed from:

$$\underline{T} = \underline{\underline{A}}^{-1} \underline{B} \tag{8-127}$$

8.9 SCALING CONSIDERATIONS

The vessel component rod and unheated conductor models, and the one-dimensional component conductor model, are used in analyses of nuclear reactors and simulations of experiments in which heat transfer between structures and the fluid are important. The models are applied in a systematic manner in nuclear reactor analyses and simulations of experiments, as summarized below:

- For nuclear reactor analyses and simulations of experiments which use nuclear fuel rods (e.g., LOFT), the fuel rods are modeled using the NUCL rod option, and the dynamic gap conductance and fuel rod deformation models are employed. If high cladding temperatures are expected, the metal-water reaction model is also employed.

- For all simulations of experiments which include heat transfer, and in which quench front modeling is important (e.g., FLECHT, ORNL, CCTF, and FEBA), similar hydraulic node sizes are used as in the PWR analysis, as well as the fine mesh rezoning model.

- The unheated conductor model and one-dimensional component conductor model are also applied in a consistent manner, for analyses of nuclear reactors and simulations of experiments.

The simulations of the experiments cited above are used to assess the WCOBRA/TRAC-TF2 models and the code uncertainty. Because of the consistent application of the models described in Section 8 in these simulations and in nuclear reactor analyses, and the use of full-length nuclear fuel rods and electrically heated rods in several of these experiments, there are no scaling uncertainties associated with the use of these models in analyses of nuclear reactors.

8.10 CONCLUSIONS

The WCOBRA/TRAC-TF2 models for heated and unheated structures provide an appropriate means for calculating the transient temperature response of the structures found in nuclear reactors and the experiments of interest. These models are applied in a consistent manner in analyses of nuclear reactors and simulations of experiments. No scaling uncertainty is required for the use of these models in nuclear reactor analyses.

[

]^{a,c}

8.11 REFERENCES

1. Bajorek, S. M., et al., 1998, "Code Qualification Document for Best Estimate LOCA Analysis," WCAP-12945-P-A, Volume 1, Revision 2, and Volumes 2 through 5, Revision 1, and WCAP-14747 (Non-Proprietary).

2. Berna, G. A., et al., 1978, "FRAPCON-1: A Computer Code for the Steady-State Analysis of Oxide Fuel Rods," CDAP-TR-032-R1, Idaho National Engineering Laboratory, Idaho Falls, Idaho.

3. Beyer, C. E., et al., 1975, "GAPCON-THERMAL-2: A Computer Program for Calculating the Thermal Behavior of an Oxide Fuel Rod," BNWL-1898, Pacific Northwest Laboratory, Richland, Washington.

4. Beyer, W. H., 1978, CRC Standard Mathematical Tables, 25th Edition, CRC Press, Inc., West Palm Beach, Fla., pp. 326-327.

5. Boegli, J. S. and Deissler, R. G., 1955, "Measured Effective Thermal Conductivity of Uranium Oxide Powder in Various Gases and Gas Mixtures," NACA RM-E54L10.

6. Bordelon, F. M., et al., 1974, "LOCTA-IV Program: Loss-of-Coolant Transient Analysis," WCAP-8301 and WCAP-8305 (Non-Proprietary), Westinghouse Electric Corporation, Pittsburgh, PA.

7. Broughton, J. M., et al., 1981, "PBF LOCA Test Series, Test LOC-3 and LOC-5 Fuel Behavior Report," NUREG/CR-2073.

8. Broughton, J. M., et al., 1983, "PBF LOCA Test LOC-6 Fuel Behavior Report," NUREG/CR-3184, EGG-2244.

9. Cathcart, J. V., Pawell, R. E., et al., 1977, "Zirconium Metal-Water Oxidation Kinetics IV - Reaction Rate Studies," ORNL/NUREG-17, Oak Ridge National Laboratory, Oak Ridge, TN.

10. Chapman, R. H., 1979, "Multirod Burst Test Program Progress Report for April-June, 1979," NUREG/CR-1023, Oak Ridge National Laboratory, Oak Ridge, TN.

11. Cooper, M. G., Mikic, B. B. and Yavonovich, M. M., 1969, "Thermal Contact Conductance," *Journal of Heat and Mass Transfer*, Vol. 12.

12. Davidson, S. L. and Nuhfer, D. L., 1990, "VANTAGE + Fuel Assembly Reference Core Report," WCAP-12610, Westinghouse Electric Corporation, Pittsburgh, PA.

13. Dearien, J. A., et al., 1977, "FRAP-S3: A Computer Code for the Steady-State Analysis of Oxide Fuel Rods – Report I, Analytical Models and Input Manual," TFBP-TR-164, Idaho National Engineering Laboratory, Idaho Falls, Idaho.

14. Deissler, R. G. and Boegli, J. S., 1958, "An Investigation of Effective Thermal Conductivities of Powders in Various Gases," *TRANS ASME*, pg. 1417.

15. Donaldson, A. T., Horwood, R. A. and Healey, T., 1982, "Biaxial Creep Deformation of Zircaloy-4 in the High Alpha Phase Temperature Range," TPRD/B/0100/N82, Central Electricity Generating Board – Berkeley Nuclear Laboratories, Berkeley, Gloucestershire, United Kingdom.

16. Donaldson, A. T., Healey, T. and Horwood, R. A., 1985, "Biaxial Creep Deformation of Zircaloy-4 PWR Fuel Cladding in the Alpha, (Alpha + Beta) and Beta Phase Temperature Ranges," *Journal of the British Nuclear Energy Society*, pp. 83-89.

17. Donaldson, A. T. and Barnes, J. P., 1989, "Creep Behavior of ZIRLO Clad at Temperatures in the Alpha Phase Range, 873-973K, and in the Beta Phase Range, 1273-1373K," RD/B/6245/R89, Central Electricity Generating Board – Berkeley Nuclear Laboratories, Berkeley, Gloucestershire, United Kingdom.

18. Donaldson, A. T., Barnes, J. P. and Hall, P. D., 1989, "Creep Behavior of ZIRLO Clad at Temperatures in the Duplex Phase Range, 1048-1183K," RD/B/6304/R89, Central Electricity Generating Board – Berkeley Nuclear Laboratories, Berkeley, Gloucestershire, United Kingdom.

19. Erbacher, F. J., et al., 1982, "Burst Criterion of Zircaloy Fuel Claddings in a Loss-of-Coolant Accident," *Zirconium in the Nuclear Industry; Fifth Conference*, AS™ STP 754, pp. 271-283.

20. Garnier, J. E. and Begej, S., 1979, "Ex-Reactor Determination of Thermal Gap and Contact Conductance Between Uranium Dioxide: Zircaloy-4 Interfaces. Stage 1: Low Gas Pressure," NUREG/CR-0330, Pacific Northwest Laboratory, Richland, Washington.

21. Hagrman, D. L. and Reymann, G. A., 1979, "MATPRO-Version 11: A Handbook of Material Properties for Use in the Analysis of Light Water Reactor Fuel Rod Behavior," NUREG/CR-0497, Idaho National Engineering Laboratory, Idaho Falls, Idaho.

22. Hagrman, D. L., Reymann, G. A. and Manson, R. E., 1980, "MATPRO-Version 11: A Handbook of Materials Properties for Use in the Analysis of Light Water Reactor Fuel Rod Behavior," NUREG/CR-0497, Revision 1, Idaho National Engineering Laboratory, Idaho Falls, Idaho.

23. Hann, C. R., Beyer, C. E. and Parchen, L. J., 1973, "GAPCON-THERMAL-1: A Computer Program for Calculating the Gap Conductance in Oxide Fuel Pins," BNWL-1778, Pacific Northwest Laboratory, Richland, Washington.

24. Kelly, J. M., 1979, "Quench Front Modeling and Reflood Heat Transfer in COBRA-TF," Paper 79-WA/HT-63, ASME Winter Annual Meeting, New York, New York.

25. Krupiczka, R., 1967, "Analysis of Thermal Conductivity in Granular Materials," *International Chemical Engineering*, Vol. 7, No. 1, pp. 122-144.

26. Lanning, D. D. and Hann, C. R., 1975, "Review of Methods Applicable to the Calculation of Gap Conductance in Zircaloy-Clad UO2 Fuel Rods," BNWL-1894, Pacific Northwest Laboratory, Richland, Washington.

27. Lanning, D. D., et al., 1978, "GAPCON-THERMAL-3 Code Description," PNL-2434, Pacific Northwest Laboratory, Richland, Washington.

28. Lloyd, W. R., et al., 1973, "Heat Transfer in Multicomponent Monatomic Gases in the Low, Intermediate, and High Pressure Regime," paper presented at the Nuclear Thermionics Conference.

29. Munson, B. R., Young, D. F. and Okiishi, T. H., 1994, Fundamentals of Fluid Mechanics, 2nd ed., John Wiley & Sons, Inc.

30. Paik, C. Y. and Hochreiter, L. E., 1986, "Analysis of FLECHT SEASET 163-Rod Blocked Bundle Data Using COBRA-TF," NUREG/CR-4166.

31. Powers, D. A., and Meyer, R. O., 1980, "Cladding Swelling and Rupture Models for LOCA Analysis," NUREG-0630, U.S. Nuclear Regulatory Commission, Washington, D.C.

32. Roache, P. J., 1972, Computational Fluid Dynamics, Hermosa Publishers, Albuquerque, NM.

33. Siefken, L. J., et al., 1979, "FRAP-T5: A Computer Code for Transient Analysis of Oxide Fuel Rods," NUREG/CR-0840, Idaho National Engineering Laboratory, Idaho Falls, Idaho.

34. Stewart, C. W., et al., 1982, "VIPRE-01 A Thermal-Hydraulics Analysis Code for Reactor Cores: Volume 1, Mathematical Modelling," NP-2511, Electric Power Research Institute, Palo Alto, California.

35. Thomas, L. B., 1967, Fundamentals of Gas-Surface Interactions, H. Saltsburg et al., Eds., Academic Press, New York, pp. 346-369.

36. Todreas, N. and Jacobs, G., 1973, "Thermal Contact Conductance of Reactor Fuel Elements," *Nuclear Science and Engineering*, Vol. 50, pg. 283.

37. Trent, D. S. and Welty, J. R., 1974, "A Summary of Numerical Methods for Solving Transient Heat Conduction Problems," Bulletin No. 49, Engineering Experimental Station, Oregon State University, Corvallis, Oregon.

38. Ullman, A., Acharya, R. and Olander, D. R., 1974, "Thermal Accommodation Coefficients of Inert Gases on Stainless Steel and UO_2," *Journal of Nuclear Materials*, Vol. 51, pp. 277-279.

39. USNRC, 1988, Compendium of ECCS Research for Realistic LOCA Analysis, NUREG-1230 R4.

Table 8-1 Cladding Thermal Expansion Correlations		
T < 1073 K (Following Formulas are Used)		
$\varepsilon_r = 6.721 \times 10^{-6} T - 0.00207$ $\varepsilon_z = 4.441 \times 10^{-6} T - 0.00124$		
1073 ≤ T ≤ 1273 K (Linear Interpolation from the Following Table is Used.)		
T	**ε_r**	**ε_z**
1073	0.00514	0.00353
1083	0.00522	0.00353
1093	0.00525	0.00350
1103	0.00528	0.00346
1113	0.00528	0.00341
1123	0.00524	0.00333
1133	0.00522	0.00321
1143	0.00515	0.00307
1153	0.00508	0.00280
1163	0.00490	0.00250
1173	0.00470	0.00200
1183	0.00445	0.00150
1193	0.00410	0.00130
1203	0.00350	0.00116
1213	0.00313	0.00113
1223	0.00297	0.00110
1233	0.00292	0.00111
1243	0.00287	0.00113
1253	0.00286	0.00120
1263	0.00288	0.00130
1273	0.00290	0.00140
T > 1273 K (Following Formulas are Used)		
$\varepsilon_r = 9.70 \times 10\text{-}6\ T - 0.00945$ $\varepsilon_z = 9.70 \times 10\text{-}6\ T - 0.0110$		

Table 8-2 Cladding Correlations for Modulus of Elasticity (E) and Shear Modulus (G)
T < 1094 K $E = 1.088 \times 10^{11} - 5.475 \times 10^{7} T$ $G = 4.04 \times 10^{10} - 2.168 \times 10^{7} T$
1094 < T < 1239 K $E = 4.893 \times 10^{10} - 4.817 \times 10^{7} (T-1094)$ $G = 1.669 \times 10^{10} - 1.622 \times 10^{7} (T-1094)$
T > 1239 K $E = 9.21 \times 10^{10} - 4.05 \times 10^{7} T$ $G = 3.49 \times 10^{10} - 1.66 \times 10^{7} T$

Table 8-3 [ ]^{a,c}

a,c

Table 8-4 [ ]a,c

a,c

Table 8-5 [		]a,c

a,c

[

Table 8-6 [ ]^{a,c}

]

a,c

a,c

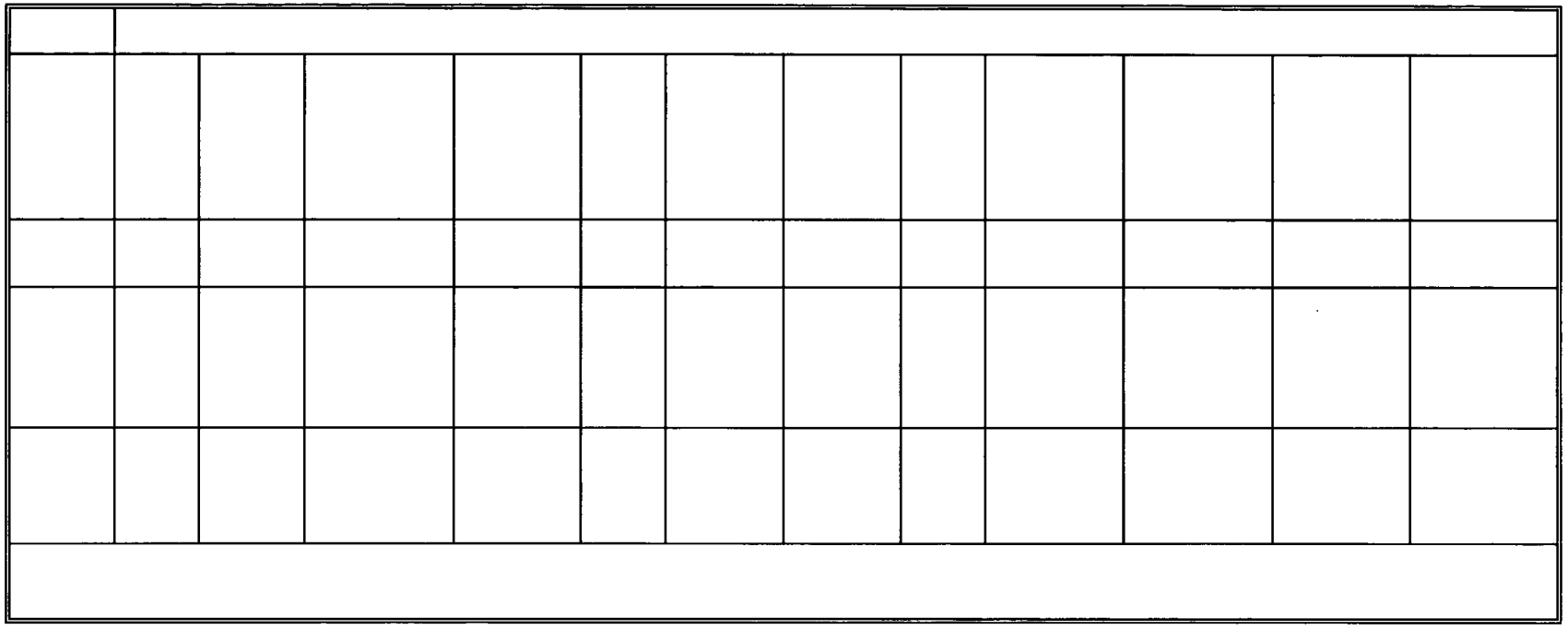

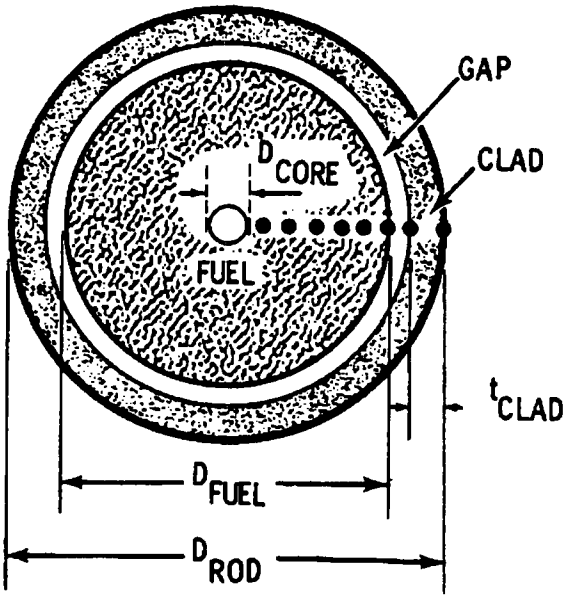

Figure 8-1 Nuclear Fuel Rod Geometry

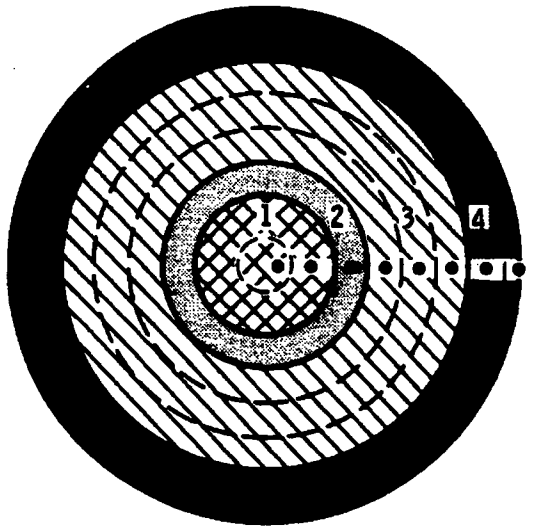

Figure 8-2 Heater Rod Geometry

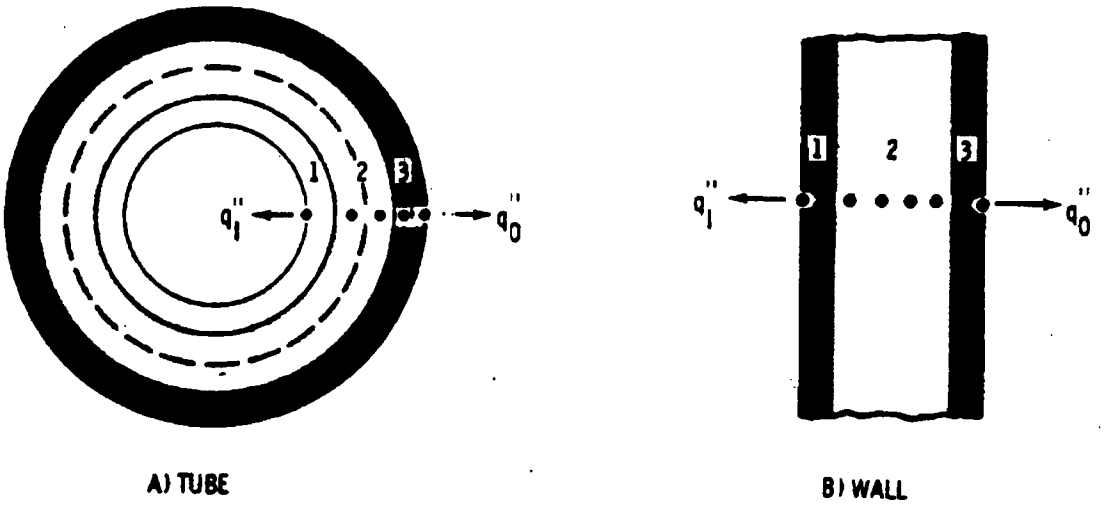

Figure 8-3 Tube and Wall Conductor Geometries

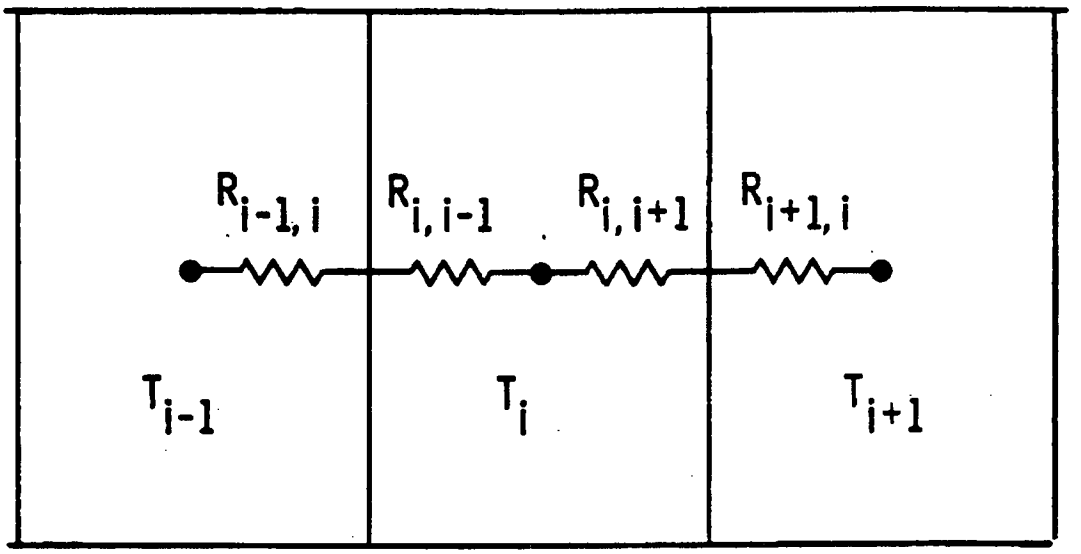

Figure 8-4 Control Volume for Heat Balance

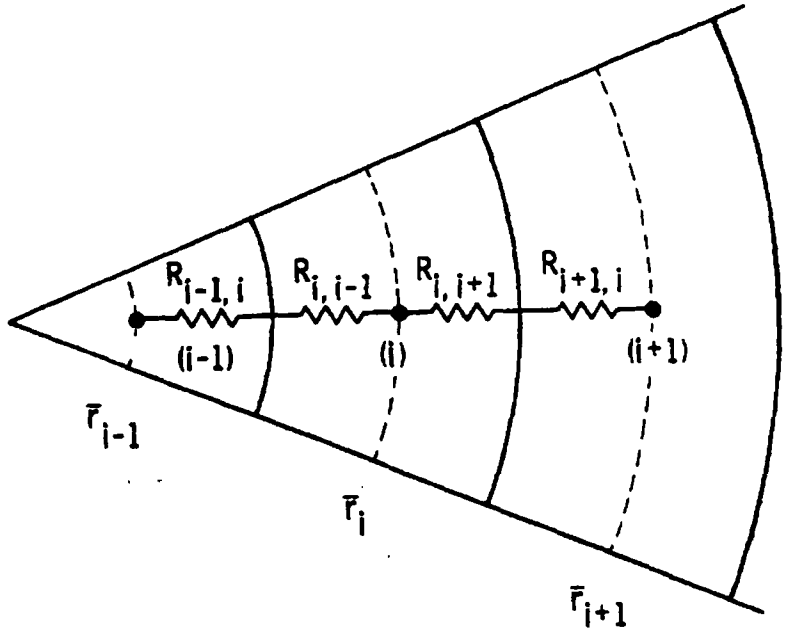

Figure 8-5 Noding for Fuel Rod Conduction Model

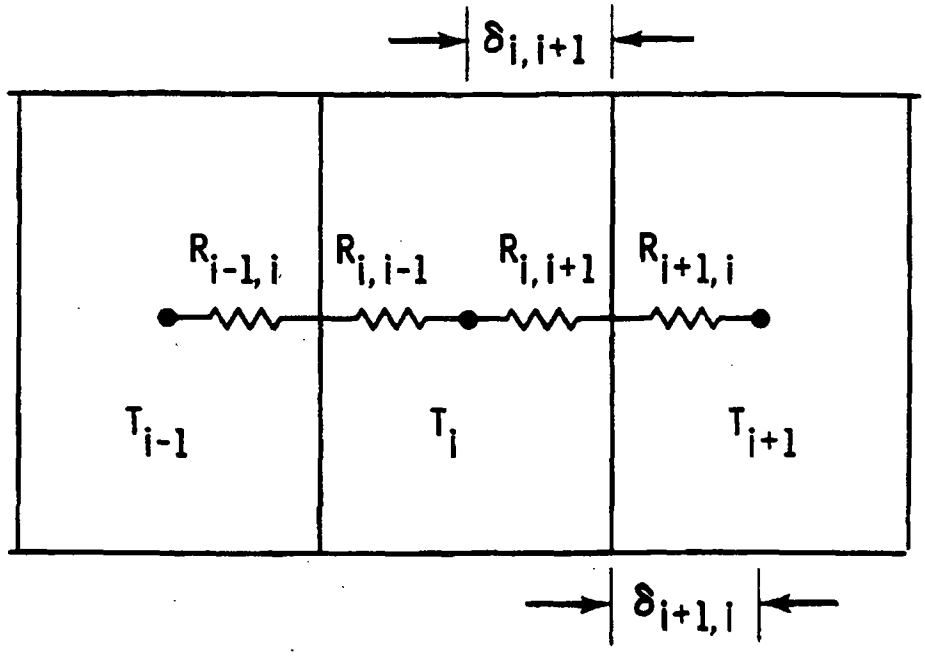

Figure 8-6 Conductance Between Nodes

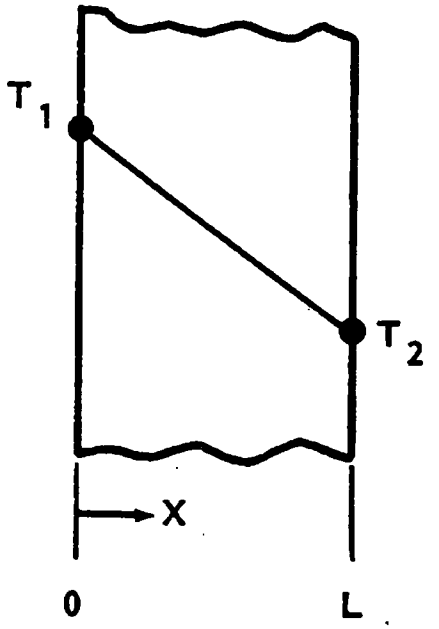

Figure 8-7 Steady-State Temperature Distribution in a Flat Plate with No Internal Heat Generation

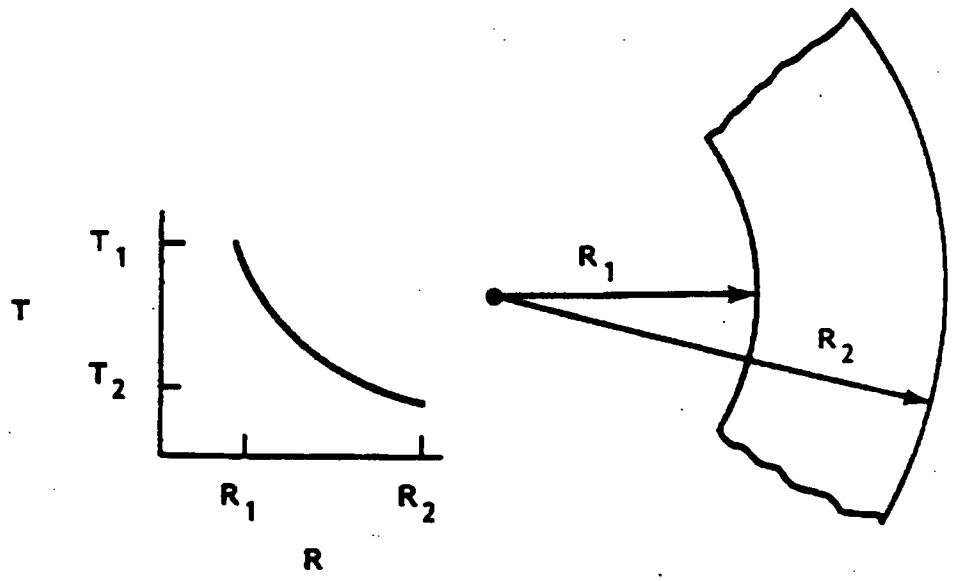

Figure 8-8 Steady-State Temperature Distribution in a Hollow Cylinder with No Internal Heat Generation

a,c

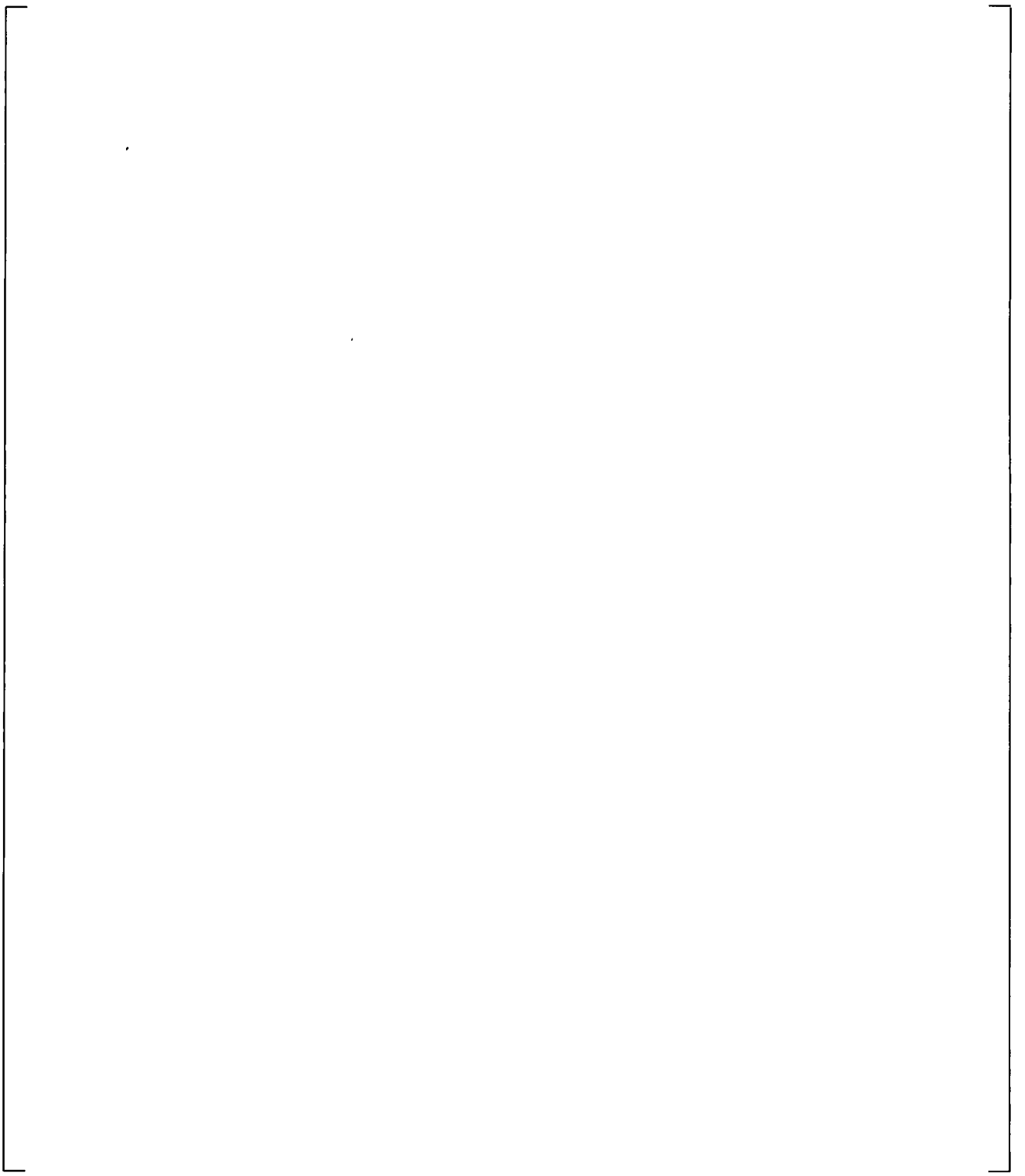

Figure 8-9 Typical Heat Transfer Noding Scheme

A) Within a Continuity Cell

B) At Continuity Cell Boundary

Figure 8-10 Examples of Heat Transfer Node Insertion

a,c

Figure 8-11 Cladding Temperature Profile with Fine Mesh Renoding

a,c

Figure 8-12 Surface Heat Flux Profile with Fine Mesh Renoding

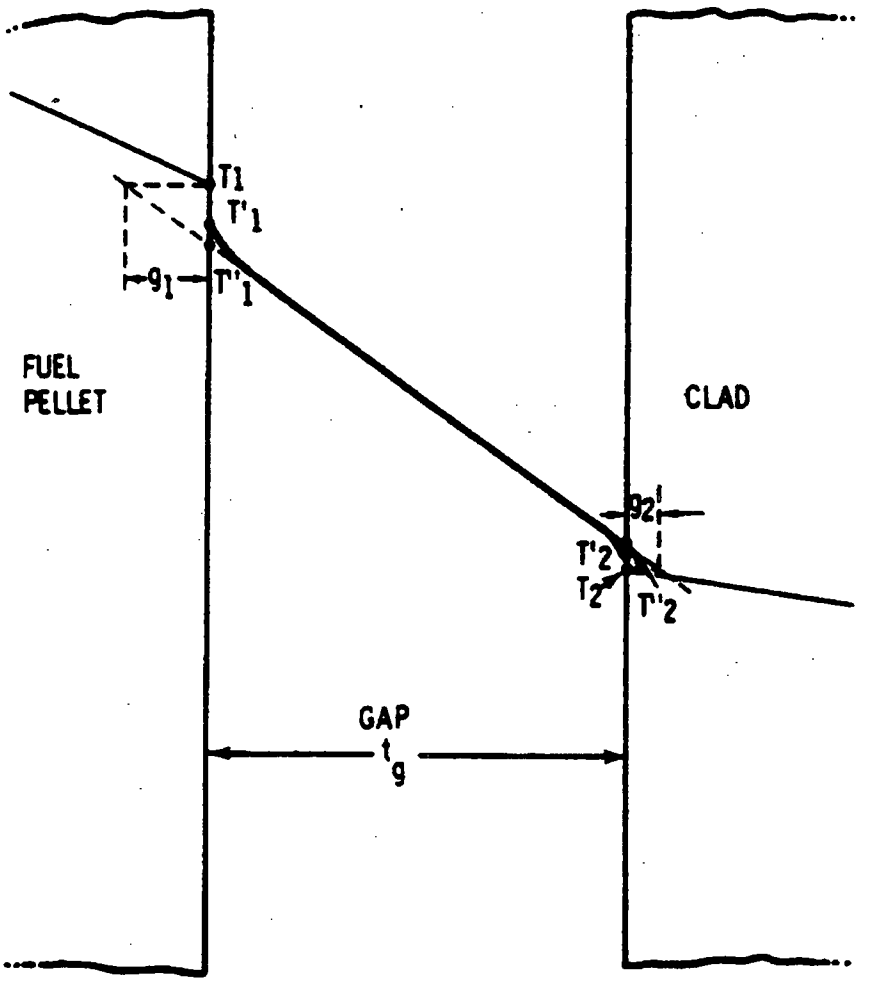

Figure 8-13 Temperature Jump Distances for an Ideal Gap

a,c

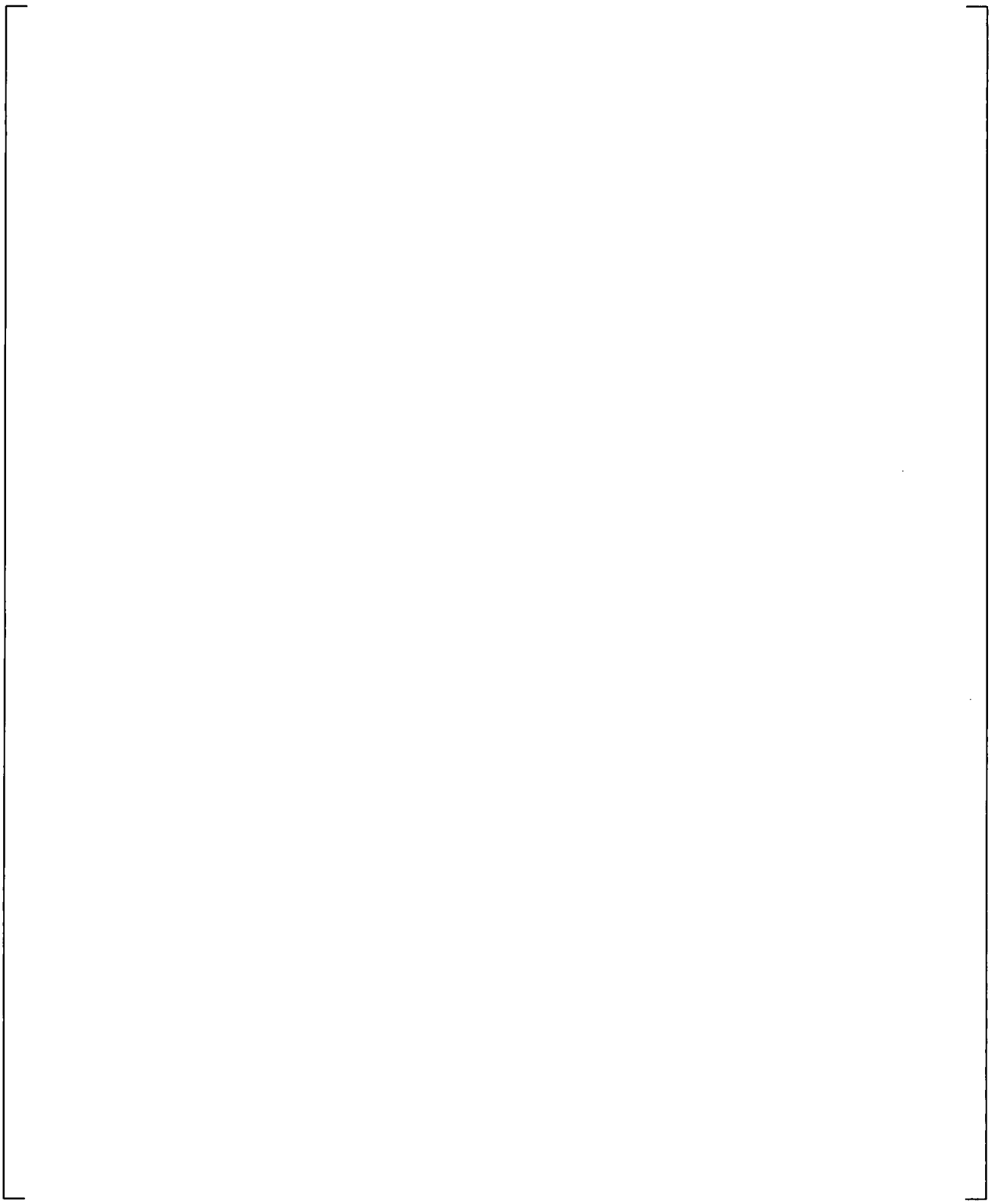

Figure 8-14 Instantaneous Creep Rates for Westinghouse Zircaloy-4 Cladding

a,c

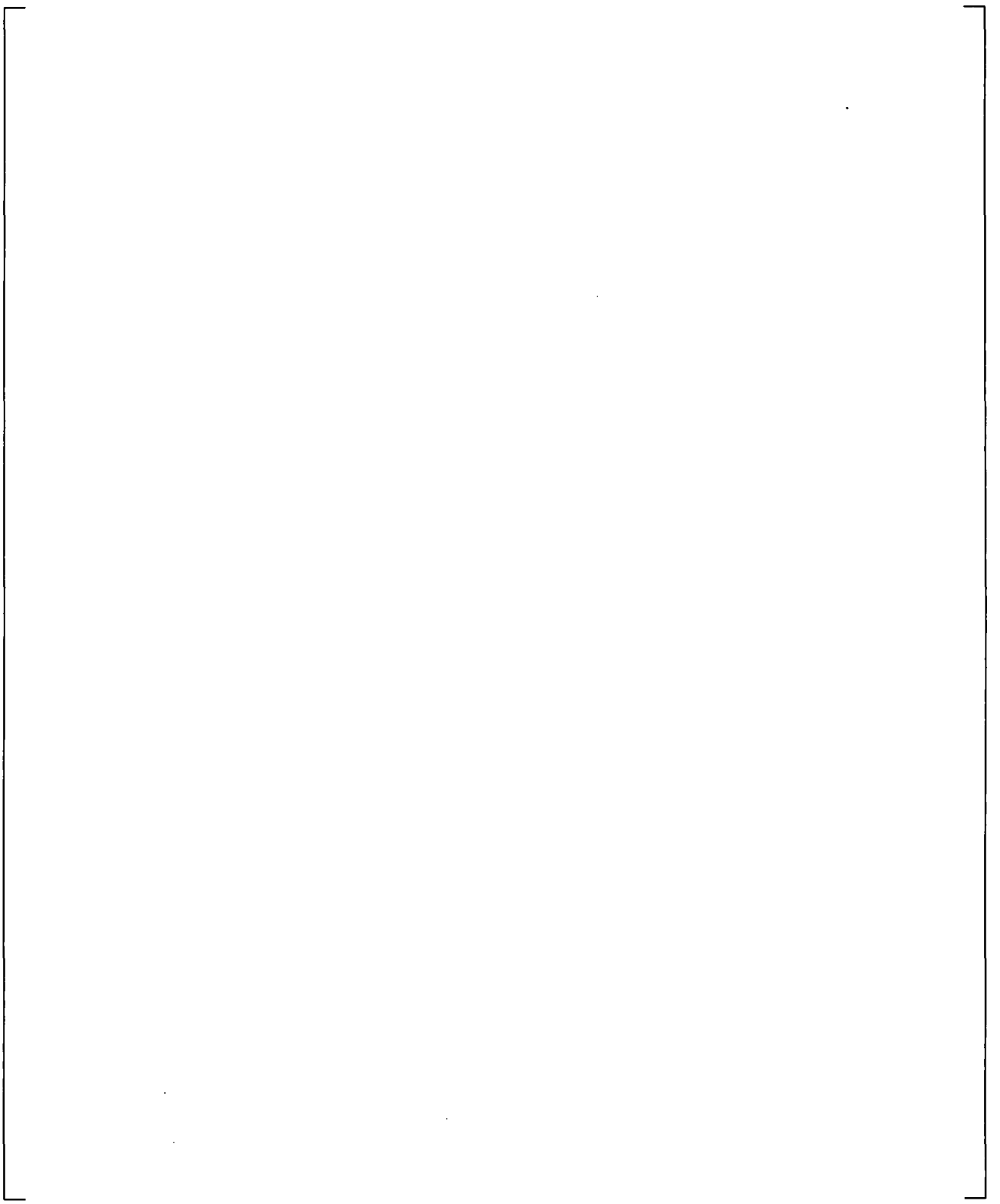

Figure 8-15 Instantaneous Creep Rates for Westinghouse ZIRLO® Cladding

a,c

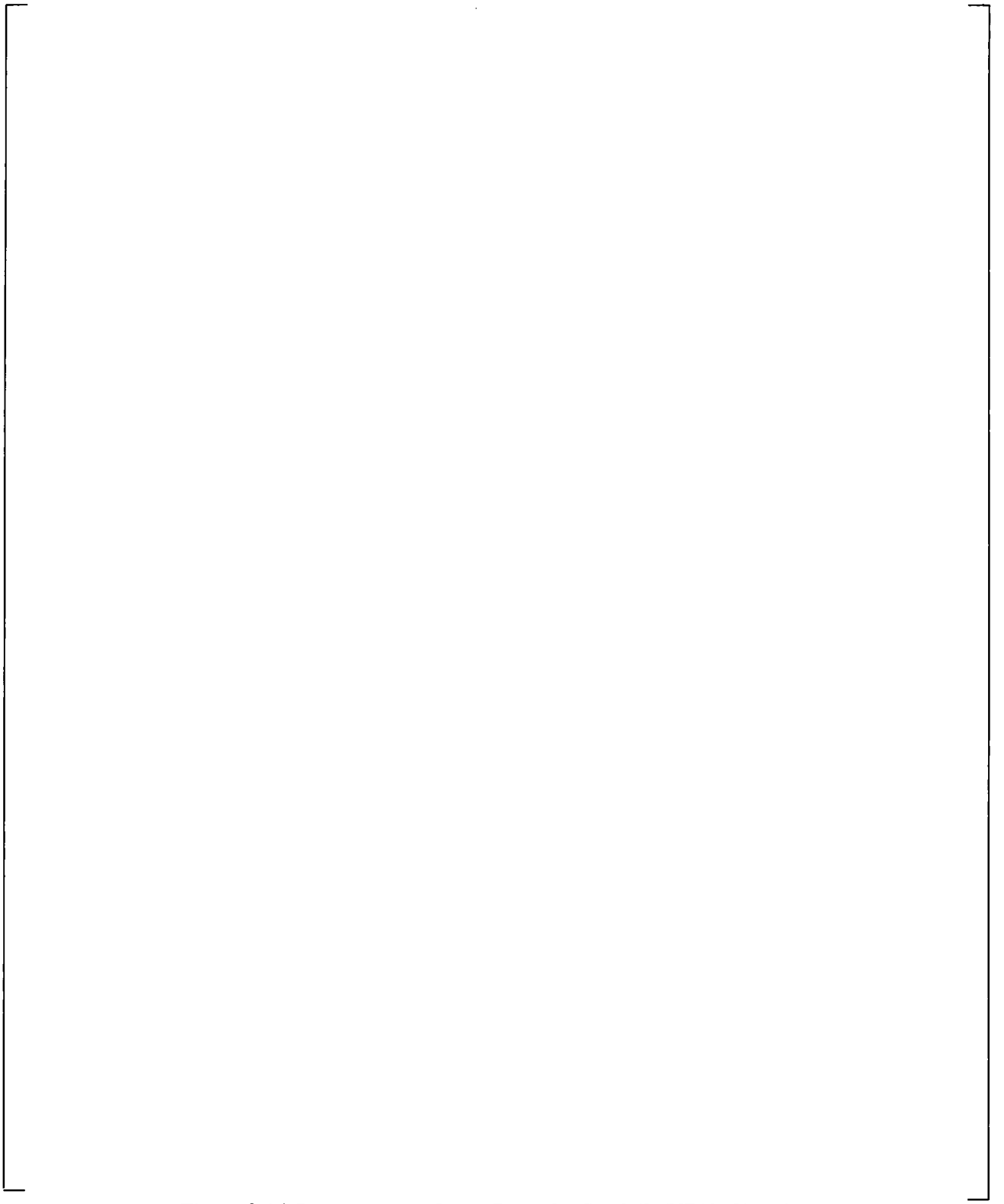

Figure 8-16 Instantaneous Creep Rates for Sandvik (NRU) Cladding

a,c

Figure 8-17 Heatup Rate Scenarios

a,c

Figure 8-18 Circumferential Strain Following Rupture – Zircaloy-4 Cladding

a,c

Figure 8-19 Burst Temperature Correlation – Westinghouse ZIRLO® Cladding

a,c

Figure 8-20 Circumferential Strain Following Rupture – Westinghouse ZIRLO® Cladding

a,c

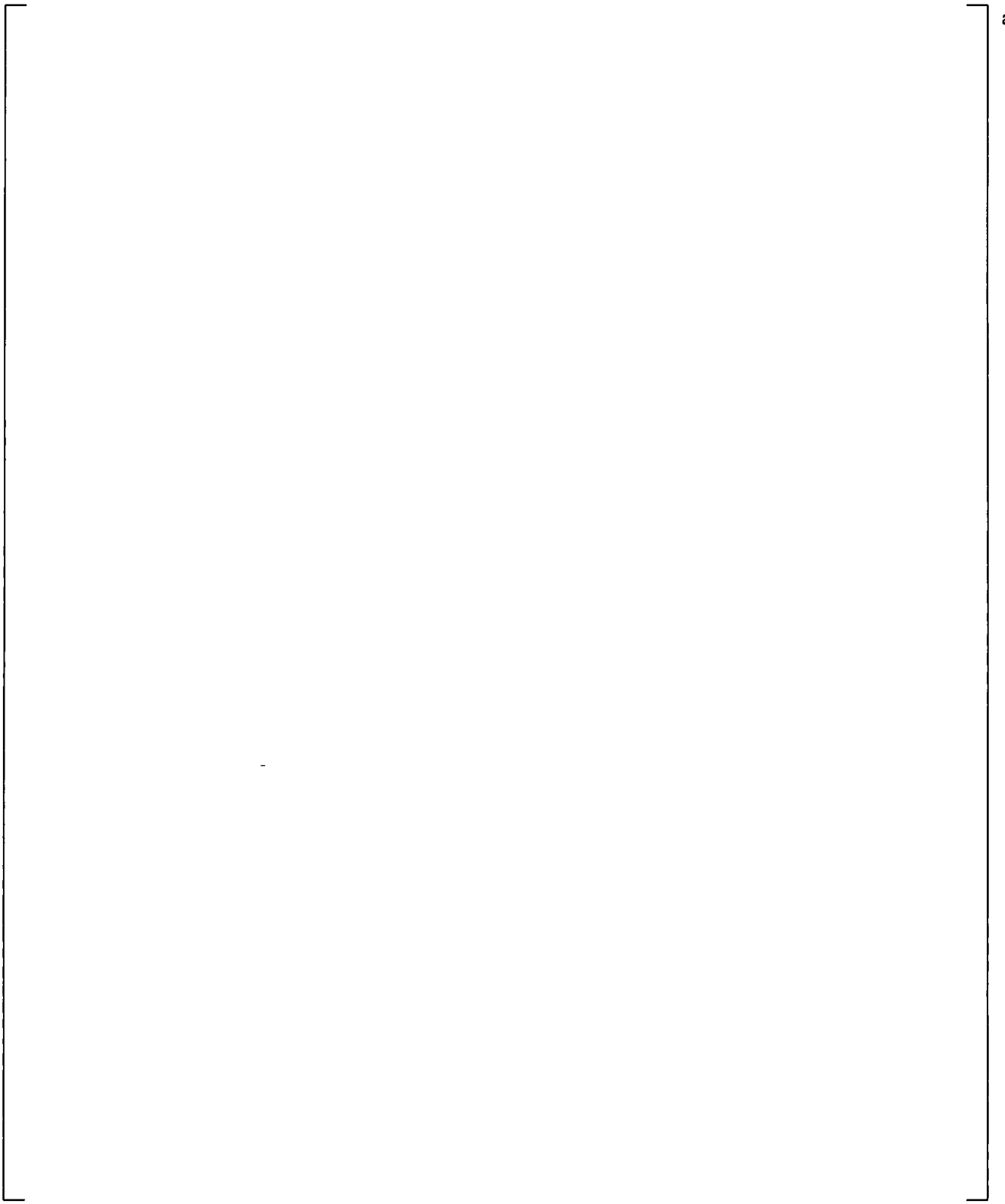

Figure 8-21 Rod Strain at Burst Elevation

a,c

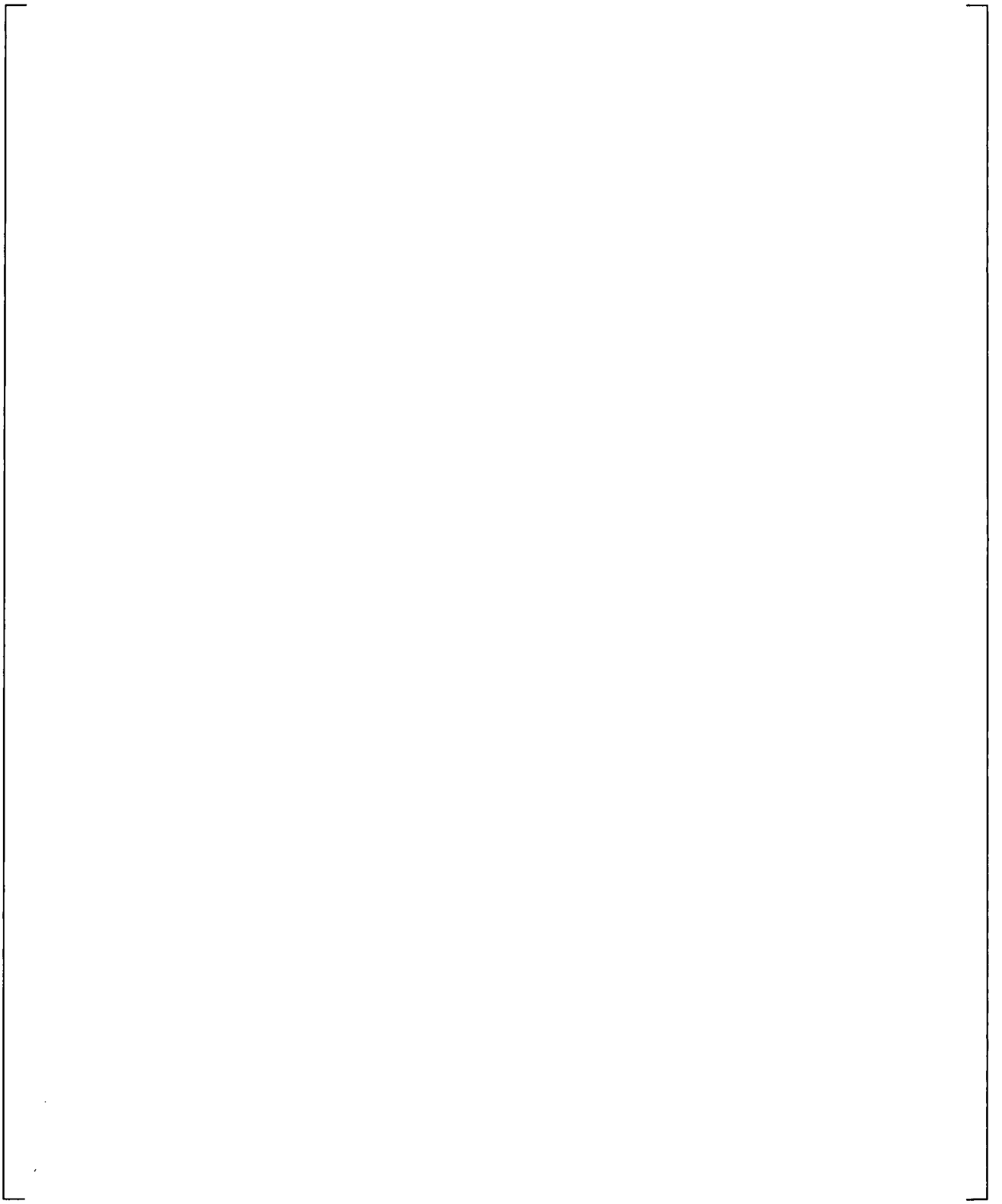

Figure 8-22 Flow Area Reduction Due to Blockage – Zircaloy-4 Cladding

a,c

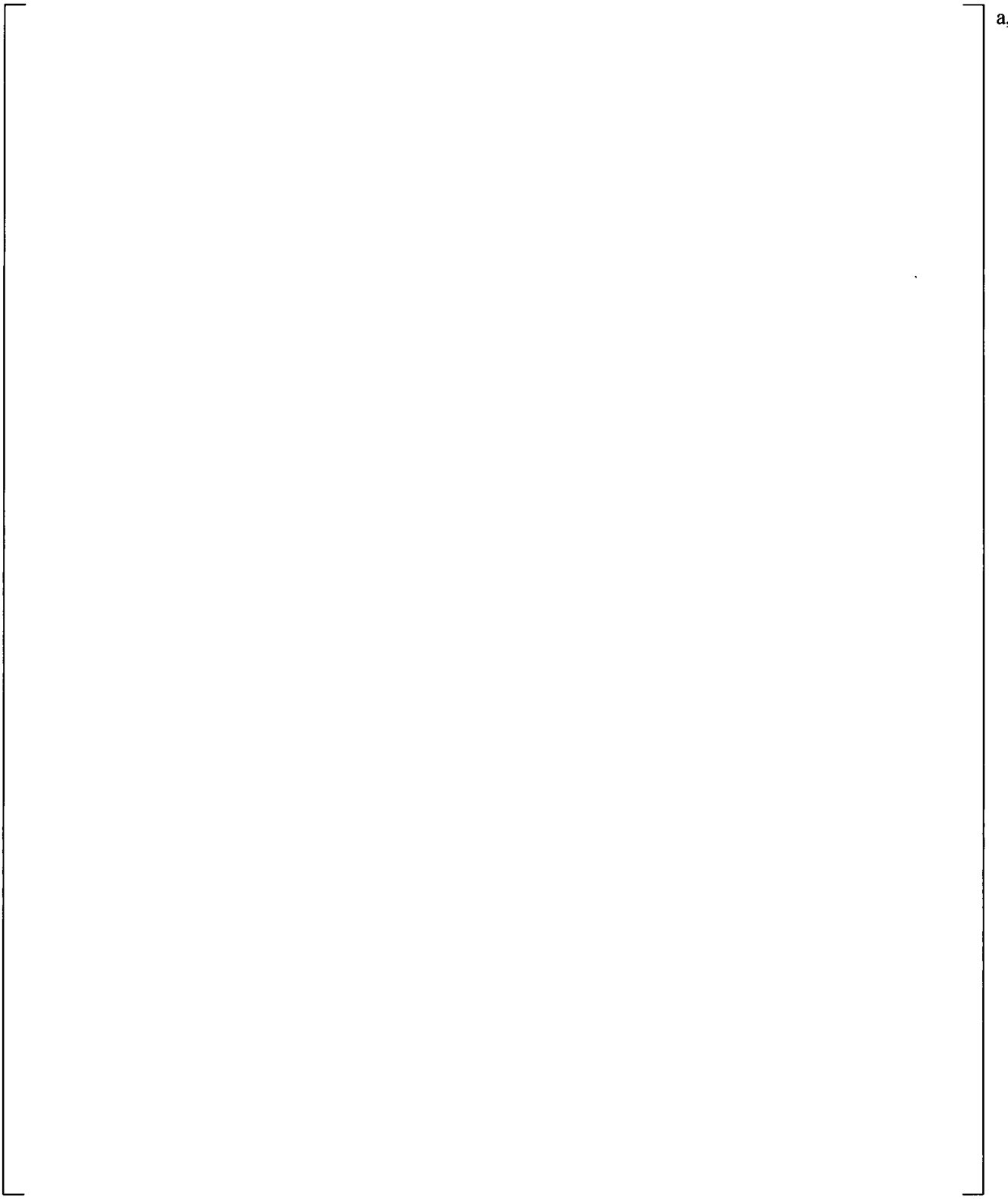

Figure 8-23 Flow Area Reduction Due to Blockage – ZIRLO® Cladding

a,c

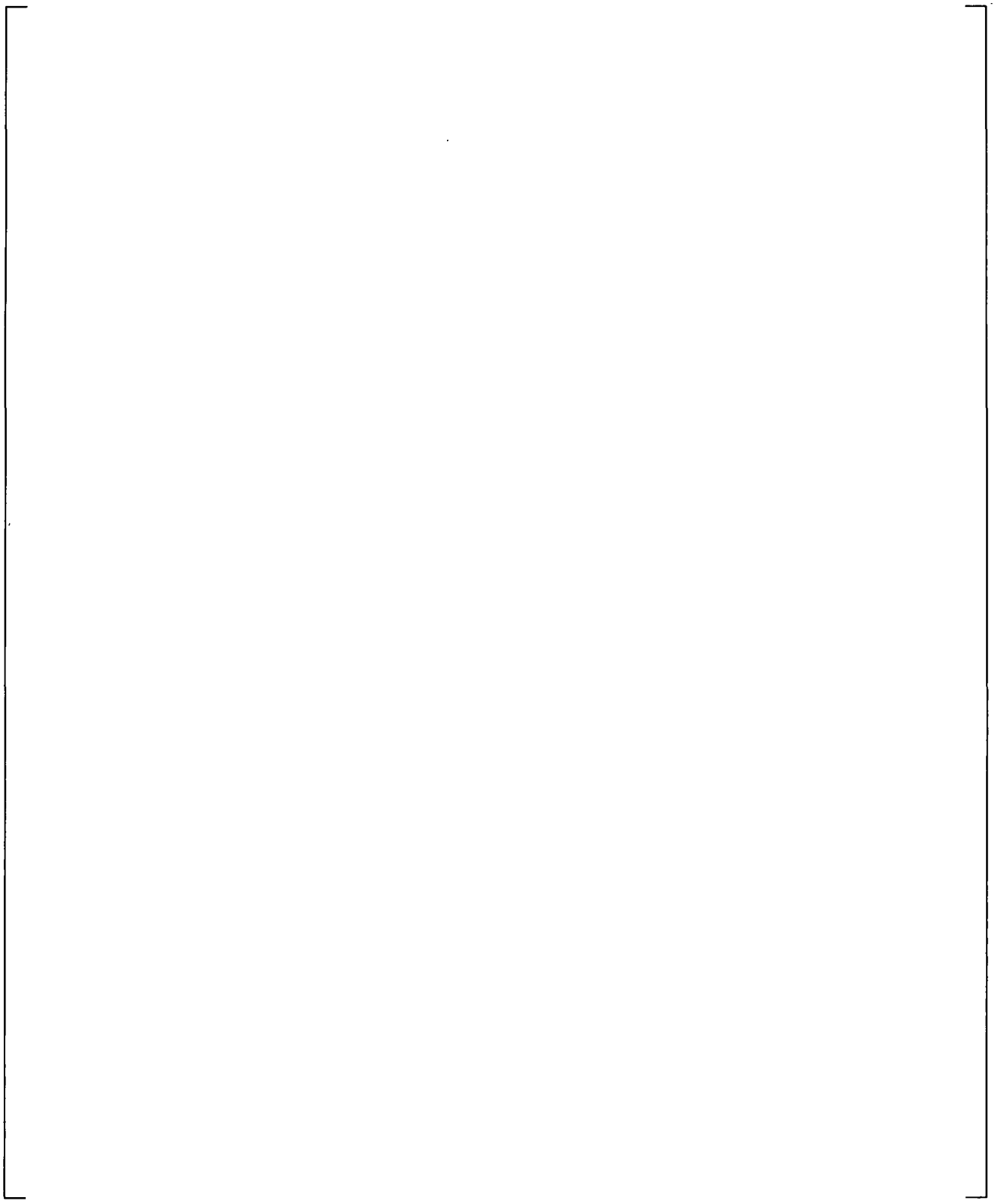

Figure 8-24 [

][a,c]

[a,c

]

Figure 8-25 [ ]^{a,c}

[a,c

]

Figure 8-26 [ ]^{a,c}

[ ] a,c

Figure 8-27 [ ]a,c

[ ] a,c

Figure 8-28 [ ]a,c

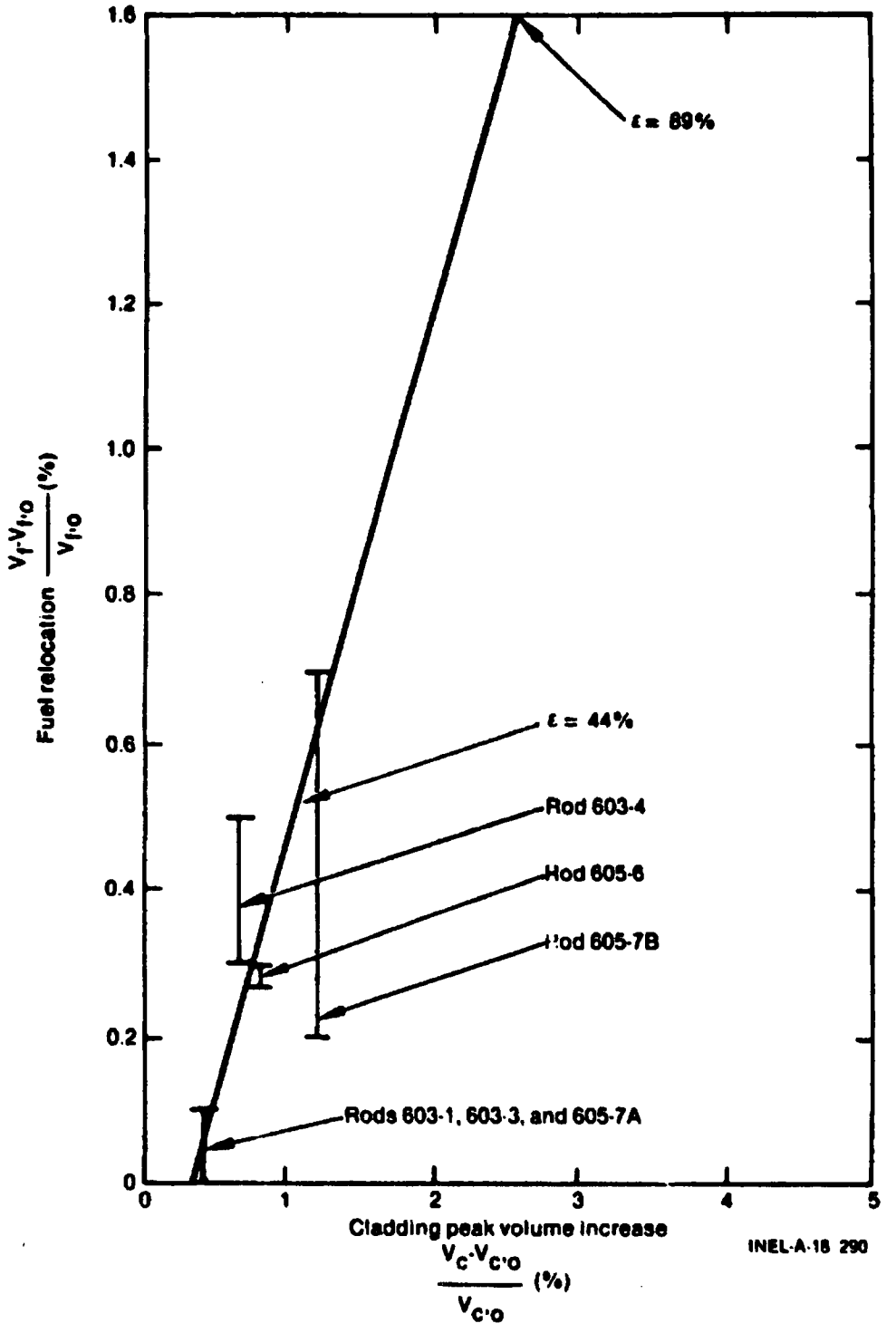

Figure 8-29 Volumetric Increase in Fuel for Corresponding Clad Volume Increase Derived from PBF Tests (Broughton, 1981)

[a,c

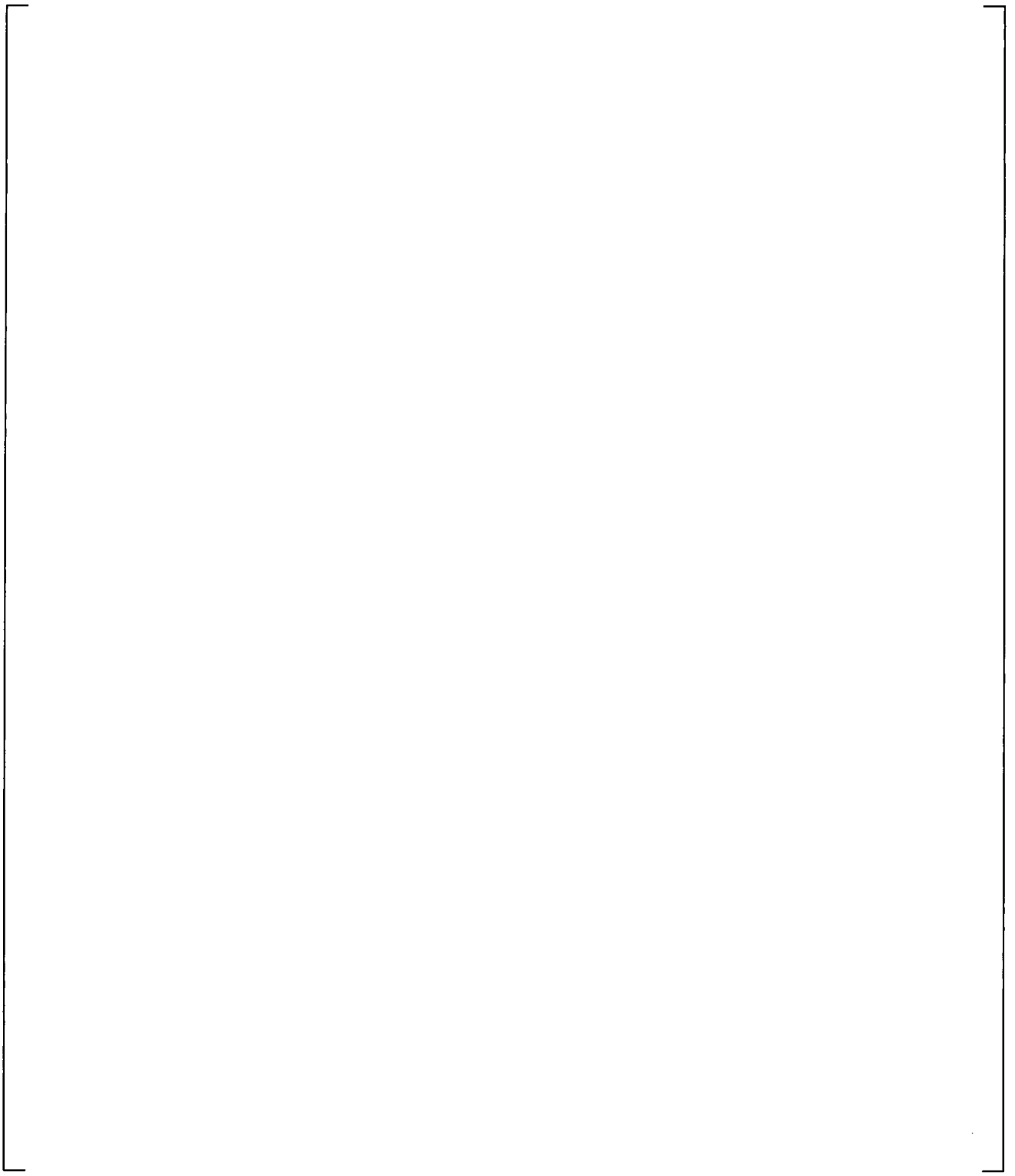

]

Figure 8-30 [

][a,c]

[a,c

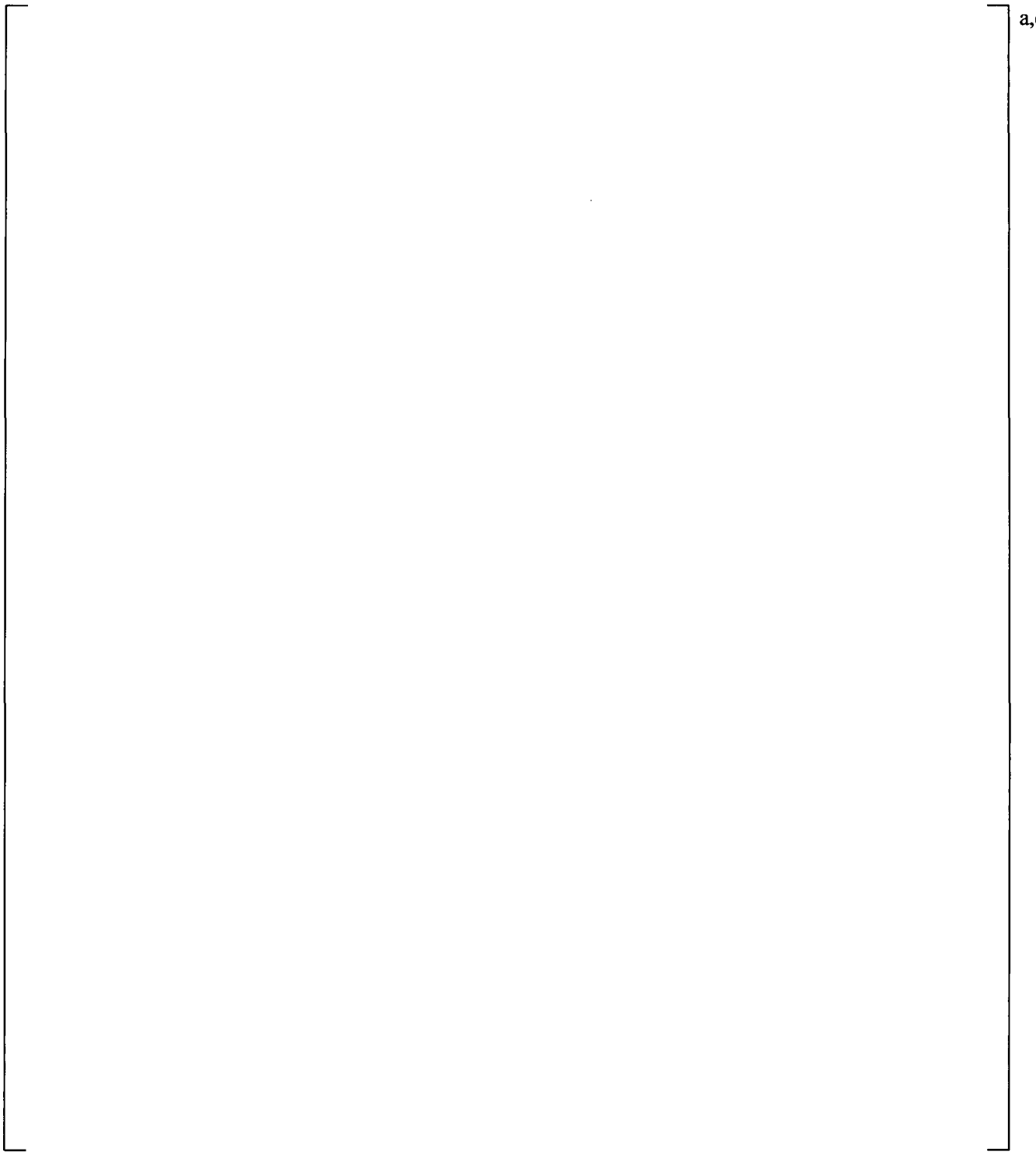

Figure 8-31 [

]a,c

a,c

Figure 8-32 [

]^{a,c}

a,c

Figure 8-33 [

]^{a,c}

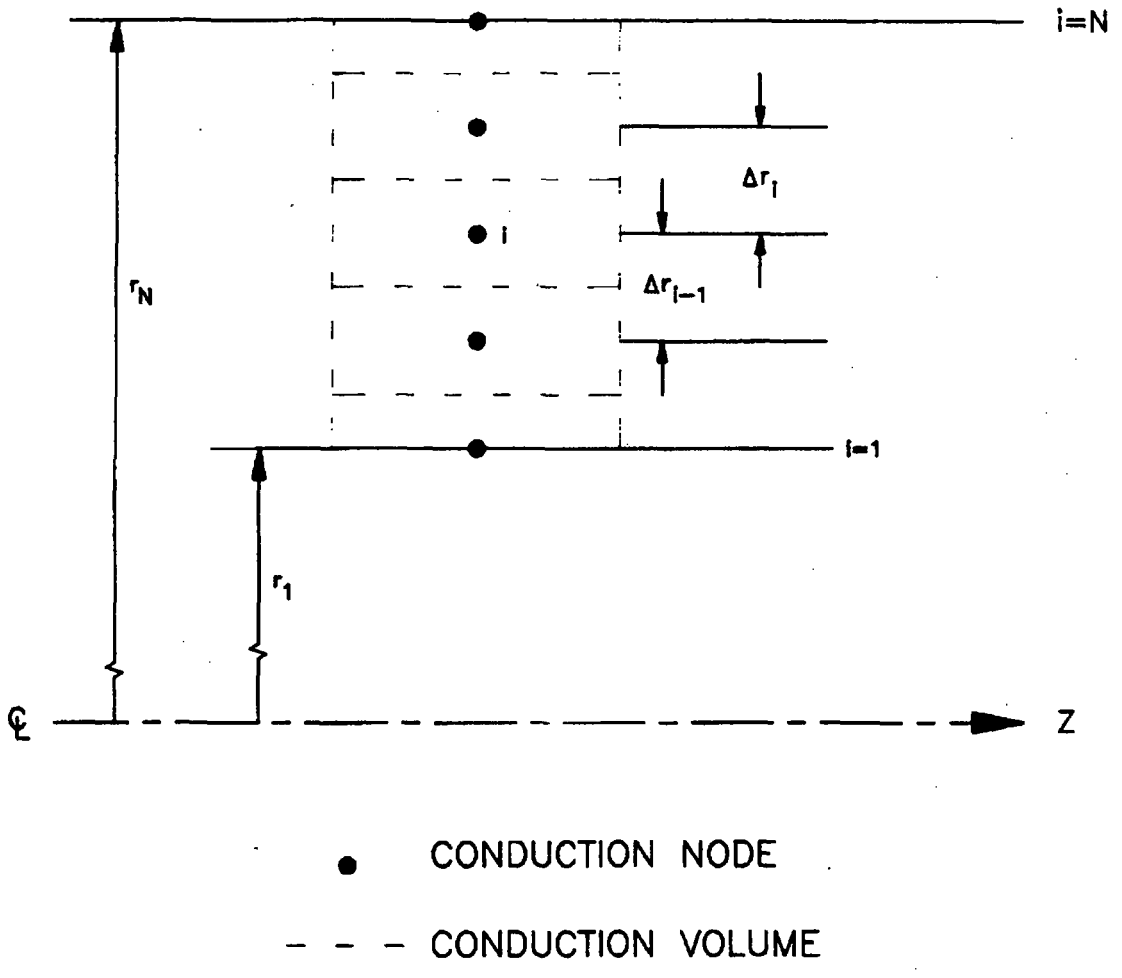

Figure 8-34 Geometry for One-Dimensional Component Conductor

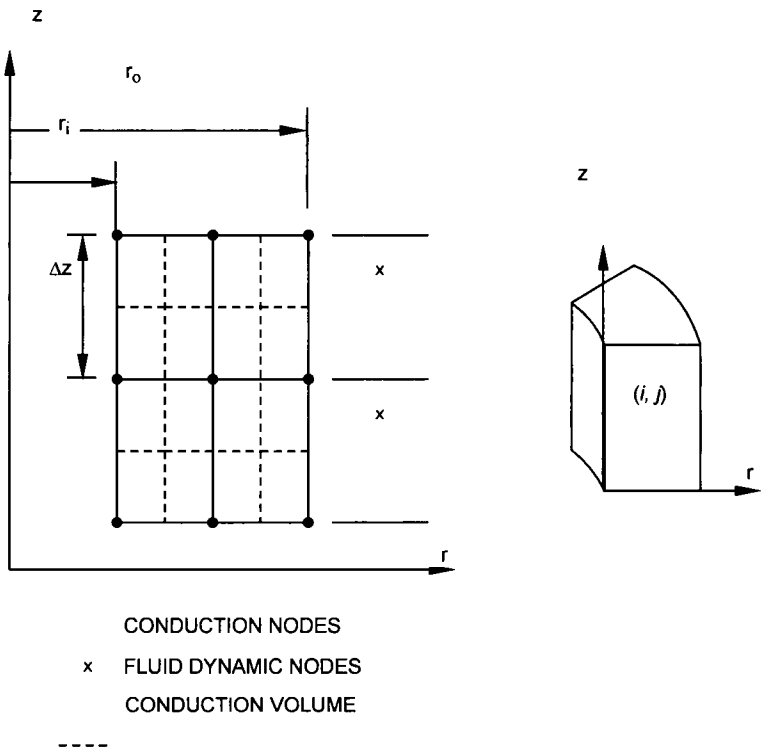

Figure 8-35 Geometry for HTSTR Component Conductor

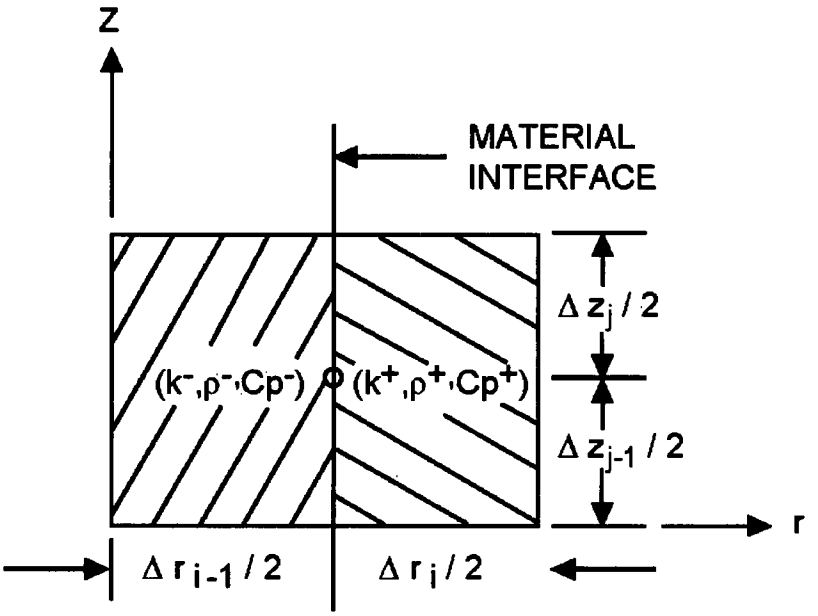

Figure 8-36 Node Located at the Interface between Two Dissimilar Materials

9 WCOBRA/TRAC-TF2 REACTOR KINETICS AND DECAY HEAT MODELS

9.1 INTRODUCTION

The heat sources during a postulated Loss-of-Coolant Accident (LOCA) are important in determining the cladding heatup. It is therefore important to include all possible heat sources in an accurate way such that the peak cladding temperature (PCT) calculated from an analysis model is realistic, without having an unnecessary penalty.

The primary heat sources during a LOCA are fission product decay heat, fission heat, actinide decay heat, and cladding chemical reaction. The objective of this section is to summarize the models related to the first three heat sources which have been programmed in the code WCOBRA/TRAC-TF2. The cladding chemical reaction was described in Section 8. The models described in this section are identical to the approved models which have been documented in Hochreiter et al. (1988).

The variables of each equation presented in this section are defined after each equation. The nomenclature of this section is independent of the nomenclature of the rest of this report.

9.2 DECAY HEAT SOURCE

Model Basis

In general, the time-dependent decay activity for a given nuclide can be solved by the following relationship:

$$\frac{d}{dt}DH^i = \alpha_i(\Sigma_F \phi) - \Gamma_i DH^i + \phi\sum_{j=1}^{n} DH^j\sigma_\alpha^j A(i,j)$$

$$+\sum_{j=1}^{n}\Gamma_j\, DH^j\, D\,(i,j) \qquad (9\text{-}1)$$

where:

DH^i	=	the decay activity of the i-th decay heat pseudo-nuclide,
α_i	=	the yield fraction of the i-th decay heat pseudo-nuclide directly from fission,
Σ_F	=	the macroscopic fission cross section,
$\Sigma_F \phi$	=	the fission rate of the reactor of interest,
Γ_i	=	the decay constant of the i-th decay heat pseudo-nuclide,
ϕ	=	the neutron flux in the reactor of interest,
σ_a^j	=	the microscopic absorption cross section of the j-th nuclide,
A(i, j)	=	the probability that absorption in the j-th isotope will produce the i-th isotope, and
D (i, j)	=	the probability that decay of the j-th nuclide will produce the i-th nuclide.

Equation 9-1 is numerically exact for the decay heat problem. However, the direct solution of Equation 9-1 involves 250 to 350 cross-coupled equations.

To simplify the preceding equation, three assumptions have been used to implement a generalized decay heat source consistent with ANSI/ANS 5.1-1971 Draft (1971) and ANSI/ANS 5.1-1979 (1978). The first two are:

- $A(i,j) = 0$
- $D(i,j) = 0$

That is, the contributions from the absorption in the j-th isotope and decay of the j-th isotope, which will produce the i-th isotope, are much less significant than the direct production ($\alpha_i \Sigma_F \phi$), and decay ($\Gamma_i DH^i$), except for very few nuclides in very high flux reactors. The third assumption is:

- Nuclides of similar time constants may be grouped into a single pseudo-nuclide with the weighted average energy yield of all the nuclides involved.

The above assumption yields fewer equations to be solved with negligible loss in accuracy when the nuclide groups are chosen appropriately.

The final form of Equation 9-1 with the above assumptions is:

$$\frac{d}{dt} DH^i = \alpha_i (\Sigma_F \phi) - \Gamma_i DH^i \tag{9-2}$$

Table 9-1 lists the standard data of α_i and Γ_i from the ANSI/ANS 5.1-1979 model for U-235, Pu-239 thermal fission, and U-238 fast fission.

The ANSI/ANS 5.1-1979 standard data are represented in an exponential form (MeV/fission):

$$DH(t,T) = \sum_{n=1}^{3} w_n(BU,\varepsilon) \left[\sum_{i=1}^{23} \frac{\alpha_i}{\Gamma_i} e^{-\Gamma_i t} (1 - e^{-\Gamma_i T}) \right]_n \tag{9-3}$$

where:

t = time after shutdown (sec),

T = irradiation time (sec), and,

$w_n(BU,\varepsilon)$ = fission fraction of the n-th fissile isotope as a function of burnup (BU) and initial enrichment (ε),

$n=1$ = U-235 Thermal Fission

n=2 = Pu-239 Thermal Fission

n=3 = U-238 Fast Fission

Equation 9-3 is the general solution of Equation 9-2 for a constant fission rate for an irradiation time T followed by a zero fission rate for time, t. WCOBRA/TRAC-TF2 solves Equation 9-2 as the generalized differential equation representation of Equation 9-3 for U-235 and Pu-239 thermal fission as well as U-238 fast fission. The energy yield constants are weighted by the appropriate fission rate fractions, $w_n(BU,\varepsilon)$, as a function of initial enrichment and burnup within WCOBRA/TRAC-TF2.

The fission rate weighting was obtained from detailed physics evaluations of PWR fuel lattice designs. Figure 9-1 illustrates the U-235 thermal fission rate weighting obtained from these evaluations. Similarly, Figures 9-2 and 9-3 illustrate the Pu-239 thermal fission and U-238 fast fission weightings, respectively. The U-235 fission rate fraction presented in Figure 9-1 was evaluated as directed by ANSI/ANS 5.1-1979, as all fissions that are not U-238 or Pu-239.

The decay heat model within WCOBRA/TRAC-TF2 has been benchmarked against the ANSI/ANS 5.1-1979 Standard. Table 9-2 presents the results of decay heat solved by Equation 9-2 in WCOBRA/TRAC-TF2 and the standard form (Equation 9-3) for U-235 only. The difference between the two approaches is negligible. Similar comparisons exist for Pu-239 and U-238. WCOBRA/TRAC-TF2 solves for the composite decay heat of the reactor of interest using the fission rate fractions derived from specific physics calculations for the fuel lattice design.

As for the ANSI/ANS 5.1-1971 model, the standard formulation is a piece-wise power fit over ranges of time from 0.1 seconds to 2×10^8 seconds (Table 9-3). The standard data have been refitted and incorporated into WCOBRA/TRAC-TF2 in the same form as Equation 9-3 except 11 groups (instead of 69 groups) of pseudo-nuclides were used.

Table 9-3 lists the fitted values of α_i and Γ_i of the ANSI/ANS 5.1-1971 model. It can be seen in Table 9-4 that the exponential form with the fitted coefficients generates results which deviate from the standard power form by about one percent.

9.3 FISSION HEAT

Model Basis

The fission heat is treated using a point kinetics model. The derivation of the final form of the point kinetics model can be found in various nuclear reactor analysis textbooks, such as Henry (1975) and Glasstone and Sesonske (1967). The most familiar form of the point kinetics model is:

$$\frac{dn}{dt} = \frac{\rho(t) - \bar{\beta}}{\ell^*} n(t) + \sum_{i=1}^{6} \lambda_i C_i + S_e \qquad (9\text{-}4)$$

and

$$\frac{dC_i}{dt} = \frac{\beta_i n(t)}{\ell^*} - \lambda_i C_i \tag{9-5}$$

where:

n	=	neutron density,
ρ	=	reactivity, (k-1)/k,
β_i	=	the i-th group delayed neutron precursor yield fraction,
$\bar{\beta}$	=	$\sum_{i=1}^{6} \beta_i$,
ℓ^*	=	effective neutron lifetime,
λ_i	=	the i-th delayed neutron precursor time constant,
C_i	=	the i-th delayed neutron precursor concentration, and
S_e	=	external source strength.

The assumptions in deriving Equations 9-4 and 9-5 are the time and space separability of the neutron density and six groups of delayed neutrons.

Once the neutron density $n(t)$ is solved from the point kinetics model, the fission power can be obtained by the equation:

$$FH(t) = \nu n(t) \kappa \Sigma_F \tag{9-6}$$

where:

ν	=	neutron velocity,
κ	=	prompt energy release per fission, and
Σ_F	=	macroscopic fission cross section.

The macroscopic fission cross section is a neutron energy dependent parameter. The moderator density affects the thermalization of neutrons. Therefore, the fission interaction frequency ($\nu\kappa\Sigma_F$) should be a function of moderator density. The moderator of a typical PWR is the primary loop coolant. During a LOCA, the coolant density will undergo a rapid change. Therefore, to assume fission interaction frequency ($\nu\kappa\Sigma_F$) is a constant throughout the transient would be overly conservative (lower coolant density should result in harder neutron energy spectrum, hence lower thermal fission rate). A water-density-dependent form of fission interaction frequency ($\nu\kappa\Sigma_F$) has been incorporated into WCOBRA/TRAC-TF2, which is:

$$\nu\kappa\Sigma_F(\rho_\ell) = A_0 + \sum_{n=1}^{6} A_n \rho_\ell^n \tag{9-7}$$

where:

ρ_ℓ = water density.

The seven coefficients ($A_0 - A_6$) are obtained by space/energy calculations for the fuel assembly of interest.

A series of detailed space/energy calculations have been performed for a typical fresh assembly to quantitatively evaluate fission rate per unit neutron density for water densities that occur during the LOCA transient. Table 9-5 lists the values of the seven coefficients and Figure 9-4 shows the calculated density dependence of $\kappa\Sigma_F$, which is normalized to the value at $\rho_\ell = 0.7 g/cm^3$. [

]^{a,c} Therefore, the modification of the fission frequency ($\nu\kappa\Sigma_F$) should be considered. This quantity, as with all other plant and reactor specific data, is modeled in WCOBRA/TRAC-TF2 using input appropriate to the specific plant and reactor design being considered.

WCOBRA/TRAC-TF2 explicitly models the burnup and initial enrichment dependence of kinetics data, i.e., groupwise delayed neutron fractions, groupwise delayed neutron time constants, prompt neutron lifetime, prompt energy release per fission, and total energy release per fission. Figure 9-5 presents the effective delayed neutron fraction as a function of burnup and initial enrichment. Figure 9-6 presents the prompt neutron lifetime as a function of initial enrichment and burnup. Figures 9-7 and 9-8 present the prompt and total energy release per fission as a function of initial enrichment and burnup, respectively. Figures 9-9 through 9-14 illustrate the groups 1 through 6 delayed neutron time constants as a function of initial enrichment and burnup. The data presented in Figures 9-5 through 9-14 were generated for typical Westinghouse fuel lattice designs.

9.4 ACTINIDE DECAY HEAT SOURCE

Model Basis

The time dependent actinide heat source due to the buildup and decay of U-239 and Np-239 is a relatively simple problem. The basic equations for U-239 and Np-239 are given below as Equations 9-8 and 9-9, respectively:

$$\frac{dU}{dt} = \bar{R}(BU,\varepsilon)(\nu\Sigma_F n(t)) - \lambda_u U(t) \tag{9-8}$$

$$\frac{dNp}{dt} = \lambda_u U(t) - \lambda_n Np(t) \tag{9-9}$$

where:

U(t) = time-dependent U-239 concentration,
$\bar{R}(BU,\varepsilon)$ = U-238 capture to fission ratio, function of initial enrichment ε, and burnup (BU),

$v\Sigma_F n(t)$ = time-dependent fission rate,
λ_u = U-239 decay constant,
$Np(t)$ = time-dependent Np-239 concentration, and
λ_n = Np-239 decay constant.

It is much more convenient to express the decay equations in terms of instantaneous decay power. Recall that decay power is simply the product of concentration, decay constant and energy release per decay as shown in Equations 9-10 and 9-11 for U-239 and Np-239, respectively:

$$P_u = q_u \lambda_u U(t) \tag{9-10}$$

$$P_n = q_n \lambda_n Np(t) \tag{9-11}$$

where:

P_u = time dependent decay power due to U-239 decay,
q_u = energy release per U-239 decay,
P_n = time dependent decay power due to Np-239 decay, and
q_n = energy release per Np-239 decay.

Equations 9-8 through 9-11 can now be combined into a form suitable for implementation as Equations 9-12 and 9-13 below:

$$\frac{dP_u}{dt} = \overline{R}\,\alpha_u\,(v\Sigma_F n(t)) - \lambda_u P_u \tag{9-12}$$

$$\frac{dP_n}{dt} = \frac{\lambda_u P_u(t)\,\alpha_n}{\alpha_u} - \lambda_n P_n \tag{9-13}$$

where:

α_u = $q_u \lambda_u$, decay power yield per capture (MeV/sec/capture) for U-239, and
α_n = $q_n \lambda_n$, decay power yield per capture (MeV/sec/capture) for Np-239.

[

]^{a,c} With this assumption, the initial conditions for U-239 and Np-239 are described by Equations 9-14 and 9-15, respectively:

[ ] a,c (9-14)

(9-15)

The values of constants required for explicit actinide representation were taken from ANSI/ANS 5.1-1979 and are presented in Table 9-6. The U-238 capture to fission ratio, $\overline{R}$, is a function of fuel lattice design, initial enrichment, and burnup. Figure 9-15 presents $\overline{R}$ for a typical PWR fuel lattice design. ENDF-B/V data were used in PWR core depletion calculations to determine variations in $\overline{R}$ with burnup and enrichment.

[

$$\left[\right]^{a,c}_{a,c} \tag{9-16}$$

where:

κ_f = total energy release per fission

9.5 SPACE DEPENDENT HEAT SOURCE MODEL

Model Basis

WCOBRA/TRAC-TF2 models the space dependent composition and initial condition dimensions of the decay heat source. This model is based upon the space/time separability assumptions of the point reactor kinetics solutions as well as the input composition and initial condition description. WCOBRA/TRAC-TF2 models decay heat using channel average compositions. Initial condition concentrations are input based on conservative irradiation history evaluations. Channel average compositions are realistic representations of decay heat in limiting evaluations.

The basic space independent equations derived in Sections 9.2 and 9.3 are repeated below:

$$\frac{dn}{dt} = \frac{\rho(t) - \overline{\beta}}{\ell^*} n(t) + \sum_{i=1}^{6} \lambda_i C_i + S_e \tag{9-4}$$

$$\frac{dC_i}{dt} = \frac{\beta_i n(t)}{\ell^*} - \lambda_i C_i \tag{9-5}$$

$$\frac{d}{dt} DH^i = \alpha_i (\Sigma_F \phi) - \Gamma_i DH^i \tag{9-2}$$

$$P(t) = FH(t) + \sum_j DH^j + AH(t) \tag{9-17}$$

$$FH(t) = \kappa v \Sigma_F(t) n(t) \tag{9-18}$$

where:

$P(t)$ = time-dependent heat source,
$n(t)$ = time-dependent neutron density,
$\rho(t)$ = time-dependent reactivity defined as (k-1)/k,
ℓ^* = prompt neutron lifetime,
$\bar{\beta}$ = effective delay neutron fraction,
λ_i = time constant for the i-th delayed neutron group,
S_e = external source strength,
$\nu\Sigma_F(t)$ = time dependent interaction frequency for fission,
β_i = effective delayed neutron fraction for the i-th group,
DH^j = energy release rate of the j-th decay heat pseudo-nuclide,
α_j = energy yield of the j-th decay heat pseudo nuclide,
Γ_j = time constant of the j-th decay heat pseudo nuclide,
κ = prompt energy release per fission,
$FH(t)$ = time dependent fission heat, and
$AH(t)$ = time dependent actinide heat.

Assuming space/time separability, Equation 9-17 can be expressed with a general time-independent space dependence for each basic heat source as Equation 9-19 below:

$$P_i(z,t) = F_i(z)\,FH(t) + \sum_j D_i^j(z)\,DH^j(t) + A_i(z)\,AH(t) \qquad (9\text{-}19)$$

where:

$P_i(z,t)$ = the heat-source as a function of elevation and time in the i-th xy channel,

$F_i(z)$ = the elevation dependence of fission heat for the i-th xy channel,

$D_i^j(z)$ = the elevation dependence of the j-th decay heat pseudo-nuclide for the i-th xy channel, and

$A_i(z)$ = the elevation dependence of actinide heat for the i-th xy channel.

[

$$\left[\right]^{a,c} \qquad \left[\right]^{a,c} \qquad (9\text{-}20)$$

[

]^{a,c}

The decay heat source is most conveniently expressed in terms of the [

]^{a,c}

[ ]^{a,c} (9-21)

where:[

]^{a,c}

Equation 9-21 is now solved for $D_i^j(z)$ as Equation 9-22 below:

[ ]^{a,c} (9-22)

The space/time dependent heat source can now be expressed in terms of the fission distribution and the initial power by substituting Equation 9-22 into Equation 9-19 as Equation 9-23 below:

[ ]^{a,c} (9-23)

Equation 9-23 can be further simplified by defining the [

]^{a,c} as defined in Equation 9-24 below:

[ ]^{a,c} (9-24)

Equation 9-24 is now solved for the initial condition for [

]^{a,c} as Equation 9-25 below:

[ ]^{a,c} (9-25)

Equation 9-25 is now substituted into Equation 9-23 to give the final form of the space/time dependent heat source as Equation 9-26 below:

[ ]^{a,c} (9-26)

The remaining task is to provide initial conditions for Equations 9-4, 9-5, and 9-2 in terms of Equation 9-26. The first of these conditions is that the input power peaking $FT_i(z)$ be normalized to a reactor average value of unity. This relation is expressed for $FT_i(z)$ as Equation 9-27 below:

$$\frac{\sum_i \int_z FT_i(z)\, V_i(z) dz}{\sum_i \int_z V_i(z) dz} = 1.0, \tag{9-27}$$

where $V_i(z)$ is the volume of the i-th channel at elevation *z*. The second initial condition is that the initial reactor power, P_{TH}, be given by Equation 9-28 below:

$$P_{TH} = \sum_i \int_z V_i(z) P_i(z,0)\, dz \tag{9-28}$$

The initial conditions of Equations 9-4, 9-5, and 9-2 can now be solved in terms of P_{TH}. First, it is necessary to derive the relations for $P_i(z, 0)$ as Equation 9-29 below (from Equations 9-26 and 9-20):

[ ]^{a,c} (9-29)

Substituting Equation 9-25 into Equation 9-29 yields a statement of initial condition in terms of [ ]^{a,c} as Equation 9-30:

[ ]^{a,c} (9-30)

Finally, Equation 9-30 can be integrated over the entire reactor as specified in Equation 9-28, and [ ]^{a,c} as shown in Equation 9-31 below:

[ ]^{a,c} (9-31)

Now, solve for the initial neutron density $n(0)$ by substituting Equation 9-18 into Equation 9-31 to yield the initial conditions in terms of initial total power P_{TH} as Equation 9-32 below:

[ ]^{a,c} (9-32)

Recall Equation 9-24 defines that:

[ ] a,c (9-33)

where the two power distributions, $D_i(z)$ and $F_i(z)$, are normalized to a reactor average value of unity.

Equation 9-22 is now substituted into Equation 9-33 to yield an expression for $AVFR^j$ in terms of the fission peaking as Equation 9-34:

[ ] a,c (9-34a)

and

[ ] a,c (9-34b)

All that remains to be done is to solve for $F_i(z)$ in terms of $FT_i(z)$. Recall that Equation 9-27 requires that $FT_i(z)$ be normalized such that $P_i(z,0)$ is given by Equation 9-35 below:

$$P_i(z,0) = P_{AV}(0)\, F_{T_i}(z), \tag{9-35}$$

where:

$$P_{AV}(0) = \frac{P_{TH}}{\sum_i \int_z V_i(z)\, dz} \tag{9-36}$$

Substituting Equation 9-30 into Equation 9-35 and rearranging gives Equation 9-37 below:

[ ] a,c (9-37)

9.6 ENERGY DEPOSITION MODELING

9.6.1 Introduction

WCOBRA/TRAC-TF2 models the energy sources within the reactor fuel in three distinct categories. These categories are prompt fission, fission product decay, and actinide nuclide decay. The specific details of the energy source modeling can be found in (Hochreiter et al., 1988). The distribution of energy sources is, however, of no interest to the thermal and hydraulic modeling of deposition resulting from the various distributed energy sources. The specific details of the methodology by which the spatial distribution of the energy sources is transformed into the spatial distribution of energy deposition are the subject of the following discussion.

The energy from fission events appears in varying forms with large differences in spatial transport characteristics. Table 9-7 illustrates a typical breakdown of the energy released due to a fission event and the relative spatial transport length of the component. The degree to which a radiation source will propagate through a medium is strongly related to whether the radiation is expressed as a charged particle (e.g., fission fragment or beta particle), an uncharged particle (e.g., neutron), or a photon, (e.g., gamma-ray). Charged particles emitted from within a nuclear fuel material are, from a practical viewpoint, unable to penetrate the confines of the fuel rod and, therefore, deposit essentially all of their energy within the fuel rod as heat. As illustrated in Table 9-7, the vast majority of the total energy released due to a fission event is expressed as the kinetic energy of the fission products. The fission fragments are emitted as highly charged particles, essentially instantaneously after the fission event, and are deposited almost exclusively within the fuel pin in which they are generated. The beta particle energy from both the decay of fission fragments and the transmutation of the actinide activation products are also charged particles which are, like the fission fragments, deposited almost exclusively within the fuel pin in which they are generated. The beta particle energy is released as a result of the radioactive decay process, which is not directly related to the fission rate; rather it is related to the concentration of the various radio-nuclides which compose the source. WCOBRA/TRAC-TF2 explicitly models the spatial distribution and temporal relationships which describe all heat sources and deposits the energy from non-penetrating radiation sources [ ]^{a,c}. The fraction of the total heat source which is deposited in this manner is independent of coolant conditions and ranges from [ ]^{a,c} during steady state operation to [ ]^{a,c}.

The balance of the energy released as a result of the fission event is expressed as uncharged particles, i.e., neutrons and gamma photon energy. These penetrating radiation sources, due to their lack of charged particles, easily escape the confines of the fuel rod and deposit their energy [ ]^{a,c}. The deposition of the energy contained within these sources is quite important to the consequences of the LOCA transient since [ ]^{a,c} of the decay power released during the LOCA transient is expressed as penetrating radiation. WCOBRA/TRAC-TF2 models the spatial deposition of spatially varying penetrating radiation sources using a generalized energy deposition model (GEDM). The GEDM is [ ]^{a,c} and relies on input to describe the energy deposition as a function of [ ]^{a,c}. The formulation of the GEDM and the methodology for the generation of the model input follows. Illustrative examples are presented for a typical application.

The application of the GEDM is restricted only to the [
]^{a,c}.

9.6.2 Generalized Energy Deposition Model

Generalized Energy Deposition Model Derivation

Model Basis

The WCOBRA/TRAC-TF2 GEDM utilizes the linear superposition of distribution sources to compute the spatial distribution of deposited energy due to a generalized distributed source. The energy deposition, modeled as either heat flux or volumetric, is based upon the results of detailed particle transport calculations which form the basis of the GEDM input. The WCOBRA/TRAC-TF2 GEDM utilizes the relationship illustrated in Equation 9-38 below to account for the energy deposition as heat flux at the point of interest due to generalized penetrating and non-penetrating radiation source spatial distribution(s).

[ ] a,c (9-38)

where:[

]^{a,c}

The WCOBRA/TRAC-TF2 GEDM utilizes the relationship in Equation 9-39 below to account for the energy deposition as volumetric coolant heating at the point of interest due to generalized penetrating and non-penetrating radiation source spatial distribution(s).

[ ] a,c (9-39)

where:[

]^{a,c}

The GEDM transfer matrices Γ^n_{ij} and ϕ^n_{ij} represent [

]^{a,c}, respectively. As stated above, the theoretical basis behind the GEDM transfer matrices is the [

]^{a,c}. The GEDM transfer matrix elements are derived from [

]^{a,c} Equation 9-40 below describes the derivation of the GEDM [ ]^{a,c} transfer matrix elements Γ^n_{ij}.

$$\left[\right]^{a,c} \tag{9-40}$$

where:[

]^{a,c}

Equation 9-41 below describes the derivation of the GEDM [ ]^{a,c} transfer matrix elements ϕ^n_{ij}.

$$\left[\right]^{a,c} \tag{9-41}$$

where:[

]^{a,c}

The numeric values of $(1-\beta_n)$ have been derived from the [

]^{a,c}. Typical values for β_n are given in Table 9-8.

Generalized Energy Deposition Model Transfer Matrix Generation

The GEDM transfer matrix elements are the product of a [

]^{a,c}

[

]^{a,c} The GEDM [ ]^{a,c} methodology was chosen because it can [ ]^{a,c}. The GEDM transfer matrices have been found to be independent of [

]^{a,c} The following discussion will present a sample set of GEDM [ ]^{a,c} calculations that have been performed using the Westinghouse 15x15 fuel design. The methodology described below applies generically to all other fuel designs.

The current model for [

]^{a,c}

Gamma Transfer Matrix Generation Methodology

A series of [ ]^{a,c} calculations were performed for a typical 15x15 OFA fuel design at typical plant conditions. The purpose of these calculations was to quantify, in a generalized fashion, the relative distribution of gamma energy as [ ]^{a,c} throughout the reactor, parameterized as a function of [ ]^{a,c}. DOT (Disney et al., 1970) was used as the dimensional particle transport code for the examples presented in this report. The methodology presented within this report does not rely on the use of DOT, but rather on [

]^{a,c}

The dimensional problem was modeled as a [

]^{a,c}

[

]^{a,c}

The basic methodology employed in the generation of GEDM transfer matrix elements is the use of a [

]^{a,c}

Nuclear particle cross sections were taken from the familiar SAILOR (1985) and BUGLE-80 (1980) library, developed at the Oak Ridge National Laboratory as part of the Radiation Shielding Information Center (RSIC). [

]^{a,c}

Gamma kerma factors were taken from the BUGLE-80 library and used as [

]^{a,c}. The SAILOR/BUGLE-80 cross-section libraries are described in ORNL RSIC reports DLC-76 and DLC-75, respectively. The SAILOR basic multigroup cross sections were [

]^{a,c} The Kerma data used in the development of the [

]^{a,c} are presented in Table 9-11 and illustrated in Figure 9-20.

The final results of the [

]^{a,c}

The results of these calculations were then used to calculate the GEDM transfer matrix elements as shown in Equations 9-40 and 9-41 for [ ]^{a,c} respectively. The results of this evaluation for the 15x15 fuel design are presented in Table 9-12.

The data presented in Table 9-12 quantifies the [ ]^{a,c}. A sample evaluation of the spatial energy deposition distributed using the data from Table 9-12 is presented in Figure 9-21 as the [ ]^{a,c}, respectively.

Figure 9-22 illustrates the [ ]^{a,c}, respectively. These figures clearly illustrate the dependence of heat flux deposition on [ ]^{a,c}.

Application of Generalized Energy Deposition Model (GEDM) within WCOBRA/TRAC-TF2

The data presented in Table 9-12 can be used directly in WCOBRA/TRAC-TF2 provided that the [

]^{a,c} can be found in Table 9-13 and demonstrates that the [

]^{a,c}

The relationship used to apply [

]^{a,c}

$$\left[\right]^{a,c} \qquad (9\text{-}42a)$$

$$\left[\right]^{a,c} \qquad (9\text{-}42b)$$

[a,c (9-42c)

where:

Γ_{ij} = problem specific transfer element,
V_i = problem specific channel volume,
Γ_{ij}^{ref} = reference transfer element, and
V_{ij}^{ref} = reference channel volume.

The relationship used to apply [

]^{a,c}

[a,c (9-43a)

(9-43b)

(9-43c)

where:

ϕ_{ij} = problem specific transfer element,
V_i = problem specific channel volume,
ϕ_{ij}^{ref} = reference transfer element, and
V_j^{ref} = reference channel volume

As discussed above, WCOBRA/TRAC-TF2 currently models [

]^{a,c}

9.7 DECAY HEAT UNCERTAINTY EVALUATION

Decay heat uncertainty has been modeled in WCOBRA/TRAC-TF2 through the use of pseudo-isotope energy yield, α_i, augmentation factors. The values of the augmentation factors are presented in Table 9-14. The values in Table 9-14 were generated using a least squares fit to the uncertainty data provided in ANSI/ANS 5.1-1979, and provide a conservative representation of the standard's quoted uncertainties.

Figures 9-23 to 9-25 show the nominal WCOBRA/TRAC-TF2 decay heat power predictions plus 2σ uncertainty as continuous functions of time for ^{235}U, ^{239}Pu, and ^{238}U, presented normalized to the nominal values. In addition, the ANSI/ANS 5.1-1979 standard decay heat power uncertainty data for ^{235}U, ^{239}Pu, and ^{238}U is presented in the same format.

Figures 9-26 to 9-28 provide curves that represent the nominal WCOBRA/TRAC-TF2 decay heat power predictions as continuous functions of time, as well as two additional curves that represent the decay heat power "upper bound" (nominal plus 2σ) and "lower bound" (nominal minus 2σ) for ^{235}U, ^{239}Pu and ^{238}U for decay time from 0.1s to 10^6 s. In addition, each plot includes the standard decay heat power values $F_i(t,\infty)$ for ^{235}U, ^{239}Pu, and ^{238}U as tabulated in ANSI/ANS 5.1-1979 Tables 4, 5, and 6, representing each value by a symbol with a two-sided Y-error bar corresponding to ± 2σ uncertainty using the uncertainty data in the ANSI/ANS 5.1-1979 tables.

9.8 REACTOR POINT KINETICS VALIDATION

The WCOBRA/TRAC-TF2 heat source model is a fully integrated model containing a total of [

]^{a,c} The decay heat model validation was presented previously in Tables 9-2 and 9-4 against the ANSI/ANS 5.1 1979 and 1971 decay heat standards, respectively. WCOBRA/TRAC-TF2 shows excellent agreement with the decay heat standard data.

The point kinetics model within WCOBRA/TRAC-TF2 has been validated on a [ ]^{a,c} for two basic test problems. The first test problem is the time-dependent solution of a step reactivity input. Figures 9-29 through 9-31 illustrate the WCOBRA/TRAC-TF2 point kinetics solution of reactor period for a step reactivity insertion of $+3.0 \times 10^{-3}$, $+1.5 \times 10^{-3}$, and -3.0×10^{-2} ΔK in the absence of external feedback mechanisms, respectively. The WCOBRA/TRAC-TF2 kinetics model stabilizes at a constant asymptotic reactor period after a short period of time. The asymptotic reactor period for a step reactivity insertion can be solved for analytically using the familiar Inhour Equation below:

$$\rho = \frac{\ell^*}{T} + \sum_{i=1}^{6} \frac{\beta_i}{1+\lambda_i T} \qquad (9\text{-}44)$$

where:

T = Asymptotic reactor period.

Table 9-15 presents the calculated and theoretical asymptotic reactor period for these step insertions. WCOBRA/TRAC-TF2 shows excellent agreement against this theoretical validation test.

[

]^{a,c}

9.9 JUSTIFICATION OF SIMPLIFICATIONS AND ASSUMPTIONS

9.9.1 Actinide Decay Power

ANSI/ANS 5.1-1979 directs the user to evaluate the impact of other actinide isotopes. As stated previously, WCOBRA/TRAC-TF2 explicitly models the decay power due to U-239 and Np-239 with the [

]^{a,c}

Detailed calculations have been performed to evaluate the impact of the total actinide heat source. Table 9-16 presents the basic physical data for the [

]^{a,c}

9.9.2 WCOBRA/TRAC-TF2 Fission Energy Accounting

WCOBRA/TRAC-TF2 explicitly accounts for the energy deposition due to fission by five basic mechanisms. Direct fission energy deposition due to fission fragments, prompt gamma reactions, and prompt beta reactions are a direct and immediate result of a fission event. These components, as well as the neutron slowing down deposition and structural material radiative capture mechanisms, are included

explicitly in the prompt energy release per fission as illustrated in Figure 9-7. The basic physics data used to generate Figure 9-7 as a function of burnup and initial enrichment is based upon ENDF-B/V as utilized at Westinghouse for standard reactor design. Table 9-17 presents the prompt fission energy release, radiative capture release, and average fission neutron energy utilized in the evaluation of the composite prompt energy release per fission. Thus, WCOBRA/TRAC-TF2 complies with the standard's requirement to evaluate the energy release per fission, including radiative capture in structural components.

9.9.3 Decay Heat Absorption Effects

ANSI/ANS 5.1-1979 directs the user that the basic decay heat data supplied within the standard is uncorrected for neutron capture effects. The standard supplies a means of correction for neutron capture as a function of irradiation time, shutdown time, and integrated fissions per initial fissile atom, as shown in Equation 9-45 below:

$$G(t) = 1.0 + (3.24E-06 + 5.23E-10t)\, T^{0.4}\, \psi \qquad (9\text{-}45)$$

where:

t	=	time after shutdown in seconds, (t < 10,000 sec)
T	=	irradiation time in seconds, (T < 1.2614E+08 sec)
ψ	=	fissions per initial fissile atom, (ψ < 3.0)

Integrated fissions per initial fissile atom have been evaluated for PWR fuel lattice designs, as illustrated in Figure 9-34, as a function [

]^{a,c} Thus, WCOBRA/TRAC-TF2 conservatively accounts for neutron capture effects in the decay heat model as required by the standard.

9.10 GENERALIZED ENERGY DEPOSITION MODEL (GEDM) VALIDATION

The GEDM has been validated in two separate manners for application within WCOBRA/TRAC-TF2. The first validation calculation was performed to validate the [

]^{a,c}

[

]^{a,c}

The final validation of the GEDM and input generation methodology was the comparison of the GEDM [

]^{a,c}. The results of this comparison are given in Table 9-18. It is apparent from the [

]^{a,c}.

9.11 INTERFACE BETWEEN NEUTRONICS AND THERMAL-HYDRAULICS MODELS

Figure 9-35 shows the calculation block diagram for WCOBRA/TRAC-TF2. The neutronics part of the calculation is performed by a subroutine within WCOBRA/TRAC-TF2 called LUCIFER (Hochreiter et al., 1988). There are two options available for the neutronics calculations in terms of the reactivity feedback to LUCIFER. The first option is the user supplied reactivity table. With this option, LUCIFER is essentially a stand-alone code for calculating the power history associated with the reactivity table. The second option is the internal feedback option. The core average fuel temperature and coolant density calculated in WCOBRA/TRAC-TF2 are fed back to LUCIFER for the reactivity calculation and the associated power history calculation. The calculated power history is then supplied to WCOBRA/TRAC-TF2 as the heat source in the thermal-hydraulics calculations.

9.12 REACTOR KINETICS, DECAY HEAT, AND INTERFACE MODELS AS CODED

WCOBRA/TRAC-TF2 solves the reactor kinetics, decay heat, and actinide decay heat models with a system of first-order ordinary differential equations of the form $y' = f(x,y)$ or $A'y = f(x,y)$ with initial conditions, where A is a matrix of order N. The solution method is the backward differentiation formula (up to order 6), also called Gear's stiff method (1971). Because the basic formula is implicit, an algebraic system of equations must be solved at each step. The matrix in this system has the form $L = A + \eta J$, where η is a small number and J is the Jacobian.

The FORTRAN coding in WCOBRA/TRAC-TF2 is consistent with the models described in this section.

9.13 REACTOR KINETICS, DECAY HEAT, AND INTERFACE MODELS SCALING CONSIDERATIONS

The models described in this section are scale independent.

9.14 CONCLUSIONS

The models and derivations described in this section have been reviewed and checked. It is concluded that the models are correct. The coding in WCOBRA/TRAC-TF2 is found to be consistent with the models described in this section.

9.15 REFERENCES

1. ANSI/ANS 5.1-1971, 1971, "Proposed ANS Standard Decay Energy Release Rates Following Shutdown of Uranium-Fueled Thermal Reactors," American Nuclear Society.

2. ANSI/ANS 5.1-1979, 1978, "Decay Heat in Light Water Reactors," American Nuclear Society.

3. BUGLE-80 Gamma Cross Sections, 1980, ORNL RSIC DLC-76.

4. Disney, R. K., et al., 1970, "Nuclear Rocket Shielding Methods, Modification, Updating, and Input Preparation," Volume 5, Two Dimensional Discrete Ordinates Transport Techniques, WANL-PR-(LL)-034, Westinghouse Astro Nuclear Laboratory.

5. DOT2W, "A Two-Dimensional Discrete Ordinates Computer Program," ORNL/RSIC CCC-89. Contributed by Westinghouse Advanced Reactors Division, Madison, PA, USA.

6. Gear, C. W., 1971, Numerical Initial Value Problems in Ordinary Differential Equations, Prentice-Hall, Englewood Cliffs, New Jersey.

7. Glasstone, S. and Sesonske, A., 1967, Nuclear Reactor Engineering, Van Nostrand, New York.

8. Henry, A. F., 1975, Nuclear-Reactor Analysis, The MIT Press, Cambridge, Mass. and London England.

9. Hochreiter, L. E., et al., 1988, "Westinghouse Large Break LOCA Best Estimate Methodology, Volume 1: Model Description and Validation, Addendum 2: Revised Appendix B: Heat Source Models," WCAP-10924-P-A, Revision 1.

10. SAILOR Gamma Cross Sections, 1985, ORNL RSIC DLC-75.

Table 9-1 ANSI/ANS 5.1-1979		
Decay Heat Standard Data for U-235 Thermal Fission		
Group	**α_i (MeV/f.sec)**	**Γ_i (sec^{-1})**
1	6.5057E-01	2.2138E+01
2	5.1264E-01	5.1587E-01
3	2.4384E-01	1.9594E-01
4	1.3850E-01	1.0314E-01
5	5.5440E-02	3.3656E-02
6	2.2225E-02	1.1681E-02
7	3.3088E-03	3.5870E-03
8	9.3015E-04	1.3930E-03
9	8.0943E-04	6.2630E-04
10	1.9567E-04	1.8906E-04
11	3.2535E-05	5.4988E-05
12	7.5595E-06	2.0958E-05
13	2.5232E-06	1.0010E-05
14	4.9948E-07	2.5438E-06
15	1.8531E-07	6.6361E-07
16	2.6608E-08	1.2290E-07
17	2.2398E-09	2.7213E-08
18	8.1641E-12	4.3714E-09
19	8.7797E-11	7.5780E-10
20	2.5131E-14	2.4786E-10
21	3.2176E-16	2.2384E-13
22	4.5038E-17	2.4600E-14
23	7.4791E-17	1.5699E-14

Table 9-1 ANSI/ANS 5.1-1979 (cont.)

Decay Heat Standard Data for Pu-239 Thermal Fission

Group	α_i (MeV/f.sec)	Γ_i (sec^{-1})
1	2.083E-01	1.002E+01
2	3.853E-01	6.433E-01
3	2.213E-01	2.186E-01
4	9.460E-02	1.004E-01
5	3.531E-02	3.728E-02
6	2.292E-02	1.435E-02
7	3.946E-03	4.549E-03
8	1.317E-03	1.328E-03
9	7.052E-04	5.356E-04
10	1.432E-04	1.730E-04
11	1.765E-05	4.881E-05
12	7.347E-06	2.006E-05
13	1.747E-06	8.319E-06
14	5.481E-07	2.358E-06
15	1.671E-07	6.450E-07
16	2.112E-08	1.278E-07
17	2.996E-09	2.466E-08
18	5.107E-11	9.378E-09
19	5.730E-11[1]	7.450E-10
20	4.138E-14	2.426E-10
21	1.088E-15	2.210E-13
22	2.454E-17	2.640E-14
23	7.557E-17	1.380E-14

Table 9-1 ANSI/ANS 5.1-1979 (cont.)

Decay Heat Standard Data for U-238 Fast Fission

Group	α_i (MeV/f.sec)	Γ_i (sec^{-1})
1	1.2311E+0	3.2881E+0
2	1.1486E+0	9.3805E-1
3	7.0701E-1	3.7073E-1
4	2.5209E-1	1.1118E-1
5	7.1870E-2	3.6143E-2
6	2.8291E-2	1.3272E-2
7	6.8382E-3	5.0133E-3
8	1.2322E-3	1.3655E-3
9	6.8409E-4	5.5158E-4
10	1.6975E-4	1.7873E-4
11	2.4182E-5	4.9032E-5
12	6.6356E-6	1.7058E-5
13	1.0075E-6	7.0465E-6
14	4.9894E-7	2.3190E-6
15	1.6352E-7	6.4480E-7
16	2.3355E-8	1.2649E-7
17	2.8094E-9	2.5548E-8
18	3.6236E-11	8.4782E-9
19	6.4577E-11	7.5130E-10
20	4.4963E-14	2.4188E-10
21	3.6654E-16	2.2739E-13
22	5.6293E-17	9.0536E-14
23	7.1602E-17	5.6098E-15

Note:

1. Entry reflects the errata in ANSI/ANS 5.1-1979

Table 9-2 ANSI/ANS 5.1-1979			
Decay Heat Model Comparison for Infinite Radiation of U-235			
Time AfterTrip (sec.)	**WCOBRA/TRAC-TF2 (MeV/fission)**	**Standard (MeV/Fission)**	**Δ%**
0	13.1825	13.183	- 0.003
1	12.3190	12.318	+ 0.008
10	9.5002	9.500	+ 0.007
20	8.4616	8.461	+ 0.003
40	7.4674	7.465	+ 0.036
100	6.2039	6.204	- 0.002
200	5.3744	5.374	+ 0.0002
400	4.6751	4.673	+ 0.04
1000	3.8013	3.801	0.0
Decay Heat Model Comparison for 10^6 Second Irradiation of U-235 From Zero Concentration			
Time AfterTrip (sec.)	**WCOBRA/TRAC-TF2 (MeV/fission)**	**Standard (MeV/Fission)**	**Δ%**
0	12.626	12.626	0.000
1	11.761	11.761	0.000
10	8.944	8.943	+ 0.015
20	7.907	7.905	+ 0.020
40	6.909	6.908	+ 0.012
100	5.648	5.647	+0.014
200	4.820	4.818	+ 0.034
400	4.118	4.117	+ 0.013
1000	3.245	3.245	0.000

Table 9-3 ANSI/ANS 5.1-1971		
Decay Heat Standard Data for U-235 Thermal Fission		
Standard Formulation		
$\frac{DH(t)}{DH_\infty} = At^B$, where,		
t(sec)	**A[1]**	**B**
$0.1 \leq t < 10$	0.07236	-0.0639
$10 \leq t < 150$	0.09192	-0.181
$150 \leq t < 4 \times 10^6$	0.156	-0.283
$4 \times 10^6 \leq t \leq 2 \times 10^8$	0.3192	-0.335
Exponential Representation[2]		
	α_i	Γ_i
1	6.587E+00	2.658E+00
2	1.490E-01	4.619E-01
3	2.730E-01	6.069E-02
4	2.173E-02	5.593E-03
5	1.961E-03	6.872E-04
6	1.025E-04	6.734E-05
7	4.923E-06	6.413E-06
8	2.679E-07	6.155E-07
9	1.452E-08	8.288E-08
10	1.893E-09	1.923E-08
11	1.633E-10	1.214E-09

Notes:

1. Includes 20% required Appendix K uncertainty.
2. Assumes 200 MeV/fission total recoverable energy.

Table 9-4 ANSI/ANS 5.1-1971			
Decay Heat Standard for U-235 Thermal Fission			
TimeAfter Trip	WCOBRA/TRAC-TF2 (MeV/fission)	Standard (MeV/fission)	Δ%
0.1	16.549	16.766	-1.29
1	14.458	14.472	-0.094
10	12.095	12.118	-0.186
20	10.757	10.689	+0.632
40	9.409	9.429	-0.213
100	8.018	7.964	+0.675
200	6.869	6.899	-0.446
400	5.674	5.725	-0.888
1000	4.479	4.417	+1.39

a,c

Table 9-5 Typical Normalized Interaction Frequency Fit Data	

Table 9-6 Actinide Heat Source Data			
Isotope	q(MeV)	α(MeV/Sec/Capture)	λ (Sec^{-1})
U-239	0.474	2.32834E-4	4.91E-4
Np-239	0.419	1.42879E-6	3.41E-6

Table 9-7 Typical Radiation Source Timing, Strength, and Range

WCOBRA/TRAC-TF2 Energy Category	Radiation Type	Timing	Energy (MeV)	Range
Fission[1]	Fragments	Prompt	161.0	Very Short
Fission	Direct Gamma	Prompt	5.0	Long
Fission[2]	Capture Gamma	Prompt	–5.0	Long
Fission	Neutron	Prompt	5.0	Medium
Fission	Neutron	Delayed	0.04	Medium
Fission Fragment Decay[3]	Gamma	Delayed	6.5	Long
Fission Fragment Decay	Beta	Delayed	6.5	Short
Actinide Decay	Gamma	Delayed	0.4	Long
Actinide Decay	Beta	Delayed	0.4	Short

Notes:

1. Typical prompt fission energy source taken from "Nuclear Heat Transport," M. M. El-Wakil, American Nuclear Society, 1978.
2. Typical BOL capture gamma energy source.
3. Typical BOL decay heat source representative of ANSI/ANS 5.1-1979.

Table 9-8 Typical Values for Redistribution Fraction Values

a,c

Table 9-9 Neutron Heating Transfer Model

a,c

Table 9-10 Gamma Photon Energy Spectrum

a,c

Table 9-11 BUGLE-80 Gamma Kerma Data[1]

a,c

Table 9-12 Typical 15x15 GEDM Gamma Transfer Matrix

a,c

[

]a,c

a,c

Table 9-13 [ ]^{a,c}

Table 9-14 Decay Group Uncertainty Factors Per One Sigma (%)

Decay Group	U-235	Pu-239	U-238
1	20.00	30.00	12.00
2	18.00	25.00	14.00
3	3.90	7.00	19.50
4	3.10	4.60	19.80
5	2.60	4.20	20.20
6	2.25	3.90	11.20
7	1.95	3.80	6.80
8	1.85	4.00	5.70
9	1.75	4.00	5.50
10	1.70	4.20	5.30
11	1.65	4.50	5.10
12	1.65	4.50	5.00
13	1.80	4.90	4.70
14	2.00	5.00	3.80
15	2.00	5.00	3.40
16	2.00	5.00	3.60
17	2.00	5.00	3.90
18	2.00	5.00	4.70
19	2.00	5.00	5.00
20	2.00	5.00	5.00
21	2.00	5.00	5.00
22	2.00	5.00	5.00
23	2.00	5.00	5.00

Note:

1. Above table quotes percent uncertainty by group for one-sigma uncertainty values from ANSI/ANS 5.1-1979. Two sigma values can be obtained by doubling the table values above.

Table 9-15 Point Reactor Kinetics Validation			
WCOBRA/TRAC-TF2		Inhour Solution[2]	
Δρ (pcm)	T(sec)[1]	Δρ (pcm)	T(sec)
-30000	-80.707	-30027.1	-80.77
+300	+9.147	+300.002	+9.147
+150	+34.14	+150.001	+34.14

Notes:

1. Observed asymptotic period.
2. Data for each solution given below.

Group	Beta	Lambda
1	3.5410E-04[1]	3.00
2	1.0104E-03	1.13
3	2.9479E-03	0.301
4	1.4271E-03	0.111
5	1.5313E-03	0.0305
6	2.2920E-04	0.0124

Notes:

ℓ = 16.06 μs, $\bar{\beta}$ = 0.0075

1. Read as 3.541×10^{-4}.

Table 9-16 Actinide Isotope Nuclear Data

a,c

Table 9-17 Prompt Fission Energy Release Data

a,c

Table 9-18 [ ][a,c]

a,c

a,c

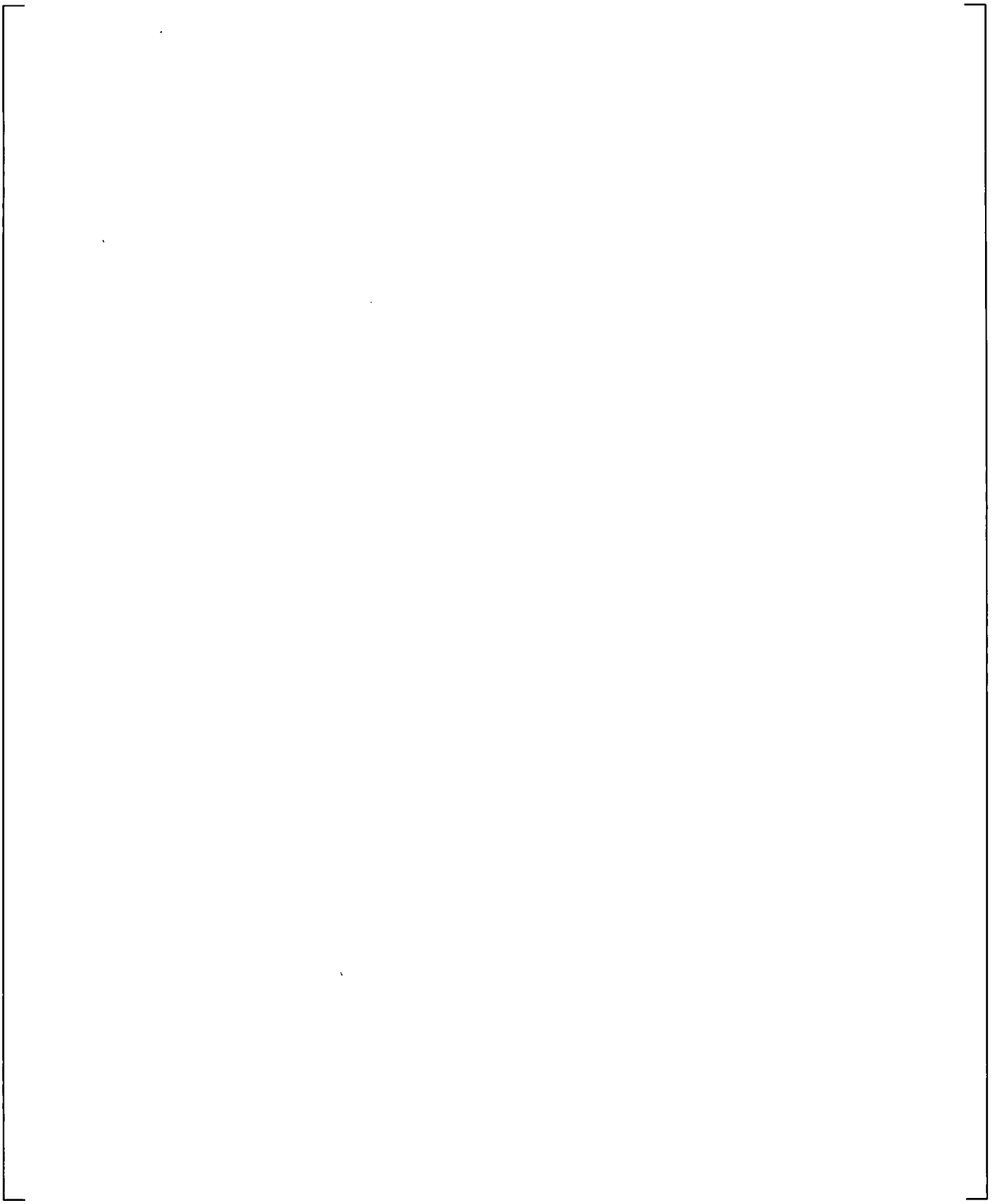

Figure 9-1 U-235 Fission Fraction

a,c

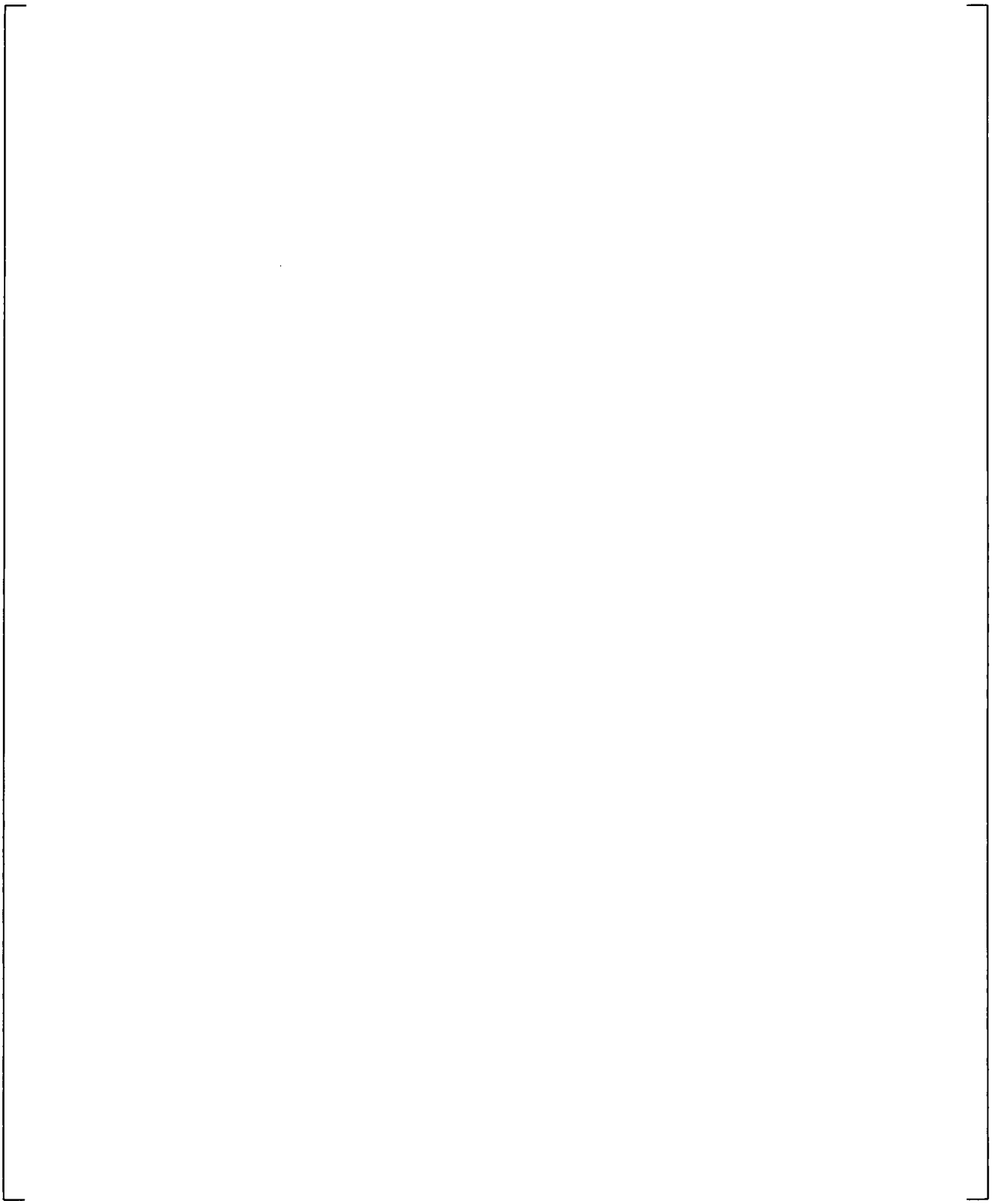

Figure 9-2 Pu-239 Fission Fraction

a,c

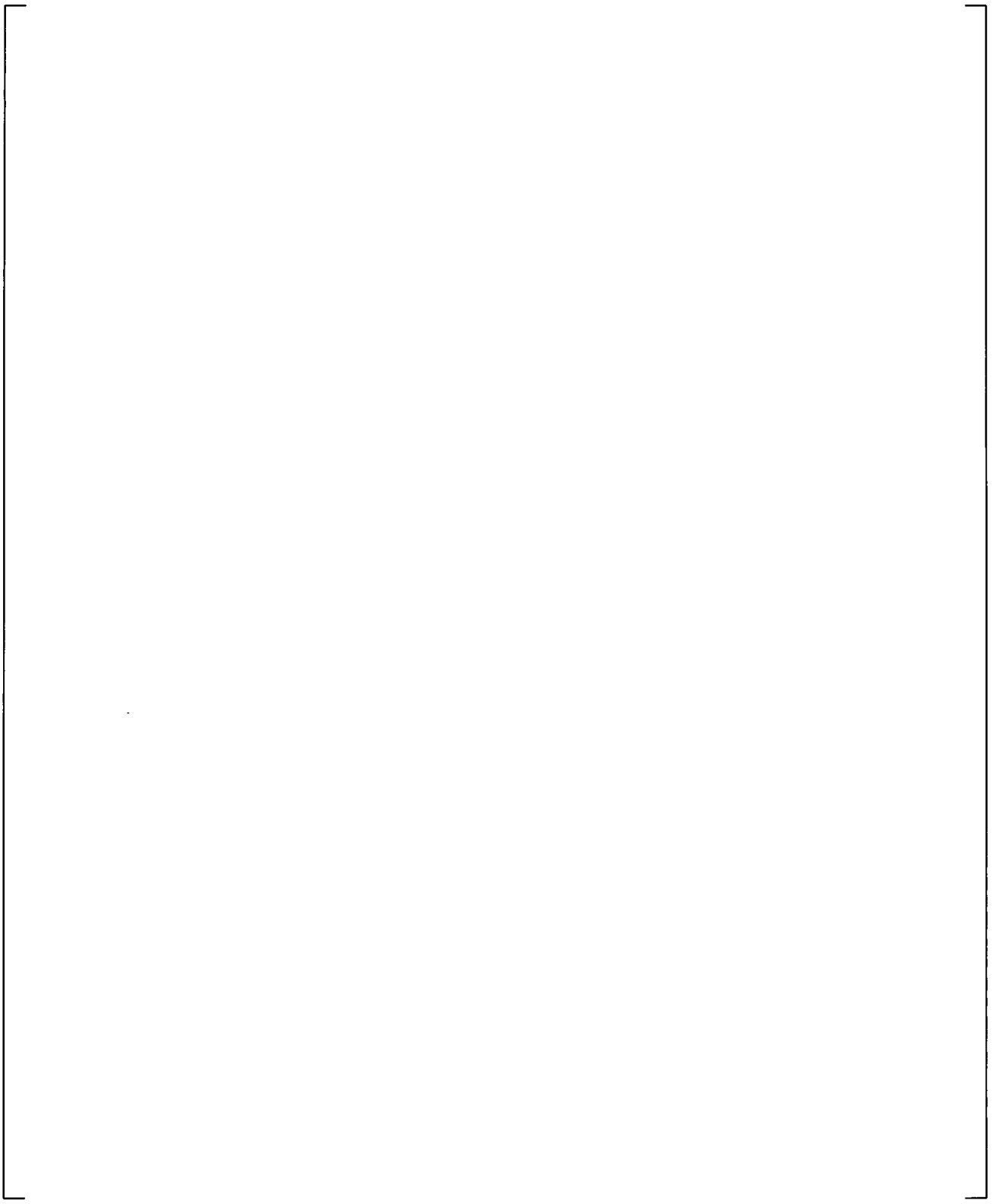

Figure 9-3 U-238 Fission Fraction

a,c

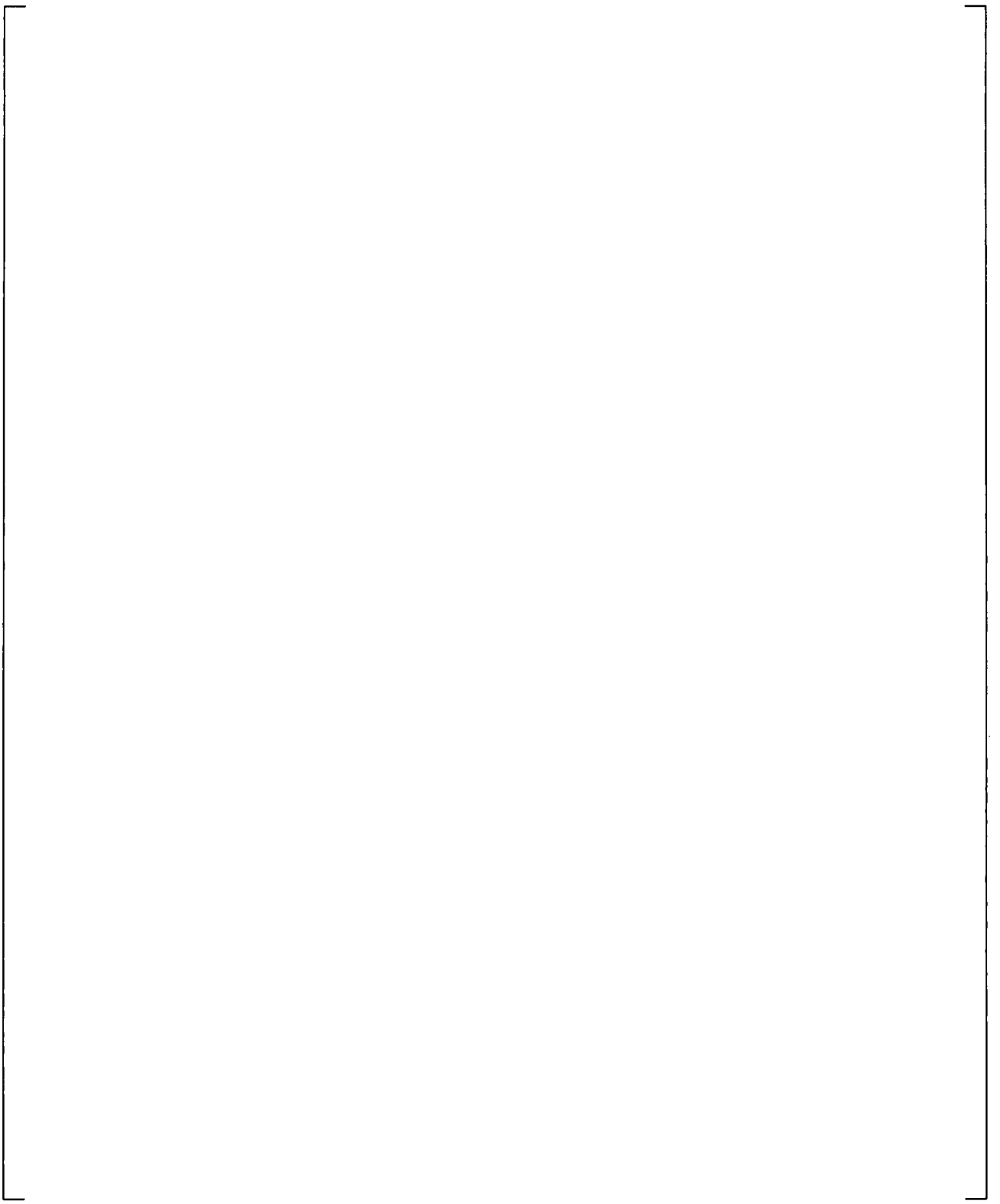

Figure 9-4 Calculated Normalized Macroscopic Cross Sections Versus Core Average Water Density

a,c

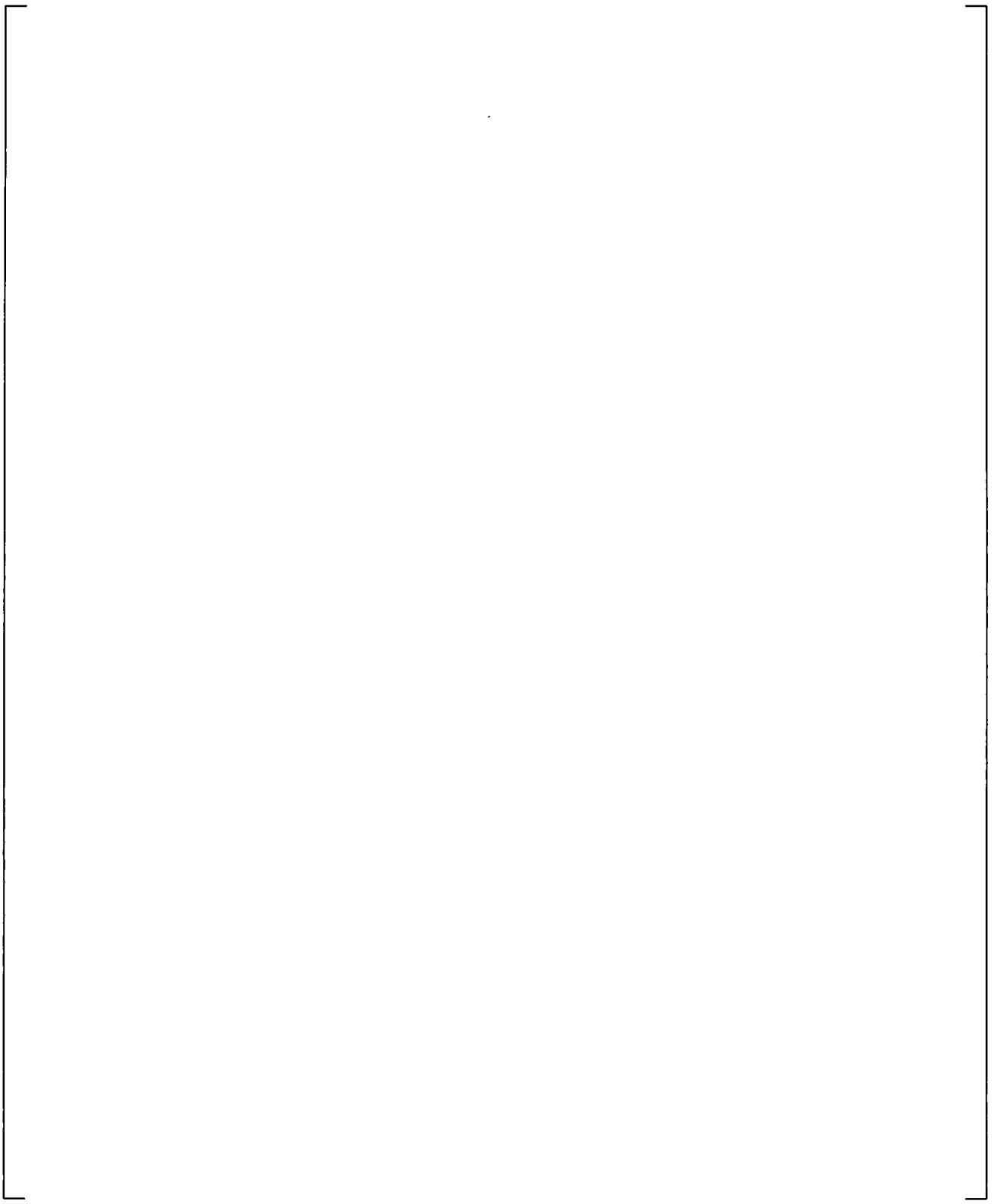

Figure 9-5 $\bar{\beta}$ vs. Burnup at Various Enrichments

a,c

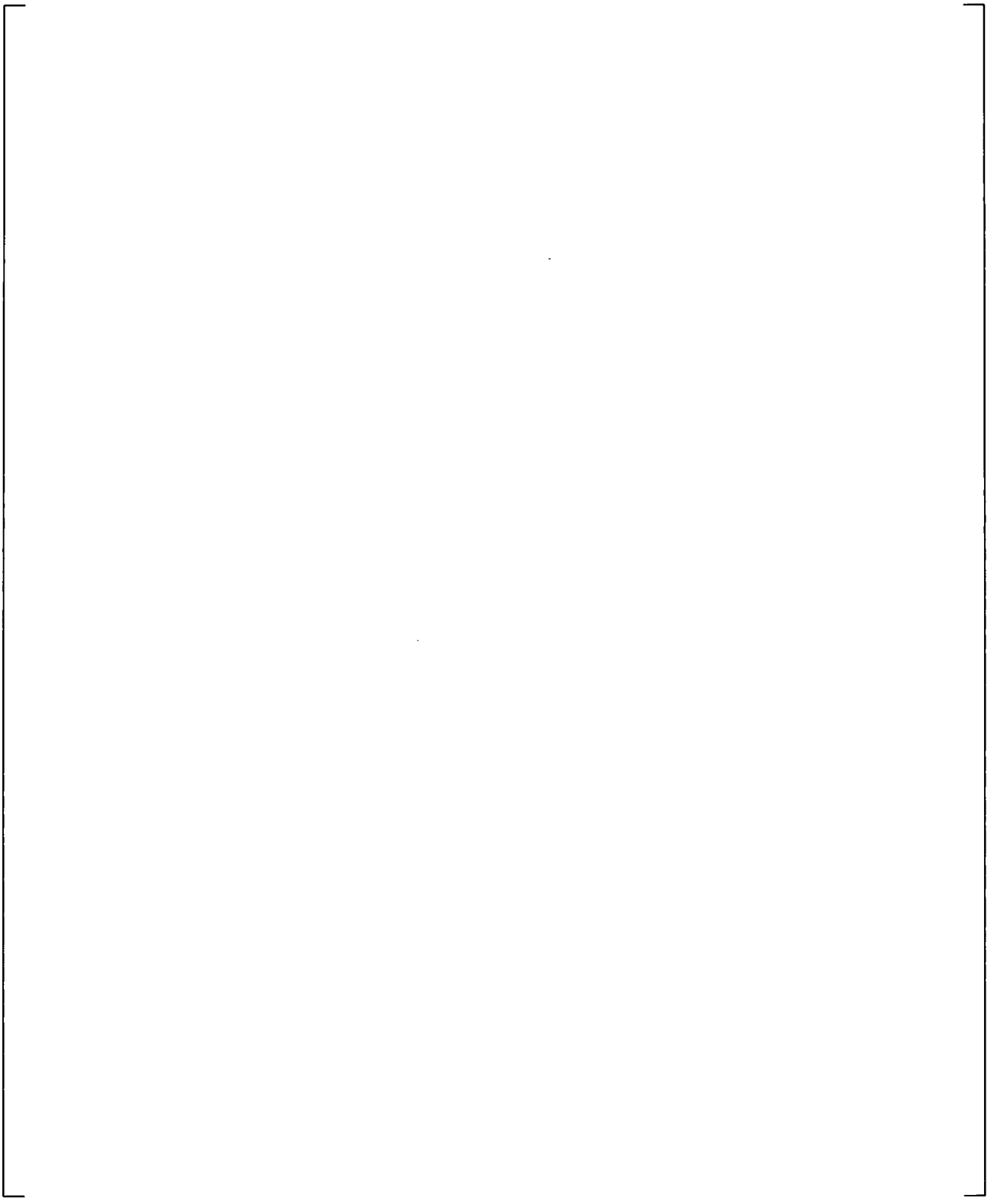

Figure 9-6 Prompt Neutron Lifetime

a,c

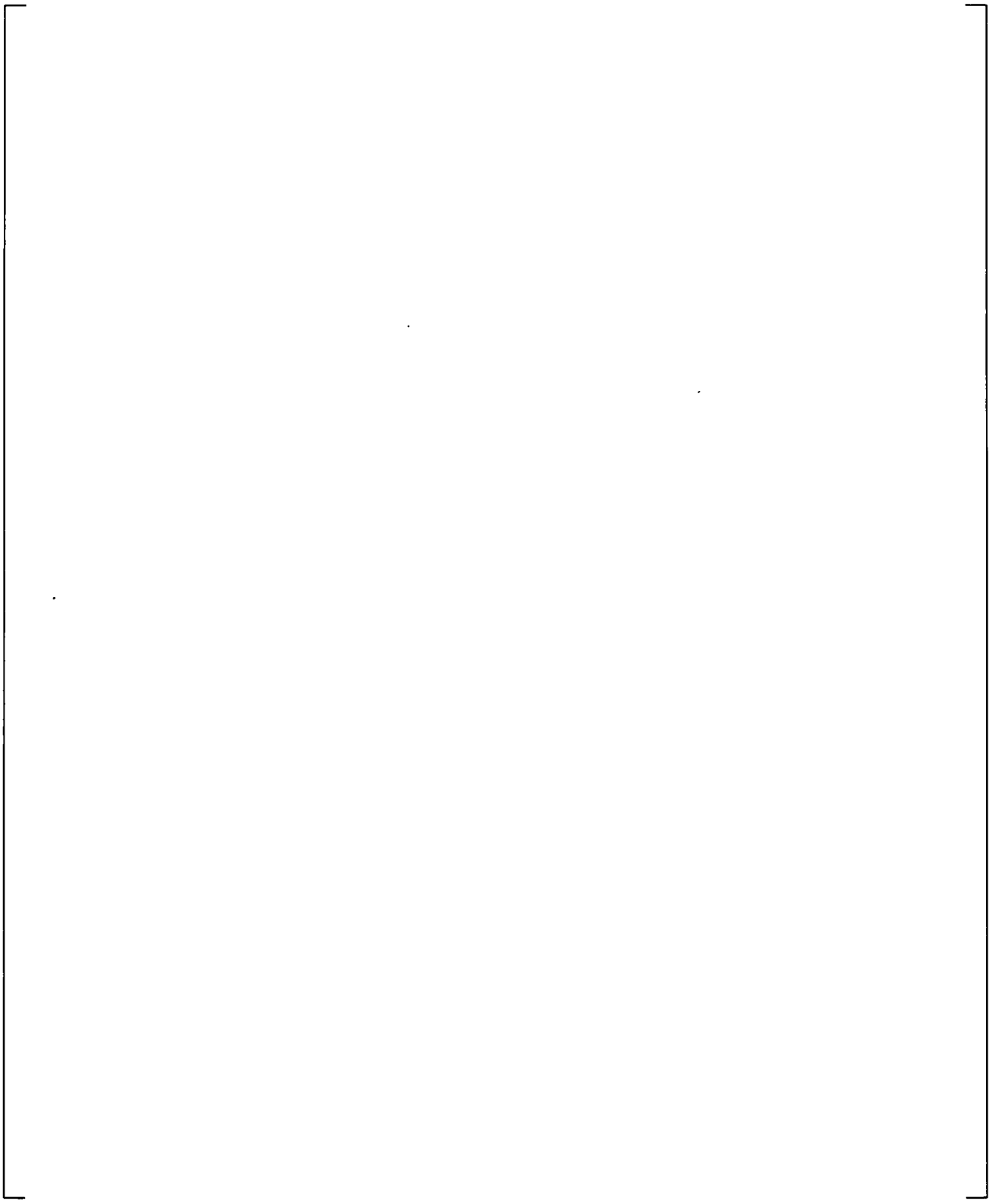

Figure 9-7 Prompt Energy Release

a,c

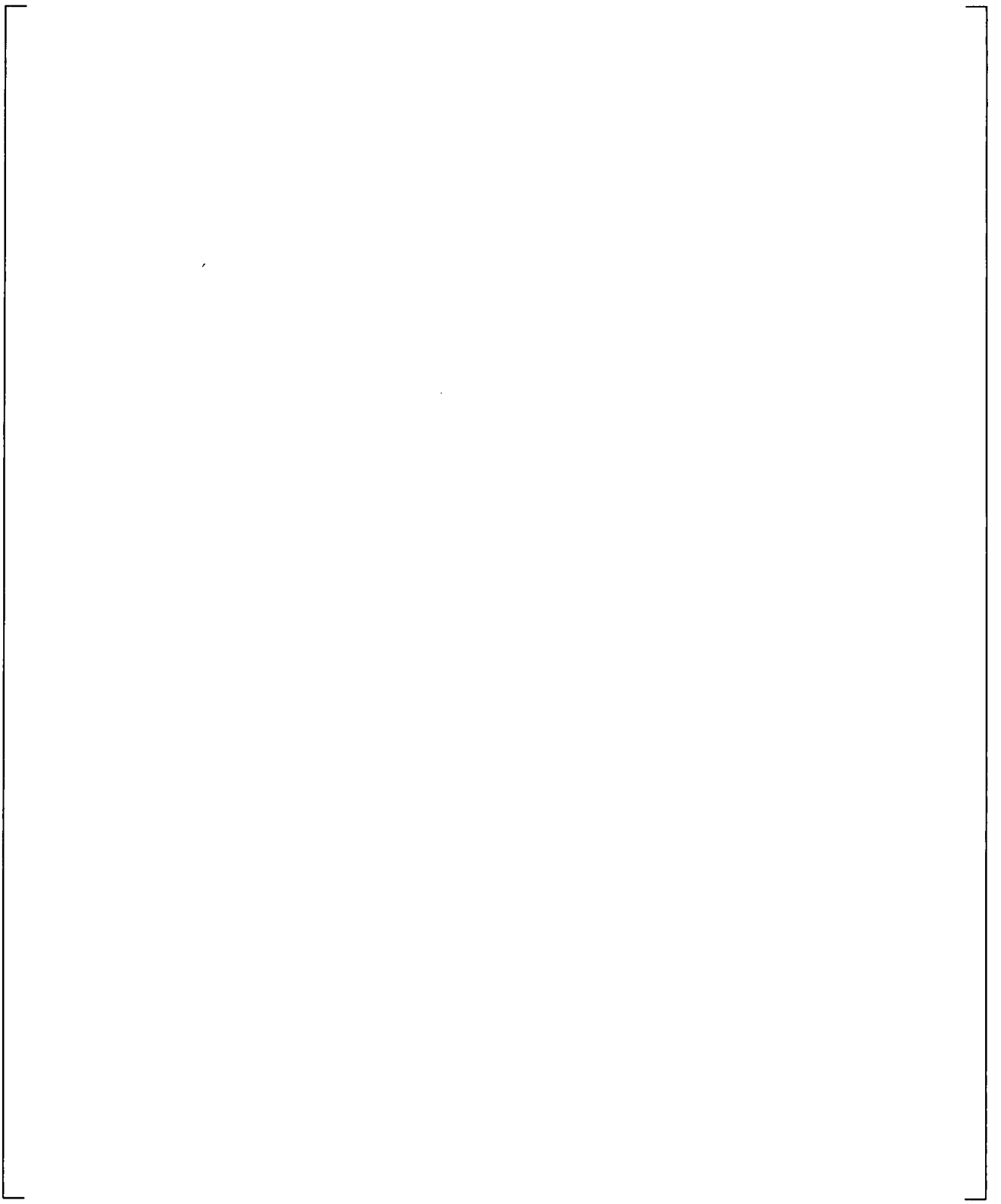

Figure 9-8 Total Energy Release

a,c

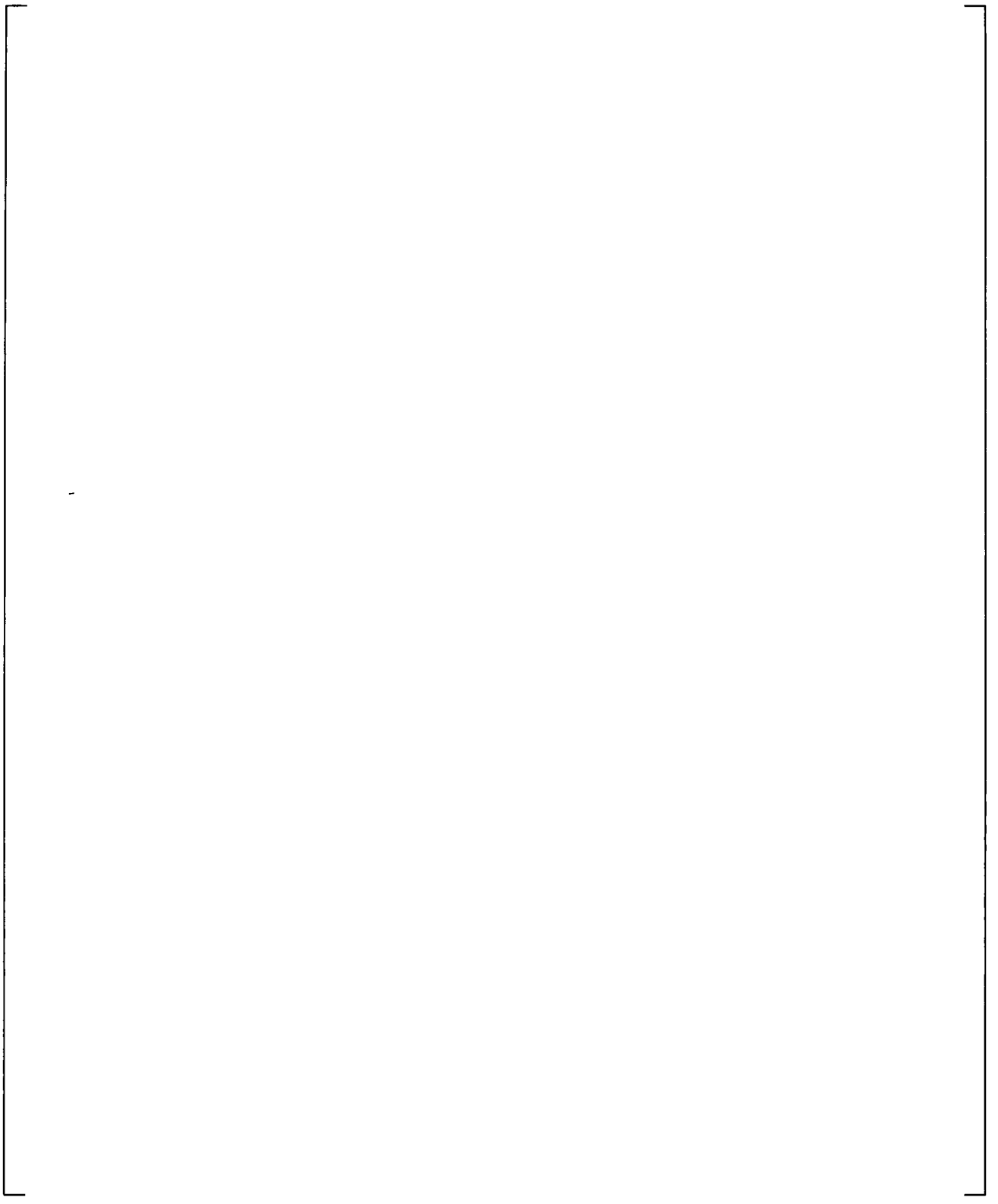

Figure 9-9 Delayed Group I Lambda

a,c

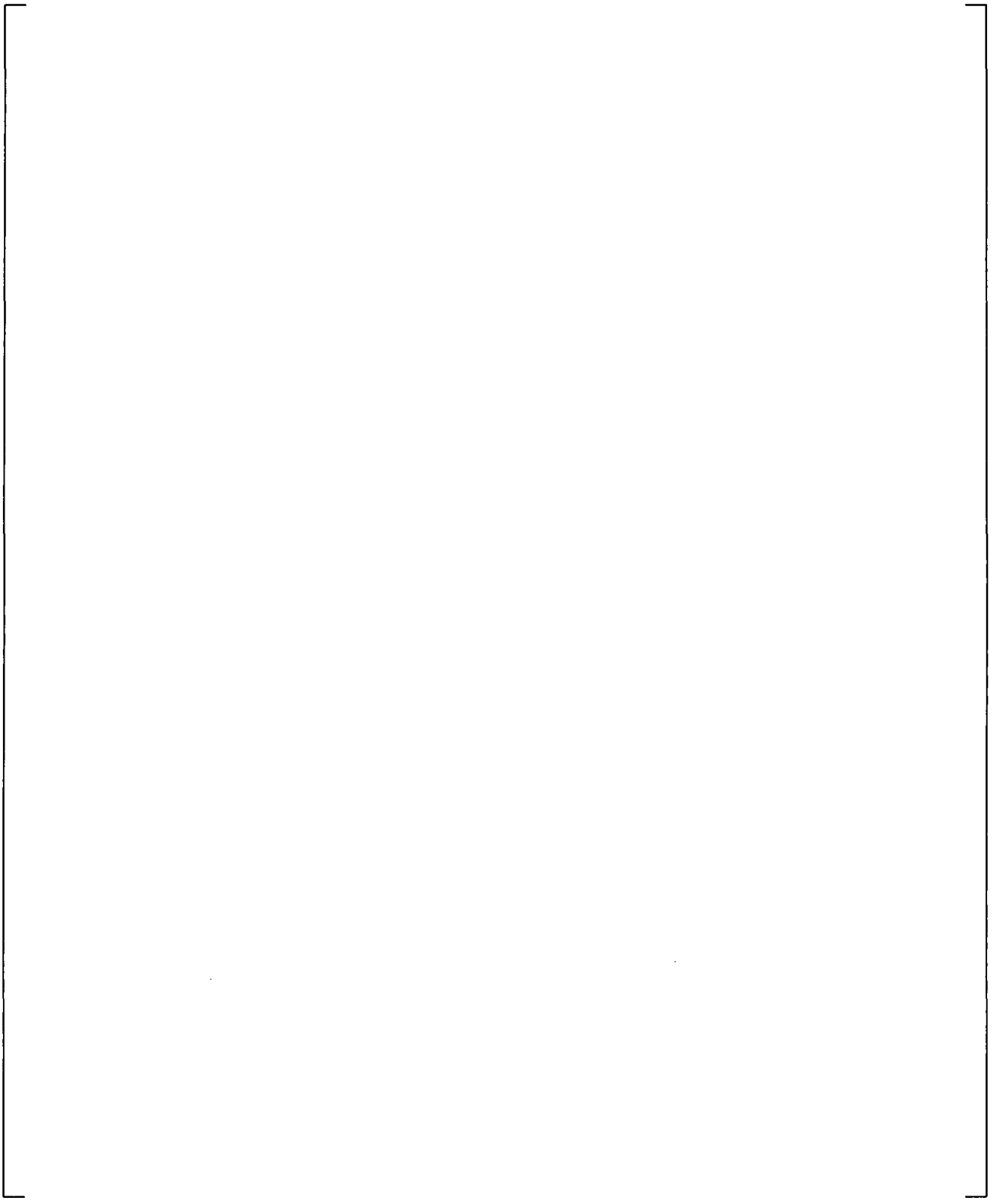

Figure 9-10 Delayed Group II Lambda

a,c

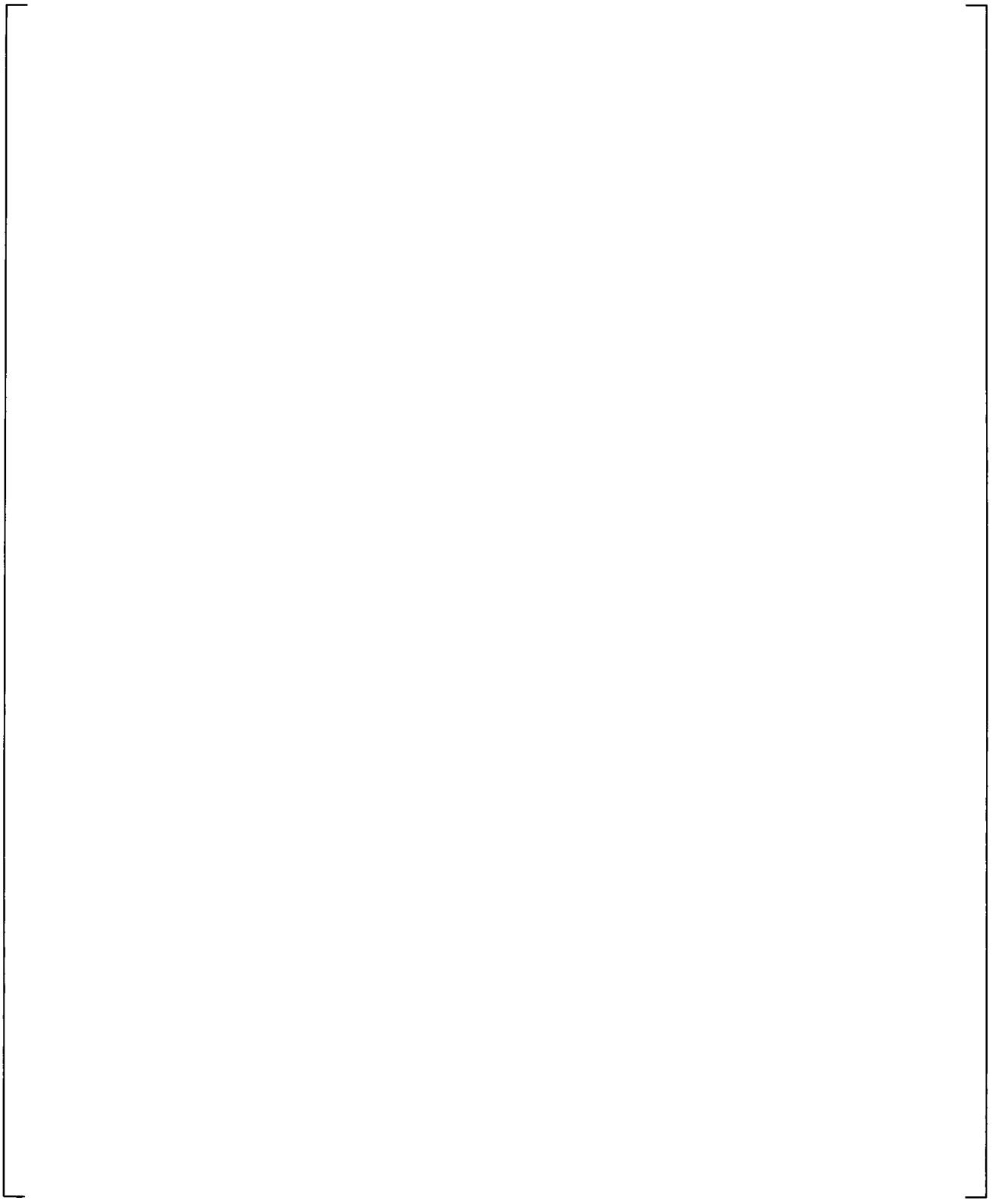

Figure 9-11 Delayed Group III Lambda

a,c

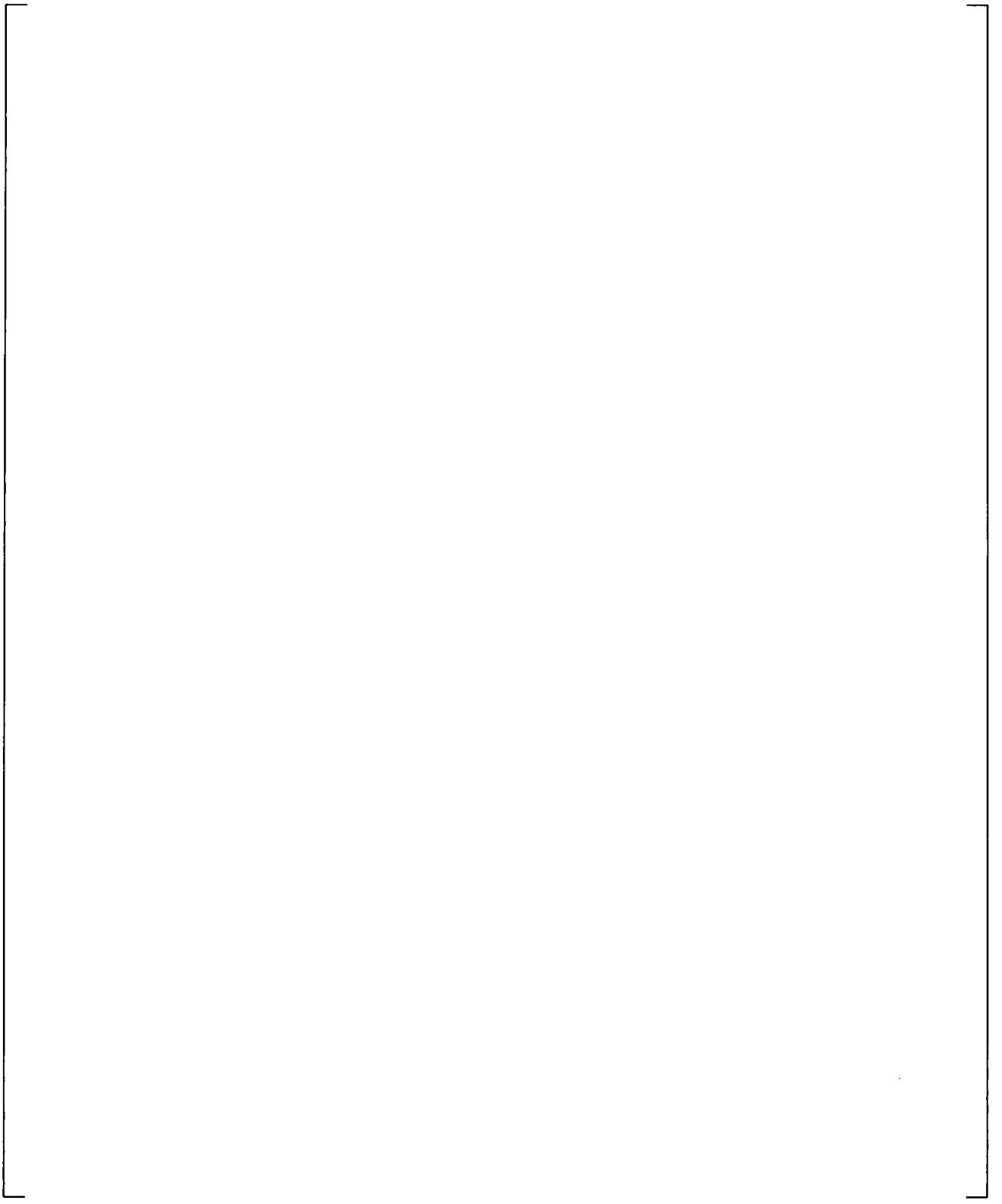

Figure 9-12 Delayed Group IV Lambda

a,c

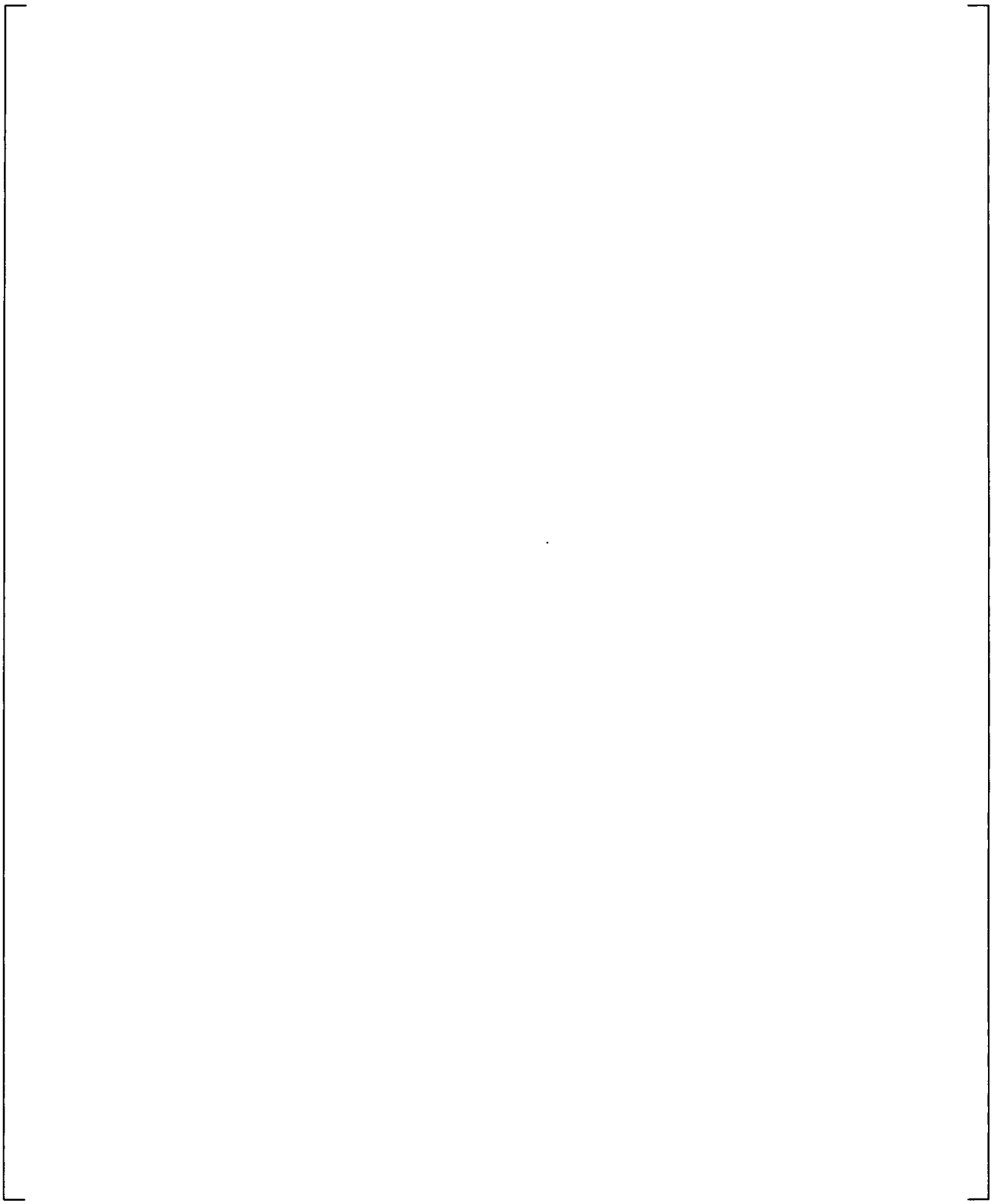

Figure 9-13 Delayed Group V Lambda

a,c

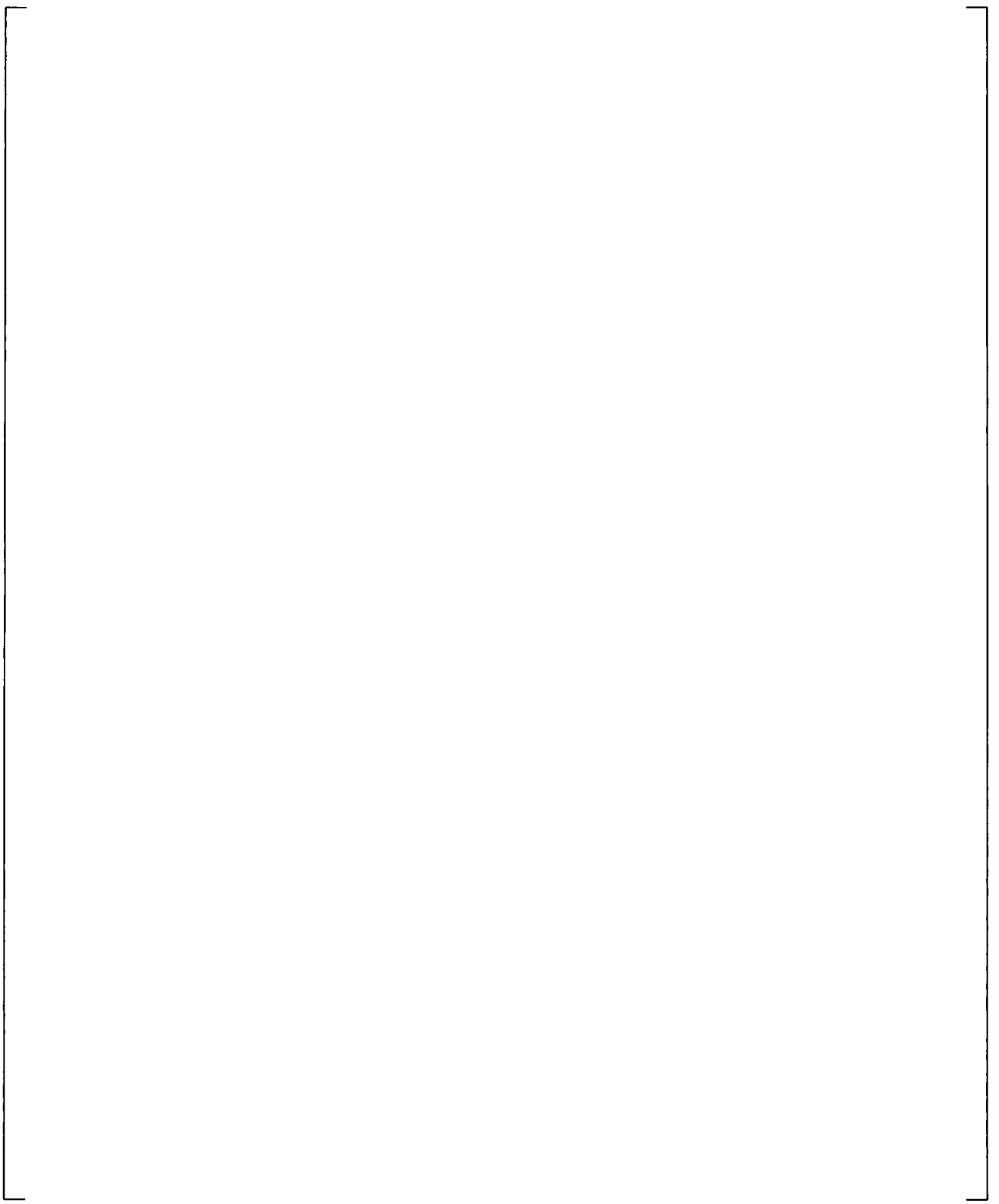

Figure 9-14 Delayed Group VI Lambda

a,c

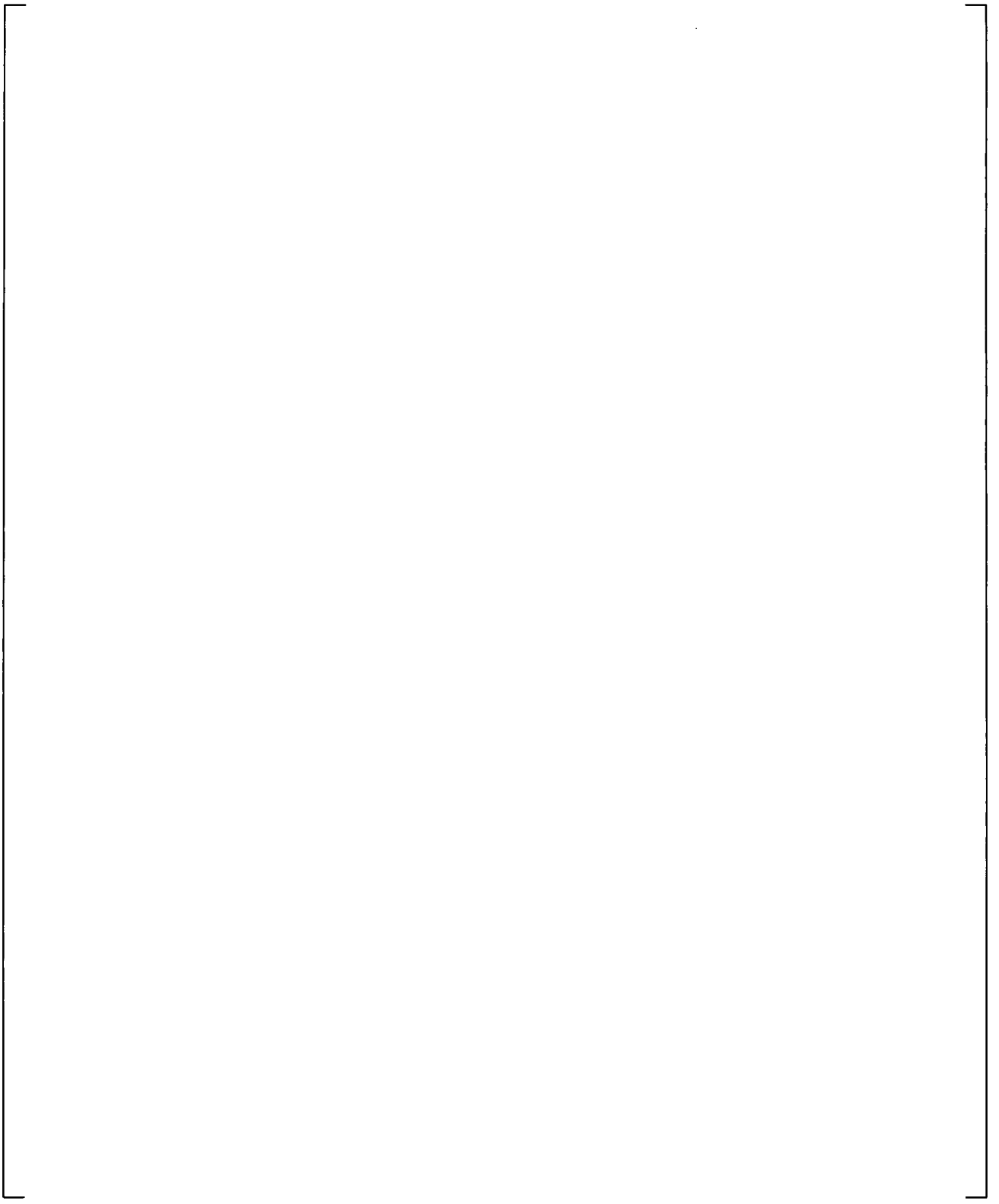

Figure 9-15 U-238 Capture/Fission Ratio as a Function of Initial Enrichment and Burnup

a,c

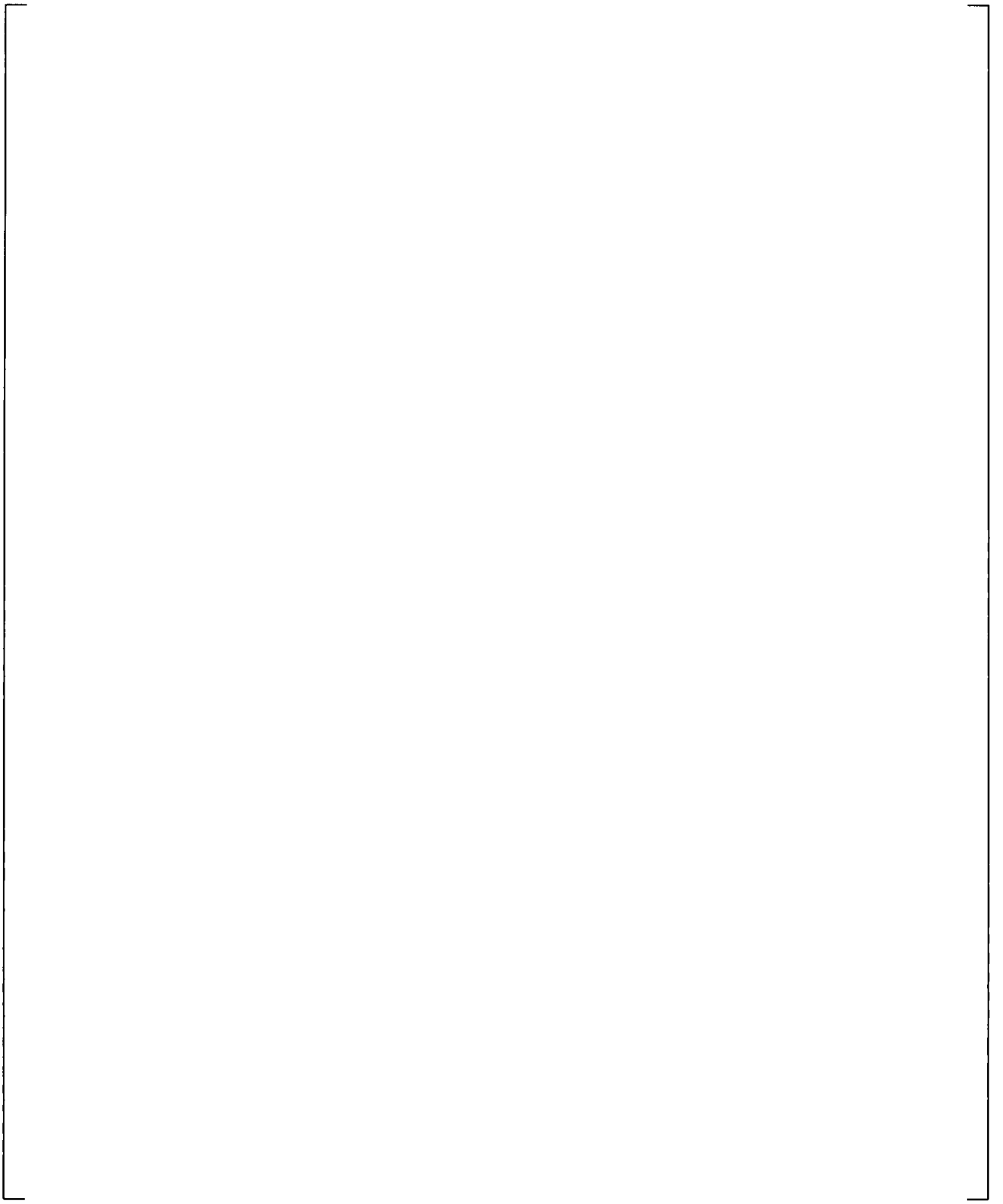

Figure 9-16 15x15 Material Composition Assignment Layout

a,c

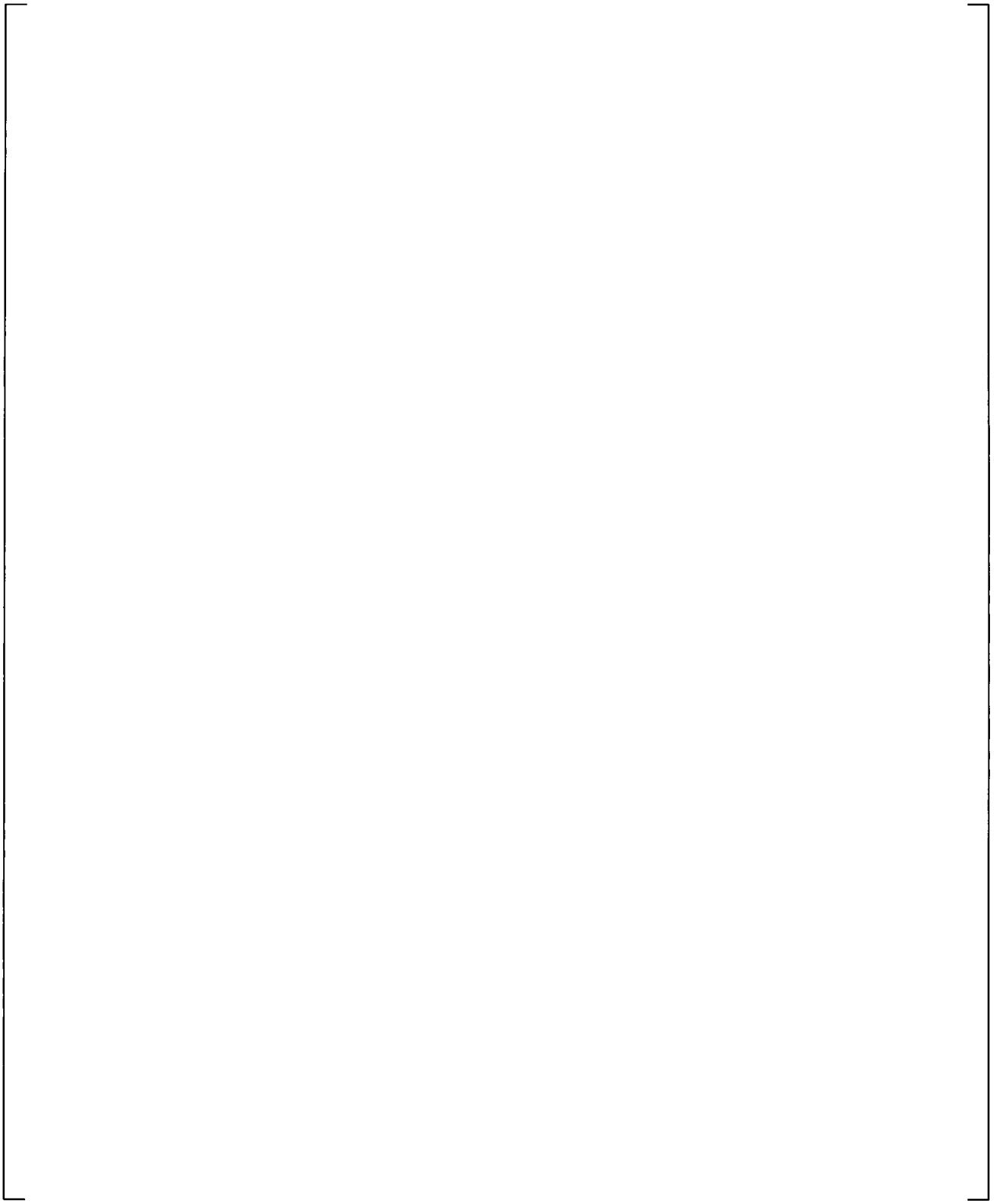

Figure 9-17 15x15 Core Balance Fixed Source Distribution

a,c

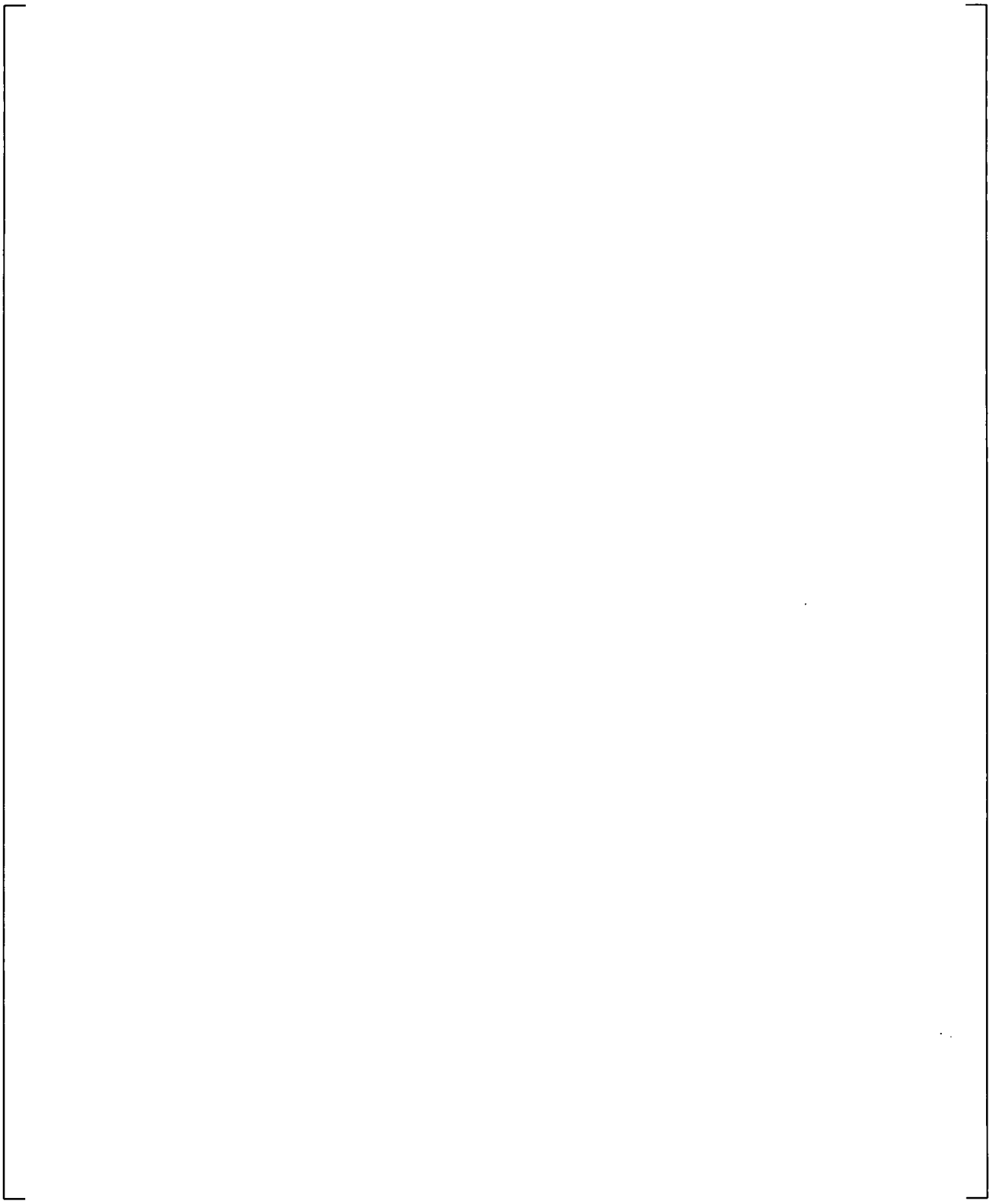

Figure 9-18 15x15 Hot Assembly Fixed Source Distribution

a,c

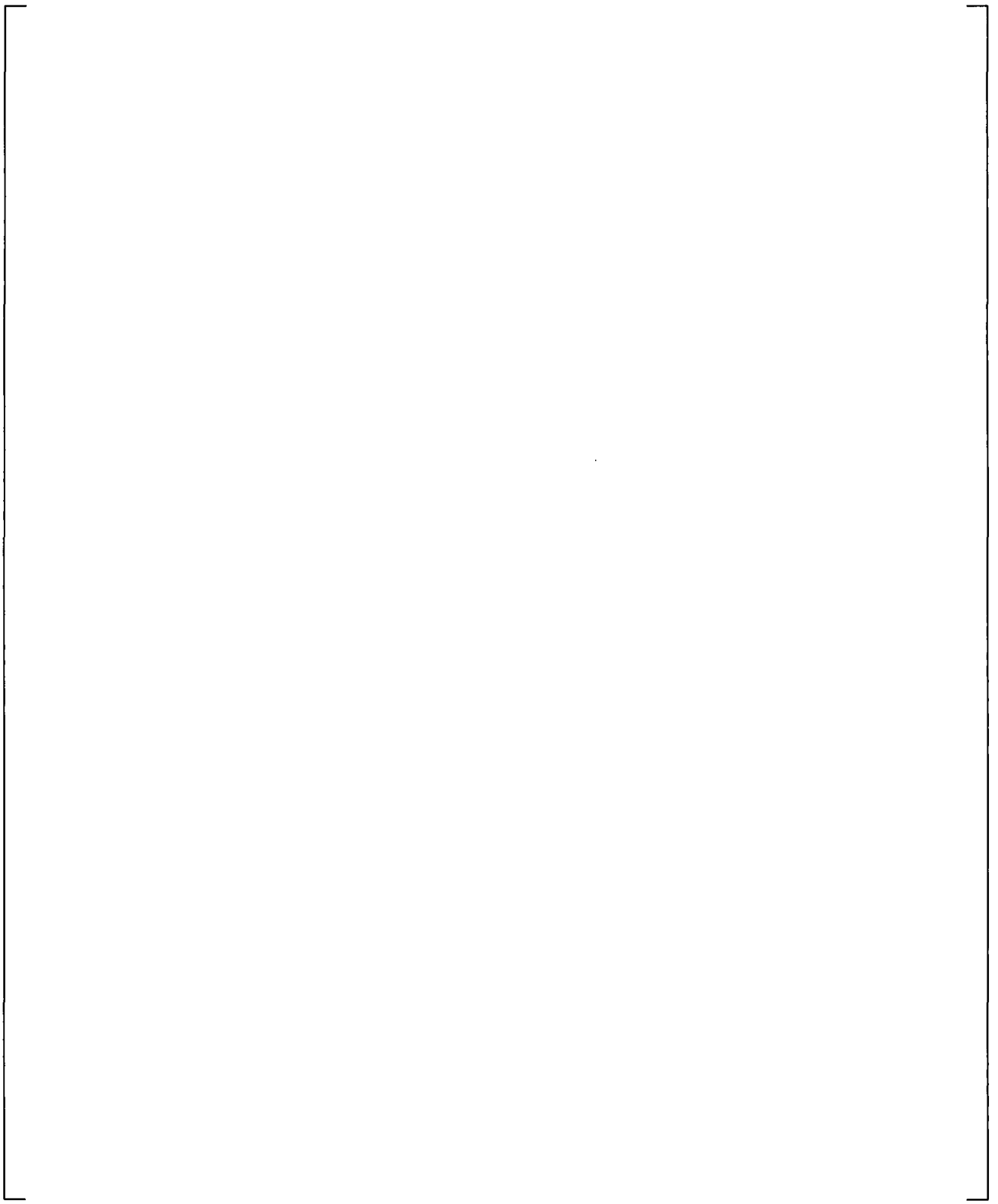

Figure 9-19 15x15 Hot Rod Fixed Source Distribution

a,c

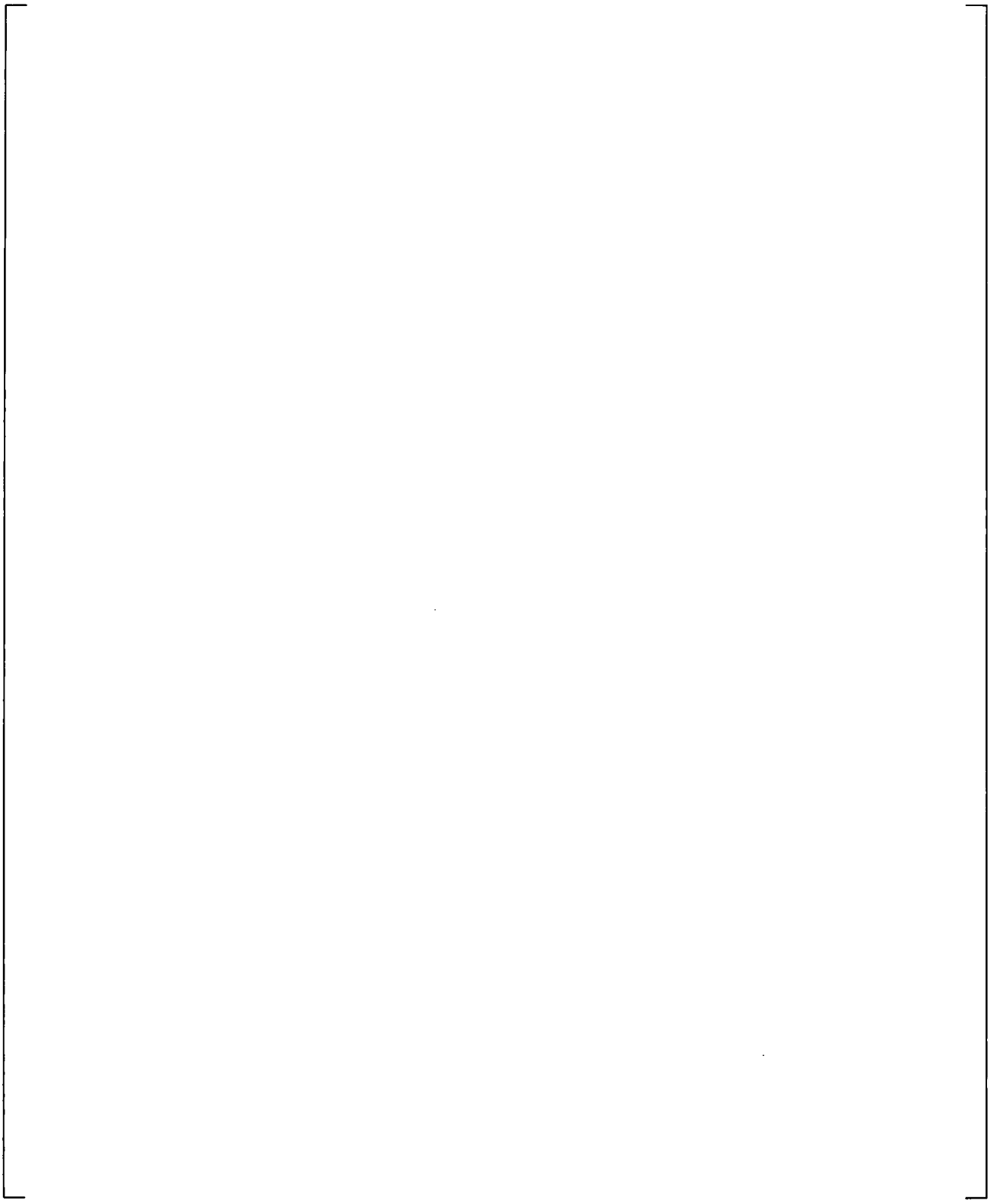

Figure 9-20 Gamma Kerma Cross Section Energy Dependence

a,c

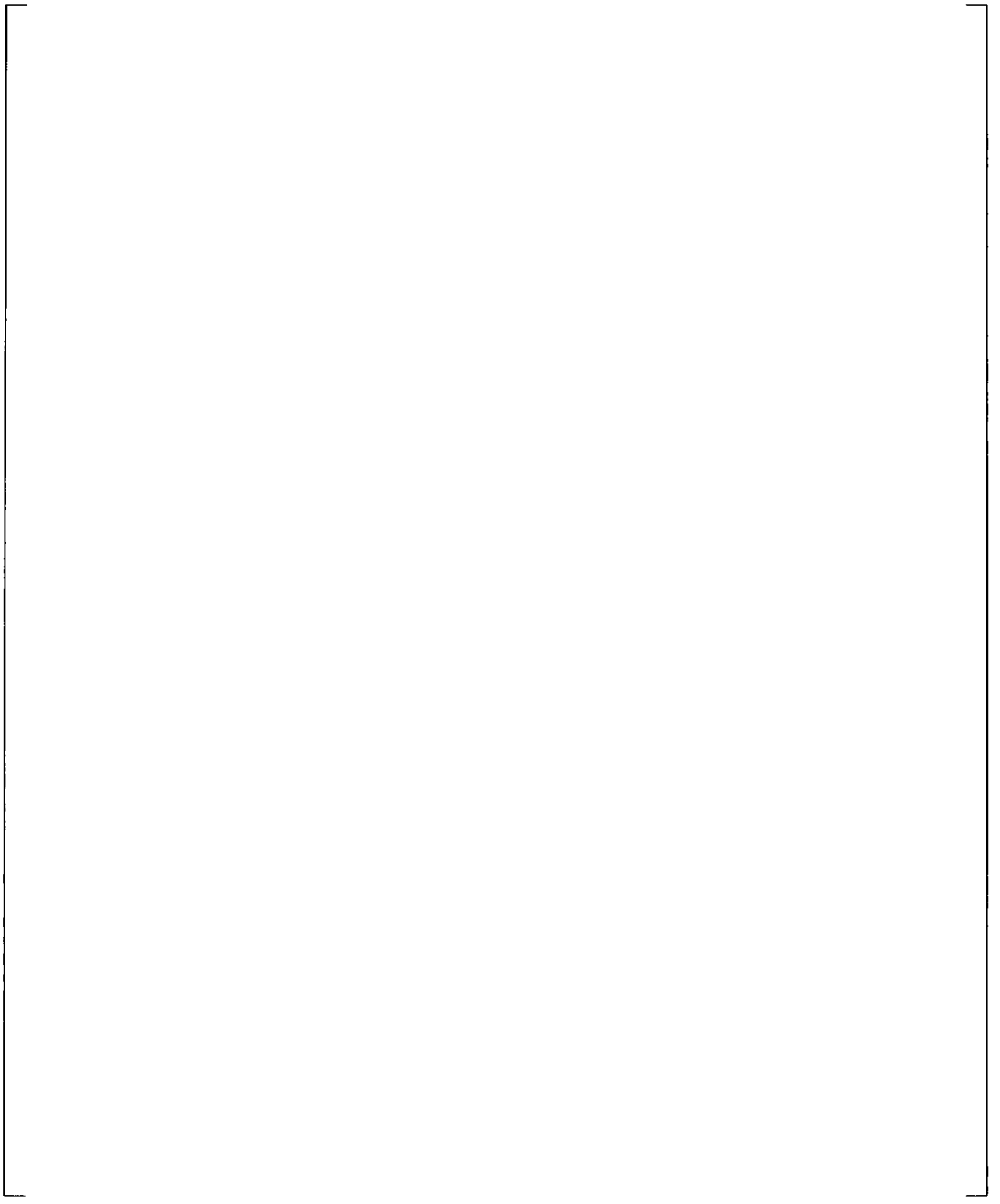

Figure 9-21 Typical Heat Flux Deposition Fractions versus Coolant Density

a,c

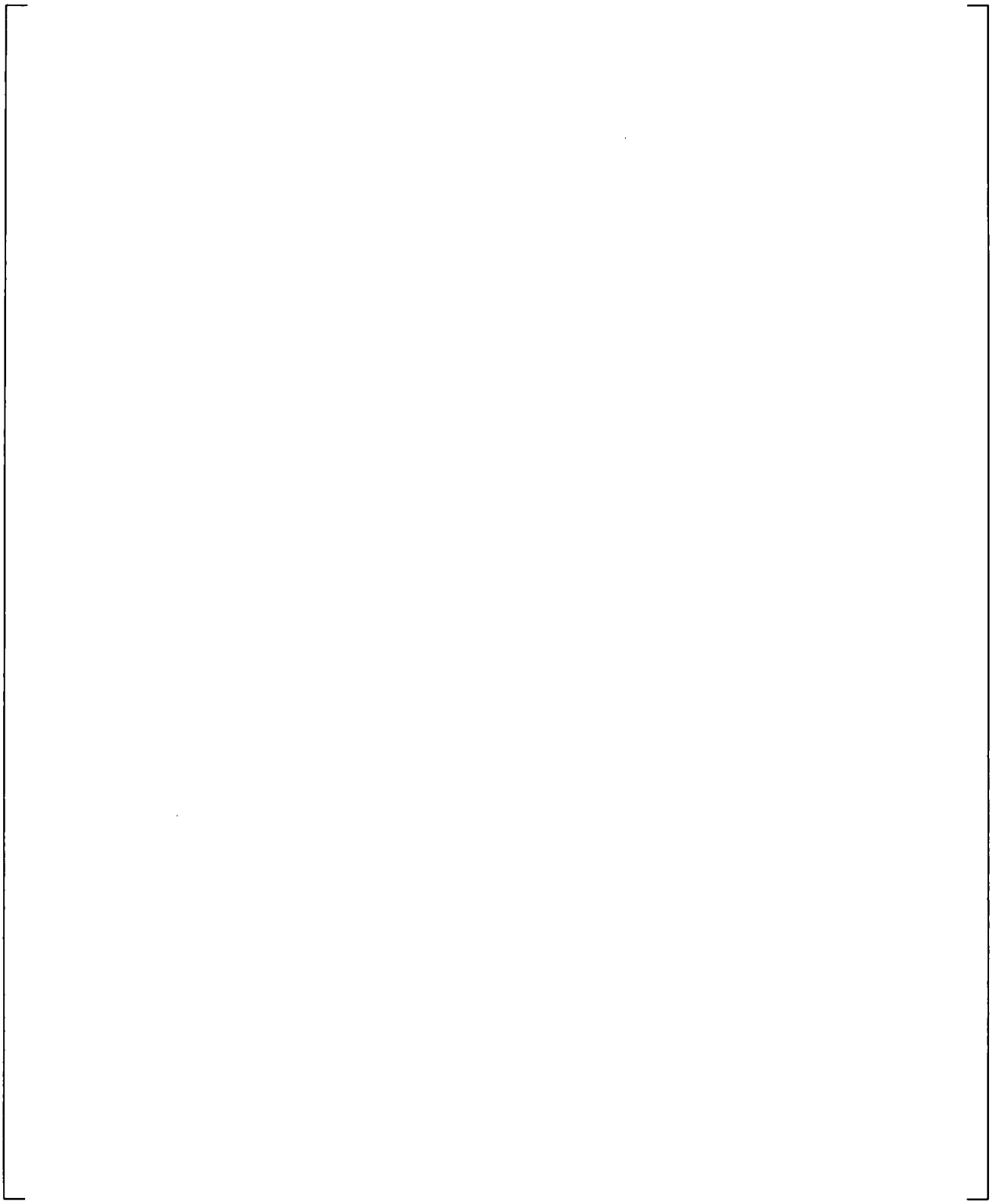

Figure 9-22 Typical Heat Flux Deposition Fractions versus Coolant Density

a,c

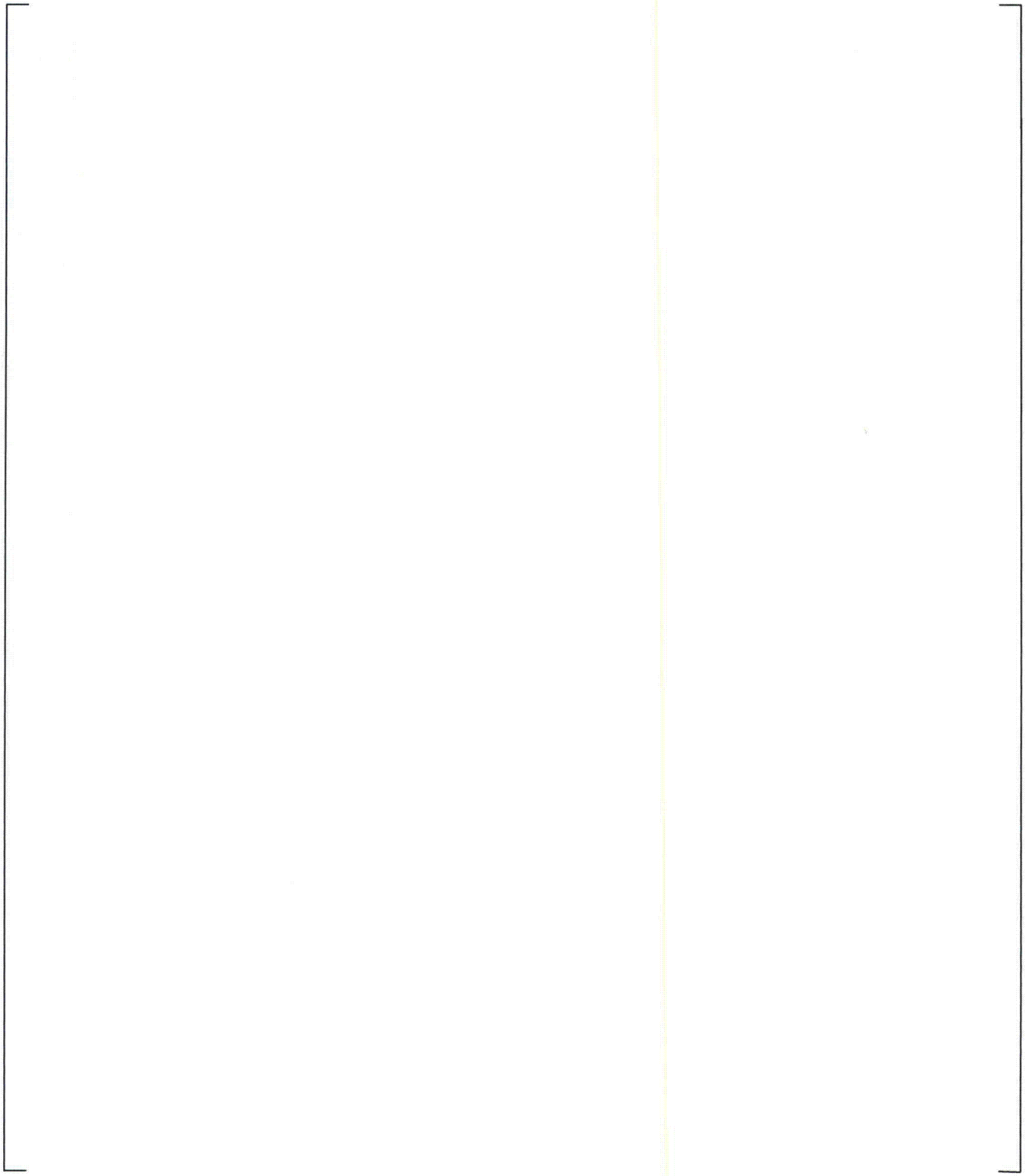

Figure 9-23 Comparison of Normalized Decay Heat Power Uncertainty Predictions for Thermal Fission of U-235 between ANSI/ANS 5.1 – 1979 Decay Heat Standard and WCOBRA/TRAC-TF2

a,c

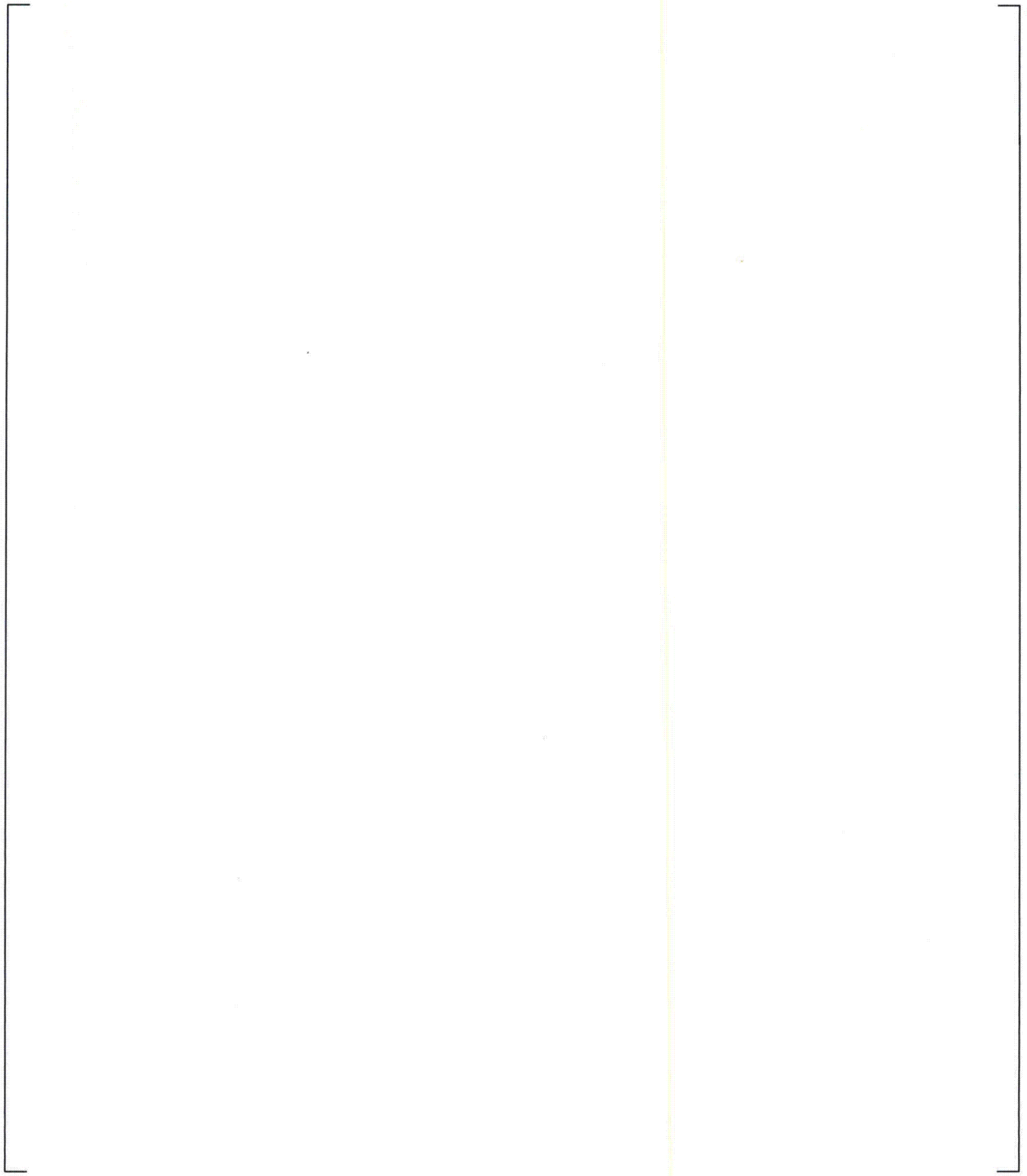

Figure 9-24 Comparison of Normalized Decay Heat Power Uncertainty Predictions for Thermal Fission of Pu-239 between ANSI/ANS 5.1 – 1979 Decay Heat Standard and WCOBRA/TRAC-TF2

a,c

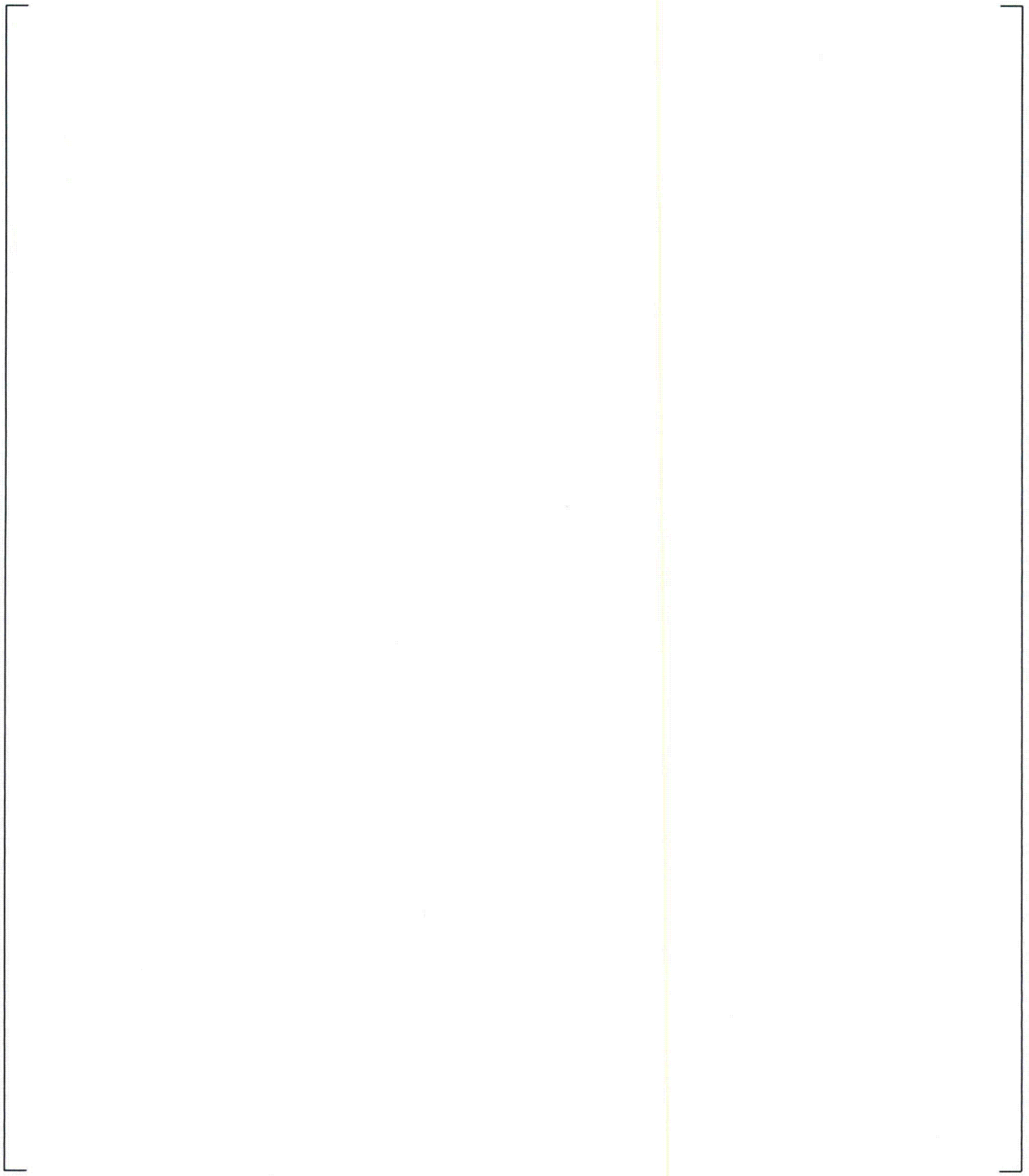

Figure 9-25 Comparison of Normalized Decay Heat Power Uncertainty Predictions for Fast Fission of U-238 between ANSI/ANS 5.1 – 1979 Decay Heat Standard and WCOBRA/TRAC-TF2

a,c

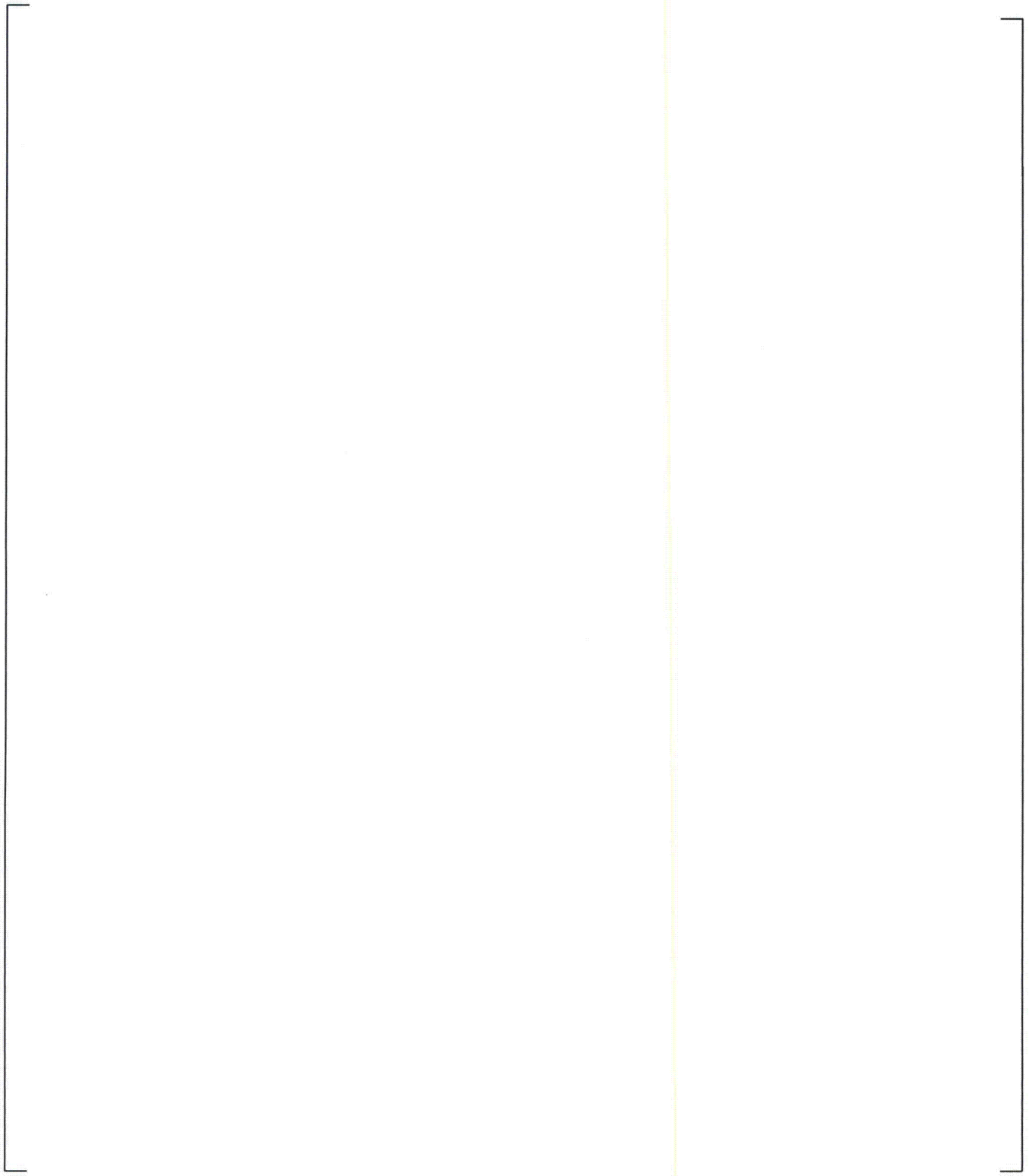

Figure 9-26 Comparison of Decay Heat Power Predictions by WCOBRA/TRAC-TF2 for Thermal Fission of U-235 with ANSI/ANS 5.1 – 1979 Decay Heat Standard

a,c

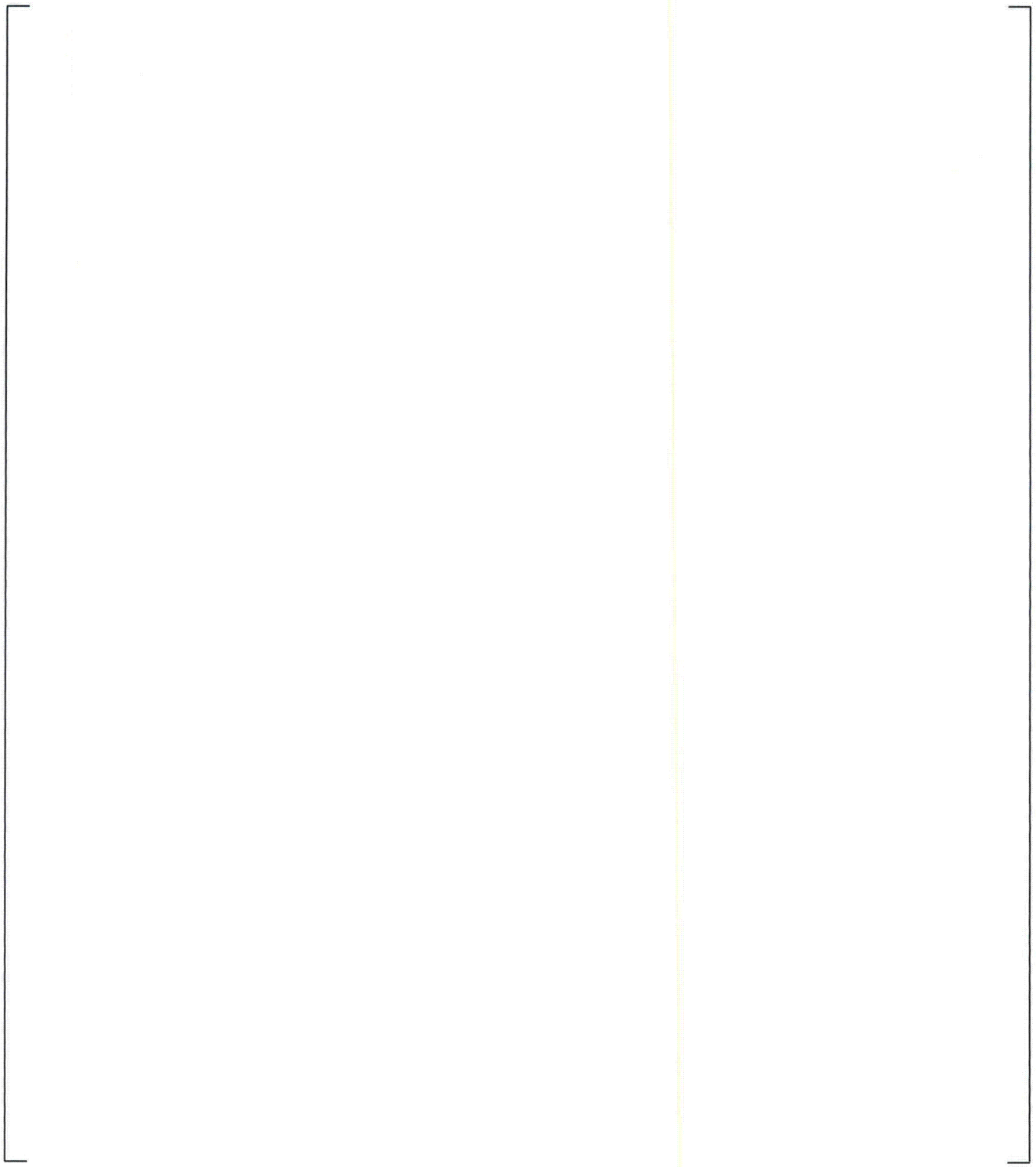

Figure 9-27 Comparison of Decay Heat Power Predictions by WCOBRA/TRAC-TF2 for Thermal Fission of Pu-239 with ANSI/ANS 5.1 – 1979 Decay Heat Standard

a,c

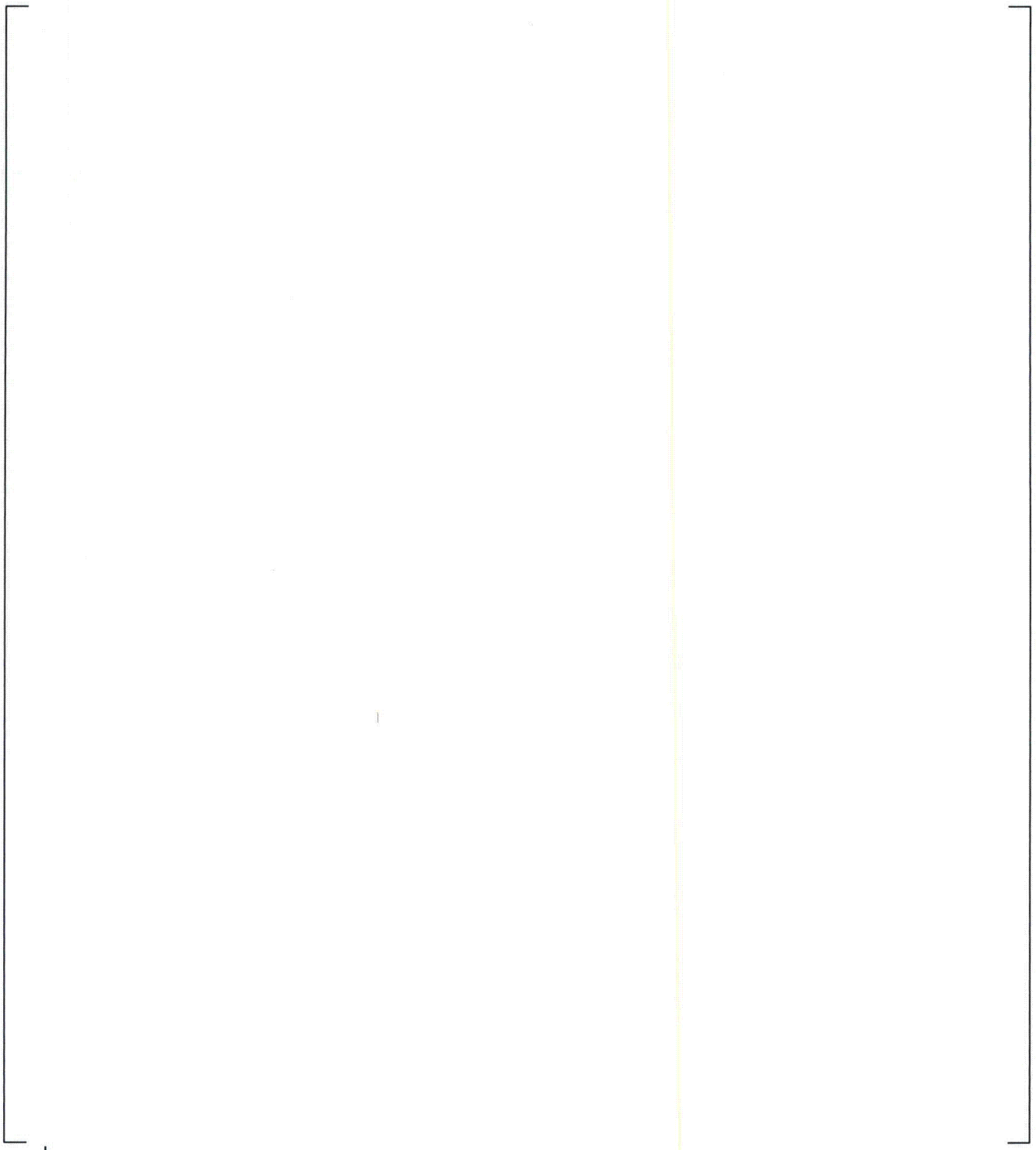

Figure 9-28 Comparison of Decay Heat Power Predictions by WCOBRA/TRAC-TF2 for Fast Fission of U-238 with ANSI/ANS 5.1 – 1979 Decay Heat Standard

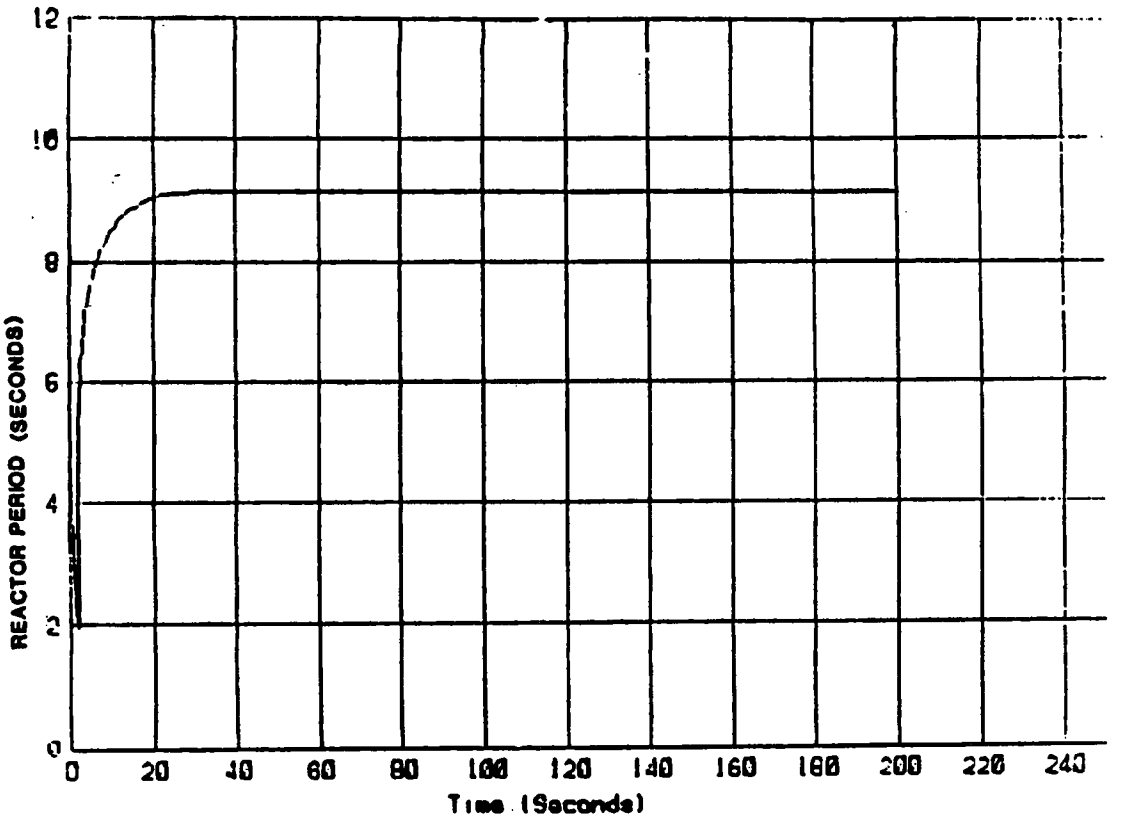

Figure 9-29 Time Dependent Reactor Period for + 0.003 ΔK Reactivity Insertion Versus Time After Insertion

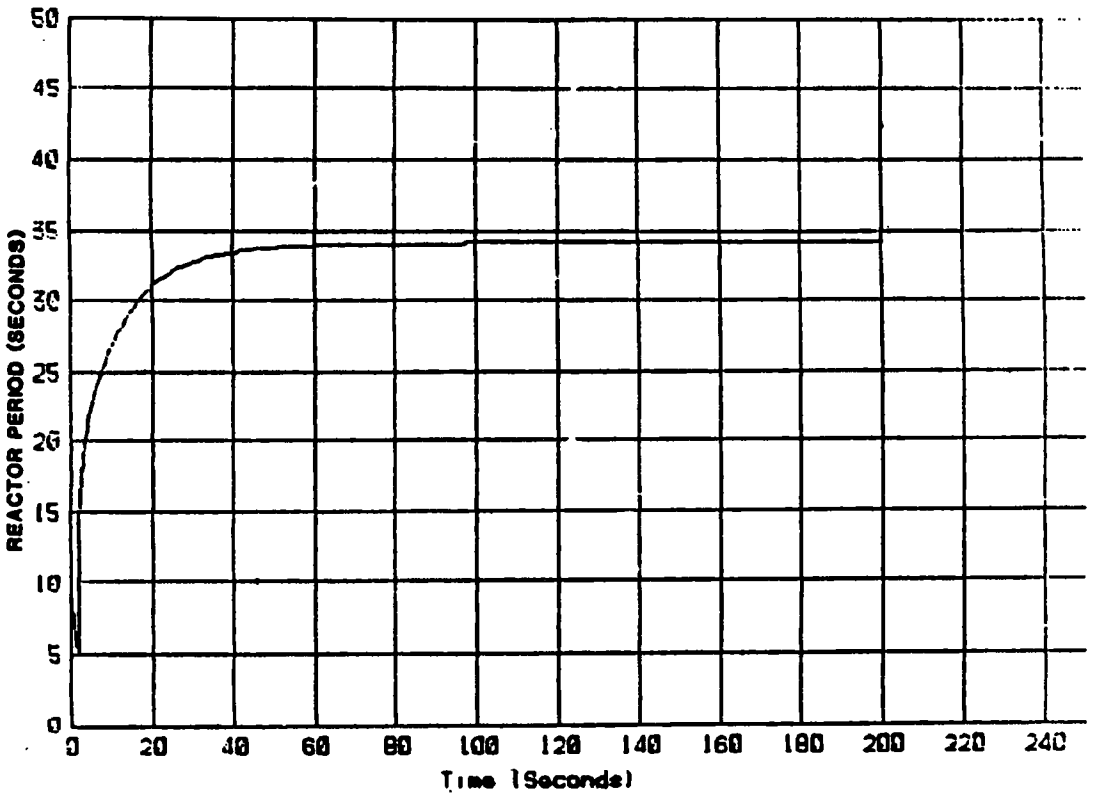

Figure 9-30 Time Dependent Reactor Period for + 0.0015 ΔK Reactivity Insertion Versus Time After Insertion

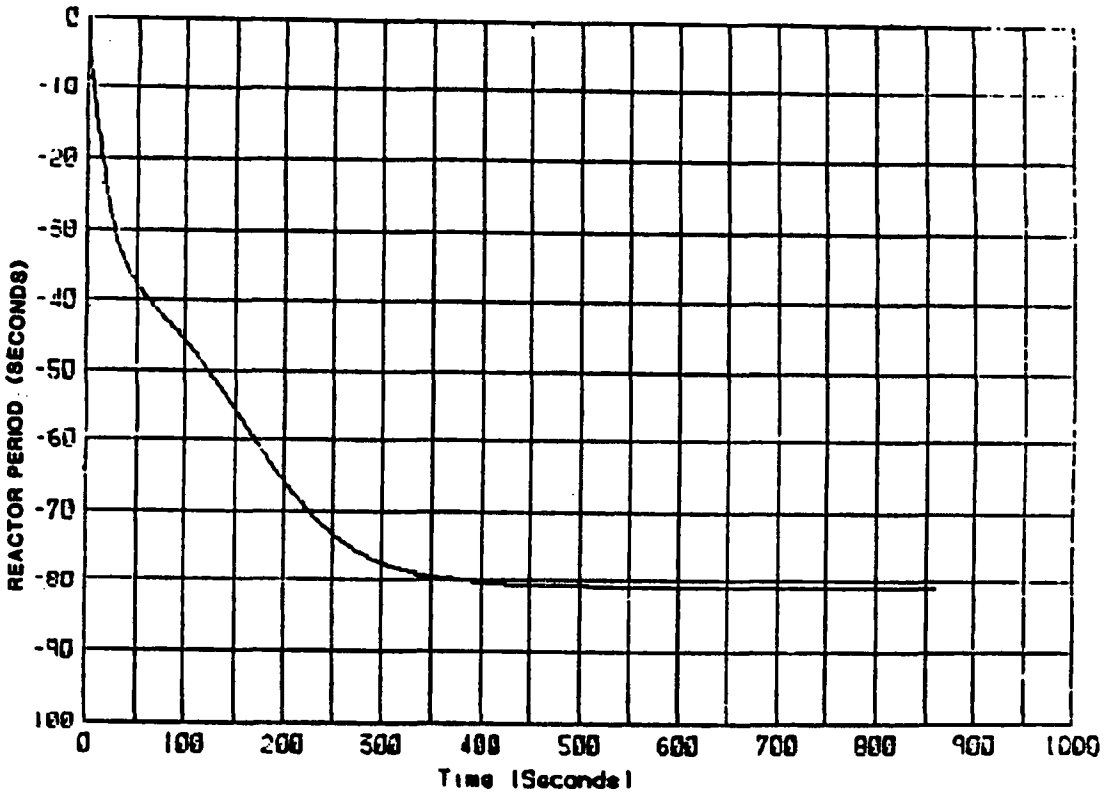

Figure 9-31 Time Dependent Reactor Period for – 0.030 ΔK Reactivity Insertion Versus Time After Insertion

a,c

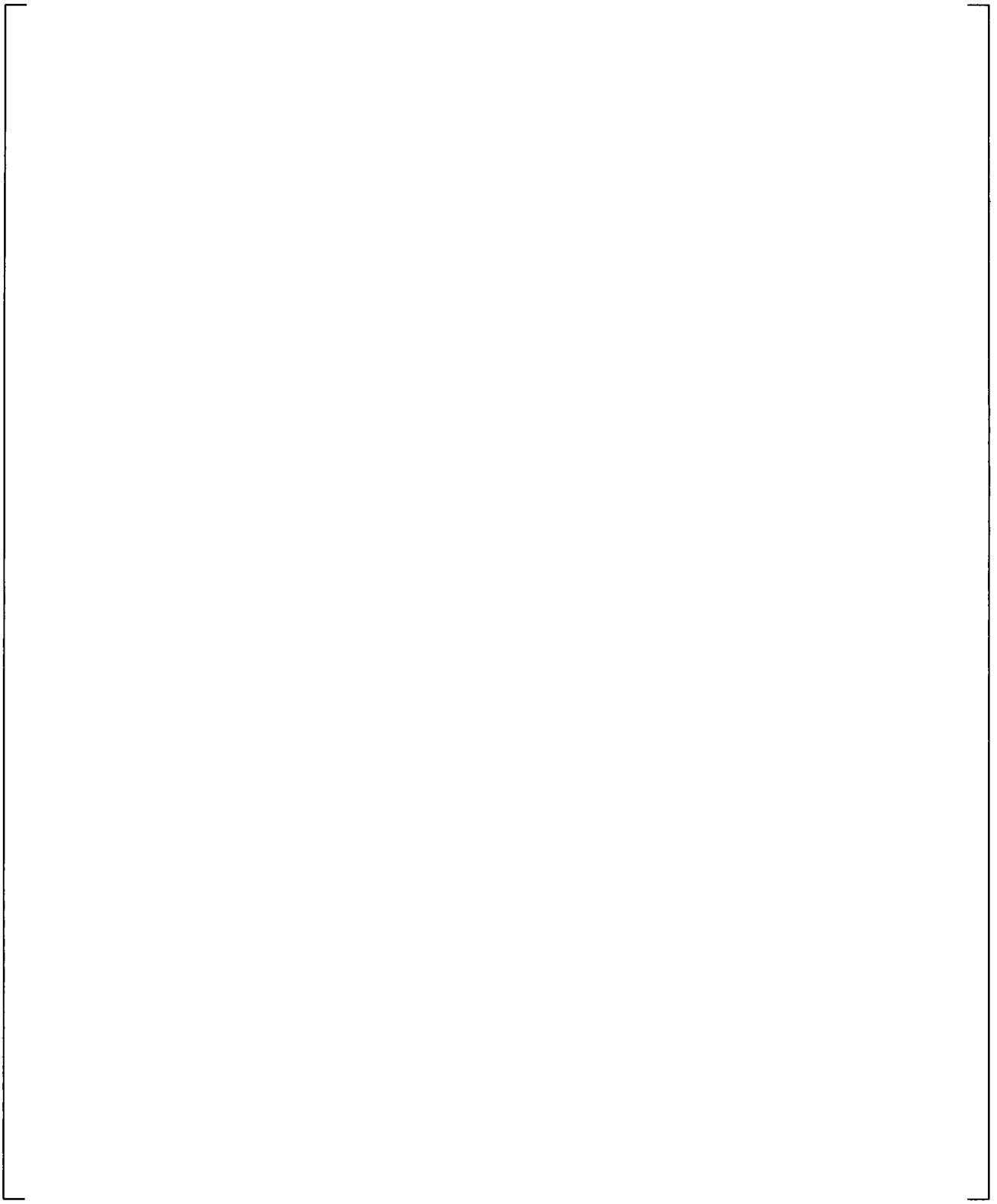

Figure 9-32 Total Actinide Decay Power Versus Burnup and Initial Enrichment

a,c

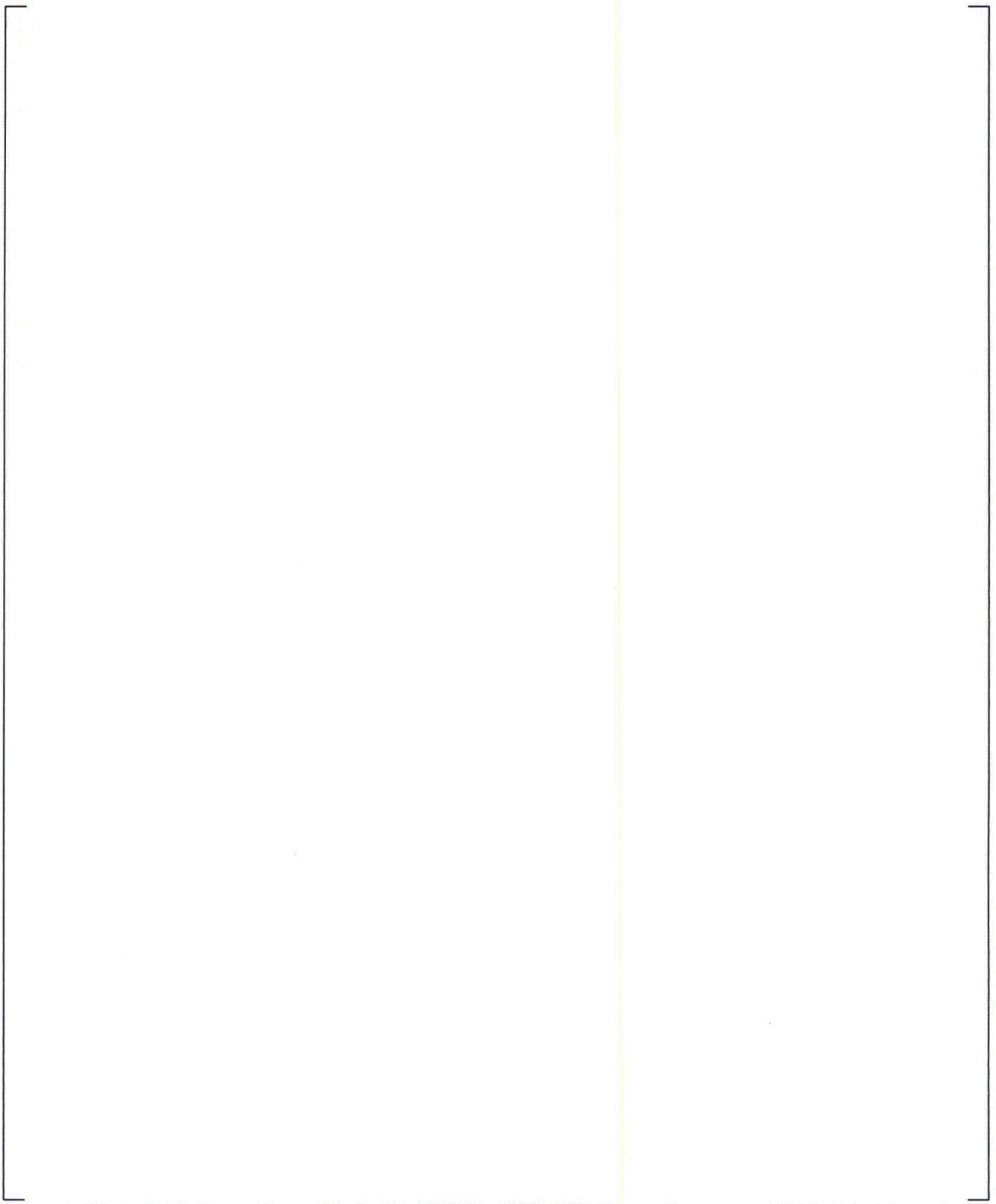

Figure 9-33 Actinide Decay Power Excluding U-239 and Np-239 Versus Burnup and Initial Enrichment

a,c

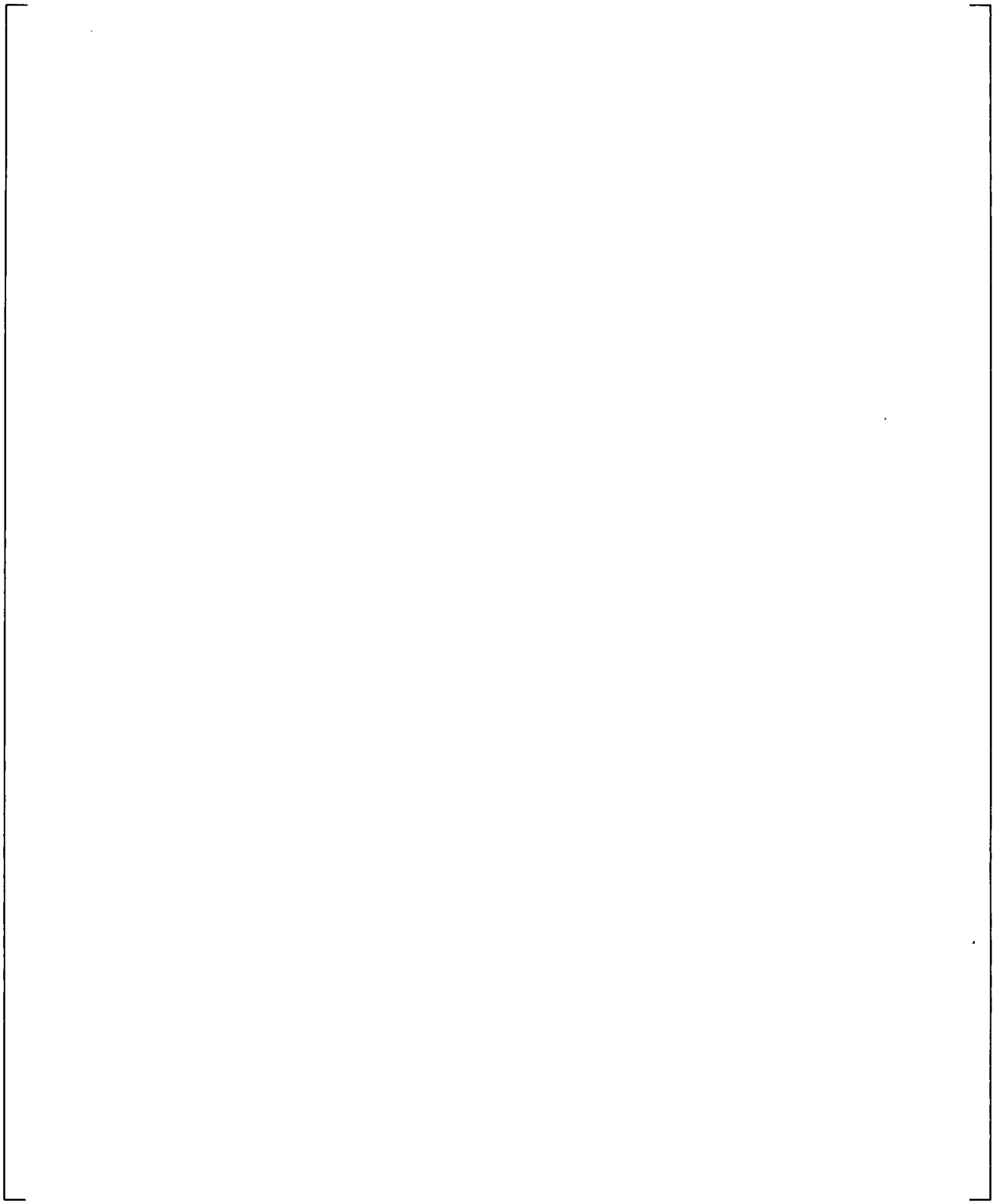

Figure 9-34 Capture Correction Versus Burnup and Initial Enrichment

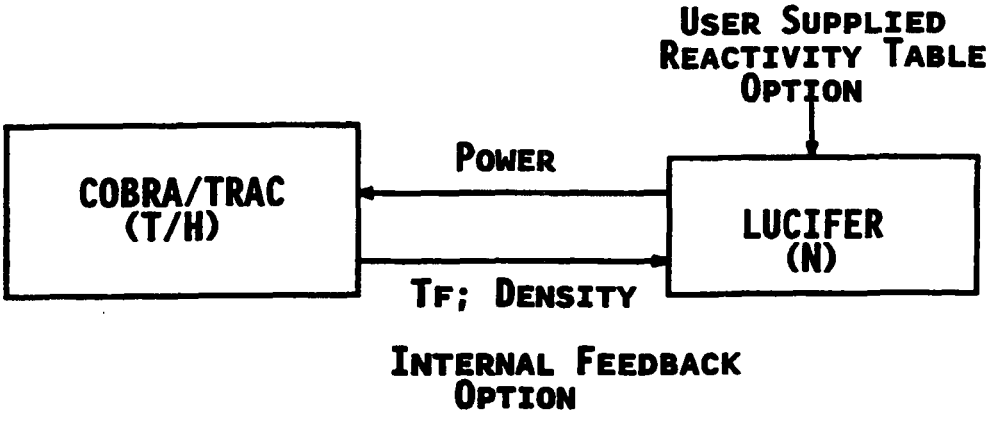

Figure 9-35 WCOBRA/TRAC-TF2 Calculation Block Diagram

10 WCOBRA/TRAC-TF2 ONE-DIMENSIONAL COMPONENT MODELS

10.1 INTRODUCTION

The one-dimensional components in WCOBRA/TRAC-TF2 are modules derived from TRAC-P [ ]^{a,c} to model the reactor primary system. These components provide models for accumulators, pressurizers, pipes, tees, pumps, steam generators, and valves. In addition, there are two modules that provide boundary conditions for parts of the system not modeled, representing either a pressure sink/source or a flow boundary condition.

The conservation equations used for the one-dimensional components are discussed in Section 3.4. The following sections will describe the features of each of the one-dimensional components and elaborate on the conventions that are used to model the component using a typical noding diagram. Many of the base modules, such as PIPE, TEE, HTSTR, VALVE and PUMP are virtually unchanged from their original TRAC-P [ ]^{a,c} counterparts, so their descriptions are very similar to those given by TRAC-M user's manual (Steinke et al., 2000). The steam generator can be modeled with a combination of PIPE, TEE, and HTSTR components. A demonstration of steam generator model is outlined in Section 10.5. In Section 10.8, the accumulator model built with a PIPE is described.

10.2 PIPE COMPONENT

Model Basis

The PIPE component is used to model one-dimensional thermal-hydraulic flow in a duct or pipe. A PIPE can be used alone in a problem, together with only BREAK and/or FILL boundary conditions, or it can connect other components together to model a system. Area changes, wall heat sources and heat transfer across the inner and outer wall surfaces can be modeled in the PIPE component.

Figure 10-1 shows as an example a typical noding diagram for a PIPE used to model a venturi with an abrupt area change. The numbers within the PIPE indicate cell numbers, and those above it are cell boundary numbers. The geometry is specified by providing a volume and length for each cell and a flow area and hydraulic diameter at each cell boundary. The junction variables JUN1 and JUN2 provide reference numbers for connecting this PIPE to other components.

Input options are available to model a two-dimensional (2D) volumetric heat source in the wall, one-dimensional (1D) wall radial conduction heat transfer, wall-surface convection heat transfer based on flow regime dependent heat transfer coefficients on the inner surface and input-specified constant heat transfer coefficients on the outer surface, and wall-surface coolant-flow friction factors. The wall heat transfer calculation is evaluated when the input number of heat transfer nodes, NODES, is greater than zero. A critical heat flux (CHF) calculation can be evaluated by setting the input parameter ICHF to 1. Wall friction and irreversible form losses caused by abrupt or gradual coolant flow-area change and coolant flow turning are evaluated by specifying appropriate option values for the input arrays, NFF and FRIC, at each cell interface.

Heat can be deposited directly in the coolant by setting the input parameter IPOW to 1. A power-to-the-fluid table defines the total power that is uniformly distributed in the coolant per unit length for all of the mesh cells of the PIPE component.

Model As Coded

The conservation equations for any PIPE component are solved as described in Section 3, with the closure relations discussed in Sections 4 through 8, referring to one-dimensional components. The thermodynamic and material properties are described in Section 11. Cylindrical pipe is assumed for the computation of interfacial area in horizontal flow regime. Additional user defined multipliers have been added in WCOBRA/TRAC-TF2 that affect specific models and correlations.

The HS_SLUG (used interchangeably with C_{hs_slug}) multiplier affects the transition between non-stratified and stratified flow regimes; specifically, it is a multiplier on the nominal relative velocity required for transition from stratified flow as described in detail in Section 4.4.5. The default value of HS_SLUG is 1.0 and can be modified through the $NAMELIST set of the model input within allowable range of $0.1 \leq$ HS_SLUG ≤ 9.99. The HS_SLUG multiplier affects the horizontal flow calculation for all the PIPE, TEE, and VALVE 1D hydraulic components.

User-specified allowance for horizontal stratification within a PIPE component can be provided through the MSTRTX and STRTX inputs. The [

]^{a,c} input. The HS_SLUG multiplier can only affect cell faces [

]^{a,c} since the flow is not allowed to stratify if neither of these conditions exists.

If needed, interfacial drag multipliers YDRGX can be defined by the user at any cell faces of the PIPE component. In addition, interfacial condensation heat transfer at user selected PIPE cells can be modified by using the CNDNX multipliers.

Critical flow calculation, using a homogeneous relaxation model (HRM) described in Section 5.12, can be invoked at a specified cell face of the PIPE component. The HRM model is activated by using the $NAMELIST input ICFLOW=3 and appropriate ICFLG input for the PIPE component. The code capability to calculate critical flow using the HRM model is documented in Section 12. The original TRAC-P [ ]^{a,c} critical flow model is retained in WCOBRA/TRAC-TF2 and is invoked using ICFLOW=2.

10.3 TEE COMPONENT

Model Basis

The TEE component models the thermal-hydraulics of three piping branches, two of which lie along a common line with the third entering at some angle Φ from the main axis of the other two. The code basically treats a TEE component as two PIPEs, as indicated in Figure 10-2. The angle Φ is from the low-numbered end of PIPE 1 to PIPE 2. The low-numbered end of PIPE 2 always connects to PIPE 1. The straight PIPE segment is numbered from cell 1 to NCELL1, with the connection to PIPE 2 at cell

JCELL. The branch PIPE segment is numbered from the cell immediately adjacent to JCELL, beginning with cell 1 and ending with cell NCELL2.

The connection to PIPE 1 from PIPE 2 is treated with mass, momentum, and energy source terms. For PIPE 2 the conditions in cell JCELL of PIPE 1 form the inlet boundary conditions. The mass and energy terms associated with the side branch flow are added to the governing mass and energy equations representing the main branch flow. The losses at the junction are modeled in terms of the momentum change resulting from the combining or dividing flow. For the combining case an additional momentum source term is added to the main branch momentum equations. This term represents the momentum source or sink associated with the secondary flow in relation to the main branch flow. The time differencing and iteration procedures guarantee conservation of scalar quantities within a convergence tolerance. Liquid or gas can be prevented from entering the TEE secondary side by setting the input value of FRIC at the interface between JCELL and secondary side cell 1 to a value greater than 10^{20} or less than -10^{20}, respectively. Actually, such a liquid or gas separator can be modeled at any mesh-cell interface.

Since the junction between PIPE 1 and PIPE 2 is always treated semi-implicitly, the velocity at that point is always included in the computation of the time step stability limit. Phase separation at the junction is calculated if the flag ISEP is set to one.

Model as Coded

Since the TEE is modeled as two connected PIPEs, the PIPE model description in Section 10.2 should be consulted for additional information. The calculational sequence for a TEE includes separate calculations of the primary and secondary sides. For the junction momentum source, an additional source term is calculated in subroutine ETEE and is incorporated in the momentum equation in TF1DS. This source term is set to zero when the TEE is a dividing tee.

The HS_SLUG multiplier, selected through the $NAMELIST input, affects calculated horizontal flow in the TEE component. Also, similar to the PIPE component, the user has the option to specify allowance for horizontal stratification in the main and side pipes through the STRTX1 and STRTX2 multipliers.

In addition, interfacial heat transfer and interfacial drag at user selected locations of the main and side pipes of the TEE component can be influenced by implementing CNDNX1/CNDNX2 and YDRGX1/YDRGX2 multipliers, respectively.

Similar to the PIPE component, critical flow calculation using a homogeneous relaxation model (HRM) described in Section 5.12, can be invoked at any specified cell face of the main and side pipe of the TEE component as well. The HRM model is activated by using the $NAMELIST input ICFLOW=3 and appropriate ICFLG input for the selected TEE component locations. When modeling the side break of a pipe, the HRM model is usually invoked at the last cell face of the side pipe.

An offtake model is incorporated into the TEE component, as described in Section 5.13. The model is invoked by specifying IENTRN=1 in the TEE component input. The offtake model is assessed in Section 12 and the related uncertainty treatment is discussed in Section 29.

An additional specialized model included in the WCOBRA/TRAC-TF2 code adds the capability of the code to calculate the local effect of direct steam condensation on the safety injection delivered in the cold leg. The model as coded is described in detail in Section 6.3.6. The assessment is documented in Section 17 and the associated uncertainty treatment is discussed in Section 29.1.6. The direct-contact cold leg condensation model validated for the purpose of the FULL SPECTRUM LOCA (FSLOCA) methodology is invoked by specifying IENTRN=3 in the TEE component input.

10.4 PUMP COMPONENT

Model Basis

The pump model employed in WCOBRA/TRAC-TF2 describes the interaction of the system fluid with a centrifugal pump. The model calculates the pressure differential across the pump and its angular velocity as a function of the fluid flow rate and the fluid properties. The model is designed to treat any centrifugal pump and can include two-phase effects.

The pump model is represented by a one-dimensional component with N cells, where N must be greater than 1. A typical noding diagram for the pump component is shown in Figure 10-3. The pump momentum is modeled as a source Ω that is included between cells 1 and 2. The source is positive for normal operation with the pressure rise occurring from cell 1 to cell 2, so it is necessary to number the cells so that the cell number increases in the normal flow direction.

The pump model is identical to the one-dimensional pipe model except that a momentum source is included in the mixture momentum equation written between cells 1 and 2:

$$\frac{V_{\ell,1+1/2}^{n+1} - V_{\ell,1+1/2}^{n}}{\Delta t} = \frac{\left\{ P_1^{n+1} - P_2^{n+1} + \left[\Delta P^n + \left(\frac{\delta \Delta P}{\delta V} \right)^n \cdot \left(V_{\ell,1+1/2}^{n+1} - V_{\ell,1+1/2}^{n} \right) \right] \right\}}{\bar{\rho}_{m,1+1/2}^{n} \Delta x_{1+1/2}} - g \cdot \cos\theta \qquad (10\text{-}1)$$

and

$$V_g^{n+1} = V_\ell^{n+1} \qquad (10\text{-}2)$$

where $\left[\Delta P^n + \left(\frac{\delta \Delta P}{\delta V} \right)^n \cdot \left(V_{\ell,1+1/2}^{n+1} - V_{\ell,1+1/2}^{n} \right) \right]$ is the SMOM first-order approximated pressure rise momentum source across the pump-impeller interface at the end of time step n+1 evaluated from the pump curve correlations. The steady state solution form of the Equation 10-1 is:

$$\Delta P = P_2 - P_1 + \bar{\rho}_{m,1+1/2}^{n} \Delta x_{1+1/2} g \cdot \cos\theta \qquad (10\text{-}3)$$

which is the desired model. Friction and form losses do not enter explicitly into the pump-impeller interface motion equation. Therefore, wall drag and additive friction losses are not modeled between the

centers of cells 1 and 2 [NFF(2) = 0 and FRIC(2) = 0.0]. The pressure rise ΔP^n and its derivative with respect to the coolant velocity $(\delta\Delta P/\delta V)^n$ for the pump-impeller interface is evaluated only once at the beginning of each time step.

This momentum source is applied in the coolant motion equation at the pump-impeller interface.

The Pump Characteristic Curves – The Homologous Curves

It has been well known that for single-phase flow the characteristics of a pump can be quite accurately obtained from those of a geometrically similar scale-model using the similarity laws. Following these laws, the head and the torque of the pump can be represented in non-dimensional forms which are independent of the scale of the pump model. The approach used to establish the so-called homologous curves is one of the methods that have utilized the similarity laws to non-dimensionalize the variables involved in pump operations. In this approach, four homologous curve segments (one curve segment represents a family of curves) are established. These curves describe in a compact manner all the operating states of the pump. The following definitions are employed in the subsequent development:

H	=	pump head = $\Delta P_{pump}/\rho$
ρ	=	fluid density at pump inlet
Q	=	volumetric flow rate through pump
ω	=	pump impeller angular speed
T	=	pump hydraulic torque

To allow one set of curves to be used for a variety of pumps, the following normalized quantities are used:

υ	=	Q/Q_R
α_N	=	ω/ω_R
h	=	H/H_R
β	=	$(T/T_R)/(\rho_R/\rho)$

where the subscript R denotes the rated conditions. Use of the pump similarity relations (Olson, 1974) shows that:

$$\frac{h}{\alpha_N^2} = f\left(\frac{\upsilon}{\alpha_N}\right) \tag{10-4}$$

and

$$\frac{\beta}{\alpha_N^2} = f\left(\frac{\upsilon}{\alpha_N}\right) \tag{10-5}$$

for:

$$\left|\frac{\upsilon}{\alpha_N}\right| \leq 1$$

and

$$\frac{h}{\upsilon^2} = f\left(\frac{\alpha_N}{\upsilon}\right) \tag{10-6}$$

and

$$\frac{\beta}{\upsilon^2} = f\left(\frac{\alpha_N}{\upsilon}\right) \tag{10-7}$$

for:

$$\left|\frac{\alpha_N}{\upsilon}\right| < 1$$

Table 10-1 shows the resulting four segments of the homologous head and torque curves that represent the complete pump operational characteristics.

Pump Single-Phase Head and Torque Homologous Curves

Figures 10-4 and 10-6 show typical single-phase homologous head and torque characteristic curves for Westinghouse designed pumps (specifically the W93A pump design).

Pump Fully-Degraded Head and Torque Homologous Curves

A basic assumption of the WCOBRA/TRAC-TF2 pump model is that the same type of scaling laws, which are applied under single-phase conditions, can also be applied under two-phase conditions. It is assumed that there exists a condition at an intermediate range of void fractions in which the pump head and torque can be described by a set of homologous curves, similar to the single-phase curves. A typical set of curves for a Westinghouse designed pump is illustrated in Figures 10-5 and 10-7.

The Head and Torque Multipliers

To provide for a transition from single- to two-phase conditions, the following correlations are used:

$$H_* = H_1 - M(\alpha)\,(H_1 - H_2) \tag{10-8}$$

and

$$T_* = T_1 - N(\alpha)(T_1 - T_2) \tag{10-9}$$

where:

M	=	head multiplier
N	=	torque multiplier
α	=	donor cell vapor void fraction at pump inlet

and the subscript 1 denotes the single-phase value, the subscript 2 denotes the two-phase value, both calculated from the homologous curves, and the subscript * denotes the derived value for a given two-phase condition.

Pump Impeller Speed

The PUMP component treats the pump impeller angular velocity as a constant value that is input each time step (and may vary) when the motor is energized. After the drive motor is tripped, the time rate of change of the pump impeller angular velocity is proportional to the sum of the moments acting on it and is calculated from:

$$I\frac{d\omega}{dt} = T_M - (T_* + T_{FR} + T_E) \tag{10-10}$$

where:

I	=	moment of inertia of the pump rotor assembly
T_M	=	torque supplied by motor (after trip, $T_M = 0.0$)
T_{FR}	=	total friction torque (including all mechanical, bearing friction and windage loss)
T_E	=	electric torque (caused by induced voltage after trip)
T_*	=	pump hydraulic torque

The total friction torque for plant applications selected by setting TFROPT = 1 is calculated as (Bordelon et al., 1974a):

$$\left[\qquad\qquad\right]^{a,c} \tag{10-11}$$

where:

[

]^{a,c}

A more generalized form of the friction torque is available within the code as follows:

$$T_{FR} = C_0 + C_1\frac{\omega}{\omega_R} + C_2\frac{\omega|\omega|}{\omega_R{}^2} + C_3\frac{\omega^3}{\omega_R{}^3} \tag{10-12}$$

where C_0, C_1, C_2, and C_3 are input constants TFR0, TFR1, TFR2, and TFR3, respectively. If the pump impeller angular velocity (pump speed) drops below the input specified value of TFRB, then a second set of constants are used to determine T_{FR}.

$$T_{FR} = C'_0 + C'_1 \frac{\omega}{\omega_R} + C'_2 \frac{\omega|\omega|}{\omega_R^2} + C'_3 \frac{\omega^3}{\omega_R^3} \tag{10-13}$$

where C'_0, C'_1, C'_2, and C'_3 are input constants TRFL0, TRFL1, TRFL2, and TRFL3, respectively. The constants C_0, C_1, C_2, C_3, C'_0, C'_1, C'_2, and C'_3 should be determined from experimental data. As the pump speed approaches zero, the C_0 and C'_0 contributions are linearly decreased to zero to ensure that there are no friction losses at a pump speed of zero. The reduction of C_0 and C'_0 contributions to T_{FR} begins when the pump speed drops to 1/10 of the rated speed. The pump hydraulic torque (T_*) is evaluated from the homologous curves and Equation 10-9 as a function of the fluid density and flow rate as well as pump angular velocity.

Pump Options and Limitations

The wall heat transfer NODES, wall friction NFF, and CHF calculation ICHF options for the PUMP module are the same as for the PIPE component. In addition, the following options are specified: pump type IPMPTY, trip-controlled pump-motor action IPMPTR, frictional and windage torque option TFROPT, reverse speed option IRP, two-phase degradation IPM option, and pump curve option OPTION.

Input variables IPMPTR and NPMPTB specify, respectively, the controlling trip ID number for pump trip action and the number of pairs of points in the pump-speed table PMPTB. If IPMPTR = 0, no pump-trip action occurs, and the pump runs for the entire calculation at the constant pump impeller angular velocity (rotational speed) OMEGAN. If IPMPTR $\neq$ 0 and the IPMPTR trip is initially OFF, the pump impeller angular velocity is defined by signal variable or control block ID number NPMPSD or by OMEGAN when NPMPSD = 0. If the IPMPTR trip is OFF after being ON, OMGOFF defines the pump impeller angular velocity. In all situations, the rate of change of the pump impeller angular velocity is constrained by its maximum rate ROMGMX.

Three types of pumps are available as presented in Table 10-2. For pump type IPMPTY = 0, the pump-impeller interface coolant-mixture velocity is defined by signal variable or control block NPMPSD when trip IPMPTR is OFF and by the PMPTB coolant-mixture velocity table when trip IPMPTR is ON. For pump type IPMPTY = 1, the pump impeller angular velocity is defined by OMEGAN when NPMPSD = 0 or by signal variable or control block NPMPSD when trip IPMPTR is OFF and by the PMPTB pump-speed table when trip IPMPTR is ON. The independent variable for the PMPTB table may be elapsed time since the trip was set ON or any signal variable or control block. For pump type IPMPTY = 1, the torque calculation is not used. Pump type IPMPTY = 2 is similar to IPMPTY = 1 except that a PMPTB pump-speed table is not input. Instead, the pump impeller angular velocity is calculated from Equation 10-10 when trip IPMPTR is ON.

Two different options are available for the calculation of the frictional and windage torque using TFROPT. TFROPT = 1 causes the frictional and windage torque to be calculated using Equation 10-11,

and is generally used for plant applications. TFROPT = 0 allows for a more flexible calculation of the frictional and windage torque. This torque is calculated using Equations 10-12 and 10-13 for TFROPT = 0.

If the IRP = 1 reverse-rotation option is specified, the pump impeller is allowed to rotate in both the forward and reverse directions. If reverse rotation is not allowed by specifying IRP = 0, the pump impeller will rotate in the forward direction only. In this case, if negative rotation is calculated (for pump type IPMPTY = 2 with trip IPMPTR ON), the pump impeller angular velocity is set to zero. If IRP = 0 and a negative pump impeller angular velocity is defined by input parameters, fatal error messages will be printed by subroutines PUMPD, PUMPX, and PUMPSR, and the calculation will abort.

If the two-phase option is turned on (IPM = 1), the degraded pump head and torque will be calculated from Equations 10-8 and 10-9. If the two-phase option is turned off (IPM = 0), only the single-phase head and torque homologous curves will be used.

The user may either specify pump homologous curves in the input by OPTION = 0 or may use the built-in pump curves of OPTION = 3. The use of OPTION = 1 or 2 (built-in Semiscale or LOFT pump curves) is not supported. Pump curves for the Westinghouse 93A pump design are built-in, and can be selected via OPTION=3. The associated pump curves are presented in Figures 10-4 through 10-7. For other types of pressurized water reactor (PWR) pumps their corresponding homologous curves and multiplier values would be specified. Because these homologous curves are dimensionless, they can describe a variety of pumps by specifying the desired rated head RHEAD, rated torque RTORK, rated volumetric flow RFLOW, rated density RRHO, and rated pump impeller rotational speed ROMEGA as input.

There are several restrictions and limitations in the current version of the pump component. Because there is no pump motor torque versus pump impeller speed model, the pump impeller rotational speed is assumed to be input if the pump motor is energized. Pump noding is restricted so that the cell numbers increase in the normal flow direction where the total number of component cells NCELLS > 2, the pump momentum source is located at the interface between cells 1 and 2 of the PUMP component, and the wall friction and additive loss coefficient between cells 1 and 2 are zero (NFF(2) = 0 and FRIC(2) = 0.0). A flow-area change should not be modeled between cells 1 and 2. Finally, the pump-head degradation multiplier $M(\alpha)$ and the torque degradation multiplier $N(\alpha)$ are assumed to apply to all operating states of the pump.

The pump model does not account for the addition of energy to the liquid caused by irreversible effects. If this is considered to be important, that energy can be added to the coolant in the first PIPE or TEE component downstream of the pump. This may be done with a power deposited in the coolant component-action table that defines the amount of energy deposited directly into the coolant based on the pump operating condition.

The PUMP module input consists of the same geometric and hydrodynamic data and initial conditions that are required for the PIPE module. In addition, information specific to the PUMP is required. The speed table (PMPTB) as well as the homologous pump curve arrays must be input.

Model as Coded

For the new timestep (n+1), Equation 10-10 is evaluated explicitly:

$$\omega^{n+1} = \omega^n + (\frac{d\omega}{dt})^n \Delta t \qquad (10\text{-}14)$$

The momentum source for a pump cell is evaluated once each timestep, and the source is applied only during the explicit pass in subroutine TF1DS. The mixture velocity and mixture density from the donor component (i.e., conditions at the upstream boundary of the pump component) are used to establish the volumetric flow rate through the pump. Standard curve fitting techniques are then used to compute the pump head. The pump source evaluation is performed by subroutine PUMPSR.

Scaling Considerations

During blowdown and reflood periods, reactor coolant pumps will be under two-phase flow conditions, and both the pump head and the pump torque will be degraded. Although the physical mechanisms responsible for the performance degradation in two-phase flows are not well understood, analysis of tests on pumps (Kamath and Swift, 1982) revealed that "scaling down the size of the pump while maintaining the same design specific speed produces very similar performance characteristics both in single and two-phase flows." The study also indicated that effects due to size and operating speed were not discernible within the range of test conditions and within experimental uncertainties. The system pressure, however, appeared to affect the rate of degradation even for the same pump. Similar results were also observed in the scaled pump experimental tests conducted by KWU (Kostner and Seeburger, 1983). These test results suggest that uncertainties due to scaling distortion from the pump are small compared to other contributors. The effect of scaling and other uncertainties is minimized in the WCOBRA/TRAC-TF2 model by using data from a 1/3-scale model similar in design to the Westinghouse pump (Snyder and Grigsby, 1982) which is also a good representation of other PWR's pumps.

Conclusions

The pump model is constructed by combining the experimentally established pump characteristic correlations and the PIPE module of WCOBRA/TRAC-TF2, based on a one-dimensional two-fluid formulation. The as-coded frictional torque correlation, defined by Equation 10-11, is also experimentally established. The pump model can handle all single- and two-phase operations (with or without phase separation) and provide accurate speed, flow, and head predictions during the transient (including coastdown). The options of the model provide the users with the flexibility to model a variety of pump operating conditions. The WCOBRA/TRAC-TF2 pump model has been assessed against Loss-of-Fluid Test (LOFT) L2-5 test data (Bayless et al., 1982) with satisfactory results. The model can be utilized to simulate any PWR pump for which the homologous characteristic curves have been adequately established.

10.5 STEAM GENERATOR

Model Basis

In a PWR, the steam generators transfer energy from the primary coolant loop to the secondary coolant to produce steam. In WCOBRA/TRAC-TF2, the steam generator is modeled with a combination of PIPE, TEE, and HTSTR components. Figure 10-8 provides an example noding diagram for a U-tube steam generator, in which the steam generator tube bundle is represented by [ ]^{a,c}. Modeling this way, the steam generator primary side and secondary side hydrodynamics are treated separately. [ ]^{a,c} It is possible to connect the secondary side junctions to any 1D component, but the most common arrangement for Loss-of-Coolant Accident (LOCA) analysis is to connect the inlet to a FILL, specifying the secondary side fluid inlet conditions and flow rate, and to a BREAK at the discharge, specifying the steam generator secondary discharge pressure.

The cylindrical heat conduction equation for a typical tube is solved as described in Section 8.8. There must be at least one wall temperature node, but three are suggested, placing one at each tube surface and one at the tube wall center. The tube material is selected from the material options given in Section 11.5. Wall friction correlations and additional frictional losses for the primary and secondary sides can be specified as described as the same as the PIPE component.

An example of the steam generator as part of the PWR model is available in Section 26.

10.6 PRESSURIZER COMPONENT (PRIZER)

Model Basis

The pressurizer in a PWR is a pressure vessel used to control the primary coolant system operating pressure and accommodate any change in the coolant volume during normal operation. During normal operation, this reservoir contains the highest-energy fluid in the primary coolant system and it controls the primary coolant system pressure by hydraulic coupling through a long surge line connected to one of the PWR hot legs. It is usually kept 50%-60% full of saturated liquid that is pressurized by saturated steam above it. The pressure is maintained at the operating setpoint value by a system of heaters and sprays which regulate the energy input to the water.

Model as Coded

The pressurizer is simulated by the PRIZER component. The component is essentially a specialized PIPE component which connects at the bottom to another one-dimensional component (PIPE or TEE) to model the connecting surge line and at the top to a zero flow FILL component to simulate the closed end. The PRIZER component has its nodes numbered from 1 to NCELLS, with node 1 being at the top of the component as in Figure 10-9.

LOCA transients are simulated by restarting from an initial transient simulation of the steady-state of the plant. A specialized function is added to help achieving such steady-state with a simplistic modeling of

the pressurizer heaters and sprays. [

]^{a,c}

[a,c]

[

]^{a,c}

[a,c] (10-15)

where:

[a,c] (10-16)

[

]^{a,c}

10.7 VALVE COMPONENT

Model Basis

VALVE components are used to simulate the controlling action of various valve fittings incorporated in the design of the PWRs. The valve action is modeled by adjustment of the flow area and form loss at a user-specified cell interface (cell face number IVPS) of a 1D (PIPE-like) hydraulic component. Any VALVE component consists of at least two fluid nodes, and its adjustable flow area may not be located at the VALVE component junction, unless that junction is connected to a BREAK component. The flow area and hydraulic diameter specified at cell face IVPS are used as the controlling parameters to model the valve operation. In all other respects, the VALVE component is identical to the PIPE component.

Many different types of valves can be modeled because of the flexibility to choose the independent variable of VALVE component-action tables and to perform table evaluation under trip control. These include simple valves to model pipe breaks or the opening of rupture disks, check valves, power-operated relief valves, banks of power operated relief valves, steam-flow control valves, turbine stop valves, turbine bypass valves, main-steam isolation valves, safety relief valves, and atmospheric dump valves.

The adjustment of the VALVE closure (or open) state is made with a step change at the beginning of a hydrodynamic time step; the VALVE state is held constant during the time step.

Model as Coded

The noding scheme typically used for a VALVE is shown in Figure 10-10. Input IVPS defines the cell face where the valve action is modeled.

Two methods are provided for specifying the valve flow area. The first method allows for the flow area at cell face IVPS, FA(IVPS) to be computed directly from a flow-area fraction (FAVLVE), provided by the user as a function of an independent variable. In this case the valve flow area is calculated according to Equation 10-17:

$$FA(IVPS) = FAVLVE \times AVLVE \tag{10-17}$$

where AVLVE is the input value for the fully open valve flow area, provided by the user.

Alternatively, using the second method, the flow area may be computed from the relative position (XPOS) of the valve stem, which assumes a guillotine-type cut of circular cross section (Figure 10-11). The relative valve-stem position of XPOS = 1 corresponds to a fully open valve with flow area AVLVE. Fully closed valve position corresponds to XPOS=0.

This calculation of the valve flow area assumes a guillotine cut of a circular cross section and is based on standard mensuration formulas. Figure 10-11 shows the assumed geometry for valve flow area calculation. When the valve is fully open, the flow area corresponds to the full circle. The stem position is assumed to be normalized such that a zero position is fully closed and a position of 1 is fully open. The calculation of the area and the corresponding hydraulic diameter is normalized similarly.

Subroutine FAXPOS performs the calculation of the normalized flow area. For a relative valve-stem position XPOS, the code calculates the normalized flow area, as described below. The flow area at the valve location is defined by a circle with a normalized radius of 1. At certain valve stem position XPOS, one can define H such that:

$$H = 1 - h = \min\left(1.0, \left|1.0 - 2 \times XPOS\right|\right) \tag{10-18}$$

where h is the dimension shown in Figure 10-11. The half of the angle subtended by the chord is given by:

$$\theta = \cos^{-1} H \tag{10-19}$$

and the resulting normalized flow area is:

$$FA = \frac{1}{\pi}\left(\theta - H\sqrt{1 - H^2}\right) \tag{10-20}$$

Because of symmetry, the total normalized flow area is:

$$A_{norm} = \begin{cases} FA & \text{if } XPOS \le 0.5 \\ 1.0 - FA & \text{if } XPOS > 0.5 \end{cases} \tag{10-21}$$

The valve flow area is then calculated as:

$$FA(IVPS) = A_{norm} \times AVLVE \tag{10-22}$$

Noting that $H\sqrt{1 - H^2} = (1/2) \times \sin(2\theta)$, by rewriting Equation 10-20 the normalized flow area A_{norm} of the VALVE can also be defined as:

$$A_{norm} = \frac{1}{2\pi}(T - \sin T) \tag{10-23}$$

where the angle $T = 2 \times \theta$, and θ can vary from 0 to π radians, such that 0 represents a fully closed valve and π a fully open valve.

For the case in which the VALVE flow area is specified, the code solves for angle T by searching for an iterative solution of the following equation:

$$F(T) = \frac{1}{2\pi}(T - \sin T) - A_{norm} = 0 \tag{10-24}$$

Equation 10-24 is solved for the angle T using the modified regula falsi method. The procedure is limited to 20 iterations and attempts to converge the solution for T to less than 1.0×10^{-8}.

The valve stem position is then calculated as:

$$XPOS = 0.5\times(1+H) \tag{10-25}$$

where

$$H = \begin{cases} \cos(T/2) & \text{if } FA \geq 0.5 \\ -\cos(T/2) & \text{if } FA < 0.5 \end{cases} \tag{10-26}$$

The FA fraction (FAVLVE) or valve-stem position (XPOS) is entered as a constant or a tabular function defined by a table. Use of a table may be trip-initiated according to the control option selected. To increase the flexibility to model various types of valves, two valve tables may be input for trip-controlled valves. The first table is used when the trip set status is $ON_{forward}$ and the second table is used when the trip set status is $ON_{reverse}$. The independent variable for the table can be any modeled-system parameter defined by a signal variable or a control block. Typically, the independent variable can be either time or pressure difference across the IVPS cell face, depending on the type of valve being modeled.

Because the hydraulic diameter is used in the wall friction calculation, the fully open valve hydraulic diameter (HVLVE user input) is not changed during a given calculation. HD(IVPS) is set equal to HVLVE during initialization and is held constant after the initialization phase. The form loss for flow through the valve is adjusted according to the valve flow area based on:

$$K = K0 + 0.5\cdot(1-b) + (1-b)^2 \tag{10-27}$$

where K0 is the fully open valve form loss and b is the ratio of the flow area at the valve location IVPS, as defined by Equations 10-17 or 10-22, to the pipe flow area. The pipe flow area is defined as FAVOL(IVPS-1)=VOL(IVPS-1)/DX(IVPS-1), where VOL is the volume and DX is the length of cell. If IVPS=1, then the pipe flow area is defined as FAVOL(IVPS)=VOL(IVPS)/DX(IVPS).

Equation 10-27 is recommended in the Crane manual (Crane Company, 1942) for gate and ball valves. It will overestimate the form loss for partially closed globe and angle valves. For globe and angle valves, K0 tends to be large and therefore the total error during opening or closing a globe or angle valve is relatively small. K0 is the value of the valve resistance, provided by the user at cell face IVPS. In the code, this value is also restricted to be greater than 0.03 since K0 of zero has been observed to provide numerical instability. The Crane manual also indicates that K0 should range from $3f$ to $400f$ or (assuming pipe friction factor $f = 0.01$) 0.03 to 4.0, depending upon the valve design.

Many different types of valves can be modeled because of the flexibility available to choose the independent variable for the valve-action table and to implement table evaluation under trip control. Simple valves that either open or close on a trip may be modeled using an OFF-ON- or ON-OFF-type trip and a table that has relative time (since trip initiation) as the independent variable to obtain the desired rate of opening or closing. Valve leakage can be simulated by restricting the table minimum FA fraction or valve-stem position to a value greater than zero. Simple valves can be used to model pipe breaks or the opening of rupture disks.

A simple check valve can be modeled by using a valve table with the appropriate pressure gradient as its independent variable. Alternatively, a check valve can be modeled as a trip-controlled valve with the pressure gradient used as the trip signal and the valve table used to control the rate of valve movement.

A steam-flow control valve [or power-operated relief valve (PORV)] can be modeled using an $ON_{reverse}$-OFF-$ON_{forward}$ trip to control it with the start closing pressure, end closing pressure, end opening pressure, and start opening pressure as the respective trip set points. The rate of opening ($ON_{forward}$ state) can be defined by the first valve table and the rate of closing ($ON_{reverse}$ state) by the second valve table. The rate of opening and closing will be the same only if the first valve table is entered.

A PORV can be modeled by using a table with pressure as the independent variable and a step-like function for the flow-area fraction or valve-stem position. In this case, it is important that the step function not be too steep or the valve flow area may oscillate because of the coupling between the flow through the valve and the pressure variable. A bank of PORVs can be modeled with a single valve component in the same manner by using a multistep function to simulate the multiple pressure set points corresponding to the various valves.

Table 10-3 provides examples of valve control logic implemented for different valve actions.

The HS_SLUG multiplier, selected through the $NAMELIST input, affects calculated horizontal flow in the VALVE component. However, the option to provide a user-specified allowance for horizontal flow, similar to the one available for the PIPE, is not available in the VALVE component model.

Condensation (CNDNX) and interfacial drag (YDRGX) multipliers can be applied at user-specified locations of the VALVE component.

10.8 ACCUMULATOR MODELING WITH THE PIPE COMPONENT

An accumulator is a pressure vessel partially filled with water and pressurized with nitrogen gas. The accumulator is isolated from the primary reactor coolant system (RCS) by a check valve. If reactor coolant pressure falls below accumulator pressure, the check valve opens and the accumulator water is forced into the RCS. This flow continues until the accumulator is empty, after which the nitrogen cover gas is discharged.

During a LOCA transient, the accumulators of a PWR will deliver emergency core cooling (ECC) water to the cold legs. The accumulator injection period may be divided into two time intervals:

Phase A: $t_{ACC} \leq t \leq t_o$
Phase B: $t_o \leq t \leq t_*$

where t_{ACC} is the time when the accumulator starts to deliver ECC water, and t_o is the time when the accumulator is empty of water, t_* is the time when the pressure in the accumulator is in equilibrium with that of the intact cold leg (ICL), and no more flow issues from the accumulator.

During phase A, only water enters the ICL. The nitrogen in the accumulator continues to expand in volume as the pressure in the accumulator decreases. The nitrogen cools as it expands. During this phase, accumulator water begins to fill the reactor vessel downcomer, lower plenum, and core. During Phase B a water/nitrogen mixture, and finally only the nitrogen gas, enters the ICL. Because of the width of the tank, the water-nitrogen interface is likely to be well-defined. Consequently, the time during which a water-nitrogen mixture flows from the tank is expected to be small. The nitrogen flow passes through the downcomer of the vessel and exhausts to the containment at the broken cold leg (BCL).

The expanding nitrogen from the accumulator will significantly increase the volumetric flow in the ICL, displacing the steam originally in the ICL. Because nitrogen is an inert gas, condensation is reduced.

As the nitrogen flows into the vessel and out the break, the ICL and the upper portion of the downcomer may be pressurized due to the presence of the nitrogen flow. This increase in pressure may affect the cooling flow entering or leaving the core.

Early versions of WCOBRA/TRAC had a specialized ACCUM component to model PWR accumulators. The special ACCUM models were included in the PIPE component of the WCOBRA/TRAC-TF2 code (which has built-in wall heat conduction that is not available in the ACCUM). WCOBRA/TRAC-TF2 provides two user-selected options in the PIPE component for modeling PWR accumulators. The PIPE component with input parameter IACC set to 1 selects the normal PIPE component (IACC = 0), plus an interface sharpener and additional output variables to monitor accumulator behavior. Setting IACC to 2 selects the features of IACC = 1, plus application of a liquid separator model at the bottom of the PIPE. Figure 10-12 shows the typical nodalization of an accumulator with respect to gravity, i.e., a vertical stack of cells with cell 1 at the top and cell NCELLS at the bottom (NCELLS is the number of cells in the PIPE component).

Model as Coded

The code sets the interfacial drag to zero at each internal interface j ($1 < j < NCELLS + 1$) in the PIPE component with IACC set to 1 or 2 to enhance the phase separation in the component. Additionally, the IACC = 2 option of the PIPE component will reset, preventing the gas phase from escaping from the component (perfect separator). However, the IACC = 2 option is not used when modeling a PWR accumulator.

10.9 BREAK AND FILL COMPONENTS

BREAK and FILL components are used to model the pressure and flow boundary conditions respectively within the network of 1D components.

The BREAK- and FILL-component-specified fluid pressure, gas volume fraction, fluid temperatures, non-condensable gas partial pressure, and solute concentration in liquid define the properties of the fluid convected into the adjacent component if an inflow condition occurs. By convention, inflow to the adjacent component corresponds to a positive velocity at the FILL component's JUN1 junction and to a negative velocity at the BREAK component's JUN1 junction. A FILL or BREAK component cannot be connected directly to a VESSEL component-source connection junction or a PLENUM component junction.

A BREAK component is used to impose a pressure boundary condition one cell away from its adjacent one-dimensional component with which it connects (Figure 10-13). The pressure boundary condition, as well as the fluid properties associated with the BREAK cell for inflow donor cell convection, may be specified by user input as constants, defined individually by signal variables or control blocks, or defined as tabular functions of a signal variable or control block. They can also be constant until a controlling trip is set ON and then evaluated based on the tabular-function BREAK tables while the controlling trip remains ON.

Inflow momentum flux from a BREAK cell is not modeled internally by WCOBRA/TRAC-TF2 because its contribution to the momentum-convection term of the junction-interface motion equation can be numerically unstable. The inflow momentum flux must be modeled by the user through input by defining a dynamic-pressure rather than a static-pressure boundary condition as:

$$P_{dynamic} = P_{static} + \rho \cdot \frac{V^2}{2} \tag{10-26}$$

A BREAK is often considered a pressure boundary condition, but it can affect the flow through more than just the pressure-gradient term in the motion equations. Lack of caution in selecting the fluid void fraction and fluid temperatures and pressure that determine the fluid microscopic densities in the BREAK mesh cell can result in unexpected gravitational pressure heads and a poor prediction of the flow regime used to compute the interfacial drag. When flow is in from a BREAK, the inflow momentum flux has been assumed to be zero in order to provide a numerically stable solution. The user can account for an inflow momentum flux by input specifying a static rather than dynamic pressure boundary condition. This requires knowing when the transient inflow from the BREAK occurs and then defining the pressure in its static rather than dynamic form. This can be done using control blocks to define the static or dynamic pressure boundary condition based on the flow direction of the BREAK junction velocity.

A FILL component imposes a coolant-velocity or mass-flow boundary condition at the junction with its adjacent component (Figure 10-14). For example, the ECC injection or secondary side feedwater may be modeled with a FILL component.

The velocity or mass-flow boundary condition, as well as its fluid properties, are specified by user input in several ways, according to the FILL type IFTY option selected. The allowed values for IFTY are:

1 = constant mixture velocity;

2 = constant mass flow;

3 = constant phase velocities;

4 = mixture velocity vs. independent-variable form table;

5 = mass flow vs. independent-variable form table;

6 = generalized state vs. independent-variable form table;

7 = constant mixture velocity until the controlling trip is set ON then velocity vs. independent variable form table;

8 = constant mass flow until the controlling trip is set ON, then mass flow vs. independent-variable form table;

9 = constant generalized state until the controlling trip is set ON, then generalized state vs. independent variable form table;

10 = Generalized-state parameters defined individually by signal variable(s) or control block(s).

For each type, the relevant parameters may be constant, interpolated from input FILL-component action tables, constant until a controlling trip is set ON to require their evaluation from their action tables, or defined by signal-variable or control-block signals. The independent variable of the FILL table's tabular data is a signal-variable modeled-system parameter or a control-block output signal. The user should exercise caution when setting up FILLs with properties that depend on nearby system parameters (especially pressure) through signal-variable (or control block based on signal-variable input) independent-variable evaluated tables. The tables are always evaluated with old-time variables, and situations can occur that are numerically unstable. These instabilities can be controlled by setting additional user inputs.

10.10 HTSTR COMPONENTS

Model Basis

The HTSTR component evaluates the dynamics of conduction, convection, and gap-gas radiation heat transfer in a fuel-rod or structure hardware element. Although the transient conduction and convection heat transfer across the cylindrical 1D flow channel wall can be evaluated in the PIPE, PRIZER, PUMP, TEE, and VALVE hydraulic components, they can be done with greater modeling flexibility by using an HTSTR component. For example, an HTSTR component can couple the hydrodynamics of the adjacent fluid cells on its inner and outer surfaces, while other hydraulic components cannot do so.

The thermal history of the reactor structure is obtained from a solution of the heat conduction equation applied to different geometries. Section 8.8 discusses in detail the thermal conduction equation and its coupling solution to the fluid phases on its boundaries.

The HTSTR component has capability to model thermal radiation heat transfer. The model is based on the radiation-enclosure method that evaluates radiative exchanges between discrete surfaces of HTSTR components that are convection heat transfer coupled to particular hydraulic component cells. An option is available to include participation of the intervening two-phase fluid coolant. If the fluid participates in the radiative exchange, the model assigns radiation-related properties to each of the fluid phases according to a radiation flow regime map based on the gas volume fraction. The net radiative heat flux at each HTSTR surface and the energy absorbed by the fluid are coupled to the overall energy conservation equations that determine the structure and fluid temperatures.

As a general heat structure component provided, HTSTR features the input options to define its power generation; a reactivity feedback model for the point-reactor kinetics evaluation of fission power generated; a decay-heat model that combines the point-kinetics fission power with the power from decaying fission product precursors to define the total thermal power generated; options to specify the 3D power distribution based on the total thermal power. However, since the fuel rods (nuclear or electrically heated) are modeled using a 3D COBRA vessel component in WCOBRA/TRAC-TF2, the TRAC-3D features mentioned in this paragraph are not discussed further.

Model as Coded

The heat transfer modeling in an HTSTR component hardware element is in either ROD cylindrical (r,z) or SLAB Cartesian (x,z) 2D geometry. The user selects the hardware-element geometry by specifying ROD or SLAB through input as the component type for the HTSTR component. Heat transfer is evaluated implicitly in the r or x direction and explicitly (NAMELIST-input NRSLV = 0 option default) or implicitly (NRSLV = 1 input) in the axial z direction when the HTSTR component axial-conduction input parameter IAXCND = 1. If IAXCND = 0 is input, WCOBRA/TRAC-TF2 does not evaluate axial conduction heat transfer.

The HTSTR component hardware element may have an inner surface, outer surface, or both inner and outer surfaces where convection heat transfer is evaluated. Figure 10-15 shows the 2D node-row and node-column conduction coupling and the convective coupling to hydraulic cells at its inner and outer surfaces (perpendicular to the r or x direction). The number of r- or x-direction and z-direction nodes is input defined by NODES and NCRZ+1, respectively. If NODES = 1, a one-node lumped-parameter heat transfer solution is evaluated in the x or r direction without axial heat transfer. Node rows defined through input must be located on hydraulic-cell interfaces in the z direction. The inner and outer surfaces are defined individually by one of three different heat transfer boundary conditions that are input specified by IDBCI and IDBCO:

0 defines an adiabatic heat transfer surface (having no r- or x-direction thermal-energy flux; dT/dr or dT/dx is zero where T is the temperature at the inner or outer surface);

1 defines a heat transfer surface with input-specified constant-value HTCs and temperatures for the gas- and liquid-coolant phases that are heat transfer coupled to the inner or outer surface; and

2 defines a heat transfer surface coupled to hydraulic-component cells that are input-specified; heat transfer coefficients and temperatures are evaluated by the WCOBRA/TRAC-TF2 hydrodynamic solution for the gas and liquid-coolant phases that are heat transfer coupled to the inner or outer surface.

The IDBCI = 2 and IDBCO = 2 boundary condition provides the WCOBRA/TRAC-TF2 user with the capability to couple any two hydraulic cells within the modeled system with a conduction and surface-convection heat transfer path. Also, any number of hydraulic cells can be coupled to a given hydraulic cell.

Arrays NHCOMI(k) and NHCELI(k) (for k=1,2,..,NCRZ+2) define the respective ID and cell number of the hydraulic 1D components coupled by convection heat transfer to the HTSRT-component's inside surface. NHCOMO(k) and NHCELO(k) (for k=1,2,..,NCRZ+2) define the ID and cell number of the 1D hydraulic components that are coupled by convection heat transfer to the HTSTR component's outside surface. The numerical signs of the NHCELI(k) and NHCELO(k) array elements allow for the direction of axial node row numbering to be the same (+) or opposite (–) as that of hydraulic-cell numbering. For example, the 1D hydraulic cells |NHCELI(k)| are between node rows k and k+1 if NHCELI(k) < 0 and between node rows k–1 and k if NHCELI(k) > 0.

When the number of ROD or SLAB elements (specified by HTSTR input variable NCRX) is > 1, each element can be coupled to the same or to a different hydraulic component by input-specifying M1D = 0 (default) or M1D = 1, respectively. When M1D = 1, the four arrays are input for each of the NCRX elements to define the difference in their hydraulic-component coupling.

An HTSTR component has the capability to dynamically add and remove additional axial fine-mesh node rows during the WCOBRA/TRAC-TF2 calculation. Under input-specified trip IRFTR control, WCOBRA/TRAC-TF2 adds and removes axial fine-mesh node rows in either of two ways.

1. When trip IRFTR is set ON, WCOBRA/TRAC-TF2 adds NFAX(k) input-specified permanent axial fine-mesh node rows to each of the k = 1, NCRZ axial-cell intervals, with equal axial spacing within each interval. These permanent axial fine-mesh node rows remain in place until the trip IRFTR is set OFF.

2. During the time that trip IRFTR is ON, WCOBRA/TRAC-TF2 may either add or remove a temporary axial fine-mesh node row. This occurs when:

    a. the surface temperature change between axial node rows coupled to the hydraulic cells (where IDBCI = 2 or/and IDBCO = 2) exceeds the input-specified DTXHT(m) {to add} or is less than DTXHT(m)/2.1 {to remove}, respectively, where m = 1 for the nucleate- and transition-boiling heat transfer regimes and m = 2 for all other heat transfer regimes,

    b. adding the axial node row will not reduce the axial distance between node rows below the input-specified DZNHT minimum value, and

    c. removing the axial node row will not result in the axial-interval spacing on each side of the adjacent node rows having a ratio (new interval with respect to remaining intervals below and above) less than 10.

The total number of axial node rows (input + permanent + temporary) cannot exceed the input-specified NZMAX. When trip IRFTR is set OFF, all temporary as well as permanent axial fine-mesh node rows are removed leaving only the input axial node rows.

To apply the radiation heat transfer model, the user specifies NAMELIST variable NENCL ≥ 1. This integer defines the number of radiation enclosures in the model. For each enclosure, the number of surfaces to be involved in radiative exchanges must be defined. Enclosure data (with one data card for

each enclosure), defining the total number of faces in each enclosure and whether the intervening fluid participates, are input at the end of the Control-Procedure Data.

Each surface of a radiation enclosure corresponds to a node on either the inner or outer surface of an HTSTR component. The radiation model requires that each HTSTR component have a single ROD or SLAB element, i.e., the model requires that NCRX = 1 (Word 1 on Card Number 2) and NRODS = 1 (Word 1 on Card Number 11). Radiative properties such as surface emissivities, geometric view factors, and average path lengths are specified as part of the input data for each of the HTSTR components involved.

10.11 COCO COMPONENT

Model Basis

The COCO computer program (Bordelon and Murphy, 1974) is used to predict the containment pressure response to a LOCA for dry containment buildings, with modeling assumptions to conservatively minimize the back pressure as described in (Bordelon et al., 1974b). The containment pressure is important for determining the break flow and ultimately the pressure throughout the RCS during a LOCA, particularly during the reflood period for larger breaks. This is identified by the assigned significance in the Phenomena Identification and Ranking Table (PIRT) presented as Table 2-1 in Section 2, Volume 1.

Prior best-estimate methods rely on the execution of the thermal-hydraulic analysis code and COCO in an iterative process: (a) execute thermal-hydraulic code assuming a containment response, (b) execute COCO using the break mass and energy flows from thermal-hydraulic code, (c) execute thermal-hydraulic code using the containment back-pressures from (b); repeating until acceptable results are achieved. In order to streamline this process and remove the iterations, the COCO calculations were merged into the WCOBRA/TRAC-TF2 code for dry containment designs.

The revised method executes the thermal-hydraulic calculations and containment calculations in unison, passing the boundary condition information back and forth at each WCOBRA/TRAC-TF2 timestep. This allows every break case to have immediate feedback with the containment. The containment calculations use the mass and energy releases at the end of the WCOBRA/TRAC-TF2 timestep. Then, the new containment conditions are used for the next WCOBRA/TRAC-TF2 timestep as boundary conditions at the BREAK. As such, there is no impact on the WCOBRA/TRAC-TF2 solution matrix or numerical solution method.

A new BREAK component type should be specified with IBTYP=101 to indicate a break which interfaces with COCO. A maximum of two BREAKs of this type can be specified, which is expected to accommodate both double-ended guillotine breaks and split breaks. If IBTYP=101 is specified for any BREAK component, an associated COCO component must be specified which contains the required inputs for the containment pressure and temperature calculation.

Model as Coded

If the BREAK component type flag IBTY is not set to 101, then the BREAK will function as described in Section 10.9. However, if IBTY is set to 101, then the BREAK will use boundary conditions calculated

by WCOBRA/TRAC-TF2 using the integrated COCO code (Bordelon and Murphy, 1974). The application of the COCO code is generally consistent with the approach described in (Bordelon et al., 1974b), and is described in Section 25.6 of this topical.

10.12 REFERENCES

1. Bayless, P. D., et al., 1982, "Experimental Data Report for LOFT Large-Break Loss-of-Coolant Experiment L2-5," NUREG/CR-2826, EGG-2210.

2. Bordelon, F. M. and Murphy, E. T., 1974, "Containment Pressure Analysis Code (COCO)," WCAP-8327 and WCAP-8306 (Non-Proprietary).

3. Bordelon, F. M., et al., 1974a, "SATAN VI Program: Comprehensive Space-Time Dependent Analysis of Loss-of-Coolant," WCAP-8302 and WCAP-8306 (Non-Proprietary).

4. Bordelon, F. M., et al., 1974b, "Westinghouse Emergency Core Cooling System Evaluation Model – Summary," WCAP-8339.

5. Kamath, P. S. and Swift, W. L., 1982, "Two-Phase Performance of Scale Models of a Primary Coolant Pump," EPRI NP-2578, Final Report.

6. Kostner, W. and Seeburger, G. J., 1983, "Pump Behaviour and Its Impact on a Loss of Coolant Accident in a Pressurized Water Reactor," Nuclear Technology, Vol. 60.

7. Olson, D. J., 1974, "Single- and Two-Phase Performance Characteristics of the MOD-1 Semiscale Pump Under Steady State and Transient Fluid Conditions," Aerojet Nuclear Company, Report ANCR-1165.

8. Snyder, P. H. and Grigsby, J. M., 1982, "EVA Project on Two-Phase Reactor Coolant Pump Performance – Data Analysis and Model," Vol. 1-3, WCAP-10109.

9. Steinke, R. G., et al., 2000, "TRAC-M/FORTRAN 90 (Version 3.0) User's Manual," LA-UR-00-834.

10. Crane Company, 1942, "Flow of Fluids," Technical Paper 409.

Table 10-1 The Four Segments of Pump Homologous Curves				
Curve Segment	**Homologous Head**	**Homologous Torque**	**Variable Range**	**Operating Condition**
1	h/α_N^2	β/α_N^2	$\lvert \upsilon/\alpha_N \rvert \le 1$	$\omega > 0$
4	h/α_N^2	β/α_N^2	$\lvert \upsilon/\alpha_N \rvert \le 1$	$\omega < 0$
2	h/υ^2	β/υ^2	$\lvert \upsilon/\alpha_N \rvert > 1$	$Q > 0$
3	h/υ^2	β/υ^2	$\lvert \upsilon/\alpha_N \rvert > 1$	$Q < 0$
Note: The condition of ($\omega < 0$) will not occur in Westinghouse PWRs due to locking devices on the pumps.				

Table 10-2 Pump Control Input Parameter				
IPMPTY Pump Option	**IPMPTR Pump Trip I.D.**	**NPMPTB Pair of Points**	**Pump Speed Table (PMPTB)**	**Algorithm**
0	x = pump trip desired	x	x	Mixture Velocity before trip
	0 = no pump trip			PMPTB after trip
1	x = pump trip desired	x	x	OMEGAN before trip
	0 = no pump trip			PMPTB after trip
2	x = pump trip desired	x		OMEGAN before trip
	0 = no pump trip	0		Code calculated after trip

Table 10-3 Valve Control Options

1. Valve is normally open and is closed instantly on a trip signal.
   Controlling logic for this action is as follows:

   Before trip,

   $A_{(valve)}$ = AVLVE
   $D_{h(valve)}$ = HVLVE

   After trip,

   $A_{(valve)}$ = 0.0
   VL = 1.E-10
   VV = 1.E-10

   where,

   AVLVE equals completely open valve area
   HVLVE equals completely open valve hydraulic diameter
   VL equals velocity of liquid phase
   VV equals velocity of gas phase

2. Valve is normally closed and is opened instantly on a trip signal.
   Controlling logic for this action is as follows:

   Before trip,

   $A_{(valve)}$ = 0.0
   VL = 1.E-10
   VV = 1.E-10

   After trip,

   $A_{(valve)}$ = AVLVE
   $D_{h(valve)}$ = HVLVE

3. Valve is normally open and is closed on a trip signal according to a time-dependent valve table.
   Controlling logic is as follows:

   Before trip,

   $A_{(valve)}$ = AVLVE
   $D_{h(valve)}$ = HVLVE

   After trip,

   $A_{(valve)}$ = AVLVE * SCALE
   $D_{h(valve)}$ = HVLVE * SCALE

   where,

   SCALE equals the linear interpolated multiplier from the user input forcing factor versus time table. IF SCALE equals 0.0,

   VL = 1.E-10
   VV = 1.E-10

Table 10-3 Valve Control Options (cont)

4. Valve is normally closed and is open on a trip signal according to a time-dependent valve table. Controlling logic is as follows:

   Before trip,

   $A_{(valve)}$ = 0.0
   VL = 1.E-10
   VV = 1.E-10

   After trip,

   $A_{(valve)}$ = AVLVE * SCALE
   $D_{h(valve)}$ = HVLVE * SCALE

   where,

   SCALE has the same definition as given above.

5. Check valve is controlled by a static pressure gradient using signal variable and tabular value of 1.0 and 0.0 defined by a table.

   The above equations are applied at each timestep until the opening or closing action has been completed.

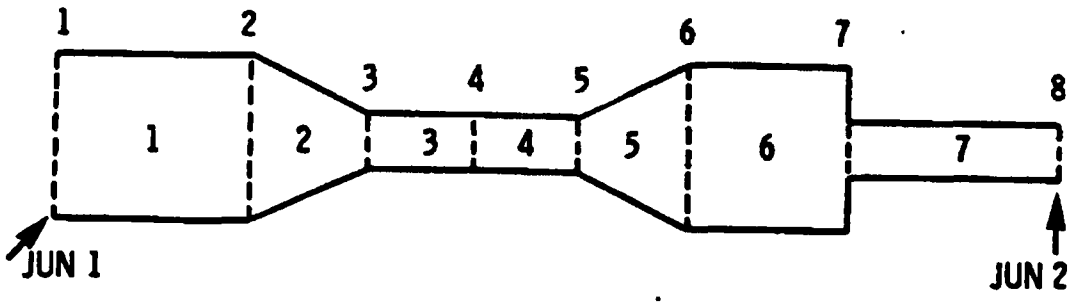

Figure 10-1 PIPE Component Noding

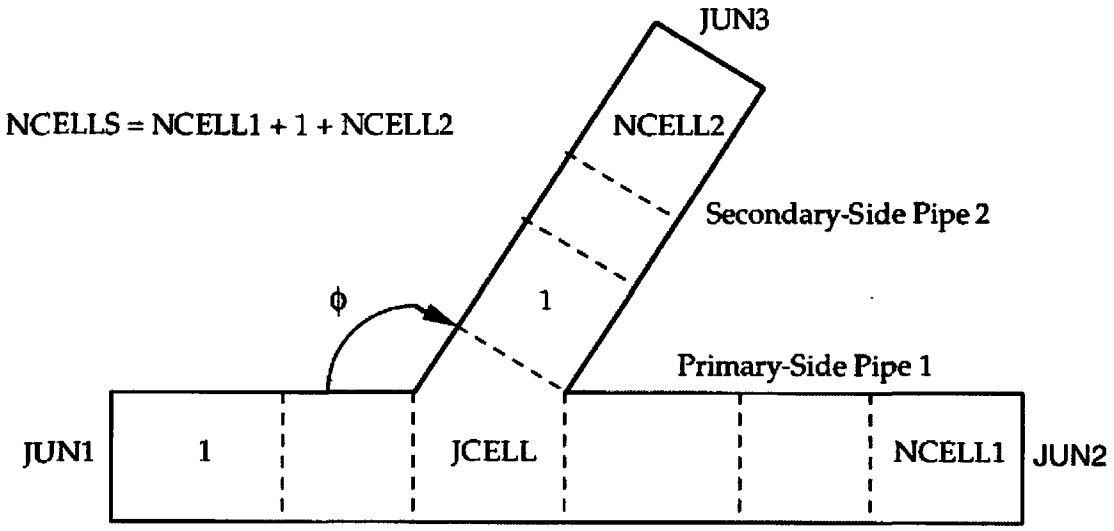

Figure 10-2 TEE Component Noding

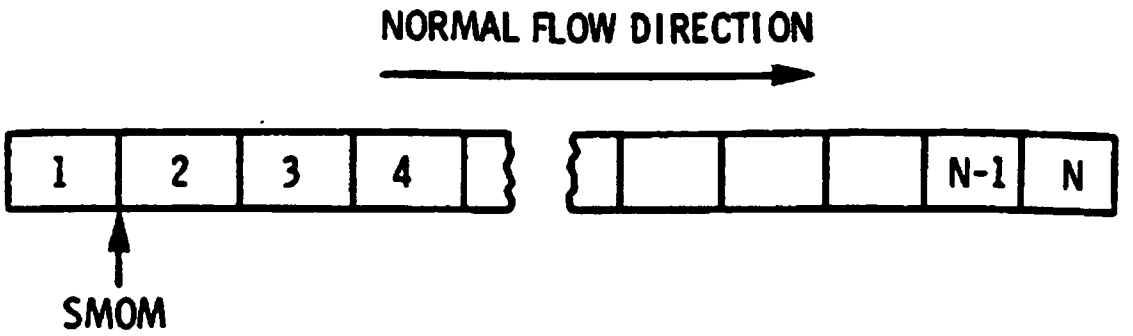

Figure 10-3 PUMP Noding Diagram

[a,c]

Figure 10-4 93A Pump Single-Phase Homologous Head Curves

a,c

Figure 10-5 93A Pump Two-Phase Homologous Head Curves

[a,c]

Figure 10-6 93A Pump Single-Phase Homologous Torque Curves

[ ] a,c

Figure 10-7 93A Pump Two-Phase Homologous Torque Curves

a,c

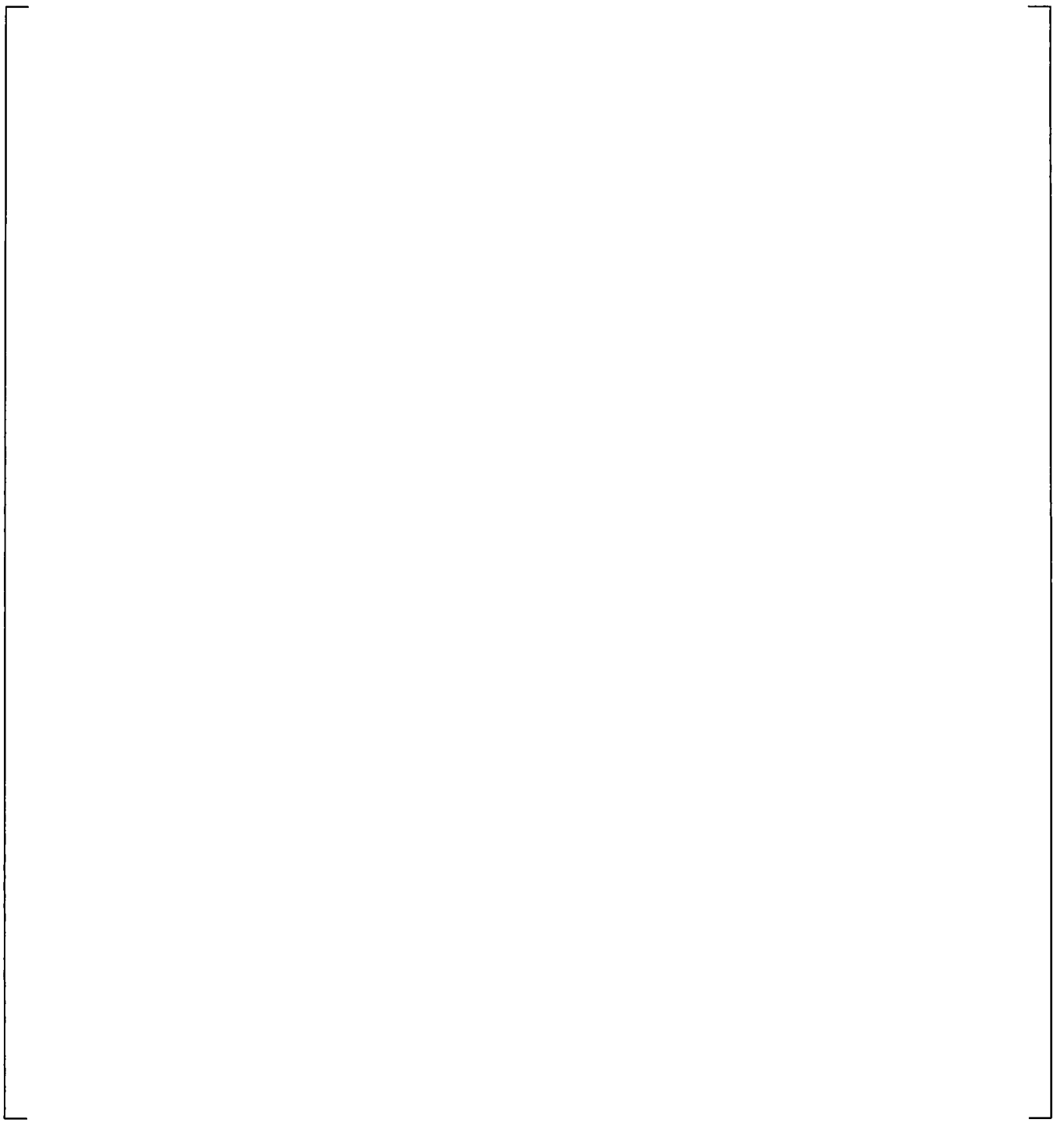

Figure 10-8 Steam Generator Noding Diagram

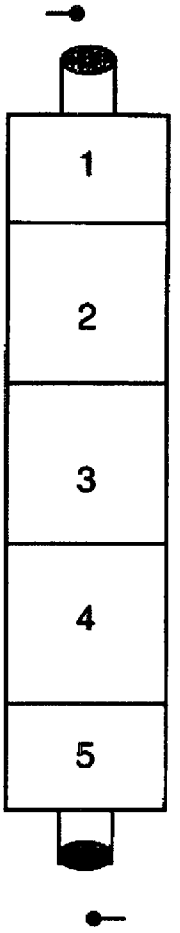

Figure 10-9 Pressurizer (PRIZER) Component Noding

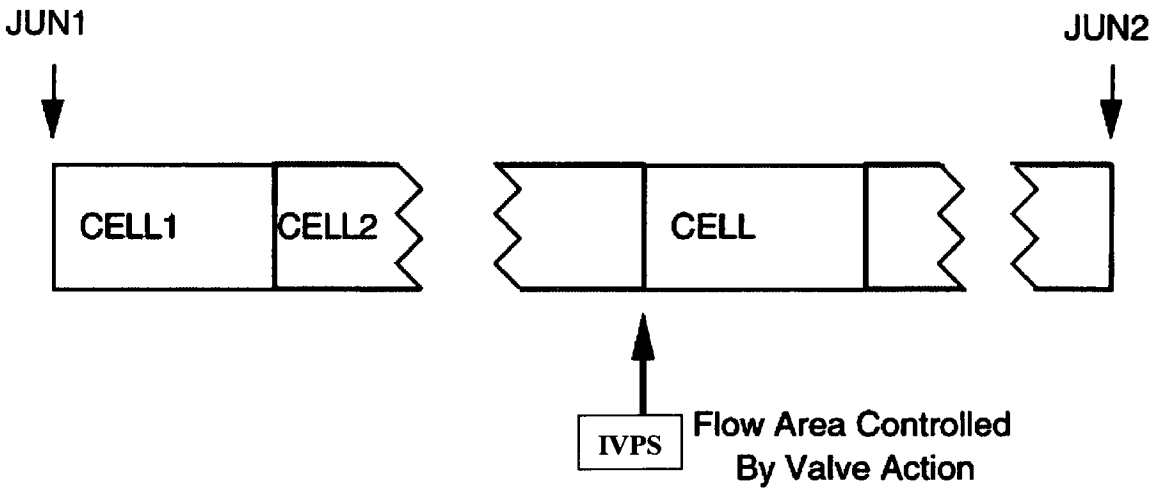

Figure 10-10 VALVE Component Noding

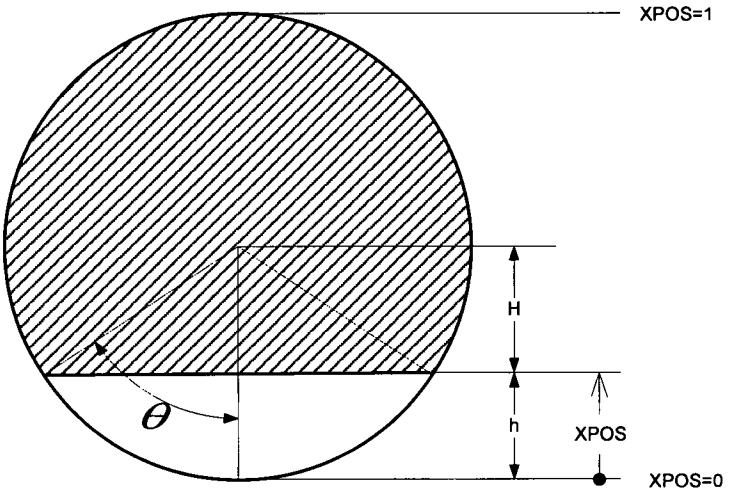

a) XPOS < 0.5

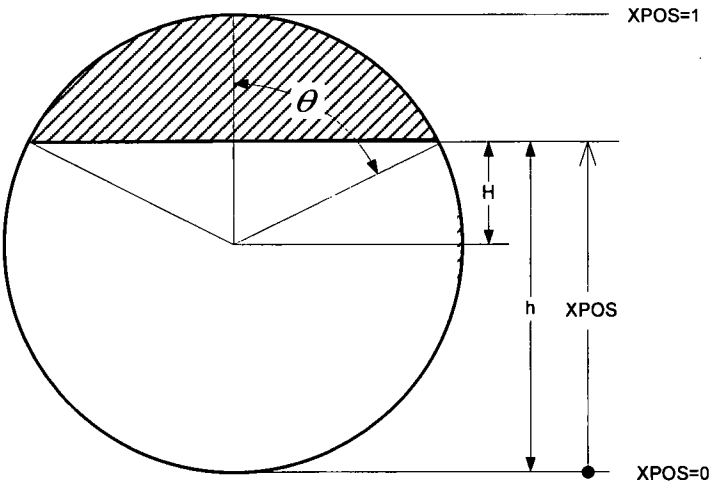

b) XPOS > 0.5

Figure 10-11 Geometry Configurations for VALVE Flow Area Calculation

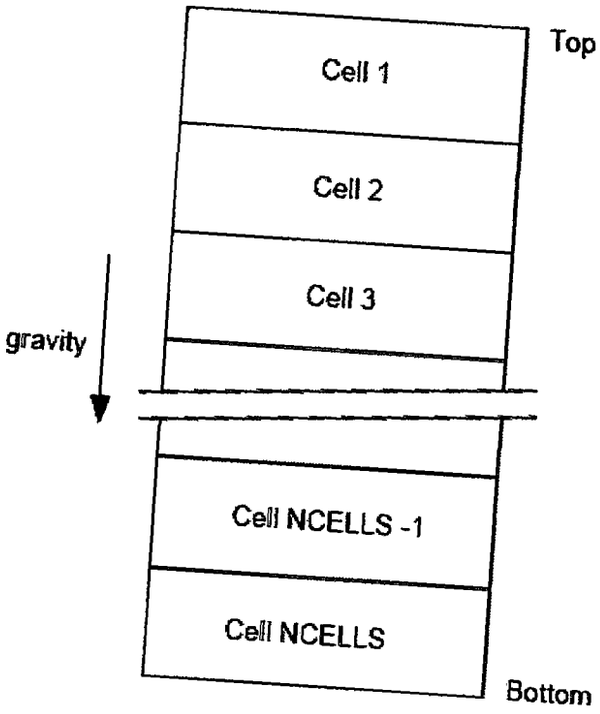

Figure 10-12 Accumulator Noding Diagram

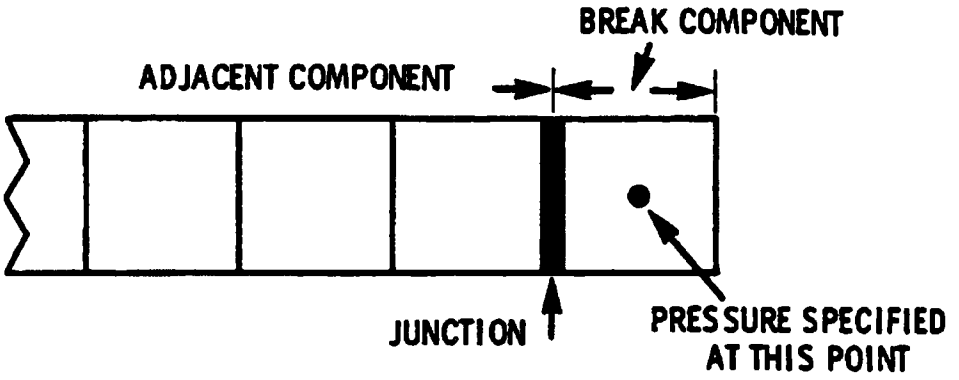

Figure 10-13 Pressure Boundary Condition Using BREAK Component

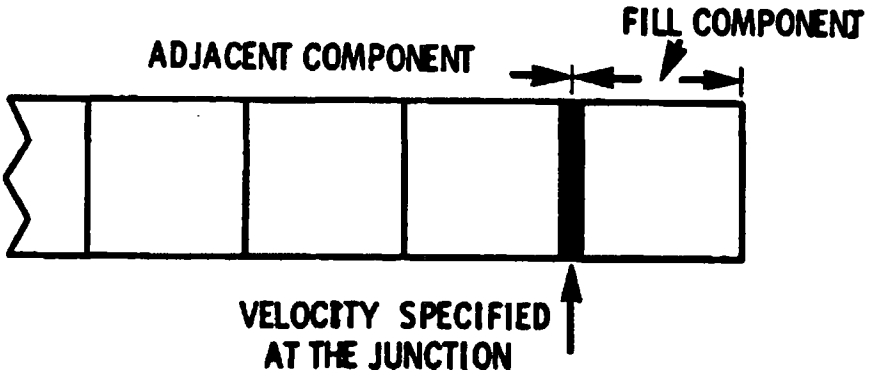

Figure 10-14 Velocity Boundary Condition Using FILL Component

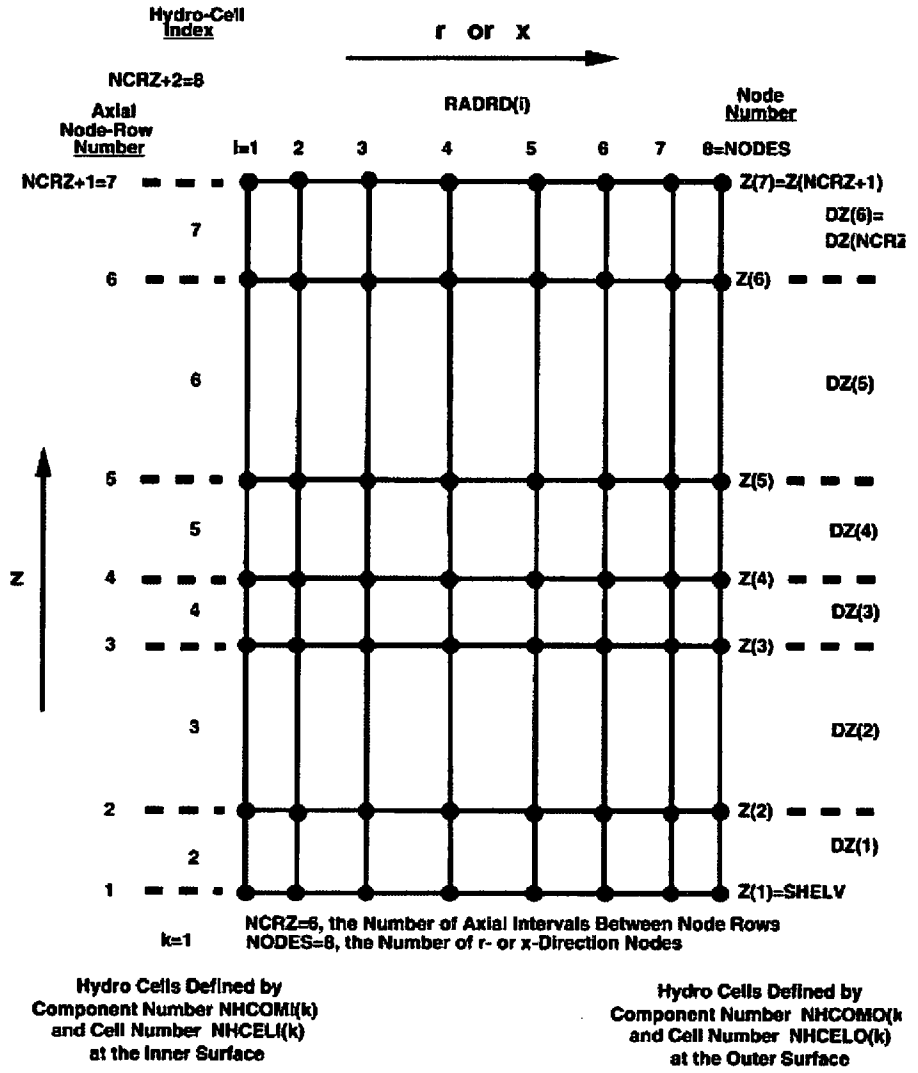

Figure 10-15 ROD or SLAB Geometry HTSTR Component with Hydraulic Cell Coupling on Both the Inner and Outer Surface

11 THERMOPHYSICAL AND TRANSPORT PROPERTIES

11.1 INTRODUCTION

WCOBRA/TRAC-TF2 includes a set of functional routines and individual correlations to calculate the thermophysical and transport properties of water, non-condensable gas, and the mixture of the steam and non-condensable gas. The calculation of the thermal properties of nuclear rods and several common structural materials is also included. The thermophysical and transport property calculations for the vessel and one-dimensional components are described in each section that follows, and the calling sequences of the property calculating subroutines in WCOBRA/TRAC-TF2 are provided in Figures 11-35 through 11-37 for vessel and 1D components, respectively. Section 11.2 describes calculation of the properties of water. Section 11.3 describes the WCOBRA/TRAC-TF2 calculation of non-condensable gas properties and its mixture properties with steam. Section 11.4 describes the thermal properties of materials used in nuclear fuel rods, clad materials, and fuel rod gap gases. WCOBRA/TRAC-TF2 can also calculate the thermal properties of several common PWR structural materials such as stainless steel. These calculations are described in Section 11.5.

11.2 THERMOPHYSICAL AND TRANSPORT PROPERTIES OF WATER

11.2.1 Vessel Component Water Properties

The thermal-hydraulic calculations performed by the WCOBRA/TRAC-TF2 vessel component frequently require the thermal conductivity, specific heat, viscosity, Prandtl number, and surface tension for water as functions of the fluid pressure and specific enthalpy. This section describes the thermodynamic property calculations performed by WCOBRA/TRAC-TF2 for saturated, superheated, and subcooled fluid conditions.

11.2.1.1 Saturated Fluid Properties

Model Basis

The saturated liquid and saturated vapor enthalpies are calculated as functions of the pressure. Values for the saturation temperature, densities of saturated liquid and vapor, thermal conductivities and viscosities of saturated liquid and vapor, saturated liquid and vapor specific heat, and the surface tension are interpolated from tables indexed by saturated liquid enthalpy. The saturated liquid and saturated vapor specific enthalpies are determined from polynomial representations of the saturation curve. This representation provides close agreement with ASME Steam Tables (1968) and the NBS/NRC Steam Tables (Haar, Gallagher, and Kell, 1984). The tables of values at saturation for the other properties (conductivities, viscosities, etc.) are also in close agreement with the standard tables.

The saturation enthalpies are calculated in Btu/lbm as functions of pressure based on expressions developed for EPRI (McFadden et al., 1980).

The polynomial expansions for saturated liquid enthalpy are:

$$H_f(P) = \sum_{n=1}^{9} A_n [\ln(P)]^{n-1} \quad (11\text{-}1)$$

if $P < 2529.9$ psia, and:

$$H_f(P) = \sum_{n=1}^{9} A_n \left[(3208.2 - P)^{0.41}\right]^{n-1} \quad (11\text{-}2)$$

for $2529.9 \leq P < 3208.0$ psia.

The constants A_n for Equations 11-1 and 11-2 are shown in Table 11-1.

The saturated vapor enthalpy is calculated using:

$$H_g(P) = \sum_{n=1}^{5} B_n [\ln(P)]^{n-1} + \sum_{n=6}^{8} B_n [\ln(P)]^{n+3} \quad (11\text{-}3)$$

if $0.1 \leq P < 1467.6$ psia, by:

$$H_g(P) = \sum_{n=1}^{9} B_n [\ln(P)]^{n-1} \quad (11\text{-}4)$$

if $1467.6 \leq P < 2586.0$ psia, and by:

$$H_g(P) = \sum_{n=1}^{9} B_n \left[(3208.2 - P)^{0.41}\right]^{n-1} \quad (11\text{-}5)$$

if $2586.0 \leq P < 3208.0$ psia.

The constants B_n for Equations 11-3 through 11-5 are listed in Table 11-2.

These expressions are compared to values from the ASME Steam Tables (1968, 1983) in Figures 11-1 and 11-2.

Table 11-3 lists values of the saturation temperature, density, viscosity, thermal conductivity, specific heat, and surface tension that are used to represent the saturation curve for those properties. The saturation curves defined by these tables are compared to values from the standard tables in Figures 11-3 through 11-11.

Model as Coded

For a known pressure P the saturated liquid enthalpy is calculated using either Equation 11-1 or 11-2 in subroutine SAT. From that calculated value of saturated liquid enthalpy, the other properties are determined in subroutine PROP by linearly interpolating between the 90 values listed in Table 11-3.

Scale Considerations

Calculation of saturated water thermophysical properties is not dependent on scale.

Conclusions

The WCOBRA/TRAC-TF2 vessel component calculates saturated liquid and saturated vapor enthalpies as functions of pressure using polynomial representations, and then uses the saturated liquid enthalpy to determine the other thermal properties by linear interpolation. All of the saturated properties agree very closely with values found in the standardized Steam Tables.

11.2.1.2 Properties of Superheated Vapor

Model Basis

Vapor Enthalpy

The enthalpy of superheated vapor as a function of pressure and temperature is calculated by the expression developed by Keenan and Keyes (1936):

$$H_v = 0.43\left[0.10129\left(F_0 P + \frac{F_1}{2}P^2 + \frac{F_3}{4}P^4 + \frac{F_{12}}{13}P^{13}\right) + F^1\right] \tag{11-6}$$

where, F_0, F_1, F_3, and F_{12} are defined by:

$$F_k = \frac{\partial}{\partial\tau}(B_k\tau), k = 0,1,3,12 \tag{11-7}$$

The coefficients B_k are defined as:

$$\tau = 1/T \tag{11-8}$$

$$B_0 = 1.89 - 2641.62\tau 10^{80870\tau^2} \tag{11-9}$$

$$B_1 = B_0^2\left(82.546\,\tau^2 - 1.6246\times10^5\tau^3\right) \tag{11-10}$$

$$B_3 = B_0^4\left(0.21828\ \tau^3 - 1.2697\times10^5\tau^5\right) \tag{11-11}$$

$$B_{12} = -B_0^{13}\left(3.635\times10^{-4}\tau^{12} - 6.768\times10^{64}\tau^{36}\right) \quad (11\text{-}12)$$

and F^1 is given by:

$$F^1 = 2502.36 + \int_{273.16}^{T}\left(1.472 + 0.00075566T + \frac{47.8365}{T}\right)dT \quad (11\text{-}13)$$

In Equations 11-6 through 11-13, T is in Kelvin (K), P is in atmospheres, and H_v is in J/g.

Vapor Temperature

Values for superheated vapor temperature as a function of pressure and enthalpy are calculated using an iterative [ ]^{a,c} interpolation.

The given enthalpy is first compared with the saturation enthalpy at the given pressure to ensure that subsequent calculation uses an enthalpy that is not lower than the saturation enthalpy.

$$H_v = \text{maximum}\begin{Bmatrix} H_0 \\ H_{sat}(P_0) \end{Bmatrix} \quad (11\text{-}14)$$

where the P_0 and H_0 are given pressure and enthalpy in the units of psia and Btu/lbm, respectively. H_{sat} is the saturation enthalpy at given P_0, in Btu/lbm.

[

]^{a,c}

[ ]^{a,c} (11-15)

[

]^{a,c}

[ ]^{a,c} (11-16)

[

]^{a,c}

[ ]^{a,c}

(11-17a)

(11-17b)

[ ]^{a,c}

[ ]^{a,c}

(11-18a)

(11-18b)

Vapor Density

The vapor specific volume is calculated as a function of pressure and enthalpy using equations from Keenan and Keyes (1936):

$$\upsilon_v = \frac{1}{\rho_v} = E_1 + E_2 P + \frac{E_3}{P} + E_4 H_v + E_5 P H_v + E_6 \frac{H_v}{P} \qquad (11\text{-}19)$$

where P is in psia, H_v is in Btu/lbm, and υ_v is in ft^3/lbm. The constants for this equation are:

E_1 = -0.81735849E-03
E_2 = 0.12378514E-04
E_3 = -0.10339904E+04
E_4 = -0.62941689E-05
E_5 = -0.872921608E-08
E_6 = 0.12460225E+01

Vapor Thermal Conductivity

The thermal conductivity for superheated vapor is calculated as a function of temperature and density using equations given in the ASME Steam Tables (1968). The expression for thermal conductivity [ ]^{a,c} is:

$$k_v = k_1 + \left(103.51 + 0.4198T - 2.771 \times 10^{-5} T^2\right)\rho_v + 2.1482 \times 10^{14} \frac{\rho_v^2}{T^{4.2}} \qquad (11\text{-}20)$$

where:

$$k_1 = 17.6 + 5.87 \times 10^{-2} T + 1.04 \times 10^{-4} T^2 - 4.51 \times 10^{-8} T^3 \qquad (11\text{-}21)$$

In Equations 11-20 and 11-21, T is in °C, ρ_v is in g/cm^3, and k_v is in mW/m-K.

[ ]^{a,c}

[ ]^{a,c} (11-22)

[ ]^{a,c}

Vapor Viscosity

The viscosity for superheated vapor is calculated as a function of temperature and density using equations given in the ASME Steam Tables (1968).

The viscosity is given by [ ]^{a,c}

$$\mu_v = \begin{cases} \mu_l - \rho(1858 - 5.9T), & \text{if } T < 340°C \\ \mu_l + 353\rho + 676.5\rho^2 + 102.1\rho^3, & \text{if } T > 365°C \end{cases} \quad (11\text{-}23)$$

$$\mu_l = 0.407 \cdot T + 80.4 \quad (11\text{-}24)$$

For values of T between 340°C and 365°C the viscosity is interpolated between the values given by the two expressions in Equation 11-23. In Equations 11-23 and 11-24, temperature is in °C, density is in g/cm^3, and viscosity is in micropoise.

[

]^{a,c}

[ ]a,c (11-25)

[ ]^{a,c}

[ ]a,c (11-26)

[

]^{a,c}

Values of superheated vapor enthalpy, temperature, density, thermal conductivity, and viscosity defined by the foregoing expressions are compared with the available data from the ASME tables (1968, 1983) and the National Bureau of Standards/National Research Council tables (Haar, Gallagher, and Kell, 1984) in Figures 11-12 through 11-16.

Model as Coded

The properties for superheated vapor represented by Equations 11-6 through 11-26 are coded as described above without modification [ ]^{a,c} Properties are not calculated if P < 0.1 psia or if P > 3208.0 psia, in which cases an error message is printed and execution is terminated.

In the calculation of vapor temperature as a function of pressure and enthalpy, Equations 11-14 through 11-18 describe an iterative method. A maximum of [ ]^{a,c} iterations are permitted.

Scaling Considerations

The equations and methods used to calculate the properties for superheated vapor are independent of scale.

Conclusions

The WCOBRA/TRAC-TF2 vessel component calculates superheated vapor enthalpy as a function of temperature and pressure, density as a function of pressure and enthalpy, and thermal conductivity as a function of temperature and density, using generalized polynomials. Temperature as a function of pressure and enthalpy is found iteratively using the enthalpy function. All of these properties agree closely with values found in standard steam tables.

11.2.1.3 Subcooled Liquid Properties

Model Basis

Subcooled liquid specific volume is calculated using the equation:

$$v_\ell = \exp\left[\sum_{i=1}^{5}\left(\sum_{j=1}^{3} C_{CXij} P^{j-1}\right) H_\ell^{i-1}\right] \tag{11-27}$$

where H_ℓ is in Btu/lbm, P is in psia, and the values of the coefficients C_{CXij} are given in Table 11-4.

The liquid temperature at enthalpy (H_ℓ) is assumed to be equal to the saturation temperature at H_ℓ. The properties C_p, k, and μ for subcooled liquid at temperature T are assumed to be equal to the saturated liquid properties at T. These properties are only weakly dependent on pressure in the low to moderate pressure range.

The liquid Prandtl number is calculated as:

$$Pr_\ell = \frac{\mu_f C_{pf}}{k_f} \tag{11-28}$$

Model as Coded

The equation for subcooled liquid specific volume is programmed as shown [ ]^{a,c} Other subcooled liquid properties are determined by linear interpolation of the saturation properties listed in Table 11-3. The liquid enthalpy is used as the index to determine the appropriate location in the table at which to perform the interpolation.

Scaling Considerations

The method in which subcooled liquid properties are determined is scale independent.

Conclusions

Subcooled liquid properties are estimated to be equal to the properties of saturated liquid corresponding to the liquid temperature. Since these properties are only weakly dependent on pressure, only a negligible error is introduced into the calculation.

11.2.2 One Dimensional Component Water Properties

The thermodynamic and transport properties for water used in the WCOBRA/TRAC-TF2 one dimensional (1D) components are based on the polynomial fits to the steam table data. The fits for transport properties were obtained from Coffman and Lynn (1966).

11.2.2.1 Saturated Fluid Thermodynamic Properties

Model Basis

Saturation Temperature and Pressure

Subroutine SATPRS calculates the saturation pressure for a given temperature, while subroutine SATTMP calculates the saturation temperature for a given pressure. Subroutine SATDER evaluates the derivative of saturation temperature with respect to saturation pressure when given the values of the saturation temperature and pressure. Four temperature and pressure regions are used to evaluate the saturation pressure, saturation temperature, and derivative of saturation temperature with respect to saturation pressure:

- **$610.8\ Pa \leq P_s < 90.56466 \times 10^3\ Pa$ and $273.15\ K \leq T_s < 370.4251\ K$**

In subroutine HEV, a linear function of temperature accurately represents the enthalpy of evaporation $h_{\ell vs}$ such that:

$$h_{\ell vs} = 3180619.59 - 2470.2120\ T_s \tag{11-29}$$

for all $T_s \leq 425.01$ K (corresponding to all $P_s \leq 0.5 \times 10^6$ Pa). The Clausius-Clapeyron equation, which assumes that steam is an ideal gas and neglects liquid volume compared to steam volume, can be written as:

$$\frac{dP_s}{dT_s} = \frac{h_{\ell vs} P_s}{R_v T_s^2} \tag{11-30}$$

where R_v is the gas constant for steam. Substituting for $h_{\ell vs}$ and integrating using the boundary condition $P_s = 24821$ Pa at $T_s = 338$ K, gives:

$$P_s = 24821.0\,(T_s/338.0)^{-5.3512} \exp\,[20.387\,(T_s - 338.0)/T_s] \tag{11-31}$$

The determination of T_s from a given P_s can be calculated by trial and error from the above equation. A simplified logic for calculating T_s is used that guarantees solution in two iterations with an error of only a fraction of a percent. First, an approximate value of T_s is calculated from:

$$T_{s,approx} = \frac{-2263.0}{0.434 \ln\left(P_s/100000.0\right) - 6.064} \tag{11-32}$$

which gives $T_{s,approx}$ within a few degrees of the actual value. Integration of the Clausius-Clapeyron equation, assuming constant $h_{\ell vs}$ between $T_{s,approx}$ and T_s, calculates the first iteration value of T_s to be:

$$T_s = \frac{T_{s,approx}}{1 - \dfrac{R_v T_{s,approx}}{h_{\ell vs,approx}} \ln\left(\dfrac{P_s}{P_{s,approx}}\right)} \tag{11-33}$$

The resulting T_s value is then input into this equation again as the new $T_{s,approx}$ value. Both $h_{\ell vs,approx}$ and $P_{s,approx}$ are calculated corresponding to $T_{s,approx}$ using the equations given above.

Inverting the Clausius-Clapeyron equation allows the derivative of the saturation temperature with respect to the saturation pressure to be evaluated, such that:

$$\frac{dT_s}{dP_s} = \frac{R_v T_s^2}{h_{\ell vs} P_s} \tag{11-34}$$

Note: For values of P_s such that:

$$1.0 \text{ Pa} \le P_s < 610.8 \text{ Pa} \tag{11-35}$$

subroutines SATTMP and SATDER reset the value of P_s to 610.8 Pa, and proceed with the calculation of T_s and dT_s/dP_s.

- **90.56466×10^3 Pa $\le P_s < 13.969971285053 \times 10^6$ Pa and $370.4251 \le T_s < 609.62462615967$ K**

Saturation temperature as a function of pressure, and saturation pressure as a function of temperature, are calculated using expressions recommended by Rivard and Torrey (1975) within this range.

These are:

$$P_s = 10^5 \left(\frac{T_s - 255.2}{117.8} \right)^{\frac{1}{0.223}} \tag{11-36}$$

and

$$T_s = 117.8 \left(10^{-5} P_s \right)^{0.223} + 255.2 \tag{11-37}$$

The derivative of saturation temperature with respect to pressure is given by:

$$\frac{dT_s}{dP_s} = \frac{0.223(T_s - 255.2)}{P_s} \tag{11-38}$$

- **$13.969971285053 \times 10^6$ Pa $\leq P_s < 22.12 \times 10^6$ Pa and 609.62462615967 K $\leq T_s <$647.3 K**

The relationships given below are based on an equation-of-state of the form:

$$\ln (P_r) = a + \frac{b}{T_r} + \frac{c}{T_r^2} \tag{11-39}$$

In the above relation,

$$P_r = \frac{P_s}{P_{critical}} \tag{11-40}$$

and

$$T_r = \frac{T_s}{T_{critical}} \tag{11-41}$$

where P_s and T_s are the saturation pressure and temperature and $P_{critical}$ and $T_{critical}$ are the critical pressure and temperature (Martin and Hou, 1955). These relationships were formulated to provide a good fit to the data and to provide a smooth transition between the preceding and the following temperature and pressure ranges:

$$P_s = 7.2166948490268 \times 10^{11} \exp \left(\frac{-8529.6481905883 + \frac{1166669.3278328}{T_s}}{T_s} \right) \tag{11-42}$$

$$T_s = \frac{4264.8240952941 + \sqrt{-13666986.708428 + 1166669.3278328 \cdot \ln(P_s)}}{27.304833093884 - \ln(P_s)} \quad (11\text{-}43)$$

and

$$\frac{dT_s}{dP_s} = \frac{-T_s^2}{P_s\left(-8529.6481905883 + \frac{2333338.6556656}{T_s}\right)} \quad (11\text{-}44)$$

- **22.12×10^6 Pa $\leq P_s \leq 45.0 \times 10^6$ Pa and 647.3 K $\leq T_s \leq$ 713.94025779311 K**

The relationships given below are based on an equation-of-state of the form:

$$\frac{d\left[\ln(P_r)\right]}{d\left[\ln\left(\frac{1}{T_r}\right)\right]} = M \quad (11\text{-}45)$$

where P_r and T_r are defined as in the previous pressure and temperature range and M is a constant (Martin and Hou, 1955):

$$P_s = 22.12 \times 10^6 \exp\left(7.6084087 - \frac{4924.9229}{T_s}\right) \quad (11\text{-}46)$$

$$T_s = \frac{4924.9229}{24.520401 - \ln(P_s)} \quad (11\text{-}47)$$

and

$$\frac{dT_s}{dP_s} = \frac{2.0304886238506 \times 10^{-4} T_s^2}{P_s} \quad (11\text{-}48)$$

Saturated Vapor Internal Energy and Enthalpy

[ ]^{a,c} main pressure regions are used in the calculation of water vapor internal energy (e_{vs}) and enthalpy (h_{vs}) at saturation, and their derivatives with respect to the partial pressure of steam, P_v. In this section, T_{sv} is the saturation temperature corresponding to P_v.

- [ ]^{a,c}

$$e_{vs} = h_{vs} - \frac{P_v}{\rho_{vs}} = h_{vs} - R_v T_{sv} \quad (11\text{-}49a)$$

and

$$\frac{de_{vs}}{dP_v} = \frac{dh_{vs}}{dP_v} - R_v \frac{dT_{sv}}{dP_v} \tag{11-49b}$$

where h_{vs} and $\frac{dh_{vs}}{dP_v}$ are calculated as described below.

Within this pressure region, the enthalpy of saturated steam at temperature T_{sv} is approximated as the sum of the enthalpy of saturated liquid water at the reference temperature of 273.15 K, plus the enthalpy necessary to raise the saturated liquid water temperature from 273.15 K to T_{sv}, plus the latent heat of vaporization needed to convert saturated liquid water at T_{sv} to saturated steam at T_{sv}. If we define the enthalpy of saturated water at 273.16 K to be exactly zero, this gives:

$$h_{vs} = 4186.8\,(273.15 - 273.16) + 4186.8\,(T_{sv} - 273.15) + h_{\ell vs} \tag{11-50a}$$

where $h_{\ell vs}$ is evaluated at T_{sv} in subroutine HEV as described earlier (Equation 11-29). The derivative with respect to the partial pressure of the vapor, P_v, becomes:

$$\frac{dh_{vs}}{dP_v} = 4186.8\frac{dT_{sv}}{dP_v} + \frac{dh_{\ell vs}}{dP_v} = (4186.8 - 2470.2120)\frac{dT_{sv}}{dP_v} \tag{11-50b}$$

- [ ]^{a,c}

[ ]^{a,c} (11-51a)

[ ]^{a,c} (11-51b)

[ ]^{a,c} (11-52a)

(11-52b)

(11-52c)

[ ]a,c (11-52d)

- [ ]a,c

A sequence of polynomials in the partial pressure of steam, P_v, is used to calculate e_{vs} and d_{evs}/dP_v as:

$$e_{vs} = AVE(i) + BVE(i)\, P_v + CVE(i)\, P_v^{\,2} + DVE(i)\, P_v^{\,3} \tag{11-53}$$

and

$$\frac{de_{vs}}{dP_v} = BVE(i) + 2\, CVE(i)\, P_v + 3\, DVE(i)\, P_v^2 \tag{11-54}$$

where:

$i=1$ for $0.5\times10^6 < p_v \le 2.0\times10^6$ Pa,
$i=2$ for $2.0\times10^6 < p_v < 5.0\times10^6$ Pa,
$i=3$ for $5.0\times10^6 \le p_v < 10.0\times10^6$ Pa,
$i=4$ for $10.0\times10^6 \le p_v < 15.0\times10^6$ Pa,
$i=5$ for $15.0\times10^6 \le p_v < 20.0\times10^6$ Pa,
$i=6$ for $20.0\times10^6 \le p_v \le 22.0\times10^6$ Pa,
$i=7$ for $22.0\times10^6 < p_v < 25.0\times10^6$ Pa,
$i=8$ for $25.0\times10^6 \le p_v < 30.0\times10^6$ Pa,
$i=9$ for $30.0\times10^6 \le p_v < 35.0\times10^6$ Pa,
$i=10$ for $35.0\times10^6 \le p_v < 40.0\times10^6$ Pa, and
$i=11$ for $40.0\times10^6 \le p_v \le 45.0\times10^6$ Pa.

The constants AVE(i), BVE(i), CVE(i), and DVE(i) for the given pressure ranges are listed in Table 11-5.

Function de_{vs}/dP_v is discontinuous near the critical point at junction point $P_v = 22.0 \times 10^6$ Pa. At this point the left side value of the function is 4.37931×10^{-3} while the right side value is 0.0, giving a fractional change across the junction point of 1.00.

A sequence of polynomials in the partial pressure of steam, P_v, is used to calculate h_{vs} and dh_{vs}/dP_v as:

$$h_{vs} = e_{vs}\gamma_s \tag{11-55}$$

and

$$\frac{dh_{vs}}{dP_v} = \gamma_s \frac{de_{vs}}{dP_v} + e_{vs} \frac{d\gamma_s}{dP_v} \tag{11-56}$$

where:

$$\gamma_s = AVG(i) + BVG(i)\, P_v + CVG(i)\, P_v^2 + DVG(i)\, P_v^3 \tag{11-57}$$

$$\frac{d\gamma_s}{dP_v} = BVG(i) + 2\, CVG(i)\, P_v + 3\, DVG(i)\, P_v^2 \tag{11-58}$$

and

$i = 1$ for $0.5 \times 10^6 < p_v \le 2.0 \times 10^6$ Pa,

$i = 2$ for $2.0 \times 10^6 < p_v < 5.0 \times 10^6$ Pa,

$i = 3$ for $5.0 \times 10^6 \le p_v < 10.0 \times 10^6$ Pa,

$i = 4$ for $10.0 \times 10^6 \le p_v < 15.0 \times 10^6$ Pa,

$i = 5$ for $15.0 \times 10^6 \le p_v < 20.0 \times 10^6$ Pa,

$i = 6$ for $20.0 \times 10^6 \le p_v \le 22.0 \times 10^6$ Pa,

$i = 7$ for $22.0 \times 10^6 < p_v < 25.0 \times 10^6$ Pa,

$i = 8$ for $25.0 \times 10^6 \le p_v < 30.0 \times 10^6$ Pa,

$i = 9$ for $30.0 \times 10^6 \le p_v < 35.0 \times 10^6$ Pa,

$i = 10$ for $35.0 \times 10^6 \le p_v < 40.0 \times 10^6$ Pa, and

$i = 11$ for $40.0 \times 10^6 \le p_v \le 45.0 \times 10^6$ Pa.

Table 11-6 lists the constants AVG(i), BVG(i), CVG(i), and DVG(i) for the given pressure ranges.

[

]^{a,c}

Functions dh_{vs}/dP_v and $d\gamma_s/dP_v$ are both discontinuous near the critical point at junction point $P_v = 22.0 \times 10^6$ Pa. At this point, the left side value of dh_{vs}/dP_v is 4.6073×10^{-3} and the right side value

is -5.1790 × 10^{-6} for a fractional change here of 1.0011. The left side value of $d\gamma_s/dp_v$ is 6.6694 × 10^{-12} and the right side value is –2.3541 × 10^{-12} [1] giving a fractional change at this junction point of 1.3530.

Saturated Liquid Internal Energy and Enthalpy

A series of polynomials in T_{sat} is used to calculate the internal energy of saturated liquid ($e_{\ell s}$) and its derivative with respect to saturation temperature T_{sat}. These are given by:

$$e_{\ell s} = ALE(i) + BLE(i)\cdot T_{sat} + CLE(i)\cdot T_{sat}^2 + DLE(i)\cdot T_{sat}^3 \tag{11-59}$$

and

$$\frac{de_{\ell s}}{dT_{sat}} = BLE(i) + 2CLE(i)\cdot T_{sat} + 3DLE(i)\cdot T_{sat}^2 \tag{11-60}$$

where:

$i=1$ for $273.15 \le T_{sat} < 423.15\,K$,
$i=2$ for $423.15 \le T_{sat} < 473.15\,K$,
$i=3$ for $473.15 \le T_{sat} < 523.15\,K$,
$i=4$ for $523.15 \le T_{sat} < 573.15\,K$,
$i=5$ for $573.15 \le T_{sat} < 623.15\,K$,
$i=6$ for $623.15 \le T_{sat} \le 645.15\,K$,
$i=7$ for $645.15 < T_{sat} < 673.15\,K$, and
$i=8$ for $673.15 \le T_{sat} \le 713.94025779311\,K$.

Table 11-7 lists the constants ALE(i), BLE(i), CLE(i), and DLE(i) for the given temperature ranges.

Saturated liquid enthalpy is calculated using the definition:

$$h_{\ell s} = e_{\ell s} + \frac{P}{\rho_{\ell s}} \tag{11-61}$$

and its derivative by:

$$\frac{dh_{\ell s}}{dP} = \frac{de_{\ell s}}{dT_{sat}}\frac{dT_{sat}}{dP} + \frac{1}{\rho_{\ell s}} - \frac{P}{\rho_{\ell s}^2}\left[\left(\frac{\partial \rho_{\ell s}}{\partial P}\right)_{T_{sat}} + \left(\frac{\partial \rho_{\ell s}}{\partial T_{sat}}\right)_{P}\frac{dT_{sat}}{dP}\right] \tag{11-62}$$

1. The value of -2.3541 × 10^{-12} is corrected from -2.3541 × 10^{-2} in the TRAC/M manual (Spore, et al., 2000).

where $e_{\ell s}$ and its derivative are evaluated as shown earlier, and where $\rho_{\ell s}$ and its derivatives are evaluated using the equations in Section 11.2.2.4 with T_ℓ equal to T_{sat}.

Saturated Vapor Specific Heat Capacity

Although the heat capacity of saturated steam is not an output variable of THERMO, subsequent steam property calculations require its definition. The heat capacity of saturated steam is:

$$c_{pvs} = ACP(i) + BCP(i)\, T_{sv} + CCP(i)\, T_{sv}^2 + DCP(i)\, T_{sv}^3 \tag{11-63}$$

and

$$\frac{dc_{pvs}}{dP_v} = \left[BCP(i) + 2\, CCP(i)\, T_{sv} + 3\, DCP(i)\, T_{sv}^2\right]\frac{dT_{sv}}{dP_v} \tag{11-64}$$

where:

$i = 1$ for $273.15 \le T_{sv} < 323.15\,K$,
$i = 2$ for $323.15 \le T_{sv} < 373.15\,K$,
$i = 3$ for $373.15 \le T_{sv} < 423.15\,K$,
$i = 4$ for $423.15 \le T_{sv} < 473.15\,K$,
$i = 5$ for $473.15 \le T_{sv} < 523.15\,K$,
$i = 6$ for $523.15 \le T_{sv} < 573.15\,K$,
$i = 7$ for $573.15 \le T_{sv} < 623.15\,K$,
$i = 8$ for $623.15 \le T_{sv} < 647.3\,K$,
$i = 9$ for $647.3 \le T_{sv} < 673.15\,K$, and
$i = 10$ for $673.15 \le T_{sv} < 713.94025779311\,K$.

Table 11-8 lists the constants ACP(i), BCP(i), CCP(i), and DCP(i) for the given temperature ranges.

Model as Coded

Subroutine THERMO supplies thermodynamic properties for WCOBRA/TRAC-TF2 one-dimensional components. The input variables are the total pressure, the partial pressure of the non-condensable gas, if any is present, and the liquid- and gas-phase temperatures, where the gas phase is a steam, or a non-condensable gas, or a steam-gas mixture. The output variables include the saturation temperature corresponding to the total pressure and its derivative with respect to the total pressure, the saturation temperature corresponding to the partial pressure of steam and its derivative with respect to the steam partial pressure, the internal energies and densities of the liquid and gas phases, and their partial derivatives with respect to pressure (at constant temperature) and with respect to temperature (at constant pressure), and finally the saturated liquid and saturated vapor enthalpies, and their derivatives with respect to the pressure.

THERMO supplies thermodynamic properties valid for temperatures and pressures within the following ranges:

$$273.15\,K \leq T_\ell \leq 713.940258\,K$$

$$273.15\,K \leq T_g \leq 3000.0\,K$$

and

[ ]^{a,c}

If THERMO is provided with a temperature outside this range, the calculation stops and it adjusts the data to the corresponding limit and issues a warning message.

Subroutine RHOLIQ calculates liquid densities and density derivatives used in THERMO.

Saturation pressure, saturation phasic densities, and saturated enthalpies as calculated by WCOBRA/TRAC-TF2 are compared with NBS/NRC tables (Haar, Gallagher, and Kell, 1984) in Figures 11-17 through 11-21.

Scaling Considerations

Not applicable.

Conclusions

The saturation conditions for the WCOBRA/TRAC-TF2 one-dimensional components are calculated using polynomial expressions that provide a close approximation to the Steam Table values. The error introduced by the WCOBRA/TRAC-TF2 routines is small and is not considered a major contributor to the overall code calculational uncertainty.

11.2.2.2 Thermophysical Properties of Superheated Vapor

Model Basis

Internal Energy

The constant pressure specific heat of steam at temperature T_v is approximated as:

$$c_{pv} = \left(\frac{\partial h_v}{\partial T_v}\right)_P = \frac{c_{pv,ideal}}{2}\left[1 + \frac{T_v}{\left(T_v^2 - \beta\right)^{1/2}}\right] \qquad (11\text{-}65)$$

where:

$$\beta = T_{sv}^2\left[1-\frac{1}{\left(\frac{2c_{pvs}}{c_{pv,ideal}}-1\right)^2}\right] \tag{11-66}$$

The term c_{pvs} is calculated as defined in Equation 11-63 and $c_{pv,ideal}$ is defined by ideal gas behavior, such that:

$$c_{pv,ideal} = \frac{R_v\gamma_{ideal}}{\gamma_{ideal}-1} \tag{11-67}$$

where R_v is the gas constant for steam (461.5 J/kg-K) and $\gamma_{ideal} = 1.3$ is the ratio of ideal specific heats for steam.

Integrating the expression for c_{pv} along a line of constant pressure P_v gives:

$$h_v = h_{vs} + \frac{c_{pv,ideal}}{2}\left[\left(T_v - T_{sv}\right) + \left(T_v^2 - \beta\right)^{1/2} - \frac{T_{sv}}{\left(\frac{2c_{pvs}}{c_{pv,ideal}}-1\right)}\right] \tag{11-68}$$

The internal energy of vapor is therefore:

$$e_v = e_{vs} + \frac{c_{pv,ideal}}{2}\left[\left(T_v - T_{sv}\right) + \left(T_v^2 - \beta\right)^{1/2} - \frac{T_{sv}}{\left(\frac{2c_{pvs}}{c_{pv,ideal}}-1\right)}\right] - P_v\left(\frac{1}{\rho_v} - \frac{1}{\rho_{vs}}\right) \tag{11-69}$$

The definitions of enthalpy and internal energy allow the density of the water vapor to be written such that:

$$\begin{aligned}\rho_v &= \frac{P_v}{h_v - e_v} = \frac{P_v}{\left[h_{vs} + c_{pv,ideal}\left(T_v - T_{sv}\right)\right] - \left[e_{vs} + c_{vv,ideal}\left(T_v - T_{sv}\right)\right]} \\ &= \frac{P_v}{\left(h_{vs} - e_{vs}\right) + \left(\gamma_{ideal} - 1\right)\left(e_v - e_{vs}\right)}\end{aligned} \tag{11-70}$$

Substitution of ρ_v and ρ_{vs}, as defined by the preceding equation, into the equation for the internal energy of the vapor gives the following equations.

For $P_v \leq 1.9 \times 10^7$ Pa,

$$e_v = e_{vs} + \frac{c_{vv,ideal}}{2} = \left[(T_v - T_{sv}) + (T_v^2 - \beta)^{\frac{1}{2}} - \frac{T_{sv}}{\left(\frac{2\, c_{pvs}}{c_{pv,ideal}} - 1 \right)} \right] \tag{11-71}$$

where $c_{vv,ideal}$ is the constant volume specific heat for steam, as defined by ideal gas behavior given by:

$$c_{vv,ideal} = \frac{R_v}{\gamma_{ideal} - 1}$$

The partial derivatives are given by:

$$\left(\frac{\partial e_v}{\partial T_v} \right)_{p_v} = \frac{c_{vv,ideal}}{\left(1 - \frac{\beta}{\kappa^2} \right)} \tag{11-72}$$

and

$$\left(\frac{\partial e_v}{\partial P_v} \right)_{T_v} = -\frac{1}{2} \left(\frac{\partial e_v}{\partial T_v} \right)_{P_v} \left[\left(1 - \frac{\beta}{\kappa^2} \right) \kappa_p' + \frac{1}{\kappa} \frac{d\beta}{dP_v} \right] \tag{11-73}$$

where:

$$\kappa = \frac{2}{c_{vv,ideal}} (e_v - e_{vs}) + T_{sv} \left[1 + \frac{1}{\frac{2\, c_{pvs}}{c_{pv,ideal}} - 1} \right]$$

and

$$\kappa_p' = -\frac{2}{c_{vv,ideal}}\frac{de_{vs}}{dP_v} + \left[1 + \frac{1}{\left(\frac{2\,c_{pvs}}{c_{pv,ideal}} - 1\right)}\right]\frac{dT_{sv}}{dP_v}$$

$$-\frac{2}{c_{pv,ideal}}\left[\frac{T_{sv}}{\left(\frac{2\,c_{pvs}}{c_{pv,ideal}} - 1\right)^2}\right]\frac{dc_{pvs}}{dP_v}$$

and

$$\frac{d\beta}{dP_v} = \frac{2}{T_{sv}}\left\{\beta\frac{dT_{sv}}{dP_v} + \frac{2}{c_{pv,ideal}}\left[\frac{T_{sv}}{\left(\frac{2\,c_{pvs}}{c_{pv,ideal}} - 1\right)}\right]^3\frac{dc_{pvs}}{dP_v}\right\}$$

For $P_v \geq 2.0 \times 10^7$ Pa,

$$e_v = e_{vs} + \frac{c_{pv,ideal}}{2\,\gamma_s}\left[\left(T_v - T_{sv}\right) + \left(T_v^2 - \beta\right)^{1/2} - \frac{T_{sv}}{\left(\frac{2\,c_{pvs}}{c_{pv,ideal}} - 1\right)}\right] \qquad (11\text{-}74)^2$$

$$\left(\frac{\partial e_v}{\partial T_v}\right)_{P_v} = \frac{c_{pv,ideal}}{2\,\gamma_s}\left(1 + \frac{T_v}{(T_v^2 - \beta)^{\frac{1}{2}}}\right) \qquad (11\text{-}75)$$

and

$$\left(\frac{\partial e_v}{\partial P_v}\right)_{T_v} = \frac{de_{vs}}{dP_v} - \frac{e_v - e_{vs}}{\gamma_s}\frac{d\gamma_s}{dP_v} + \frac{c_{pv,ideal}}{2\gamma_s}\cdot\left[\left(-\frac{dT_{sv}}{dP_v}\right) - \frac{1}{2}\frac{d\beta}{dP_v}\frac{1}{(T_v^2 - \beta)^{\frac{1}{2}}}\right] \qquad (11\text{-}76)$$

2. Equation 11-74 is corrected from the original one in the TRAC/M manual (Spore, et al., 2000).

$$-\frac{dT_{sv}}{dP_v}\cdot\left(\frac{1}{\frac{2\,c_{pvs}}{c_{pv,ideal}}-1}\right)+\frac{2}{c_{pv,ideal}}\left[\frac{T_{sv}}{\left(\frac{2\,c_{pvs}}{c_{pv,ideal}}-1\right)^2}\right]\frac{dc_{pvs}}{dP_v}\Bigg]$$

where:

$$\frac{d\beta}{dP_v}=\frac{2}{T_{sv}}\left\{\beta\frac{dT_{sv}}{dP_v}+\frac{2}{c_{pv,ideal}}\left[\frac{T_{sv}}{\left(\frac{2\,c_{pvs}}{c_{pv,ideal}}-1\right)}\right]^3\frac{dc_{pvs}}{dP_v}\right\}$$

For 1.9×10^7 Pa $< P_v < 2.0 \times 10^7$ Pa, the values of e_v and its derivatives are calculated by interpolating between the values of the two curve fits.

Density

If $P_v \leq 1.9 \times 10^7$ Pa, the vapor density is calculated as:

$$\rho_v=\frac{P_v}{(\gamma_s-1)e_{vs}+(\gamma_{ideal}-1)\cdot(e_v-e_{vs})} \tag{11-77}$$

Therefore, the partial derivatives are calculated by:

$$\left(\frac{\partial\rho_v}{\partial T_v}\right)_{p_v}=-\left(\frac{\partial e_v}{\partial T_v}\right)_{p_v}\frac{(\gamma_{ideal}-1)\rho_v}{(\gamma_s-1)e_{vs}+(\gamma_{ideal}-1)(e_v-e_{vs})} \tag{11-78}$$

and

$$\left(\frac{\partial\rho_v}{\partial P_v}\right)_{T_v}=\left\{1-\rho_v\left[e_{vs}\frac{d\gamma_s}{dP_v}+(\gamma_s-\gamma_{ideal})\frac{de_{vs}}{dP_v}\right]\right\}\cdot\left[\frac{1}{(\gamma_s-1)e_{vs}+(\gamma_{ideal}-1)(e_v-e_{vs})}\right]+\left(\frac{\partial\rho_v}{\partial e_v}\right)_{P_v}\left(\frac{\partial e_v}{\partial P_v}\right)_{T_v} \tag{11-79}$$

where:

$$\left(\frac{\partial\rho_v}{\partial e_v}\right)_{P_v}=-\frac{(\gamma_{ideal}-1)\rho_v}{[(\gamma_s-1)e_{vs}+(\gamma_{ideal}-1)\cdot(e_v-e_{vs})]} \tag{11-80}$$

If $P_v \geq 2.0 \times 10^7$ Pa, the vapor density is calculated as:

$$\rho_v = \frac{P_v}{(\gamma_s - 1)\, e_v} \tag{11-81}$$

Therefore,

$$\left(\frac{\partial \rho_v}{\partial T_v}\right)_{P_v} = \left(\frac{\partial \rho_v}{\partial e_v}\right)_{P_v} \left(\frac{\partial e_v}{\partial T_v}\right)_{P_v} \tag{11-82}$$

and

$$\left(\frac{\partial \rho_v}{\partial P_v}\right)_{T_v} = \left(1 - \rho_v e_v \frac{d\gamma_s}{dP_v}\right) \frac{1}{(\gamma_s - 1) e_v} + \left(\frac{\partial \rho_v}{\partial e_v}\right)_{p_v} \left(\frac{\partial e_v}{\partial P_v}\right)_{T_v} \tag{11-83}$$

where:

$$\left(\frac{\partial \rho_v}{\partial e_v}\right)_{P_v} = -\frac{\rho_v}{e_v} \tag{11-84}$$

If $1.9 \times 10^7 < P_v < 2.0 \times 10^7$ Pa, the vapor density and its derivatives are calculated by linearly interpolating between the values of the two curve fits.

Enthalpy

The enthalpy of superheated vapor is calculated using the definition of enthalpy,

$$h_v = e_v + \frac{P_v}{\rho_v} \tag{11-85}$$

where e_v is calculated from Equation 11-71 and Equation 11-74, and ρ_v is calculated using Equations 11-77 and 11-81.

Model as Coded

Thermodynamic properties for superheated water vapor are calculated in subroutine THERMO as described in this section. For superheated vapor, however, minimum and maximum limits are placed on the calculated values of the density, and its partial derivatives. In low pressure regions where the above equations may predict a negative density, the density and its derivatives are recalculated based on ideal gas behavior. If ρ_v is less than zero, the vapor density and its derivatives are superseded by:

$$\rho_v = \frac{P_v}{R_v T_v}$$

$$\left(\frac{\partial \rho_v}{\partial T_v}\right)_{p_v} = -\frac{\rho_v}{T_v}$$

and

$$\left(\frac{\partial \rho_v}{\partial P_v}\right)_{T_v} = \frac{\rho_v}{P_v}$$

Near the critical point, it is necessary to impose the following limit on the density ratio:

$$\frac{\rho_v}{\rho_\ell} \leq 0.999$$

to avoid singularities when calculating certain parameters. If the calculated value of ρ_v exceeds 0.999 ρ_ℓ, the vapor density and its derivatives are superseded by:

$$\rho_v = 0.999\,\rho_\ell$$

$$\left(\frac{\partial \rho_v}{\partial T_v}\right)_{P_v} = 0.999\left(\frac{\partial \rho_\ell}{\partial T_\ell}\right)_P$$

and

$$\left(\frac{\partial \rho_v}{\partial P_v}\right)_{T_v} = 0.999\left(\frac{\partial \rho_\ell}{\partial P}\right)_{T_\ell}$$

Scaling Considerations

Not applicable.

Conclusions

The thermodynamic properties for superheated vapor in WCOBRA/TRAC-TF2 one-dimensional components are calculated from thermodynamic first principles. The calculated values are in good agreement with those found in the Steam Tables. The error introduced by the WCOBRA/TRAC-TF2 routines is small and thus is not considered a major contributor to the overall code calculational uncertainty.

11.2.2.3 Subcooled Vapor Thermophysical Properties

Model Basis

Internal Energy

The internal energy and its derivatives for subcooled vapor are calculated as:

$$e_v = e_{vs} + (T_v - T_{sv})\frac{c_{pvs}}{\gamma_{ideal}} \tag{11-86}$$

$$\left(\frac{\partial e_v}{\partial T_v}\right)_{P_v} = \frac{c_{pvs}}{\gamma_{ideal}} \tag{11-87}$$

$$\left(\frac{\partial e_v}{\partial P_v}\right)_{T_v} = \frac{de_{vs}}{dP_v} + \left(\frac{e_v - e_{vs}}{c_{pvs}}\right)\frac{dc_{pvs}}{dP_v} - \left(\frac{\partial e_v}{\partial T_v}\right)_{P_v}\frac{dT_{sv}}{dP_v} \tag{11-88}$$

where T_{sv} is the saturation temperature corresponding to the vapor pressure P_v.

Density

Subcooled vapor density and its derivatives are determined using the same method of calculation as in the case of superheated vapor for $P_v \leq 1.9\times10^7$ Pa (Equation 11-77 through Equation 11-80 in Section 11.2.2.2).

Enthalpy

The enthalpy of subcooled vapor is calculated using the definition of enthalpy,

$$h_v = e_v + \frac{P_v}{\rho_v} \tag{11-89}$$

where e_v is calculated from Equation 11-86, and ρ_v is calculated using Equation 11-77 or 11-81.

Model as Coded

The thermodynamic properties for subcooled vapor are calculated directly as described in this section, in subroutine THERMO. The enthalpy is calculated in subroutine FPROP.

Scaling Considerations

Not applicable.

Conclusions

The thermodynamic properties for subcooled vapor in WCOBRA/TRAC-TF2 one-dimensional components are calculated in a manner consistent with calculations for superheated vapor, which are derived from thermodynamic first principles. Subcooled vapor occurs only infrequently during a LOCA transient. As such, the error introduced by WCOBRA/TRAC-TF2 subcooled vapor property calculations is assumed minor and is not considered a contributor to the code uncertainty.

11.2.2.4 Subcooled Liquid Thermophysical Properties

Model Basis

Internal Energy

For a liquid at a subcooled temperature T_ℓ and pressure P the liquid internal energy associated with that state is calculated starting with the internal energy of the saturated liquid state described by T_ℓ and $P_{sat}(T_\ell)$, which is the saturation pressure corresponding to T_ℓ, and adding an additional term which represents the change in internal energy from the state $(T_\ell, P_{sat}(T_\ell))$ to the state (T_ℓ, P). That is

$$e_\ell(T_\ell, P) = e_{\ell s}(T_\ell) + \theta_\ell(P, T_\ell) \tag{11-90}$$

The additional term θ_ℓ, which represents the change in energy required to move along the isotherm at T_ℓ between two different pressure values, namely $P_{sat}(T_\ell)$ and P, is represented as:

$$\theta_\ell(P, T_\ell) = (P - P_{sat}(T_\ell))\left(\frac{\partial e_\ell}{\partial P}\right)_{T_\ell} \tag{11-91}$$

where:

$$\left(\frac{\partial e_\ell}{\partial P}\right)_{T_\ell} = -8.329595\times10^{-4}\left[1-\exp\left(-1.450382\times10^{-6}\cdot P_{sat}(T_\ell)\right)\right] - 2.245825\times10^{-17}\cdot P_{sat}(T_\ell)^2 \tag{11-92}[3]$$

Therefore, the partial derivative with respect to T_ℓ of the internal energy is calculated as:

$$\left(\frac{\partial e_\ell}{\partial T_\ell}\right)_p = \frac{de_{\ell s}}{dT_{sat}} + ERT$$

3. The value of -1.450382 × 10^{-6} is corrected from 1.450382 × 10^{-6} in the TRAC/M manual (Spore, et al., 2000).

where:

$$ERT = \left[\frac{\partial \theta_\ell(P, T_\ell)}{\partial T_\ell}\right]_p = \{-8.329595\times10^{-4}\left[-1+\exp\left(-1.450382\times10^{-6}\cdot P_{sat}(T_\ell)\right)\right.$$
$$\left.\cdot\left[1+1.450382\times10^{-6}\left(P-P_{sat}(T_\ell)\right)\right]\right] \quad (11\text{-}93)$$
$$-2.245825\times10^{-17}(2P\cdot P_{sat}(T_\ell)-3\,P_{sat}(T_\ell)^2)\,\}\frac{dP_{sat}(T_\ell)}{dT_\ell}$$

and $de_{\ell s}/dT_{sat}$ is calculated as in Equation 11-60.

Density

Initial Calculation

Given the pressure P and temperature T_ℓ of liquid water, Tait's equation-of-state in the form:

$$\frac{v(0,T_\ell)-v(P,T_\ell)}{v(0,T_\ell)} = \frac{1}{n}\ln\left[1+\frac{P}{B(T_\ell)}\right] \quad (11\text{-}94)$$

is used to determine the liquid density and its partial derivatives, where v is the specific volume of the liquid. The constant n is quoted in work by Richardson, Arons, and Halverson (1947) to be 7.146. The terms $v(0, T_\ell)$ and $B(T_\ell)$ are third-order polynomials of liquid temperature fitted to steam table data, such that:

$$v(0,T_\ell) = AVO(i)+BVO(i)\,T_\ell+CVO(i)\,T_\ell^2+DVO(i)\,T_\ell^3$$

and

$$B(T_\ell) = AFN(i)+BFN(i)\,T_\ell+CFN(i)\,T_\ell^2+DFN(i)\,T_\ell^3$$

where:

$i=1$ for $273.15 \le T_\ell < 373.15\,K$,
$i=2$ for $373.15 \le T_\ell < 473.15\,K$,
$i=3$ for $473.15 \le T_\ell < 573.15\,K$,
$i=4$ for $573.15 \le T_\ell < 603.15\,K$,
$i=5$ for $603.15 \le T_\ell < 613.15\,K$,
$i=6$ for $613.15 \le T_\ell < 623.15\,K$,
$i=7$ for $623.15 \le T_\ell < 633.15\,K$,
$i=8$ for $633.15 \le T_\ell < 643.15\,K$,
$i=9$ for $643.15 \le T_\ell < 653.15\,K$,
$i=10$ for $653.15 \le T_\ell < 663.15\,K$,
$i=11$ for $663.15 \le T_\ell < 673.15\,K$, and
$i=12$ for $673.15 \le T_\ell \le 713.94025779311\,K$.

Table 11-9 lists the constants AVO(i), BVO(i), CVO(i), DVO(i), AFN(i), BFN(i), CFN(i), and DFN(i) for the given temperature ranges.

This allows the density, ρ_ℓ, to be calculated as:

$$\rho_\ell = \frac{1}{v(0,T_\ell)\left\{1.0 - \frac{1}{7.146}\ln\left[1.0 + \frac{P}{B(T_\ell)}\right]\right\}} \tag{11-95}$$

Therefore,

$$\left(\frac{\partial \rho_\ell}{\partial P}\right)_{T_\ell} = \frac{\rho_\ell^2 v(0,T_\ell)}{7.146\,[P + B(T_\ell)]} \tag{11-96}$$

and

$$\left(\frac{\partial \rho_\ell}{\partial T_\ell}\right)_P = -\rho_\ell \frac{v'(0,T_\ell)}{v(0,T_\ell)} - B'(T_\ell)\frac{P}{B(T_\ell)}\left(\frac{\partial \rho_\ell}{\partial P}\right)_{T_\ell} \tag{11-97}$$

where:

$$v'(0,T_\ell) = BVO(i) + 2\,CVO(i)\,T_\ell + 3\,DVO(i)\,T_\ell^2$$

and

$$B'(T_\ell) = BFN(i) + 2\,CFN(i)\,T_\ell + 3\,DFN(i)\,T_\ell^2$$

The polynomial constants for $v'(0,T_\ell)$ and $B'(T_\ell)$ are the same as for $v(0,T_\ell)$ and $B(T_\ell)$ and are given in Table 11-9.

Model as Coded

The thermodynamic properties for subcooled liquid are calculated in subroutine THERMO as described in the previous paragraphs.

Scaling Considerations

Not applicable.

Conclusions

The subcooled water thermodynamic property routines used in WCOBRA/TRAC-TF2 for one dimensional components have been compared to the standard steam table data. The agreement is good over a wide range of pressure (14.7 psi < P_ℓ < 3000. psi) and liquid subcooling.

11.2.2.5 Transport Properties

Model Basis

This section describes the WCOBRA/TRAC-TF2 calculations performed to obtain the specific heat, fluid viscosity, thermal conductivity, and surface tension for one-dimensional components. The equations used for these quantities are polynomial fits to data.

Specific Heat

Function CPLL calculates the constant pressure specific heat for liquid water in J/(kg-K) as a function of enthalpy (H_ℓ) and pressure (P) by:

$$c_{p\ell} = \left\{H_\ell\left[H_\ell\left(D_{o\ell} + D_{1\ell}P\right) + \left(C_{o\ell} + C_{1\ell}P\right)\right] + B_{o\ell} + B_{1\ell}P\right\}^{-1} \tag{11-98}$$

Function CPVV1 calculates the steam constant-pressure specific heat, such that:

$$c_{pv} = C_{1v} + C_{2v}T_v + \frac{C_{3v}P}{\left(C_{5v}T_v - C_{6v}\right)^{2.4}} + \frac{C_{4v}P^3}{\left(C_{5v}T_v - C_{6v}\right)^9} \tag{11-99}$$

where the coefficients of Equations 11-98 and 11-99 are listed in Table 11-10.

Liquid Viscosity

Calculation of liquid viscosity is divided into three different ranges in VISCL based on the liquid enthalpy (H_ℓ).

For $H_\ell \leq 0.276\times10^6$ J/kg, the liquid viscosity in N-s/m^2 is:

$$\mu_\ell = \left\{A_{0\ell} + A_{1\ell}\chi + A_{2\ell}\chi^2 + A_{3\ell}\chi^3 + A_{4\ell}\chi^4\right\} - \left[B_{0\ell} + B_{1\ell}\eta + B_{2\ell}\eta^2 + B_{3\ell}\eta^3\right]\cdot(P - P_o) \quad (11\text{-}100)$$

where:

$$\chi = (H_\ell - c_{0n})H_0 \quad (11\text{-}101)$$

and

$$\eta = (H_\ell - e_{c0n})e_{h0} \quad (11\text{-}102)$$

For $0.276\times10^6 \text{ J/kg} < H_\ell \leq 0.394\times10^6 \text{ J/kg}$ the liquid viscosity is,

$$\mu_\ell = \left[E_{0\ell} + E_{1\ell}H_\ell + E_{2\ell}H_\ell^2 + E_{3\ell}H_\ell^3\right] + \left[F_{0\ell} + F_{1\ell}H_\ell + F_{2\ell}H_\ell^2 + E_{3\ell}H_\ell^3\right](P - P_o) \quad (11\text{-}103)$$

and for $H_\ell > 0.394\text{x}10^6$ J/kg,

$$\mu_\ell = \left[D_{0\ell} + D_{1\ell}z + D_{2\ell}z^2 + D_{3\ell}z^3 + D_{4\ell}z^4\right] \quad (11\text{-}104)$$

where:

$$z = (H_\ell - c_n)H_{00} \quad (11\text{-}105)$$

The coefficients for the liquid viscosity equations are found in Table 11-11.

Vapor Viscosity

Vapor viscosity is calculated the same way using Equations 11-23 through 11-26 in Section 11.2.1.2.

Liquid Thermal Conductivity

The liquid thermal conductivity is calculated in THCL and given as W/m-K by:

$$k_\ell = A_{\ell0} + A_{\ell1}\chi_\kappa + A_{\ell2}\chi_\kappa^2 + A_{\ell3}\chi_\kappa^3 \quad (11\text{-}106)$$

where:

$$\chi_\kappa = \frac{H_\ell}{H_0} \tag{11-107}$$

and constants $A_{\ell 0}$, $A_{\ell 1}$, $A_{\ell 2}$, $A_{\ell 3}$ and H_0 are listed in Table 11-12.

Vapor Thermal Conductivity

Vapor thermal conductivity is calculated the same way using Equations 11-20 through 11-22 in Section 11.2.1.2.

Surface Tension

Function SIGMA calculates the surface tension of liquid water using two ranges of saturation temperature corresponding to the total pressure. The units for surface tension are N/m.

- **$273.15\ K \leq T_{sat} \leq 582.435\ K$**

Within this range, the surface tension of liquid water is calculated using the following ASME Steam Tables (1983) Recommended Interpolation Equation:

$$\sigma = 0.2358\left(1 - 0.625\frac{647.15 - T_{sat}}{647.15}\right)\left(\frac{647.15 - T_{sat}}{647.15}\right)^{1.256} \tag{11-108}$$

The ASME Steam Tables state that this equation is valid for temperatures between the triple point (273.16 K) and the critical point, which the reference assumes to be 647.15 K. It is necessary in WCOBRA/TRAC-TF2, however, to place a lower limit on the calculated value of the surface tension to avoid singularities when evaluating such things as the Chen nucleate boiling relation. For this reason, the surface tension is set equal to a constant value for the remaining temperature range, 582.435 K to 713.94025779311 K.

- **$582.435\ K < T_{sat} \leq 713.94025779311\ K$**

A constant value of surface tension is calculated in this range to keep the surface tension from becoming too low. Constraining the temperature difference ratio to be no less than 0.1 gives:

$$\sigma = 0.2358\,[1 - 0.625\,(0.1)\,]\,(0.1)^{1.256} = 0.012261 \tag{11-109}$$

Model as Coded

Subroutine FPROP is used to obtain transport properties for liquid- and vapor-phase water. The input variables for this subroutine are the saturation temperature corresponding to the total pressure; the internal energies, densities, and temperatures of the liquid and gas phases where the gas is either steam, non-condensable gas, or steam-gas mixture; the total pressure; and the partial pressure of the non-condensable gas, if any is present. The output transport variables include the latent heat of

vaporization, the constant pressure specific heats, viscosities, and thermal conductivities of the liquid and gas phases, and the surface tension of the liquid.

The transport property calls are function calls within the FPROP subroutine. Function CPLL calculates the constant pressure specific heat of the liquid, while function CPVV1 determines the value of the constant pressure specific heat of the vapor. [

]^{a,c} Finally, function SIGMA calculates the surface tension.

The equations shown are coded directly. Sample curves of liquid and vapor specific heat, viscosity, thermal conductivity, and the surface tension calculated by these routines along the saturation line are shown in Figures 11-22 through 11-28.

In some instances, upper and lower limits are maintained on the calculated values of the transport properties. These limits are summarized as follows.

Specific Heat

The maximum permitted value for the liquid specific heat is $c_{p\ell} = 4.0 \times 10^4$ J/(kg-K). If the calculation of $c_{p\ell}$ by Equation 11-98 performed by function CPLL yields a value greater than this, $c_{p\ell}$ is reset to 4.0×10^4 J/(kg-K). No limits are placed on the calculation of the vapor specific heat.

Viscosity

No limits are imposed on the vapor and liquid phase viscosities, [

]^{a,c}

Thermal Conductivity

The minimum permitted value of the liquid thermal conductivity is $k_\ell = 0.09$ W/m-K. If, in function THCL, Equation 11-106 yields a value lower than this, k_ℓ is reset to 0.09 W/m-K.

No limits are imposed on the vapor phase thermal conductivity [ ]^{a,c}

Surface Tension

If $T_{sat} > 582.435$ K, the surface tension is set to $\sigma = 0.012261$ N/m.

Scaling Considerations

Not applicable.

Conclusions

The subcooled water transport properties routines used in WCOBRA/TRAC-TF2 for one dimensional components have been compared to the standard steam table data. The agreement is good over a wide range of pressure (14.7 psi< P_f < 3000 psi) and liquid subcooling.

11.3 THERMOPHYSICAL AND TRANSPORT PROPERTIES OF NON-CONDENSABLE GASES AND STEAM GAS MIXTURES

11.3.1 Vessel Component

Model Basis

WCOBRA/TRAC-TF2 can perform calculations for a thermal hydraulic system which is either an air only system or a nitrogen and water (liquid and steam) system. This section describes the thermodynamic properties which are defined for air and nitrogen in the WCOBRA/TRAC-TF2 vessel component.

11.3.1.1 Air

Enthalpy

The enthalpy of air is calculated as:

$$H_{air} = c_{p,air,ref}\left(T_{air} - T_{ref,air}\right) + H_{ref,air} \tag{11-110}$$

where the reference values are $T_{ref,air}$ = 40.0°F, $H_{ref,air}$ = 188.49 Btu/lbm, and $c_{p,air,ref}$ = 0.249 Btu/lbm-°F.

Density

The density of air is calculated from the ideal gas law with the gas constant for air assumed to be $R_{air} = \frac{8314.339\ \text{J/(kmol - K)}}{28.96461\ \text{kg/kmol}} = 287.0516\ \text{J/(kg - K)}$. Thus, the density of air is given by:

$$\rho_{air} = \frac{P}{R_{air}\left(T_{air} + 273.15\right)} \tag{11-111}$$

Temperature

The air temperature is estimated from the enthalpy using the inverse of Equation 11-110.

Specific Heat

The specific heat for air in BTU/(lbm-°F) is determined in two different temperature ranges.

If $T_{air} \leq 600K$,

$$c_p = 0.244388 + A_1 T_{air} + A_2 T_{air}^2 + A_3 T_{air}^3 \quad (11\text{-}112)$$

and if $T_{air} > 600K$,

$$c_p = 0.208831 + B_1 T_{air} + B_2 T_{air}^2 + B_3 T_{air}^3 \quad (11\text{-}113)$$

where the coefficients A_i and B_i are listed in Table 11-13, and T_{air} is in Kelvin (K).

11.3.1.2 Nitrogen

Enthalpy

The enthalpy of nitrogen is calculated [ ]^{a,c}

[ ]^{a,c}

$$H_{N_2}(T) = 1041.6 \cdot T \quad (11\text{-}114)$$

[ ]^{a,c}

[ ]^{a,c} (11-115)

[

]^{a,c}

Density

The density of nitrogen is calculated from the ideal gas law with the gas constant for nitrogen assumed to be $R_{N_2} = 296.80\ J/(kmol \cdot K)$. Thus, the density of nitrogen is given by:

$$\rho_{N_2} = \frac{P}{R_{N_2}\left(T_{N_2} + 273.15\right)} \tag{11-116}$$

Temperature

The nitrogen temperature is estimated from the enthalpy using the inverse of Equations 11-114 and 11-115.

Specific Heat

The specific heat for nitrogen is determined [ ]^{a,c} in kJ/kg-K

[ ]^{a,c}

[a,c] (11-117)

[ ]^{a,c}

$$c_{p,N_2}(T) = 1.0416 \tag{11-118}$$

Model as Coded

The equations used to calculate the thermodynamic properties of air and nitrogen, Equations 11-110 through 11-118, are coded as shown without modification. No upper or lower limits are imposed on the values calculated. [ ]^{a,c}

Scaling Considerations

Not applicable.

Conclusions

The WCOBRA/TRAC-TF2 vessel component can perform calculations to estimate the thermodynamic properties of air and nitrogen. However, only the option of selecting nitrogen as the non-condensable gas in the water system is allowed by the current code.

11.3.2 One-Dimensional Components

Model Basis

This section describes the calculation of thermodynamic and transport properties in WCOBRA/TRAC-TF2 one-dimensional components for the non-condensable gas – nitrogen.

Internal Energy

The internal energy and its derivatives for nitrogen are given by:

$$e_a = c_{v,a} \cdot T \tag{11-119}$$

$$\left(\frac{\partial e_a}{\partial T}\right)_{P_a} = c_{v,a} \tag{11-120}$$

and

$$\left(\frac{\partial e_a}{\partial P_a}\right) = 0.0 \tag{11-121}$$

The constant volume specific heat of the non-condensable gas $c_{v,a}$ is calculated as:

$$c_{v,a} = c_{p,a} - R_c/M_a \tag{11-122}$$

where $c_{p,a}$ is the constant pressure specific heat, $R_c = 8314.339$ J/(kmol·K) is the universal gas constant and M_a is the molecular weight.

For nitrogen, the correlations used to calculate c_{p,N_2} are described in the Equation 11-117 and Equation 11-118 [ ]^{a,c}

The molecular weight for nitrogen is $M_{N_2} = 28.01352$ kg/kmol.

Density

The density and its derivatives are based on the Ideal Gas Law and are given by:

$$\rho_a = \frac{P_a}{R_a T} \tag{11-123}$$

$$\left(\frac{\partial \rho_a}{\partial P_a}\right)_T = \frac{1}{R_a T} \tag{11-124}$$

$$\left(\frac{\partial \rho_a}{\partial T}\right)_{P_a} = -R_a \rho_a \left(\frac{\partial \rho_a}{\partial P_a}\right)_T \quad (11\text{-}125)$$

where:

$$R_a = R_c / M_a \quad J/(kg \cdot K) \quad (11\text{-}126)$$

Viscosity

The viscosity of nitrogen is calculated [

]^{a,c}

[ ]^{a,c} (11-127)

and

[ ]^{a,c} (11-128)

[

]^{a,c}

Thermal Conductivity

[ ]^{a,c}, the thermal conductivity nitrogen is calculated [

]^{a,c}

[ ]^{a,c} (11-129)

[

]^{a,c}

Model as Coded

[

]^{a,c}

Scaling Considerations

Not applicable.

Conclusions

The WCOBRA/TRAC-TF2 one-dimensional components calculate thermodynamic properties for the non-condensable gas assuming it behaves as ideal gas. The transport properties are based on polynomial fits to data or the kinetic theory. The correlations approximately calculate properties for the nitrogen at low density.

11.3.3 Steam and Non-Condensable Gas Mixtures

Model Basis

This section describes the calculations of steam and gas mixture thermodynamic specific heat and internal energy [ ]^{a,c} and the steam gas mixture transport properties (viscosity and thermal conductivity) [

]^{a,c}

Specific Heat

Specific heat of the steam and gas mixture is calculated in CPVV1H as:

$$c_p = \frac{\rho_v c_{p,v} + \rho_a c_{p,a}}{\rho_v + \rho_a} \tag{11-130}$$

Density

Subroutine THERMOH calculates the steam and non-condensable gas mixture density as:

$$\rho_m = \rho_v + \rho_a \tag{11-131}$$

Internal Energy

Subroutine THERMOH calculates the steam and non-condensable gas mixture internal energy as:

$$e_m = \frac{\rho_v e_v + \rho_a e_a}{\rho_v + \rho_a} \tag{11-132}$$

Enthalpy

Subroutine COBRAI calculates the steam and non-condensable gas mixture Enthalpy for the VESSEL components as:

$$h_m = \frac{\rho_v h_v + \rho_a h_a}{\rho_v + \rho_a} = e_m + \frac{P}{\rho_m} \tag{11-133}$$

Binary Diffusion Coefficient

[

]^{a,c}

[ ] a,c

(11-134)

[

]^{a,c}

[

,]^{a,c}

[ ] a,c

[

]^{a,c}

[ ] a,c

(11-135)

[ ]^{a,c}

Viscosity

[

]^{a,c}

$$\left[\qquad\qquad\right]^{a,c} \tag{11-136}$$

[ ]^{a,c}

$$\left[\qquad\qquad\right]^{a,c} \tag{11-137}$$

[

]^{a,c}

Thermal Conductivity

[

]^{a,c}

$$\left[\qquad\qquad\right]^{a,c} \tag{11-138}$$

[ ]^{a,c}

$$\left[\qquad\qquad\right]^{a,c} \tag{11-139}$$

[ ]^{a,c}

[ ]^{a,c} (11-140)

[ ]^{a,c} (11-141)

[ ]^{a,c} (11-142)

[ ]^{a,c} (11-143)

[ ]^{a,c} (11-144)

Scaling Considerations

Not applicable.

Conclusions

The WCOBRA/TRAC-TF2 one-dimensional components calculate transport properties for the non-condensable gas and steam mixture [ ]^{a,c}

11.4 THERMAL PROPERTIES OF NUCLEAR FUEL ROD MATERIALS

A typical nuclear fuel rod is composed of uranium-dioxide fuel pellets and a zirconium based clad material. The gap between the fuel pellets and the clad is filled with the initial backfill gas and fission gas. As part of the WCOBRA/TRAC-TF2 default nuclear fuel rod model, the material properties of uranium-dioxide, Zircaloy-4, ZIRLO alloy, and of gas mixtures are included. This section describes the calculation of the thermal properties for these fuel rod materials.

[

]^{a,c}

11.4.1 Uranium Dioxide

Model Basis

The material properties of uranium dioxide are based on MATPRO-9 (MacDonald et al., 1976) and on MATPRO-11, Rev. 1 (Hagrman, Reymann, and Mason, 1980) calculations, with exception to the thermal conductivity model, which is the Nuclear Fuels Industries (NFI) model as modified in FRAPCON 3.3 (Lanning et al., 2005).

Density

The (cold) density for uranium-dioxide is assumed to be:

$$\rho_{UO_2} = 684.86 f_D \tag{11-145}$$

where f_D is the fraction of theoretical density and is input by the user. The density ρ_{UO_2} has units of lbm/ft^3.

Thermal Conductivity

The UO_2 thermal conductivity model accounts for the effects of burnup on thermal conductivity. The Nuclear Fuels Industries (NFI) model (Ohira and Itagaki, 1997) was selected as the starting point for a replacement of the Lucuta model (Lucuta et al., 1996) for FRAPCON 3.3 (Lanning et al., 2005). The Lucuta formula for uranium oxide pellet thermal conductivity was found to have two inaccuracies. First, it predicts values at high temperature (>2200 K) that are too large relative to credible modern data for un-irradiated fuel pellet material (Ronchi et al., 1999). Secondly, it has too little burnup degradation compared to both in-cell laser-flash diffusivity measurements on high-burnup pellet samples and in-reactor fuel temperatures measured at nominal to high burnup. For especially this second reason, the NFI model as modified in FRAPCON 3.3 is considered most appropriate. Section 2.3 in (Lanning et al., 2005) shows that the modified NFI model compares well against zero burnup (unirradiated) and irradiated test results.

The NFI model, similar to most other thermal conductivity models utilized in fuel performance codes, consists of a lead term that is inversely proportional to a temperature function A + BT (phonon term), with burnup dependence factors in its denominator, plus terms that model the electronic contribution to fuel heat transfer at high temperature. The modified NFI model implemented in WCOBRA/TRAC-TF2 is defined as follows:

$$K_{95} = \frac{1}{A + B \cdot T + f(Bu) + \left(1 - 0.9 \cdot \exp(-0.04 \cdot Bu)\right) \cdot g(Bu) \cdot h(T)} + \frac{E}{T^2} \cdot \exp(-F/T) \quad (11\text{-}146)$$

where:

K_{95} = Thermal Conductivity, W/m-K, for as fabricated fuel density of 95% of theoretical density (TD)

T = Temperature, K

Bu = Burnup, GWD/MTU

f(Bu) = effect of fission products in crystal matrix (solution)

$$= 0.00187 \cdot Bu \quad (11\text{-}147)$$

g(Bu) = effect of irradiation defects,

$$= 0.038 \cdot Bu^{0.28} \quad (11\text{-}148)$$

h(T) = Temperature dependence of annealing on irradiation defects

$$= \frac{1}{1 + 396 \cdot \exp(-Q/T)} \quad (11\text{-}149)$$

Q = Temperature dependence parameter = 6380 K

A = 0.0452 m-K/W

B = 2.46E-4 m/W

E = 3.5E9 W-K/m

F = 16361 K

The model is adjusted for 'as fabricated' fuel densities different from 95% TD using the Lucuta recommendation for spherical-shaped pores (Lucuta et al., 1996), as follows:

$$K_d = 1.0789 \cdot K_{95} \cdot \{d/[1.0 + 0.5 \cdot (1 - d)]\} \quad (11\text{-}150)$$

where:

K_d	=	Thermal Conductivity, W/m-K, for as-fabricated fuel density "d"
d	=	density in fraction of TD

The range of applicability of the modified NFI correlation is provided by volume 4 of the NUREG/CR-6534 (Lanning et al., 2005) as follows:

Temperature	=	300 – 3000 K
Rod-Average Burnup	=	0 – 62 GWD/MTU
As-fabricated Density	=	92 – 97 % TD

Specific Heat

The specific heat in Btu/lbm-°F for uranium dioxide is given by:

$$c_{P_{UO_2}} = \left(2.388\times10^{-4}\right)\left\{\frac{K_1\theta^2\exp(\theta/T_K)}{T_K^2\left[\exp(\theta/T_K)-1\right]^2} + K_2T_K + \frac{F_{OM}}{2}\frac{K_3E_D}{RT_K^2}\exp(-E_D/RT_K)\right\} \quad (11\text{-}151)$$

where T_K is the temperature in Kelvin (K) and

θ	=	Einstein temperature (535.285 K)
R	=	8.3143 (J/mol-K)
K_1	=	296.7 (J/kg-K)
K_2	=	2.43×10^{-2} (J/kg-K^2)
K_3	=	8.745×10^{7}(J/kg)
E_D	=	1.577×10^{5} (J/mol)
F_{OM}	=	oxygen/metal ratio (2.0)

Model as Coded

The equations representing the density, thermal conductivity and specific heat for uranium dioxide are coded into WCOBRA/TRAC-TF2 as described by Equations 11-145 through 11-151 without modification.

Calculations for uranium dioxide density are performed in subroutine SETUP, those for thermal conductivity in subroutines SSTEMP and TEMP, and those for specific heat in subroutines TEMP and MOVE. Values of conductivity and specific heat versus temperature are shown in Figures 11-29, 11-30 and 11-31.

Scaling Considerations

Not applicable.

Conclusions

The WCOBRA/TRAC-TF2 correlations for UO_2 density and specific heat are based on MATPRO-9 and MATPRO-11. The correlation for UO_2 thermal conductivity is the modified NFI model used in FRAPCON 3.3. The models and correlations for these properties were used in simulations of LOFT. Therefore, the uncertainty and reliability of these models is accounted for in the overall code bias and uncertainty.

11.4.2 Zircaloy-4

Model Basis

The material properties of Zircaloy-4 are based on MATPRO-9 and MATPRO-11 calculations.

Density

The (cold) density of Zircaloy-4 clad material is assumed to be $\rho_{Zr} = 409.0 lbm/ft^3$.

Thermal Conductivity

The thermal conductivity in Btu/hr-ft-°F for Zircaloy-4 clad is given by:

$$k_{Zr} = 0.5779 \cdot \left[7.51 + 0.0209 T_K - \left(1.45 \times 10^{-5}\right) T_K^2 + \left(7.67 \times 10^{-9}\right) T_K^3\right] \quad (11\text{-}152)$$

where T_K is temperature in Kelvin (K).

Specific Heat

WCOBRA/TRAC-TF2 calculates the specific heat for Zircaloy-4 by linearly interpolating between values from a built-in table. Table 11-14 lists the values used to determine the specific heat of Zircaloy-4.

Model as Coded

The equations for the density, thermal conductivity and specific heat of Zircaloy-4 are coded into WCOBRA/TRAC-TF2 as described above without modification. Density is calculated in subroutine SETUP and HEAT, conductivity in subroutines STEMP, TEMP, and HEAT and specific heat in subroutines TEMP, HEAT, and MOVE. Curves of conductivity and specific heat versus temperature are shown in Figures 11-32 and 11-33.

Scaling Considerations

Not applicable.

Conclusions

The WCOBRA/TRAC-TF2 correlations for the density, thermal conductivity, and specific heat of Zircaloy-4 are based on MATPRO-9 and MATPRO-11. These property relations were used in simulations of LOFT.

11.4.3 ZIRLO Alloy

Model Basis

The ZIRLO alloy developed by Westinghouse represents a modification to Zircaloy-4 which was achieved by reducing the tin and iron content, eliminating the chromium, and adding a nominal one percent niobium. Table 11-15 shows a comparison of the two alloys.

Since tin is an alpha phase stabilizer and niobium is a beta phase stabilizer, the reduction in tin and the addition of niobium result in reductions in the temperatures at which the ZIRLO alloy undergoes the alpha to beta phase change, relative to Zircaloy-4. Measurements performed by Westinghouse show that the ZIRLO alloy starts the transformation at 1023 K and ends at 1213 K.

Since the ZIRLO and Zircaloy-4 alloys are both about 98 percent zirconium, it should not be expected that the material properties are significantly different, except to the extent that they are affected by the differences in the phase change temperatures. Density, thermal expansion, thermal conductivity, and specific heat of both alloys have been measured by the Properties Research Laboratory using samples cut from Westinghouse production tubing (Taylor, Groot, and Larimore, 1989). Evaluation of the test results indicated that the materials are sufficiently similar that the Zircaloy-4 material properties can be used for the ZIRLO alloy, with the exception of the specific heat (Davidson and Nuhfer, 1990). The specific heat of the ZIRLO alloy is based on an adjustment to Table 11-14, which considers the difference in phase change temperatures.

Density

The (cold) density of the ZIRLO cladding material is taken to be identical to that of Zircaloy-4 (409.0 lbm/ft^3).

Thermal Conductivity

The thermal conductivity of the ZIRLO cladding material is taken to be identical to that of Zircaloy-4, given by Equation 11-152.

Specific Heat

The specific heat shown in Table 11-14 for Zircaloy-4 includes both the true specific heat and the alpha to beta phase heat of transformation. The specific heat for the ZIRLO cladding material was obtained by adjusting Table 11-14 to account for the difference in phase change temperatures, assuming both the true specific heat and the heat of transformation are the same for the two alloys. The true specific heat is taken

to be equal to the total specific heat in Table 11-14 for T ≤ 1090 K, 0.085 Btu/lbm-°F for T ≥ 1213 K, and:

[ ]a,c (11-153)

[

]a,c

[ ]a,c (11-154)

where:

[ ]a,c (11-155)

WCOBRA/TRAC-TF2 calculates the specific heat for the ZIRLO cladding material using the resulting total specific heat values, shown in Table 11-16.

Model as Coded

The density, thermal conductivity, and specific heat of the ZIRLO cladding material are coded into WCOBRA/TRAC-TF2 as described above, without modification. Figure 11-34 shows a comparison of specific heat for ZIRLO cladding material with that of Zircaloy-4.

Scaling Considerations

Not applicable.

Conclusions

Comparisons of the material properties for the ZIRLO and Zircaloy-4 cladding materials have shown that the Zircaloy-4 relations for density and thermal conductivity can also be applied to the ZIRLO alloy. The difference in the phase change temperatures of the two alloys requires that different specific heat correlations be used. The specific heat correlation for the ZIRLO alloy is based on an adjustment to the Zircaloy-4 correlation, which accounts for the different phase change temperature range. This correlation will be used for analyses of nuclear reactors which utilize the ZIRLO cladding material.

[

]a,c

11.4.4 Fuel Rod Gas Mixtures

Model Basis

For the gas mixture in the fuel-clad gap, only the thermal conductivity is calculated. The fill gas in the WCOBRA/TRAC-TF2 fuel rod model assumes that the gas is a mixture composed of helium, xenon, argon, krypton, hydrogen, and nitrogen. The thermal conductivity of the gas mixture as a function of temperature is determined, as described in MATPRO-11 Rev. 1 (Hagrman, Reymann, and Mason, 1980), from the relation:

$$k_{gas} = \sum_{i=1}^{N} \frac{k_i}{1 + \sum_{\substack{j=1 \\ j \neq i}}^{N} \psi_{ij} \frac{n_j}{n_i}} \tag{11-156}$$

where N = number of component gases, and where:

$$\psi_{ij} = \Phi_{ij}\left[1 + 2.41\frac{(M_i - M_j)(M_i - 0.142M_j)}{(M_i + M_j)^2}\right] \tag{11-157}$$

and

$$\Phi_{ij} = \frac{\left[1 + \left(\frac{k_i}{k_j}\right)^{1/2}\left(\frac{M_i}{M_j}\right)^{1/4}\right]^2}{2^{3/2}\left(1 + \frac{M_i}{M_j}\right)^{1/2}} \tag{11-158}$$

where:

M_i	=	molecular weight of gas species i
n_i	=	mole fraction of gas species i
k_i	=	thermal conductivity of gas species i

The thermal conductivities of the six component gases are evaluated in Btu/hr-ft-°F as a function of temperature from the following relations:

Gas	k(Btu/hr-ft-°F)	
Helium	$\left(1.314\times10^{-3}\right)T_{gas}^{0.668}$	(11-159)
Argon	$\left(1.31\times10^{-3}\right)T_{gas}^{0.701}$	(11-160)

Krypton	$\left(1.588\times10^{-5}\right)T_{gas}^{0..92331}$	(11-161)
Xenon	$\left(1.395\times10^{-5}\right)T_{gas}^{0.872}$	(11-162)
Hydrogen	$\left(5.834\times10^{-4}\right)T_{gas}^{0.8213}$	(11-163)
Nitrogen	$\left(7.35\times10^{-5}\right)T_{gas}^{0.846}$	(11-164)

where:

T_{gas} = gas temperature (°R)

Model as Coded

Equations 11-156 through 11-164 for gap gas thermal conductivity are coded in WCOBRA/TRAC-TF2 as described without modification in subroutine GTHCON.

Scaling Consideration

Not applicable.

Conclusions

Thermal conductivity for the gas mixture in the fuel-clad gap is calculated using the equations in MATPRO-11 Rev. 1 (Hagrman, Reymann, and Mason, 1980).

11.5 THERMAL PROPERTIES OF STRUCTURAL MATERIALS

11.5.1 Vessel Component Structural Material Properties

Model Basis

The density, specific heat, and thermal conductivity for structural materials within the vessel are specified by the user for a range of temperatures. Values for each material are obtained from standard references for thermal properties such as Touloukian (1967). When available, material properties provided by the material supplier are used.

Model as Coded

Values for the material specific heat and thermal conductivity are linearly interpolated with temperature. A warning message is printed if the temperature is outside of the range supplied by the user.

Scaling Considerations

Not applicable.

Conclusion

Material thermal properties are supplied by the user. This permits the representation of the material properties by the actual measured values and minimizes uncertainty.

11.5.2 One-Dimensional Component Structural Material Properties

Model Basis

A library of temperature-dependent material properties is incorporated in WCOBRA/TRAC-TF2 for the one-dimensional components. There are five sets of material properties that make up the library. Each set supplies values for the density, thermal conductivity, specific heat, and spectral emissivity for use in heat transfer calculations. The material sets are for Types 304, 316, and 347 Stainless Steel, Medium Carbon Steel, Inconel 600 and Inconel 690.

In the following expressions,

ρ = density $\left(\frac{kg}{m^3}\right)$

c_p = specific heat $\left(\frac{J}{kg-K}\right)$

k = thermal conductivity $\left(\frac{W}{m-K}\right)$

T_K = temperature (K)

T_F = temperature (°F)

Stainless Steel, Type 304

The density is given by:

$$\rho(T_F) = 8054.65 - 0.2595T_F \tag{11-165}$$

Specific heat is given by:

$$\begin{aligned} c_p(T_F) = {} & 426.17 + 0.43816T_F - \left(6.3759\times10^{-4}\right)T_F^2 \\ & + \left(4.4803\times10^{-7}\right)T_F^3 - \left(1.0729\times10^{-10}\right)T_F^4 \end{aligned} \tag{11-166}$$

Thermal conductivity is calculated by:

$$k(T_F) = 14.79 + 0.00714T_F \tag{11-167}$$

Stainless Steel, Type 316

Density is given by:

$$\rho(T_K) = 8084.0 - 0.4209T_K - \left(3.894 \times 10^{-5}\right)T_K^2 \quad (11\text{-}168)$$

Specific heat is given by Equation 11-166 and thermal conductivity is given by:

$$k(T_K) = 9.248 + 0.01571T_K \quad (11\text{-}169)$$

Stainless Steel, Type 347

The density is assumed constant at:

$$\rho = 7913\frac{kg}{m^3} \quad (11\text{-}170)$$

The specific heat is given by:

$$c_p(T_F) = 502.416 + 0.0984(T_F - 240) \quad (11\text{-}171)$$

and the thermal conductivity is:

$$k(T_F) = 14.1926 + \left(7.269 \times 10^{-3}\right)T_F \quad (11\text{-}172)$$

Carbon Steel

The density for carbon steel is assumed constant:

$$\rho = 7855.23\frac{kg}{m^3} \quad (11\text{-}173)$$

The specific heat is given by:

$$c_p(T_F) = 400.48 + 0.4582T_F - \left(6.5532 \times 10^{-4}\right)T_F^2 + \left(5.3706 \times 10^{-7}\right)T_F^3 \quad (11\text{-}174)$$

and the thermal conductivity is given by:

$$k(T_F) = 48.43 - 0.011366T_F \quad (11\text{-}175)$$

Inconel 600

The density for Inconel 600 is assumed constant,

$$\rho = 8409.45\frac{kg}{m^3} \quad (11\text{-}176)$$

The specific heat is given by:

$$c_p(T_F) = 4184.\left[0.1014456 + \left(4.378952\times10^{-5}\right)T_F - \left(2.046138\times10^{-8}\right)T_F^2 + \left(3.418111\times10^{-11}\right)T_F^3 - \left(2.060318\times10^{-13}\right)T_F^4 + \left(3.682836\times10^{-16}\right)T_F^5 - \left(2.458648\times10^{-19}\right)T_F^6 + \left(5.597571\times10^{-23}\right)T_F^7\right] \quad (11\text{-}177)$$

and thermal conductivity is given by:

$$k(T_F) = 1.730\left[8.011332 + \left(4.643719\times10^{-3}\right)T_F + \left(1.872857\times10^{-6}\right)T_F^2 - \left(3.914512\times10^{-9}\right)T_F^3 + \left(3.475513\times10^{-12}\right)T_F^4 - \left(9.936696\times10^{-16}\right)T_F^5\right] \quad (11\text{-}178)$$

Inconel 690

The density for Inconel 690 is [ ]^{a,c}

$$\left[\quad\right]^{a,c} \quad (11\text{-}179)$$

The specific heat is given by:

$$\left[\quad\right]^{a,c} \quad (11\text{-}180)$$

and thermal conductivity is given by:

$$\left[\quad\right]^{a,c} \quad (11\text{-}181)$$

Model as Coded

The correlations described by Equations 11-165 through 11-181 are programmed as shown without modification in subroutine MSTRCT and C_MSTRCT.

Scaling Considerations

Not applicable.

Conclusions

The WCOBRA/TRAC-TF2 code uses built-in correlations to calculate the thermal properties of common structural materials modeled by one dimensional components. The one-dimensional components generally remain at low temperature during a LOCA transient and the use of these correlations introduces only a small uncertainty into the transient calculation.

11.6 CONCLUSIONS

WCOBRA/TRAC-TF2 routines provide appropriate means for calculation of thermodynamic and transport properties of liquid water, steam, mixture of nitrogen and steam and air for the vessel

component and for one-dimensional components. Routines to calculate properties of fuel rod materials, i.e., fuel, cladding, and gap gas, are also included. Properties of structural materials in the vessel component are interpolated from user-provided tables. For one-dimensional components, routines to calculate properties of common structural materials are included. The routines generally calculate properties in the form of equations, for example as functions of temperature and pressure, or by linear interpolation in built-in tables. These property calculations have been compared with standard references and found to agree satisfactorily over the range of conditions expected for PWR LOCA calculations. No scaling uncertainty is required for the use of these models in reactor analysis.

11.7 REFERENCES

1. ASME Steam Tables, 1968, American Society of Mechanical Engineers, 2nd Edition.

2. ASME Steam Tables, 1983, Thermodynamic and Transport Properties of Steam, 5th Ed., The American Society of Mechanical Engineers, New York.

3. Bird, R. B., Stewart, W. E. and Lightfoot, E. N., 2002, Transport Phenomena, John Wiley & Sons Inc, 2nd Edition.

4. Coffman, W. A. and Lynn, L. L., 1966, "WATER: A Large Range Thermodynamic and Transport Water Property FORTRAN-IV Computer Program," Bettis Atomic Power Laboratory Report WAPD-TM-568.

5. Davidson, S. L. and Nuhfer, D. L., 1990, "VANTAGE+ Fuel Assembly Reference Core Report," WCAP-12610, Westinghouse Electric Corporation, Pittsburgh, Pennsylvania.

6. Haar, L., Gallagher, J. S. and Kell, G. S., 1984, NBS/NRC Steam Tables, Hemisphere Publishing Corporation, New York.

7. Hagrman, D. L., Reymann, G. A. and Mason, R. E., 1980, "MATPRO – Version 11 (Revision 1): A Handbook of Materials Properties for Use in the Analysis of Light Water Reactor Fuel Rod Behavior," USNRC Report NUREG/CR-0497, TREE-1280, Revision 1.

8. Keenan, J. H. and Keyes, F. G., 1936, Thermodynamic Properties of Steam, John Wiley & Sons, New York.

9. Lanning, D. D., Beyer, C. E. and Geelhood, K. J, 2005, "FRAPCON-3 Updates, Including Mixed-Oxide Fuel Properties," Pacific Northwest National Laboratory, NUREG/CR-6534, Vol. 4.

10. Lucuta, P. G., Matzke, H. J. and Hastings, I. J., 1996, "A pragmatic approach to modelling thermal conductivity of irradiated UO_2 fuel: review and recommendations," *Journal of Nuclear Materials*, Vol. 232, pp. 166-180.

11. MacDonald, P. E., et al., 1976, "MATPRO – Version 9: A Handbook of Materials Properties for Use in the Analysis of Light Water Reactor Fuel Rod Behavior," Idaho National Engineering Laboratories, TREE-NUREG-1005.

12. Martin, J. J. and Hou, Y., 1955, "Development of an Equation of State for Gases," *J. AIChE*, Vol. 1 (2), pp. 142-151.

13. McFadden, J. H., et al., 1980, "RETRAN-02 A Program for Transient Thermal-Hydraulic Analysis of Complex Fluid Flow Systems, Volume 1: Equations and Numerics," Report NP-1850, Electric Power Research Institute, Palo Alto, California.

14. Ohira, K., and N. Itagaki. 1997, "Thermal Conductivity Measurements of High Burnup UO2 Pellet and a Benchmark Calculation of Fuel Center Temperature," in *Proceedings of the ANS International Topical Meeting on LWR Fuel Performance*, pp. 541-549, March 2-6, 1997, Portland, Oregon.

15. Poling, B. E., Prausnitz, J. M. and O'Connell J., 2000, The Properties of Gases and Liquids, McGraw-Hill Professional Publishing.

16. Richardson, J. M., Arons, A. B. and Halverson, R. R., 1947, "Hydrodynamic Properties of Sea Water at the Front of a Shock Wave," *J. Chemical Physics*, Vol. 15 (11), pp. 785-794.

17. Rivard, W. C. and Torrey, M. D., 1975, "Numerical Calculation of Flashing from Long Pipes Using a Two-Field Model," Los Alamos Scientific Laboratory Report LA-6104-MS.

18. Ronchi, C., Sheindlin, M., Musella, M. and Hyland, G. J., 1999, "Thermal conductivity of uranium dioxide up to 2900 K from simultaneous measurement of the heat capacity and thermal diffusivity," *Journal of Applied Physics*, Vol. 85 (2), pp. 776-789.

19. Spore, J. W., Elson, J. S., et al., 2000, "TRAC-M/FORTRAN 90 (VERSION 3.0) Theory Manual," Los Alamos National Laboratory & Pennsylvania State University.

20. Schueren, P., 2006, "Optimized ZIRLO™", WCAP-12610-P-A & CENPD-404-P-A, Addendum 1-A.

21. Taylor, R. E., Groot, H. and Larimore, J., 1989, "Thermophysical Properties of ZR-4 and ZIRLO," PRL-820, Properties Research Laboratory, West Lafayette, Indiana. [PROPRIETARY].

22. Touloukian, Y. S., 1967, Thermophysical Properties of High Temperature Solid Materials, Thermophysical Properties Research Center, Purdue University, The Macmillan Co., New York.

Table 11-1 Constants for Saturated Liquid Enthalpy			
	Pressure (psia)		
A_n	$0.1 \leq P < 898.7$	$898.7 \leq P < 2529.9$	$2529.9 \leq P \leq 3208$
1	0.6970887859E+02	0.8408618802E+06	0.9060030436E+03
2	0.3337529994E+02	0.3637413208E+06	-0.1426813520E+02
3	0.2318240735E+01	-0.4634506669E+06	0.1522233257E+01
4	0.1840599513E+00	0.1130306339E+06	-0.6973992961E+00
5	-0.5245502294E-02	-0.4350217298E+03	0.1743091663E+00
6	0.2878007027E-02	-0.3898988188E+04	-0.2319717696E-01
7	0.1753652324E-02	0.6697399434E+03	0.1694019149E-02
8	-0.4334859620E-03	-0.4730726377E+02	-0.6454771710E-04
9	0.3325699282E-04	0.1265125057E+01	0.1003003098E-05

Table 11-2 Constants for Saturated Vapor Enthalpy			
	Pressure (psia)		
B_n	$P < 1467.6$	$1467.6 \leq P < 2586.0$	$2586.0 \leq P \leq 3208.0$
1	0.1105836875E+04	0.5918671729E+06	0.9059978254E+03
2	0.1436943768E+02	-0.2559433320E+06	0.5561957539E+01
3	0.8018288621E+00	0.3032474387E+05	0.3434189609E+01
4	0.1617232913E-01	0.4109051958E+01	-0.6406390628E+00
5	-0.1501147505E-02	0.3475066877E+00	0.5918579484E-01
6	-0.1237675562E-04	-0.3026047262E+00	-0.2725378570E-02
7	0.3004773304E-05	-0.1022018012E+02	0.5006336938E-04
8	-0.2062390734E-06	0.1591215116E+01	0.0
9	0.0	-0.6768383759E-01	0.0

Table 11-3 Vessel Component Saturated Water Thermal Properties

P_{sat} (psia)	T_{sat} (°F)	ρ_f (lbm/ft^3)	ρ_g (lbm/ft^3)	H_f (Btu/lbm)	H_g (Btu/lbm)	μ_f (lbm/hr/ft)	μ_g (lbm/hr/ft)	k_f (Btu/hr/ft/F)	k_g (Btu/hr/ft/F)	C_{pf} (Btu/lbm/F)	C_{pg} (Btu/lbm/F)	σ (lbf/ft)
0.1	41.97	62.42	0.000	10.00	1079.83	3.61570	0.02262	0.33023	0.01002	1.00440	0.44426	0.00513
0.2	51.93	62.40	0.001	20.00	1084.18	3.06850	0.02295	0.33627	0.01022	1.00320	0.44477	0.00508
0.3	61.91	62.36	0.001	30.00	1088.55	2.64160	0.02331	0.34218	0.01041	1.00140	0.44542	0.00502
0.4	71.90	62.29	0.001	40.00	1092.92	2.30190	0.02368	0.34791	0.01062	0.99975	0.44623	0.00496
0.5	81.91	62.20	0.002	50.00	1097.28	2.02710	0.02406	0.35338	0.01083	0.99851	0.44723	0.00491
0.7	91.93	62.09	0.002	60.00	1101.62	1.80170	0.02445	0.35848	0.01105	0.99776	0.44844	0.00484
1.0	101.95	61.97	0.003	70.00	1105.94	1.61440	0.02485	0.36334	0.01128	0.99743	0.44988	0.00478
1.4	111.98	61.83	0.004	80.00	1110.23	1.45700	0.02526	0.36765	0.01152	0.99745	0.45157	0.00472
1.8	122.00	61.68	0.005	90.00	1114.49	1.32340	0.02568	0.37183	0.01177	0.99774	0.45353	0.00465
2.3	132.02	61.52	0.007	100.00	1118.70	1.20900	0.02611	0.37530	0.01203	0.99823	0.45577	0.00459
3.0	142.04	61.34	0.009	110.00	1122.86	1.11020	0.02654	0.37863	0.01230	0.99888	0.45832	0.00452
3.9	152.04	61.15	0.011	120.00	1126.97	1.02440	0.02698	0.38146	0.01258	0.99965	0.46117	0.00445
5.0	162.04	60.95	0.014	130.00	1131.04	0.94915	0.02742	0.38403	0.01287	1.00050	0.46435	0.00438
6.3	172.02	60.75	0.017	140.00	1135.03	0.88297	0.02787	0.38624	0.01318	1.00150	0.46786	0.00432
7.9	182.01	60.53	0.021	150.00	1138.98	0.82425	0.02832	0.38814	0.01349	1.00270	0.47172	0.00424
9.7	191.96	60.31	0.025	160.00	1142.85	0.77208	0.02877	0.38984	0.01381	1.00390	0.47591	0.00417
12.0	201.92	60.07	0.031	170.00	1146.66	0.72533	0.02923	0.39115	0.01415	1.00530	0.48047	0.00410
14.7	211.84	59.83	0.037	180.00	1150.39	0.68345	0.02969	0.39236	0.01449	1.00690	0.48538	0.00403
17.8	221.78	59.58	0.045	190.00	1154.05	0.64561	0.03015	0.39320	0.01486	1.00860	0.49067	0.00396
21.4	231.66	59.32	0.053	200.00	1157.62	0.61149	0.03061	0.39397	0.01523	1.01050	0.49633	0.00388
25.7	241.55	59.05	0.063	210.00	1161.12	0.58043	0.03107	0.39444	0.01561	1.01260	0.50239	0.00381
30.6	251.39	58.78	0.074	220.00	1164.50	0.55228	0.03153	0.39481	0.01601	1.01490	0.50882	0.00373
36.2	261.22	58.50	0.087	230.00	1167.79	0.52655	0.03199	0.39496	0.01642	1.01740	0.51569	0.00366

Table 11-3 (cont.) Vessel Component Saturated Water Thermal Properties

P_{sat} (psia)	T_{sat} (°F)	ρ_f (lbm/ft^3)	ρ_g (lbm/ft^3)	H_f (Btu/lbm)	H_g (Btu/lbm)	μ_f (lbm/hr/ft)	μ_g (lbm/hr/ft)	k_f (Btu/hr/ft/F)	k_g (Btu/hr/ft/F)	C_{pf} (Btu/lbm/F)	C_{pg} (Btu/lbm/F)	σ (lbf/ft)
42.5	271.02	58.21	0.101	240.00	1170.98	0.50302	0.03245	0.39498	0.01684	1.02010	0.52299	0.00358
49.8	280.80	57.92	0.117	250.00	1174.05	0.48145	0.03291	0.39485	0.01727	1.02300	0.53075	0.00351
58.0	290.54	57.61	0.135	260.00	1177.01	0.46163	0.03337	0.39456	0.01772	1.02610	0.53899	0.00343
67.2	300.26	57.30	0.155	270.00	1179.84	0.44339	0.03383	0.39418	0.01817	1.02940	0.54775	0.00335
77.6	309.93	56.99	0.177	280.00	1182.54	0.42656	0.03429	0.39358	0.01864	1.03290	0.55706	0.00327
89.1	319.58	56.66	0.202	290.00	1185.10	0.41101	0.03474	0.39293	0.01912	1.03670	0.56696	0.00320
101.8	329.19	56.34	0.229	300.00	1187.53	0.39661	0.03520	0.39205	0.01962	1.04060	0.57748	0.00312
116.0	338.76	56.00	0.260	310.00	1189.82	0.38325	0.03565	0.39113	0.02012	1.04470	0.58869	0.00304
131.6	348.28	55.66	0.293	320.00	1191.95	0.37083	0.03610	0.39000	0.02064	1.04910	0.60063	0.00296
148.6	357.77	55.31	0.329	330.00	1193.94	0.35927	0.03655	0.38882	0.02116	1.05380	0.61336	0.00288
167.4	367.21	54.95	0.368	340.00	1195.77	0.34849	0.03699	0.38743	0.02170	1.05870	0.62693	0.00280
187.8	376.61	54.59	0.411	350.00	1197.44	0.33842	0.03744	0.38597	0.02225	1.06390	0.64141	0.00272
210.0	385.96	54.22	0.458	360.00	1198.96	0.32898	0.03788	0.38435	0.02281	1.06940	0.65687	0.00264
234.0	395.26	53.85	0.508	370.00	1200.30	0.32014	0.03832	0.38265	0.02338	1.07530	0.67338	0.00256
260.0	404.50	53.47	0.563	380.00	1201.48	0.31182	0.03876	0.38078	0.02396	1.08150	0.69101	0.00248
288.0	413.69	53.08	0.622	390.00	1202.49	0.30399	0.03920	0.37881	0.02455	1.08820	0.70984	0.00240
318.1	422.83	52.69	0.686	400.00	1203.32	0.29660	0.03964	0.37667	0.02516	1.09540	0.72995	0.00232
350.4	431.90	52.29	0.755	410.00	1203.97	0.28961	0.04008	0.37441	0.02578	1.10300	0.75144	0.00224
384.9	440.91	51.88	0.828	420.00	1204.44	0.28299	0.04052	0.37199	0.02642	1.11130	0.77439	0.00216
421.6	449.86	51.47	0.907	430.00	1204.71	0.27670	0.04095	0.36946	0.02707	1.12010	0.79891	0.00208
460.7	458.73	51.05	0.992	440.00	1204.79	0.27072	0.04139	0.36679	0.02773	1.12970	0.82510	0.00200
502.1	467.53	50.62	1.082	450.00	1204.67	0.26501	0.04183	0.36401	0.02841	1.13990	0.85307	0.00192
546.0	476.26	50.18	1.178	460.00	1204.34	0.25954	0.04227	0.36106	0.02912	1.15100	0.88295	0.00185
592.2	484.91	49.74	1.281	470.00	1203.79	0.25431	0.04271	0.35800	0.02984	1.16290	0.91488	0.00177

Table 11-3 (cont.) Vessel Component Saturated Water Thermal Properties

P_{sat} (psia)	T_{sat} (°F)	ρ_f (lbm/ft^3)	ρ_g (lbm/ft^3)	H_f (Btu/lbm)	H_g (Btu/lbm)	μ_f (lbm/hr/ft)	μ_g (lbm/hr/ft)	k_f (Btu/hr/ft/F)	k_g (Btu/hr/ft/F)	C_{pf} (Btu/lbm/F)	C_{pg} (Btu/lbm/F)	σ (lbf/ft)
641.2	493.51	49.29	1.391	480.00	1203.02	0.24926	0.04315	0.35472	0.03059	1.17590	0.94916	0.00169
692.1	501.94	48.84	1.507	490.00	1202.04	0.24444	0.04359	0.35138	0.03136	1.18980	0.98549	0.00161
745.9	510.35	48.37	1.631	500.00	1200.81	0.23976	0.04404	0.34782	0.03218	1.20490	1.02460	0.00154
802.0	518.65	47.90	1.762	510.00	1199.35	0.23524	0.04450	0.34426	0.03300	1.22130	1.06650	0.00146
860.5	526.84	47.42	1.901	520.00	1197.64	0.23086	0.04495	0.34043	0.03390	1.23890	1.11140	0.00139
921.3	534.91	46.93	2.048	530.00	1195.69	0.22662	0.04541	0.33660	0.03480	1.25800	1.15940	0.00132
984.4	542.86	46.44	2.204	540.00	1193.50	0.22250	0.04588	0.33255	0.03581	1.27870	1.21100	0.00124
1050.0	550.72	45.93	2.368	550.00	1191.03	0.21846	0.04636	0.32846	0.03684	1.30120	1.26690	0.00117
1117.8	558.47	45.42	2.543	560.00	1188.31	0.21452	0.04685	0.32427	0.03795	1.32560	1.32710	0.00111
1187.8	566.10	44.89	2.727	570.00	1185.33	0.21067	0.04734	0.31999	0.03915	1.35220	1.39240	0.00104
1259.9	573.61	44.36	2.922	580.00	1182.08	0.20689	0.04785	0.31571	0.04038	1.38120	1.46330	0.00097
1334.0	580.98	43.82	3.127	590.00	1178.57	0.20318	0.04837	0.31134	0.04174	1.41290	1.54050	0.00091
1410.0	588.22	43.27	3.344	600.00	1174.80	0.19953	0.04891	0.30694	0.04324	1.44770	1.62510	0.00084
1487.8	595.33	42.71	3.574	610.00	1170.75	0.19594	0.04946	0.30255	0.04486	1.48590	1.71800	0.00078
1567.2	602.29	42.14	3.816	620.00	1166.42	0.19239	0.05004	0.29817	0.04663	1.52810	1.82060	0.00073
1648.2	609.11	41.56	4.072	630.00	1161.76	0.18889	0.05063	0.29382	0.04854	1.57490	1.93450	0.00067
1730.4	615.77	40.96	4.343	640.00	1156.76	0.18543	0.05125	0.28954	0.05069	1.62710	2.06150	0.00061
1813.8	622.28	40.36	4.629	650.00	1151.40	0.18200	0.05190	0.28531	0.05307	1.68570	2.20410	0.00056
1898.2	628.62	39.74	4.931	660.00	1145.66	0.17859	0.05258	0.28115	0.05565	1.75180	2.36520	0.00051
1983.9	634.84	39.11	5.253	670.00	1139.49	0.17518	0.05330	0.27709	0.05848	1.82770	2.55010	0.00046
2069.5	640.84	38.47	5.593	680.00	1132.96	0.17181	0.05405	0.27314	0.06173	1.91440	2.76120	0.00042
2155.4	646.65	37.81	5.953	690.00	1126.01	0.16845	0.05485	0.26926	0.06527	2.01490	3.00550	0.00037
2241.1	652.28	37.14	6.335	700.00	1118.63	0.16509	0.05570	0.26545	0.06919	2.13280	3.29110	0.00033
2326.3	657.69	36.46	6.740	710.00	1110.82	0.16173	0.05661	0.26186	0.07374	2.27250	3.62830	0.00029

Table 11-3 (cont.) Vessel Component Saturated Water Thermal Properties

P_{sat} (psia)	T_{sat} (°F)	ρ_f (lbm/ft^3)	ρ_g (lbm/ft^3)	H_f (Btu/lbm)	H_g (Btu/lbm)	μ_f (lbm/hr/ft)	μ_g (lbm/hr/ft)	k_f (Btu/hr/ft/F)	k_g (Btu/hr/ft/F)	C_{pf} (Btu/lbm/F)	C_{pg} (Btu/lbm/F)	σ (lbf/ft)
2410.6	662.89	35.76	7.170	720.00	1102.59	0.15837	0.05758	0.25836	0.07854	2.44030	4.03110	0.00025
2494.0	667.89	35.03	7.630	730.00	1093.91	0.15497	0.05863	0.25520	0.08401	2.64650	4.52210	0.00022
2575.2	672.62	34.29	8.117	740.00	1084.90	0.15156	0.05975	0.25212	0.08983	2.90110	5.12290	0.00019
2653.8	677.08	33.53	8.635	750.00	1075.52	0.14813	0.06096	0.24935	0.09704	3.22290	5.87350	0.00016
2729.8	681.29	32.75	9.190	760.00	1065.74	0.14464	0.06228	0.24673	0.10465	3.64070	6.14500	0.00013
2801.8	685.18	31.95	9.777	770.00	1055.59	0.14113	0.06371	0.24493	0.11447	4.19150	6.14500	0.00011
2869.6	688.77	31.12	10.403	780.00	1045.00	0.13755	0.06526	0.24313	0.12429	4.94400	6.14500	0.00008
2931.9	692.01	30.27	11.066	790.00	1034.06	0.13393	0.06694	0.24418	0.13890	5.99630	6.14500	0.00007
2988.5	694.90	29.39	11.771	800.00	1022.75	0.13024	0.06878	0.24576	0.15442	6.14500	6.14500	0.00005
3038.4	697.40	28.48	12.513	810.00	1011.17	0.12649	0.07076	0.24734	0.16993	6.14500	6.14500	0.00004
3081.4	699.53	27.55	13.293	820.00	999.32	0.12268	0.07291	0.25288	0.19158	6.14500	6.14500	0.00002
3116.7	701.26	26.60	14.101	830.00	987.40	0.11885	0.07520	0.26470	0.22270	6.14500	6.14500	0.00002
3144.7	702.62	25.63	14.927	840.00	975.50	0.11500	0.07761	0.29237	0.27220	6.14500	6.14500	0.00001
3165.7	703.63	24.65	15.750	850.00	963.98	0.11119	0.08008	0.81017	0.80644	6.14500	6.14500	0.00000
3180.5	704.34	23.68	16.541	860.00	953.38	0.10744	0.08253	2.55507	2.55265	6.14500	6.14500	0.00000
3190.3	704.81	22.72	17.243	870.00	944.22	0.10382	0.08475	4.29997	4.29886	6.14500	6.14500	0.00000
3196.0	705.08	21.78	17.759	880.00	937.47	0.10034	0.08642	10.00000	10.00000	6.14500	6.14500	0.00000
3198.3	705.19	20.87	17.987	890.00	934.25	0.09704	0.08717	50.00000	50.00000	6.14500	6.14500	0.00000
3206.4	705.39	20.16	19.244	900.00	917.46	0.09704	0.08717	100.00000	100.00000	6.14500	6.14500	0.00000

Table 11-4 Subcooled Water Density Constants					
	C_{CXij}				
i=	1	2	3	4	5
j=1	-0.413450E1	0.13252E-4	0.15812E-5	-0.21959E-8	0.21683E-11
j=2	-0.59428E-5	0.63377E-7	-0.39974E-9	0.69391E-12	-0.36159E-15
j=3	0.15681E-8	-0.40711E-10	0.25401E-12	-0.52372E-15	0.32503E-18

Table 11-5 Saturated Steam Internal Energy Constants				
i	AVE(i)	BVE(i)	CVE(i)	DVE(i)
1	2.4949771766385E+06	2.0855856331827E–01	-1.3553894579716E-07	2.8522684989198E–14
2	2.5600870370371E+06	3.1086111111026E–02	-6.8988888888580E-09	4.3203703703379E–16
3	2.5915500000006E+06	8.7749999997567E–03	-1.7499999999663E-09	4.2999999998503E–17
4	2.6606000000024E+06	-1.3545000000581E-02	6.4250000004682E–10	-4.2100000001248E-17
5	3.8201600000097E+06	-2.3019900000170E-01	1.4068900000098E–08	-3.1786000000187E-16
6	-1.2103411633350E+08	1.8018803375785E+01	-8.7442426507726E-07	1.4091076856088E-14
7	2.2000000000000E+06	0.	0.	0.
8	2.2000000000000E+06	0.	0.	0.
9	2.2000000000000E+06	0.	0.	0.
10	2.2000000000000E+06	0.	0.	0.
11	2.2000000000000E+06	0.	0.	0.

Table 11-6 Saturated Steam Enthalpy Constants				
i	AVG(i)	BVG(i)	CVG(i)	DVG(i)
1	1.0666845123419E+00	2.8310838172462E-08	–2.1151097428905E-14	4.7404001285964E–21
2	1.0735412407407E+00	2.6518055555551E-09	-6.3461111111128E-16	3.9824074074117E-23
3	1.0777730000000E+00	-2.4300000008021E-11	-7.1979999998378E-17	4.8799999990422E-25
4	1.0851130000007E+00	-1.9307000001824E-09	8.9100000014826E-17	-3.8960000003946E-24
5	1.1639800000015E+00	-1.6338350000254E-08	9.5856000001448E-16	-2.1194000000274E-23
6	3.8898867259868E+00	-3.8595945559811E-07	1.7476370114910E-14	-2.6377008249858E-22
7	2.7168710524682E+00	-2.2832718294604E-07	1.0417331983836E-14	-1.5842822199773E-22
8	3.9749829999964E+00	-3.0657099999960E-07	1.0637899999985E-14	-1.2257999999981E-22
9	1.2946929999997E+00	-2.4834999999979E-08	7.8979999999944E-16	-8.0799999999948E-24
10	1.0590519999963E+00	-2.4615999996941E-09	8.8399999991573E-17	-8.0799999992269E-25
11	1.1430199999838E+00	-7.7095999988588E-09	1.9335999997331E-16	-1.4639999997924E-24

Table 11-7 Saturated Liquid Internal Energy Constants				
i	ALE(i)	BLE(i)	CLE(i)	DLE(i)
1	-1.1436668993222E+06	4.1868000000000E+03	0.	0.
2	8.0957542810383E+06	-5.7008855264640E+04	1.3443632119671E+02	-9.7879669155946E-02
3	-1.9373932457007E+06	9.7492797103351E+03	-1.3299615999876E+01	1.0879999999922E-02
4	-5.3245827703670E+06	2.9179372045334E+04	-5.0452192000967E+01	3.4560000000583E-02
5	-6.3583523639930E+07	3.2873715263424E+05	-5.6371182000208E+02	3.2760000000116E-01
6	-6.6239163195929E+09	3.1605562257270E+07	-5.0263730855532E+04	2.6650075114186E+01
7	-5.4759091078157E+09	2.4635618770681E+07	-3.6931079506707E+04	1.8454719393083E+01
8	-7.1536399439453E+07	3.0560801674842E+05	-4.2424553999630E+02	1.9719999999823E-01

Table 11-8 Constants for Saturated Steam Specific Heat

i	ACP(i)	BCP(i)	CCP(i)	DCP(i)
1	-7.9678485852270E+02	2.8187658437259E+01	-1.0180624999920E-01	1.2499999999912E-04
2	-9.7082632232795E+02	2.8324981030402E+01	-9.7656200001157E-02	1.1600000000110E-04
3	-1.6649701690752E+03	3.3159363169596E+01	-1.0861179999898E-01	1.2399999999915E-04
4	-6.1420486441088E+03	6.3630987079837E+01	-1.7762319999965E-01	1.7599999999975E-04
5	-8.2289951961933E+04	5.3773958896061E+02	-1.1612491999609E+00	8.5599999997375E-04
6	-6.5842104212475E+05	3.7934294783212E+03	-7.2924928000022E+00	4.7040000000014E-03
7	3.4561620732510E+05	-2.2129380791446E+02	-2.4524285999925E+00	3.1479999999958E-03
8	1.9798369474597E+06	-1.4782551342826E+04	3.1656481897637E+01	-2.0843356864237E-02
9	-9.6249385211359E+07	4.3633668884423E+05	-6.5887615106930E+02	3.3146147264269E-01
10	-1.1074934463333E+07	4.8073794630970E+04	-6.9212173247881E+01	3.3091693999800E-02

Table 11-9 Liquid Density Constants				
i	AVO(i)	BVO(i)	CVO(i)	DVO(i)
1	1.7057666777468E-03	-6.0320895569365E-06	1.5944423965594E-08	-1.2149418561177E-11
2	5.2145931517155E-04	3.5189228252915E-06	-9.7304881862624E-09	1.0856688130631E-11
3	-1.4931865836934E-02	9.7931556400429E-05	-2.0172817692512E-07	1.4080475270259E-10
4	-4.9334201381918E-01	2.5928571576499E-03	-4.5387107397840E-06	2.6537936475365E-09
5	-3.4558955902321E+00	1.7351793841884E-02	-2.9047483637289E-05	1.6220227777320E-08
6	-1.1952528427292E+01	5.8904962031842E-02	-9.6786687447220E-05	5.3029284583415E-08
7	-3.7446629978341E+01	1.8173474403006E-01	-2.9404991620713E-04	1.5863005350824E-07
8	-3.9713284923576E+02	1.8801824705202E+00	-2.9673900150051E-03	1.5612171739106E-06
9	-2.3142714272157E+03	1.0710216457395E+01	-1.6521763202064E-02	8.4955209566212E-06
10	2.0481569977849E+03	-9.3452783115489E+00	1.4212077056589E-02	-7.2037202704367E-06
11	-7.3864713248117E+01	3.3144939132191E-01	-4.9608715522591E-04	2.4771793009809E-07
12	-2.1891320674084E+01	9.6758467414310E-02	-1.4289074953436E-04	7.0567217785700E-08
i	AFN(i)	BFN(i)	CFN(i)	DFN(i)
1	-4.2486354144244E+09	3.7516769853867E+07	-1.0064945851796E+05	8.7507285129715E+01
2	-2.7936308563236E+08	5.5663179995300E+06	-1.4921749894688E+04	1.0834095198280E+01
3	-1.1761210016041E+08	4.3832221802974E+06	-1.2088373365747E+04	8.6034520917150E+00
4	-4.5415129389018E+09	2.7368608704680E+07	-5.1894794477625E+04	3.1581281016141E+01
5	-4.0104325667716E+10	2.0292575433752E+08	-3.4075971373732E+05	1.9000660267975E+02
6	-6.0173879922257E+10	2.9984925450490E+08	-4.9675963282729E+05	2.7368658401451E+02
7	2.0678826351719E+10	-8.9503807129603E+07	1.2822787819385E+05	-6.0722291833340E+01
8	8.3793557728900E+10	-3.8997180562867E+08	6.0502628698976E+05	-3.1291965911464E+02
9	9.2402374347985E+10	-4.2674923965292E+08	6.5695613829284E+05	-3.3711122197289E+02
10	-2.7547713637194E+10	1.2580004134443E+08	-1.9147491048695E+05	9.7136148925404E+01
11	6.8608195287374E+08	-3.0636028439513E+06	4.5613625244005E+03	-2.2642074876391E+00
12	4.3458430609231E+07	-1.8379937116289E+05	2.5971646178490E+02	-1.2244044950391E-01

Table 11-10 Constant Pressure Specific Heat Constants	
$B_{0\ell} = 2.394907 \times 10^{-4}$	$B_{1\ell} = -5.196250 \times 10^{-13}$
$C_{0\ell} = 1.193203 \times 10^{-11}$	$C_{1\ell} = 2.412704 \times 10^{-18}$
$D_{0\ell} = -3.944067 \times 10^{-17}$	$D_{1\ell} = -1.680771 \times 10^{-24}$
$C_{1\upsilon} = 1.68835968 \times 10^{3}$	
$C_{2\upsilon} = 0.6029856$	
$C_{3\upsilon} = 4.820979623 \times 10^{2}$	
$C_{4\upsilon} = 2.95317905 \times 10^{7}$	
$C_{5\upsilon} = 1.8$	
$C_{6\upsilon} = 4.60 \times 10^{2}$	

Table 11-11 Liquid Viscosity Constants	
$A_{0\ell} = 1.298102340 \times 10^{-3}$ $A_{1\ell} = -9.264032108 \times 10^{-4}$ $A_{2\ell} = 3.81047061 \times 10^{-4}$ $A_{3\ell} = -8.219444458 \times 10^{-5}$ $A_{4\ell} = 7.022437984 \times 10^{-6}$	$B_{0\ell} = -6.5959 \times 10^{-12}$ $B_{1\ell} = 6.763 \times 10^{-12}$ $B_{2\ell} = -2.88825 \times 10^{-12}$ $B_{3\ell} = 4.4525 \times 10^{-13}$
$D_{0\ell} = 3.026032306 \times 10^{-4}$ $D_{1\ell} = -1.836606896 \times 10^{-4}$ $D_{2\ell} = 7.567075775 \times 10^{-5}$ $D_{3\ell} = -1.647878879 \times 10^{-5}$ $D_{4\ell} = 1.416457633 \times 10^{-6}$	$E_{0\ell} = 1.4526052612 \times 10^{-3}$ $E_{1\ell} = -6.9880084985 \times 10^{-9}$ $E_{2\ell} = 1.5210230334 \times 10^{-14}$ $E_{3\ell} = -1.2303194946 \times 10^{-20}$
$F_{0\ell} = -3.8063507533 \times 10^{-11}$ $F_{1\ell} = 3.9285207677 \times 10^{-16}$ $F_{2\ell} = -1.2585799292 \times 10^{-21}$ $F_{3\ell} = 1.2860180788 \times 10^{-27}$	$H_0 = 8.581289699 \times 10^{-6}$ $c_{0n} = 4.265884 \times 10^{4}$ $P_0 = 6.894575293 \times 10^{5}$
$H_{00} = 3.892077365 \times 10^{-6}$ $e_{c0n} = 5.53588 \times 10^{4}$	$e_{h0} = 6.484503981 \times 10^{-6}$ $c_n = 4.014676 \times 10^{5}$

Table 11-12 Liquid Thermal Conductivity Constants
$A_{\ell 0} = 0.573738622$ $A_{\ell 1} = 0.2536103551$ $A_{\ell 2} = -0.145468269$ $A_{\ell 3} = -0.01387472485$
$H_0 = 5.815 \times 10^5$

Table 11-13 Constants for Specific Heat of Air		
i	A_i	B_i
1	-4.20419E-05	7.71027E-05
2	9.61128E-08	-8.56726E-09
3	-1.16383E-11	-4.75772E-12

Table 11-14 Specific Heat of Zircaloy-4	
T(K)	**C_p (Btu/lbm – °F)**
300.0	0.0671
400.0	0.0721
640.0	0.0790
1090.0	0.0896
1093.0	0.1199
1113.0	0.1409
1133.0	0.1469
1153.0	0.1717
1173.0	0.1949
1193.0	0.1839
1213.0	0.1478
1233.0	0.1120
1248.0	0.0850
>1248.0	0.0850

Table 11-15 Chemical Composition of ZIRLO and Zircaloy-4 Alloys		
Element (wt %)	**ZIRLO Alloy**	**Zircaloy-4 Alloy**
Sn	0.8-1.2	1.2-1.7
Fe	0.09-0.13	0.18-0.24
Cr	--	0.07-0.13
Fe + Cr	--	0.28-0.37
Nb	0.8-1.2	--
Zr	Balance	Balance

Table 11-16 Specific Heat of ZIRLO Alloy

a,c

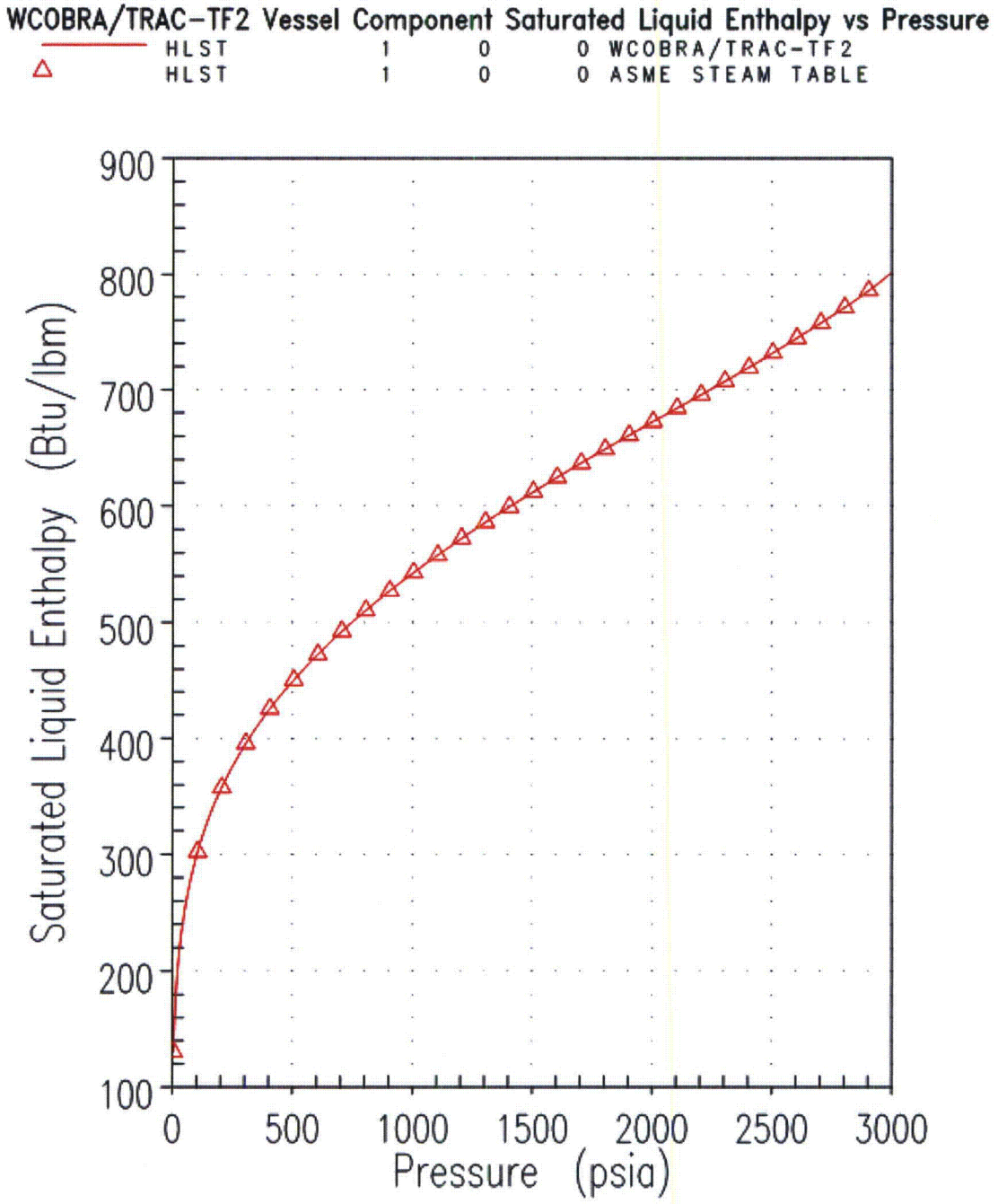

Figure 11-1 WCOBRA/TRAC-TF2 Vessel Component Saturated Liquid Enthalpy Function

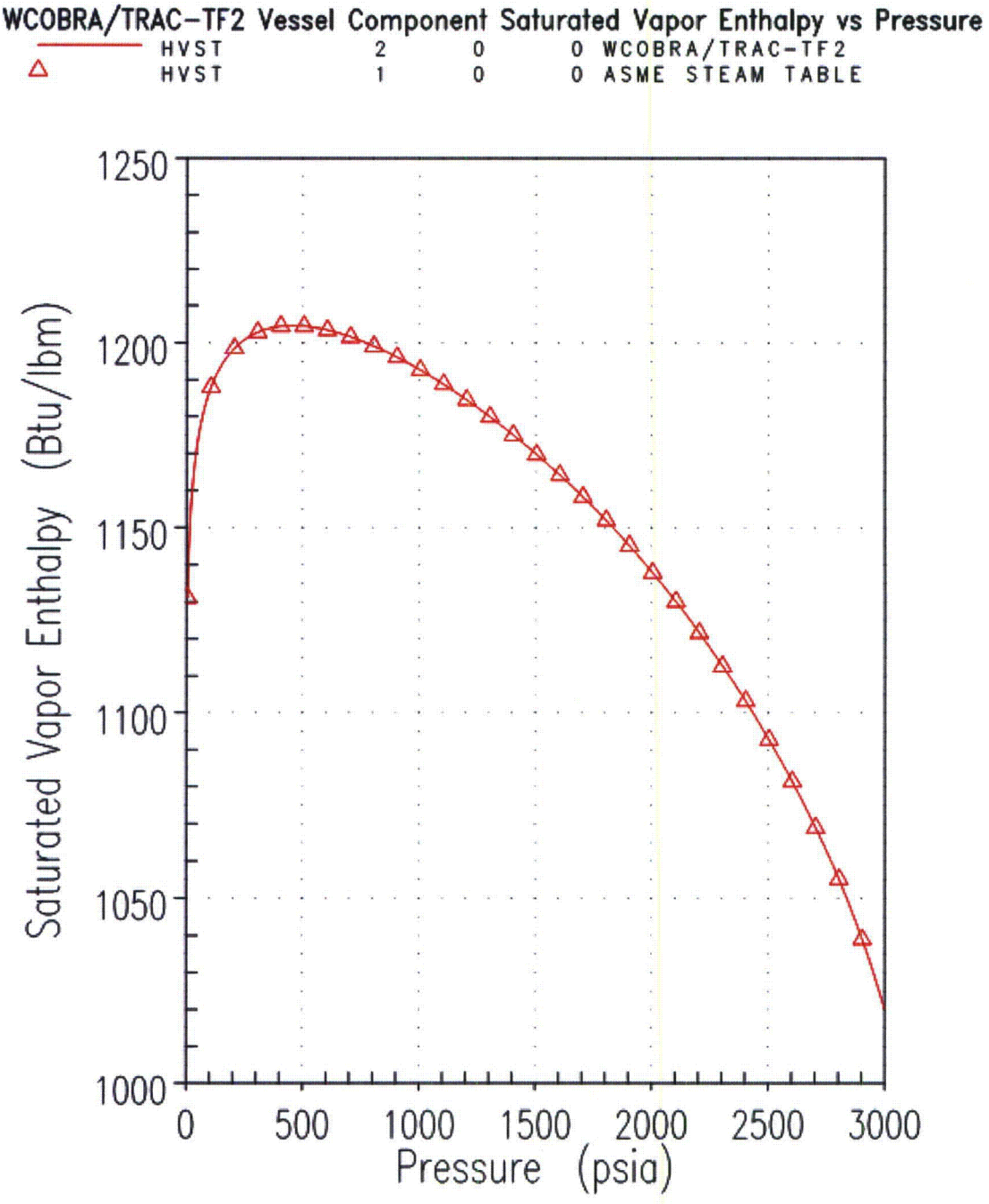

Figure 11-2 WCOBRA/TRAC-TF2 Vessel Component Saturated Vapor Enthalpy Function

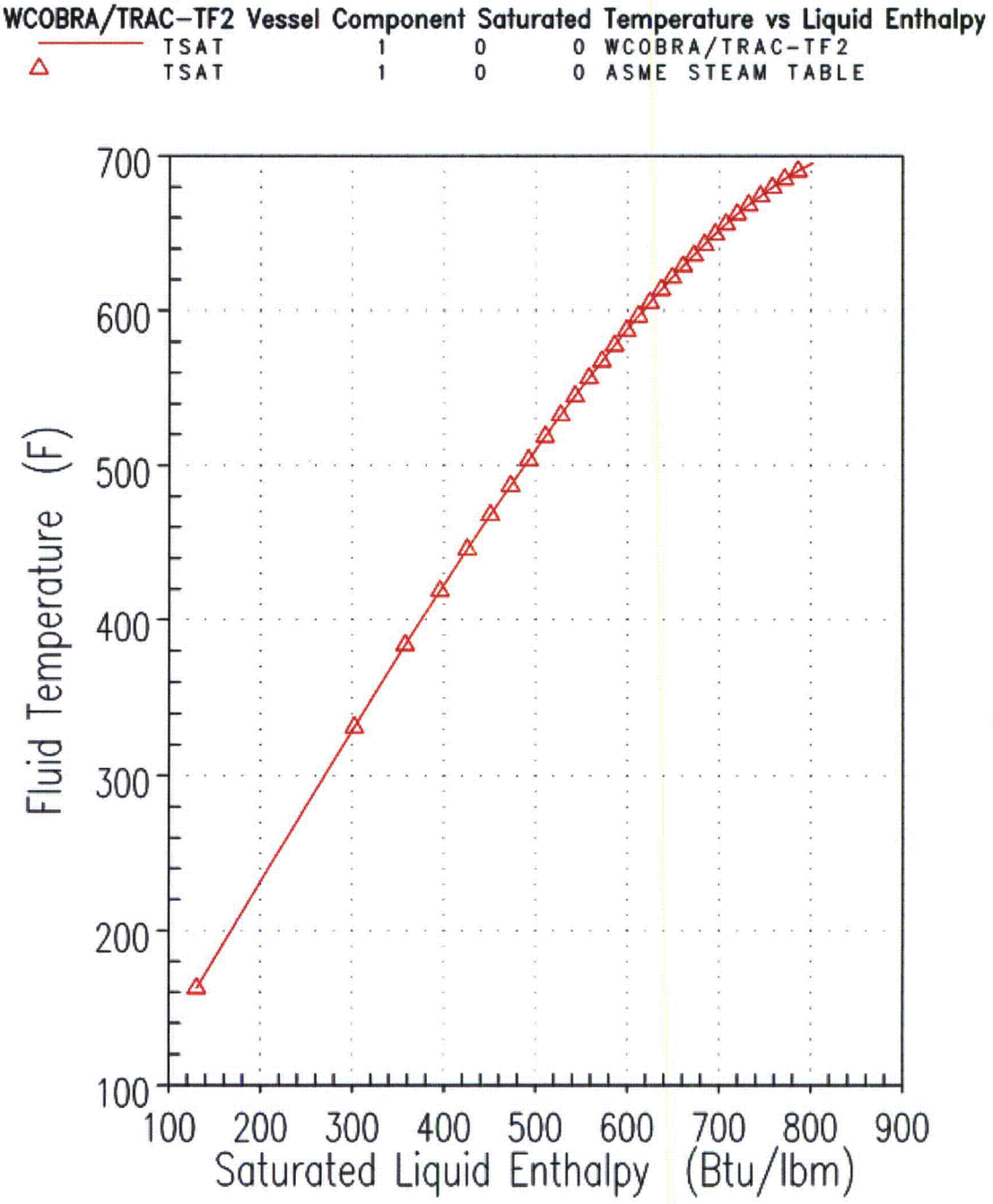

Figure 11-3 WCOBRA/TRAC-TF2 Vessel Component Saturation Temperature

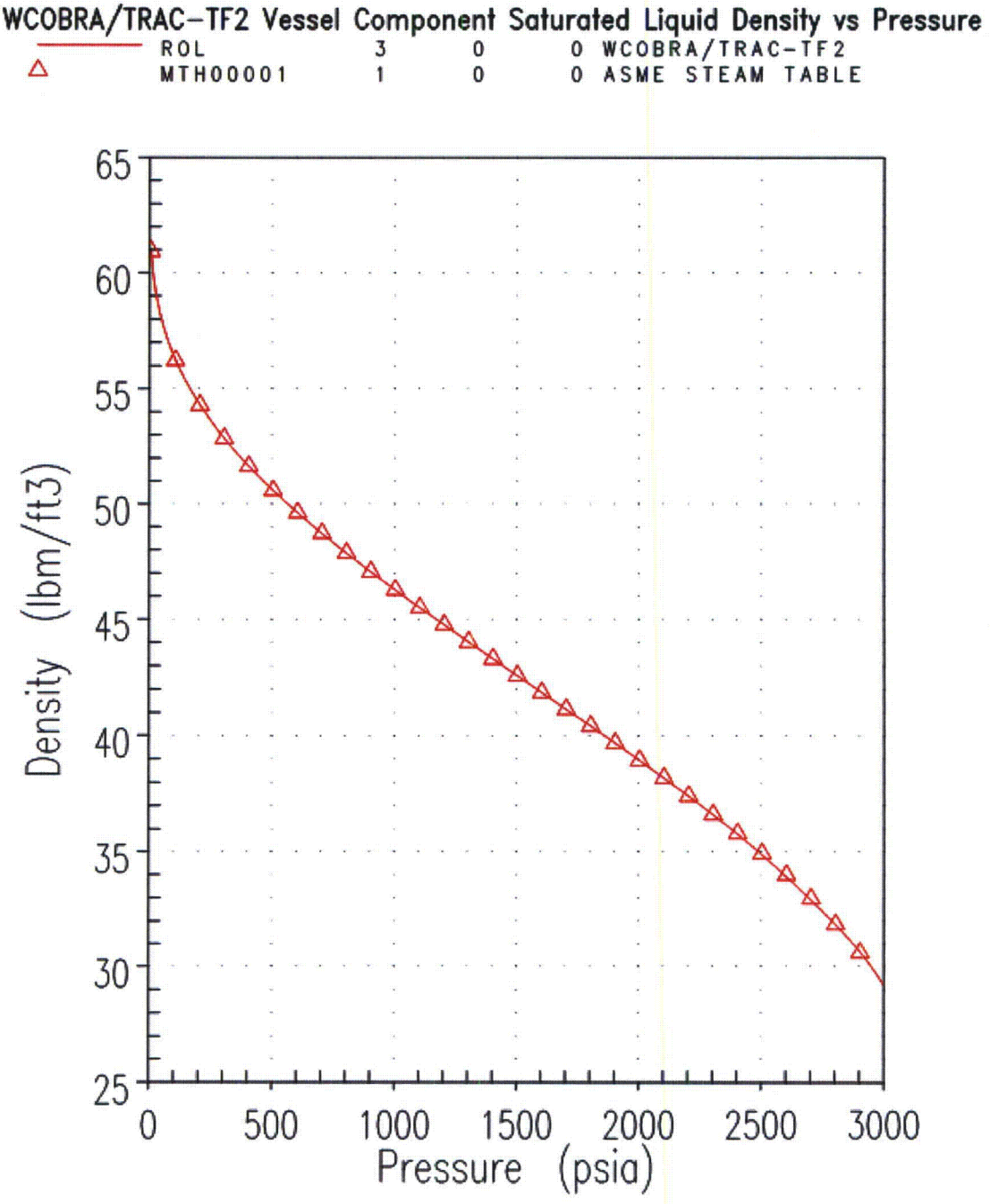

Figure 11-4 WCOBRA/TRAC-TF2 Vessel Component Saturated Liquid Density

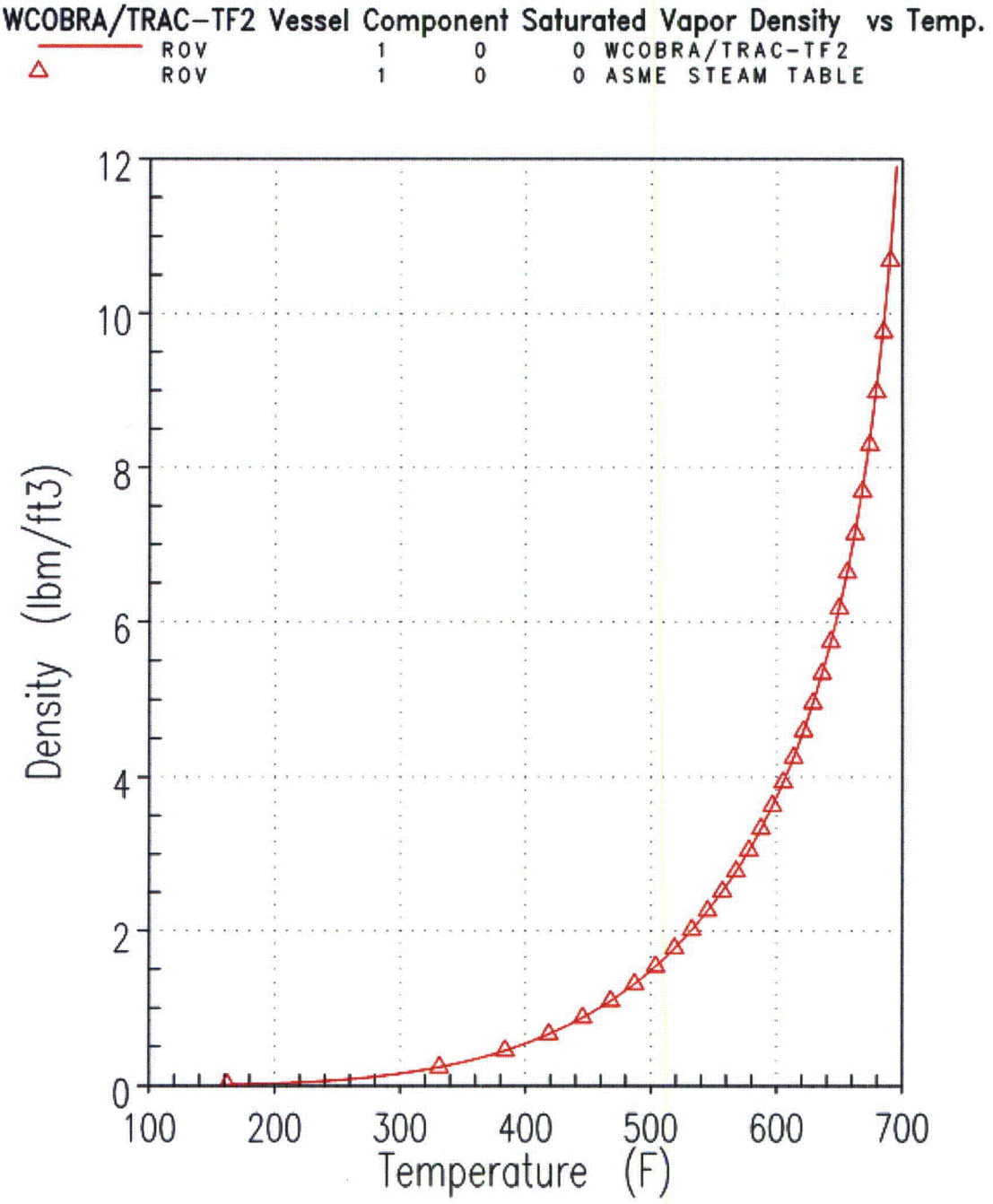

Figure 11-5 WCOBRA/TRAC-TF2 Vessel Component Saturated Vapor Density

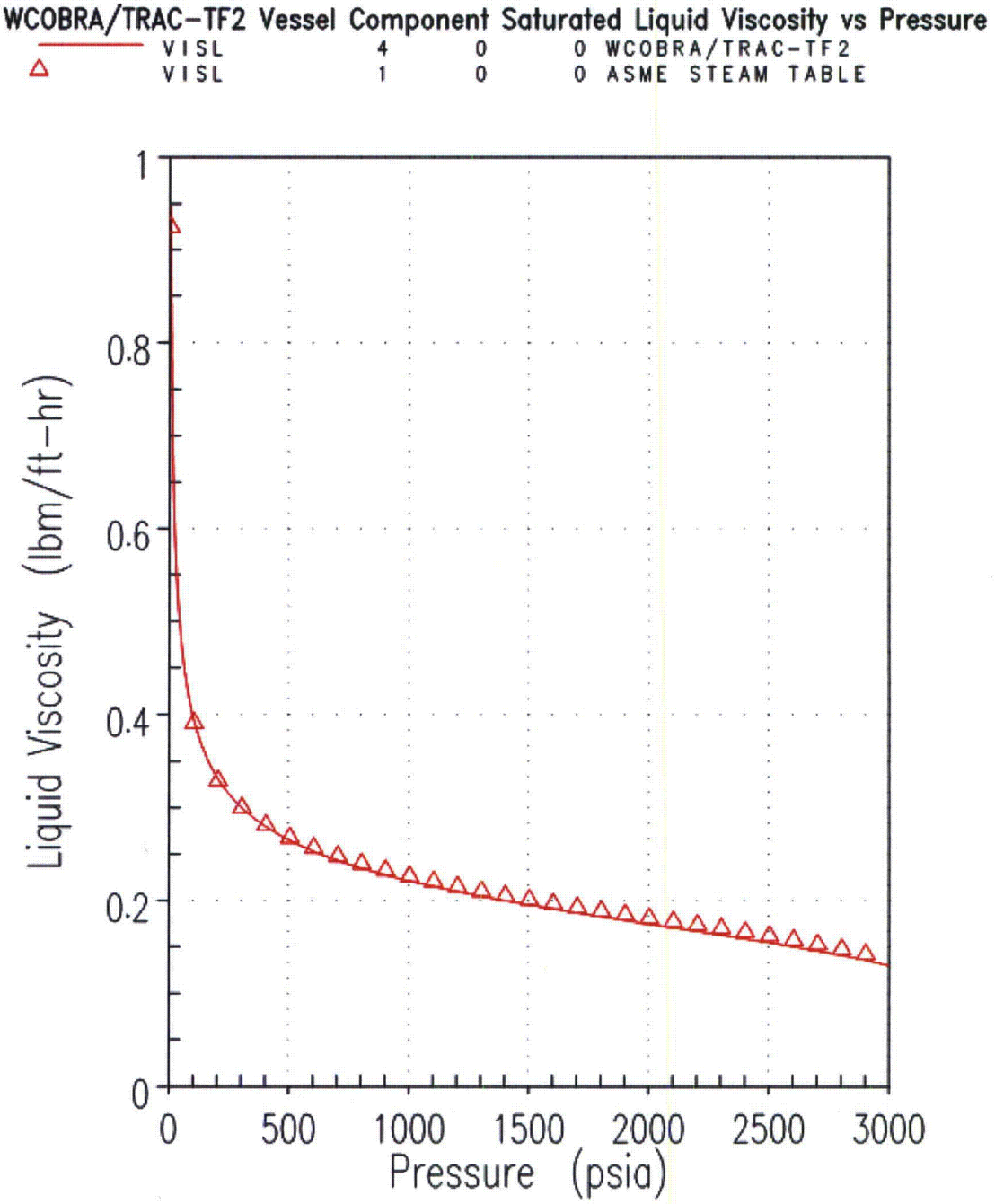

Figure 11-6 WCOBRA/TRAC-TF2 Vessel Component Saturated Liquid Viscosity

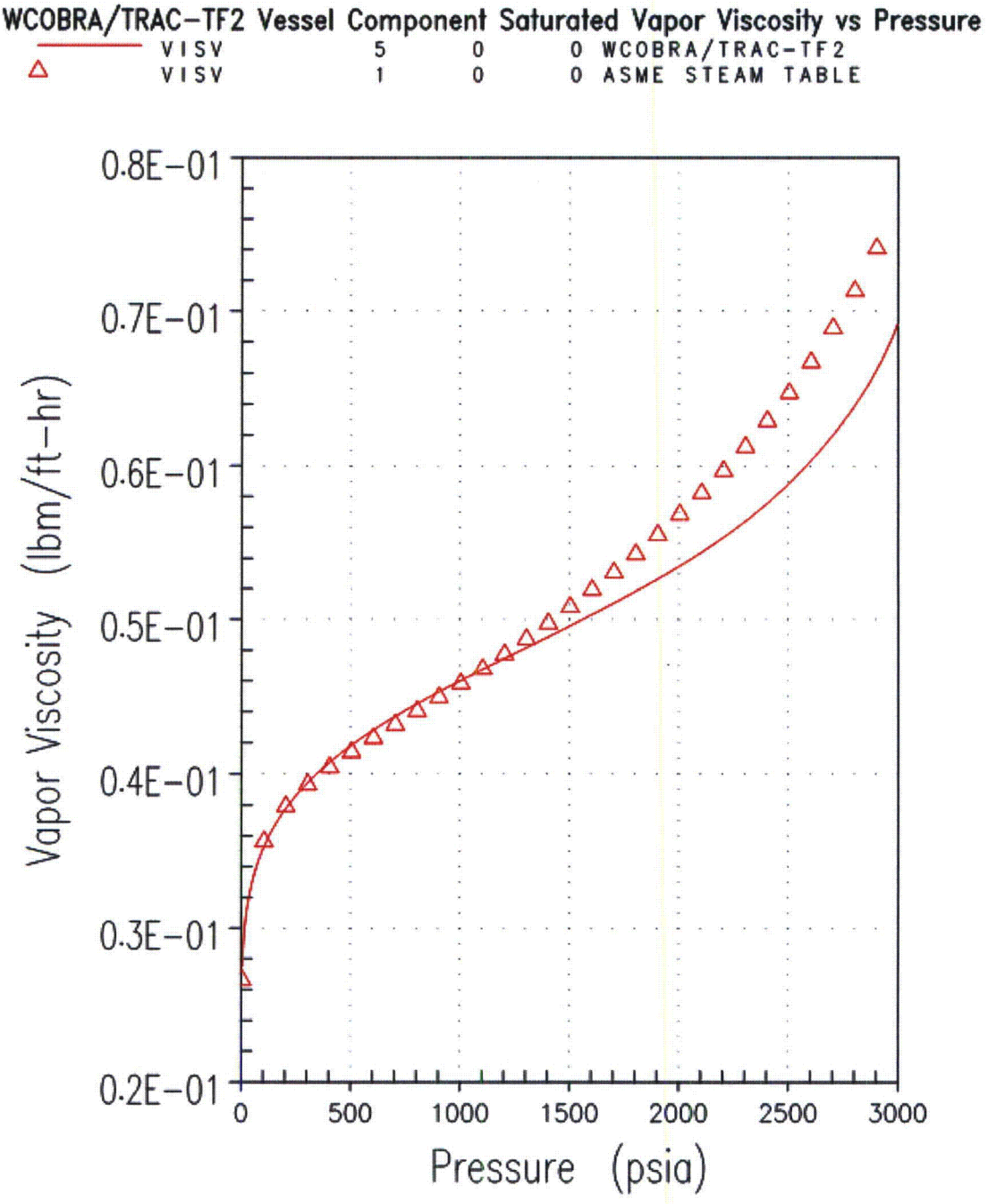

Figure 11-7 WCOBRA/TRAC-TF2 Vessel Component Saturated Vapor Viscosity

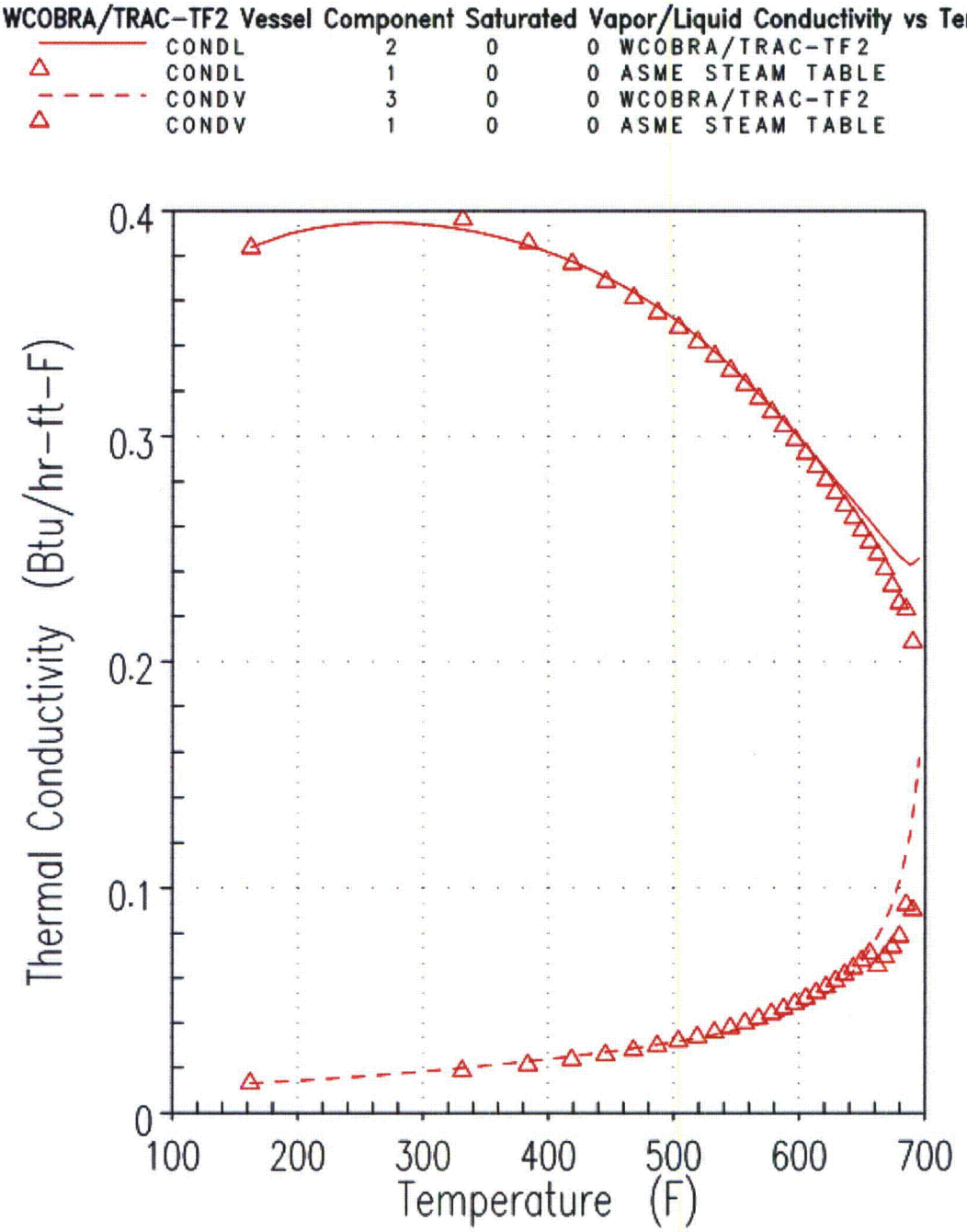

Figure 11-8 WCOBRA/TRAC-TF2 Vessel Component Saturated Liquid and Vapor Thermal Conductivity

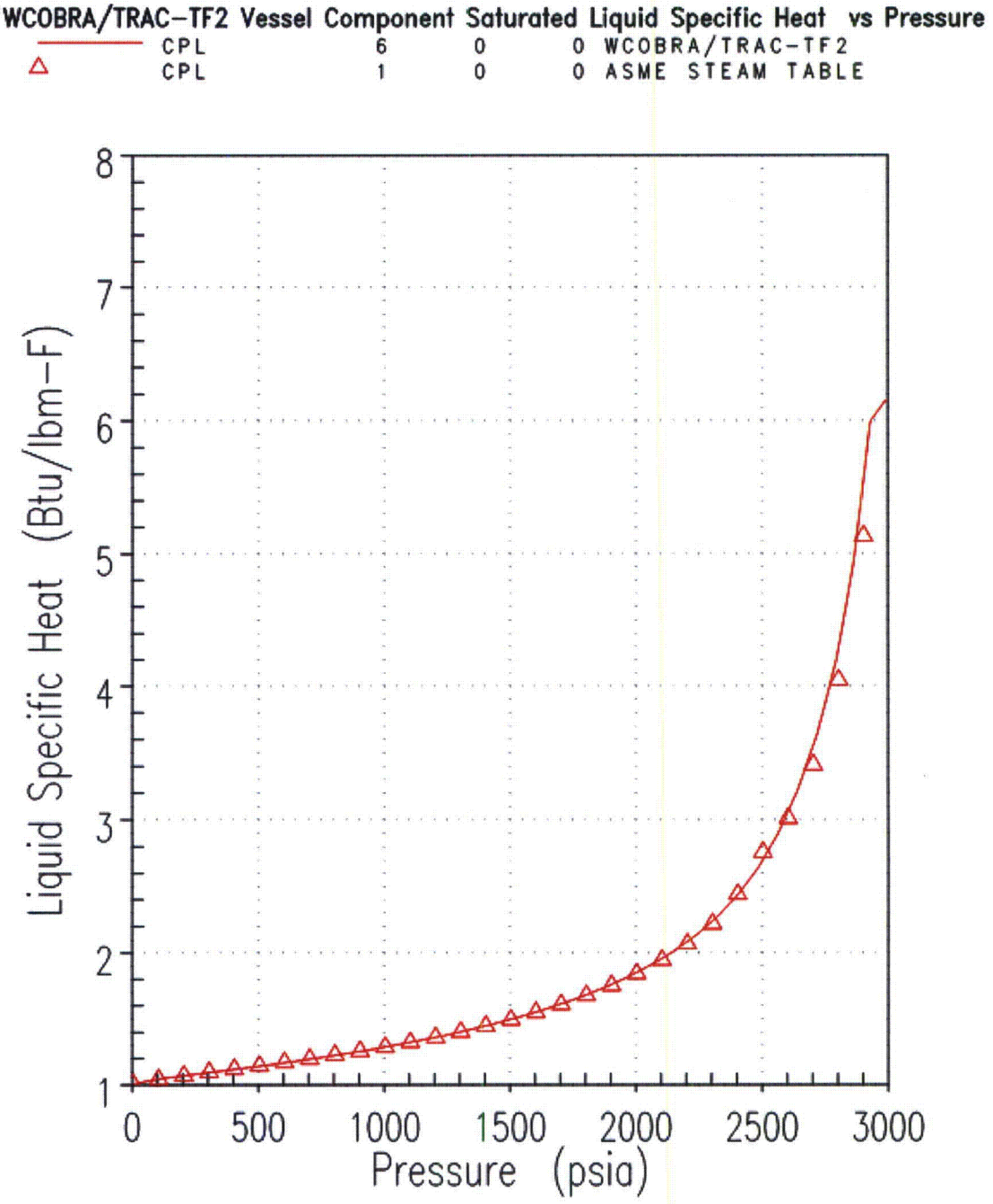

Figure 11-9 WCOBRA/TRAC-TF2 Vessel Component Saturated Liquid Specific Heat

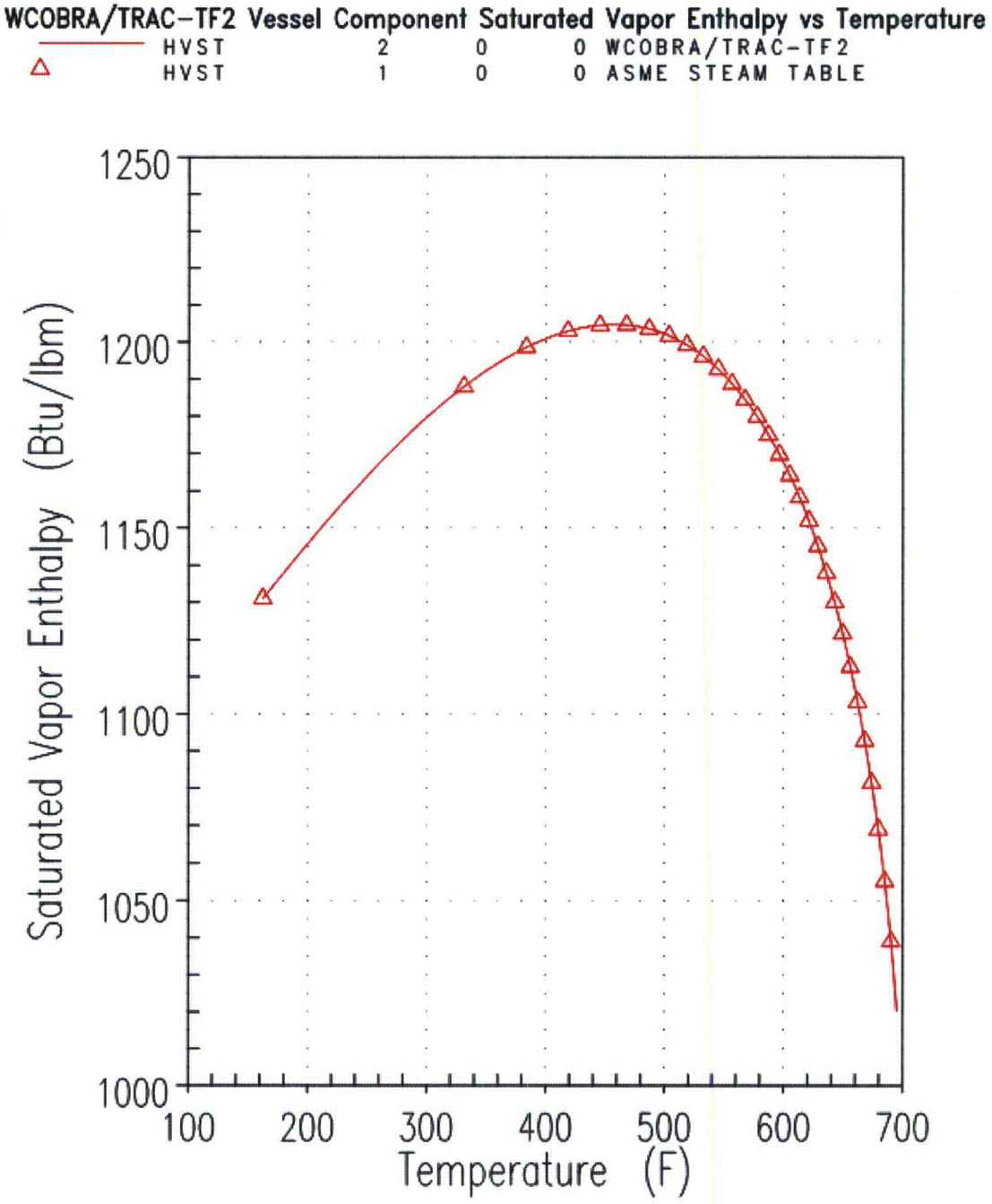

Figure 11-10 WCOBRA/TRAC-TF2 Vessel Component Saturated Vapor Enthalpy

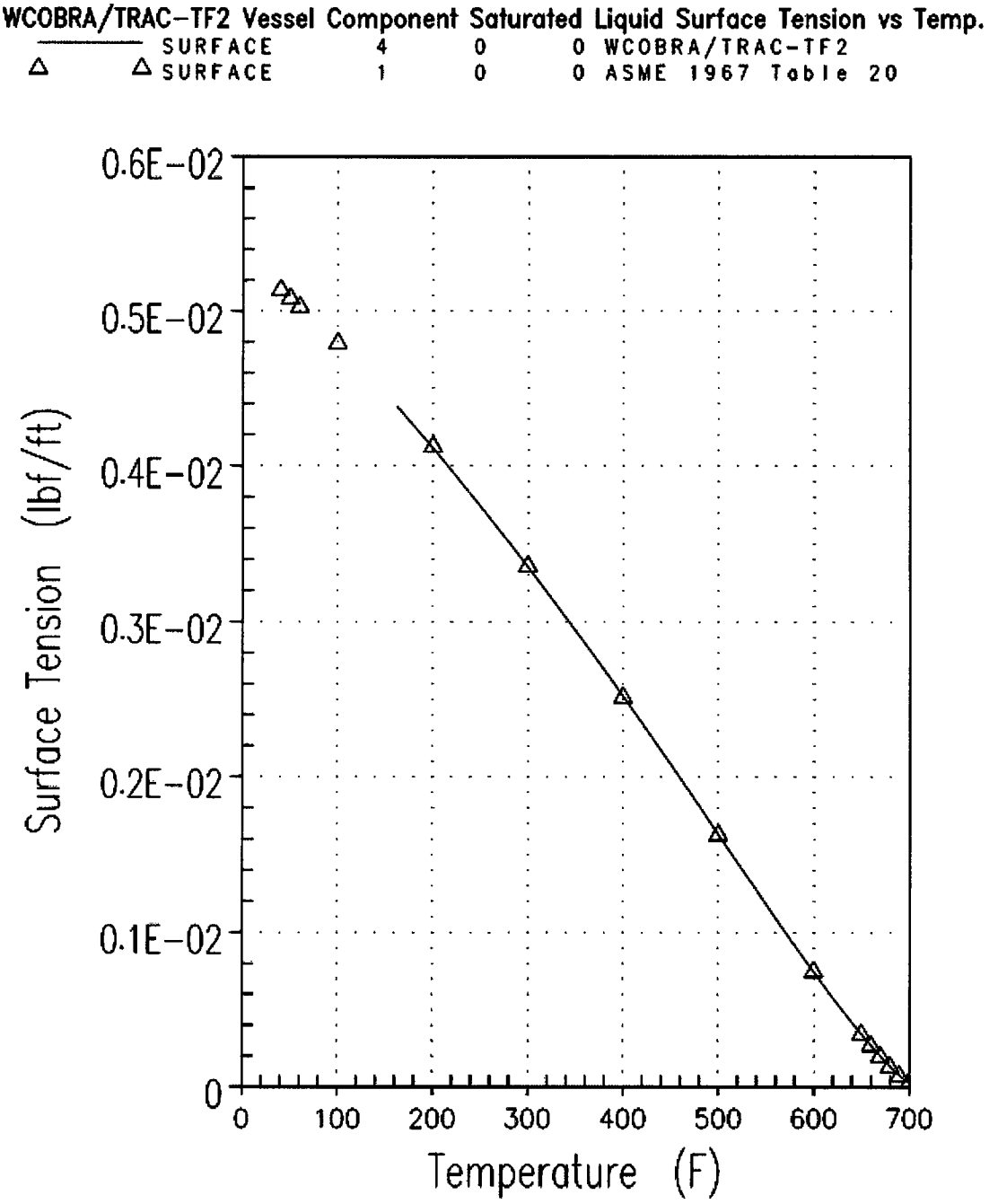

Figure 11-11 WCOBRA/TRAC-TF2 Vessel Component Saturated Liquid Surface Tension

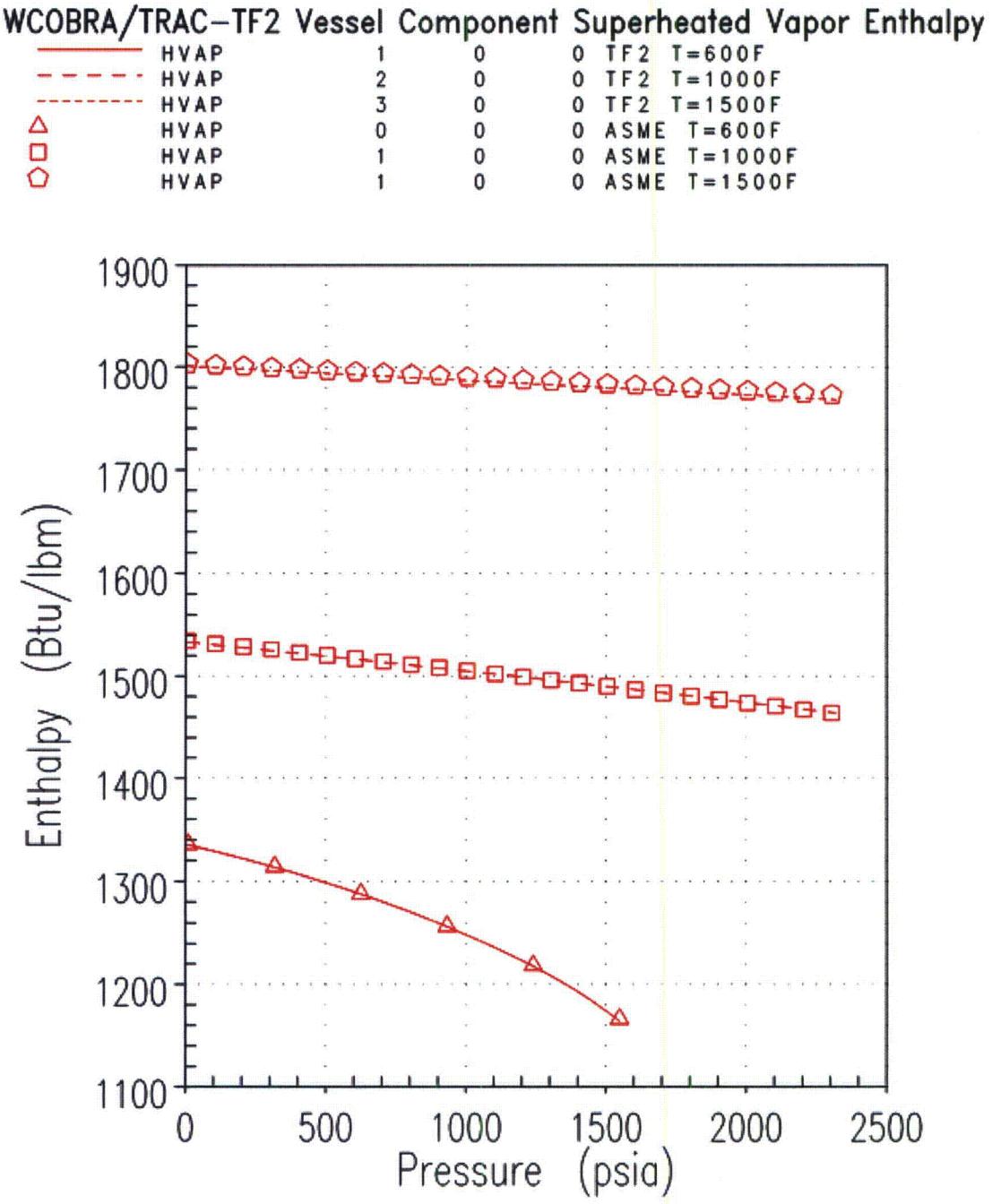

Figure 11-12 WCOBRA/TRAC-TF2 Vessel Component Superheated Vapor Enthalpy

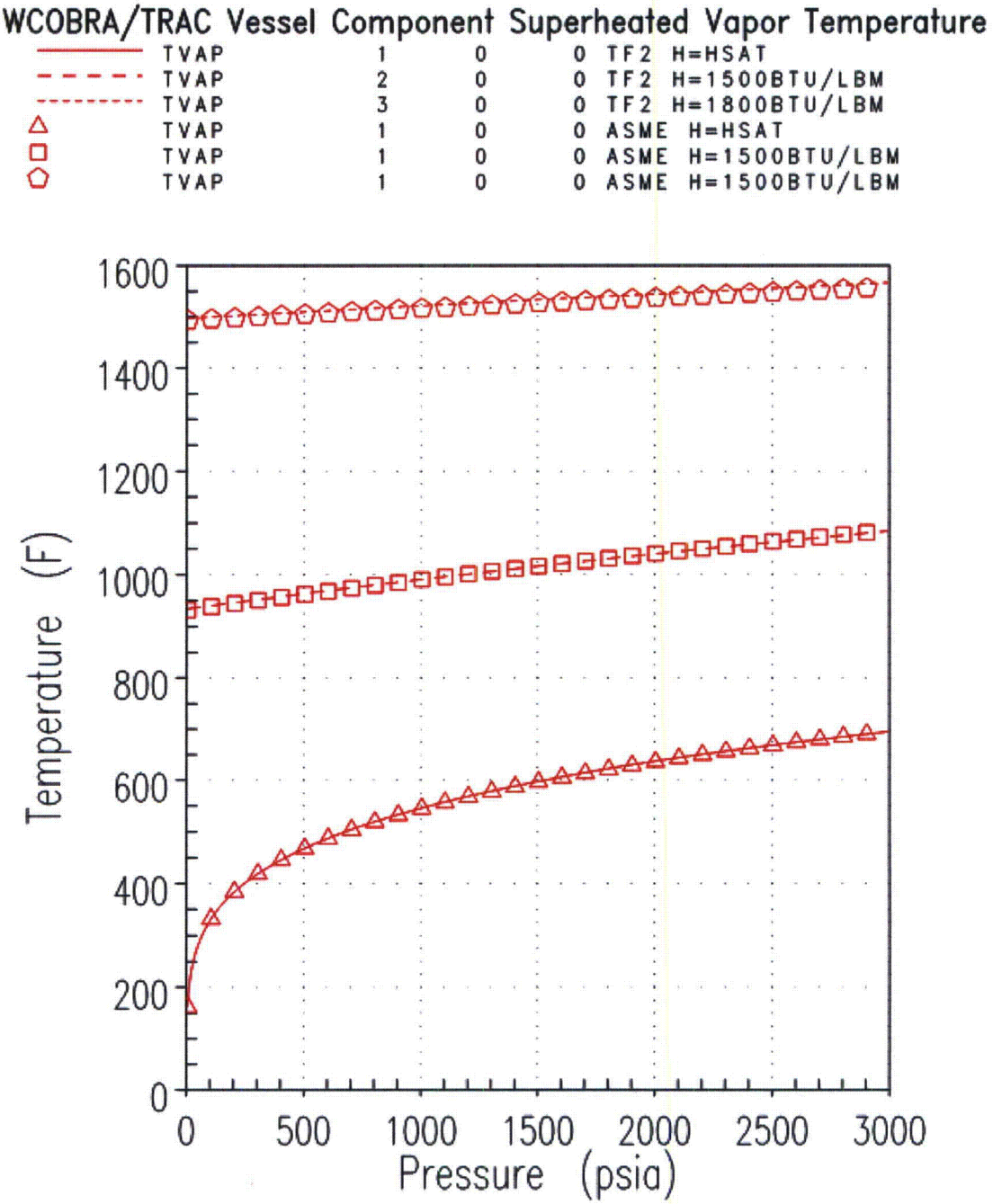

Figure 11-13 WCOBRA/TRAC-TF2 Vessel Component Superheated Vapor Temperature

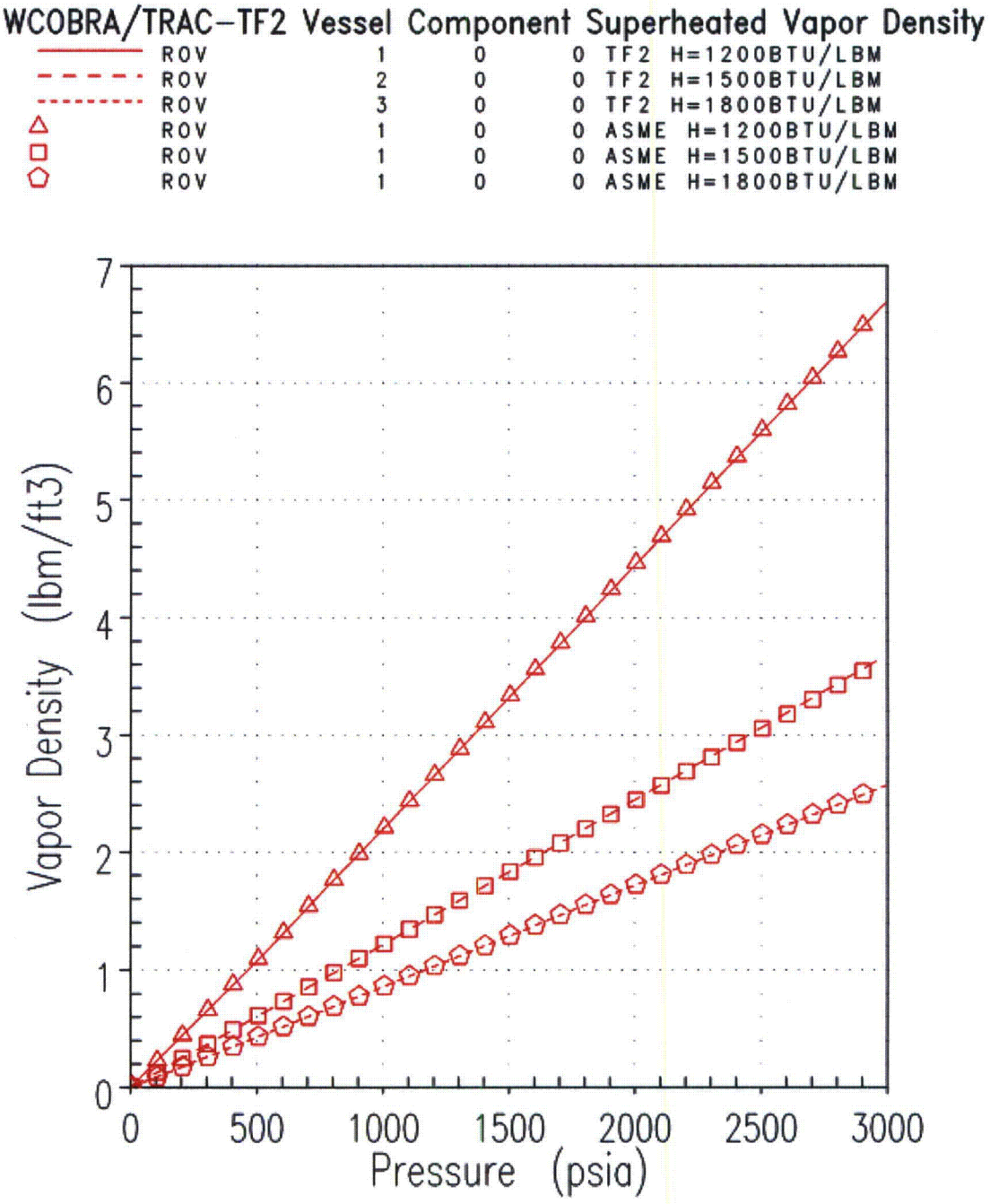

Figure 11-14 WCOBRA/TRAC-TF2 Vessel Component Superheated Vapor Density

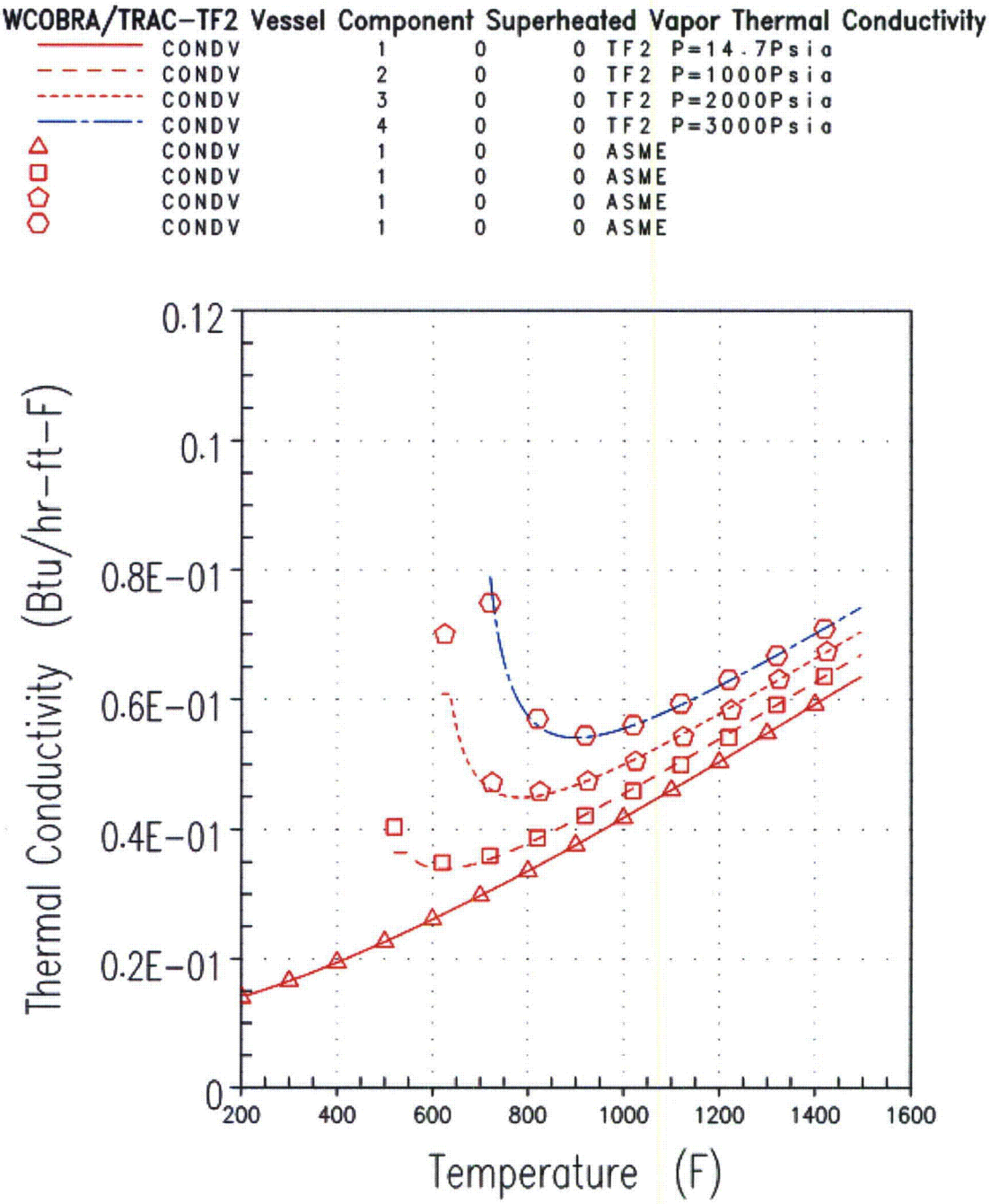

Figure 11-15 WCOBRA/TRAC-TF2 Vessel Component Superheated Vapor Thermal Conductivity

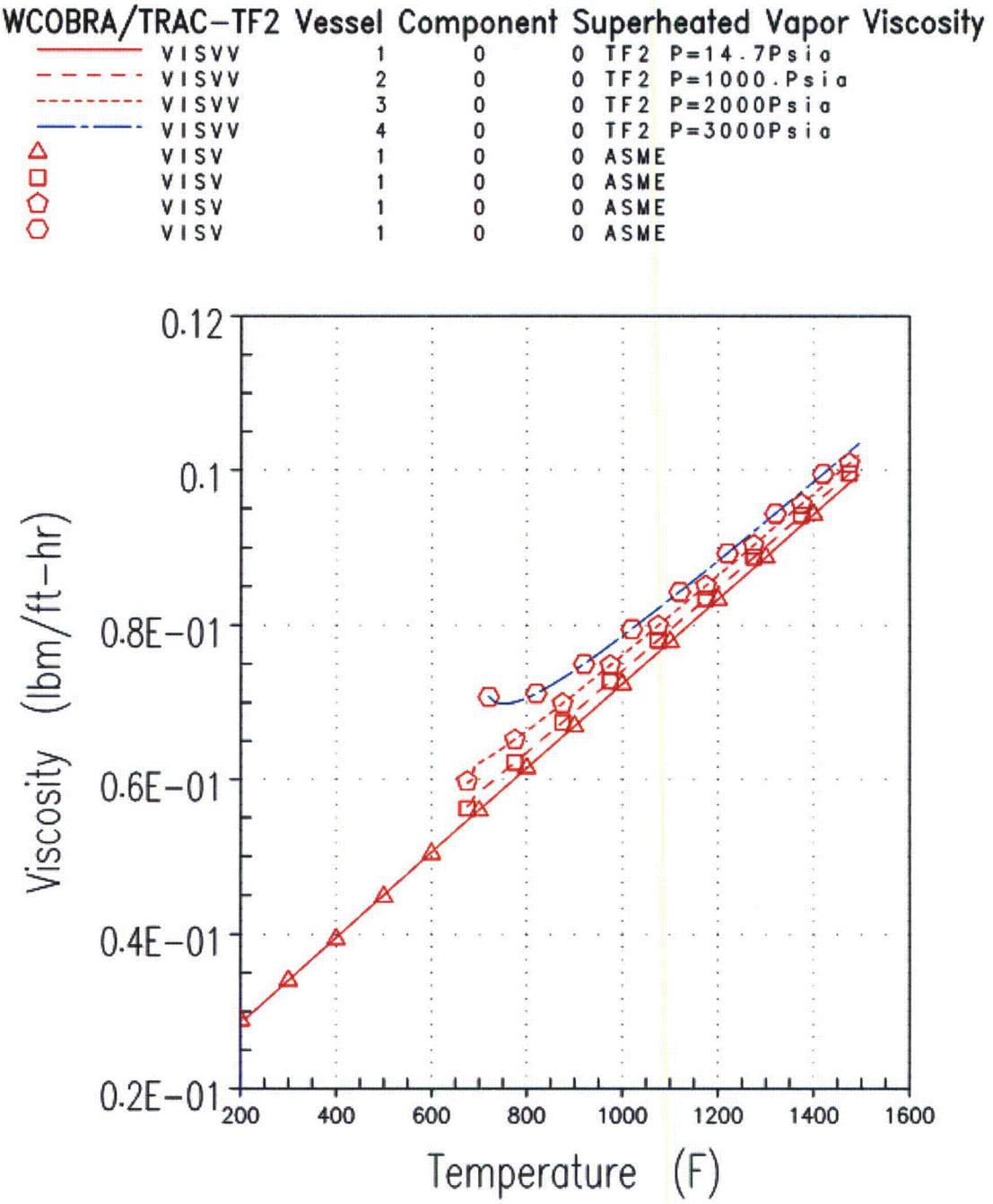

Figure 11-16 WCOBRA/TRAC-TF2 Vessel Component Superheated Vapor Viscosity

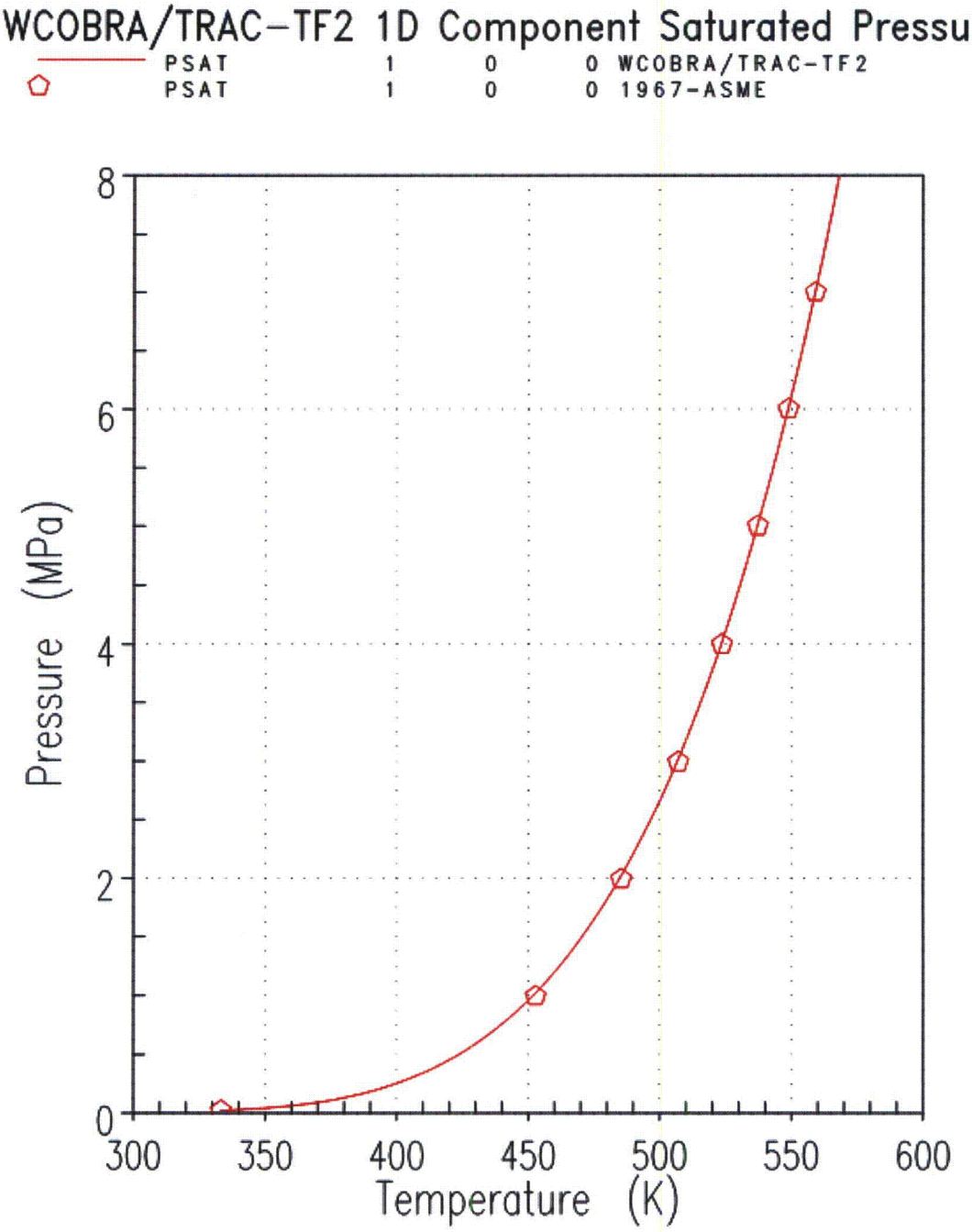

Figure 11-17 WCOBRA/TRAC-TF2 1D Component Saturation Pressure

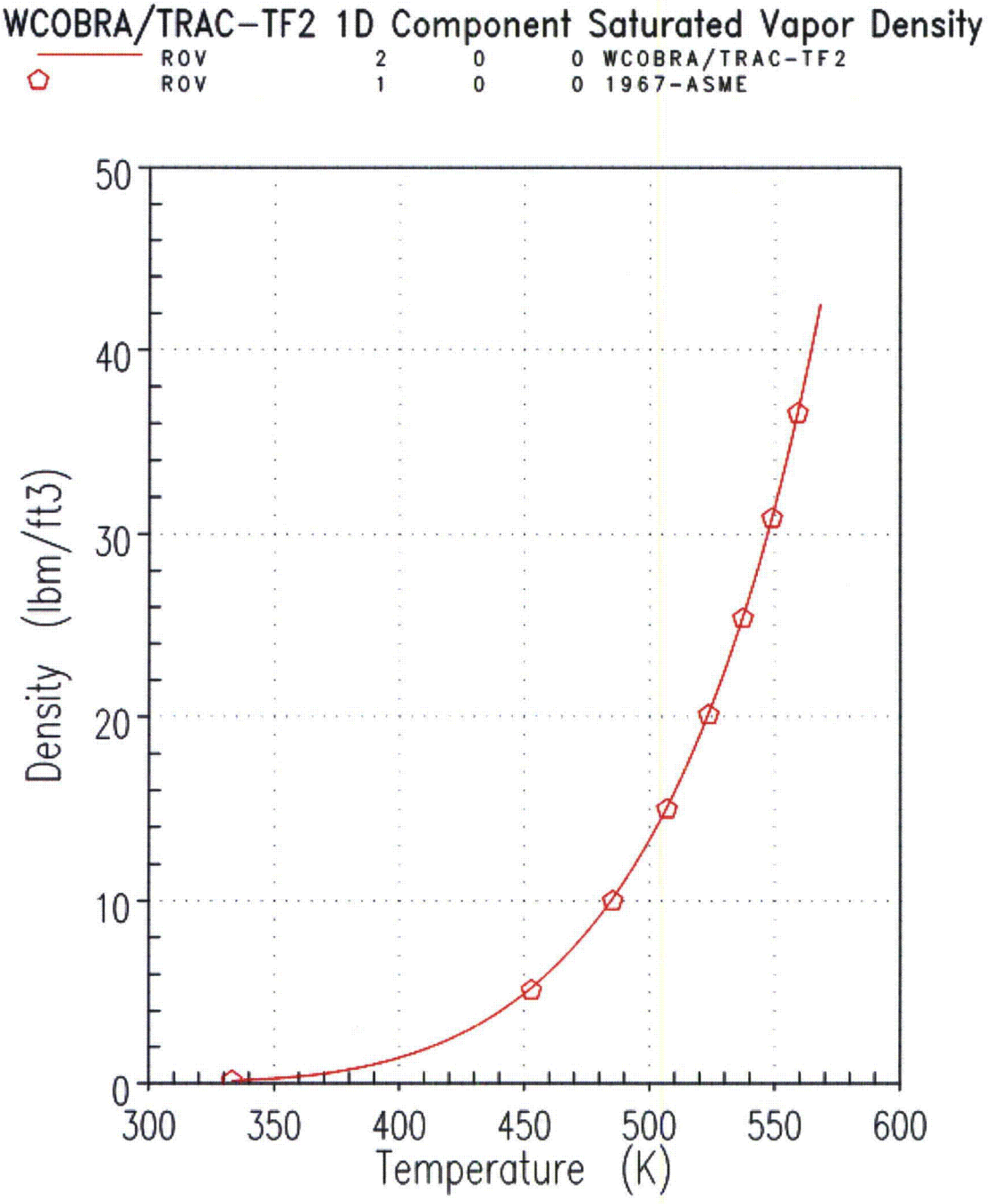

Figure 11-18 WCOBRA/TRAC-TF2 1D Component Saturated Vapor Density

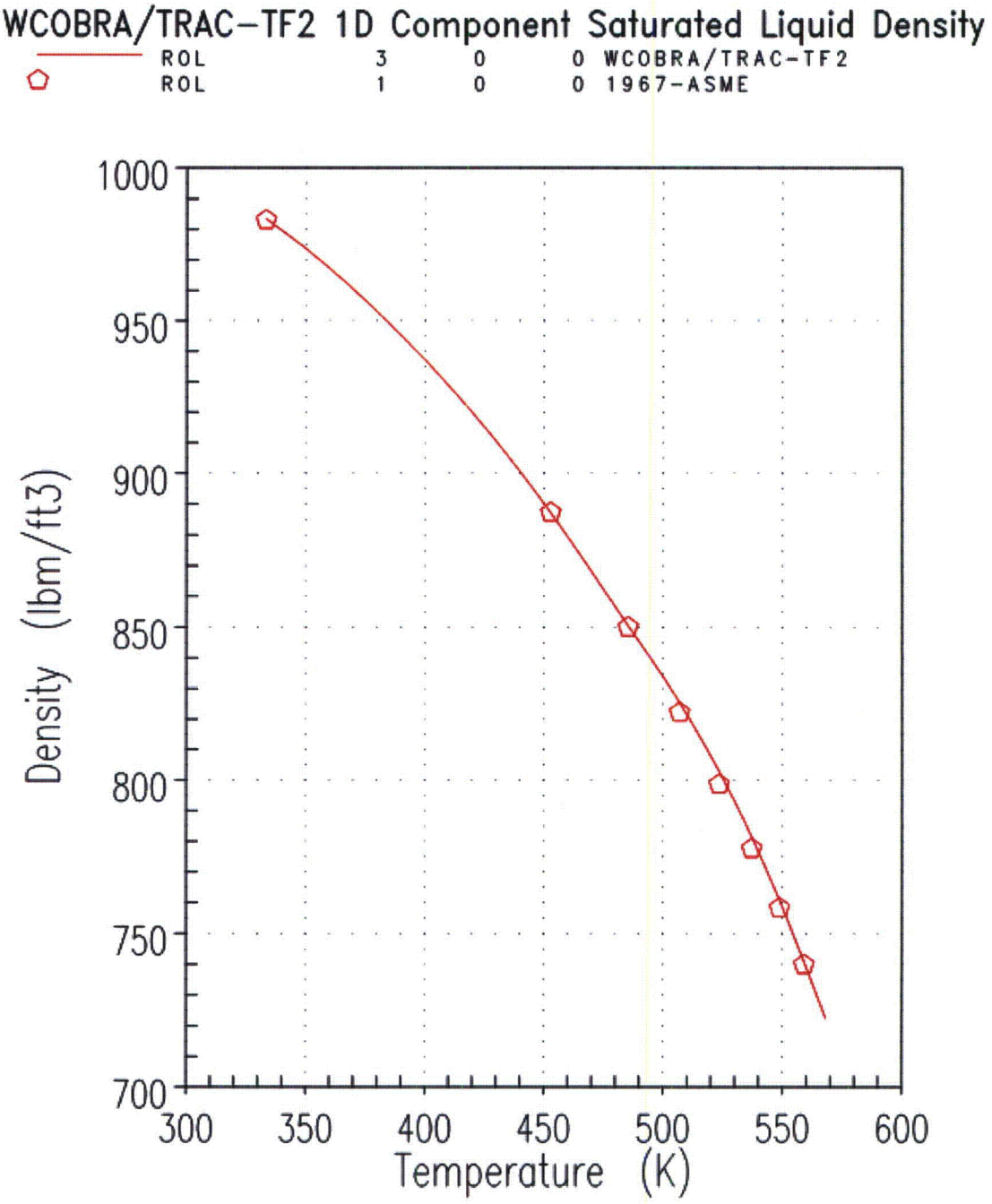

Figure 11-19 WCOBRA/TRAC-TF2 1D Component Saturated Liquid Density

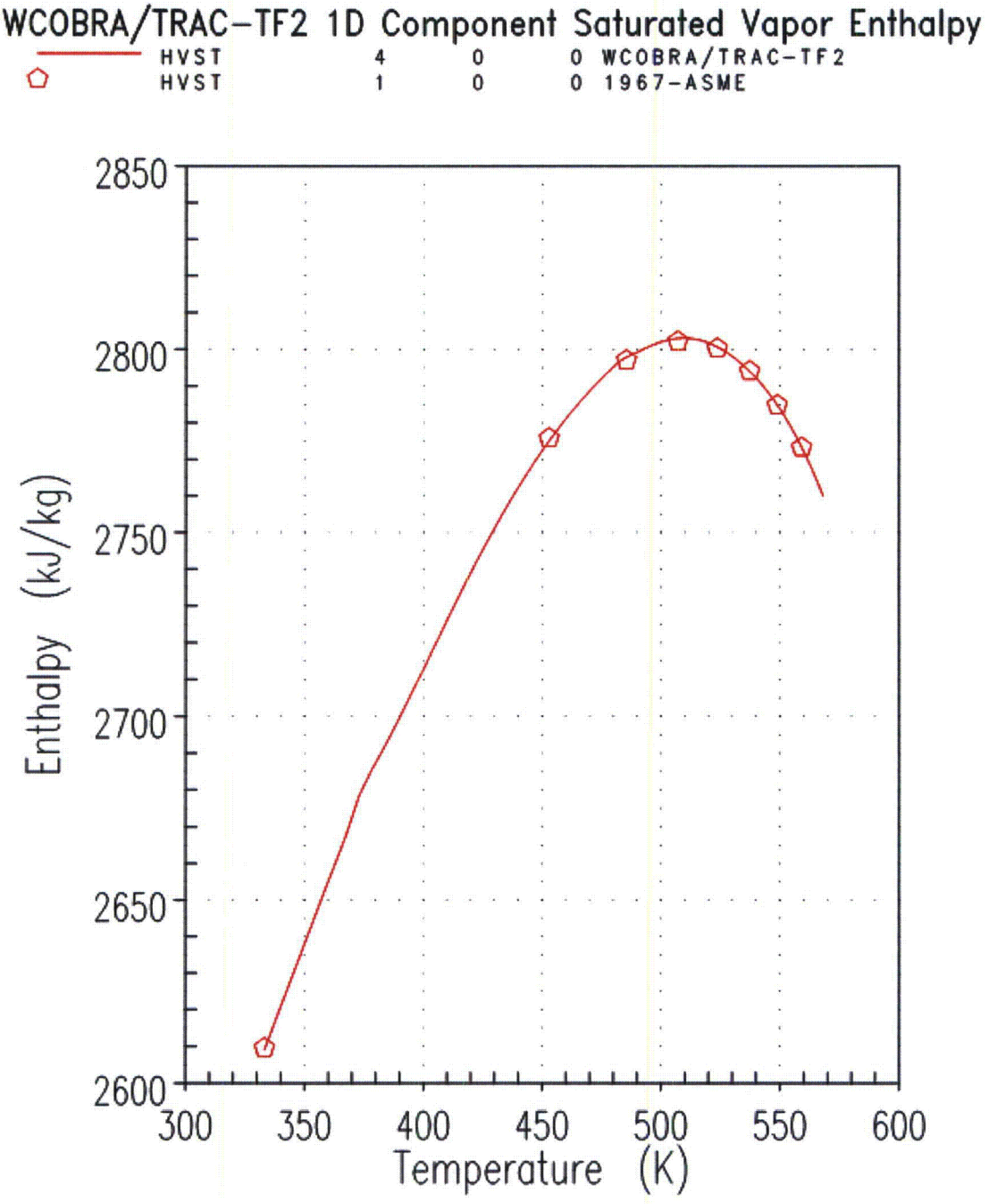

Figure 11-20 WCOBRA/TRAC-TF2 1D Component Saturated Vapor Enthalpy

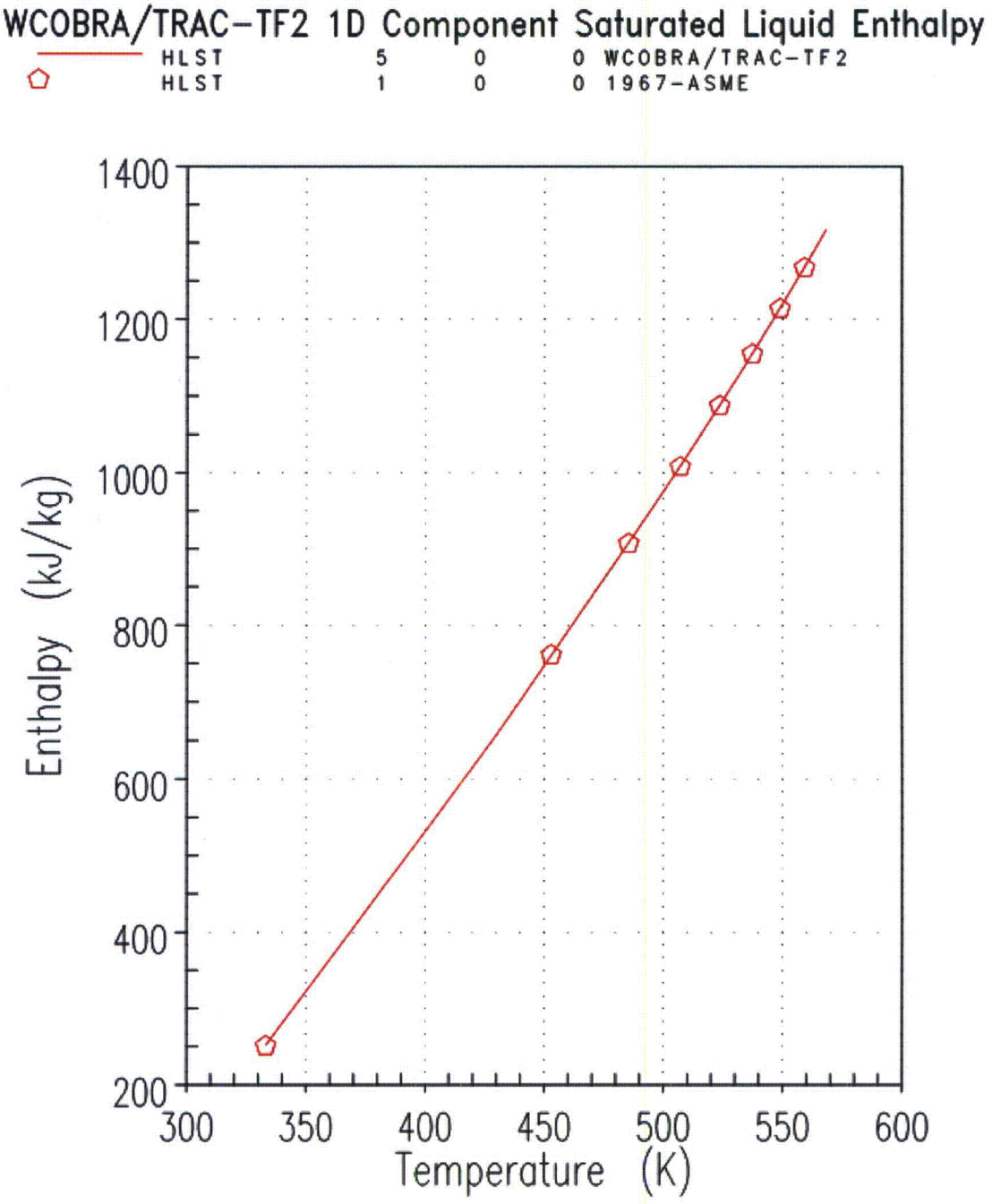

Figure 11-21 WCOBRA/TRAC-TF2 1D Component Saturated Liquid Enthalpy

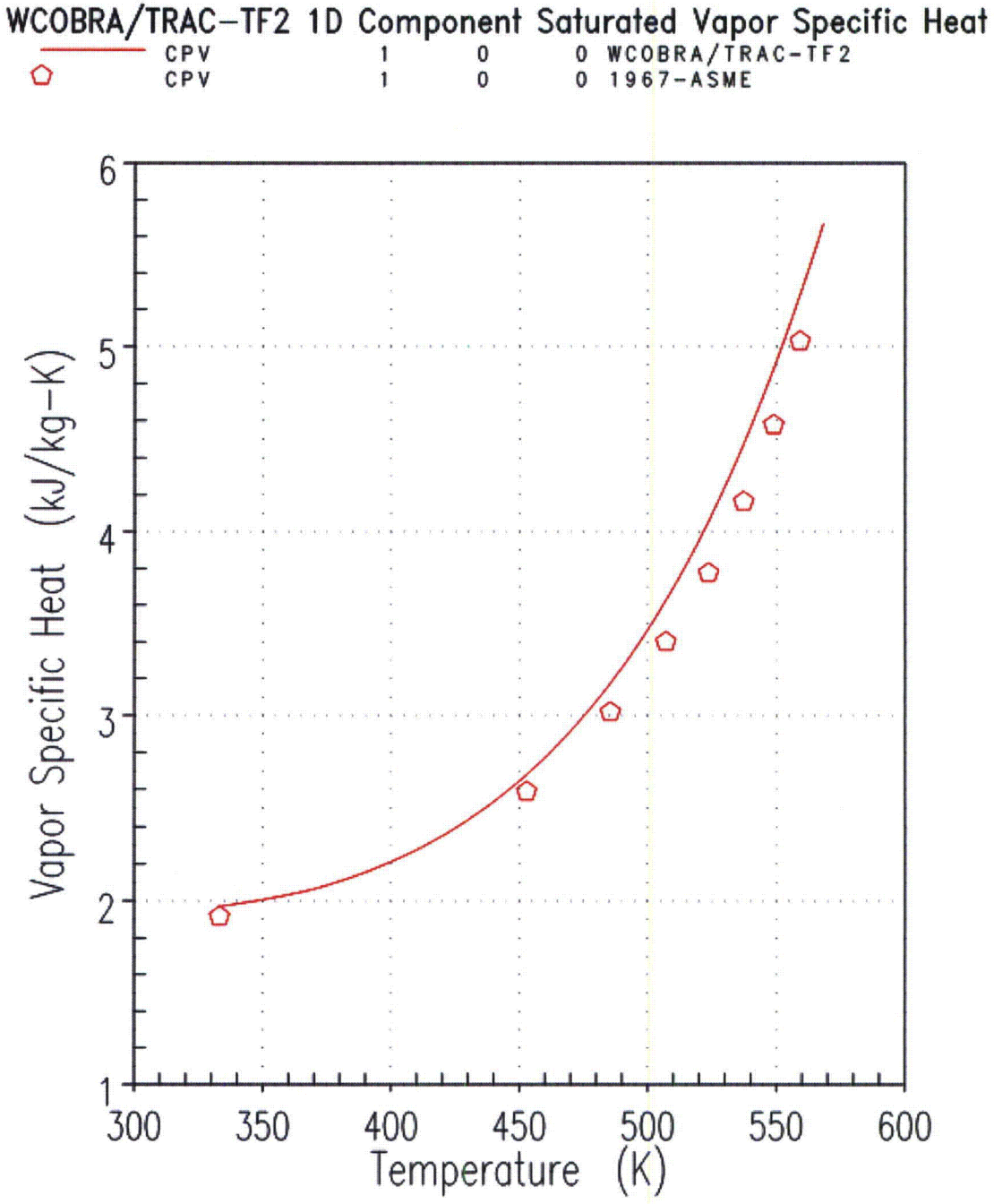

Figure 11-22 WCOBRA/TRAC-TF2 1D Component Saturated Vapor Specific Heat

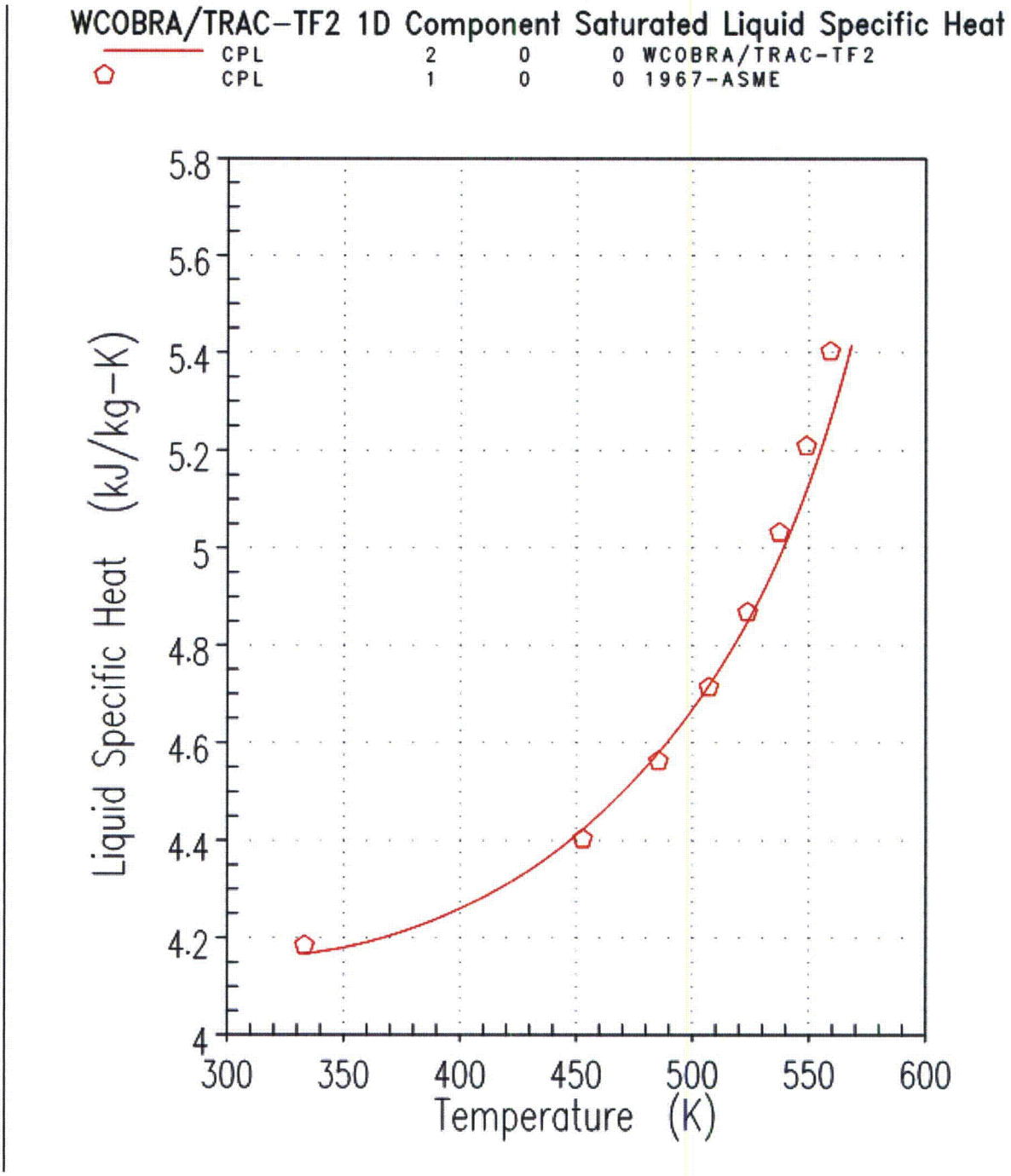

Figure 11-23 WCOBRA/TRAC-TF2 1D Component Saturated Liquid Specific Heat

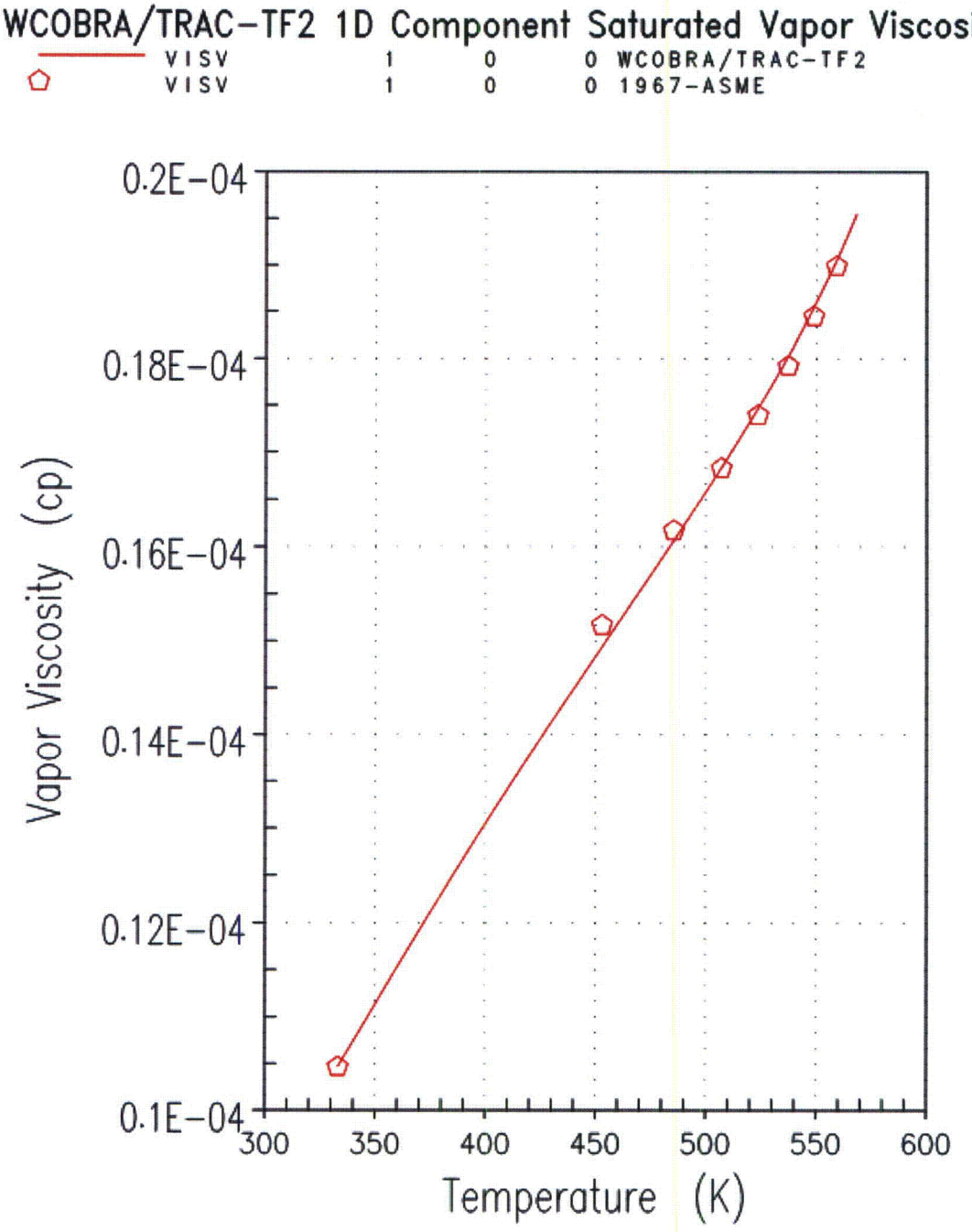

Figure 11-24 WCOBRA/TRAC-TF2 1D Component Saturated Vapor Viscosity

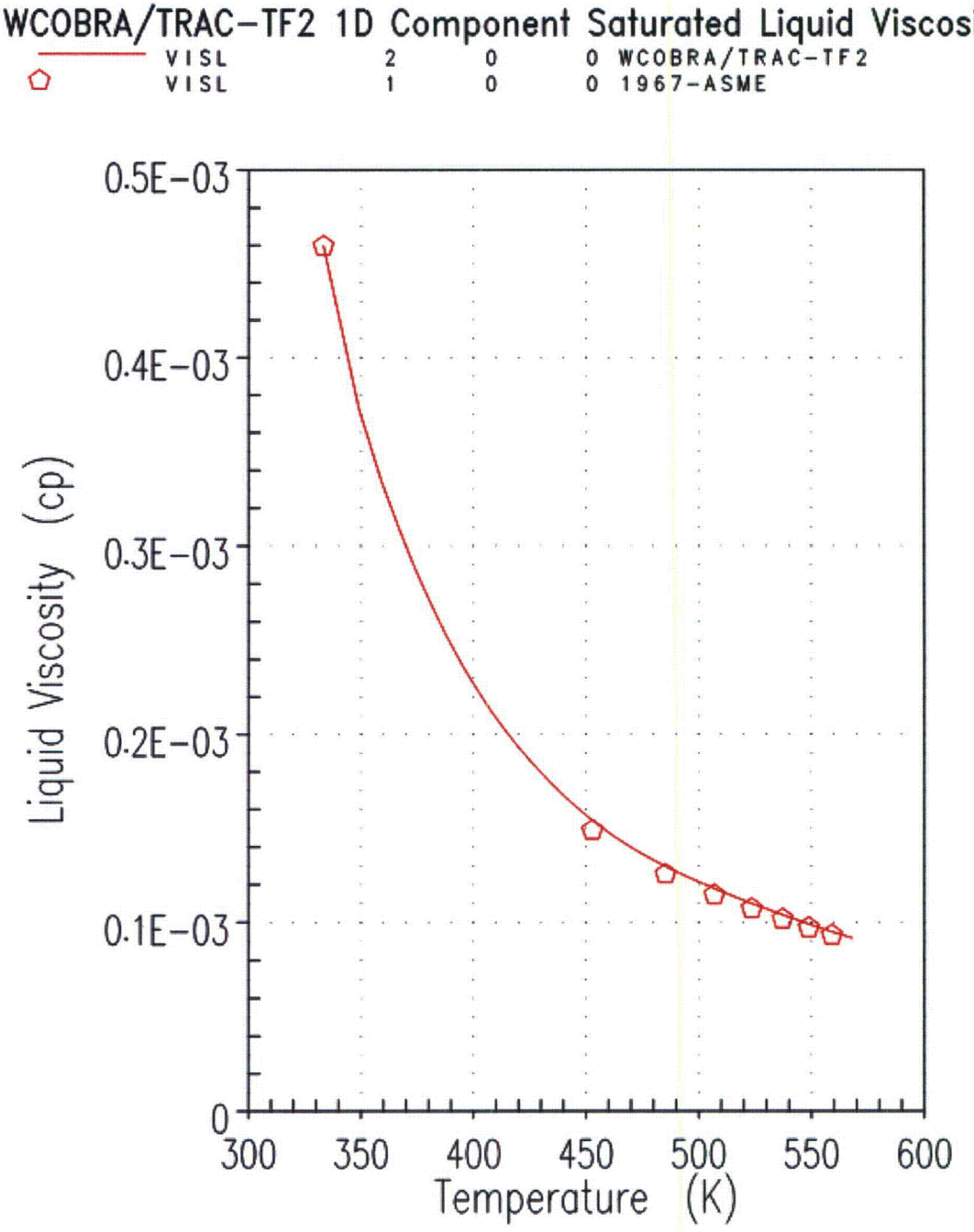

Figure 11-25 WCOBRA/TRAC-TF2 1D Component Saturated Liquid Viscosity

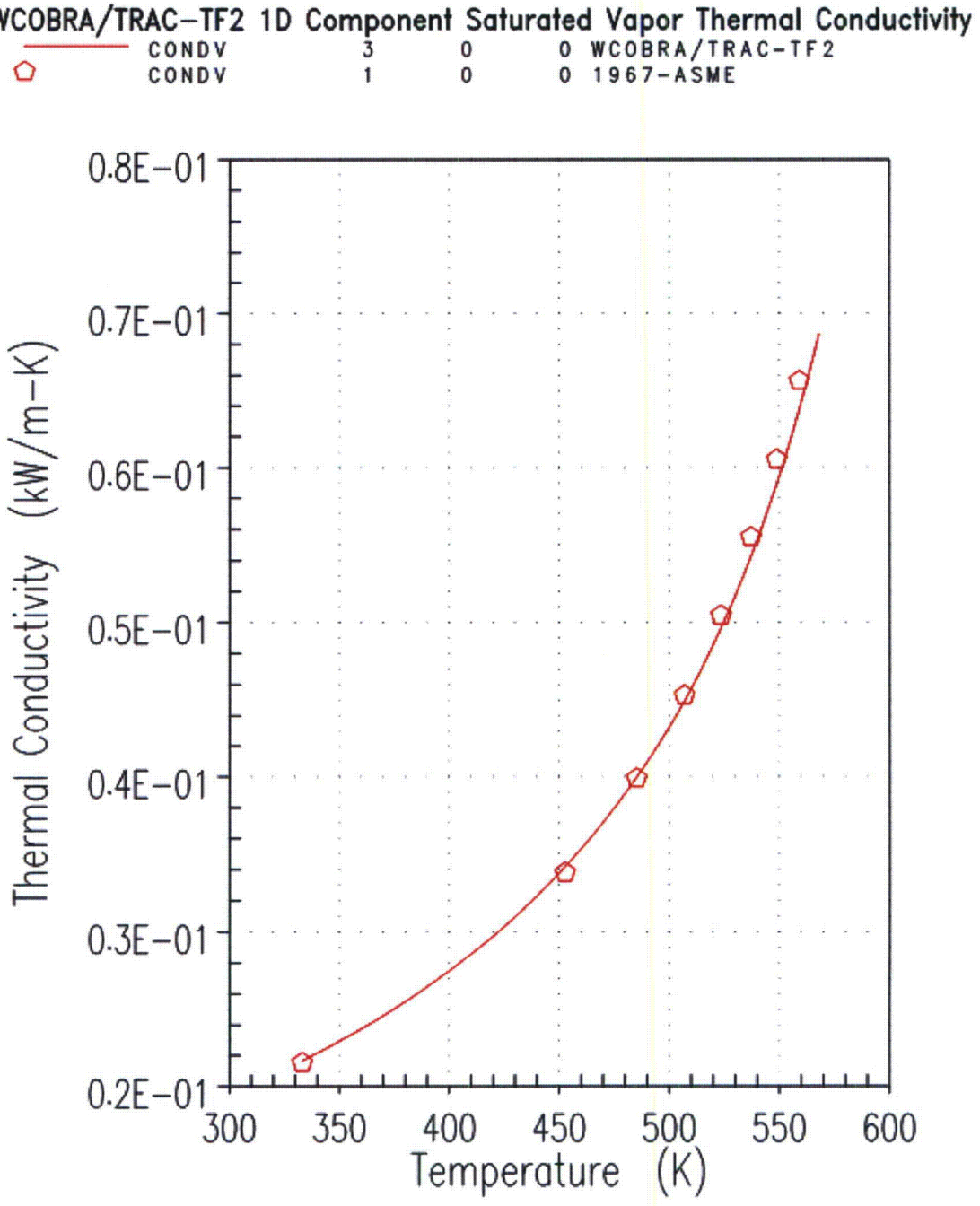

Figure 11-26 WCOBRA/TRAC-TF2 1D Component Saturated Vapor Thermal Conductivity

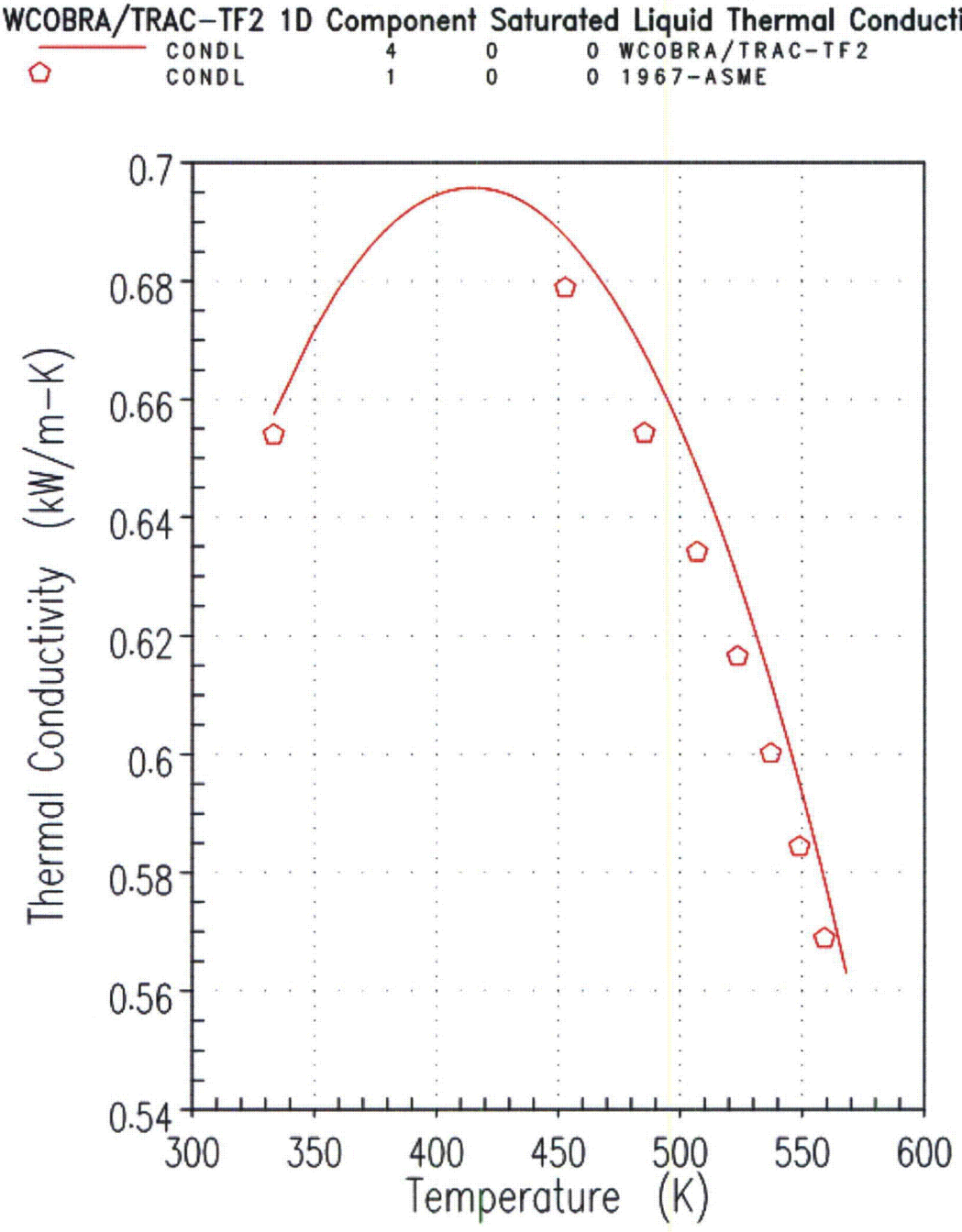

Figure 11-27 WCOBRA/TRAC-TF2 1D Component Saturated Liquid Thermal Conductivity

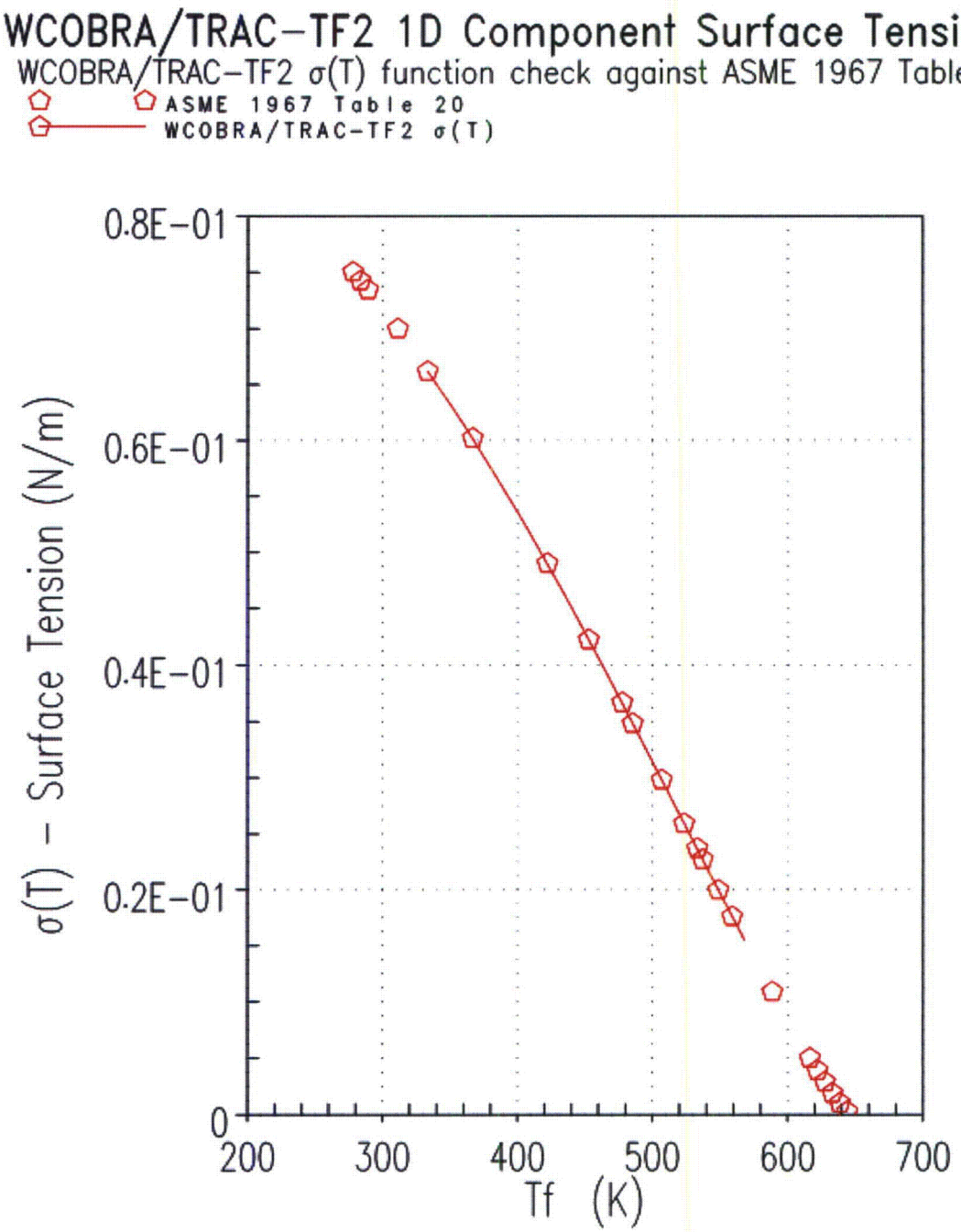

Figure 11-28 WCOBRA/TRAC-TF2 1D Component Surface Tension

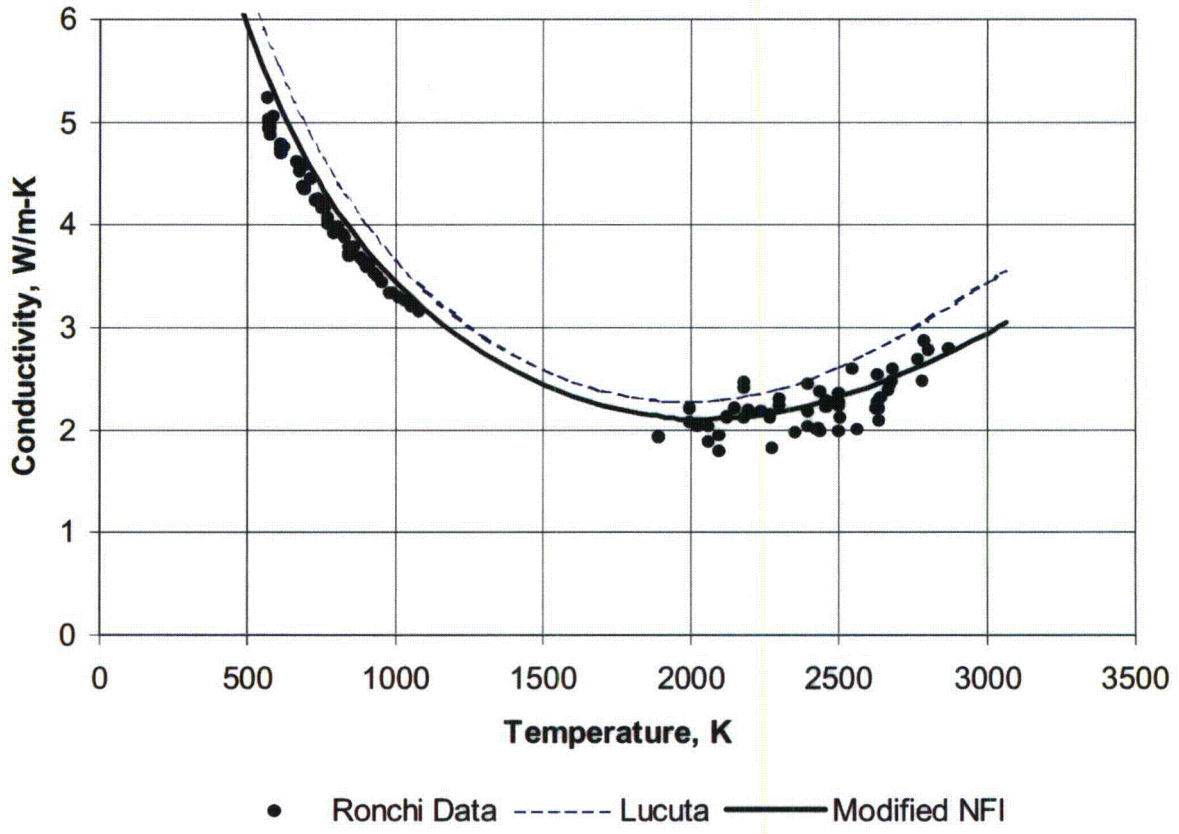

Figure 11-29 Modified NFI and Lucuta Model Predictions Compared to Measured Conductivity on Unirradiated Pellet Material (Ronchi et al., 1999), from Figure 2.4 of (Lanning et al., 2005)

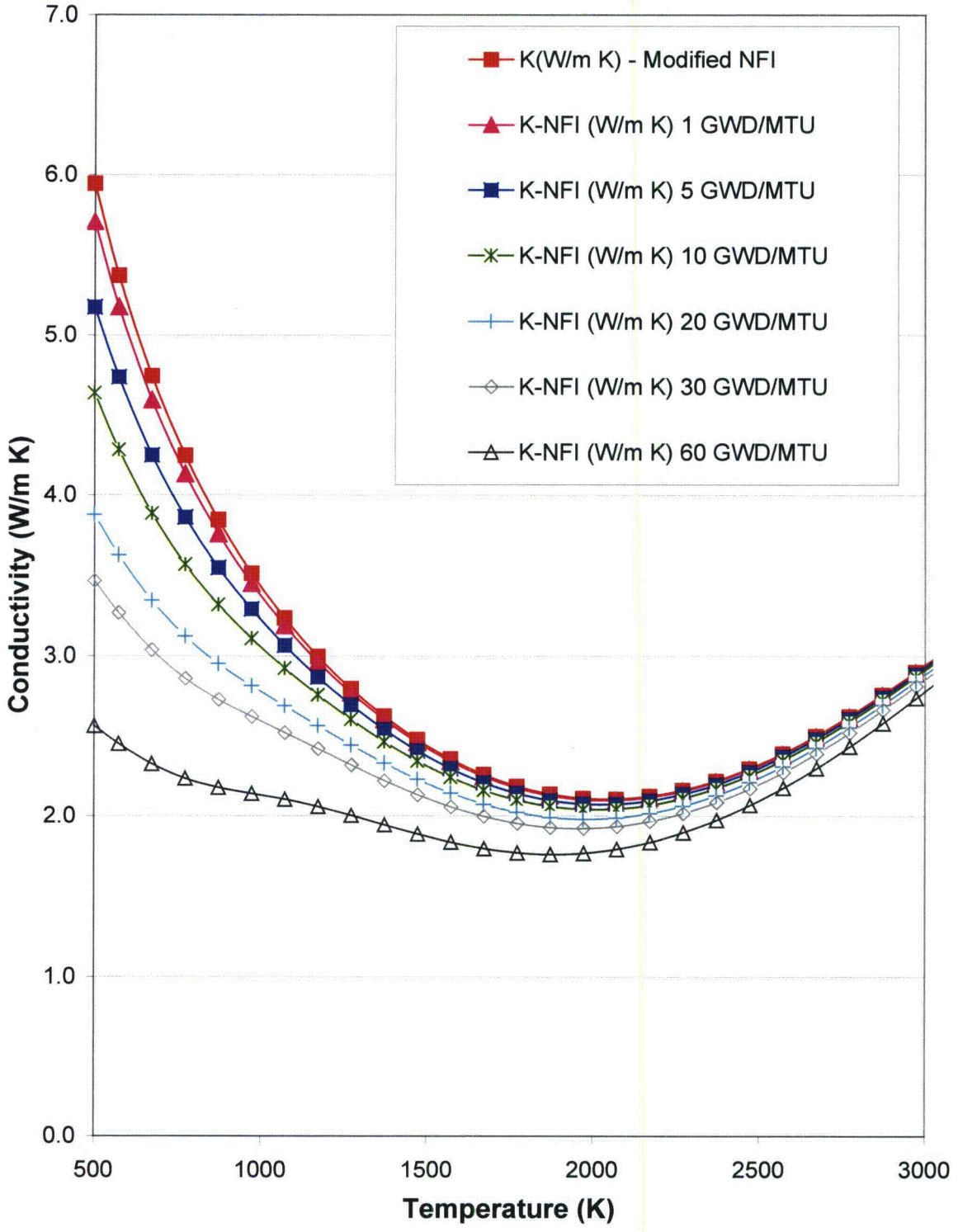

Figure 11-30 Modified NFI Thermal Conductivity for fuel density of 95% TD as a function of Burnup

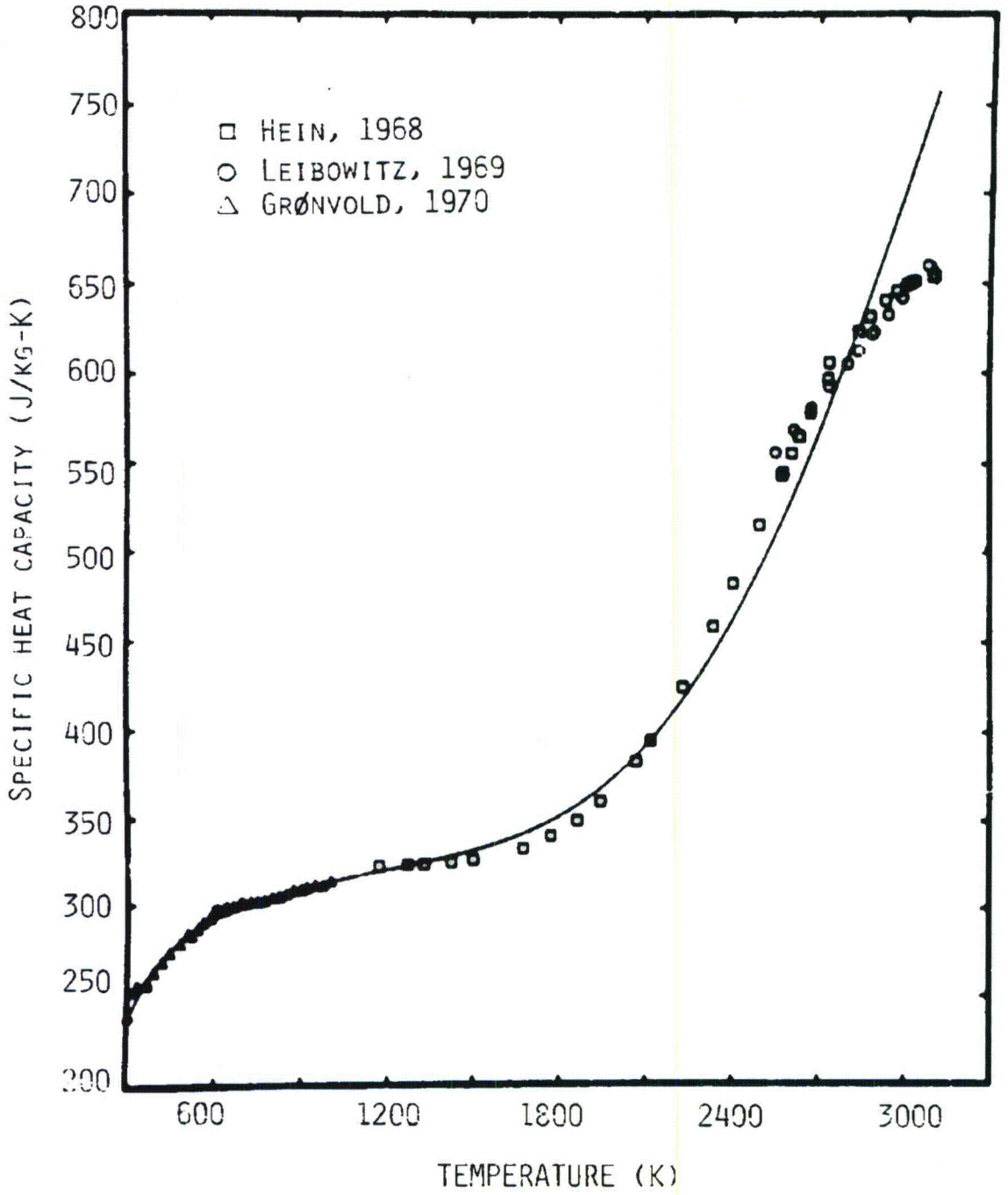

Figure 11-31 WCOBRA/TRAC-TF2 UO_2 Specific Heat Model

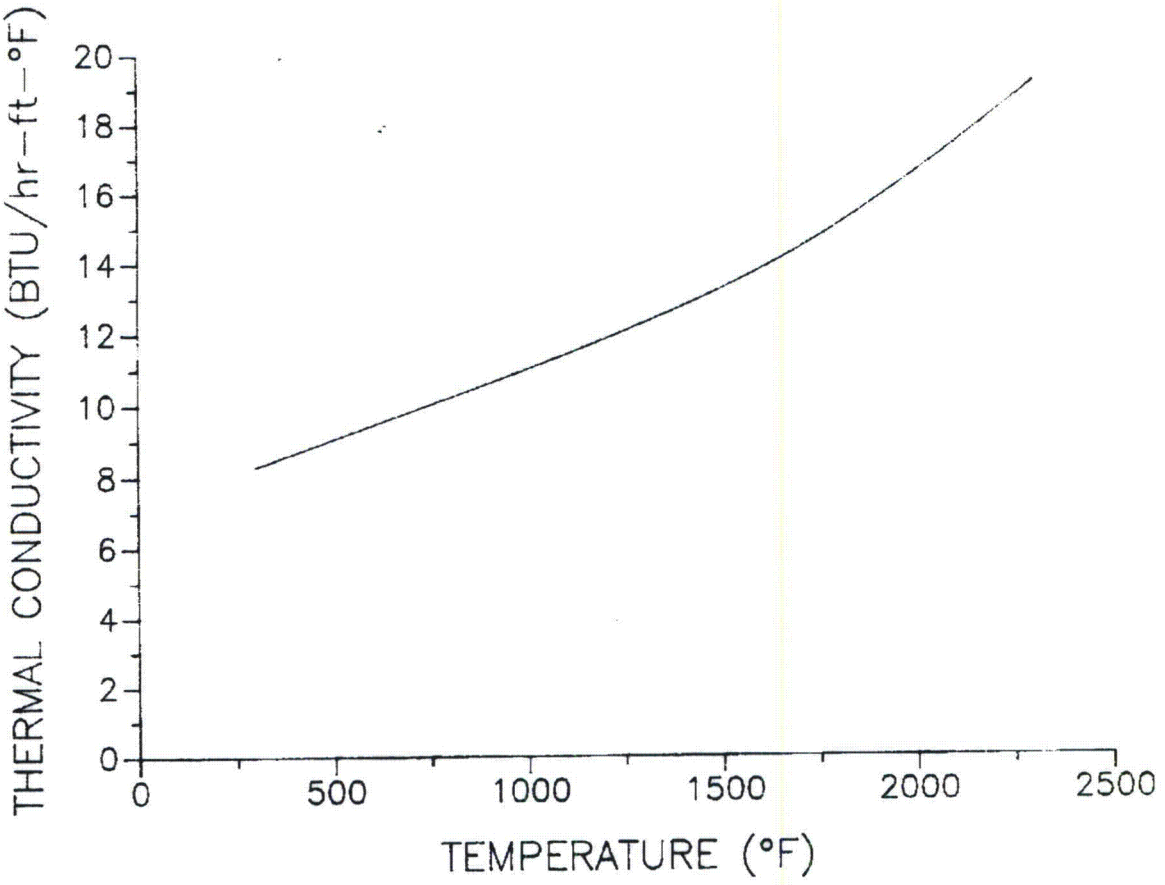

Figure 11-32 WCOBRA/TRAC-TF2 Zircaloy-4 Thermal Conductivity Model

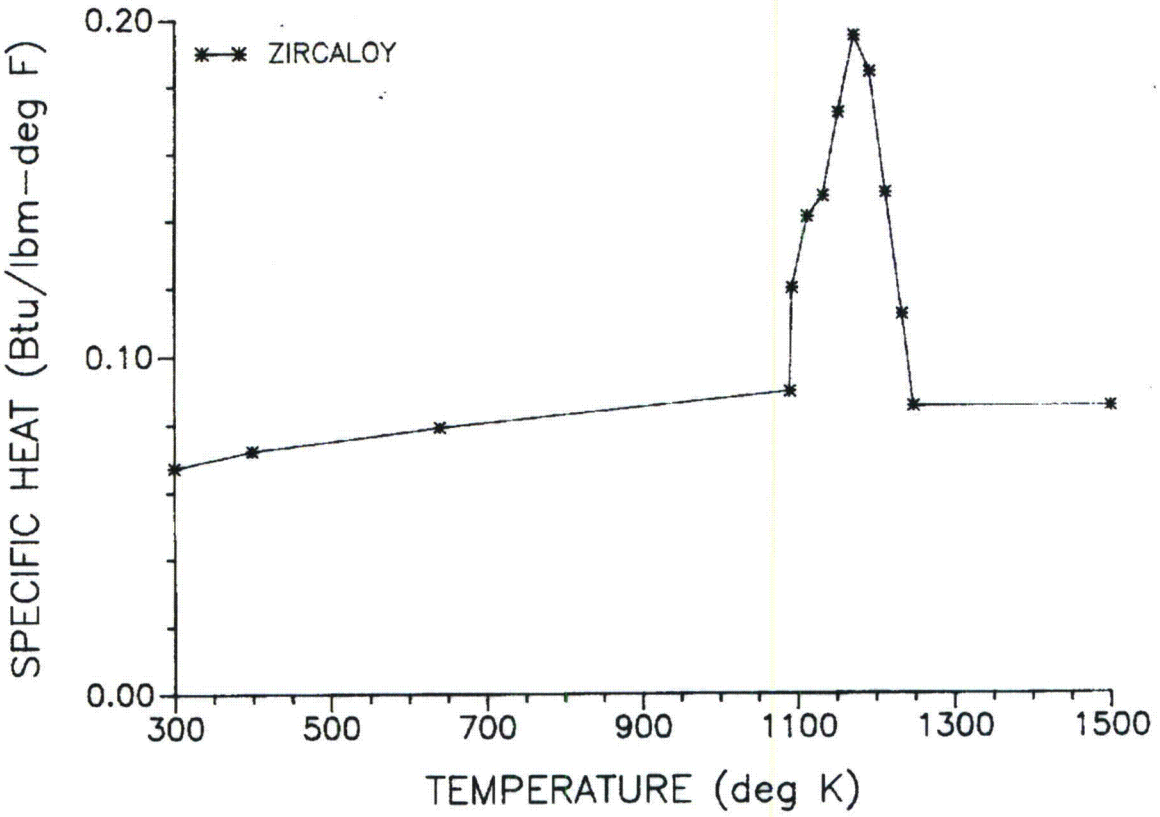

Figure 11-33 WCOBRA/TRAC-TF2 Zircaloy-4 Specific Heat Model

a,c

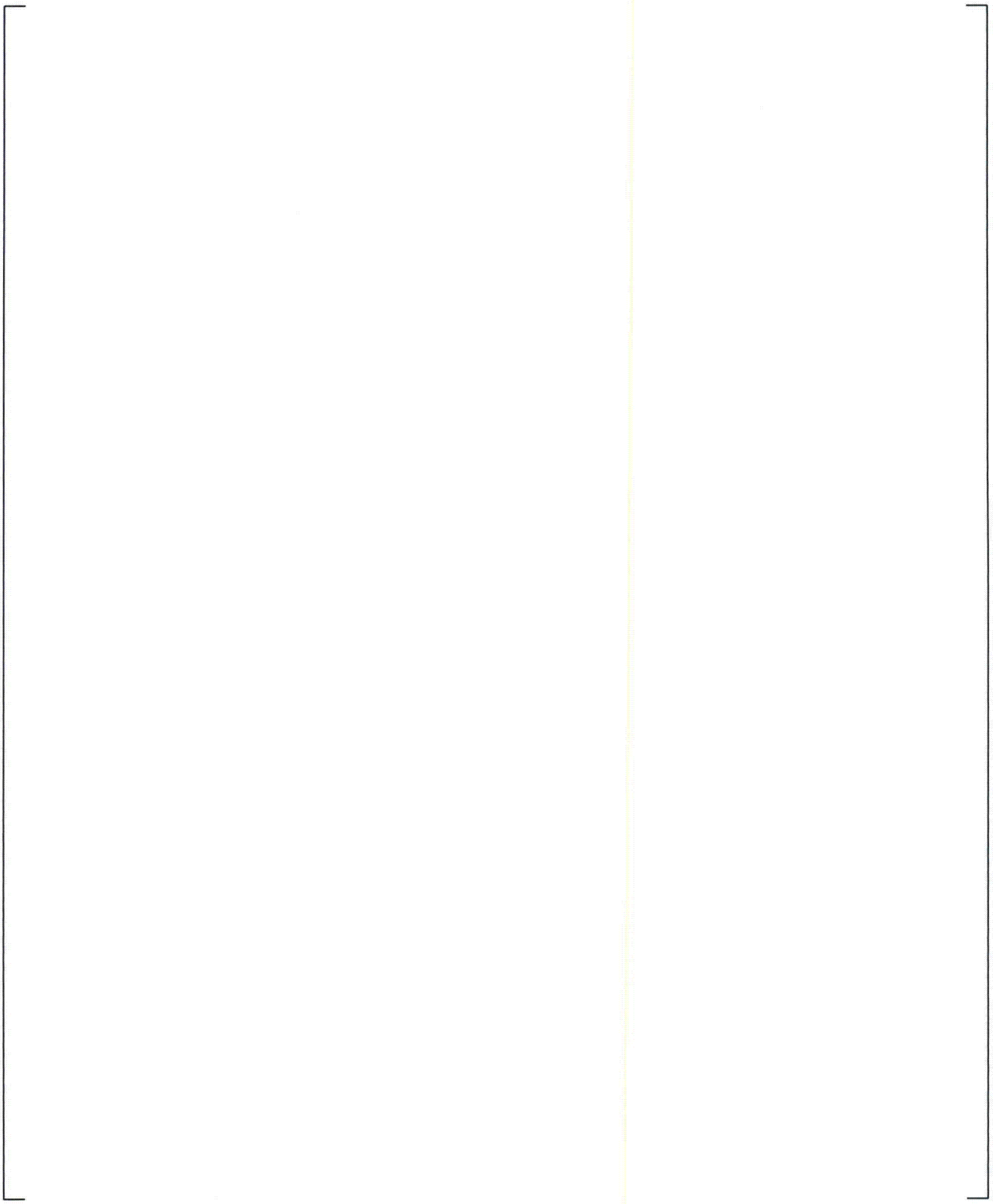

Figure 11-34 [ ][a,c]

[a,c

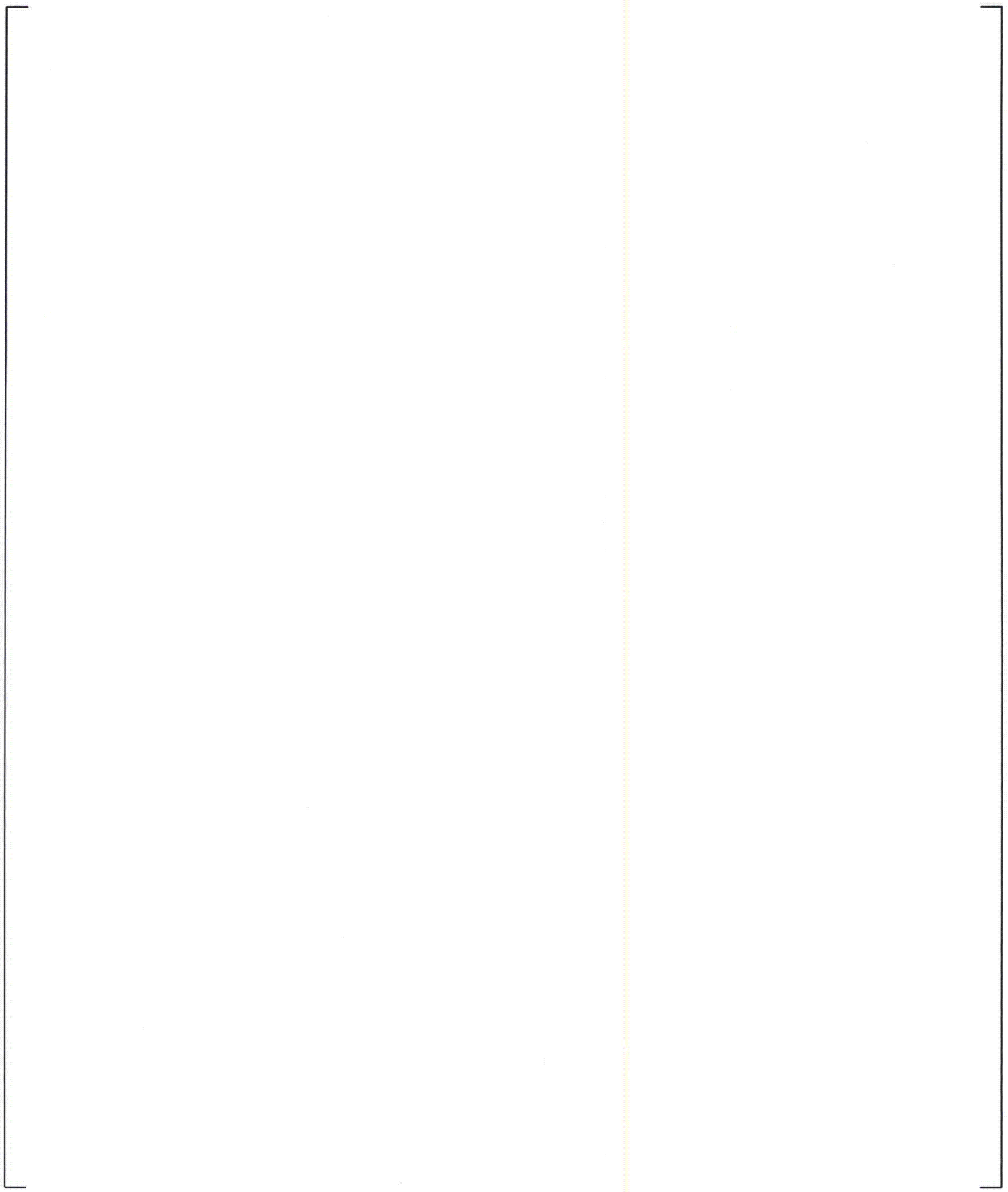

Figure 11-35 [

]a,c

[a,c

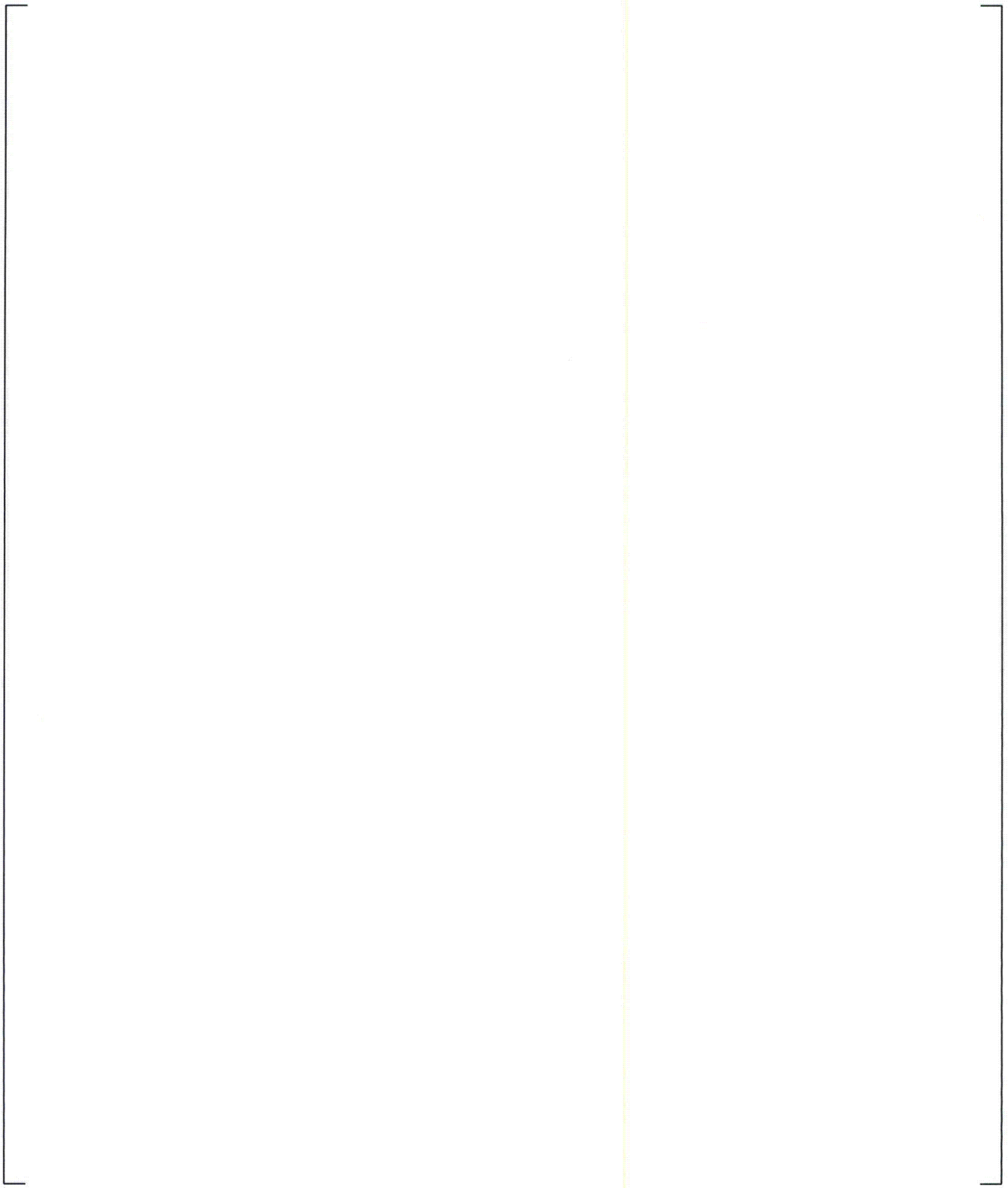

Figure 11-36 [

]^{a,c}

a,c

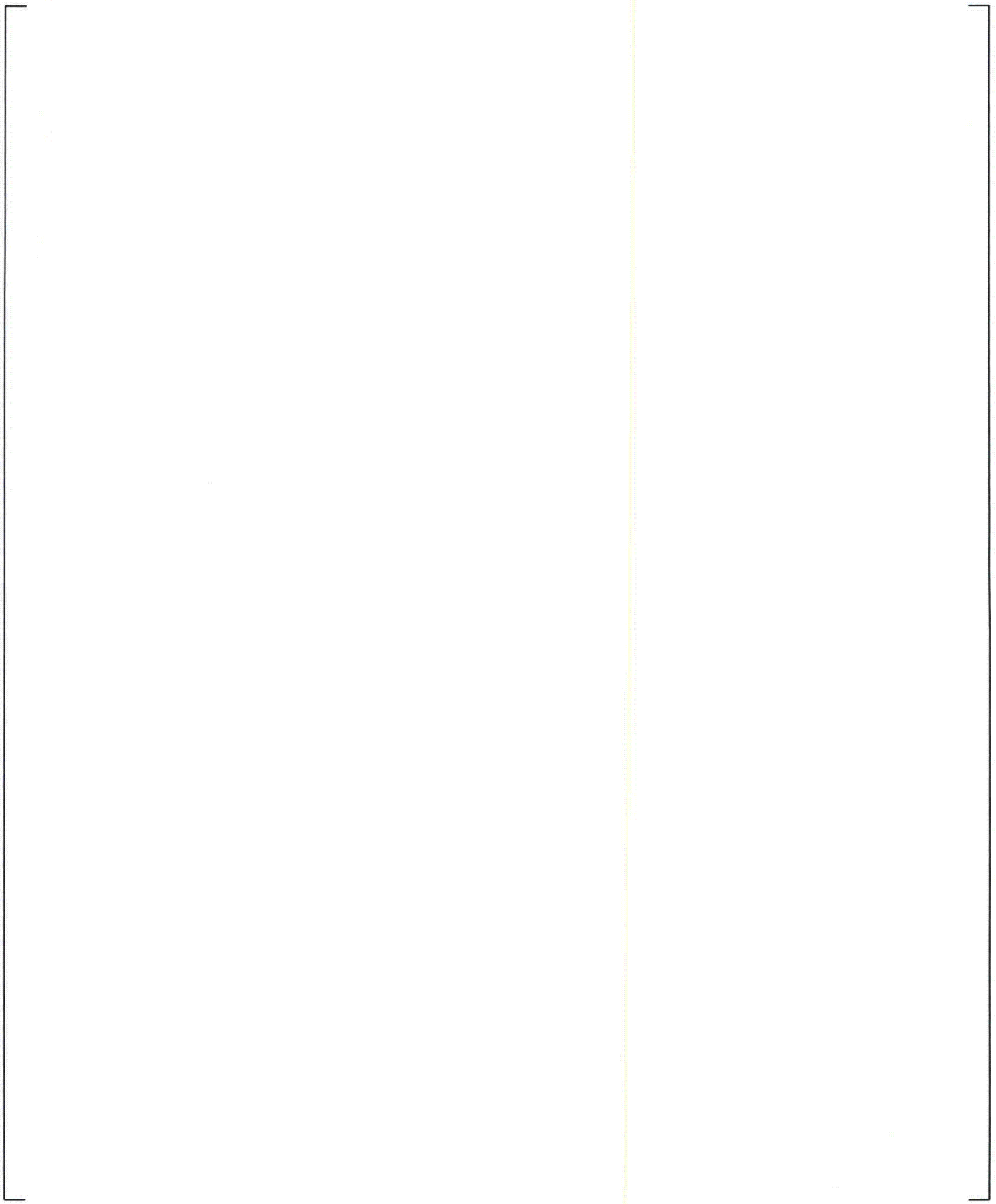

Figure 11-37 [

][a,c]